JUNE 1987

LIDS-TH-1674

Research Supported By:

NASA Ames and Langley Research Centers Grant NASA/NAG-2-297

Office of Naval Research Contract ONR/N00014-82-K-0582

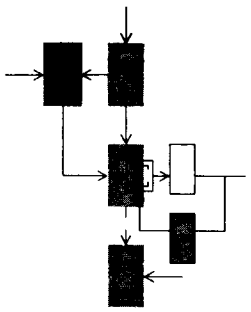

ROBUST TIME AND FREQUENCY DOMAIN ESTIMATION METHODS IN ADAPTIVE CONTROL

Richard Orville Lamaire

Laboratory for Information and Decision Systems

MASSACHUSETTS INSTITUTE OF TECHNOLOGY, CAMBRIDGE, MASSACHUSETTS 02139

MAY 1987

LIDS-TH-1674

ROBUST TIME AND FREQUENCY DOMAIN ESTIMATION METHODS IN ADAPTIVE CONTROL

By

RICHARD ORVILLE LAMAIRE

This report is based on the unaltered thesis of Richard O. LaMaire submitted in partial fulfillment of the requirements for the Degree of Doctor of Philosophy at the Massachusetts Institute of Technology in May 1987. The research was conducted at the M.I.T. Laboratory for Information and Decision Systems with support provided by NASA Ames and Langley Research Centers under grant NASA/NAG-2-297, and by the Office of Naval Research under contract ONR/N00014-82-K-0582.

Laboratory for Information and Decision Systems
Massachusetts Institute of Technology
Cambridge, MA. 02139

ROBUST TIME AND FREQUENCY DOMAIN ESTIMATION METHODS IN ADAPTIVE CONTROL

by

Richard Orville LaMaire

B.S., Carnegie-Mellon University
(1981)

S.M., Massachusetts Institute of Technology
(1983)

E.E., Massachusetts Institute of Technology
(1986)

Submitted to the Department of

ELECTRICAL ENGINEERING AND COMPUTER SCIENCE

in partial fulfillment of the requirements

for the degree of

DOCTOR OF PHILOSOPHY

at the

MASSACHUSETTS INSTITUTE OF TECHNOLOGY

May 1987

Signature of Author Richard O. LaMaire
Department of Electrical Engineering and Computer Science
May, 1987

Certified by Michael Athans
Michael Athans
Thesis Co-Supervisor

Certified by Lena Valavani
Lena Valavani
Thesis Co-Supervisor

Accepted by _____
Arthur C. Smith
Committee on Graduate Students

ROBUST TIME AND FREQUENCY DOMAIN ESTIMATION METHODS IN ADAPTIVE CONTROL

by

Richard Orville LaMaire

Submitted to the Department of Electrical Engineering and Computer Science on May 15, 1987 in partial fulfillment of the requirements for the degree of Doctor of Philosophy.

ABSTRACT

A new robust identification method is developed for use in an adaptive control system. The new type of estimator is called the robust estimator, since it is robust to the effects of both unmodeled dynamics and an unmeasurable disturbance. The development of the robust estimator was motivated by a need to provide guarantees in the identification part of an adaptive controller. To enable the design of a robust control system, a nominal model as well as a frequency-domain bounding function on the modeling uncertainty associated with this nominal model must be provided. The results of this thesis provide this information.

Two estimation methods are presented for finding parameter estimates and, hence, a nominal model. One of these methods is based on the well developed field of time-domain parameter estimation. In a second method of finding parameter estimates, a type of weighted least-squares fitting to a frequency-domain estimated model is used. The frequency-domain estimator is shown to perform better, in general, than the time-domain parameter estimator. In addition, a new methodology for finding a frequency-domain bounding function on the modeling uncertainty is presented. A frequency-domain bounding function on the disturbance is used to compute a frequency-domain bounding function on the additive modeling error due to the effects of the disturbance and the use of finite-length data.

The performance of the robust estimator in both open-loop and closed-loop situations is examined through the use of simulations. The excitation conditions for the robust estimator, and the issues concerning the introduction of a probing signal in a closed-loop context, are also analyzed in the thesis.

Thesis Co-Supervisor: Dr. Michael Athans
Title: Professor of Systems Science and Engineering

Thesis Co-Supervisor: Dr. Lena Valavani
Title: Assistant Professor of Aeronautics and Astronautics

ACKNOWLEDGEMENTS

I am grateful to my thesis co-supervisors, Professors Michael Athans and Lena Valavani, for their guidance, support and patience during the course of this research. In particular, I thank Professor Athans for teaching me how to ask the right questions when doing research; and Professor Valavani for teaching me the "ropes" of adaptive control. I also thank my thesis readers, Professors Gunter Stein and Fred C. Schweppe, for their many helpful comments and suggestions. I thank Professor Stein for his willingness to teach me when I became confused; and Professor Schweppe for his many insights concerning system identification. I also thank Professor Lennart Ljung for several helpful discussions during the initial stages of my research.

In addition, I thank my fellow students at the Laboratory for Information and Decision Systems, for their friendship and valuable technical opinions. Over the years, I have had the opportunity to know and learn from George Goodman, Dan Grunberg, Petros Kapasouris, Wilma Quinn, David Milich, Tony Rodriguez, Jeff Shamma, and Jim Walton. I also thank Fifa Monserrate for her assistance and ever cheerful attitude.

I thank my family for their strong support of my extended schooling. In particular, I thank my wife, Susan, for her love and for her limitless patience during the preparation of this document.

This research was conducted at the M.I.T. Laboratory for Information and Decision Systems with support provided by the NASA Ames and Langley Research Centers under grant NASA/NAG-2-297, by the Office of Naval Research under contract ONR/N00014-82-K-0582 (NR 606-003), by the National Science Foundation under grant NSF/ECS-8210960, and by AFOSR-Eglin A.F.B. under grant F08635-87-K-0031. In addition, the author acknowledges the computing resources support that was provided by the JVNC Allocation Committee under allocation number JVNC-NAC-603.

CONTENTS

LIST OF FIGURES

LIST OF TABLES

GLOSSARY

$A(z)$	Denominator polynomial of the discrete-time nominal model structure
$B(z)$	Numerator polynomial of the discrete-time nominal model structure
c	Compensator gain, see Eqn. (7.3.4) or (9.6.1)
c_{tcl}	Target closed-loop compensator gain, see Eqn. (7.4.10)
$d(t)$, $d[n]$	Disturbance signal
d_{max}	Maximum magnitude of $d[n]$
$D_N^n(\omega_k)$	DFT of N points of $d[m]$ ending with n
$\overline{\overline{D}}_N(\omega_k)$	Magnitude bound on $D_N^n(\omega_k)$ for $n \geq N-1$
$e[n]$	Prediction error, see Eqn. (4.5.3)
$e_1[n]$	Equation error signal due to both the unmodeled dynamics and the disturbance
$e_2[n]$	Equation error signal due to the unmodeled dynamics alone
$e_3[n]$	Equation error signal due to the disturbance alone
$e_t[n]$	Tracking error
$E_{cumf,N}^n(\omega_k)$	Cumulative frequency-domain bounding function, see Eqn. (5.3.3)
$\overline{E}_{cumf,N}^n(\omega_k)$	Magnitude bound on $E_{cumf,N}^n(\omega_k)$, see Eqn. (5.3.1)
$E_N^n(\omega_k)$	Estimation error due to the use of finite-length data, see Eqn. (5.2.2)
$\overline{E}_N^n(\omega_k)$	Magnitude bound on $E_N^n(\omega_k)$, see Eqn. (5.2.4)
$E_{f,N}^n(\omega_k)$	Frequency-domain estimation error, see Eqn. (5.2.12)
$\overline{E}_{f,N}^n(\omega_k)$	Frequency-domain bounding function on $\lvert E_{f,N}^n(\omega_k)\rvert$, see Eqn. (5.2.14)
$\overline{E}_{wcf,N}^n(\omega_k)$	Worst-case frequency-domain bounding function, see Eqn. (8.3.7)
$\overline{E}_{rem}$	Remainder term, see Eqn. (5.2.5)
$F(z)$	Filter for time-domain parameter estimator
$g[n,\theta]$	Impulse response of the nominal discrete-time plant
$g_{true}(t)$	Impulse response of the true continuous-time plant

$g_{true}[n]$	Impulse response of the true discrete-time plant
$G^c_{true}(s)$	True continuous-time plant
$G^c(s,\theta^c_0)$	Nominal continuous-time plant
$G(z,\theta_0)$	Nominal discrete-time plant
$G_{cumf,N}{}^n(\omega_k)$	Cumulative frequency-domain estimate, see Eqn. (5.3.2)
$G_{true}(z)$	True discrete-time plant
$h_d[n,\theta]$	Impulse response from the disturbance signal to the equation error $e_1[n]$
$\overline{h}_d[n]$	Magnitude bound on $h_d[n,\theta]$, see Eqn. (4.3.7)
$h_u[n,\theta]$	Impulse response from the input signal to the equation error $e_1[n]$
$\overline{h}_u[n]$	Magnitude bound on $h_u[n,\theta]$, see Eqn. (4.4.17)
$h_{g\delta}[n,\theta]$	Impulse response of the additive plant error $G(z,\theta)\,\delta(z)$, see Eqn. (4.4.7)
$\overline{h}_{g\delta}[n]$	Magnitude bound on $h_{g\delta}[n,\theta]$
$H_d(z,\theta)$	Transfer function from the disturbance signal to the equation error $e_1[n]$
$H_u(z,\theta)$	Transfer function from the input signal to the equation error $e_1[n]$
$K(z)$	Discrete-time compensator
M	Memory length
n	Discrete time index
N	General symbol for the DFT length
N_f	DFT length used in the frequency-domain parameter estimator
N_t	DFT length used in the time-domain parameter estimator
$P[n]$	Projection matrix in the time-domain parameter estimator, see Eqn. (4.5.8)
p_{tcl}	Target discrete-time pole of the nominal closed-loop system
$r(t)$, $r[n]$	Closed-loop reference signal
t	Continuous time
T	Sampling period
$u(t)$, $u[n]$	Plant input control signal

$u_f[n]$	Filtered version of u[n], see Eqn. (4.2.11)
u_{max}	Maximum magnitude of u[n]
$U_N^n(\omega_k)$	DFT of N points of u[m] ending with n
v[n]	Probing signal
$V_N(\omega_k)$	DFT of the probing signal v[n]
y(t), y[n]	Plant output signal
$y_f[n]$	Filtered version of y[n], see Eqn. (4.2.12)
$Y_N^n(\omega_k)$	DFT of N points of y[m] ending with n
$\delta^c_u(s)$	Continuous-time unstructured uncertainty (unmodeled dynamics)
$\Delta^c_u(j\omega)$	Magnitude bound on continuous-time unstructured uncertainty
$\nabla^c_u(e^{j\omega T})$	Continuous-time smoothness condition, a magnitude bound on $d\delta^c_u(j\omega) / d\omega$
$\delta_u(z)$	Discrete-time unstructured uncertainty (unmodeled dynamics)
$\tilde{\delta}_u[n]$	Impulse response of the unstructured uncertainty $\delta_u(z)$
$\Delta_u(e^{j\omega T})$	Magnitude bound on the discrete-time unstructured uncertainty
$\nabla_u(e^{j\omega T})$	Discrete-time smoothness condition, a magnitude bound on $d\delta_u(e^{j\omega T}) / d\omega$
$\delta_s(z, \hat{\theta})$	Discrete-time structured uncertainty, see Eqn. (5.6.3)
$\delta_{su}(z, \hat{\theta})$	Total discrete-time uncertainty including the effects of both structured and unstructured uncertainty
$\Delta_{su}(e^{j\omega T}, \hat{\theta})$	Uncertainty bounding function, a magnitude bound on $\delta_{su}(e^{j\omega T}, \hat{\theta})$
$\Delta_{su}^n(e^{j\omega_k T}, \hat{\theta})$	Uncertainty bounding function at time index n, see Eqn. (5.5.6)
$\hat{\Delta}_{su}^n(e^{j\omega_k T}, \hat{\theta})$	Robust uncertainty bounding function at time index n, see Eqn. (5.6.12)
$\tilde{\Delta}_{su}^n(e^{j\omega_k T}, \hat{\theta})$	Smoothed uncertainty bounding function at time index n, see Eqn. (5.7.37)

$\overline{\Delta}_{su}^{n}(e^{j\omega_k T}, \hat{\theta})$	Uncertainty bounding function including safety factor, see Eqn. (5.8.3)
$\nabla_{su,wc}(e^{j\omega T})$	Worst-case bounding function on $\lvert d\delta_{su}(e^{j\omega T}, \hat{\theta}) / d\omega \rvert$, see Eqn. (5.7.11)
$\nabla_{su}^{n}(e^{j\omega T})$	Bounding function on $\lvert d\delta_{su}(e^{j\omega T}, \hat{\theta}) / d\omega \rvert$ at time index n, see Eqn. (5.7.18)
$\phi[n]$	Signal regression vector, see Eqn. (4.2.7)
$\phi_f[n]$	Filtered signal regression vector, see Eqn. (4.2.16)
$\kappa\{\bullet\}$	Denotes the condition number of a matrix
θ^c_0	True continuous-time parameter vector
Θ^c	Bounded set that contains the continuous-time parameter vector θ^c_0
θ_0	True discrete-time parameter vector
Θ	Bounded set that contains the discrete-time parameter vector θ_0
$\hat{\theta}[n]$	Estimate of the discrete-time parameter vector
$\tilde{\theta}[n]$	Error of the discrete-time parameter vector estimate, $\tilde{\theta}[n] = \hat{\theta}[n] - \theta_0$
$\theta^*[n]$	Projected estimate of the discrete-time parameter vector
$\tilde{\theta}^*[n]$	Error of the projected parameter vector estimate, $\tilde{\theta}^*[n] = \theta^*[n] - \theta_0$
$\sigma_{max}\{\bullet\}$	Denotes the maximum singular value of a matrix
$\sigma_{min}\{\bullet\}$	Denotes the minimum singular value of a matrix
$\upsilon[n]$	Dead-zone signal in time-domain parameter estimator, see Eqn. (4.5.9)
ω_{inc}	Discrete frequency spacing, $\omega_{inc} = \omega_s / N$
ω_k	General notation for a discrete frequency point, $\omega_k = (k / N)\, \omega_s$
ω_s	Sampling frequency
ω_{tcl}	Target closed-loop bandwidth

CHAPTER 1.
INTRODUCTION

1.1 Overview

1.1.1 Motivation

The use of feedback control in systems having large amounts of uncertainty requires the use of algorithms that learn or adapt in an on-line situation. A control system that is designed using only a priori knowledge results in a relatively low bandwidth closed-loop system so as to guarantee stable operation in the face of large uncertainty. An adaptive control algorithm, which can identify the plant on-line, thereby decreasing the amount of plant uncertainty, can yield a closed-loop system that has a reduced sensitivity function, higher bandwidth and thus better performance than a non-adaptive algorithm. There are many problems with the adaptive control algorithms that have been developed, to date. In particular, most adaptive control algorithms available are not robust to unmodeled dynamics and unmeasurable disturbances, particularly in the absence of a persistently-exciting input signal.

In this thesis, we develop and test a set of plant identification algorithms which can be used with confidence in an adaptive control setting. We attempt to improve performance, while providing ironclad guarantees that the closed-loop system remains stable in the presence of high-frequency modeling errors and disturbances. As we shall see, such stability guaranitees have a price; extensive real-time calculations in the frequency-domain are required.

In this subsection, we will motivate the robust estimation problem by first discussing the adaptive control problem, in general, and then presenting a perspective on the robust adaptive control problem. Further, we justify the choice of an infrequent adaptation strategy before discussing the main focus of the thesis, the development of a robust estimator.

The Adaptive Control Problem

The adaptive control problem has received considerable attention during the past thirty years. However, while many different algorithms and analysis methods have been developed, a pragmatic adaptive control design methodology has not, as yet, been developed. The primary difficulty with current adaptive control algorithms is that they make restrictive (non-practical) assumptions about the plant. In addition, these algorithms often assume that the system operates in an ideal environment. Recent research efforts have focused both on reducing the restrictiveness of the plant assumptions, as well as the issue of robustness to unmodeled dynamics and unmeasurable

disturbances. However, an algorithm that requires reasonable a priori information about the plant, and that can provide guarantees of global stability in the absence of persistent excitation and in the face of reasonable classes of unmodeled dynamics and unmeasurable disturbances, is still an unreached goal. Although many researchers have suggested "safety nets" for specific applications, a general "safety net" methodology is not available. This thesis represents a contribution in that direction.

Stability of Adaptive Control Algorithms

The use of current adaptive control algorithms yields systems that are nonlinear and possibly time-varying. Thus, the closed-loop stability of these systems depends on the inputs and disturbances, as well as the plant (including any unmodeled dynamics) and the compensator. However, the stability properties of a linear time-invariant (LTI) feedback system depend only on the plant and compensator, not the inputs and disturbances. Because of this fact, we take the point of view that it is desirable to make the system "as LTI as possible". Of course, our motivation for using adaptive control is to achieve a performance improvement (increased bandwidth) over the best non-adaptive LTI compensator. So, there is the ever present tradeoff between performance and robustness.

The preceding argument can be used to justify an infrequent control-law update strategy. It is envisioned that a discrete-time estimator (identifier) will be used to continually update the estimates of the plant as long as there is useful information in the input/output data of the plant. The continuous-time plant is in a closed-loop that is controlled by a fixed-structure, discrete-time compensator whose parameters are updated infrequently. It can be shown that, if the compensator parameters are updated sufficiently infrequently, then the LTI stability of the frozen-time system at every point in time guarantees the exponential stability of the time-varying system. In this way, the control system looks nearly LTI and consequently is more robust to disturbances, than a highly nonlinear adaptive controller. It is emphasized here that a robust adaptive controller that slowly learns and produces successively better LTI compensators is the end product envisioned in this thesis. The work presented in this thesis aims to develop only the estimation part of this robust adaptive controller. On the other end of the adaptive control spectrum are algorithms that quickly adapt to a changing system. However, these systems have poor robustness properties in that they are highly sensitive to unmodeled dynamics and unmeasurable disturbances, particularly in the absence of persistent excitation.

A Perspective on the Robust Adaptive Control Problem

With the solution of the adaptive control problem for the ideal case, that is, when there are no unmodeled dynamics nor unmeasurable disturbances, the problem of robustness has become a focus of current research. Recently, a new perspective on the robust adaptive control problem has appeared in the literature [1]. Briefly, a "robust" adaptive controller is viewed as a combination of a "robust" parameter estimator and a "robust" control law. Indeed, researchers have coined the term "adaptive robust control" to emphasize this new perspective. This is an appealing point of view. For example, if the robust parameter estimator is not getting any useful information and, consequently, is not able to improve on the current knowledge of the plant parameters, then the adaptation aspect of the algorithm can be disabled and the adaptive controller reduces to a robust control law. That is, in a situation where the adaptive algorithm is not learning, the adaptive controller becomes simply the best robust LTI control law that one could design based only on a priori information and any additional information learned since the algorithm began. As an aside we mention the fact that currently the control field doesn't provide a method for designing the best-performing, robustly-stable, LTI control law in the face of uncertainty. A second benefit of the new adaptive control perspective is that it, like all indirect adaptive control approaches, enables us to view the adaptive control problem as having two parts, the parameter estimator and the control law. Alternatively, the direct adaptive control approaches combine the estimation and control-law design aspects of the problem. That is, in the direct approach the control law parameters are estimated directly instead of first estimating the plant and then computing the new control law parameters as is done in the indirect approach. Since we use the indirect approach in this thesis, we will able to use previous results in the fields of parameter estimation and robust control. The field of LTI control is well established for questions of stability robustness and offers several possible robust control algorithms for use in an adaptive controller. However, the problem of robust estimation (identification) has received less attention by researchers. This area of robust identification is where the thesis makes its main contribution.

Brief Statement of the Robust Estimation Problem

The main focus of this thesis is the development of a robust estimator for use in an adaptive control system. In non-adaptive robust control, the designer must perform two identification steps; he must obtain both a nominal model and some measure of its goodness. A useful measure of goodness is a frequency-domain bounding function on the modeling errors as this permits the use of frequency-domain stability robustness tests. Now, since non-adaptive robust control requires

both of the above steps, the same steps must implicitly, or explicitly, be present in a robust adaptive control scheme, the difference being that the steps are carried out on-line rather than off-line. Thus, we assume that our robust estimator must supply:

1) a nominal plant model,

2) a bounding function on the magnitude of the modeling error vs. frequency of this nominal model with respect to the true plant.

So, given an a priori assumed model structure, the robust estimator must provide an estimate of the parameters of the plant, as well as a frequency-domain error bounding function corresponding to this estimate. That is, we define a robust estimator as one that generates a model of the plant along with guarantees about how good the model is. Given this information, several robust control-law design methodologies could be used. This adaptive control scenario is shown in Figure 1.1.

In this thesis, we present two methodologies for estimating the parameters of the nominal model, one based on time-domain methods and one based on frequency-domain methods. In addition, we will present one method for computing a frequency-domain bounding function on the modeling uncertainty. It will be shown in the simulations that the specific time-domain parameter estimator that is described in this thesis has some weaknesses. Thus, frequency-domain methods will be used to provide both parameter estimates and the aforementioned frequency-domain bounding function on the modeling uncertainty. The frequency-domain calculations of these methods require significant real-time computations.

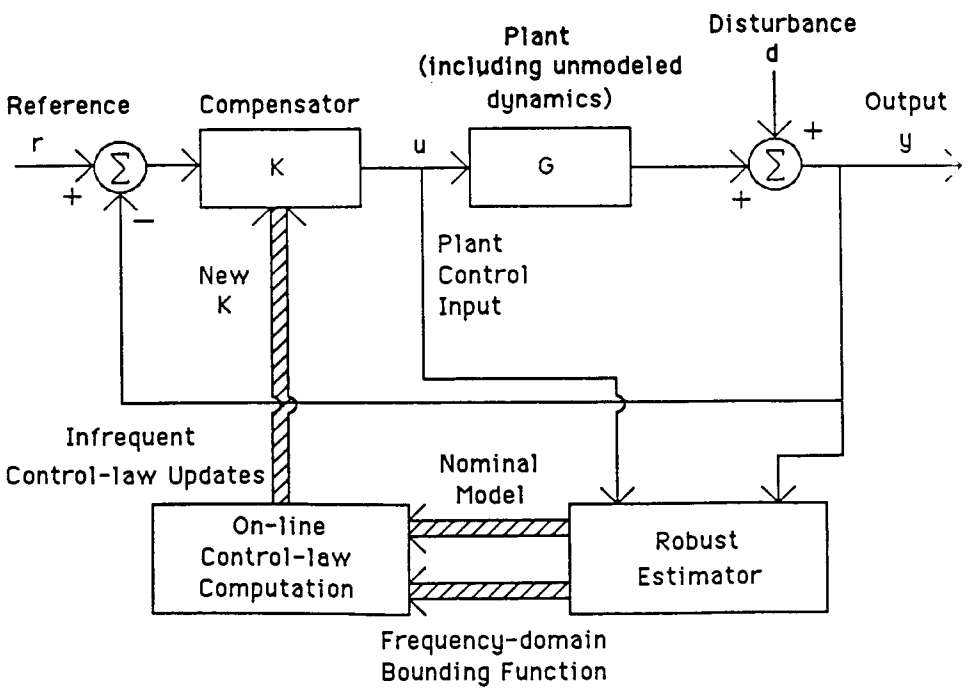

Figure 1.1: Robust Adaptive Control System.

The goal of the robust estimator is to enable improved closed-loop performance through the reduction of the modeling uncertainty. The modeling error or uncertainty has two components: 1) an unstructured component due to the modeling mismatch error between the finite-dimensional plant model and the plant, and 2) a structured component due to errors in the parameters of the nominal model. The function of the robust estimator is to eliminate the structured uncertainty of the plant model. That is, the robust estimator seeks to yield a better performing closed-loop system by reducing the structured uncertainty. The robust estimator will be of most use in situations where there is significant structured uncertainty. We do not require the robust estimator to eliminate the inherent unstructured uncertainty due to high-frequency unmodeled dynamics. The role of the robust estimator is illustrated in Figure 1.2.

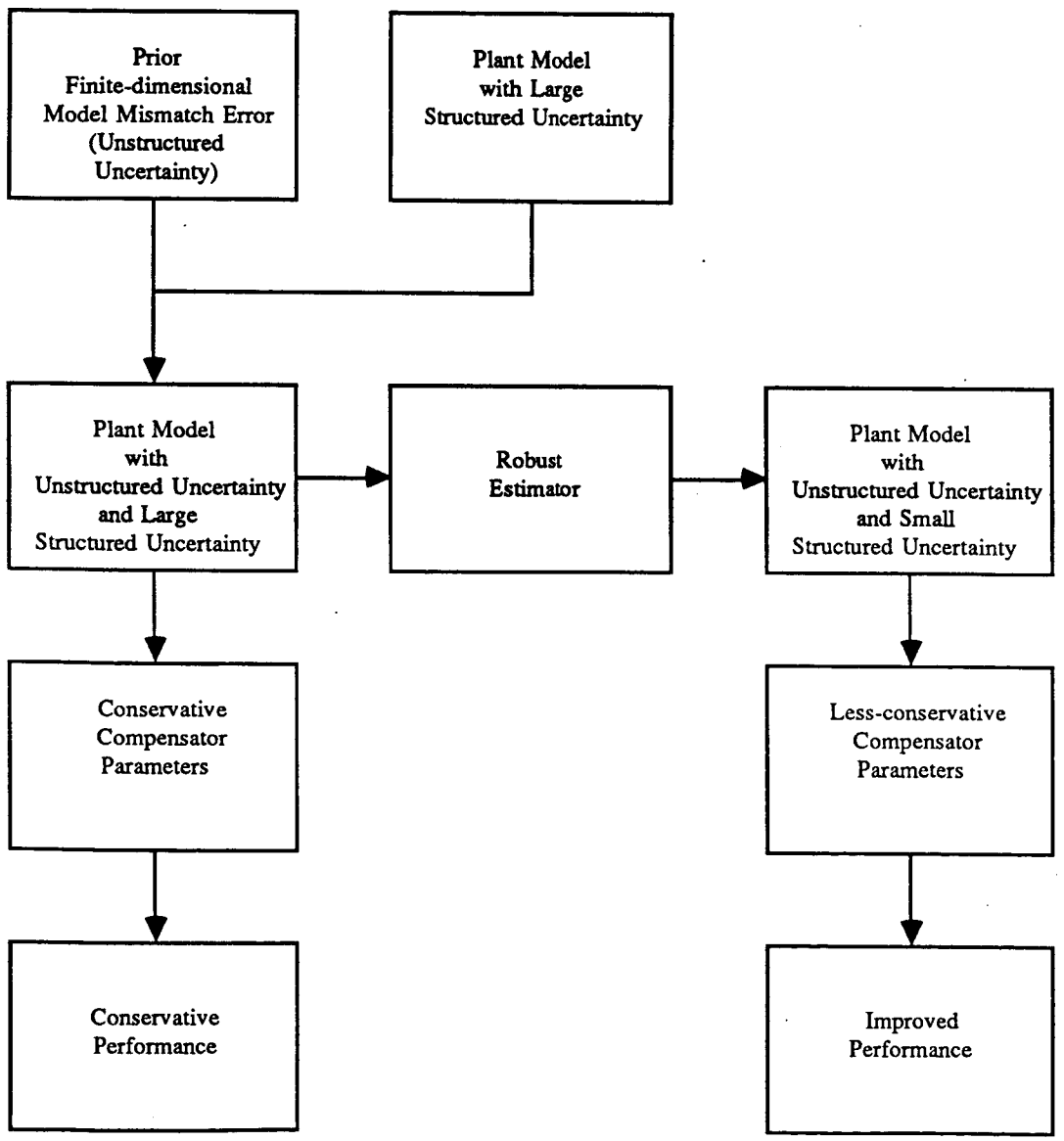

Figure 1.2: The Role of the Robust Estimator.

1.1.2 Contributions of the Thesis

The results of this thesis represent a major step toward a more complete understanding of the robust adaptive control problem. The primary technical contributions are in the area of robust estimation (identification), however, the thesis provides insight as to the future of robust adaptive control. We now discuss the novel features of the robust estimator and then summarize some of the contributions of the thesis.

The robust estimator is the first of its kind in that it provides frequency-domain guarantees concerning the accuracy of the nominal plant model. The author is not aware of any other algorithm that provides these frequency-domain guarantees. As was mentioned earlier, we use a frequency-domain bound on the modeling errors since this allows us to use existing stability robustness results. We emphasize that the identification part of an adaptive controller must provide some kind of guarantee concerning the nominal model, or else the resulting control-law cannot guarantee the stability of the closed-loop system. We will use a deterministic framework throughout the thesis since guarantees of stability are sought.

The key technical contribution of the thesis is the development of new signal processing theorems that enable the explicit bounding of frequency-domain estimation errors due to the use of finite-length data. These theorems are essential for the on-line computation of guaranteed bounds on the modeling uncertainty. The robust estimator uses discrete Fourier transforms (DFTs) to compute a frequency-domain estimate of the plant and then uses these signal processing theorems to compute the required frequency-domain bounding function.

In contrast to some current adaptive control algorithms, the robust estimator uses pragmatic assumptions concerning the a priori known information about the plant. Specifically, in practice, engineers are generally able to determine the following:

a) the structure of the (low-frequency) nominal model,

b) an approximate idea of the parameters of the nominal model,

c) a frequency-domain bounding function on the size of the unmodeled dynamics, (i.e. a magnitude bounding function on the Fourier transform),

d) an approximate idea of how smooth the unmodeled dynamics are in the frequency-domain,

e) a frequency-domain bounding function on the magnitude of the Fourier transform of the unmeasurable disturbance (i.e. where the disturbance has its energy), and

f) a coarse bounding function on the impulse response of the plant, and coarse time-domain magnitude bounds on both the unmeasurable disturbance and the input signal.

The development of the robust estimator assumes that the plant is stable, so the impulse response of f) above is bounded. The robust estimator uses the above information and blends it with the information gleaned on-line from the input/output data. It is the first such estimator to use a priori

frequency-domain information about the unmodeled dynamics. The above continuous-time assumptions are translated to an analogous set of discrete-time assumptions. The robust estimation problem is then stated and solved in discrete-time. All on-line frequency-domain calculations are computed using DFTs.

The development of the robust estimator entailed the study of techniques for robust time-domain parameter estimation. Some time-domain bounding results are developed in the thesis so that we can robustify a time-domain parameter estimator. This is done through the use of a time-varying dead-zone. It will later be shown that this type of robust time-domain parameter estimator performs unsatisfactorily. This poor performance motivates our development of a frequency-domain parameter estimator which is found to perform much better than the time-varying dead-zone approach.

Further contributions of this thesis are the insights gained concerning the closed-loop operation of an adaptive system that uses the robust estimator. A simple adaptive control system that uses the robust estimator is developed for a limited class of plants. The simulation of this simple adaptive control system allows us to assess the potential of the robust estimator. In addition, in this thesis we consider the introduction of probing signals into the closed-loop system. The robust adaptive control system that is shown in Figure 1.1, is essentially a passive system in that it only learns and, hence, updates the compensator parameters when there is useful information available to it, in the form of a rich control input signal. If it is essential that the robust adaptive controller improve on its a priori information and the control input signal is not rich, in the sense that the robust estimator cannot improve its estimate, then an external probing signal must be introduced at the plant input to enhance identification. That is, in some closed-loop situations it will be necessary to add a probing signal so that identification can occur. We analyze the excitation conditions that are required by a robust adaptive control system that uses the robust estimator. This enables us to devise a probing signal strategy that can be used to attain a target closed-loop bandwidth.

The simulation results of this thesis suggest that the robust estimator (using the frequency-domain parameter estimator) can provide performance improving information to the control-law under reasonable excitation conditions. The cost of this improved closed-loop performance with stability-robustness guarantees is the extensive real-time calculations of the robust estimator.

1.1.3 Organization of the Thesis

The thesis is organized into ten chapters and several appendices. Figure 1.3 illustrates the logical interdependence of the various chapters with the exception of the introductory and

concluding chapters. In Chapter 2 we present the notation that will be used throughout the thesis. In addition, this chapter contains derivations of several new signal processing theorems that will be used in the later parts of the thesis. The statement of the robust estimation problem is presented in Chapter 3 where the assumptions of the robust estimator are first stated in continuous-time and then used to form an analogous set of discrete-time assumptions. Chapter 4 presents a robust time-domain parameter estimator while Chapter 5 presents a frequency-domain based method of finding parameter estimates as well as a frequency-domain method for bounding modeling uncertainty. Chapter 6 addresses the many design issues of the robust estimator in the context of closed-loop adaptive control. In addition, Chapter 6 investigates how the assumption of a frequency-domain bounding function can or cannot be satisfied by various disturbance models. Computational issues are also discussed in Chapter 6. Chapter 7 ties together the results of the previous chapters by presenting a robust adaptive control system, which uses the robust estimator, and that can be applied to a restricted class of plants. Chapters 8 and 9 provide a two part presentation of several illustrative simulation examples. In particular, we provide a closed-loop simulation example that demonstrates the potential of adaptive controllers that use the robust estimator. Finally, Chapter 10 presents conclusions and directions for future research. The appendices contain useful results that are referenced, as needed, in the main body of the thesis itself.

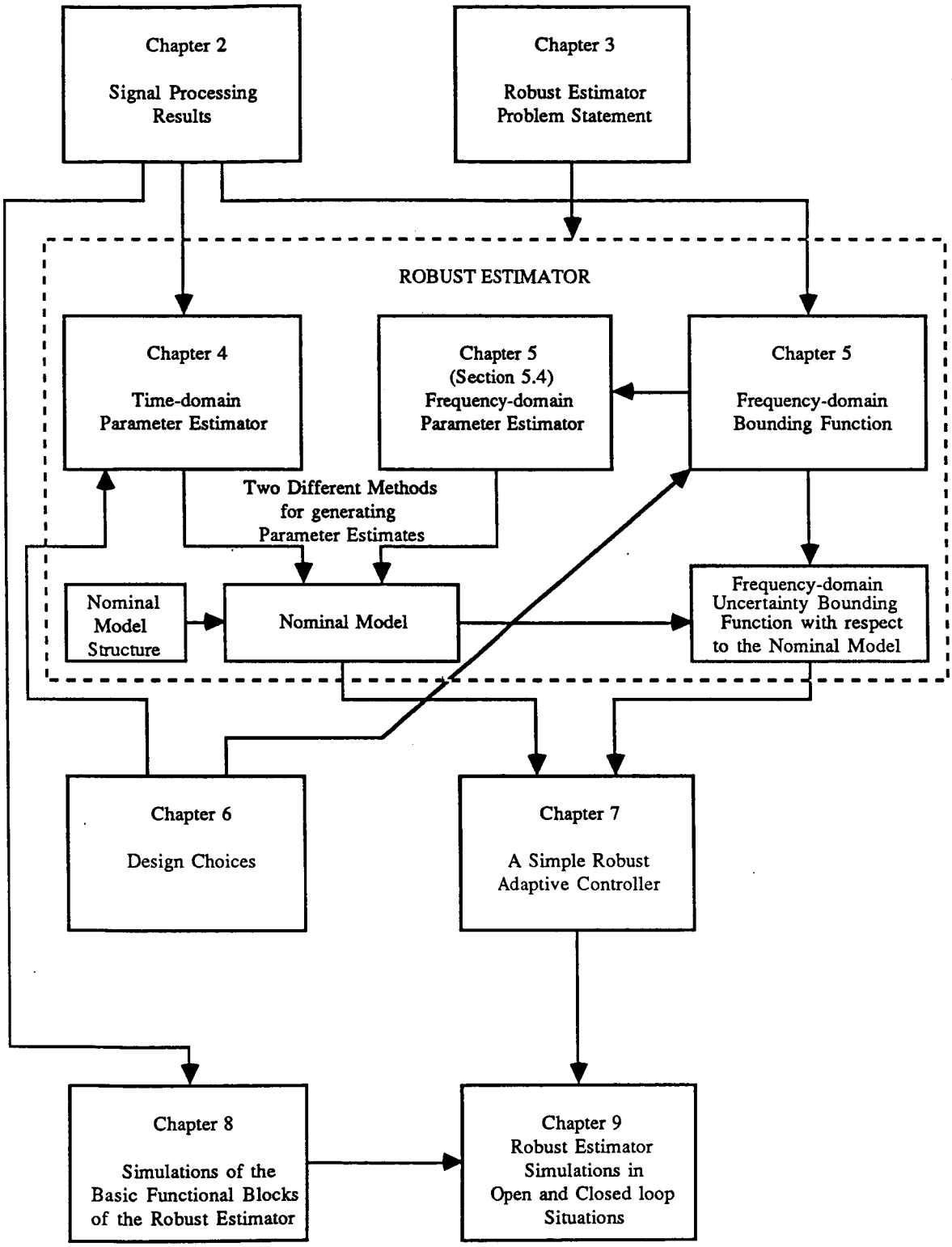

Figure 1.3: Logical Interdependence of Thesis Chapters.

1.2 Previous Work and Related Literature

1.2.1 Robust Adaptive Control

During the late 1970s, global stability results for Model Reference Adaptive Controllers (MRAC), in the absence of unmodeled dynamics and unmeasurable disturbances, were derived by Narendra and Valavani [3], Narendra, Lin and Valavani [4], and Feuer and Morse [5]. These results made several restrictive assumptions concerning the plant. It was assumed that the SISO plant was: 1) minimum phase, 2) of known relative degree, 3) of known sign on high-frequency gain, 4) of known maximum order, and 5) of known upper bound on the high-frequency gain. These assumptions were necessary in order to prove global asymptotic stability of the continuous-time adaptive control algorithms. A different adaptive control approach, the Self-Tuning Regulator (STR) was developed by Astrom et al. [6,7] for discrete-time systems. Stability results were not developed for the STR algorithms as they were derived in a stochastic framework; rather, convergence properties were later shown to be true. A third approach was pursued by Goodwin, Ramadge and Caines [8] who presented an algorithm and stability proof of a projection-type adaptive controller for discrete-time systems. As in the MRAC case, unmodeled dynamics and unmeasurable disturbances were not considered. In addition, the STR and projection-type algorithms both make restrictive assumptions about the plant as in the MRAC case.

In the early '80s it became apparent with the work of Rohrs et al. [9,10] that there were robustness problems with all of the previously developed adaptive control algorithms. These problems stemmed from the nonlinear nature of the adaptive control problem and were different than the stabilty-robustness problems encountered in the design of LTI compensators. Rohrs et al. [9,10] showed that the presence of unmodeled dynamics and unmeasurable disturbances would cause the current adaptive algorithms to become unstable when a persistently-exciting input signal was absent. This realization initiated investigations into the development of robust adaptive control algorithms.

In recent years, several different approaches to the robust adaptive control problem have been pursued. In 1982, Ioannou and Kokotovic [11] introduced the use of an exponential forgetting factor to achieve a measure of robustness in adaptive control systems. At about the same time, Peterson and Narendra [12] incorporated a fixed dead-zone mechanism into a continuous-time MRAC and proved that the system was globally stable in the presence of a bounded, unmeasurable disturbance. When the output error of Peterson and Narendra's algorithm was less than the error that might be due to the bounded disturbance, the adaptation mechanism was disabled. They did not consider the effects of unmodeled dynamics. This fixed dead-zone mechanism for intermittent adaptation has also been used in discrete-time systems [13]. While a fixed dead-zone is useful for

obtaining robustness with respect to a bounded disturbance, it cannot be used to provide robustness to unmodeled dynamics. This is because the output error due to the unmodeled dynamics cannot be absolutely bounded but, rather, depends on the size of the states of the plant. Thus, a time-varying deadzone which depends on the plant states (or alternatively the plant inputs and outputs) must be included in the system to provide robustness to both unmodeled dynamics and unmeasurable disturbances.

In 1984, Orlicki et al. [14,15] incorporated a time-varying dead-zone into a continuous-time MRAC and proved that the system was simultaneously robust to both unmodeled dynamics and certain classes of disturbances, including bounded disturbances. Orlicki's algorithm implicitly assumed that the plant was open-loop stable. He used on-line spectral calculations of the plant input and output to determine when useful information was available for the adaptation algorithm. Recently, Kreisselmeier and Anderson [16] introduced what they call a "relative dead-zone" to provide robustness to unmodeled dynamics in discrete-time MRACs. The system is permitted to adapt unless the error due to the unmodeled dynamics is larger than the current output error. They bound the output error due to unmodeled dynamics using a stable difference equation driven by a weighted sum of the current plant input and output. Goodwin et al. [17,18] have extended this work to include the treatment of both unmodeled dynamics and bounded disturbances, by adding a fixed component to the dead-zone of Kreisselmeier and Anderson to account for a bounded disturbance. In addition, this new type of time-varying dead-zone is used by Goodwin et al. [17,18] in a modified least-squares algorithm. This new modified least-squares algorithm will be used in this thesis. However, we will use on-line spectral calculations to bound the output error due to unmodeled dynamics, rather than Kreisselmeier and Anderson's bounding mechanism.

A different approach to the robust adaptive control problem advocates the use of the basic ideal-case adaptive control algorithms in combination with a supervisory level, which is added to the algorithm. Such a supervisory level provides a type of "safety net" that can detect the conditions under which an adaptive control algorithm has problems, such as lack of excitation. When these conditions are detected the adaptive algorithm is temporarily disabled so as to avoid degradation of the parameter estimates and, hence, possibly unstable behavior. Both Astrom [19], and Isermann and Lachmann [20] have suggested this kind of approach. These supervisory type algorithms are ad-hoc and have not been shown to provide "safety nets" that guarantee stability. In a sense, the results of this thesis represent a kind of "safety net" in that the robust estimator based adaptive controller of this thesis seeks to achieve the same type of goals. That is, the robust estimator doesn't update the plant parameters and, hence, the control-law doesn't change when there is not any useful information in the input/output data.

A last result from the robust adaptive control area that will be used in the thesis is the recent work of Rohrs et al. [21,22]. In 1985, Rohrs et al. showed an approximate relationship between

the unmodeled dynamics of a continuous-time plant and the unmodeled dynamics of a discrete-time model of the plant. This relationship gives insight as to how to choose the sampling period in a sampled-data adaptive control system so as to avoid the deleterious effects of the high-frequency unmodeled dynamics. This result is used in the thesis to translate the continuous-time assumptions of the robust estimator to an analogous set of discrete-time assumptions.

1.2.2 Parameter Estimation

The thesis will use several results from the field of parameter estimation. Young [23] provides a thorough survey of this field up to 1980. As has already been mentioned in the preceding subsection, time-domain parameter estimators such as the least-squares algorithm will be used. Goodwin and Sin [13] provide a good summary of projection and least-squares type parameter estimators. In addition to time-domain estimation techniques, we will be using frequency-domain estimation techniques. Ljung and Glover [24] discuss the complementary nature of time and frequency-domain estimation techniques. In Ljung [25,26] the "empirical transfer function estimate" (ETFE) is introduced. This ETFE is computed using the Fourier transforms of finite-length input/output data of the plant. In [25], Ljung finds bounds on the effects of using finite-length data to compute the ETFE, for strictly stable plants. The extensive work of Ljung provides the background for the development of the frequency-domain estimation techniques of this thesis. The area of closed-loop identification is surveyed in the 1977 paper by Gustavsson, Ljung and Soderstrom [27].

1.2.3 Signal Processing and Sampled-data Control

To implement the various spectral calculations involved in our robust estimator, we will have to make use of some results from the signal processing field. Most of the needed results are well-known and are contained in the books by Oppenheim and Schafer [28], and Rabiner and Gold [29]. We will also make use of many results from the area of sampled-data control. In particular, the books by Franklin and Powell [30], Astrom and Wittenmark [31], and Ackermann [32] will be used.

CHAPTER 2.
MATHEMATICAL PRELIMINARIES

In this chapter, we will present the notation and definitions that will be used in the thesis as well as some results and theorems that will be useful later on. Specifically, we will present theorems that will enable us to bound the error due to using finite-length data in our computation of frequency-domain estimates.

2.1 Preliminaries and Notation

2.1.1 Notation

In this subsection, we present some definitions. The following notation will be used to represent various transforms of the signal x. We denote a continuous-time signal by x(t). The Laplace and Fourier transforms of x(t) are denoted by $X^c(s)$ and $X^c(j\omega)$, respectively, where the superscript 'c' denotes the fact that they are transforms of a continuous-time signal. We denote the time-sampled version of the continuous-time signal x(t) by the discrete-time signal x[n] where n is an integer and x[n]=x(nT) where T is the sampling period. The z-transform of the discrete-time signal x[n] is defined by

$$X(z) = \sum_{n=-\infty}^{\infty} x[n]\, z^{-n} = \mathcal{Z}\{ x[n] \}. \qquad (2.1.1)$$

The z-transform of x[n] on the unit circle is called the discrete-time Fourier transform (DTFT) and is defined as follows

$$X(e^{j\omega T}) = \sum_{n=-\infty}^{\infty} x[n]\, e^{-j(\omega T)n}. \qquad (2.1.2)$$

We define $W_N = e^{-j(2\pi/N)}$ where N is a positive integer. (2.1.3)

This allows us to define the N-point discrete Fourier transform (DFT) of x[n], at the N frequency points,

$$\omega_k = (k/N)\, \omega_s, \qquad \text{for } k = 0, \ldots, N-1, \qquad (2.1.4)$$

where $\omega_s = 2\pi/T$ is the sampling frequency. We denote the N-point DFT by

$$X_N(\omega_k) = \mathcal{F}_N\{ x[n] \} \Big|_{k=\omega_k N/\omega_s} \quad \text{where k is an integer and}$$

$$X_N(\omega_k) = \sum_{n=0}^{N-1} x[n]\, W_N^{kn} \qquad \text{for } k = 0, \ldots, N-1. \tag{2.1.5}$$

Further, we define the inverse N-point discrete Fourier transform of $X_N(\omega_k)$ as follows,

$$x[n] = \mathcal{F}^{-1}{}_N\{ X_N(\omega_k) \} \text{ where}$$

$$x[n] = \frac{1}{N} \sum_{k=0}^{N-1} X_N(\omega_k)\, W_N^{-kn} \qquad \text{for } n = 0, \ldots, N-1 \tag{2.1.6}$$

Since we will not always be working with N-point sequences that begin at 0, we define the following version of the DFT and inverse DFT for a sequence of N points ending with time index n.

$$X_N^n(\omega_k) = \mathcal{F}_N^n\{ x[n] \} \Big|_{k=\omega_k N/\omega_s} = \sum_{m=n-N+1}^{n} x[m]\, W_N^{km} \tag{2.1.7}$$

$$\text{for } k = 0, \ldots, N-1$$

$$x[m] = \mathcal{F}^{-1}{}_N^n\{ X_N^n(\omega_k) \} = \frac{1}{N} \sum_{k=0}^{N-1} X_N^n(\omega_k)\, W_N^{-km} \tag{2.1.8}$$

$$\text{for } m = n-N+1, \ldots, n.$$

A useful recursive equation for computing $X_N^n(\omega_k)$ from $X_N^{n-1}(\omega_k)$ can be derived from the above definitions and is given as follows

$$X_N^n(\omega_k) = X_N^{n-1}(\omega_k) + (x[n] - x[n-N])\, W_N^{kn}, \quad \text{for } k = 0, \ldots, N-1. \tag{2.1.9}$$

We will now derive a simpler version of Eqn. (2.1.9) to yield a recursion that doesn't have W_N^{kn} as a multiplier. Define the spectrum of N-points of x[n] by

$$\tilde{X}_N^n(\omega_k) = \sum_{m=n-N+1}^{n} x[m]\, W_N^{k(m-n)} = X_N^n(\omega_k)\, W_N^{-kn} \qquad (2.1.10)$$

for k = 0, . . . , N-1.

Thus, the spectrum of x[n] and its DFT, as defined in Eqn. (2.1.7), have the same magnitude. Now, using Eqn. (2.1.9) we can show that

$$\tilde{X}_N^n(\omega_k) = \tilde{X}_N^{n-1}(\omega_k)\, W_N^{-k} + (x[n] - x[n-N]), \quad \text{for } k = 0, \ldots, N-1. \qquad (2.1.11)$$

See Rabiner and Gold [29, p.387] for more details.

2.1.2 Sampling of Continuous-time Signals

In this subsection, we show the relationships between: 1) the Fourier transform of a continuous-time signal x(t); 2) the DTFT of the corresponding discrete-time signal x[n] resulting from the sampling of x(t); and 3) the DFT of x[n]. Further, we note some special cases of these relationships.

The DTFT of x[n] can be found from the Fourier transform of x(t) as follows

$$X(e^{j\omega T}) = \frac{1}{T} \sum_{r=-\infty}^{\infty} X^c(j\omega + jr\omega_s), \qquad (2.1.12)$$

where r is an integer and again ω_s is the sampling frequency. If we assume that $X^c(j\omega)$ is bandlimited to the range $-(\omega_s/2) < \omega < (\omega_s/2)$, then

$$X(e^{j\omega T}) = (1/T)\, X^c(j\omega). \qquad (2.1.13)$$

If x[n] is of finite duration, for example if $x[n] \neq 0$ only for n=0, . . , N-1, then the N-point DFT of x[n] and the DTFT of x[n] are equal at ω_k,

$$X_N(\omega_k) = X(e^{j\omega T}) \Big|_{\omega=\omega_k} \qquad \text{for } k = 0, \ldots, N-1. \qquad (2.1.14)$$

However, consider the infinite-length signal y[n] and the finite-length signal $y_{fl}[n]$ defined as

$$y_{fl}[n] = \begin{cases} y[n], & \text{for } n = 0, \ldots, N-1 \\ 0, & \text{otherwise} \end{cases} \qquad (2.1.15)$$

We can write

$$y_{fl}[n] = w[n]\, y[n] \tag{2.1.16}$$

where

$$w[n] = \begin{cases} 1, \text{ for } n = 0, \ldots, N-1 \\ 0, \text{ otherwise.} \end{cases} \tag{2.1.17}$$

It can be shown that the DTFT of w[n] is

$$W(e^{j\omega T}) = e^{-j\omega T((N-1)/2)}\, \sin(\omega TN/2) / \sin(\omega T/2). \tag{2.1.18}$$

The well-known relationship between the DTFTs of $y_{fl}[n]$ and y[n] follows. See Oppenheim and Schafer [28, p.239] for details.

$$Y_{fl}(e^{j\omega T}) = (T/2\pi) \int_{-\pi/T}^{\pi/T} Y(e^{j\upsilon T})\, W(e^{j(\omega-\upsilon)T})\, d\upsilon. \tag{2.1.19}$$

Finally, since the DTFT and the N-point DFT of $y_{fl}[n]$ are equal at ω_k, we find that

$$Y_N(\omega_k) = (T/2\pi) \int_{-\pi/T}^{\pi/T} Y(e^{j\upsilon T})\, W(e^{j(\omega_k-\upsilon)T})\, d\upsilon, \text{ for } k = 0, \ldots, N-1. \tag{2.1.20}$$

In summary, we have shown how to compute the DFT of a sampled signal given the Fourier transform of the infinite-length, continuous-time signal from which the sampled signal was derived. First, Eqn. (2.1.12) is used to compute the DTFT of the sampled signal from the Fourier transform, and then Eqn. (2.1.20) is used to compute the DFT from the DTFT.

2.2 Signal Processing Theorems

In this section, we will develop new results that can be used to bound the effects of using finite-length data to compute frequency-domain quantities. Later, in Section 5.2, the frequency-domain estimate of a stable, causal, transfer function $H(e^{j\omega T})$ will be computed based on the N-point DFTs of the transfer function input and output signals. We will now derive a new theorem that can be used to bound the error in the frequency domain between this DFT derived frequency-domain estimate and the true transfer function.

Theorem 2.1: Let $y[m] = h[m]*u[m]$, where $h[m]$ is an infinite-length, causal, impulse response with all its poles in the open unit disk. We denote the DTFT of $h[m]$ by $H(e^{j\omega T})$; and the DFTs of the N-points of $u[m]$ and $y[m]$ ending with time index n, by $U_N^n(\omega_k)$ and $Y_N^n(\omega_k)$, respectively. Then,

$$Y_N^n(\omega_k) = H(e^{j\omega_k T})\, U_N^n(\omega_k) + E_N^n(\omega_k), \qquad \text{for } k = 0, \ldots, N-1, \tag{2.2.1}$$

where the discrete function $E_N^n(\omega_k)$ is given by

$$E_N^n(\omega_k) = \sum_{p=1}^{\infty} h[p]\, W_N^{kp}\, (U_N^{n-p}(\omega_k) - U_N^n(\omega_k)), \quad \text{for } k = 0, \ldots, N-1, \tag{2.2.2}$$

where W_N is defined in Eqn. (2.1.3).

Remark 1: The function $E_N^n(\omega_k)$ is the error in the frequency domain, at time index n, due to the use of finite-length data. That is, if the DTFTs (based on infinite-length data) of $u[m]$ and $y[m]$ were used in Eqn. (2.2.1) instead of the DFTs (based on finite-length data), then there would be no error term $E_N^n(\omega_k)$. Note that the function $E_N^n(\omega_k) / U_N^n(\omega_k)$ is the error in the frequency domain between the DFT derived frequency-domain estimate of $H(e^{j\omega_k T})$ and the true transfer function $H(e^{j\omega_k T})$.

Proof: We know that

$$Y(e^{j\omega_k T}) = H(e^{j\omega_k T})\, U(e^{j\omega_k T}), \qquad \text{for } k = 0, \ldots, N-1, \tag{2.2.3}$$

where $U(e^{j\omega_k T})$ and $Y(e^{j\omega_k T})$ are the DTFTs of $u[n]$ and $y[n]$, respectively. Since

$$Y(e^{j\omega_k T}) = \sum_{m=-\infty}^{n-N} y[m]\, W_N^{km} + Y_N^n(w_k) + \sum_{m=n+1}^{\infty} y[m]\, W_N^{km}, \tag{2.2.4}$$

$$\text{for } k = 0, \ldots, N-1,$$

and a similar expression holds for $U(e^{j\omega_k T})$, we can write

$$Y_N^n(\omega_k) = H(e^{j\omega_k T}) \left[\sum_{m=-\infty}^{n-N} u[m]\, W_N^{km} + U_N^n(\omega_k) + \sum_{m=n+1}^{\infty} u[m]\, W_N^{km} \right]$$

$$- \left[\sum_{m=-\infty}^{n-N} y[m]\, W_N^{km} + \sum_{m=n+1}^{\infty} y[m]\, W_N^{km} \right] \qquad (2.2.5)$$

for k = 0, . . , N-1.

It can be shown that

$$\sum_{m=-\infty}^{n-N} y[m]\, W_N^{km} = h[0] \left\{ \sum_{m=-\infty}^{n-N} u[m]\, W_N^{km} \right\}$$

$$+ \sum_{p=1}^{\infty} h[p]\, W_N^{kp} \left\{ \sum_{m=-\infty}^{n-N} u[m]\, W_N^{km} - \sum_{m=n-N-p+1}^{n-N} u[m]\, W_N^{km} \right\} \qquad (2.2.6)$$

for k = 0, . . , N-1.

So, we can show that

$$H(e^{j\omega_k T}) \sum_{m=-\infty}^{n-N} u[m]\, W_N^{km} - \sum_{m=-\infty}^{n-N} y[m]\, W_N^{km} =$$

$$+ \sum_{p=1}^{\infty} h[p]\, W_N^{kp} \left\{ \sum_{m=n-N-p+1}^{n-N} u[m]\, W_N^{km} \right\} \qquad (2.2.7)$$

for k = 0, . . , N-1.

Similarly, it can be shown that

$$H(e^{j\omega_k T}) \sum_{m=n+1}^{\infty} u[m]\, W_N^{km} - \sum_{m=n+1}^{\infty} y[m]\, W_N^{km} =$$

$$- \sum_{p=1}^{\infty} h[p]\, W_N^{kp} \left\{ \sum_{m=n-p+1}^{n} u[m]\, W_N^{km} \right\} \qquad (2.2.8)$$

for k = 0, . . , N-1.

Using Eqns. (2.2.1), (2.2.5) and (2.2.7-8) we find that

$$E_N^n(\omega_k) = \sum_{p=1}^{\infty} h[p]\, W_N^{kp} \left\{ \sum_{m=n-N-p+1}^{n-N} u[m]\, W_N^{km} - \sum_{m=n-p+1}^{n} u[m]\, W_N^{km} \right\} \qquad (2.2.9)$$

for k = 0, . . , N-1.

Eqn. (2.2.2) now follows using the definition of Eqn. (2.1.7).

Q. E. D.

Later, in Section 5.2, it will be useful to be able to find a magnitude bound on $E_N^n(\omega_k)$. The following theorem provides such a bounding function by using only a finite summation and therefore can be implemented in practice.

Theorem 2.2: Under the assumptions of Theorem 2.1 we find that given some finite integer M, the magnitude of $E_N^n(\omega_k)$ is bounded for each k as follows,

$$|E_N^n(\omega_k)| \le \sum_{p=1}^{M-1} |h[p]|\,|U_N^{n-p}(\omega_k) - U_N^n(\omega_k)| + 2\,u_{max} \sum_{p=M}^{\infty} p\,|h[p]|, \quad \text{for } k = 0, \ldots, N-1, \tag{2.2.10}$$

where $u_{max} = \sup_m |u[m]|$.

Proof: Using the triangle inequality and Eqns. (2.2.2) and (2.2.9) we find,

$$|E_N^n(\omega_k)| \le \sum_{p=1}^{M-1} |h[p]|\,|U_N^{n-p}(\omega_k) - U_N^n(\omega_k)| + \sum_{p=M}^{\infty} |h[p]|\,\left| \sum_{m=n-N-p+1}^{n-N} u[m]\,W_N^{km} - \sum_{m=n-p+1}^{n} u[m]\,W_N^{km} \right| \tag{2.2.11}$$

for k = 0, . . , N-1.

Since,

$$\left| \sum_{m=n-N-p+1}^{n-N} u[m]\,W_N^{km} - \sum_{m=n-p+1}^{n} u[m]\,W_N^{km} \right| \le \sum_{m=n-N-p+1}^{n-N} |u[m]| + \sum_{m=n-p+1}^{n} |u[m]| \le 2\,u_{max}\,p \tag{2.2.12}$$

we conclude that Eqn. (2.2.10) is true.

Q. E. D.

Corollary 2.1: Under the assumptions of Theorem 2.2,

$$|E_N^n(\omega_k)| \le 2\, u_{max} \sum_{p=1}^{\infty} p\, |h[p]|, \quad \text{for } k = 0, \ldots, N-1. \tag{2.2.13}$$

Proof: Choose M=1 in Theorem 2.2. This corollary is closely related to Theorem 2.1 in Ljung [26].

For later reference, we rewrite Eqn. (2.2.10) in terms of the spectrum of u[n] as defined in Eqn. (2.1.10).

$$|E_N^n(\omega_k)| \le \sum_{p=1}^{M-1} |h[p]|\, |\tilde{U}_N^{n-p}(\omega_k)\, W_N^{-kp} - \tilde{U}_N^n(\omega_k)| + 2\, u_{max} \sum_{p=M}^{\infty} p\, |h[p]|, \text{ for } k = 0, \ldots, N-1. \tag{2.2.14}$$

Note that the above bounding function also bounds the magnitude of the error between $\tilde{Y}_N^n(\omega_k)$ and $H(e^{j\omega_k T})\, \tilde{U}_N^n(\omega_k)$ for k=0, . . , N-1.

Later, in Sections 4.3 and 4.4, we will be interested in computing the maximum output signal of a transfer function for which we have a magnitude bounding function in the frequency domain. The following theorem will be useful in this respect.

Theorem 2.3: Let y[m] = h[m]*u[m], where h[m] is an infinite-length, causal, impulse response with all its poles in the open unit disk. We denote the DTFT of h[m] by $H(e^{j\omega_k T})$, and the DFT of the N-points of u[m] ending with time index n, by $U_N^n(\omega_k)$. Then,

$$y[n] = \frac{1}{N} \sum_{k=0}^{N-1} H(e^{j\omega_k T})\, U_N^n(\omega_k)\, W_N^{-kn} + e[n], \tag{2.2.15}$$

where

$$e[n] = \sum_{p=N}^{\infty} h[p]\, (\, u[n-p] - u[n-(p \text{ modulo } N)]\,). \tag{2.2.16}$$

Remark 2: The signal e[n] is the error due to the fact that the impulse response h[n] is of infinite length. We note from Eqn. (2.2.16) that if h[p]=0 for $p \geq N$, then e[n]=0, $\forall n$.

Proof: From the definition of Eqn. (2.1.8) we find that

$$y[n] = \frac{1}{N} \sum_{k=0}^{N-1} Y_N^n(\omega_k)\, W_N^{-kn}. \tag{2.2.17}$$

Using Eqn. (2.2.1) from Theorem 2.1, we find that

$$y[n] = \frac{1}{N} \sum_{k=0}^{N-1} H(e^{j\omega_k T})\, U_N^n(\omega_k)\, W_N^{-kn} + \frac{1}{N} \sum_{k=0}^{N-1} E_N^n(\omega_k)\, W_N^{-kn}. \tag{2.2.18}$$

Thus, the second term of the above equation is equal to e[n]. This will allow us to use Eqn. (2.2.9) from Theorem 2.1 to find e[n]. However, first we will find an alternate form of Eqn. (2.2.9). We observe that

$$\sum_{m=n-N-p+1}^{n-N} u[m]\, W_N^{km} - \sum_{m=n-p+1}^{n} u[m]\, W_N^{km} = \sum_{m=n-p+1}^{n} (\, u[m-N] - u[m]\,)\, W_N^{km}$$

$$\text{for } k = 0, \ldots, N-1, \tag{2.2.19}$$

since $W_N^{-kN} = 1$ for integer k. Then, using Eqns. (2.2.9) and (2.2.19) and the inverse DFT of Eqn. (2.1.8), we can express e[n] as follows.

$$e[n] = \frac{1}{N} \sum_{k=0}^{N-1} \sum_{p=1}^{\infty} h[p]\, W_N^{kp} \sum_{m=n-p+1}^{n} (\, u[m-N] - u[m]\,)\, W_N^{km}\, W_N^{-kn} \tag{2.2.20}$$

Rearranging the summations yields

$$e[n] = \sum_{p=1}^{\infty} h[p] \sum_{m=n-p+1}^{n} (\, u[m-N] - u[m]\,)\, \frac{1}{N} \sum_{k=0}^{N-1} W_N^{k(m-n+p)}. \tag{2.2.21}$$

Noting that

$$\frac{1}{N} \sum_{k=0}^{N-1} W_N^{k(m-n+p)} = \begin{cases} 1, & \text{for } m = n - p + i\,N \\ 0, & \text{otherwise} \end{cases} \tag{2.2.22}$$

where 'i' is an integer, we find

$$\sum_{m=n-p+1}^{n} (u[m-N] - u[m]) \frac{1}{N} \sum_{k=0}^{N-1} W_N^{k(m-n+p)}$$

$$= \begin{cases} 0, \text{ for } p = 1, \ldots, N-1 \\ u[n-p] - u[n-(p \text{ modulo } N)], \text{ for } p \geq N. \end{cases} \tag{2.2.23}$$

Eqn. (2.2.16) follows from Eqns. (2.2.21) and (2.2.23).

Q. E. D.

We want to be able to find a magnitude bounding function on y[n]. The following theorem provides such a bounding function by using the inverse DFT and the results of Theorem 2.3.

Theorem 2.4: Under the assumptions of Theorem 2.3 we find that, for a real-valued impulse response h[n] and a real-valued signal u[n], the magnitude of y[n] is bounded at each n as follows,

$$|y[n]| \leq \frac{1}{N} \{ |H(e^{j\omega_0 T})| \, |U_N^n(\omega_0)| + 2 \sum_{k=1}^{(N/2)-1} |H(e^{j\omega_k T})| \, |U_N^n(\omega_k)|$$

$$+ |H(e^{j\omega(N/2)T})| \, |U_N^n(\omega_{(N/2)})| \} + 2 u_{max} \sum_{p=N}^{\infty} |h[p]|, \tag{2.2.24}$$

where $u_{max} = \sup_m |u[m]|$, and where we have assumed that N is even. An alternate form of the theorem can easily be proven for the case of an odd value of N.

Proof: By applying the triangle inequality to Eqn. (2.2.15) and noting that $|W_N^{-kn}|=1$ we find,

$$|y[n]| \leq \frac{1}{N} \sum_{k=0}^{N-1} |H(e^{j\omega_k T})| \, |U_N^n(\omega_k)| + |e[n]|. \tag{2.2.25}$$

From Eqn. (2.2.16) we obtain a bound on |e[n]|,

$$|e[n]| \leq \sum_{p=N}^{\infty} |h[p]| \, |(u[n-p] - u[n-(p \text{ modulo } N)])| \leq 2 u_{max} \sum_{p=N}^{\infty} |h[p]|. \tag{2.2.26}$$

To complete the proof, we observe that since h[n] and u[n] are real-valued sequences, then

$$|H(e^{j\omega_k T})| = |H(e^{j\omega_{(N-k)} T})|, \tag{2.2.27}$$

$$|U_N^n(\omega_k)| = |U_N^n(\omega_{(N-k)})|, \tag{2.2.28}$$

respectively, for k=1, . . , (N/2)-1. Eqn. (2.2.24) follows from Eqns. (2.2.25-8).

Q. E. D.

In this chapter, we have derived several new signal processing results which will be used in the later parts of this thesis. Specifically, we will use the time-domain bounding results of Theorems 2.3 and 2.4 in Chapter 4 where we develop a robustified time-domain parameter estimator. In addition, the frequency-domain bounding results of Theorems 2.1 and 2.2 will be used in our development of the frequency-domain bounding method in Chapter 5.

CHAPTER 3.
ROBUST ESTIMATION PROBLEM STATEMENT

3.1 Introduction

The purpose of this chapter is to define the robust estimation problem. First, we will describe the adaptive control scenario in which we plan to use the robust estimator. Then, in Section 3.2, we list the assumptions concerning the continuous-time plant and the disturbance. In Section 3.3, we will develop a discrete-time model of the continuous-time plant. Discrete-time impulse response bounds for the plant and disturbance DFT bounds are derived in Sections 3.4 and 3.5, respectively. The results of these sections will enable us, in Section 3.6, to form a list of assumptions concerning the discrete-time plant model and the disturbance. These assumptions can be derived from the assumptions of Section 3.2 concerning the continuous-time plant and the disturbance or, alternatively, they can serve as a starting point for the statement of the robust estimation problem entirely in discrete-time. In Section 3.7, we present the technical details of the robust estimation problem statement and provide an overview of the solution.

Problem Scenario: Sampled-data Adaptive Control

It is assumed in this thesis that a continuous-time plant is being controlled by a discrete-time controller, as is shown in Figure 3.1. The continuous-time, single-input single-output (SISO) plant $G^c_{true}(s)$ is controlled by a discrete-time compensator K(z). $G^c_{true}(s)$ has unmodeled dynamics and an additive output disturbance d(t). The sensor noise $\eta(t)$ has most of its energy at high frequencies. In this thesis, we will assume that the sensor noise $\eta(t)$ can be effectively eliminated by the low-pass, anti-aliasing filter $F_a(s)$ or by the low-pass nature of the plant itself. Consequently, for the remainder of the thesis, we will ignore the effects of sensor noise. Since the plant is preceded by a zero-order hold, we can use a discrete-time model to represent the transfer function from u[n] to $y_0[n]$ as is shown in Figure 3.2. Finally, we can represent the closed-loop control system, ignoring the sensor noise and the filter $F_a(s)$, by the discrete-time system that is shown in Figure 3.3. In this figure, the discrete-time signals r[n], d[n] and y[n] are the sampled versions of r(t), d(t) and y(t), respectively.

One of the goals of this thesis is the development of a discrete-time robust estimator which can be used to identify $G_{true}(z)$ in a closed-loop and provide this information to an on-line

control-law update algorithm. Specifically, the plant is controlled by a fixed-structure, discrete-time compensator whose parameters are updated infrequently using information from the robust estimator. This adaptive control scheme is illustrated in Figure 3.4. In order to develop a discrete-time model of the partially known plant, we must make some assumptions about the continuous-time plant. In the following section, we list these assumptions as well as assumptions concerning the disturbance and the input signal.

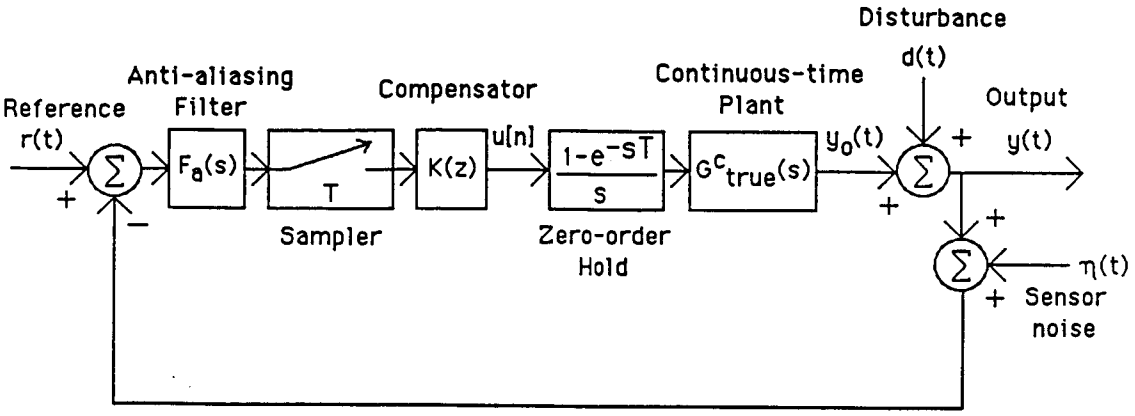

Figure 3.1: Discrete-time Control of a Sampled-data System.

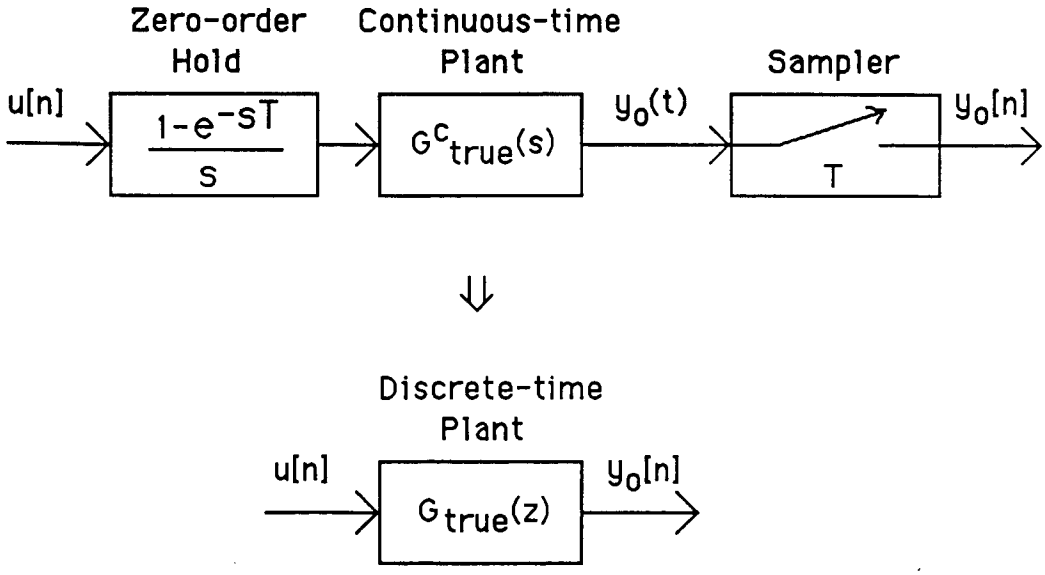

Figure 3.2: Discrete-time Model of the Continuous-time Plant.

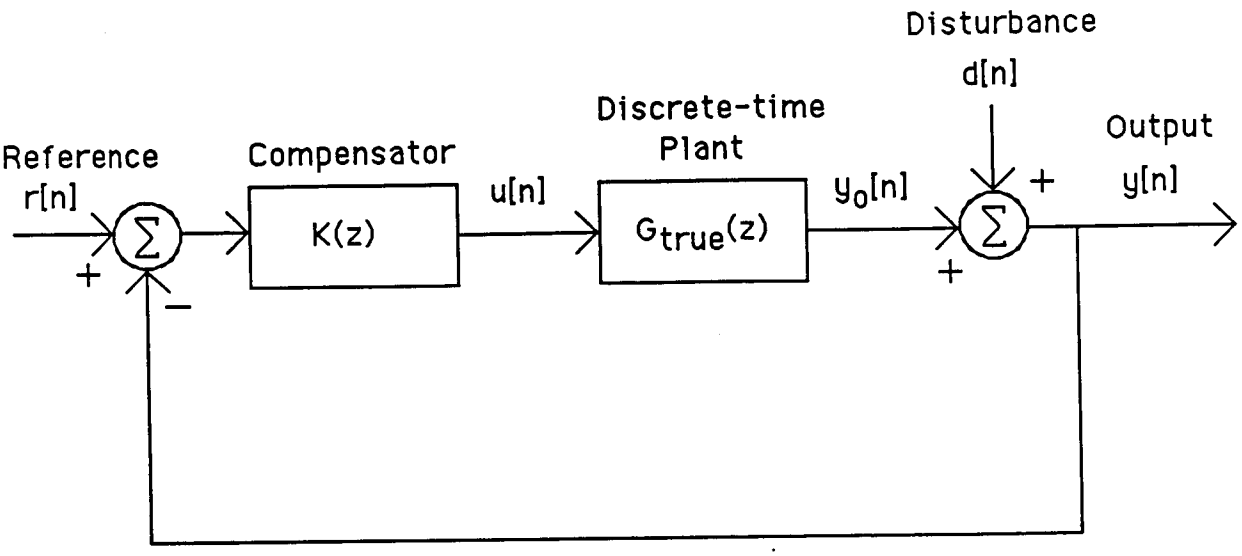

Figure 3.3: Discrete-time Closed-loop System.

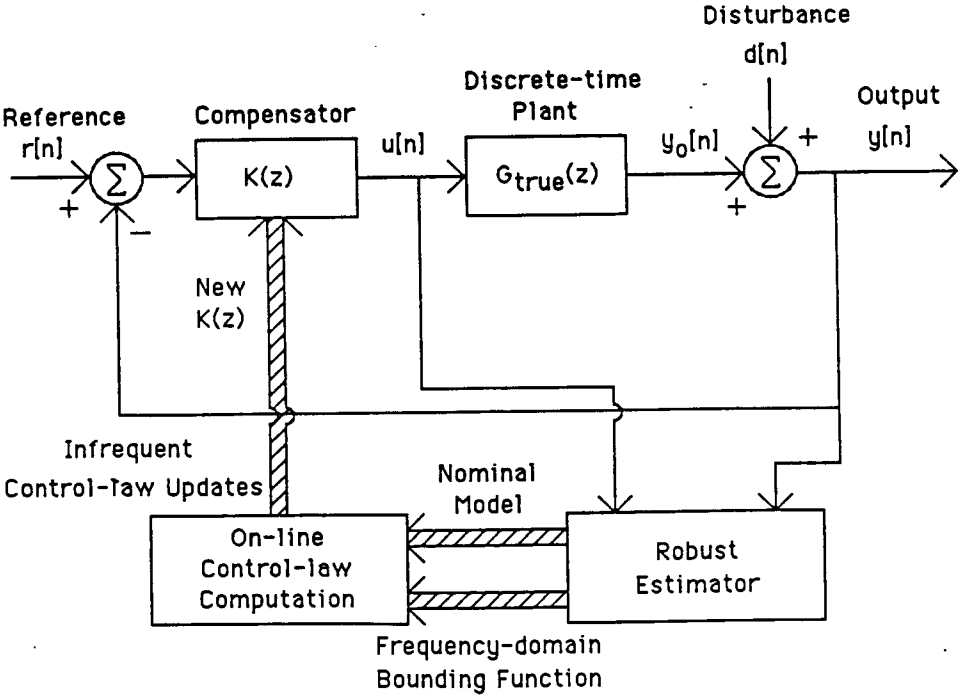

Figure 3.4: Discrete-time Adaptive Control System.

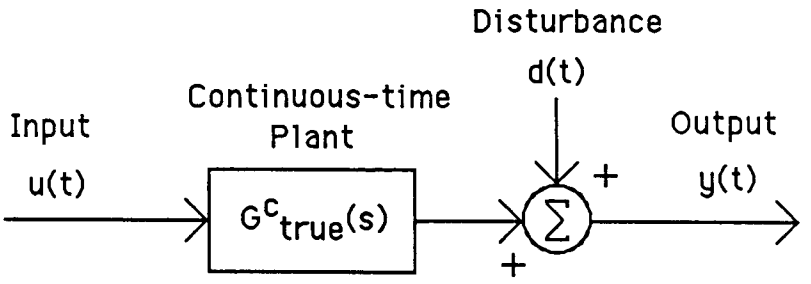

Figure 3.5: Continuous-time Plant and Disturbance.

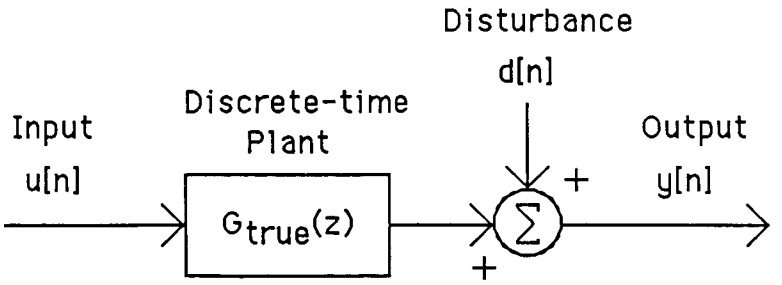

Figure 3.6: Discrete-time Plant and Disturbance.

3.2 Continuous-time Assumptions on the Plant and Disturbance

Consider the system of Figure 3.5 where the continuous-time plant $G^c_{true}(s)$, which we are trying to identify, has input u(t), output y(t), and an additive output disturbance d(t). We make the following assumptions, which we label for later reference with the letters 'AC' referring to the fact that they are assumptions concerning the continuous-time plant, disturbance and input. In the remaining sections of this chapter we will develop a set of discrete-time assumptions from the following list of continuous-time assumptions. When the discrete-time assumptions are enumerated in Section 3.6 we will discuss why each assumption is needed.

AC1) Plant Assumptions. We assume a structure for the nominal model of $G^c_{true}(s)$ and a magnitude bounding function on the unstructured uncertainty. That is, we assume that

$$G^c_{true}(s) = G^c(s,\theta^c_0)\,[1 + \delta^c_u(s)] \tag{3.2.1}$$

where $G^c(s,\theta^c_0)$ is a nominal model, $\delta^c_u(s)$ denotes the unstructured uncertainty of the plant, θ^c_0 is a vector of plant parameters and we assume,

AC1.1) $G^c(s,\theta^c_0) = B^c(s) / A^c(s)$, (3.2.2)

where the polynomials $B^c(s)$ and $A^c(s)$ for the continuous-time system are,

$$B^c(s) = b^c_0 s^{mc_1} + b^c_1 s^{(mc_1-1)} + \ldots + b^c_{mc1}, \tag{3.2.3}$$

$$A^c(s) = s^{nc_1} - a^c_1 s^{(nc_1-1)} + \ldots - a^c_{nc1}, \quad nc_1 > mc_1, \tag{3.2.4}$$

and where the parameter vector of the continuous-time plant is,

$$\theta^c_0 = [\, a^c_1 \ldots a^c_{nc1} \;\; b^c_0 \;\; b^c_1 \ldots b^c_{mc1} \,]^T. \tag{3.2.5}$$

AC1.2) $\theta^c_0 \in \Theta^c$, where Θ^c is a known bounded set. (3.2.6)

This assumptions means that we have some coarse prior idea of what the parameters are.

AC1.3) $|\delta^c_u(j\omega)| \le \Delta^c_u(j\omega), \;\forall\omega.$ (3.2.7)

This assumption is our characterization of the high-frequency unmodeled dynamics. While other characterizations are possible, this frequency-domain approach has been shown to have pragmatic utility [34].

AC1.4) $|d\delta^c_u(j\omega)/d\omega| \le \nabla^c_u(j\omega), \;\forall\omega.$ (3.2.8)

This assumption tells us how smooth the unmodeled dynamics are. This assumption is required since we will be using DFTs to perform our frequency-domain calculations and will

need to compute the maximum variation of the plant in between the discrete frequency points.

AC1.5) $G^c(s,\theta^c_0)$ and $\delta^c_u(s)$ and, hence, $G^c(s,\theta^c_0)\,\delta^c_u(s)$ have all their poles in the open left-half plane for all $\theta^c_0 \in \Theta^c$. Thus, we assume that the true plant is asymptotically stable.

AC1.6) A bounding function on the magnitude of the impulse response of the true plant, denoted by $g_{true}(t)$, is known such that

$$|g_{true}(t)| \le \sum_{i=1}^{I_0^c} b_i\, t^{(r_i)}\, e^{(-a_i t)}, \quad \text{for } t \ge 0 \tag{3.2.9}$$

where r_i is a positive integer, and $b_i > 0$, $a_i > 0$ (i.e. poles in the open left-half plane) and r_i are known for $i=1, \ldots, I_0^c$. $g_{true}(t)$ is assumed to be causal. This assumption is saying that we know some coarse bounding function on the impulse response of the partially known plant. If we know that the system has no double pole, then a simple decaying exponential $b\,e^{-at}$ of appropriate time constant and gain satisfies this assumption. If the system is known to have a double pole, then we must use a bounding function of the form $b\,t\,e^{-at}$. Eqn. (3.2.9) is a general expression allowing summations of impulse response bounds, for example $b_1\,e^{(-a_1 t)} + b_2\,t\,e^{(-a_2 t)}$.

AC1.7) A bounding function on the magnitude of the impulse response of the additive plant error, that is, we assume we know a bounding function of the same form as Eqn. (3.2.9) on $|g_{true}(t) - g(t,\theta_0^c)|$, for all $\theta^c_0 \in \Theta^c$, where $g(t,\theta_0^c)$ is the impulse response of $G^c(s,\theta^c_0)$. This assumption means that we know some coarse bounding function on the impulse response of the additive plant error that is due to the unmodeled dynamics.

AC1.8) zero initial conditions.

Thus, our a priori assumptions are that we know mc_1 and nc_1, the degrees of $B^c(s)$ and $A^c(s)$, respectively, and the bounding functions $\Delta^c_u(j\omega)$ and $\nabla^c_u(j\omega)$. Further, we assume that the parameter vector θ^c_0 is in some known bounded set Θ^c, which is only a coarse and, hence, large a priori estimate of the parameter space.

AC2) Disturbance Assumptions. We assume that the unmeasurable disturbance d(t) satisfies:

$$\text{AC2.1)}\ |d(t)| \leq d_{max},\ \forall t, \text{ and} \tag{3.2.10}$$

$$\text{AC2.2)}\ |D^c(j\omega)| \leq \overline{D}^c(j\omega),\ \forall \omega. \tag{3.2.11}$$

where the constant d_{max} and the function $\overline{D}^c(j\omega)$ are known a priori.

AC3) Input and Output Signal Assumptions. We assume that both the input signal u(t) and the output signal y(t) are measurable and that u(t) is bounded.

$$\text{AC3.1)}\ |u(t)| \leq u_{max},\ \forall t, \text{ where } u_{max} \text{ is known a priori.} \tag{3.2.12}$$

Remark 1: Assumption AC1.7 will only be used in the development of the time-domain parameter estimator of Chapter 4.

Remark 2: Assumptions AC1.2-1.4 and AC1.6-1.7 are quite different from the classical MRAC assumptions, which are listed in Subsection 1.2.1. We do assume knowledge of the structure of the "nominal" plant model, and hence its relative degree and its maximum order. However, we do not assume that the plant is minimum phase nor do we make non-pragmatic assumptions about the plant, such as knowledge of: 1) the sign of the high-frequency gain and 2) an upper bound on the high-frequency gain.

3.3 Development of a Discrete-time Plant Model

In this section, we will show how the assumptions of the previous section, concerning the continuous-time plant and the disturbance, can be used to find their discrete-time counterpart, which is very similar. In Subsections 3.3.1-3, we will assume that the continuous-time nominal model of the plant is known along with magnitude bounding functions on the continuous-time unstructured uncertainty and the derivative of the continuous-time unstructured uncertainty as assumed in AC1.3-4. In Subsection 3.3.4, we will discuss the issues that arise due to the fact that we do not know the parameters of the nominal model; rather, we only know that they lie in some known bounded set.

3.3.1 Development of a Discrete-time Nominal Plant Model

In this subsection, we consider the continuous-time plant $G^c_{true}(s)$ whose input is generated by a zero-order hold. We will use the zero-order hold equivalent of the continuous-time plant to find a discrete-time model of the plant. The anti-aliasing filter, in Figure 3.1, could be considered as part of the plant. However, for simplicity, we will ignore the effects of the anti-aliasing filter in this development. The true discrete-time plant, using a zero-order hold equivalence is given by,

$$G_{true}(z) = (1 - z^{-1})\, \mathcal{Z}\{ (1/s)\, G^c_{true}(s) \}. \tag{3.3.1}$$

Similarly, given a continuous-time nominal model $G^c(s)$, the discrete-time nominal model $G(z)$ can be found as follows,

$$G(z) = (1 - z^{-1})\, \mathcal{Z}\{ (1/s)\, G^c(s) \}. \tag{3.3.2}$$

See Franklin and Powell [30, p.62] for details.

3.3.2 Development of a Bounding Function on the Magnitude of the Discrete-time Unstructured Uncertainty

We seek a bounding function on the magnitude of the discrete-time unstructured uncertainty. To find this, we must first make several definitions. The transfer function of a zero-order hold is given by,

$$H_{zoh}(s) = (1 - e^{-sT}) / s, \tag{3.3.3}$$

which allows us to define the transfer function of the true plant and the zero-order hold,

$$G^c_{true,zoh}(s) = H_{zoh}(s)\, G^c_{true}(s). \tag{3.3.4}$$

Since there will always be some unstructured uncertainty in the continuous-time system, we write

$$G^c_{true}(s) = G^c(s)\, [1 + \delta^c_u(s)] \tag{3.3.5}$$

where $G^c(s)$ is a nominal model and $\delta^c_u(s)$ is the unstructured uncertainty. We assume a magnitude bounding function on the continuous-time unstructured uncertainty, that is,

$$|\delta^c_u(j\omega)| \le \Delta^c_u(j\omega), \ \forall\omega, \tag{3.3.6}$$

as was assumed in AC1.3. For later use, we define

$$G^c_{zoh}(s) = H_{zoh}(s)\, G^c(s). \tag{3.3.7}$$

We develop a similar kind of plant description in discrete time. The discrete-time model of the plant that results from sampling the continuous-time transfer function of the plant and the zero-order hold is,

$$G_{true}(e^{j\omega T}) = \frac{1}{T} \sum_{r=-\infty}^{\infty} G^c_{true,zoh}(j\omega + jr\omega_s), \tag{3.3.8}$$

where ω_s is the sampling frequency and T is the sampling period. Using Eqns. (3.3.4-5) and (3.3.7-8) yields

$$G_{true}(e^{j\omega T}) = \frac{1}{T} \sum_{r=-\infty}^{\infty} G^c_{zoh}(j\omega + jr\omega_s)\,[1 + \delta^c_u(j\omega + jr\omega_s)]. \tag{3.3.9}$$

We define the desired form of the true discrete-time plant,

$$G_{true}(z) = G(z)\,[1 + \delta_u(z)] \tag{3.3.10}$$

where the discrete-time nominal model G(z) is defined by Eqn. (3.3.2). It can be shown, using Theorem 4.1 of Astrom and Wittenmark [31], that

$$G(e^{j\omega T}) = (1 - e^{-j\omega T})\, \mathcal{Z}\{ (1/s)\, G^c(s) \} \Big|_{z=e^{j\omega T}} \tag{3.3.11}$$

$$= \frac{1}{T} \sum_{r=-\infty}^{\infty} G^c_{zoh}(j\omega + jr\omega_s). \tag{3.3.12}$$

It was shown by Rohrs et al. [21] that, with reference to the nominal model of Eqn. (3.3.12), which we have shown is the same as the nominal model of Eqn. (3.3.2),

$$\delta_u(e^{j\omega T}) = \{ \frac{1}{T} \sum_{r=-\infty}^{\infty} G^c_{zoh}(j\omega + jr\omega_s)\, \delta^c_u(j\omega + jr\omega_s) \} / G(e^{j\omega T}), \ \forall\omega. \tag{3.3.13}$$

Eqn. (3.3.13) follows from Eqns. (3.3.9-12). Then, using the triangle inequality and Eqn. (3.3.6) yields,

$$|\delta_u(e^{j\omega T})| \le \Delta_u(e^{j\omega T}), \ \forall\omega \tag{3.3.14}$$

where

$$\Delta_u(e^{j\omega T}) = \{ \frac{1}{T} \sum_{r=-\infty}^{\infty} |G^c_{zoh}(j\omega + jr\omega_s)|\, \Delta^c_u(j\omega + jr\omega_s) \} / |G(e^{j\omega T})|, \forall\omega. \tag{3.3.15}$$

Recalling the definition of $G^c_{zoh}(j\omega)$ and observing that

$$(1 - e^{-(j\omega+jr\omega_s)T}) = (1 - e^{-j\omega T}), \ \forall\omega \tag{3.3.16}$$

we can factor this term out of the numerator of Eqn. (3.3.15) to yield

$$\Delta_u(e^{j\omega T}) =$$

$$|1-e^{-j\omega T}| \{ \frac{1}{T} \sum_{r=-\infty}^{\infty} |G^c(j\omega+jr\omega_s) / (j\omega+jr\omega_s)| \Delta^c_u(j\omega+jr\omega_s) \} / |G(e^{j\omega T})|, \ \forall\omega. \tag{3.3.17}$$

In practice, the sums in Eqns. (3.3.12), and (3.3.13) will usually be dominated by the r=0 terms. When the r=0 terms dominate the sums, Eqn. (3.3.13) yields the approximate equality,

$$\delta_u(e^{j\omega T}) \approx \delta^c_u(j\omega), \quad \text{for } -\omega_s/2 < \omega < \omega_s/2. \tag{3.3.18}$$

Similarly, it can be shown that

$$\Delta_u(e^{j\omega T}) \approx \Delta^c_u(j\omega), \quad \text{for } -\omega_s/2 < \omega < \omega_s/2, \tag{3.3.19}$$

when the r=0 terms dominate the sums.

In summary, in this subsection we have shown how to find a magnitude bounding function on the discrete-time unstructured uncertainty. To find this bounding function, we needed a continuous-time nominal model from which we found a discrete-time nominal model; in addition, we needed a magnitude bounding function on the continuous-time unstructured uncertainty. Later, in Section 9.2, it will be shown through an example that Eqn. (3.3.19) will be a good approximation for many problems. Thus, for many problems it will not be necessary to compute Eqn. (3.3.17). Appendix A contains several useful results that can aid in the computation of Eqn. (3.3.17) should the need arise.

3.3.3 Development of a Bounding Function on the Magnitude of the Derivative of the Discrete-time Unstructured Uncertainty

We seek a bounding function on the magnitude of the derivative of the discrete-time unstructured uncertainty. This derivative bounding function is a description of how smooth the discrete-time unstructured uncertainty is. Taking the derivative of Eqn. (3.3.13) yields

$$d\delta_u(e^{j\omega T}) / d\omega =$$

$$\{ G(e^{j\omega T}) [\frac{1}{T} \sum_{r=-\infty}^{\infty} ((dG^c_{zoh} / d\omega) \delta^c_u + G^c_{zoh} (d\delta^c_u / d\omega))] \tag{3.3.20}$$

$$- [\frac{1}{T} \sum_{r=-\infty}^{\infty} G^c_{zoh} \delta^c_u] (dG(e^{j\omega T}) / d\omega) \} / G(e^{j\omega T})^2, \ \forall\omega,$$

where we have omitted the arguments of the summands for clarity. From Eqn. (3.3.12) we find that

$$dG(e^{j\omega T}) / d\omega = \frac{1}{T} \sum_{r=-\infty}^{\infty} (dG^c_{zoh}(j\upsilon) / d\upsilon) \Big|_{\upsilon=\omega+r\omega_s}. \tag{3.3.21}$$

Combining Eqns. (3.3.13), and (3.3.20-1) yields

$$d\delta_u(e^{j\omega T}) / d\omega = \{ \frac{1}{T} \sum_{r=-\infty}^{\infty} [(\delta^c_u(j\omega+jr\omega_s) - \delta_u(e^{j\omega T})) (dG^c_{zoh}(j\upsilon) / d\upsilon) \Big|_{\upsilon=\omega+r\omega_s}$$

$$+ G^c_{zoh}(j\omega+jr\omega_s) (d\delta^c_u(j\upsilon) / d\upsilon) \Big|_{\upsilon=\omega+r\omega_s}] \} / G(e^{j\omega T}), \ \forall\omega. \tag{3.3.22}$$

We note that if the r=0 terms dominate the sums in Eqns. (3.3.12-13) and (3.3.22), then Eqn. (3.3.18) is true and

$$d\delta_u(e^{j\omega T}) / d\omega \approx d\delta^c_u(j\omega) / d\omega, \text{ for } -\omega_s/2 < \omega < \omega_s/2. \tag{3.3.23}$$

We can now find a magnitude bounding function on $d\delta_u(e^{j\omega T})/d\omega$ by using the triangle inequality, assumptions AC1.3-4, and Eqn. (3.3.22). Thus,

$$|d\delta_u(e^{j\omega T}) / d\omega| \le \nabla_u(e^{j\omega T}), \ \forall\omega \tag{3.3.24}$$

where

$$\nabla_u(e^{j\omega T}) = \{ \frac{1}{T} \sum_{r=-\infty}^{\infty} [(\Delta^c_u(j\omega+jr\omega_s) + \Delta_u(e^{j\omega T})) |dG^c_{zoh}(s) / ds| \Big|_{s=j\omega+jr\omega_s}$$

$$+ |G^c_{zoh}(j\omega+jr\omega_s)| \nabla^c_u(j\omega+jr\omega_s)] \} / |G(e^{j\omega T})|, \ \forall\omega. \tag{3.3.25}$$

and where

$$|G^c_{zoh}(j\omega+jr\omega_s)| = |1-e^{-j\omega T}|\,|G^c(j\omega+jr\omega_s)| / |j\omega+jr\omega_s|,\ \forall\omega \tag{3.3.26}$$

and

$$\left|\frac{dG^c_{zoh}(s)}{ds}\right|_{s=j\omega+jr\omega_s} = |1-e^{-j\omega T}|\left|\frac{d(G^c(s)/s)}{ds}\right|_{s=j\omega+jr\omega_s} + T\,|G^c(j\omega+jr\omega_s)| / |j\omega+jr\omega_s|,\ \forall\omega. \tag{3.3.27}$$

In Eqn. (3.3.25) we have been forced to use a very conservative magnitude bound for the term $(\delta^c_u(j\omega+jr\omega_s) - \delta_u(e^{j\omega T}))$ since we do not have any phase information about δ^c_u and δ_u. It may be possible to derive other, less conservative, bounding functions on the magnitude of the derivative of the discrete-time unstructured uncertainty. That is, from Eqn. (3.18) we expect considerable cancellation in the term $(\delta^c_u(j\omega+jr\omega_s) - \delta_u(e^{j\omega T}))$ so that a new bounding function using this cancellation could be significantly tighter than Eqn. (3.3.25).

In summary, in this subsection we have shown how to find a magnitude bounding function on the derivative of the discrete-time unstructured uncertainty. To find this bounding function, we needed a continuous-time nominal model from which we found a discrete-time nominal model; in addition, we needed magnitude bounding functions on the continuous-time unstructured uncertainty and the derivative of the continuous-time unstructured uncertainty. Later, in Section 9.2, it will be shown through an example that Eqn. (3.3.23) is a good approximation for many problems. Thus, for many problems it will not be necessary to compute Eqn. (3.3.25). Appendix A contains several useful results that can aided in the computation of Eqn. (3.3.25) should the need arise.

3.3.4 Treatment of the Case of Nominal Models with Structured Uncertainty

In this subsection, we will discuss the modifications in the results of Subsections 3.3.1-3 that are necessary when the continuous-time nominal model has structured uncertainty. That is, it was assumed in these subsections that we knew the continuous-time nominal model from which we could find the discrete-time nominal model. In fact, with reference to assumptions AC1.1-2, while we know the structure of the continuous-time nominal model, we do not know its parameters. We only know that the nominal model parameters lie in some bounded set Θ^c.

Using Eqn. (3.3.2), we can find the structure of the discrete-time nominal model from

AC1.1. In addition, using Eqn. (3.3.2) and given assumption AC1.2, that is, $\theta^c \in \Theta^c$, we can find a set Θ such that the parameter vector θ of the discrete-time nominal model satisfies $\theta \in \Theta$. That is, Eqn. (3.3.2) implicitly defines a map from the bounded parameter space Θ^c to the parameter space Θ. We denote this map by f(•). Ackermann [32, p.95] summarizes the relationship between the continuous-time and discrete-time parameters using a state-space representation of these systems. In this thesis, we view the map f(•) as an explicit map that can be found for any given example using the methods in Franklin and Powell [30]. This methodology will later be illustrated by an example, in Section 9.2.

In summary, from AC1.1-2 and the application of Eqn. (3.3.2), we have the following continuous-time and corresponding discrete-time nominal model structures,

$$G^c(s,\theta^c), \text{ with } \theta^c \in \Theta^c, \text{ and} \tag{3.3.28}$$

$$G(z,\theta), \text{ with } \theta = f(\theta^c) \in \Theta\ , \tag{3.3.29}$$

where the set Θ is defined as follows,

$$\Theta = \{\ \theta \mid \theta = f(\theta^c), \text{ for } \theta^c \in \Theta^c\ \}. \tag{3.3.30}$$

We can now find modified forms of the results of Subsections 3.3.2-3. The new magnitude bounding functions will be formed by maximizing the expressions of Eqn. (3.3.17) and Eqn. (3.3.25) over the parameter space Θ^c. Thus, from Eqn. (3.3.17), the new bounding function on the discrete-time unstructured uncertainty is given by

$$\Delta_u(e^{j\omega T}) = |1-e^{-j\omega T}| \bullet$$

$$\sup_{\theta^c \in \Theta^c} \left[\left\{ \frac{1}{T} \sum_{r=-\infty}^{\infty} \left(|G^c(j\omega+jr\omega_s,\theta^c) / (j\omega + jr\omega_s)|\ \Delta^c_u(j\omega+jr\omega_s) \right) \right\} / \ |G(e^{j\omega T},f(\theta^c))| \ \right], \forall\omega. \tag{3.3.31}$$

Further, from Eqn. (3.3.25), the new bounding function on the derivative of the discrete-time unstructured uncertainty is given by

$$\nabla_u(e^{j\omega T}) =$$

$$\sup_{\theta^c \in \Theta^c} \left[\left\{ \frac{1}{T} \sum_{r=-\infty}^{\infty} \left((\Delta^c{}_u(j\omega+jr\omega_s) + \Delta_u(e^{j\omega T})) \left| dG^c{}_{zoh}(s,\theta^c) / ds \right| \right|_{s=j\omega+jr\omega_s} \right.\right.$$

$$\left.\left. + \left| G^c{}_{zoh}(j\omega+jr\omega_s,\theta^c) \right| \nabla^c{}_u(j\omega+jr\omega_s) \right) \right\} / \left| G(e^{j\omega T}, f(\theta^c)) \right| \right], \ \forall\omega. \qquad (3.3.32)$$

where

$$\left| G^c{}_{zoh}(j\omega+jr\omega_s,\theta^c) \right| = \left| 1-e^{-j\omega T} \right| \left| G^c(j\omega+jr\omega_s,\theta^c) \right| / \left| j\omega+jr\omega_s \right|, \ \forall\omega, \text{ and} \qquad (3.3.33)$$

$$\left| dG^c{}_{zoh}(s,\theta^c) / ds \right|_{s=j\omega+jr\omega_s} = \left| 1-e^{-j\omega T} \right| \left| d(G^c(s,\theta^c)/s) / ds \right|_{s=j\omega+jr\omega_s}$$

$$+ \ T \left| G^c(j\omega+jr\omega_s,\theta^c) / \left| j\omega+jr\omega_s \right| \right., \ \forall\omega. \qquad (3.3.34)$$

The bounding function of Eqn. (3.3.31) can be used for $\Delta_u(e^{j\omega T})$ in Eqn. (3.3.32). Alternatively, one could substitute the expression of Eqn. (3.3.31) into Eqn. (3.3.32) and compute the supremum for this expression, however, it would make the computation of this expression quite complex.

3.4 Discrete-time Impulse Response Bounding

In this section, we will show how the magnitude of the discrete-time impulse response of a system formed using the zero-order hold equivalence, can be bounded by using a magnitude bounding function on the impulse response of the corresponding continuous-time plant. We will use these results to derive a discrete-time impulse response bounding function from the continuous-time bounding function of assumption AC1.6. From Franklin and Powell [30, p.62] we find that if the zero-order hold equivalence is used, then the discrete-time impulse response $g_{true}[n]$ is related to the continuous-time impulse response $g_{true}(t)$ as follows.

$$g_{true}[n] = \int_{(n-1)T}^{nT} g_{true}(t)\, dt, \ \forall n. \qquad (3.4.1)$$

If $g_{true}(t)$ satisfies the magnitude bounding function of assumption AC1.6 of Section 3.2, then we find

$$|g_{true}[n]| \le \int_{(n-1)T}^{nT} |g_{true}(t)|\,dt \le \sum_{i=1}^{I_0^c} b_i \int_{(n-1)T}^{nT} t^{(r_i)}\, e^{(-a_i t)}, \text{ for } n \ge 1. \quad (3.4.2)$$

For the case of r=0, corresponding to a bounding function that is a simple exponential decay $b\,e^{-at}$, it is easily seen that

$$b \int_{(n-1)T}^{nT} e^{-at}\,dt = (b/a)\,(1 - e^{-aT})\,e^{-aT(n-1)}, \text{ for } n \ge 1. \quad (3.4.3)$$

Next, we consider the case of r=1, which corresponds to the bounding function $b\,t\,e^{-at}$. This bounding function is the impulse response of a double pole system, that is, a system with two identical real poles. In Appendix B, it is shown that for this case,

$$b \int_{(n-1)T}^{nT} t\,e^{-at}\,dt = (b/a)\,\{\,[\,(1/a)\,(1 - e^{-aT}) - T\,] + [\,nT\,(1 - e^{-aT})\,]\,\}\,e^{-aT(n-1)}, \text{ for } n \ge 1. \quad (3.4.4)$$

A general method for the treatment of larger values of r is also presented in Appendix B. For example, in Appendix B we treat the case of r=2, which corresponds to the impulse response of a triple pole system. However, most practical situations will not require more than the case of r=1, which corresponds to a system with a double pole.

3.5 Bounding the DFT of the Disturbance

3.5.1 The Basic Technique

In this section, we consider the problem of finding a magnitude bounding function on the DFT of the time-sampled disturbance d[n], given a magnitude bounding function on the Fourier transform of d(t). Thus, as in assumption AC2.2 of Section 3.2, we assume that we know a magnitude bounding function $\overline{D}^c(j\omega)$ on the Fourier transform of d(t), $\mathcal{F}\{d(t)\}$, which we denote by $D^c(j\omega)$. That is,

$$|\mathcal{F}\{d(t)\}| = |D^c(j\omega)| \le \overline{D}^c(j\omega), \ \forall\omega. \quad (3.5.1)$$

From Eqn. (2.1.12) we find that the magnitude of the DTFT of d[n], which we denote by $D(e^{j\omega T})$, is bounded by the function $\overline{D}(e^{j\omega T})$ as follows

$$|D(e^{j\omega T})| \le \bar{D}(e^{j\omega T}) = \frac{1}{T} \sum_{r=-\infty}^{\infty} \bar{D}^c(j\omega + jr\omega_s), \ \forall\omega. \tag{3.5.2}$$

Using Eqns. (2.1.18) and (2.1.20) it can be shown that

$$|D_N(\omega_k)| \le (T/2\pi) \int_{-\pi/T}^{\pi/T} \bar{D}(e^{j\upsilon T}) \, |\sin((\omega_k-\upsilon)TN/2) / \sin((\omega_k-\upsilon)T/2)| \, d\upsilon$$

$$\text{for } k = 0, \ldots, N-1. \tag{3.5.3}$$

It is a property of the DTFT that if the DTFT of w[m] is $W(e^{j\omega T})$, then the DTFT of w[m-n] is $e^{-jn\omega T}W(e^{j\omega T})$. Thus, a shift in time doesn't change the magnitude of the DTFT. This fact allows us to conclude that

$$|D_N^n(\omega_k)| \le (T/2\pi) \int_{-\pi/T}^{\pi/T} \bar{D}(e^{j\upsilon T}) \, |\sin((\omega_k-\upsilon)TN/2) / \sin((\omega_k-\upsilon)T/2)| \, d\upsilon$$

$$\text{for } k = 0, \ldots, N-1. \tag{3.5.4}$$

for all n, where $D_N^n(\omega_k)$ is defined as in Eqn. (2.1.7).

3.5.2 Treatment of the Start-up Situation

In this subsection, we consider the effects of the disturbance on the robust estimator. We must consider the situation that occurs when the estimator starts up. That is, from the viewpoint of the estimator, the disturbance d[n] is zero for $n < 0$. Thus, we define the disturbance,

$$d^+[n] = \begin{cases} d[n], & \text{for } n = 0, 1, \ldots \\ 0, & \text{for } n < 0. \end{cases} \tag{3.5.5}$$

The N-point DFT of $d^+[m]$ for the last N points ending with 'n' is defined, as in Eqn. (2.1.7) by

$$D_N^{+n}(\omega_k) = \sum_{m=n-N+1}^{n} d^+[m] \, W_N^{km}, \qquad \text{for } k = 0, \ldots, N-1. \tag{3.5.6}$$

We are really concerned with the properties of $D_N^{+n}(\omega_k)$, rather than $D_N^n(\omega_k)$, since $D_N^{+n}(\omega_k)$ appears in all of our algorithms. However, we note that

$$D_N^{+n}(\omega_k) = \begin{cases} \sum_{m=0}^{n} d^+[m]\, W_N^{km}, & \text{for } n = 0, 1, \ldots, N\text{-}2, \\ D_N^{n}(\omega_k), & \text{for } n \geq N\text{-}1, \end{cases} \qquad \text{for } k = 0, \ldots, N\text{-}1. \tag{3.5.7}$$

Thus, we need only be concerned with the differences between the DFT of $D_N^{+n}(\omega_k)$ and $D_N^{n}(\omega_k)$ for n=0, . . , N-2, that is, during start-up. To treat this start-up situation, we first define the signal,

$$\tilde{d}^+[m] = w^n[m]\, d[m] \tag{3.5.8}$$

where the window $w^n[m]$ is given by,

$$w^n[m] = \begin{cases} 1, & \text{for } m = 0, \ldots, n \\ 0, & \text{otherwise.} \end{cases} \tag{3.5.9}$$

From Eqn. (2.1.18) we know that the DTFT of $w^n[m]$ is given by

$$W^n(e^{j\omega T}) = e^{-j\omega T(n/2)} \sin(\omega T(n+1)/2) / \sin(\omega T/2). \tag{3.5.10}$$

Thus, the DTFT of $\tilde{d}^+[n]$ is given by the convolution,

$$W^n(e^{j\omega T}) * D(e^{j\omega T}), \tag{3.5.11}$$

which, from the discussion of Section 2.1, we know is equal to the N-point DFT of $d^+[m]$ for the last N points ending with time index n, for $\omega=\omega_k$. Using this information, it can be shown that,

$$|D_N^{+n}(\omega_k)| \leq \overline{D}_N^{+n}(\omega_k), \tag{3.5.12}$$

where

$$\overline{D}_N^{+n}(\omega_k) = \begin{cases} (T/2\pi) \int_{-\pi/T}^{\pi/T} \overline{D}(e^{j\upsilon T}) \left|\sin((\omega_k-\upsilon)T(n+1)/2) / \sin((\omega_k-\upsilon)T/2)\right| d\upsilon, & \text{for } n = 0, \ldots, N\text{-}2, \\ \overline{\overline{D}}_N(\omega_k), & \text{for } n \geq N\text{-}1, \end{cases} \qquad \text{for } k = 0, \ldots, N\text{-}1, \tag{3.5.13}$$

and where we know from Eqns. (3.5.4) and (3.5.7) that

$$\overline{\overline{D}}_N(\omega_k) = (T/2\pi) \int_{-\pi/T}^{\pi/T} \overline{D}(e^{j\upsilon T}) \left|\sin((\omega_k-\upsilon)TN/2) / \sin((\omega_k-\upsilon)T/2)\right| d\upsilon$$

$$\text{for } k = 0, \ldots, N-1. \qquad (3.5.14)$$

In summary, we have shown how to compute a magnitude bounding function on the DFT of the time-sampled disturbance given a magnitude bounding function on the Fourier transform of the infinite-length, continuous-time disturbance from which the sampled signal was derived. The expressions that were derived in this section are rather complex. Thus, in practice, we will work directly with the DFT of some disturbance for which we have some sort of time-domain model. However, it is important to note that the kind of bounding functions that we have derived in this section can all be found in terms of the magnitude bounding function on the Fourier transform of the continuous-time disturbance. The bounding functions of Eqns. (3.5.13-14) will eventually be used to compute a bound on the error associated with the frequency-domain estimate of the plant.

3.6 Restatement of Assumptions in Discrete-time

In this section, we list assumptions about the discrete-time plant in preparation for the statement of the robust estimation problem in Section 3.7. In addition, using the results of Sections 3.2-5, we show that the information assumed in this section about the discrete-time plant and the disturbance can be obtained from the assumptions about the continuous-time plant and the disturbance that were listed in Section 3.2.

Consider the system of Figure 3.6 where the discrete-time plant $G_{true}(z)$, is the zero-order hold equivalent of the continuous-time plant of Section 3.2. $G_{true}(z)$ has input u[n], output y[n], and an additive output disturbance d[n]. We make the following assumptions, which we label for later reference with the letters 'AD' referring to the fact that they are assumptions concerning the discrete-time plant, disturbance and input.

AD1) Plant Assumptions. We assume a structure for the nominal model of $G_{true}(z)$ and a magnitude bounding function on the unstructured uncertainty. That is, we assume that

$$G_{true}(z) = G(z,\theta_0) [1 + \delta_u(z)] \qquad (3.6.1)$$

where $G(z,\theta_0)$ is a nominal model, $\delta_u(z)$ denotes the unstructured uncertainty of the plant, θ_0 is a

vector of plant parameters and we assume,

AD1.1) $G(z,\theta_0) = B(z) / A(z)$, (3.6.2)

where the polynomials B(z) and A(z) for the discrete-time system are,

$$B(z) = b_0 z^{(m_1-n_1)} + b_1 z^{(m_1-n_1-1)} + \ldots + b_{m1} z^{-n_1}, \quad (3.6.3)$$

$$A(z) = 1 - a_1 z^{-1} + \ldots - a_{n1} z^{-n_1}, \quad n_1 > m_1, \quad (3.6.4)$$

and where the parameter vector of the discrete-time plant is,

$$\theta_0 = [\, a_1 \ldots a_{n1} \;\; b_0 \;\; b_1 \ldots b_{m1} \,]^T. \quad (3.6.5)$$

AD1.2) $\theta_0 \in \Theta$, where Θ is a known bounded set. (3.6.6)

This assumptions means that we have some coarse prior idea of what the discrete-time parameters are. The bounded set Θ will be used to compute various a priori bounds in Chapters 5 and 6.

AD1.3) $|\delta_u(e^{j\omega T})| \le \Delta_u(e^{j\omega T}), \; \forall\omega.$ (3.6.7)

This assumption is our characterization of the discrete-time unmodeled dynamics. In Section 4.4, we use this assumption to find a time-domain bound on the effects of unstructured uncertainty. In addition, it is used in Section 5.6 to make the frequency-domain estimation method robust.

AD1.4) $|d\delta_u(e^{j\omega T})/d\omega| \le \nabla_u(e^{j\omega T}), \; \forall\omega.$ (3.6.8)

This assumption tells us how smooth the discrete-time unmodeled dynamics are. In Sections 5.7 and 5.8, we use this assumption to smooth out our bound on the uncertainty and to bound the inter-sample variations of the uncertainty between the discrete frequency samples of our bounding function.

AD1.5) $G_{true}(z)$ and $G(z,\theta_0)$ have all their poles in the open unit disk for all $\theta_0 \in \Theta$.

Thus, we assume that the true discrete-time plant is asymptotically stable. This assumption is required by the frequency-domain estimation method. The relaxation of this assumption is discussed in Section 10.2.

AD1.6) A bounding function on the magnitude of the impulse response of the true plant, denoted by $g_{true}[n]$, is known such that

$$|g_{true}[n]| \le \sum_{i=1}^{I_0} g_i \, n^{(r_i)} \, p_i^n, \quad (3.6.9)$$

where r_i is a positive integer, and $g_i > 0$, $0 < p_i < 1$ (i.e. all the poles of $g_{true}[n]$ are in the open unit disk) and r_i are known for $i=1, \ldots, I_0$. $g_{true}[n]$ is assumed to be causal. This assumption is saying that we know some coarse bounding function on the impulse response of the partially known discrete-time plant. In Section 5.2, this assumption is used to compute a frequency-domain bounding function on the estimation error.

AD1.7) A bounding function on the magnitude of the impulse response of the additive plant error, that is, we assume we know a bounding function of the same form as Eqn. (3.6.9) on $|g_{true}[n] - g[n,\theta_0]|$, for all $\theta_0 \in \Theta$, where $g[n,\theta_0]$ is the impulse response of $G(z,\theta_0)$. This assumption means that we know some coarse bounding function on the impulse response of the additive plant error that is due to the unmodeled dynamics. In Section 4.4, this assumption is used to make the time-domain parameter estimator robust to the effects of the unstructured uncertainty.

AD1.8) zero initial conditions.

Thus, our a priori assumptions are that we know m_1 and n_1, the degrees of B(z) and A(z), respectively, and the bounding functions $\Delta_u(e^{j\omega T})$ and $\nabla_u(e^{j\omega T})$. Further, we assume that the parameter vector θ_0 is in some known bounded set Θ, which is only a coarse and, hence, large a priori estimate of the parameter space. We do not assume that the plant is minimum phase as is done in the classical MRAC approach.

AD2) Disturbance Assumptions. We assume that the unmeasurable disturbance d[n] satisfies:

AD2.1) $|d[n]| \leq d_{max}$, $\forall n$, and (3.6.10)

AD2.2) the N-point DFT of the signal $d^+[n]$, defined as in Eqn. (3.5.5), satisfies

$$|D_N^{+n}(\omega_k)| \leq \begin{cases} \overline{D}_N^{+n}(\omega_k), & \text{for } n = 0, 1, \ldots, N-2 \\ \overline{\overline{D}}_N(\omega_k), & \text{for } n \geq N-1, \end{cases} \qquad (3.6.11)$$

$$\text{for } k = 0, \ldots, N-1,$$

where the constant d_{max} is known and the time function $\overline{D}_N^{+n}(\omega_k)$ and the constant $\overline{\overline{D}}_N(\omega_k)$ are known, for each ω_k.

AD3) Input and Output Signal Assumptions. We assume that both the input signal u[n] and the output signal y[n] are measurable and that u[n] is bounded.

AD3.1) $|u[n]| \leq u_{max}$, $\forall n$, where u_{max} is known a priori. (3.6.12)

Remark 1: We note that the assumption of a stable plant (AD1.5) and a bounded plant input (AD3.1) implies the boundness of the plant output. Thus, even in a closed-loop situation the plant output is bounded. However, such a closed-loop system could exhibit wild oscillations with u[n] oscillating between $+u_{max}$ and $-u_{max}$. We emphasize that this is not the kind of stability that we are looking for. Instead, we seek a closed-loop system that has all its poles in the open unit disk. In this case, if the plant control input never saturates, that is, $|u[n]|$ remains less than u_{max}, then we have an exponentially stable closed-loop system.

Remark 2: The parameter vector θ_0 can be thought of as a specific value. However, based on input/output measurements alone we cannot determine a specific θ_0 for the nominal model because of the unstructured uncertainty. That is, if we assume the structure of AD1.1 above and assume only that

$$\delta_u(z) \in \mathbf{S} \text{ where } \mathbf{S} = \{ \delta(z) \mid |\delta(e^{j\omega T})| \leq \Delta_u(e^{j\omega T}), \forall \omega \}, \quad (3.6.13)$$

then we can define a smallest set

$$\Theta^* = \{ \theta \mid G_{true}(z) = G(z,\theta)\,[1 + \delta_u(z)] \text{ and } \delta_u(z) \in \mathbf{S} \} \quad (3.6.14)$$

in which θ_0 lies. Thus, $\theta_0 \in \Theta^* \subset \Theta$ where only Θ is known a priori. Note that, in general, Θ^* will be a point only when $\Delta_u(e^{j\omega T})=0$ for all ω.

Remark 3: As has already been noted, assumptions AD1-3 above can be satisfied using the information of assumptions AC1-3 of Section 3.2. Specifically,

1) AD1.1-2 follow from AC1.1-2 and the results of Subsections 3.3.1 and 3.3.4.
2) AD1.3 follows from AC1.3 plus AC1.1-2 and the results of Subsections 3.3.2 and 3.3.4.
3) AD1.4 follows from AC1.4 plus AC1.1-3 and the results of Subsections 3.3.3 and 3.3.4.
4) AD1.5 follows from AC1.5.

5) AD1.6 and AD1.7 follow from AC1.6 and AC1.7, respectively, and the results of Section 3.4.
7) AD1.8 follows from AC1.8 and the assumption that the zero-order hold has zero initial conditions.
8) AD2.1 and 3.1 follow from AC2.1 and 3.1, respectively.
9) AD2.2 follows from AC2.2 and the results of Section 3.5.

3.7 Discrete-time Statement of the Robust Estimation Problem and Solution Summary

In this section, we will state the robust estimation problem and then outline the problem solution which will be developed in the following chapters of this thesis.

3.7.1 Robust Estimation Problem Statement

Since complex adaptive control algorithms will ultimately be implemented on a digital computer, we focus on the development of discrete-time estimation methods. We can use a discrete-time estimator to identify the zero-order hold equivalent of a continuous-time plant. It was shown in Sections 3.3-3.5, how the continuous-time assumptions AC1-3 of Section 3.2 could be used to satisfy the discrete-time assumptions AD1-3 of Section 3.6. Thus, we will use these discrete-time assumptions as a starting point for our problem statement.

We rewrite the true discrete-time plant of Eqn. (3.6.1), formed via the zero-order hold equivalence of the continuous-time plant, as

$$G_{true}(z) = G(z,\hat{\theta})\,[1 + \delta_{su}(z,\hat{\theta})],\quad \hat{\theta} \in \Theta \tag{3.7.1}$$

where again $G(z,\hat{\theta})$ is the nominal model using an estimate $\hat{\theta}$ of the true parameter vector θ_0 in the structure of assumption AD1.1, and $\delta_{su}(z,\hat{\theta})$ denotes the modeling error due to both structured and unstructured uncertainty. That is, since a priori we only know that $\hat{\theta} \in \Theta$, where $\hat{\theta}$ is not necessarily in Θ^*, there is structured uncertainty associated with this choice of $\hat{\theta}$ as well as the ever present unstructured uncertainty.

Problem Statement: The robust estimator must provide:

1) a parameter estimate $\hat{\theta}$ and, hence, a nominal model $G(z, \hat{\theta})$,

2) a corresponding bounding function, $\Delta_{su}^{n}(e^{j\omega T}, \hat{\theta})$, such that

$$|\delta_{su}(e^{j\omega T}, \hat{\theta})| \leq \Delta_{su}^{n}(e^{j\omega T}, \hat{\theta}), \ \forall\omega. \tag{3.7.2}$$

That is, at a given sample time n we want to generate a new nominal model $G(z, \hat{\theta})$, and a corresponding bounding function $\Delta_{su}^{n}(e^{j\omega T}, \hat{\theta})$ in the frequency domain indicating how good the current nominal model is. The robust estimator need only provide the above information at the times that a control-law update is computed.

The goal of the robust estimator is to find a $\hat{\theta}$ in Θ^* and have $\Delta_{su}^{n}(e^{j\omega T}, \hat{\theta})$ approach $\Delta_u(e^{j\omega T})$. The viewpoint taken here is that the unstructured uncertainty $\Delta_u(e^{j\omega T})$ is the best we can do given the structure of our nominal model. If the bound $\Delta_u(e^{j\omega T})$ is chosen to be larger than the actual unmodeled dynamics, then parameters can be found for the finite-dimensional nominal model that yield a smaller uncertainty bound than $\Delta_u(e^{j\omega T})$. Thus, the robust estimator can yield a total uncertainty bound $\Delta_{su}^{n}(e^{j\omega T}, \hat{\theta})$ that is even smaller than $\Delta_u(e^{j\omega T})$. In the robust estimator, we will not let $\Delta_{su}^{n}(e^{j\omega T}, \hat{\theta})$ become smaller than our a priori assumed bound $\Delta_u(e^{j\omega T})$, when computing control-law updates. We view the function $\Delta_u(e^{j\omega T})$ as the desirable lower bound of the function $\Delta_{su}^{n}(e^{j\omega T}, \hat{\theta})$.

The problem that we have described in this subsection will be referred to as the robust estimation problem. An algorithm which satisfies this problem will be referred to as a robust estimator since it provides a nominal model of the plant as well as a guaranteed frequency-domain bounding function on the accuracy of this nominal model.

3.7.2 Outline of Problem Solution

In the following two chapters of this thesis, we will develop a solution to the robust estimation problem stated in the previous subsection. First, in Chapter 4, we will describe a robust time-domain parameter estimator for plants with unstructured uncertainty and an unmeasurable disturbance. Then, in Chapter 5, we will describe a frequency-domain parameter estimation method. Thus, we will present two methods of generating a parameter estimate and, hence, the nominal model, one being a time-domain method and the other being a frequency-domain method. Later, in the simulations, we will reveal some weaknesses of the specific algorithm employed in the time-domain parameter estimation method of Chapter 4, so we will choose to use the frequency-domain parameter estimator over the time-domain parameter estimator. In Chapter 5 we will also develop a frequency-domain bounding methodology that will yield a set of points versus frequency which upper bound the magnitude of the function $\delta_{su}(e^{j\omega T}, \hat{\theta})$ at those frequency points. We will see that the frequency-domain methods of Chapter 5 will require extensive real-time computations.

CHAPTER 4.
ROBUST TIME-DOMAIN PARAMETER ESTIMATION

4.1 Introduction

In this chapter, we will develop a new type of deterministic, discrete-time parameter estimator. First, we will motivate the use of a robust time-domain parameter estimator. Then, in Sections 4.2-4, we will develop a mechanism to bound, in the time-domain, the effects of both unmodeled dynamics and an unmeasurable disturbance. Lastly, in Section 4.5 this bounding mechanism will be used together with a time-varying dead-zone to make a least-squares parameter estimator robust.

Most current parameter estimation techniques provide unreliable estimates in the presence of unmodeled dynamics and an unmeasurable disturbance. For example, assume that a large, persistently exciting, sufficiently rich signal was present for a long time so that the algorithm's parameter estimates were good. Then, assume that the input signal suddenly became zero but the disturbance continued to excite the system. In this case, the parameter estimates would diverge from their previously good values. As another example, consider what happens when the plant input signal excites the high-frequency unmodeled dynamics, that is, the dynamics we constrain with the unstructured uncertainty bound. In this case, the plant output signal is greatly affected by the high-frequency unmodeled dynamics so that the parameter estimates yielded by standard estimation techniques will have very little to do with the actual parameters of the low-frequency nominal model. We need an algorithm which will adjust the parameter estimates when there is good information about the parameters in the input/output data but we want the algorithm to stop updating the estimates when there is no useful information available.

It is the goal of this chapter to develop an algorithm that can be used with confidence in the presence of unmodeled dynamics and an unmeasurable disturbance. The resultant time-domain parameter estimator is actually a combination of the bounding mechanism that we develop in Sections 4.2-4 and a modified least-squares algorithm that was developed by Goodwin et al. [17,18]. This modified least-squares algorithm is made robust through the use of a time-varying dead-zone. The new contribution of this chapter is the development of the time-domain bounding mechanism of Sections 4.2-4. This mechanism uses the assumptions of the robust estimator, for example the assumption of a frequency-domain bound on the unstructured uncertainty. Goodwin et al. [17,18] use a different bounding mechanism in their development of a robust parameter estimator. Their bounding mechanism requires different types of assumptions than those used in development of the robust estimator.

4.2 Development of the Linear Regression Form of the Plant

4.2.1 Development of DARMA Form

Before presenting the time-domain parameter estimation algorithm, we will give some definitions that allow us to represent our previous discrete-time transfer function of the nominal model in a deterministic autoregressive moving-average (DARMA) form. We again consider the discrete-time system of Figure 3.6 where

$$y[n] = g_{true}[n] * u[n] + d[n]. \tag{4.2.1}$$

and where '*' denotes convolution. We can use the forward shift operator q in the polynomials of assumption AD1 of Section 3.6, to write

$$y[n] = [G_{true}(q)]\, u[n] + d[n] \tag{4.2.2}$$

$$= [\, (\, B(q) / A(q)\,)\, [1 + \delta_u(q)]\,]\, u[n] + d[n]. \tag{4.2.3}$$

So,

$$y[n] = [B(q) / A(q)]\, u[n] + [B(q)\, \delta_u(q) / A(q)]\, u[n] + d[n]. \tag{4.2.4}$$

Multiplying both sides by the operator [A(q)] yields

$$[A(q)]\, y[n] = [B(q)]\, u[n] + [B(q)\, \delta_u(q)]\, u[n] + [A(q)]\, d[n]. \tag{4.2.5}$$

Rewriting yields,

$$y[n] = [1-A(q)]\, y[n] + [B(q)]\, u[n] + [B(q)\, \delta_u(q)]\, u[n] + [A(q)]\, d[n]. \tag{4.2.6}$$

We define the signal regression vector,

$$\phi[n-1] = [\, y[n-1] \;\; y[n-2] \;\; \ldots \;\; y[n-n_1] \;\; u[n-n_1+m_1] \;\; u[n-n_1+m_1-1] \;\; \ldots \;\; u[n-n_1]\,]^T. \tag{4.2.7}$$

Now, Eqn. (4.2.5) can be rewritten as,

$$y[n] = \phi[n-1]^T \theta_0 + e_0[n], \tag{4.2.8}$$

where

$$e_0[n] = [B(q)\, \delta_u(q)]\, u[n] + [A(q)]\, d[n], \tag{4.2.9}$$

and where θ_0 is the true parameter vector of the nominal model, as defined in AD1. Goodwin et al. [17] observe that Eqn. (4.2.8) will, in general, be unsuitable for parameter estimation since the error $e_0[n]$ involves "near differentiation" of the input and the disturbance. As suggested in [17], we will prefilter both the input and the output signals, u[n] and y[n], to avoid this problem. We

define the filter in the forward shift operator,

$$F(q) = q^{(n_1)} / W(q) \tag{4.2.10}$$

where the polynomial W(q) has order n_1 or greater and has all its zeros in the open unit disk. Now, we define the filtered versions of the input and output signals,

$$u_f[n] = [F(q)]\, u[n], \tag{4.2.11}$$

$$y_f[n] = [F(q)]\, y[n]. \tag{4.2.12}$$

Multiplying both sides of Eqn. (4.2.5) by the operator [F(q)] yields

$$[A(q)\, F(q)]\, y[n] = [B(q)\, F(q)]\, u[n] + [B(q)\, F(q)\, \delta_u(q)]\, u[n] + [A(q)\, F(q)]\, d[n] \tag{4.2.13}$$

or

$$[A(q)]\, y_f[n] = [B(q)]\, u_f[n] + [B(q)\, F(q)\, \delta_u(q)]\, u[n] + [A(q)\, F(q)]\, d[n]. \tag{4.2.14}$$

Rearranging yields,

$$y_f[n] = [1-A(q)]\, y_f[n] + [B(q)]\, u_f[n] + [B(q)\, F(q)\, \delta_u(q)]\, u[n] + [A(q)\, F(q)]\, d[n]. \tag{4.2.15}$$

We define the signal regression vector containing the filtered signals,

$$\phi_f[n-1] = [\, y_f[n-1] \;\; y_f[n-2] \;\ldots\; y_f[n-n_1] \;\; u_f[n-n_1+m_1] \;\; u_f[n-n_1+m_1-1] \;\ldots\; u_f[n-n_1]\,]^T. \tag{4.2.16}$$

Now, we see that Eqn. (4.2.15) can be written as,

$$y_f[n] = \phi_f[n-1]^T \theta_0 + e_1[n], \tag{4.2.17}$$

where

$$e_1[n] = [B(q)\, F(q)\, \delta_u(q)]\, u[n] + [A(q)\, F(q)]\, d[n]. \tag{4.2.18}$$

In summary, we have developed a DARMA model for the discrete-time plant of Chapter 3. Further, we have used filtering to avoid "near differentiation" of the signals, u[n] and d[n].

4.2.2 Decomposition of the Error Signal

In this subsection, we will introduce several definitions so that we can decompose the error signal $e_1[n]$ defined in Eqn. (4.2.18). First, we define the transfer functions

$$H_u(z) = B(z)\, F(z)\, \delta_u(z), \tag{4.2.19}$$

$$H_d(z) = A(z)\, F(z). \tag{4.2.20}$$

As can be seen from Eqn. (4.2.18), $H_u(z)$ is the transfer function from the plant input to the equation error $e_1[n]$. This transfer function describes the effect of the additive plant error, which is due to the unmodeled dynamics, on the equation error. As can also be seen from Eqn. (4.2.18), $H_d(z)$ is the transfer function from the disturbance to the equation error $e_1[n]$. We can rewrite Eqn. (4.2.18) as

$$e_1[n] = h_u[n] * u[n] + h_d[n] * d[n]. \tag{4.2.21}$$

where the impulse responses of $H_u(z)$ and $H_d(z)$ are denoted by $h_u[n]$ and $h_d[n]$, respectively. We decompose Eqn. (4.2.21) by defining

$$e_1[n] = e_2[n] + e_3[n], \tag{4.2.22}$$

where

$$e_2[n] = h_u[n] * u[n] \tag{4.2.23}$$

$$e_3[n] = h_d[n] * d[n] \tag{4.2.24}$$

The signal $e_2[n]$ is the part of the equation error $e_1[n]$ that is due only to the unmodeled dynamics. The signal $e_3[n]$ is the part of the equation error $e_1[n]$ that is due only to the disturbance. To bound $e_1[n]$ at each time index n, we will find a time-varying magnitude bound on $e_2[n]$ and $e_3[n]$ individually. That is,

$$|e_1[n]| \leq |e_2[n]| + |e_3[n]|. \tag{4.2.25}$$

4.2.3 Outline of the Time-domain Error Bounding Technique

In the following two sections we will develop magnitude bounding functions on the component parts, $e_2[n]$ and $e_3[n]$, of the equation error $e_1[n]$ using the results of Theorem 2.4 of Chapter 2. It will be advantageous to first find a bounding function on $e_3[n]$ since the results found in this process will be useful in trying to find a bounding function on $e_2[n]$. Given such a bound, we will later be able to robustify the standard least-squares algorithm to the effects of unstructured uncertainty and an unmeasurable disturbance.

Since the following two chapters are rather involved in their derivations of these bounds, it is important to keep a perspective on what the important parts of the development are. As can be seen from Theorem 2.4, we will be using essentially a frequency-domain methodology to find the required time-domain bounding functions for $e_2[n]$ and $e_3[n]$. However, we must also consider the effect of the remainder terms due to the infinite-length of the impulse responses. To bound this

effect, we must use a complicated, conservative scheme in the case of $e_2[n]$, since we chose to use only the assumptions listed in Section 3.6. We are forced to take this approach since we want guaranteed bounds. It is stressed that, although the development is lengthy, the bounding of the remainder terms due to the infinite-length of the impulse responses, is only a relatively minor part of our development. We want to provide rigorous bounds, however, the chief contribution to our time-domain bounds will be due to the frequency-domain summations, not the generally smaller remainder terms.

4.3 Time-domain Error Bounding of Disturbance Effects

4.3.1 Different Bounding Methodologies

In this section, we will find a magnitude bounding function on $e_3[n]$. This signal is the effect of the disturbance on the equation error. We note that $H_d(z)$, which is the transfer function from the disturbance to the equation error, must have all its poles in the open unit disk since F(z) has all its poles in the open unit disk. This means that the frequency-domain methods that were developed in Section 2.2 can be applied. The signal $e_2[n]$ can be bounded using one of three methods, each of which we outline below:

Method 1: **We compute a magnitude bounding function on the DTFT of d[n] using assumption** AC2.2 and Eqn. (2.1.12). Then, we find a magnitude bounding function on $H_d(e^{j\omega T})$. These two magnitude bounding functions are used, along with the equation for the inverse DTFT to compute a magnitude bound on $e_3[n]$, in a way similarly to that used for the inverse DFT in Theorem 2.4.

Method 2: We compute a magnitude bounding function on $h_d[n]$, which will be of the same form as the bounding function of assumption AD1.6,

$$\sum_{i=1}^{I_0} g_i \, n^{(r_i)} \, p_i^n. \tag{4.3.1}$$

Then, the summation formulas in Appendix C can be used to compute the constant bounding function,

$$|e_3[n]| \leq d_{max} \{ \sum_{n=0}^{\infty} |h_d[n]| \}, \qquad (4.3.2)$$

where d_{max} is known from assumption AD2.1.

Method 3: We compute a magnitude bounding function on $H_d(e^{j\omega_k T})$ for each k, and a magnitude bounding function on $h_d[n]$ which again, will be of the form of Eqn. (4.3.1). Then we use assumption AD2.1-2 and Theorem 2.4 to find a magnitude bounding function on $e_3[n]$.

Discussion:

We choose to use method 3 from above since it uses assumptions AD2.1-2 rather than AC2.2, as does method 1. Later, we will concentrate on the investigation of the properties of the DFTs of different disturbance models. It would complicate matters if we were instead to work with the Fourier transform of the disturbance and then have to perform the frequency-domain folding of Eqn. (2.1.12). In addition, later in the frequency-domain bounding methodology of Chapter 5, we will also be using a magnitude bounding function on the DFT of the disturbance, that is, the function of assumption AD2.2. Thus, we choose to work entirely with the DFT of d[n]. However, we do note that method 1 does not require knowledge of a magnitude bound on d[n], as do both methods 2 and 3. This is because our ultimate goal here is to bound the error signal $e_3[n]$, not the disturbance itself.

Method 2 is not used since it will, in general, be more conservative than method 3. This statement of relative conservativeness actually depends on how good the different bounds of AD2.1 and AD2.2 are relative to one another. For example, if a tight bound on the magnitude of the DFT of the disturbance is known and only a coarse bound on |d[n]| is known, then method 3 will yield a tighter bounding function on $|e_3[n]|$ than method 2. However, if only a coarse bound on the magnitude of the DFT of the disturbance is known and a tight bound on |d[n]| is known, then method 2 could yield a tighter bound on $|e_3[n]|$.

As a final note, we point out that method 3 actually contains elements of both methods 1 and 2. That is, method 1 is essentially a purely frequency-domain methodology, and method 2 is a purely time-domain methodology, while method 3 uses both frequency-domain and time-domain bounding methodologies, as is evident from Theorem 2.4.

4.3.2 Development of a Bounding Function using Method 3

First, we find a magnitude bounding function on $H_d(e^{j\omega_k T})$, for k=0, . . , (N/2), where we assume that N is even. Recall that ω_k is defined in Eqn. (2.1.4). At this point in our development, we must include the fact that the transfer function $H_d(z)$ is actually a function of the parameter vector θ, which is only coarsely known . That is, using Eqn. (4.2.20), and assumptions AD1.1-2,

$$H_d(z,\theta) = A(z,\theta)\, F(z) \text{ , where } \theta \in \Theta. \tag{4.3.3}$$

Thus, we find that,

$$|H_d(e^{j\omega_k T},\theta)| \le \overline{H}_d(e^{j\omega_k T}), \text{ for } k = 0, \ldots, (N/2), \tag{4.3.4}$$

where

$$\overline{H}_d(e^{j\omega_k T}) = \sup_{\theta\in\Theta} \{ |A(e^{j\omega_k T},\theta)| \}\, |F(e^{j\omega_k T})|, \text{ for } k = 0, \ldots, (N/2). \tag{4.3.5}$$

The above bounding function is computed off-line as part of the design procedure.

To find a magnitude bounding function on the impulse response of $h_d[n]$ we must include its θ dependence. The structure of $H_d(z,\theta)$ is known, as is apparent from Eqn. (4.3.3), so we can find an expression for $h_d[n,\theta]$ in terms of the parameter vector θ. Thus, assumptions AD1.1-2 have allowed us to define the following bounding function,

$$|h_d[n,\theta]| \le \overline{h}_d[n], \ \forall n, \tag{4.3.6}$$

where

$$\overline{h}_d[n] = \sup_{\theta\in\Theta} \{ |h_d[n,\theta]| \}, \text{ for } n = 0, 1, \ldots \tag{4.3.7}$$

Since the transfer function F(z) has all its poles in the open unit disk, the bound of Eqn. (4.3.7) will be of the form,

$$\overline{h}_d[n] = \sum_{i=1}^{I_0} g_i\, n^{(r_i)}\, p_i^n, \tag{4.3.8}$$

where $0 < p_i < 1$, $\forall i$, and the largest p_i corresponds to the slowest pole of F(z). For simplicity, we assume here that

$$\overline{h}_d[n] = g_1\, p_1^n, \text{ for } n = 0, 1, \ldots \tag{4.3.9}$$

Given Eqns. (4.3.4-5), the bounding function $\overline{h}_d[n]$, plus d_{max} and $\overline{D}_N^{+n}(e^{j\omega_k T})$ from AD2.1, we can use Theorem 2.4 to find,

$$|e_3[n]| \leq \overline{e}_3[n], \tag{4.3.10}$$

where

$$\overline{e}_3[n] = \frac{1}{N}\{\overline{H}_d(e^{j\omega_0 T})\,\overline{D}_N^{+n}(\omega_0) + 2\sum_{k=1}^{(N/2)-1}\overline{H}_d(e^{j\omega_k T})\,\overline{D}_N^{+n}(\omega_k)$$

$$+ \overline{H}_d(e^{j\omega_{(N/2)} T})\,\overline{D}_N^{+n}(\omega_{(N/2)})\} + 2\,d_{max}\sum_{p=N}^{\infty}\overline{h}_d[p], \tag{4.3.11}$$

$$\text{for } n = 0, \ldots, N-2,$$

and where using Eqn. (4.3.9) and Eqn. (C.4) of Appendix C, we find

$$\sum_{p=N}^{\infty}\overline{h}_d[p] = g_1\,p_1^{\,N}/(1 - p_1). \tag{4.3.12}$$

For $n \geq N-1$, $\overline{e}_3[n]$ equals $\overline{e}_3$, a constant. Thus, with reference to assumption AD2.2,

$$\overline{e}_3 = \frac{1}{N}\{\overline{H}_d(e^{j\omega_0 T})\,\overline{D}_N(\omega_0) + 2\sum_{k=1}^{(N/2)-1}\overline{H}_d(e^{j\omega_k T})\,\overline{D}_N(\omega_k)$$

$$+ \overline{H}_d(e^{j\omega_{(N/2)} T})\,\overline{D}_N(\omega_{(N/2)})\} + 2\,d_{max}\sum_{p=N}^{\infty}\overline{h}_d[p]. \tag{4.3.13}$$

In summary, we have computed a time-varying bound on the magnitude of $e_3[n]$, which is the component of the equation error that is due to the disturbance. For $n \geq N-1$, the bounding function becomes a constant. A method for bounding the remainder term due to the fact that $h_d[n]$ has an infinite-length rather than finite-length impulse response has been developed. This method has been illustrated through the use of a simple first-order bounding function. The bounding function of Eqn. (4.3.11) and the bound of Eqn. (4.3.13) are computed off-line as part of the design procedure.

4.4 Time-domain Error Bounding of the Effects of Unstructured Uncertainty

In this section, we will find a magnitude bounding function on $e_2[n]$. This signal represents the effect of the unstructured uncertainty on the equation error. We note that $H_u(z)$ must have all its poles in the open unit disk since we know that both F(z) and $B(z)\delta(z)$, via assumption AD1.5, have all their poles in the open unit disk. Thus, we can apply the frequency-domain methods developed in Section 2.2. While it is possible to use any of the three methods listed in Subsection 4.3.1, we will be using method 3, since we will be able to find a good frequency-domain bounding function on $|H_u(e^{j\omega_k T})|$, but will only be able to find a very conservative bounding function on $|h_u[n]|$. A magnitude bounding function on the DFT of the input signal will be computed on-line and used in combination with a precomputed bounding function on $|H_u(e^{j\omega_k T})|$ to compute, on-line, a time-varying bound on $|e_2[n]|$.

4.4.1 Computation of a Magnitude Bounding Function on $H_u(e^{j\omega_k T})$

First, we find a magnitude bounding function on $H_u(e^{j\omega_k T})$, for k=0, . . , (N/2), where we assume that N is even. Again, recall that ω_k is defined in Eqn. (2.1.4). Now, we must include the fact that the transfer function $H_u(z)$ is actually a function of the parameter vector θ, which is only coarsely known . That is, using Eqn. (4.2.19), and assumptions AD1.1-2,

$$H_u(z,\theta) = B(z,\theta)\, F(z)\, \delta_u(z), \text{ where } \theta \in \Theta. \tag{4.4.1}$$

Using AD1.1-3, we find

$$|H_u(e^{j\omega_k T},\theta)| \le \overline{H}_u(e^{j\omega_k T}), \text{ for } k = 0, \ldots, (N/2), \tag{4.4.2}$$

where

$$\overline{H}_u(e^{j\omega_k T}) = \sup_{\theta\in\Theta} \{ |B(e^{j\omega_k T},\theta)| \}\, |F(e^{j\omega_k T})|\, \Delta_u(e^{j\omega_k T}). \tag{4.4.3}$$

$$\text{for } k = 0, \ldots, (N/2).$$

The above bounding function is computed off-line as part of the design procedure.

4.4.2 Computation of a Magnitude Bounding Function on $h_u[n]$

The magnitude bounding function on $h_u[n]$ is difficult to compute. Recall that $h_u[n]$ is the impulse response of the transfer function from the plant input to the equation error. The required bounding function will be found using assumptions AD1.1-2 and AD1.7; however, the resulting bounding function will be conservative. Consider the model for the true plant which was introduced in AD1,

$$G_{true}(z) = G(z,\theta)\,[1 + \delta_u(z)]. \tag{4.4.4}$$

Then the impulse response of $G_{true}(z)$ can be written as,

$$g_{true}[n] = g[n,\theta] + g[n,\theta] * \tilde{\delta}_u[n] \tag{4.4.5}$$

where the impulse responses of $G(z,\theta)$ and $\delta_u(z)$ are denoted by $g[n,\theta]$ and $\tilde{\delta}_u[n]$, respectively. Now, we find that

$$|g[n,\theta] * \tilde{\delta}_u[n]| = |g_{true}[n] - g[n,\theta]|. \tag{4.4.6}$$

In order to simplify our notation, we define the impulse response

$$h_{g\delta}[n,\theta] = g[n,\theta] * \tilde{\delta}_u[n]. \tag{4.4.7}$$

From assumption AD1.7 and Eqns. (4.4.6-7), we know a bounding function $\bar{h}_{g\delta}[n]$ such that

$$|h_{g\delta}[n,\theta]| \le \bar{h}_{g\delta}[n], \ \forall n, \tag{4.4.8}$$

where $\bar{h}_{g\delta}[n]$ is of the form of assumption AD1.6, that is,

$$\bar{h}_{g\delta}[n] = \sum_{i=1}^{I_0} g_i\, n^{(r_i)}\, p_i{}^n. \tag{4.4.9}$$

Note that the largest p_i of Eqn. (4.4.9) corresponds to the slowest pole of $G_{true}(z)$. At this point, we will assume for simplicity that $|h_{g\delta}[n,\theta]|$ can be bounded by a simple first-order system, that is, we assume that

$$\bar{h}_{g\delta}[n] = g_2\, p_2{}^n, \ \text{for } n = 0, 1, \ldots \tag{4.4.10}$$

Thus, we have not explicitly bounded $|\tilde{\delta}_u[n]|$, but have instead bounded $|g[n,\theta] * \tilde{\delta}_u[n]|$. We will

be able to use this bounding function on $|h_{g\delta}[n,\theta]|$ to find a bounding function on $|e_2[n]|$.

First, we observe that the transfer function corresponding to the impulse response $h_{g\delta}[n,\theta]$ is given by

$$G(z,\theta)\,\delta_u(z) = B(z,\theta)\,\delta_u(z) / A(z,\theta). \tag{4.4.11}$$

We find from Eqns. (4.2.19-20) and (4.4.11) that,

$$H_u(z,\theta) = H_d(z,\theta)\,G(z,\theta)\,\delta_u(z), \text{ where } \theta \in \Theta. \tag{4.4.12}$$

The magnitude of the impulse response of $H_d(z,\theta)$ has already been bounded by the function of Eqn. (4.3.7). From Eqn. (4.4.12) we find that

$$h_u[n,\theta] = h_d[n,\theta] * h_{g\delta}[n,\theta]. \tag{4.4.13}$$

or

$$h_u[n,\theta] = \sum_{m=-\infty}^{\infty} h_d[m,\theta]\,h_{g\delta}[n-m,\theta] = \sum_{m=0}^{n} h_d[m,\theta]\,h_{g\delta}[n-m,\theta] \tag{4.4.14}$$

since $h_d[n,\theta]$ and $h_{g\delta}[n,\theta]$ are causal impulse responses. Now, we find that

$$|h_u[n,\theta]| \le \sum_{m=0}^{n} |h_d[m,\theta]|\,|h_{g\delta}[n-m,\theta]|. \tag{4.4.15}$$

So, using Eqns. (4.3.6) and (4.4.8) yields

$$|h_u[n,\theta]| \le \overline{h}_u[n], \ \forall n, \tag{4.4.16}$$

where

$$\overline{h}_u[n] = \sum_{m=0}^{n} \overline{h}_d[m]\,\overline{h}_{g\delta}[n-m]. \tag{4.4.17}$$

We now can use the assumed forms of Eqns. (4.3.9) and (4.4.10) in Eqn. (4.4.17) to find

$$\overline{h}_u[n] = \sum_{m=0}^{n} g_1\,p_1^{\,m}\,g_2\,p_2^{\,n-m}. \tag{4.4.18}$$

Manipulation yields

$$\overline{h}_u[n] = \{ g_1 g_2 \sum_{m=0}^{n} (p_1 / p_2)^m \} p_2^n. \tag{4.4.19}$$

We consider two possibilities in Eqn. (4.4.19). The following results are from Appendix D.

Case 1. ($p_1 \neq p_2$) In this case,

$$\overline{h}_u[n] = g_1 g_2 [(p_2^{n+1} - p_1^{n+1}) / (p_2 - p_1)]. \tag{4.4.20}$$

Case 2. ($p_1 = p_2$) In this case,

$$\overline{h}_u[n] = \{ g_1 g_2 (n+1) \} p_1^n. \tag{4.4.21}$$

More complex forms of the bounding functions $\overline{h}_d[n]$ and $\overline{h}_{g\delta}[n]$ are also considered in Appendix D.

Given Eqn. (4.4.2), the bounding function $\overline{h}_u[n]$, u_{max} from assumption AD3.1, and the on-line computed values of $|U_N^n(e^{j\omega_k T})|$ we can use Theorem 2.4 to find,

$$|e_2[n]| \leq \overline{e}_2[n], \tag{4.4.22}$$

where

$$\overline{e}_2[n] = \frac{1}{N} \{ \overline{H}_u(e^{j\omega_0 T}) |U_N^n(\omega_0)| + 2 \sum_{k=1}^{(N/2)-1} \overline{H}_u(e^{j\omega_k T}) |U_N^n(\omega_k)| + \overline{H}_u(e^{j\omega_{(N/2)} T}) |U_N^n(\omega_{(N/2)})| \} + 2 u_{max} \sum_{p=N}^{\infty} \overline{h}_u[p], \text{ for } n = 0, 1, . . \tag{4.4.23}$$

Further, for the two illustrative cases of Eqns. (4.4.20-21), we find bounds on the infinite sum.

Case 1. ($p_1 \neq p_2$) In this case, using Eqn. (C.4) from Appendix C we find that

$$\sum_{p=N}^{\infty} \overline{h}_u[p] = [g_1 g_2 / (p_2 - p_1)] [p_2^{N+1} / (1 - p_2) - p_1^{N+1} / (1 - p_1)] \tag{4.4.24}$$

Case 2. ($p_1 = p_2$) In this case, using Eqn. (C.4) and (C.10) we find

$$\sum_{p=N}^{\infty} \overline{h}_u[p] = g_1 g_2 p_1^N (N (1 - p_1) + 1) / (1 - p_1)^2 . \tag{4.4.25}$$

In summary, we have computed a time-varying bound on the magnitude of $e_2[n]$, which is the component of the equation error that is due to the unstructured uncertainty. A method for bounding the remainder term due to the fact that $h_u[n]$ has an infinite-length rather than finite-length impulse response has been developed. This method has been illustrated using simple first-order bounding functions. More complex forms of the various bounding functions are considered in Appendix D. The bounding function of Eqn. (4.4.23) is based on a priori calculations and the on-line computation of the DFT of the input signal.

4.5 Robustified Least-squares Parameter Estimation with Regularization

In this section, we will present a robust form of the standard least-squares parameter estimator. This algorithm was developed by Goodwin et al. [17,18]. However, Goodwin et al. use a different mechanism to find a time-varying bound on the equation error in reference [17] than that used in this thesis. We utilize the assumed frequency-domain bounding function on the unstructured uncertainty, as was discussed in Section 4.4, whereas, Goodwin et al. use a time-domain method to compute their time-varying bound.

4.5.1 Completion of Equation Error Bounding

In this subsection, we will combine the results of Sections 4.2-4 and complete our development of the bounding of the equation error signal $e_1[n]$, which is the error due to the effects of unstructured uncertainty and the disturbance as is defined by Eqn. (4.2.18). Using Eqns. (4.2.25), (4.3.10) and (4.4.22) we find that

$$|e_1[n]| \leq \bar{e}_1[n], \ \forall n. \tag{4.5.1}$$

where

$$\bar{e}_1[n] = \bar{e}_2[n] + \bar{e}_3[n], \tag{4.5.2}$$

and $\bar{e}_2[n]$ and $\bar{e}_3[n]$ are given by Eqns. (4.4.23) and (4.3.11), respectively.

4.5.2 Goodwin et al.'s Robustified Least-squares Algorithm

In this subsection, we will present a modified least-squares algorithm that was developed by Goodwin et al. [17,18]. This algorithm includes a time-varying dead-zone in a least squares parameter estimator. This time-varying dead-zone is a robustifying mechanism that seeks to sort

out good and bad information using a type of thresholding in the time-domain. Recently, this method has appeared in the literature in efforts to achieve robustness in adaptive controllers. As was discussed earlier, we will be using a different mechanism to bound $|e_1[n]|$ than that used by Goodwin et al. in [17]. Before we present the algorithm, we must first make several definitions.

With reference to Section 4.2, we define the prediction error

$$e[n] = y_f[n] - \phi_f[n-1]^T \hat{\theta}[n-1] \tag{4.5.3}$$

where $\phi_f[n-1]$ and $y_f[n]$ are given by Eqns. (4.2.16) and (4.2.17), respectively, and $\hat{\theta}$ denotes the estimate of the parameter vector θ_0. Further, we define the parameter error vector as follows

$$\tilde{\theta}[n] = \hat{\theta}[n] - \theta_0. \tag{4.5.4}$$

Using Eqn. (4.2.17) in (4.5.3) yields

$$e[n] = - \phi_f[n-1]^T \tilde{\theta}[n-1] + e_1[n]. \tag{4.5.5}$$

Thus, the prediction error e[n] depends on both the parameter error vector and the error signal $e_1[n]$ due to the unstructured uncertainty and the disturbance. Since we have a time-varying magnitude bound on $e_1[n]$ given by Eqn. (4.5.2), we can make the least-squares algorithm robust. In preparation for the definition of the parameter estimation algorithm, we define the dead-zone function,

$$f\{g,e\} = \begin{cases} e - g, & \text{if } e > g \\ 0, & \text{if } |e| \le g \\ e + g, & \text{if } e < -g\,. \end{cases} \tag{4.5.6}$$

We now present the robustified least-squares algorithm. From [18],

$$\hat{\theta}[n] = \hat{\theta}[n-1] + \frac{\upsilon[n]\, P[n-2]\, \phi_f[n-1]}{1 + \phi_f[n-1]^T P[n-2]\, \phi_f[n-1]}\, e[n] \tag{4.5.7}$$

$$P[n-1] = P[n-2] - \frac{\upsilon[n]\, P[n-2]\, \phi_f[n-1]\, \phi_f[n-1]^T\, P[n-2]}{1 + \phi_f[n-1]^T P[n-2]\, \phi_f[n-1]} \tag{4.5.8}$$

with $\hat{\theta}[0]$ and P[-1] given where $P[-1] = P[-1]^T > 0$, and where

$$\upsilon[n] = \alpha\, s[n] \tag{4.5.9}$$

with

$$s[n] = \begin{cases} 0, & \text{if } |e[n]| \le \beta\, \overline{e}_1[n] \\ f\{\, \beta\, \overline{e}_1[n],\, e[n]\,\} / e[n], & \text{otherwise,} \end{cases} \tag{4.5.10}$$

where we choose $\alpha \in (0,1)$ and β is defined by

$$\beta = \sqrt{1 / (1 - \alpha)}. \tag{4.5.11}$$

Figure 4.1 illustrates the relationship between e[n] and s[n].

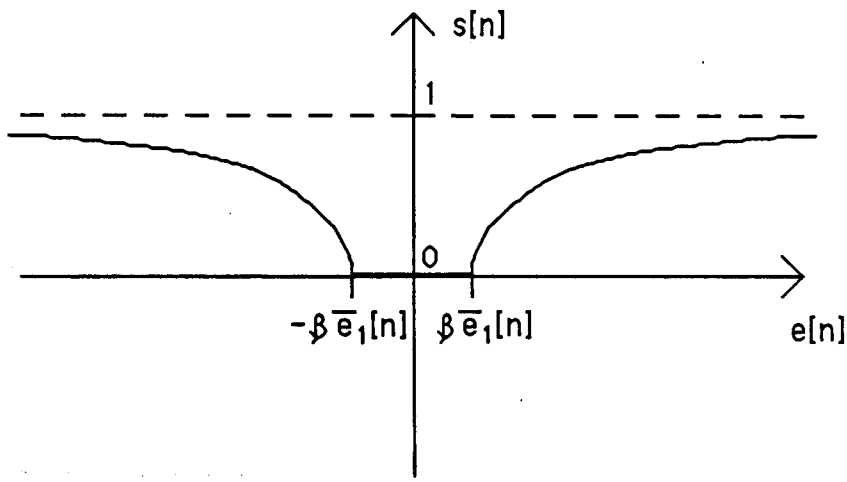

Figure 4.1: Dead-zone Illustration.

Remark 1: From Eqns. (4.5.10-11) and the definition of $\upsilon[n]$, we see that there is a trade-off between the adaptation gain α and the size of the dead-zone as controlled by the parameter β. If we choose the gain α large, that is, near unity, then β will be much greater than unity so the dead-zone will be very large and the algorithm will be turned-off most of the time.

We will now present a theorem that lists the properties of the robustified least-squares

algorithm that has been described in this section. In the following theorem, we show that the robustified least-squares algorithm has properties that are similar to the standard least-squares algorithm. The first and third properties listed in the following theorem are the same as the properties of the standard "least-squares" algorithm that are proven in [13]. The second property listed below is similar to an analogous result for the standard "least-squares" algorithm except that in the result for the standard least-squares algorithm the error signal $e[n]^2$ appears instead of $f\{\beta\, \overline{e}_1[n], e[n]\}^2$. The proof of Theorem 4.1 has been outlined in the literature [17,18].

Theorem 4.1: If Eqn. (4.5.1) holds, then the preceding algorithm has the following properties:

$$1)\ \|\tilde{\theta}[n]\| \le \sqrt{\kappa\{P[-1]\}}\ \|\tilde{\theta}[0]\|,\ n \ge 1 \tag{4.5.12}$$

where $\kappa\{P[-1]\}$ denotes the condition number of P[-1].

$$2)\ \lim_{n\to\infty} \frac{f\{\beta\, \overline{e}_1[n], e[n]\}^2}{1 + \phi_f[n-1]^T P[n-2]\, \phi_f[n-1]} = 0. \tag{4.5.13}$$

$$3)\ \lim_{n\to\infty} \|\hat{\theta}[n] - \hat{\theta}[n-1]\| = 0. \tag{4.5.14}$$

Proof: See Appendix E.

Remark 2: It can also be shown, see Appendix E, that

$$\|\tilde{\theta}[n]\| \le \sqrt{\kappa\{P[n-2]\}}\ \|\tilde{\theta}[n-1]\|,\ n \ge 1. \tag{4.5.15}$$

Thus, if the condition number of P is unity we see that the norm of the parameter error vector is non-increasing. Later, in the simulations, we will see that the algorithm generally performs better than the guaranteed properties of Eqns. (4.5.12) and (4.5.15).

Remark 3: If the signal vector $\phi_f[n-1]$ and the matrix P[n-2] are bounded, that is, both $\|\phi_f[n-1]\|$ and $\|P[n-2]\|$ are finite, then property 2 of Theorem 4.1 implies that the error signal e[n] will eventually be in the dead-zone. A further property of the above algorithm, which is proven in Appendix E, is that

$$\|P[n-1]\| \le \|P[-1]\| < \infty,\ n \ge 1. \tag{4.5.16}$$

Thus, for bounded signals we conclude that the error signal eventually ends up in the dead-zone.

4.5.3 The Regularized Constant Trace Modification to the Least-squares Algorithm

As is discussed in Goodwin et al. [17;18], the update given by Eqn. (4.5.8) causes P to be non-increasing and, in practice, the algorithm essentially turns itself off as $n \to \infty$. The problem is the same as that encountered in the standard least-squares algorithm as is discussed in Goodwin and Sin [13]. In practice, assuming that the input is rich, the basic robustified least-squares algorithm has a very fast initial convergence rate, but the algorithm gain reduces dramatically when the P matrix becomes small. To prevent this from happening, the robustified least-squares algorithm can be modified. This will help maintain an overall fast convergence rate. We choose to use the "regularized constant trace" modification that was introduced in [1]. This modification yields a P matrix that has a constant trace. Thus, it keeps P from becoming small. The robustified, regularized least-squares algorithm is described by using the same equations as in Subsection 4.5.2, except that instead of using Eqn. (4.5.8) to compute P, we use the following algorithm.

Regularized Constant Trace Algorithm:

Let c_0 and c_1 denote two positive constants, $c_1 > c_0$. Further, let m denote the number of parameters and define

$$\tau = \text{trace}\{\overline{P}[n-1]\}. \tag{4.5.17}$$

The algorithm is as follows,

a) Set $P[-1] = (c_1 / m)\, I.$ (4.5.18)

b) Compute

$$\overline{P}[n-1] = P[n-2] - \frac{\nu[n]\, P[n-2]\, \phi_f[n-1]\, \phi_f[n-1]^T\, P[n-2]}{1 + \phi_f[n-1]^T\, P[n-2]\, \phi_f[n-1]}. \tag{4.5.19}$$

c) Let

$$P[n-1] = \begin{cases} \bar{P}[n-1] + ((c_1 - \tau)/m)\, I, & \text{if } \tau \geq c_0 \\ (c_0/\tau)\, \bar{P}[n-1] + ((c_1 - c_0)/m)\, I, & \text{if } \tau < c_0. \end{cases} \tag{4.5.20}$$

We will now present a theorem that lists the properties of the robustified least-squares algorithm with the "regularized constant trace" modification. Ideally, we would like to be able to prove the same properties as those listed in Theorem 4.1. In fact, we are able to prove the second and third properties of Theorem 4.1 for our modified algorithm; however, we are forced to relax the first property of Theorem 4.1 as we see below. Most of the proof of Theorem 4.2 has appeared in the literature [1].

Theorem 4.2: If Eqn. (4.5.1) holds, then the modified algorithm defined by the use of Eqns. (4.5.17-20) has the following properties:

$$1)\ \|\tilde{\theta}[n]\| \leq \sqrt{\sigma_{max}\{P[n-1]\}/\sigma_{min}\{P[-1]\}}\ \|\tilde{\theta}[0]\| \leq \sqrt{m}\ \|\tilde{\theta}[0]\|,\ n \geq 1 \tag{4.5.21}$$

where $\sigma_{max}\{\cdot\}$ and $\sigma_{min}\{\cdot\}$ denote the maximum and minimum singular values of a matrix, respectively.

$$2)\ \lim_{n\to\infty} \frac{f\{\beta\, \bar{e}_1[n], e[n]\}^2}{1 + \phi_f[n-1]^T P[n-2]\, \phi_f[n-1]} = 0. \tag{4.5.22}$$

$$3)\ \lim_{n\to\infty} \|\hat{\theta}[n] - \hat{\theta}[n-1]\| = 0. \tag{4.5.23}$$

Proof: See Appendix E.

Remark 4: It can also be shown, see Appendix E, that

$$\|\tilde{\theta}[n]\| \leq \sqrt{\sigma_{max}\{P[n-1]\}/\sigma_{min}\{P[n-2]\}}\ \|\tilde{\theta}[n-1]\|,\ n \geq 1. \tag{4.5.24}$$

Since the trace of P is kept constant by the modified algorithm, we find that if the condition number

of P is unity for times n-1 and n-2, then Eqn. (4.5.24) would imply that the norm of the parameter error vector would be non-increasing.

Remark 5: A further property of the above modified algorithm is that

$$\|P[n-1]\| \leq \text{trace}\{P[n-1]\} = c_1, \quad n \geq 1. \tag{4.5.25}$$

Thus, for bounded signals we can conclude, as in remark 3, that the error signal eventually ends up in the dead-zone.

In this section, we have described what we call the "robustified least-squares" algorithm. This algorithm, due to Goodwin et al. [17,18], uses a time-varying dead-zone to achieve robustness. A theorem listing the properties of this algorithm was presented. In addition, we introduced a modification to prevent this parameter estimation algorithm from "turning-off". In a second theorem, we showed that the modified version of the robustified least-squares algorithm has properties that are similar to the basic robustified least-squares algorithm.

4.6 Summary

In this chapter, we have developed a modified least-squares parameter estimator that is robust to the effects of unstructured uncertainty and an unmeasurable disturbance. This robustified, regularized algorithm uses only assumptions AD1-3 of Section 3.6. A flowchart illustrating the development of this chapter is presented in Figure 4.2. First, we developed a bound on the part of the equation error $e_1[n]$ that was due to the disturbance. The computation of this bound is an off-line operation. We then set up a mechanism for computing a time-varying bound on the part of the equation error that was due to the unstructured uncertainty. This time-varying bound is computed on-line using the current DFT of the input signal. These component bounds are added to form a bound on the equation error $e_1[n]$. This equation error bound is used by the robustified, regularized algorithm of Section 4.5 to control the time-varying dead-zone. Thus, we have presented a complete methodology for robust time-domain parameter estimation.

Combining the parameter estimate of the algorithm of this chapter with the nominal model structure of assumption AD1 yields a nominal model that can be used for the computation of control-law updates. Later, in the simulations, we will show that the dead-zone based parameter estimator of this chapter has some weaknesses. Specifically, the dead-zone mechanism tends to disable the parameter estimator much of the time, so the resulting parameter estimates are poor. In the following chapter, a second method for generating parameter estimates for the nominal model will be described. This alternate method is frequency-domain based and does not suffer from the

problems of the dead-zone based parameter estimator.

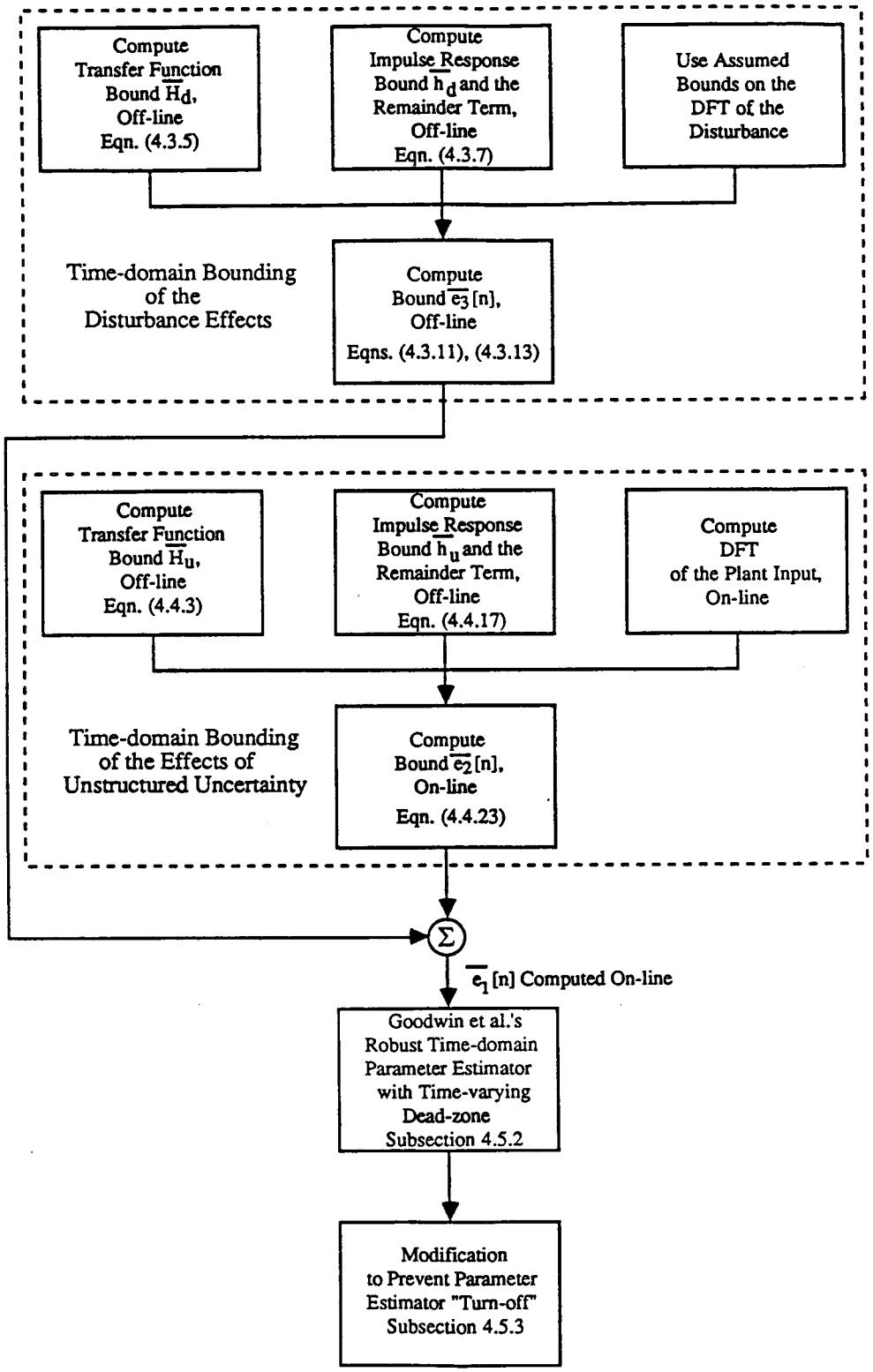

Figure 4.2: Development of the Robust Time-domain Parameter Estimator.

CHAPTER 5.
FREQUENCY-DOMAIN PARAMETER ESTIMATION AND UNCERTAINTY BOUNDING

5.1 Introduction

In this chapter, we will present a frequency-domain bounding methodology that yields a frequency-domain estimate of the true plant as well as a bounding function on the modeling error in the frequency domain. Using this frequency-domain estimate, we will compute a parameter vector estimate using a type of weighted least-squares fit in the frequency-domain. Given the parameter vector estimate and, hence, a nominal model, we will compute a bounding function on the modeling error with respect to this nominal model. The methodology will yield a set of points versus frequency which bound the magnitude of the function $\delta_{su}(e^{j\omega T}, \hat{\theta})$ at those frequency points. A smoothness condition is then used to compute a continuous bounding function on the magnitude of $\delta_{su}(e^{j\omega T}, \hat{\theta})$. To compute this continuous bounding function, we must bound the variations of $\delta_{su}(e^{j\omega T}, \hat{\theta})$ between the discrete frequency samples. The chapter is organized as follows.

First, in Section 5.2 we develop the basic frequency-domain bounding algorithm. Then, in Section 5.3 we address the problem of combining frequency-domain information that has been learned during different time intervals. Frequency-domain parameter estimation is discussed in Section 5.4 . In Section 5.5, the computation of the error bounding function with respect to the nominal model is discussed. In Section 5.6, two different philosophies concerning the modeling of the unstructured uncertainty are presented. A methodology for smoothing our uncertainty bounding function is presented in Section 5.7. In Section 5.8 we show how to bound inter-sample variations of $|\delta_{su}(e^{j\omega T}, \hat{\theta})|$. Finally, in Section 5.9 we summarize our results. The key contribution of this chapter is the development of the frequency-domain bounding methodology. This new methodology is the most important part of the robust estimator in that it provides the bounds on the frequency-domain estimation errors.

5.2 Frequency-domain Estimation and Error Bounding

In this section, we will develop a methodology for finding a frequency-domain estimate of the true plant and a corresponding error bounding function on the frequency-domain modeling

error.

5.2.1 Development of the Basic Methodology

Consider the true discrete-time plant $g_{true}[n]$, whose input is u[n] and whose disturbance-corrupted output is y[n]. Assuming zero initial conditions, we know that

$$y[n] = g_{true}[n]*u[n] + d[n]. \tag{5.2.1}$$

Then, using the notation of Section 2.1 and Theorem 2.1, we find that for some time index n,

$$Y_N^n(\omega_k) = G_{true}(e^{j\omega_k T})\, U_N^n(\omega_k) + E_N^n(\omega_k) + D_N^n(\omega_k) \tag{5.2.2}$$

$$\text{for } k = 0, \ldots, N-1,$$

where from Theorem 2.2 we know that for some integer M,

$$|E_N^n(\omega_k)| \le \overline{E}_N^n(\omega_k), \text{ for } k = 0, \ldots, N-1 \tag{5.2.3}$$

with

$$\overline{E}_N^n(\omega_k) = \sum_{p=1}^{M-1} |g_{true}[p]|\, |U_N^{n-p}(\omega_k) - U_N^n(\omega_k)| + \overline{E}_{rem}, \text{ for } k = 0, \ldots, N-1, \tag{5.2.4}$$

where the remainder term is defined as

$$\overline{E}_{rem} = 2\, u_{max} \sum_{p=M}^{\infty} p\, |g_{true}[p]|, \tag{5.2.5}$$

and where we know u_{max} from assumption AD3.1. The integer M will be referred to as the memory length. The choice of this important design parameter will be discussed later, in Section 6.6. Now, rewriting our assumptions for convenience, we know from AD1.6 that

$$|g_{true}[n]| \le \overline{g}_{true}[n], \tag{5.2.6}$$

where

$$\overline{g}_{true}[n] = \sum_{i=1}^{I_0} g_i\, n^{r_i}\, p_i^n \tag{5.2.7}$$

and where r_i is a positive integer, and $g_i > 0$, $0 < p_i < 1$, and r_i are known for $i=1, \ldots, I_0$. Since $\overline{g}_{true}[n]$ is of the form of Eqn. (5.2.7), we can use the results of Appendix C to evaluate the infinite summation term. For simplicity, we assume that

$$\overline{g}_{true}[n] = g_2\, p_2^n, \text{ for } n = 0, 1, \ldots \tag{5.2.8}$$

In this case, we use Eqn. (C.10) to compute the bounding function,

$$\overline{E}_N^n(\omega_k) = \sum_{i=1}^{M-1} g_2\, p_2^i\, |U_N^{n-i}(\omega_k) - U_N^n(\omega_k)| + 2\, u_{max}\, g_2\, p_2^M\, (M - M p_2 + p_2) / (1 - p_2)^2, \text{ for } k = 0, \ldots, N-1. \tag{5.2.9}$$

The bounding function of Eqn. (5.2.9) can be computed on-line by using the current N-point DFT of u[n] along with M-1 old N-point DFTs of u[n]. We note that the second line of the previous equation can be made arbitrarily small by choosing M to be sufficiently large. However, as M is increased so does the amount of the on-line calculations. This tradeoff will be discussed further in Chapter 6.

Now, we define the frequency-domain estimate $G_{f,N}^n(\omega_k)$ and the corresponding frequency-domain error $E_{f,N}^n(\omega_k)$.

$$G_{f,N}^n(\omega_k) = Y_N^n(\omega_k) / U_N^n(\omega_k) \tag{5.2.10}$$

$$E_{f,N}^n(\omega_k) = G_{f,N}^n(\omega_k) - G_{true}(e^{j\omega_k T}), \text{ for } k = 0, \ldots, N-1 \tag{5.2.11}$$

From Eqn. (5.2.2),

$$E_{f,N}^n(\omega_k) = (E_N^n(\omega_k) + D_N^n(\omega_k)) / U_N^n(\omega_k) \tag{5.2.12}$$

and using the triangle inequality we find,

$$|E_{f,N}^n(\omega_k)| \le \overline{E}_{f,N}^n(\omega_k) \tag{5.2.13}$$

where

$$\overline{E}_{f,N}^n(\omega_k) = (\overline{E}_N^n(\omega_k) + \overline{D}_N^n(\omega_k)) / |U_N^n(\omega_k)|, \tag{5.2.14}$$

and where $\overline{E}_N^n(\omega_k)$ is given by Eqn. (5.2.4) and

$$|D_N^n(\omega_k)| \le \overline{D}_N^n(\omega_k), \text{ for } k = 0, \ldots, N-1. \tag{5.2.15}$$

We will refer to $G_{f,N}^n(\omega_k)$ as our frequency-domain estimate of the true plant at time index n. Note that $G_{f,N}^n(\omega_k)$ is the set of N complex numbers computed using the N-point DFTs of

u[n] and y[n], which are computed on-line. Further, we will refer to $\overline{E}_{f,N}^{n}(\omega_k)$ as the frequency-domain error bounding function at time index n. In Eqn. (5.2.14), the bounding function $\overline{E}_{N}^{n}(\omega_k)$ and $|U_N^n(\omega_k)|$ are computed on-line at each time index n, while the function $\overline{D}_{N}^{n}(\omega_k)$ is known from assumption AD2.2. If we assume that $n \geq N-1$, that is, we assume that at least N non-zero points of data have been collected so that, with reference to AD2.2,

$$\overline{D}_{N}^{n}(\omega_k) = \overline{\overline{D}}_{N}(\omega_k) \text{ when } n \geq N-1, \text{ for } k = 0, \ldots, N-1, \tag{5.2.16}$$

then Eqn. (5.2.13) becomes

$$\overline{E}_{f,N}^{n}(\omega_k) = (\overline{E}_{N}^{n}(\omega_k) + \overline{\overline{D}}_{N}(\omega_k)) / |U_N^n(\omega_k)|, \text{ when } n \geq N-1, \tag{5.2.17}$$
$$\text{for } k = 0, \ldots, N-1.$$

We note that Eqn. (5.2.17) gives us an idea of how large the input signal must be to achieve some error bounding function $\overline{E}_{f,N}^{n}(\omega_k)$ given the disturbance DFT bounding function $\overline{\overline{D}}_{N}(\omega_k)$. This equation will be useful later, in Chapter 7, where we consider what kind of probing signal should be introduced into the closed-loop adaptive system to enhance identification.

5.3 The Cumulative Frequency-domain Estimate and Error Bounding Function

In this section, we will discuss a straightforward technique for combining the frequency-domain estimates and corresponding error bounding functions from different time intervals. That is, we show how to combine all of the past frequency-domain information into a cumulative estimate and cumulative error bounding function. The basic idea is that, at a given frequency point ω_k, we use the value of $G_{f,N}^{n}(\omega_k)$ that has the smallest corresponding error bounding function $\overline{E}_{f,N}^{n}(\omega_k)$, at that frequency. To formalize this we define the cumulative error bounding function at ω_k,

$$\overline{E}_{cumf,N}^{n}(\omega_k) = \min_{p \leq n} \{ \overline{E}_{f,N}^{p}(\omega_k) \}, \tag{5.3.1}$$

and the cumulative frequency-domain estimate at ω_k,

$$G_{cumf,N}^{n}(\omega_k) = \{ G_{f,N}^{m}(\omega_k) \mid \overline{E}_{f,N}^{m}(\omega_k) = \overline{E}_{cumf,N}^{n}(\omega_k) \}. \quad (5.3.2)$$

The subscript "cumf" in Eqns. (5.3.1-2) denotes the fact that they are the "cumulative frequency-domain" estimate and error bounding function. We define, for time index n,

$$E_{cumf,N}^{n}(\omega_k) = G_{cumf,N}^{n}(\omega_k) - G_{true}(e^{j\omega_k T}), \text{ for } k = 0, \ldots, N-1. \quad (5.3.3)$$

Then Eqn. (5.3.2) ensures that at time index n,

$$|E_{cumf,N}^{n}(\omega_k)| \leq \overline{E}_{cumf,N}^{n}(\omega_k), \text{ for } k = 0, \ldots, N-1. \quad (5.3.4)$$

In practice, the following simple recursive algorithm will be used to compute $G_{cumf,N}^{n}(\omega_k)$ and $\overline{E}_{cumf,N}^{n}(\omega_k)$ at a given frequency ω_k.

Algorithm:

If $\overline{E}_{f,N}^{n}(\omega_k) < \overline{E}_{cumf,N}^{n-1}(\omega_k)$, then set

$$\overline{E}_{cumf,N}^{n}(\omega_k) = \overline{E}_{f,N}^{n}(\omega_k), \text{ and}$$

$$G_{cumf,N}^{n}(\omega_k) = G_{f,N}^{n}(\omega_k). \quad (5.3.5)$$

else, set

$$\overline{E}_{cumf,N}^{n}(\omega_k) = \overline{E}_{cumf,N}^{n-1}(\omega_k), \text{ and}$$

$$G_{cumf,N}^{n}(\omega_k) = G_{cumf,N}^{n-1}(\omega_k).$$

For initial conditions, we use the a priori plant assumptions AD1. If the initial guess for the plant corresponds to the parameter vector θ_1, then for n=0 we set the cumulative frequency-domain estimate to the nominal model using θ_1, and set the cumulative error bounding function to the best bounding function we can find using only a priori information. So, using our earlier notation, we write

Initial Conditions: (n = 0)

$$G_{cumf,N}^{n}(\omega_k) = G(e^{j\omega_k T},\theta_1) \tag{5.3.6}$$

$$\overline{E}_{cumf,N}^{n}(\omega_k) = \sup_{\theta\in\Theta} \{\, |G(e^{j\omega_k T},\theta_1) - G(e^{j\omega_k T},\theta)| + |G(e^{j\omega_k T},\theta)|\, \Delta_u(e^{j\omega_k T}) \,\} \tag{5.3.7}$$

$$\text{for } k = 0, \ldots, N-1.$$

The above supremum are computed off-line. An important property of the above algorithm is that it only updates the cumulative frequency-domain estimate and the corresponding cumulative error bounding function when useful information is learned, at a given frequency.

As a final note, we observe that, since we are working with real-valued time-domain signals, the properties of the DFTs of real-valued signals can be used to show that

$$G_{cumf,N}^{n}(\omega_k) = G^{*}_{cumf,N}{}^{n}(\omega_{N-k}), \tag{5.3.8}$$

$$\overline{E}_{cumf,N}^{n}(\omega_k) = \overline{E}_{cumf,N}^{n}(\omega_{N-k}), \text{ for } k = 1, \ldots, (N/2)-1, \tag{5.3.9}$$

where '*' denotes complex conjugate and where we have assumed that N is even. This means that the information for frequency points k=0, . . , N-1 is contained in the information for the frequency points k=0, . . , N/2. We only need to estimate the plant for frequency points k=0, . . , N/2.

5.4 Frequency-domain Parameter Estimation

In this section, we will show how the cumulative frequency-domain estimate of the previous section can be used to find parameter estimates for the nominal model. We use the structure of the nominal model and a type of weighted least-squares fit to the frequency-domain estimate $G_{cumf,N}^{n}(\omega_k)$. There are many ways that one could choose the nominal model parameters to fit the cumulative frequency-domain estimate. The method that we present in this section is computationally efficient, since it only requires the solution of linear equations.

The procedure is best illustrated by an example. Consider the nominal model,

$$G(z,\theta_0) = (b_0 z + b_1) / (z^2 - a_1 z - a_2), \text{ where} \tag{5.4.1}$$

$$\theta_0 = [\, a_1 \;\; a_2 \;\; b_0 \;\; b_1 \,]^T. \tag{5.4.2}$$

Using this nominal model structure we can write

$$(z^2 - a_1 z - a_2)\, G(z,\theta_0) = b_0 z + b_1, \tag{5.4.3}$$

or

$$z^2\, G(z,\theta_0) = [\, z\, G(z,\theta_0) \;\; G(z,\theta_0) \;\; z \;\; 1\,]\, [\, a_1 \;\; a_2 \;\; b_0 \;\; b_1\,]^T \tag{5.4.4}$$

$$= [\, z\, G(z,\theta_0) \;\; G(z,\theta_0) \;\; z \;\; 1\,]\, \theta_0. \tag{5.4.5}$$

Since the parameters are assumed to be real-valued, we find

$$\mathrm{Re}\{z^2\, G(z,\theta_0)\} = [\, \mathrm{Re}\{z\, G(z,\theta_0)\} \;\; \mathrm{Re}\{G(z,\theta_0)\} \;\; \mathrm{Re}\{z\} \;\; 1\,]\, \theta_0, \tag{5.4.6}$$

$$\mathrm{Im}\{z^2\, G(z,\theta_0)\} = [\, \mathrm{Im}\{z\, G(z,\theta_0)\} \;\; \mathrm{Im}\{G(z,\theta_0)\} \;\; \mathrm{Im}\{z\} \;\; 0\,]\, \theta_0. \tag{5.4.7}$$

Thus, if we know the complex value of $G(z,\theta_0)$ for some known z, we can find two linear equations in the parameters. Our frequency-domain estimation method yields an estimate of the plant at frequencies ω_k for k = 0, . . , N/2. So, letting $z = e^{j\omega_k T}$ for k = 0, . . , N/2, we can define a (N+2)×4 matrix A whose elements depend upon the complex values of some discrete function of frequency. We write $A(\, G(e^{j\omega_k T},\theta_0)\,)$ to denote the fact that the matrix A depends upon the values of the specific frequency function $G(e^{j\omega_k T},\theta_0)$. We now define the form of the matrix A and show how its elements depend on the values of the discrete frequency function that is used as its argument.

$$A(\, G(e^{j\omega_k T},\theta_0)\,) =$$

$$\begin{bmatrix}
\mathrm{Re}\{e^{j\omega_0 T} G(e^{j\omega_0 T},\theta_0)\} & \mathrm{Re}\{G(e^{j\omega_0 T},\theta_0)\} & \mathrm{Re}\{e^{j\omega_0 T}\} & 1 \\
\vdots & \vdots & \vdots & \vdots \\
\mathrm{Re}\{e^{j\omega_{(N/2)} T} G(e^{j\omega_{(N/2)} T},\theta_0)\} & \mathrm{Re}\{G(e^{j\omega_{(N/2)} T},\theta_0)\} & \mathrm{Re}\{e^{j\omega_{(N/2)} T}\} & 1 \\
\mathrm{Im}\{e^{j\omega_0 T} G(e^{j\omega_0 T},\theta_0)\} & \mathrm{Im}\{G(e^{j\omega_0 T},\theta_0)\} & \mathrm{Im}\{e^{j\omega_0 T}\} & 0 \\
\vdots & \vdots & \vdots & \vdots \\
\mathrm{Im}\{e^{j\omega_{(N/2)} T} G(e^{j\omega_{(N/2)} T},\theta_0)\} & \mathrm{Im}\{G(e^{j\omega_{(N/2)} T},\theta_0)\} & \mathrm{Im}\{e^{j\omega_{(N/2)} T}\} & 0
\end{bmatrix} \tag{5.4.8}$$

Similarly, we define the form of the (N+2) vector B and show how its elements depend on the values of the discrete frequency function that is used as its argument.

$$B(G(e^{j\omega_k T},\theta_0)) = \begin{bmatrix} \mathrm{Re}\{e^{2j\omega_0 T}G(e^{j\omega_0 T},\theta_0)\} \\ \vdots \\ \mathrm{Re}\{e^{2j\omega_{(N/2)} T}G(e^{j\omega_{(N/2)} T},\theta_0)\} \\ \mathrm{Im}\{e^{2j\omega_0 T}G(e^{j\omega_0 T},\theta_0)\} \\ \vdots \\ \mathrm{Im}\{e^{2j\omega_{(N/2)} T}G(e^{j\omega_{(N/2)} T},\theta_0)\} \end{bmatrix} \quad (5.4.9)$$

Using Eqns. (5.4.2) and (5.4.6-9) we can write,

$$A(G(e^{j\omega_k T},\theta_0))\,\theta_0 = B(G(e^{j\omega_k T},\theta_0)). \quad (5.4.10)$$

This matrix equation is just a statement of Eqn. (5.4.3) at the frequency points $z = e^{j\omega_k T}$ for $k = 0, \ldots, N/2$.

In summary, we have shown how knowledge of the complex values of $G(e^{j\omega_k T},\theta_0)$ at the $(N/2)+1$ frequencies $\omega_0, \ldots, \omega_{(N/2)}$ can be used to write N+2 linear equations in the parameters. In the ideal situation, where one could exactly find frequency values that correspond to a system with the nominal structure $G(e^{j\omega_k T},\theta_0)$ for k=0, . ., (N/2), the matrix equation (5.4.10) will have a solution. That is, since we assume that N is greater than the number of parameters, Eqn. (5.4.10) will have more linear equations than the number of parameters. In this case, for Eqn. (5.4.10) to have a solution, the frequency values that are used in the A and B matrices must correspond to a system with the assumed structure of the nominal model. However, in practice we will only have our cumulative frequency-domain estimate $G_{cumf,N}^{n}(\omega_k)$ with which to estimate the parameters. If we use $G_{cumf,N}^{n}(\omega_k)$ instead of $G(e^{j\omega_k T},\theta_0)$ in Eqns. (5.4.8-9), then the equation

$$A(G_{cumf,N}^{n}(\omega_k))\,\hat{\theta} = B(G_{cumf,N}^{n}(\omega_k)) \quad (5.4.11)$$

will not, in general, have a solution. In Eqn. (5.4.11) we denote the matrices A and B whose elements depend on the discrete function of frequency $G_{cumf,N}^{n}(\omega_k)$ by $A(G_{cumf,N}^{n}(\omega_k))$ and $B(G_{cumf,N}^{n}(\omega_k))$, respectively. The elements of $A(G_{cumf,N}^{n}(\omega_k))$ and $B(G_{cumf,N}^{n}(\omega_k)$

depend on the complex values of $G_{cumf,N}^{n}(\omega_k)$ in the same way that $A(G(e^{j\omega_k T},\theta_0))$ and $B(G(e^{j\omega_k T},\theta_0))$ depend on $G(e^{j\omega_k T},\theta_0)$ in Eqns. (5.4.8-9). We note that Eqn. (5.4.11) is in the form of the standard least-squares problem that is discussed in Strang [33].

We will choose the parameter estimate $\hat{\theta}$ as the vector that minimizes the frequency weighted norm of the error vector,

$$A(G_{cumf,N}^{n}(\omega_k))\ \hat{\theta} - B(G_{cumf,N}^{n}(\omega_k)). \tag{5.4.12}$$

We define, with reference to Eqns. (5.4.8-9), the diagonal frequency weighting matrix,

$$W = diag[\ f(\omega_0)\ \ f(\omega_1),\ \ldots, f(\omega_{(N/2)})\ \ f(\omega_0)\ \ f(\omega_1),\ \ldots, f(\omega_{(N/2)})\ ]. \tag{5.4.13}$$

where $f(\omega)$ is the frequency weighting function. The parameter estimate that minimizes the norm of the error vector

$$W\ (\ A(G_{cumf,N}^{n}(\omega_k))\ \hat{\theta} - B(G_{cumf,N}^{n}(\omega_k))\ ) \tag{5.4.14}$$

is given by the well-known result,

$$\hat{\theta} = (A^T W^T W A)^{-1}\ A^T W^T W B \tag{5.4.15}$$

where the A and B matrices in this equation depend on the values of the estimate $G_{cumf,N}^{n}(\omega_k)$.

To gain insight as to what weighting function to choose, we examine Eqns. (5.4.3-5). Consider the use of the above methodology using the estimate $\hat{G}(z)$. Then, we find that the error

$$z^2 \hat{G}(z) - [\ z\hat{G}(z)\ \ \hat{G}(z)\ \ z\ \ 1\ ]\ \theta_0 = (z^2 - a_1 z - a_2)\hat{G}(z) - (b_0 z + b_1) \tag{5.4.16}$$

$$= (z^2 - a_1 z - a_2)\ (\ \hat{G}(z) - G(z,\theta_0)\ ) \tag{5.4.17}$$

So,

$$|\hat{G}(z) - G(z,\theta_0)| = |\ z^2 \hat{G}(z) - [\ z\hat{G}(z)\ \ \hat{G}(z)\ \ z\ \ 1\ ]\ \theta_0\ |\ /\ |z^2 - a_1 z - a_2|. \tag{5.4.18}$$

From Eqn. (5.4.18) we see that, if we want our parameter estimation method to be a least-squares fit in the frequency-domain, then we want to choose a weighting function that is one over the magnitude of the denominator of the nominal model. That is, if we choose the frequency weighting function

$$f_1(\omega) = 1\ /\ |\ e^{j2\omega T} - a_1\ e^{j\omega T} - a_2| \tag{5.4.19}$$

then using $z = e^{j\omega T}$ in Eqn. (5.4.18), we can write

C-2 .

$$|\hat{G}(e^{j\omega T}) - G(e^{j\omega T},\theta_0)| = f_1(\omega)\,|e^{j2\omega T}\,\hat{G}(e^{j\omega T}) - [\,e^{j\omega T}\,\hat{G}(e^{j\omega T})\quad \hat{G}(e^{j\omega T})\quad e^{j\omega T}\quad 1\,]\,\theta_0|$$

(5.4.20)

Thus, by using the weighting function of Eqn. (5.4.19), we actual find the parameter estimate that corresponds to a least-squares fit, in the frequency-domain, between the estimate and the nominal model. Of course, we do not know what the parameters a_1 and a_2 really are. We only have our coarse a priori bound on the parameter space. So, one can only approximately choose the frequency weighting function of Eqn. (5.4.19) using our coarse a priori knowledge of the parameters a_1 and a_2.

5.5 An Uncertainty Bounding Function for the Nominal Model

In this section, we discuss the computation of a discrete, frequency-domain error bounding function for the nominal model $G(e^{j\omega_k T},\hat{\theta})$. In addition, we will compute a magnitude bounding function, $\Delta_{su}^{n}(e^{j\omega_k T},\hat{\theta})$, on the uncertainty $\delta_{su}(e^{j\omega_k T},\hat{\theta})$ at the frequency points corresponding to ω_k for k=0, . . . , N-1. In the following sections, we will shown how to obtain a continuous, frequency-domain bounding function on $|\delta_{su}(e^{j\omega T},\hat{\theta})|$ for all ω, using the discrete bounding function that will be computed in this section.

The nominal model at time index n is obtained by using the nominal model structure and the current parameter vector estimate $\hat{\theta}$. Thus, we can compute the value of the nominal model $G(e^{j\omega_k T},\hat{\theta})$ for k=0, . . , N-1.

Using the triangle inequality, we find that at time index n, and for frequency ω_k,

$$|G(e^{j\omega_k T},\hat{\theta}) - G_{true}(e^{j\omega_k T})| \le$$

$$|G(e^{j\omega_k T},\hat{\theta}) - G_{cumf,N}^{n}(\omega_k)| + |G_{cumf,N}^{n}(\omega_k) - G_{true}(e^{j\omega_k T})|. \qquad (5.5.1)$$

and, using Eqns. (5.3.3-4),

$$|G(e^{j\omega_k T},\hat{\theta}) - G_{true}(e^{j\omega_k T})| \le |G(e^{j\omega_k T},\hat{\theta}) - G_{cumf,N}^{n}(\omega_k)| + \overline{E}_{cumf,N}^{n}(\omega_k). \qquad (5.5.2)$$

We can now find a bound on $\delta_{su}(e^{j\omega_k T},\hat{\theta})$. Rewriting Eqn. (3.7.1),

$$G_{true}(e^{j\omega_k T}) = G(e^{j\omega_k T}, \hat{\theta})\,[1 + \delta_{su}(e^{j\omega_k T}, \hat{\theta})], \text{ for } k = 0, \ldots, N-1. \quad (5.5.3)$$

So, rearranging yields,

$$\delta_{su}(e^{j\omega_k T}, \hat{\theta}) = [\, G_{true}(e^{j\omega_k T}) - G(e^{j\omega_k T}, \hat{\theta})\,] \,/\, G(e^{j\omega_k T}, \hat{\theta}). \quad (5.5.4)$$

Using Eqn. (5.5.2), we find the bounding function,

$$|\delta_{su}(e^{j\omega_k T}, \hat{\theta})| \le \Delta_{su}^{n}(e^{j\omega_k T}, \hat{\theta}), \quad (5.5.5)$$

where

$$\Delta_{su}^{n}(e^{j\omega_k T}, \hat{\theta}) =$$

$$\{\; |G(e^{j\omega_k T}, \hat{\theta}) - G_{cumf,N}^{n}(\omega_k)| + \overline{E}_{cumf,N}^{n}(\omega_k) \;\} \,/\, |G(e^{j\omega_k T}, \hat{\theta})|,$$
$$\text{for } k = 0, \ldots, N-1. \quad (5.5.6)$$

and where we have included a superscript 'n' after the Δ_{su} to denote the fact that this bound on $|\delta_{su}(e^{j\omega_k T}, \hat{\theta})|$ depends on the time index n, since $G_{cumf,N}^{n}(\omega_k)$, $\overline{E}_{cumf,N}^{n}(\omega_k)$ and also $\hat{\theta}$ depend on n. The uncertainty bounding function of Eqn. (5.5.6) need only be computed before a control-law update.

In summary, we have shown how to compute a discrete function $\Delta_{su}^{n}(e^{j\omega_k T}, \hat{\theta})$ that bounds the net effect of structured and unstructured uncertainty of the current nominal model $G(e^{j\omega_k T}, \hat{\theta})$ relative to the true plant, at the frequencies, $\omega_0, \omega_1, \ldots \omega_{N-1}$. We used the nominal model structure of AD1.1, the current parameter estimate $\hat{\theta}$, and the cumulative frequency-domain estimate $G_{cumf,N}^{n}(\omega_k)$ and corresponding cumulative error bounding function $\overline{E}_{cumf,N}^{n}(\omega_k)$ that were developed in Section 5.3.

5.6 The Effects of Unstructured Uncertainty on Frequency-domain Estimation

In this section, we will present two philosophies concerning the treatment of the unstructured uncertainty $\delta_u(z)$. We discuss how to treat the unstructured uncertainty when it is: 1) time-invariant, and 2) time-varying. The time-varying philosophy will require a modification of our estimation methodology. This discussion is important since it describes how to modify the

robust estimator for situations where the phase of the unstructured uncertainty can change with time.

5.6.1 Components of the Modeling Uncertainty

In this subsection, we examine the components of the multiplicative modeling uncertainty $\delta_{su}(z)$. From Eqns. (3.6.1) and (3.7.1) we know that,

$$G_{true}(z) = G(z,\theta_0)\,[1 + \delta_u(z)] = G(z,\hat{\theta})\,[1 + \delta_{su}(z,\hat{\theta})] \tag{5.6.1}$$

where we do not show the time dependence of $\hat{\theta}$ for convenience of notation. Rearranging yields,

$$\delta_{su}(z,\hat{\theta}) = [\,G(z,\theta_0) - G(z,\hat{\theta})\,] / G(z,\hat{\theta}) \;+\; [\,G(z,\theta_0) / G(z,\hat{\theta})\,]\,\delta_u(z). \tag{5.6.2}$$

We define the structured uncertainty,

$$\delta_s(z,\hat{\theta}) = [\,G(z,\theta_0) - G(z,\hat{\theta})\,] / G(z,\hat{\theta}), \tag{5.6.3}$$

and the transfer function,

$$H_{su1}(z,\theta_0,\hat{\theta}) = G(z,\theta_0) / G(z,\hat{\theta}) \tag{5.6.4}$$

so that we can write

$$\delta_{su}(z,\hat{\theta}) = \delta_s(z,\hat{\theta}) + H_{su1}(z,\theta_0,\hat{\theta})\,\delta_u(z). \tag{5.6.5}$$

The methodology of Sections 5.1-5 can be used to find a frequency-domain bounding function on $|\delta_{su}(e^{j\omega_k T},\hat{\theta})|$ where sign cancellations can occur between the two terms in Eqn. (5.6.5).

5.6.2 Modeling the Unstructured Uncertainty: Two Philosophies

In Sections 5.1-5, we assumed that the partially known plant was linear and time invariant. If the plant is truly time invariant, then the uncertainty bounding function of Eqn. (5.5.6) will be able to bound the total uncertainty due to both structured and unstructured uncertainty. In this case, we are actually identifying the unstructured uncertainty, although it is lumped together in the total uncertainty. Since, in practice, the unstructured uncertainty may not be modeled well by a linear time-invariant system, we suggest an engineering modification to the approach of Sections 5.1-5. We suggest that the final uncertainty bounding function should not be permitted to become less than the a priori bounding function on the unstructured uncertainty Δ_u. Said another way, we don't

require our frequency-domain estimation method to identify the unstructured uncertainty. By making sure that our final bounding function doesn't become less than Δ_u, we guarantee that our robust adaptive control system will, at least, be robust to the presence of the unstructured uncertainty. We can take a more rigorous approach to this problem.

If we view the unstructured uncertainty δ_u as being able, at any time, to have any phase and any magnitude that is less than the bounding function Δ_u, then we must modify our frequency-domain bounding methodology. We will develop an approach that bounds not $|\delta_{su}(e^{j\omega_k T}, \hat{\theta})|$ but, instead,

$$|\delta_s(e^{j\omega_k T}, \hat{\theta})| + |H_{su1}(e^{j\omega_k T}, \theta_0, \hat{\theta})\, \delta_u(e^{j\omega_k T})|. \tag{5.6.6}$$

Although we continue to view the low-frequency dynamics of the plant as being time-invariant, we allow in this second philosophy for the high-frequency unmodeled dynamics to be time-varying. By bounding Eqn. (5.6.6), we are implicitly saying that the unstructured uncertainty can change to any phase and our frequency-domain uncertainty bound will still be valid. We are guarding against the possibility that during one period of time, the phases of the two terms in Eqn. (5.6.5) are opposite, and during a later time period the phases of the two terms are the same. So, if we identified the plant during the period when the terms were of opposite phases, and updated the compensator based on this information, then the system would not be robustly stable in the face of the later situation where the terms add. In this philosophy, we only want to ask our frequency-domain bounding methodology to identify the structured uncertainty. We use our a priori bounding function to account for the unstructured uncertainty. If we want our robust adaptive controller to be truly robust in an environment where the unstructured uncertainty can be changed, but must always satisfy our a priori bound, then the following methodology must be used.

5.6.3 Computing a Robust Uncertainty Bounding Function for the Time-varying Case

In this subsection, we will compute a frequency-domain bounding function on Eqn. (5.6.6) using the bounding function $\Delta_{su}{}^n(e^{j\omega_k T}, \hat{\theta})$ of Eqn. (5.5.6) that satisfies

$$|\delta_{su}(e^{j\omega_k T}, \hat{\theta})| \le \Delta_{su}{}^n(e^{j\omega_k T}, \hat{\theta}), \text{ for } k = 0, \ldots, N\text{-}1. \tag{5.6.7}$$

Using the triangle inequality and Eqn. (5.6.5) we find that

$$|\delta_s(e^{j\omega_k T}, \hat{\theta})| \le |\delta_{su}(e^{j\omega_k T}, \hat{\theta})| + |H_{su1}(e^{j\omega_k T}, \theta_0, \hat{\theta})\, \delta_u(e^{j\omega_k T})| \tag{5.6.8}$$

$$\le \Delta_{su}{}^n(e^{j\omega_k T}, \hat{\theta}) + |H_{su1}(e^{j\omega_k T}, \theta_0, \hat{\theta})|\, \Delta_u(e^{j\omega_k T}). \tag{5.6.9}$$

Thus, we find that

$$|\delta_s(e^{j\omega_k T}, \hat{\theta})| + |H_{su1}(e^{j\omega_k T}, \theta_0, \hat{\theta})\, \delta_u(e^{j\omega_k T})| \tag{5.6.10}$$

$$\le \Delta_{su}{}^n(e^{j\omega_k T}, \hat{\theta}) + 2\,|H_{su1}(e^{j\omega_k T}, \theta_0, \hat{\theta})|\, \Delta_u(e^{j\omega_k T}). \tag{5.6.11}$$

This allows us to define the robust frequency-domain bounding function $\hat{\Delta}_{su}{}^n$ that satisfies

$$|\delta_{su}(e^{j\omega_k T}, \hat{\theta})| \le |\delta_s(e^{j\omega_k T}, \hat{\theta})| + |H_{su1}(e^{j\omega_k T}, \theta_0, \hat{\theta})\, \delta_u(e^{j\omega_k T})| \le \hat{\Delta}_{su}{}^n(e^{j\omega_k T}, \hat{\theta}),$$

$$\text{for } k = 0, \ldots, N\text{-}1 \tag{5.6.12}$$

where

$$\hat{\Delta}_{su}{}^n(e^{j\omega_k T}, \hat{\theta}) = \Delta_{su}{}^n(e^{j\omega_k T}, \hat{\theta}) + 2\,\overline{\overline{H}}_{su1}(e^{j\omega_k T}, \theta_0, \hat{\theta})\, \Delta_u(e^{j\omega_k T}) \tag{5.6.13}$$

and where

$$\overline{\overline{H}}_{su1}(e^{j\omega_k T}) = \min\{\ [1+\Delta_{su}{}^n(e^{j\omega_k T}, \hat{\theta})] / [1 - \Delta_u(e^{j\omega_k T})],$$

$$\sup_{\theta_0, \hat{\theta} \in \Theta} |H_{su1}(e^{j\omega_k T}, \theta_0, \hat{\theta})|\ \}. \tag{5.6.14}$$

The first term of the above minimum is considered only when $\Delta_u(e^{j\omega_k T}) < 1$. The supremum in Eqn. (5.6.14) can be computed off-line; however, $\overline{\overline{H}}_{su1}$ must be computed on-line since it uses the on-line computed function $\Delta_{su}{}^n$. The first term in the minimum of Eqn. (5.6.14) is derived from the fact that

$$|G(e^{j\omega_k T}, \theta_0) / G(e^{j\omega_k T}, \hat{\theta})| = |[1+\delta_{su}(e^{j\omega_k T}, \hat{\theta})] / [1+\delta_u(e^{j\omega_k T})]|. \tag{5.6.15}$$

which can be shown using Eqn. (5.6.1).

5.6.4 Section Summary

In this section, we have discussed two different ways to find a bounding function on the uncertainty. If we assume that the unstructured uncertainty is time-invariant, then we use the

bounding function Δ_{su}^{n} that was derived in Eqn. (5.5.6). However, if the unstructured uncertainty can change its phase with time, then we must use the robust bounding function $\hat{\Delta}_{su}^{n}$ that was derived in Eqn. (5.6.13). In Sections 5.7 and 5.8, we will use the bounding function Δ_{su}^{n}, corresponding to the time-invariant philosophy, in all of the derivations. If the time-varying philosophy is more appropriate in a given problem, then the robust bounding function $\hat{\Delta}_{su}^{n}$ could be used in place of Δ_{su}^{n}, in the equations of Sections 5.7 and 5.8. The robust bounding function $\hat{\Delta}_{su}^{n}$ is more conservative than the bounding function Δ_{su}^{n} for the time-invariant philosophy.

5.7 A Smoothed Uncertainty Bounding Function

In this section, we discuss the computation of a smoothed, magnitude bounding function, $\tilde{\Delta}_{su}^{n}(e^{j\omega T}, \hat{\theta})$, on $\delta_{su}(e^{j\omega T}, \hat{\theta})$ through the use of the magnitude bounding function $\Delta_{su}^{n}(e^{j\omega_k T}, \hat{\theta})$, which was computed in Section 5.6, and a smoothness condition. This smoothness condition is the magnitude bounding function on the derivative of δ_{su}. First, we will derive a conservative value of the smoothness condition using only a priori information. Then, a tighter smoothness condition will be computed using the on-line knowledge of the bounding function $\Delta_{su}^{n}(e^{j\omega_k T}, \hat{\theta})$.

5.7.1 Computing a Worst-case Bounding Function on the Magnitude of the Derivative of δ_{su} Using Only a priori Information

In this subsection, we will use only a priori information to compute a worst-case bounding function on $|d\delta_{su}(e^{j\omega T}, \hat{\theta}) / d\omega|$. We will express the derivative of δ_{su} in terms of the derivative of δ_u so that assumption AD1.4 of Section 3.6 can be used. From Eqn. (5.6.1) we know that,

$$\delta_{su}(z,\hat{\theta}) = [G(z,\theta_0) / G(z,\hat{\theta})]\,[1 + \delta_u(z)] \; - \; 1. \tag{5.7.1}$$

We seek a magnitude bounding function on the derivative of $\delta_{su}(z,\hat{\theta})$ with respect to frequency. We find,

$$d\delta_{su}(e^{j\omega T},\hat{\theta}) / d\omega \; = \; (d\delta_{su}(z,\hat{\theta}) / dz) \; \Big|_{z=e^{j\omega T}} \; (de^{j\omega T} / d\omega). \tag{5.7.2}$$

So,

$$|d\delta_{su}(e^{j\omega T},\hat{\theta}) / d\omega| = \; T\,|d\delta_{su}(z,\hat{\theta}) / dz| \Big|_{z=e^{j\omega T}}. \tag{5.7.3}$$

A similar equation holds for $d\delta_u(e^{j\omega T})/d\omega$. From Eqn. (5.7.1) we find that,

$$d\delta_{su}(z,\hat{\theta}) / dz \; = \; \frac{[\,G(z,\hat{\theta})\,(dG(z,\theta_0) / dz) - G(z,\theta_0)\,(dG(z,\hat{\theta}) / dz)\,]\,[1 + \delta_u(z)]}{G(z,\hat{\theta})^2} \; +$$

$$+ \; [G(z,\theta_0) / G(z,\hat{\theta})]\,(d\delta_u(z) / dz). \tag{5.7.4}$$

We define,

$$H_{su2}(z,\theta_0,\hat{\theta}) = \frac{[\,G(z,\hat{\theta})\,(dG(z,\theta_0) / dz) - G(z,\theta_0)\,(dG(z,\hat{\theta}) / dz)\,]}{G(z,\hat{\theta})^2} \tag{5.7.5}$$

so that we can write,

$$d\delta_{su}(z,\hat{\theta}) / dz = H_{su2}(z,\theta_0,\hat{\theta})\,[1 + \delta_u(z)] + H_{su1}(z,\theta_0,\hat{\theta})\,(d\delta_u(z) / dz), \tag{5.7.6}$$

where H_{su1} was defined in Eqn. (5.6.4). We note that, when $\hat{\theta}$ is close to θ_0, then $H_{su1} \approx 1$ and $H_{su2} \approx 0$. So,

$$d\delta_{su}(z,\hat{\theta}) / dz \; \approx d\delta_u(z) / dz. \tag{5.7.7}$$

Continuing our bounding development, it can be shown, using the triangle inequality, Eqns. (5.7.3) and (5.7.6), and assumptions AD1.3-4, that

$$|d\delta_{su}(e^{j\omega T},\hat{\theta}) / d\omega| \; \leq$$

$$T\,|H_{su2}(e^{j\omega T},\theta_0,\hat{\theta})|\,[1 + \Delta_u(e^{j\omega T})] + |H_{su1}(e^{j\omega T},\theta_0,\hat{\theta})|\,\nabla_u(e^{j\omega T}), \;\; \forall\omega. \tag{5.7.8}$$

In the above equation, we know that $\theta_0 \in \Theta$; however, we must include an additional fact concerning the estimated parameter vector $\hat{\theta}$. Since we know that the true parameter vector θ_0 is in Θ, it is reasonable to constrain our parameter vector estimate $\hat{\theta}$ to be in Θ. We note that the parameter vector estimate resulting from either of our parameter estimation methods is not necessarily in Θ. Thus, the raw parameter vector estimate yielded by these estimators will be projected onto the set Θ to produce the final parameter vector estimate. This is the justification for the statement.

Fact: $\hat{\theta} \in \Theta$ (5.7.9)

Now, using Eqns. (5.7.8-9) we compute a "worst-case" a priori bounding function,

$$|d\delta_{su}(e^{j\omega T}, \hat{\theta}) / d\omega| \leq \nabla_{su,wc}(e^{j\omega T}) \tag{5.7.10}$$

where,

$$\nabla_{su,wc}(e^{j\omega T}) =$$

$$\sup_{\theta_0, \hat{\theta} \in \Theta} \{ T\,|H_{su2}(e^{j\omega T}, \theta_0, \hat{\theta})|\,[1 + \Delta_u(e^{j\omega T})] + |H_{su1}(e^{j\omega T}, \theta_0, \hat{\theta})|\,\nabla_u(e^{j\omega T}) \},\ \forall\omega \tag{5.7.11}$$

This bounding function is computed off-line.

5.7.2 Computing a Tighter Bounding Function on the Magnitude of the Derivative of δ_{su}

Using On-line Information

In this subsection, we will derive a tighter bounding function on the magnitude of the derivative of δ_{su} by using knowledge of δ_{su} that is gained on-line. The worst-case bounding function of Eqn. (5.7.11) can be very conservative. That is, in Eqn. (5.7.11) we must assume that θ_0 and $\hat{\theta}$ can take any values in the parameter space. While, θ_0 and $\hat{\theta}$ may be far from one another initially, if there is sufficient excitation, then $\hat{\theta}$ will eventually become closer to θ_0. In this case, we can compute a tighter bounding function using our on-line knowledge of the magnitude

bounding function on δ_{su}, which tells us how close our estimate is to the true plant.

Now, from Eqns. (5.6.1) we know that,

$$1 + \delta_{su}(z, \hat{\theta}) = G_{true}(z) / G(z, \hat{\theta}) = G(z,\theta_0) [1 + \delta_u(z)] / G(z, \hat{\theta}). \tag{5.7.12}$$

We seek a magnitude bounding function on the derivative of $\delta_{su}(z, \hat{\theta})$ with respect to frequency. Using Eqns. (5.7.4) and (5.7.12) it can be shown that,

$$d\delta_{su}(z, \hat{\theta}) / dz = \left[\frac{(dG(z,\theta_0)/dz)}{G(z,\theta_0)} - \frac{(dG(z,\hat{\theta})/dz)}{G(z,\hat{\theta})} \right] [1 + \delta_{su}(z, \hat{\theta})] +$$

$$+ [G(z,\theta_0) / G(z, \hat{\theta})] (d\delta_u(z) / dz). \tag{5.7.13}$$

We define,

$$H_{su3}(z,\theta_0, \hat{\theta}) = \left[\frac{(dG(z,\theta_0)/dz)}{G(z,\theta_0)} - \frac{(dG(z,\hat{\theta})/dz)}{G(z,\hat{\theta})} \right] \tag{5.7.14}$$

so that we can write,

$$d\delta_{su}(z, \hat{\theta}) / dz = H_{su3}(z,\theta_0, \hat{\theta}) [1 + \delta_{su}(z, \hat{\theta})] + H_{su1}(z,\theta_0, \hat{\theta}) (d\delta_u(z) / dz) \tag{5.7.15}$$

where H_{su1} was defined in Eqn. (5.6.4). Continuing our bounding development it can be shown, using the triangle inequality, Eqns. (5.7.3) and (5.7.15), and assumption AD1.4, that

$$|d\delta_{su}(e^{j\omega T}, \hat{\theta}) / d\omega| \le T |H_{su3}(e^{j\omega T},\theta_0, \hat{\theta})| [1 + \Delta_{su}{}^n(e^{j\omega T}, \hat{\theta})] + |H_{su1}(e^{j\omega T},\theta_0, \hat{\theta})| \nabla_u(e^{j\omega T}),$$

$$\forall \omega. \tag{5.7.16}$$

Now, using Eqns. (5.7.16) and (5.7.9), we compute the bounding function,

$$|d\delta_{su}(e^{j\omega T}, \hat{\theta}) / d\omega| \le \nabla_{su}{}^n(e^{j\omega T}) \tag{5.7.17}$$

with

$$\nabla_{su}{}^n(e^{j\omega T}) = \sup_{\theta_0, \hat{\theta} \in \Theta} \{ T |H_{su3}(e^{j\omega T},\theta_0, \hat{\theta})| \} [1+\Delta_{su}{}^n(e^{j\omega T}, \hat{\theta})] + \overline{\overline{H}}_{su1}(e^{j\omega T}) \nabla_u(e^{j\omega T}) \},$$

$$\forall \omega, \tag{5.7.18}$$

where $\overline{\overline{H}}_{su1}(e^{j\omega T})$ was defined in Eqn. (5.6.14).

The above bounding function of Eqn. (5.7.18) can be generated using the on-line computed bounding function $\Delta_{su}{}^n(e^{j\omega T}, \hat{\theta})$. Thus, as $\Delta_{su}{}^n(e^{j\omega T}, \hat{\theta})$ becomes smaller, so does our

bounding function $\nabla_{su}{}^{n}(e^{j\omega T})$. In Eqn. (5.7.18) and in Eqn. (5.6.14), which is used in Eqn. (5.7.18), the supremums for H_{su1} and H_{su3} are computed off-line.

5.7.3 Using the Smoothness Condition to Find a Tighter Bound on the Magnitude of δ_{su}

In this subsection, we will use the bounding function on the magnitude of the derivative of δ_{su} that was derived in the previous subsection, and the discrete bounding function on $|\delta_{su}|$ that was found in Section 5.5, to compute a tighter bound on $|\delta_{su}|$. This development is motivated by the observation that, depending upon the spectrum of the input signal, one may have a very jagged bounding function on the modeling uncertainty $|\delta_{su}(e^{j\omega_k T}, \hat{\theta})|$. That is, at the frequency point ω_k the bound $\Delta_{su}{}^{n}(e^{j\omega_k T}, \hat{\theta})$ may be very tight, however, at an adjacent frequency point ω_{k+1} the bound $\Delta_{su}{}^{n}(e^{j\omega_{k+1} T}, \hat{\theta})$) may be very poor. This situation is illustrated in Figure 5.1.

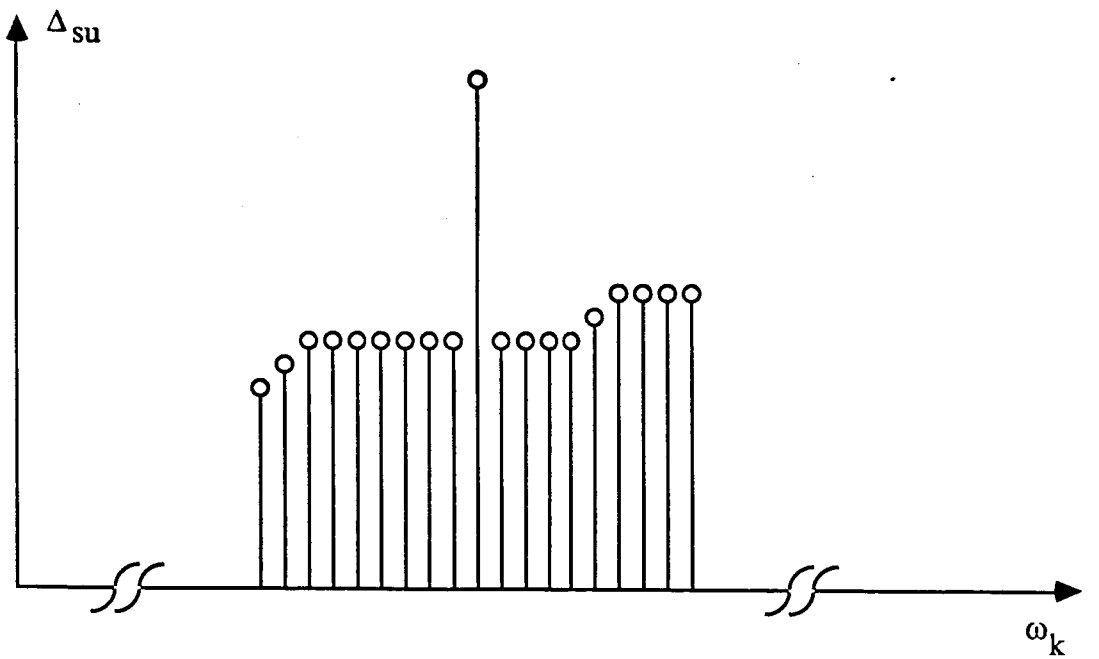

Figure 5.1: Illustration of the Need for Smoothing.

We can use the derivative bounding function $\nabla_{su}^{n}(e^{j\omega T})$ to smooth our raw bounding function $\Delta_{su}^{n}(e^{j\omega_k T}, \hat{\theta})$. However, we must first prove the following theorem.

Theorem 5.1: Let g(z) be a complex-valued function of a complex variable and let it be analytic on an open set that includes the unit circle. If a real constant h is known such that

$$h = \sup_{v \in [a,b]} |dg(e^{jv}) / dv| \tag{5.7.19}$$

then

$$|g(e^{jv})| \leq h\,|v - a| + |g(e^{ja})|, \text{ for } v \in [a,b]. \tag{5.7.20}$$

Proof: Expressing g(z) in polar form,

$$g(z) = r(z)\, e^{j\theta(z)} \tag{5.7.21}$$

we define the composite function

$$g(e^{jv}) = r(e^{jv})\, e^{j\theta(e^{jv})} \tag{5.7.22}$$

where $r(e^{jv})$ and $\theta(e^{jv})$ are real-valued composite functions of the real variable v. We differentiate to find

$$dg(e^{jv}) / dv = (dr(e^{jv}) / dv)\, e^{j\theta(e^{jv})} + r(e^{jv})\, e^{j\theta(e^{jv})}\, j\, (d\theta(e^{jv}) / dv) \tag{5.7.23}$$

$$= [\, (dr(e^{jv}) / dv) + j\, r(e^{jv})\, (d\theta(e^{jv}) / dv)\,]\, e^{j\theta(e^{jv})}. \tag{5.7.24}$$

So, we find

$$|dg(e^{jv}) / dv|^2 = |dr(e^{jv}) / dv|^2 + |r(e^{jv})\, (d\theta(e^{jv}) / dv)|^2 \tag{5.7.25}$$

$$\Rightarrow \quad |dr(e^{jv}) / dv| \leq |dg(e^{jv}) / dv|. \tag{5.7.26}$$

Since g(z) is analytic in an open region that includes the unit circle, we know that the real-valued composite function $r(e^{jv})$ of the real variable v is differentiable. Using the mean-value theorem yields,

$$r(e^{jv}) = (dr(e^{jv}) / dv) \Big|_{v=c} (v - a) + r(e^{ja}), \text{ for } v \in [a,b], \text{ where } c \in (a,b), \tag{5.7.27}$$

$$\Rightarrow \quad r(e^{jv}) \le |dr(e^{jv})/dv| \Big|_{v=c} |v - a| + r(e^{ja}), \text{ for } v \in [a,b], \text{ where } c \in (a,b). \tag{5.7.28}$$

Eqn. (5.7.20) follows from Eqns. (5.7.19), (5.7.26) and (5.7.28).

Q.E.D.

Assuming the analyticity of δ_{su}, it can be shown, using Theorem 5.1, that

$$|\delta_{su}(e^{j\omega T}, \hat{\theta})| \le |\delta_{su}(e^{j\omega_k T}, \hat{\theta})| + |\omega - \omega_k| \nabla_{su,i}^{n}(\omega_k, \omega_{k+1}) \tag{5.7.29}$$

and

$$|\delta_{su}(e^{j\omega T}, \hat{\theta})| \le |\delta_{su}(e^{j\omega_{k+1} T}, \hat{\theta})| + |\omega_{k+1} - \omega| \nabla_{su,i}^{n}(\omega_k, \omega_{k+1}) \tag{5.7.30}$$

for $\omega \in [\omega_k, \omega_{k+1}]$ where

$$\nabla_{su,i}^{n}(\omega_k, \omega_{k+1}) = \sup_{\omega \in [\omega_k, \omega_{k+1}]} \{ \nabla_{su}^{n}(e^{j\omega T}) \}, \tag{5.7.31}$$

and $\nabla_{su}^{n}(e^{j\omega T})$ is given by Eqn. (5.7.18). Using Eqns. (5.7.29-31) we see that

$$|\delta_{su}(e^{j\omega_{k+1} T}, \hat{\theta})| \le |\delta_{su}(e^{j\omega_k T}, \hat{\theta})| + |\omega_{k+1} - \omega_k| \nabla_{su,i}^{n}(\omega_k, \omega_{k+1}) \tag{5.7.32}$$

and

$$|\delta_{su}(e^{j\omega_k T}, \hat{\theta})| \le |\delta_{su}(e^{j\omega_{k+1} T}, \hat{\theta})| + |\omega_{k+1} - \omega_k| \nabla_{su,i}^{n}(\omega_k, \omega_{k+1}). \tag{5.7.33}$$

From these equations we see that it may be possible to obtain a tighter bound on $|\delta_{su}(e^{j\omega_k T}, \hat{\theta})|$ than $\Delta_{su}^{n}(e^{j\omega_k T}, \hat{\theta})$, by using the bound at an adjacent frequency point, $\Delta_{su}^{n}(e^{j\omega_{k-1} T}, \hat{\theta})$ or $\Delta_{su}^{n}(e^{j\omega_{k+1} T}, \hat{\theta})$, along with the smoothness information of $\nabla_{su,i}$. This observation is useful, since an input signal can have a lot of energy at a given frequency point but very little energy at an adjacent frequency point. By rippling our new lower bound from, first the right and then the left, in terms of the ordering of the frequency points, we can find two new, tighter bounds on $|\delta_{su}(e^{j\omega_k T}, \hat{\theta})|$. That is, we improve on our bound first by using information from the left (lower frequencies) and then by using information from the right (higher frequencies). In Figure 5.2, we show how information can be used from the lower frequency point ω_{k-1} and the higher frequency

point ω_{k+1} to find a tighter bound at frequency ω_k. In this figure, the information from the lower frequency point ω_{k-1} provides the tightest bound at frequency ω_k.

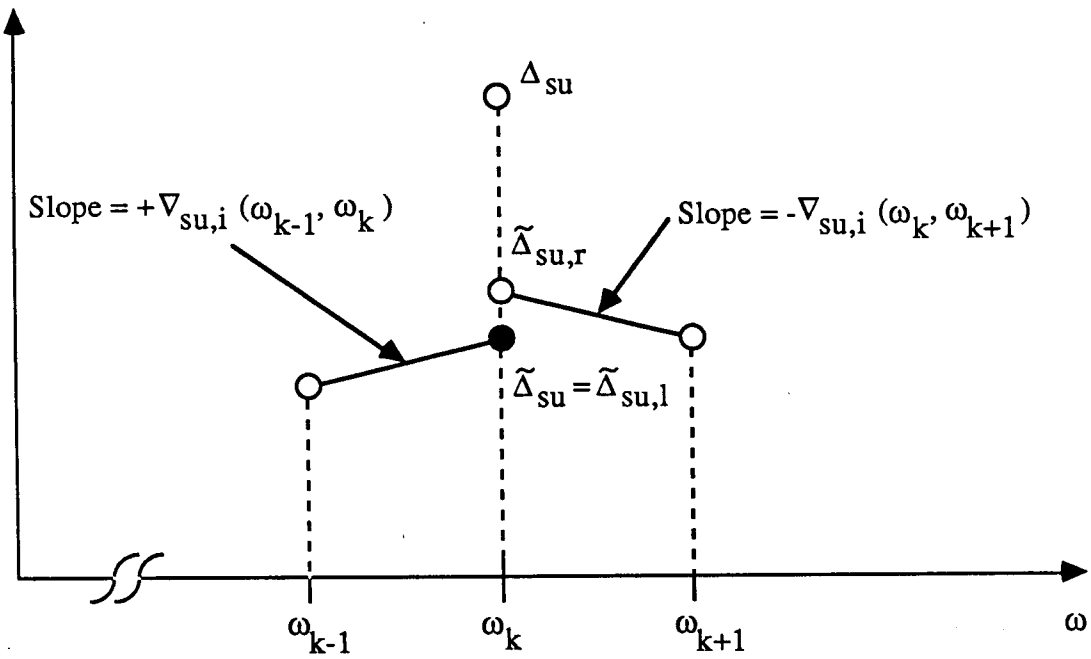

Figure 5.2: Illustration of Smoothing.

The notation for this figure is defined below. However, we first define

$$\omega_{inc} = \omega_{k+1} - \omega_k = \omega_s / N \tag{5.7.34}$$

where again ω_s is the sampling frequency. Then, the two smoothed bounding functions are given by the following recursive equations where the 'l' and 'r' denote rippling the new bounds from the left and the right, respectively.

Left Bound:

$$\tilde{\Delta}_{su,l}{}^{n}(e^{j\omega_k T}, \hat{\theta}) = \min \{ \tilde{\Delta}_{su,l}{}^{n}(e^{j\omega_{k-1} T}, \hat{\theta}) + \omega_{inc} \nabla_{su,i}{}^{n}(\omega_{k-1}, \omega_k),\ \Delta_{su}{}^{n}(e^{j\omega_k T}, \hat{\theta}) \}$$

$$\text{for } k = 1, 2, \ldots, N/2$$

$$\text{where } \tilde{\Delta}_{su,l}{}^{n}(e^{j\omega_0 T}, \hat{\theta}) = \Delta_{su}{}^{n}(e^{j\omega_0 T}, \hat{\theta}). \tag{5.7.35}$$

Right Bound:

$$\tilde{\Delta}_{su,r}^{n}(e^{j\omega_k T},\hat{\theta}) = \min\{\ \tilde{\Delta}_{su,r}^{n}(e^{j\omega_{k+1} T},\hat{\theta})+\omega_{inc}\nabla_{su,i}^{n}(\omega_k,\omega_{k+1}),\ \Delta_{su}^{n}(e^{j\omega_k T},\hat{\theta})\ \}$$

$$\text{for } k = (N/2) - 1, (N/2) - 2, \ldots, 0$$

$$\text{where } \tilde{\Delta}_{su,r}^{n}(e^{j\omega(N/2)T},\hat{\theta}) = \Delta_{su}^{n}(e^{j\omega(N/2)T},\hat{\theta}). \tag{5.7.36}$$

We define the composite smoothed bounding function,

$$\tilde{\Delta}_{su}^{n}(e^{j\omega_k T},\hat{\theta}) = \min\{\ \tilde{\Delta}_{su,l}^{n}(e^{j\omega_k T},\hat{\theta}),\ \tilde{\Delta}_{su,r}^{n}(e^{j\omega_k T},\hat{\theta})\ \}$$

$$\text{for } k = 0, \ldots, N/2, \tag{5.7.37}$$

which satisfies

$$|\delta_{su}(e^{j\omega_k T},\hat{\theta})| \le \tilde{\Delta}_{su}^{n}(e^{j\omega_k T},\hat{\theta}) \le \Delta_{su}^{n}(e^{j\omega_k T},\hat{\theta}),\ \text{for } k = 0, \ldots, N/2. \tag{5.7.38}$$

Since the impulse response corresponding to the transfer function $\delta_{su}(z,\hat{\theta})$, is real-valued, we know that,

$$|\delta_{su}(e^{j\omega(N-k)T},\hat{\theta})| = |\delta_{su}(e^{j\omega_k T},\hat{\theta})| \le \tilde{\Delta}_{su}^{n}(e^{j\omega_k T},\hat{\theta}) \le \Delta_{su}^{n}(e^{j\omega_k T},\hat{\theta}),$$

$$\text{for } k = 1, \ldots, (N/2)-1. \tag{5.7.39}$$

Thus, we need only compute the various bounding functions for $k = 0, \ldots, N/2$, since the information for the frequency points $k = (N/2)+1, \ldots, N-1$ is contained in the information for the frequency points $k = 0, \ldots, (N/2)$.

As a final note, we point out that the on-line computed bounding function Δ_{su}^{n} is used to compute the derivative bounding function that is used along with Δ_{su}^{n} itself to compute a new, smoothed bounding function $\tilde{\Delta}_{su}^{n}$. Thus, the newest smoothed bounding function could be used recursively to yield yet a tighter smoothed bounding function. That is, the newest smoothed bounding function could be used to compute a tighter derivative bounding function and, hence, a tighter new smoothed bound. We will not pursue the possibilities for recursion further, as it is not likely to greatly improve the bounding function. As a final note, we point out that the computation of the smoothed bounding function is an on-line operation that cannot be performed in a parallel fashion. That is, we must compute in a series fashion, the recursion of Eqns. (5.7.35-36) for each frequency point.

5.8 Bounding Inter-sample Variations

In this section, we discuss the computation of a safety factor that must be added to the smoothed, discrete bounding function $\tilde{\Delta}_{su}^{n}(e^{j\omega_k T}, \hat{\theta})$ to account for inter-sample variations. Ultimately, the uncertainty bounding function at discrete frequency points will be used in stability-robustness tests to update the compensator. The stability-robustness tests really use an uncertainty bounding function that is a continuous function of frequency. Since the actual computations will be performed with the uncertainty bounding function that is a discrete function of frequency, we must add the aforementioned safety factor to the discrete function to account for the worst possible peaks that may occur between frequency samples ω_k. We will choose this additive safety factor in such a way that the largest inter-sample variations lie below a line drawn between the final values of the uncertainty bounding function at two adjacent frequency samples. This idea is illustrated in Figure 5.3, where we have yet to define the notation in the figure. Now, since $\delta_{su}(e^{j\omega T}, \hat{\theta})$ is assumed to be analytic, we can use Eqns. (5.7.29-30) to find,

$$|\delta_{su}(e^{j\omega T}, \hat{\theta})| \le \min \{ |\delta_{su}(e^{j\omega_k T}, \hat{\theta})| + |\omega - \omega_k| \nabla_{su,i}^{n}(\omega_k,\omega_{k+1}),$$

$$|\delta_{su}(e^{j\omega_{k+1} T}, \hat{\theta})| + |\omega_{k+1} - \omega| \nabla_{su,i}^{n}(\omega_k,\omega_{k+1}) \} \qquad (5.8.1)$$

for $\omega \in [\omega_k,\omega_{k+1}]$. Thus, we define a discrete bounding function $\overline{\Delta}_{su}^{n}(e^{j\omega_k T}, \hat{\theta})$ that includes the additive safety factor and that satisfies

$$|\delta_{su}(e^{j\omega_k T}, \hat{\theta})| \le \overline{\Delta}_{su}^{n}(e^{j\omega_k T}, \hat{\theta}), \qquad (5.8.2)$$

where, using Eqn. (5.8.1), we choose

$$\overline{\Delta}_{su}^{n}(e^{j\omega_k T}, \hat{\theta}) = \tilde{\Delta}_{su}^{n}(e^{j\omega_k T}, \hat{\theta}) + (\omega_{inc} / 2) \max \{ \nabla_{su,i}^{n}(\omega_{k-1},\omega_k), \nabla_{su,i}^{n}(\omega_k,\omega_{k+1}) \},$$

$$\text{for } k = 1, \ldots, (N/2)-1, \qquad (5.8.3)$$

where

$$\overline{\Delta}_{su}^{n}(e^{j\omega_0 T}, \hat{\theta}) = \tilde{\Delta}_{su}^{n}(e^{j\omega_0 T}, \hat{\theta}) + (\omega_{inc} / 2) \nabla_{su,i}^{n}(\omega_0,\omega_1) \qquad (5.8.4)$$

$$\overline{\Delta}_{su}^{n}(e^{j\omega_{(N/2)} T}, \hat{\theta}) = \tilde{\Delta}_{su}^{n}(e^{j\omega_{(N/2)} T}, \hat{\theta}) + (\omega_{inc} / 2) \nabla_{su,i}^{n}(\omega_{(N/2)-1},\omega_{(N/2)}). \qquad (5.8.5)$$

Again, the values of $\overline{\Delta}_{su}^{n}(e^{j\omega_k T}, \hat{\theta})$ for k=(N/2)+1, . . , N-1 can be found from the values of $\overline{\Delta}_{su}^{n}(e^{j\omega_k T}, \hat{\theta})$ for k=1, . . , (N/2)-1. By using the bounding function of Eqns. (5.8.3-5), we guarantee that a line drawn between the values of $\overline{\Delta}_{su}^{n}(e^{j\omega_k T}, \hat{\theta})$ and $\overline{\Delta}_{su}^{n}(e^{j\omega_{k+1} T}, \hat{\theta})$ will bound $|\delta_{su}(e^{j\omega T}, \hat{\theta})|$ for $\omega \in [\omega_k, \omega_{k+1}]$. This is illustrated in Figure 5.3.

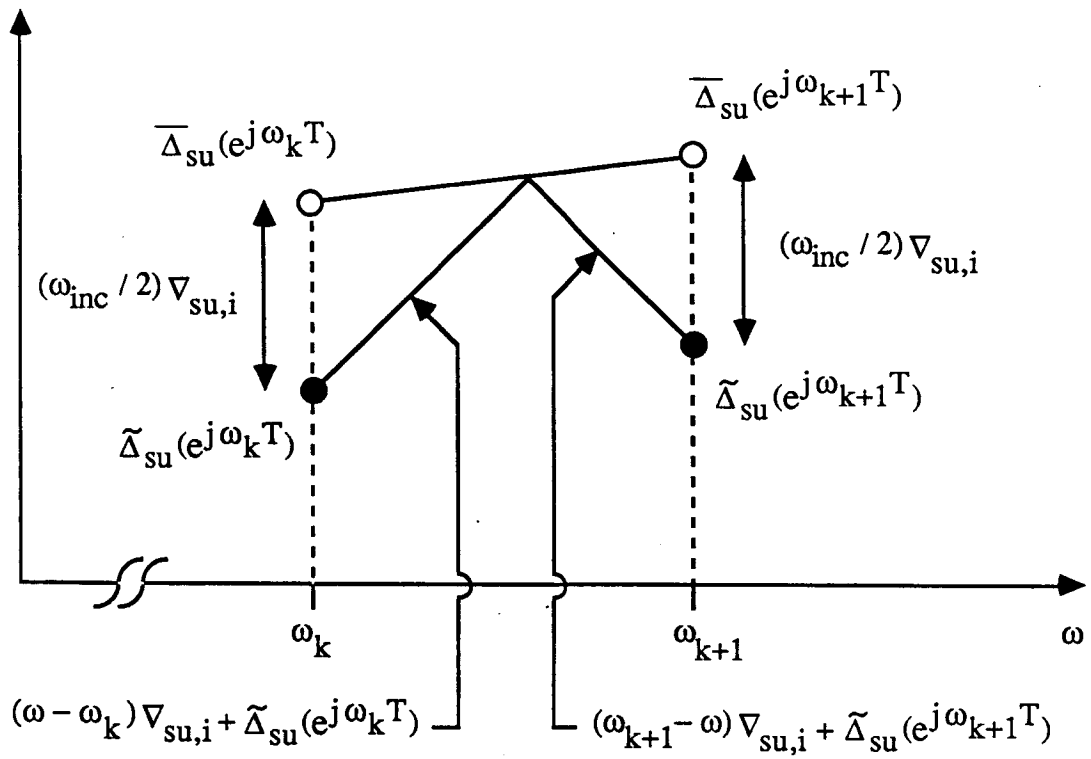

Figure 5.3: Bounding Inter-sample Variations.

5.9 Summary

In this brief section, we will place the results of this chapter in perspective and then summarize the methodology for computing the final uncertainty bounding function. In this chapter, we have developed frequency-domain methodologies for 1) finding a parameter estimate and, hence, a nominal plant model; and 2) finding a frequency-domain bounding function on the modeling uncertainty corresponding to this nominal model. It is emphasized that the frequency-domain error bounding methodology requires only a parameter vector estimate to do its job. This parameter estimate can come from either the robustified least-squares parameter

estimator, which uses time-varying dead-zone, or the frequency-domain parameter estimator of Section 5.4. Later, in the simulations, it will be shown that the dead-zone based parameter estimator has some weaknesses, so the frequency-domain parameter estimator will be the parameter estimator of choice.

Since the development of this chapter has been quite involved, we present the summarizing flowchart of Figure 5.4. This flowchart shows what computations are done off-line, on-line at every sample time, and on-line before a control-law update. Further, since the computation of the final uncertainty bounding function requires several steps, we summarize the steps of this procedure.

Uncertainty Bounding Procedure:

1) Compute the raw bounding function, Δ_{su}^{n}, on $|\delta_{su}|$ [Eqn. (5.5.6)].

   a) Time-invariant Unstructured Uncertainty Philosophy: Use Δ_{su}^{n} in Step 2.

   b) Time-varying Unstructured Uncertainty Philosophy: Use $\hat{\Delta}_{su}^{n}$ in Step 2 [Eqn. (5.6.13)].

2) Compute the smoothness condition, ∇_{su}^{n}, on $|d\delta_{su}/d\omega|$ based on Δ_{su}^{n} (or $\hat{\Delta}_{su}^{n}$) [Eqn. (5.7.18)].

3) Compute the smoothed bounding function, $\tilde{\Delta}_{su}^{n}$, on $|\delta_{su}|$ using Δ_{su}^{n} (or $\hat{\Delta}_{su}^{n}$) and ∇_{su}^{n} [Eqn. (5.7.37)].

4) Compute the final uncertainty bounding function, $\overline{\Delta}_{su}^{n}$, including the safety factor, on $|\delta_{su}|$ using $\tilde{\Delta}_{su}^{n}$ and ∇_{su}^{n} [Eqns. (5.8.3-5)].

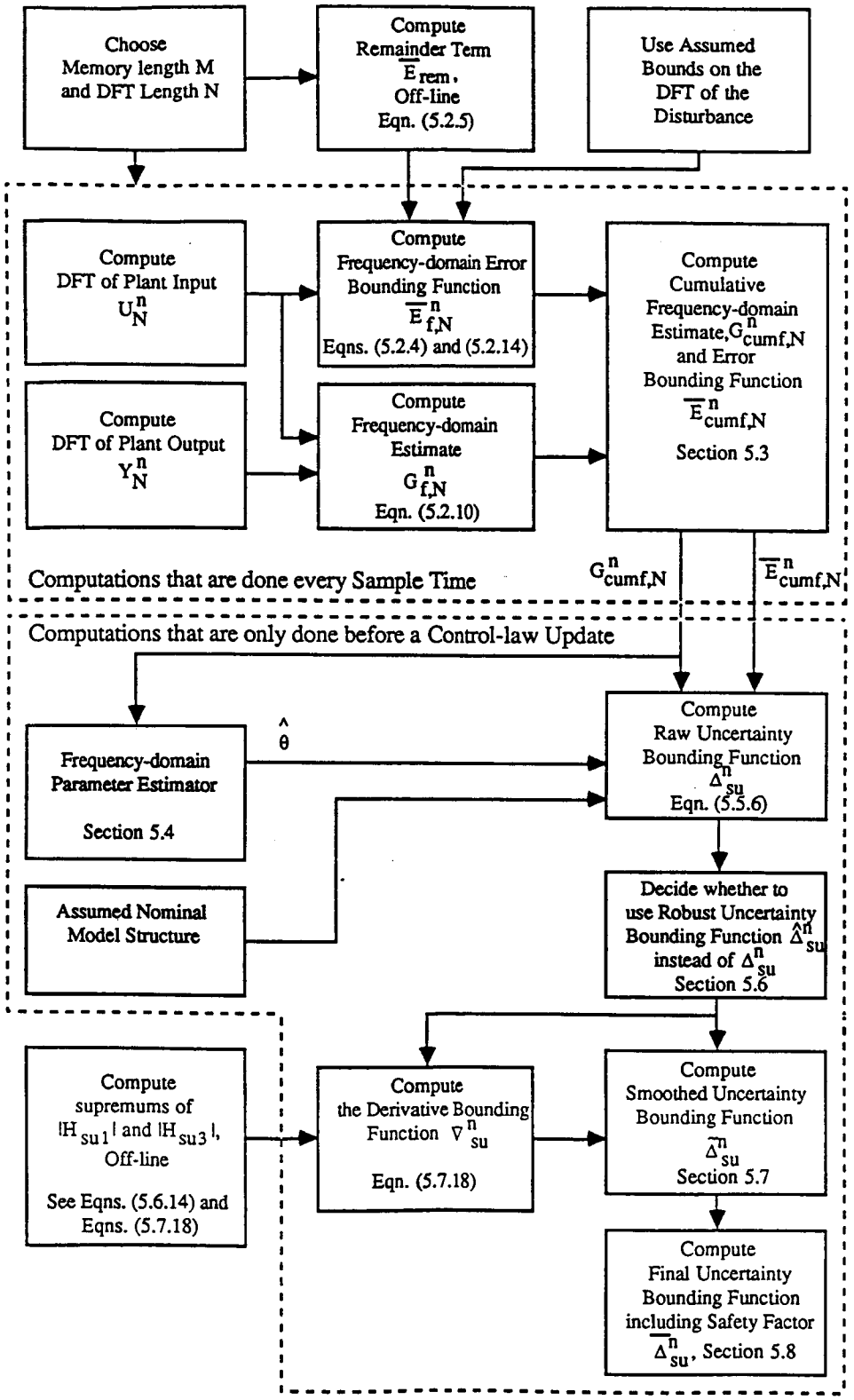

Figure 5.4: Development of the Frequency-domain Bounding Method and the Frequency-domain Parameter Estimator.

CHAPTER 6.
DESIGN CHOICES, DISTURBANCE MODELING AND COMPUTATIONAL ISSUES

6.1 Introduction

In this chapter, we will discuss how to choose various design parameters, such as the sampling period, the DFT length for both the time-domain parameter estimator and the frequency-domain estimation method, and the memory length M. In addition, questions of how to specify the bounding functions in the assumptions of the robust estimator and how to model the disturbance are examined in this chapter. We also consider the computational requirements of the robust estimator.

First, in Section 6.2, we consider the choice of the sampling period that is used in our sampled-data control system, which controls the continuous-time plant. Since we are interested in the robust estimator primarily for the purpose of closed-loop control, we must consider both the identification and control impact of the sampling period choice. Several different models for the additive output disturbance are examined in Section 6.3. The specification of the bounding assumptions of the robust estimator are discussed in Section 6.4. We will examine the design choices for the time-domain parameter estimator and the frequency-domain bounding methodology in Sections 6.5 and 6.6, respectively. In Section 6.5, we will consider the choice of the DFT length from the perspective of the time-domain parameter estimator alone. That is, it would be convenient if the DFT length that is used in the bounding mechanism of the time-domain parameter estimator was the same as the DFT length that is used in the frequency-domain bounding methodology, since then we would only have to compute one DFT of the input signal at each time index. However, we shall see in this chapter that the time-domain parameter estimator of Chapter 4 will, in general, require a shorter DFT length than the frequency-domain bounding methodology of Chapter 5. Thus, in the respective sections, we will use the notation N_t and N_f to refer to the DFT lengths corresponding to the time and frequency domain methods, respectively. In Section 6.7, we examine the computational requirements of robust estimator by examining. The key contributions of this chapter are the completion of the robust estimator design methodology and the investigation of the extensive computational requirements of the robust estimator.

6.2 Choice of Sampling Period and Closed-loop Objectives

The choice of the sampling period in the robust estimator involves a tradeoff between the target closed-loop bandwidth which we're trying to achieve and the deleterious effects of the high-frequency unmodeled dynamics on the identifier. To better understand this tradeoff, in Subsections 6.2.1 and 6.2.2, we will first investigate how the choice of sampling period affects our achievable closed-loop bandwidth and the performance of our robust estimator. Then, in Subsection 6.2.3, we will examine the tradeoff that arises.

6.2.1 Sampling Period Choice and the Closed-loop Bandwidth

In this subsection, we assume that the designer has some target closed-loop bandwidth that he wishes to achieve. In the field of digital control, sampling rates are typically chosen to be between 6 and 10 times the target closed-loop bandwidth, which we denote by ω_{tcl}. This is only a rule of thumb since some applications require faster sampling rates. The phase shift at ω_{tcl}, due to the delay of the discrete-time control system, can be computed as follows.

$$\text{Phase shift at } \omega_{tcl} \text{ (in degrees)} = -360° / (\omega_s / \omega_{tcl}) \tag{6.2.1}$$

where again the sampling frequency is given by

$$\omega_s = 2\pi / T \tag{6.2.2}$$

where T is the sampling period. We compute the following values.

Table 6.1: Sampling Period Choice and the Phase Shift at the Target Closed-loop Bandwidth.

$(\omega_s / \omega_{tcl})$	Phase shift at ω_{tcl} (in degrees)
5	-72°
10	-36°
15	-24°
20	-18°

Thus, given no other constraints, we want to choose the sampling period as small as possible so as not to introduce a large negative phase shift near the crossover frequency of the system.

6.2.2 Sampling Period Choice and the Disturbance

In Subsection 2.1.2, we saw that to avoid aliasing effects, we must choose the sampling

frequency ω_s such that $\omega_s/2$ is greater than the largest frequency at which the disturbance has significant energy. In practice, the anti-aliasing filter of Figure 3.1, whose presence we do not include in the analysis of this thesis, will attenuate the disturbance at high frequencies. See Astrom and Wittenmark [31, p.28] for a discussion of anti-aliasing filters. Since we explicitly include aliasing effects into our bounds, as in Eqn. (3.5.2), we will not consider this point further.

6.2.3 Sampling Period Choice and Identification Objectives

In this subsection, we consider how to choose the sampling period so as to have good performance of our robust estimator. Our goal is to choose the sampling period so that the high-frequency unmodeled dynamics will appear small in magnitude, in the discrete-time model of the plant. It was shown by Rohrs et al. [21], see Section 3.3, that the larger the sampling period is, the smaller the continuous-time unmodeled dynamics will appear in the discrete-time plant. Figures 6.1-2 illustrate how the choice of sampling period affects the discrete-time unmodeled dynamics. In Figures 6.1 and 6.2, we show the magnitude bounding function on the discrete-time unstructured uncertainty for two different choices of sampling period, T_a and T_b, where $(\omega_s)_a$ and $(\omega_s)_b$ are the corresponding sampling frequencies. It can be seen that the smaller the sampling frequency is, the smaller the magnitude of the unstructured uncertainty will be. Thus, slow-sampling leads to a discrete-time system that can be modeled accurately by the low-frequency nominal model.

6.2.4 The Tradeoff Between Closed-loop Bandwidth and Identification Goals

In this subsection, we summarize the tradeoff involved in the choice of the sampling period. We want our sampling frequency ω_s to be 6-10 times the target closed-loop bandwidth ω_{tcl} and we want $\omega_s/2$ to be smaller than the frequency at which the unmodeled dynamics magnitude bound becomes greater than unity. Figure 6.3 illustrates this situation. In this figure, we have denoted the frequency at which the unstructured uncertainty magnitude bound becomes greater than unity by ω_{mcl}, the maximum closed-loop bandwidth. That is, the closed-loop system cannot have a bandwidth greater than ω_{mcl} and still be robustly stable to the unstructured uncertainty shown in

the figure. With this notation in mind, we consider the following examples.

Example 1: If $\omega_{mcl} = 10\ \omega_{tcl}$ and we choose $\omega_s = 10\ \omega_{tcl}$, then $(\omega_s / 2) = (1 / 2)\ \omega_{mcl}$. In this example, we are able to meet all of our objectives for the choice of the sampling period. That is, since $(\omega_s / 2) < \omega_{mcl}$, the unstructured uncertainty will appear small in the discrete-time plant for this choice of sampling frequency. Now, we consider a more difficult case.

Example 2: If $\omega_{mcl} = \omega_{tcl}$ and we choose $\omega_s = 10\ \omega_{tcl}$, then $(\omega_s / 2) = 5\ \omega_{mcl}$. In this example, we see that $(\omega_s / 2) > \omega_{mcl}$ so the unstructured uncertainty will appear large in the discrete-time plant. Thus, for this example, we see that when the maximum closed-loop bandwidth that is consistent with stability-robustness requirements is desired, the unstructured uncertainty will have a large effect on the robust estimator.

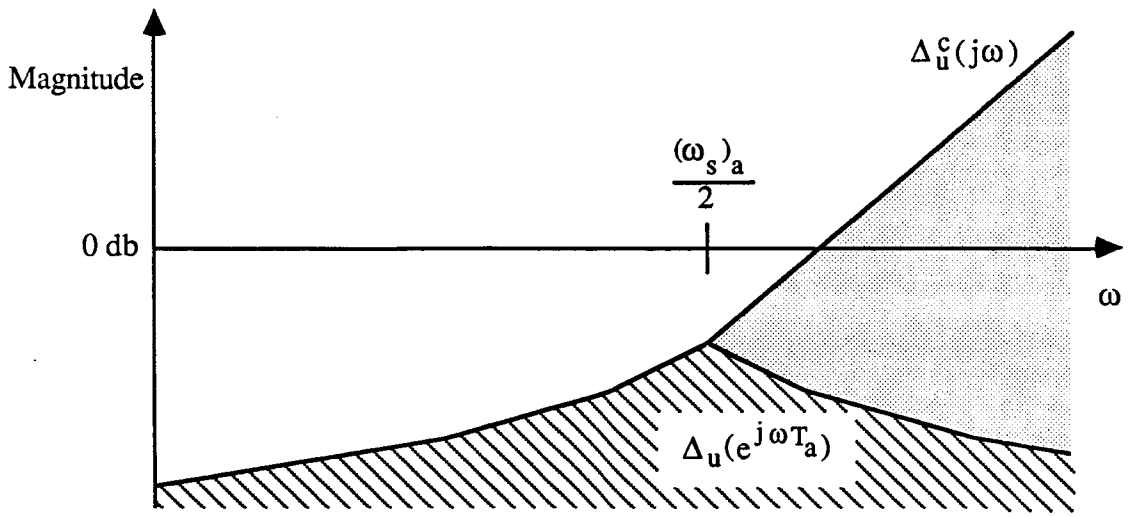

Figure 6.1: Continuous and Discrete time Unmodeled Dynamics for Sampling Period T_a.

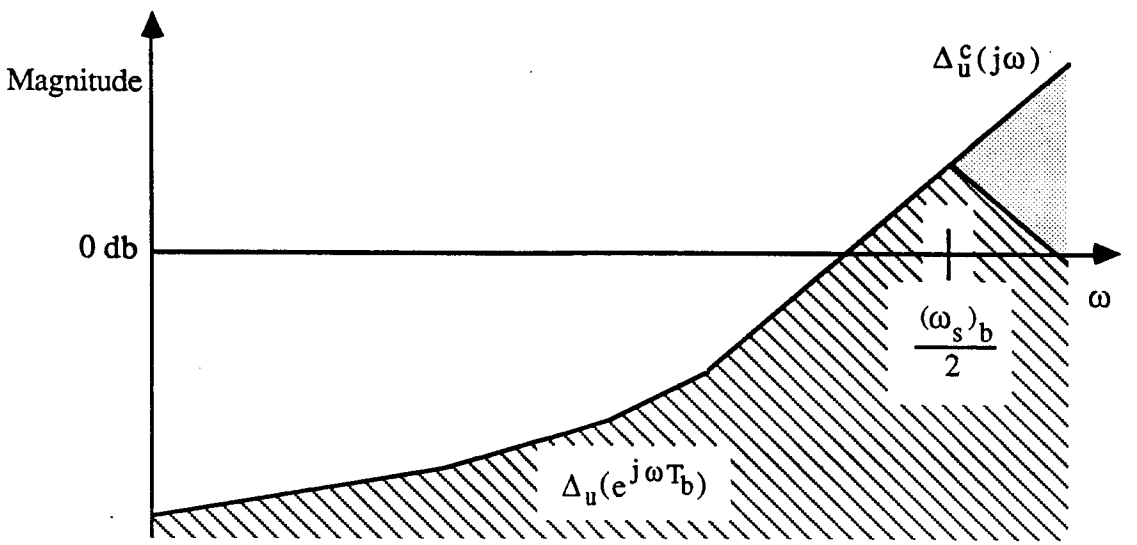

Figure 6.2: Continuous and Discrete time Unmodeled Dynamics for Sampling Period $T_b < T_a$.

Notice that for the faster sampling period, the unmodeled dynamics bound is larger at high frequencies.

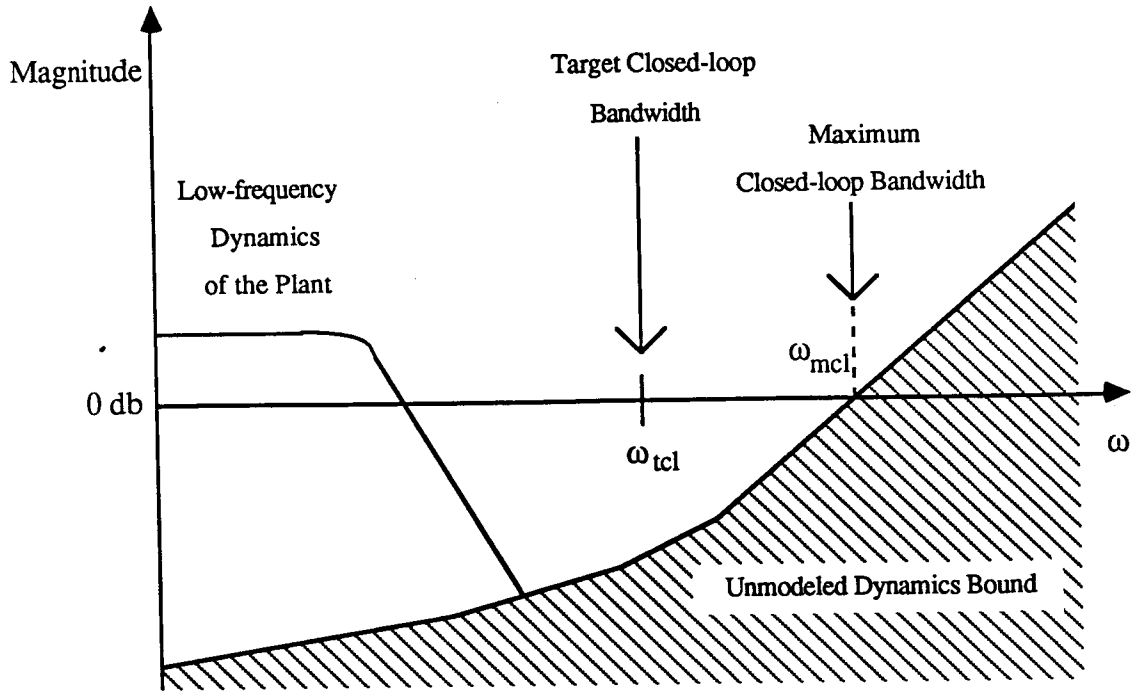

Figure 6.3: Frequency Diagram for Sampling Period Choice.

6.3 Specification of the Bounding Functions in the Assumptions

6.3.1 Introduction

The specification of the bounding functions of assumptions AC1.3-4 and, hence, AD1.3-4 of Chapter 3, are examined in this section. The landmark paper by Doyle and Stein [34] provides an insightful discussion of the multiplicative, unstructured uncertainty plant representation which we use throughout this thesis. This paper motivates the use of the unstructured uncertainty plant representation and mentions various physical phenomena that can be characterized in this way. Later, in the simulation part of this thesis, we shall generate the magnitude bounding function on the unstructured uncertainty in a rather artificial way, since we are not motivated by a specific physical example.

While the bounding function of assumption AC1.3 (or AD1.3) has become a widely used uncertainty representation, the smoothness assumption of AC1.4 (or AD1.4) has not been used previously in the literature. The specification of a magnitude bounding function on the derivative of the unstructured uncertainty is even more difficult than the specification of a magnitude bounding

function on the, only coarsely known, unstructured uncertainty itself. The specification, from physical principles, of the smoothness condition of AC1.4 may be difficult. In the following subsection, we will examine several examples in an effort to better understand the requirement of assumption AC1.4.

6.3.2 Understanding Assumptions AC1.3-4 and AD1.3-4

In this subsection, we will examine three examples of high-frequency unmodeled dynamics and will compute the bounding function of assumption AC1.4 for each. Intuitively, the unmodeled dynamics are largest in the high-frequency range, that is, in the frequency range above the crossover frequency of the system. The low-frequency dynamics of the plant are assumed to be captured by the low-frequency nominal model, in which the uncertainty is structured. We now consider three simple examples to gain insight.

Example 1: (First-order pole) Consider the hypothetical multiplicative uncertainty,

$$1 + \delta^c_u(s) = a / (s + a), \text{ where } a > 0 \text{ and} \tag{6.3.1}$$

where, in practice, 'a' is a high-frequency pole, relative to the poles of the nominal model. Then, we find that,

$$\delta^c_u(s) = - s / (s + a). \tag{6.3.2}$$

We compute,

$$|\delta^c_u(j\omega)| = \omega / \sqrt{\omega^2 + a^2}, \text{ and} \tag{6.3.3}$$

$$|d\delta^c_u(j\omega) / d\omega| = a / (\omega^2 + a^2). \tag{6.3.4}$$

We consider the following special cases:

Low-frequency Case: If $\omega << a$, then

$$|\delta^c_u(j\omega)| \approx \omega / a, \tag{6.3.5}$$

$$|d\delta^c_u(j\omega) / d\omega| \approx 1 / a. \tag{6.3.6}$$

High-frequency Case: If $\omega >> a$, then

$$|\delta^c_u(j\omega)| \approx 1, \tag{6.3.7}$$

$$|d\delta^c_u(j\omega) / d\omega| \approx a / \omega^2. \tag{6.3.8}$$

The values of $|\delta^c_u(j\omega)|$ and $|d\delta^c_u(j\omega)/d\omega|$ are shown in Figure 6.4 for a=1 rad/sec. Thus, if we know that the multiplicative uncertainty is composed only of a first-order pole, then we can bound $|d\delta^c_u(j\omega)/d\omega|$ using a lower bound on 'a', the magnitude of the high-frequency pole.

Example 2: (Second-order pole) Consider the hypothetical multiplicative uncertainty,

$$1 + \delta^c_u(s) = \omega_n^2 / (s^2 + 2\,\zeta\,\omega_n\, s + \omega_n^2), \tag{6.3.9}$$

where we assume $\zeta \leq 1$ and note that, in practice, ω_n is a high frequency relative to the natural frequencies of the nominal model. Then, we find

$$\delta^c_u(s) = -\,s\,(s + 2\,\zeta\,\omega_n) / (s^2 + 2\,\zeta\,\omega_n\, s + \omega_n^2). \tag{6.3.10}$$

We compute,

$$|\delta^c_u(j\omega)| = \omega \sqrt{\omega^2 + 4\,\zeta^2\,\omega_n^2} \;/\; \sqrt{(\omega^2 - \omega_n^2)^2 + 4\,\zeta^2\,\omega_n^2\,\omega^2}\,, \text{ and} \tag{6.3.11}$$

$$|d\delta^c_u(j\omega) / d\omega| = 2\,\omega_n^2 \sqrt{\omega^2 + \zeta^2\,\omega_n^2} \;/\; [\,(\omega^2 - \omega_n^2)^2 + 4\,\zeta^2\,\omega_n^2\,\omega^2\,]. \tag{6.3.12}$$

We consider the following special cases:

Low-frequency Case: If $\omega << \omega_n$, then

$$|\delta^c_u(j\omega)| \approx (2\,\zeta / \omega_n)\,\omega, \tag{6.3.13}$$

$$|d\delta^c_u(j\omega) / d\omega| \approx 2\,\zeta / \omega_n \leq 2 / \omega_n. \tag{6.3.14}$$

Resonant-frequency Case: If $\omega = \omega_n$, then

$$|\delta^c_u(j\omega)| \approx \sqrt{1 + 4\,\zeta^2}\,/\,(2\,\zeta), \tag{6.3.15}$$

$$|d\delta^c_u(j\omega) / d\omega| = \sqrt{1 + \zeta^2}\,/\,(2\,\zeta^2\,\omega_n). \tag{6.3.16}$$

High-frequency Case: If $\omega >> \omega_n$, then

$$|\delta^c_u(j\omega)| \approx 1, \tag{6.3.17}$$

$$|d\delta^c_u(j\omega) / d\omega| \approx 2\,\omega_n^2 / \omega^3. \tag{6.3.18}$$

The values of $|\delta^c_u(j\omega)|$ and $|d\delta^c_u(j\omega)/d\omega|$ for this example are shown in Figure 6.5 for ζ=0.2 and ω_n=1 rad/sec. From Eqn. (6.3.16) we see that if $\zeta << 1$, then for the resonant frequency case,

$$|\delta^c_u(j\omega)| \approx 1 / (2\,\zeta), \tag{6.3.19}$$

$$|d\delta^c_u(j\omega) / d\omega| \approx 1 / (2\,\zeta^2\,\omega_n), \tag{6.3.20}$$

both of which can be very large. Thus, if we know that the multiplicative uncertainty is composed only of a second-order system (with complex poles), then we can bound $|\delta^c_u(j\omega)|$ by using a lower bound on ζ, and we can bound $|d\delta^c_u(j\omega)/d\omega|$ by using a lower bound on both ζ and ω_n.

Example 3: (Time delay) Consider the hypothetical multiplicative uncertainty,

$$1 + \delta^c_u(s) = e^{-s(T_d)}, \tag{6.3.21}$$

where T_d is the time delay. Then we find that,

$$\delta^c_u(s) = e^{-s(T_d)} - 1. \tag{6.3.22}$$

We compute

$$|\delta^c_u(j\omega)| = |e^{-j\omega(T_d)} - 1| = 2\,|\sin(\omega\,T_d / 2)|, \text{ and} \tag{6.3.23}$$

$$|d\delta^c_u(j\omega) / d\omega| = T_d. \tag{6.3.24}$$

Thus, if we know that the multiplicative uncertainty is composed only of a time delay, then we can bound $|d\delta^c_u(j\omega)/d\omega|$ using an upper bound on T_d, the time delay.

These three examples provide insight as to how to generate the bounding functions of assumptions AC1.3-4. In Subsection 3.3.2, it was noted that the discrete-time unstructured uncertainty is approximately equal to the continuous-time unstructured uncertainty, if the plant rolls-off sufficiently fast. That is, we showed

$$\delta(e^{j\omega T}) \approx \delta^c_u(j\omega), \text{ for } -\omega_s/2 < \omega < \omega_s/2. \tag{6.3.25}$$

This means that the low-frequency cases given by Eqns. (6.3.5) and (6.3.13) are the most significant approximations since, typically, the poles of the unmodeled dynamics will be at high frequencies relative to $\omega_s/2$. However, if the damping ratio of a second-order system is very small,

then $|\delta^c_u(j\omega)|$ can be quite large as was seen in Eqn. (6.3.19). In this case, the full frequency-folding summation must be used to compute the discrete-time bounding function, since the plant, including the large resonant peak, may not have rolled-off enough to make the approximation of Eqn. (6.3.25) accurate.

In Subsection 3.3.3, it was noted that the derivative of the discrete-time unstructured uncertainty is approximately equal to the derivative of the continuous-time unstructured uncertainty if the plant rolls-off sufficiently fast. That is, we showed

$$d\delta(e^{j\omega T}) / d\omega \approx d\delta^c_u(j\omega) / d\omega, \text{ for } -\omega_s/2 < \omega < \omega_s/2. \tag{6.3.26}$$

Again, since the poles of the unmodeled dynamics will be at high frequencies relative to $\omega_s/2$, the low-frequency cases given by Eqns. (6.3.6) and (6.3.14) are the most significant approximations. However, if the damping ratio of a second-order system is very small, then $|d\delta^c_u(j\omega)/d\omega|$ can be large as was seen in Eqn. (6.3.20). In this case, as for the unstructured uncertainty itself, the full frequency-folding summation must be used to compute the discrete-time bounding function, since the plant, including the large resonant peak, may not have rolled-off enough to make the approximation of Eqn. (6.3.26) accurate. The use of the frequency-folding summation, see Eqn. (3.3.25), will result in a bound that is conservative, as was discussed in Subsection 3.3.3. Further, the use of Eqn. (3.3.25) requires considerable analytical and computational work.

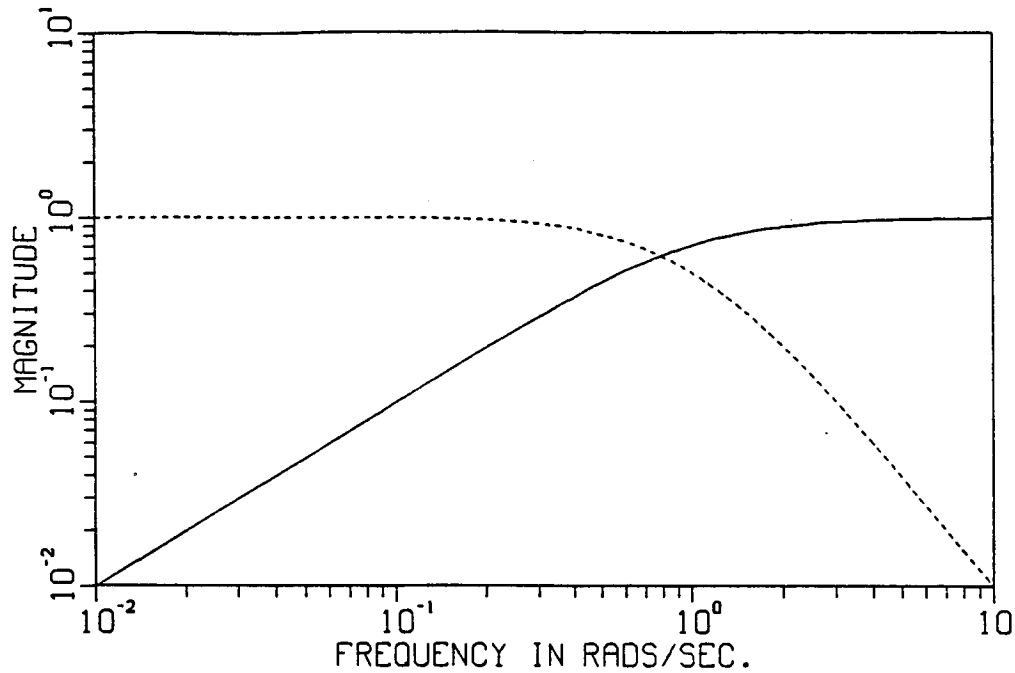

Figure 6.4: Bounding Functions for First-order Unmodeled Dynamics.

($|\delta^c_u(j\omega)|$ = ——, $|d\delta^c_u(j\omega)/d\omega|$ = - - - -)

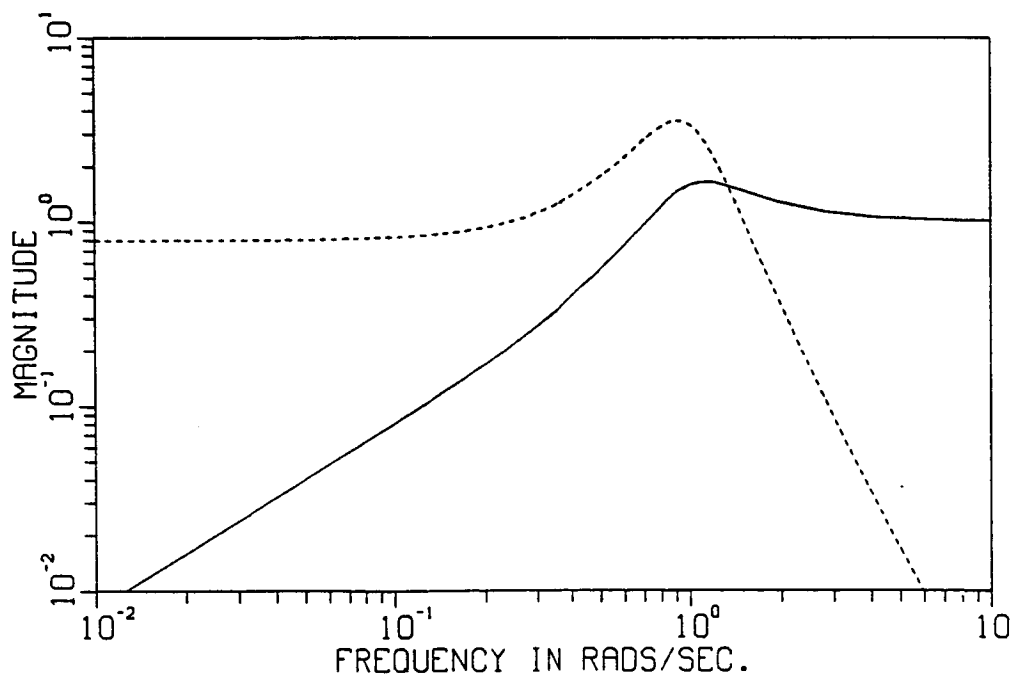

Figure 6.5: Bounding Functions for Second-order Unmodeled Dynamics.

($|\delta^c_u(j\omega)|$ = ——, $|d\delta^c_u(j\omega)/d\omega|$ = - - - -)

6.4 Disturbance Modeling and Bounding the Disturbance DFT

In this section, we will discuss the satisfaction of disturbance assumptions of Chapter 3. In practice, the specification of the DFT bounding function for the disturbance will probably be based on empirical measurements of the disturbance spectrum. However, in this section, we do not discuss the empirical generation of the bounding functions further, but instead will examine the relationship between several disturbance models and the disturbance assumptions required by the robust estimator. Specifically, we will discuss how different disturbance models can or cannot be used to find a bounding function on the magnitude of the DFT of the disturbance. The relationship between the Fourier transform of the continuous-time disturbance d(t) and the DFT of the time-sampled disturbance d[n] was discussed in Section 3.5.1. Since this relationship was rather complicated we will work directly with discrete-time disturbance models, in this section. That is, we will consider the DFT of the disturbance signal directly instead of performing the integrals of Eqns. (3.5.13-14). In order to be able to be used in the robust estimator, a disturbance model must be able to satisfy assumptions AD2.1-2.2 of Section 4.4. As we will see, all bounded disturbances satisfy AD2.1-2.2.

6.4.1 Bounded-but-Unknown Models

In this subsection, we examine a bounded-but-unknown disturbance model. That is, we assume that the discrete-time signal d[n] satisfies,

$$\underline{\text{Bounded-but-Unknown Model:}}\ |d[n]| \le d_{max},\ \forall n. \tag{6.4.1}$$

It's clear that this model satisfies assumption AD2.1; however, it's less obvious how the model satisfies AD2.2. Consider the expression for the DFT of the disturbance, from Eqns. (2.1.5) and (2.1.3),

$$D_N(\omega_k) = \sum_{m=0}^{N-1} d[m]\, e^{-j(2\pi/N)km}. \tag{6.4.2}$$

Given only the information that d[m] is bounded and real-valued, we must assume that d[m] is the disturbance that maximizes $|D_N(\omega_k)|$ for a given bound d_{max}. From Eqn. (6.4.2) its clear that if complex-valued disturbances were permitted, then the disturbance signal that maximizes $|D_N(\omega_k)|$ would be $d_{max}e^{j(2\pi/N)km}$, which would yield $D_N(\omega_k)=N$. Since d[m] must be real-valued, we

instead consider the use of a sinusoid with magnitude d_{max}. The author believes that the maximizing real-valued disturbance is given by

$$d[m] = d_{max} \cos(\tilde{\omega} T m + \phi) = (d_{max}/2)\{e^{j(\tilde{\omega}Tm+\phi)} + e^{-j(\tilde{\omega}Tm+\phi)}\}, \quad (6.4.3)$$

whose DFT is

$$D_N(\omega_k) = (d_{max}/2)\{ e^{j\phi} e^{-j[(N-1)(\omega_k-\tilde{\omega})T/2]} (\sin(N(\omega_k-\tilde{\omega})T/2) / \sin((\omega_k-\tilde{\omega})T/2)) +$$

$$+ e^{-j\phi} e^{-j[(N-1)(\omega_k+\tilde{\omega})T/2]} (\sin(N(\omega_k+\tilde{\omega})T/2) / \sin((\omega_k+\tilde{\omega})T/2)) \}. \quad (6.4.4)$$

In Eqn. (6.4.4) for a given ω_k and $\tilde{\omega}$, the phase shift ϕ can always be chosen such that the two terms have the same phase and, hence, their magnitudes may be added. With reference to the development of Section 3.5 and assumption AD2.2, we find that for the disturbance of Eqn. (6.4.3), the following bounding function on the disturbance can be computed at the frequency ω_k.

$$\overline{D}_N(\omega_k) = (d_{max}/2)(\sup_{\tilde{\omega}\in[0,\omega_s]} \{ |\sin(N(\omega_k-\tilde{\omega})T/2) / \sin((\omega_k-\tilde{\omega})T/2)| +$$

$$+ |\sin(N(\omega_k+\tilde{\omega})T/2) / \sin((\omega_k+\tilde{\omega})T/2)| \}) \quad (6.4.5)$$

This bounding function is shown in Figure 6.6, for N=20, d_{max}=1 and T=1 sec. Analogously, the start-up bounding function in AD2.2 is given by

$$\overline{D}_N^{+n}(\omega_k) = (d_{max}/2)(\sup_{\tilde{\omega}\in[0,\omega_s]} \{ |\sin((n+1)(\omega_k-\tilde{\omega})T/2) / \sin((\omega_k-\tilde{\omega})T/2)| +$$

$$+ |\sin((n+1)(\omega_k+\tilde{\omega})T/2) / \sin((\omega_k+\tilde{\omega})T/2)| \}). \quad (6.4.6)$$

Thus, given only that d[m] is real-valued and satisfies the bounded-but-unknown model of Eqn. (6.4.1), we can compute the preceding bounding functions on the DFT of the disturbance and, hence, satisfy assumption AD2.2. Since Eqns. (6.4.5-6) are complicated, the following simpler, but more conservative, bounding functions can be used

$$\overline{D}_N(\omega_k) = d_{max} N, \text{ and} \quad (6.4.7)$$

$$\overline{D}_N^{+n}(\omega_k) = d_{max}\,(n+1), \text{ for } k = 0, \ldots, N-1. \tag{6.4.8}$$

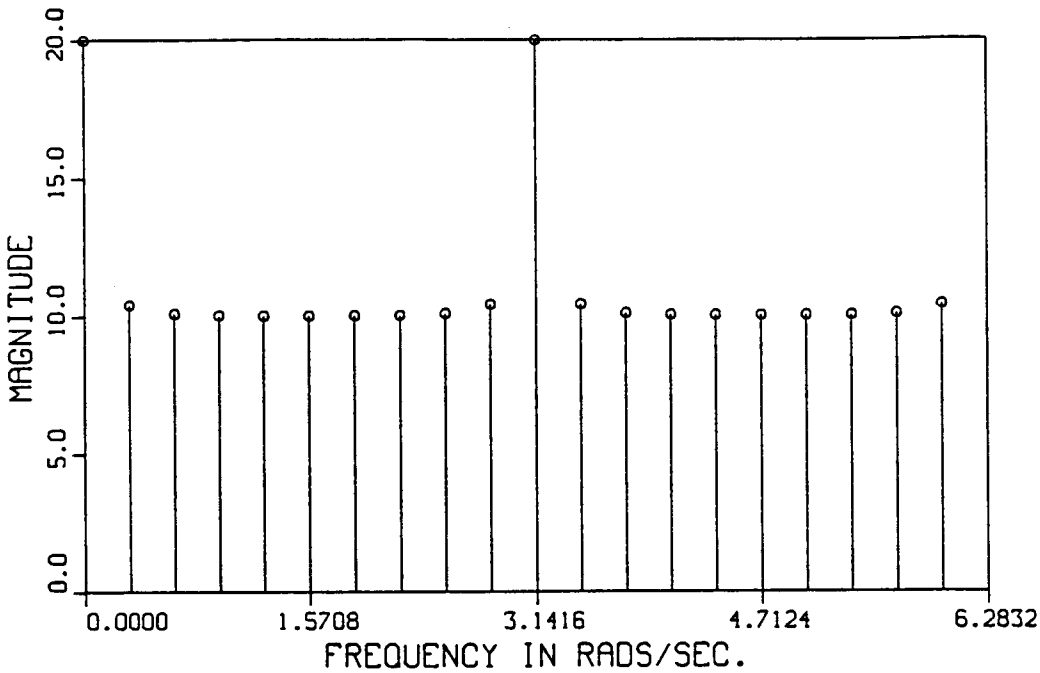

Figure 6.6: DFT Bounding Function for Unknown-but-bounded Disturbance.

6.4.2 Finite-Energy Models

In this subsection, we examine both continuous and discrete time, finite-energy disturbance models. Consider the continuous-time finite-energy disturbance that satisfies,

$$\text{Continuous-time Finite-energy Model:} \quad \int_{-\infty}^{\infty} d(t)^2\,dt \le \overline{D}^c{}_{fe} < \infty, \tag{6.4.9}$$

where $\overline{D}^c{}_{fe}$ is a known constant. This model does not imply that the sampled disturbance is bounded, since the samples d[n] could correspond to peaks of d(t) that have zero measure. That is, even though d(t) is square-integrable, we cannot conclude that |d[n]| is bounded nor can we conclude that the DFT of d[n] is bounded. However, if d(t) is finite in energy and has its energy at low frequencies relative to the sampling frequency, then we find that

$$\int_0^{NT} d(t)^2\,dt \approx \sum_{n=0}^{N-1} d[n]^2\,T. \tag{6.4.10}$$

So, from Eqns. (6.4.9-10) we see that, if d[n] has its energy at low frequencies, then we can approximately bound the finite sum of $d[n]^2$ in terms of the energy bound on the continuous-time disturbance. This leads us to the following discrete-time finite-energy disturbance model.

$$\underline{\text{Discrete-time Finite-energy Model:}} \quad \sum_{n=0}^{N-1} d[n]^2 \leq \overline{D}_{fe} < \infty. \tag{6.4.11}$$

where $\overline{D}_{fe}$ is a known constant. From Eqn. (6.4.11) it can be shown that

$$|d[n]| \leq \sqrt{\overline{D}_{fe}}, \quad \forall n, \tag{6.4.12}$$

which satisfies assumption AD2.1. Parseval's relation for our definition of the DFT is given by

$$\sum_{n=0}^{N-1} d[n]^2 = (1/N) \sum_{k=0}^{N-1} |D_N(\omega_k)|^2. \tag{6.4.13}$$

Using Eqns. (6.4.11) and (6.4.13) we find

$$|D_N(\omega_k)| \leq \sqrt{N \overline{D}_{fe}}, \text{ for } k = 0, \ldots, N-1. \tag{6.4.14}$$

So, we find that

$$\overline{D}_N(\omega_k) = \sqrt{N \overline{D}_{fe}}, \tag{6.4.15}$$

and, using this energy approach, we cannot do any better than

$$\overline{D}_N{}^{+n}(\omega_k) = \sqrt{N \overline{D}_{fe}}, \text{ for } k = 0, \ldots, N-1. \tag{6.4.16}$$

Thus, a discrete-time finite-energy model can be used to satisfy assumption AD2.2.

6.4.3 Stochastic Models

In this brief subsection, we will discuss stochastic disturbance models. If the disturbance is modeled by a stochastic process that is bounded, such as a white process that has an uniform distribution, then the bound on the disturbance model can be used in the bounded-but-unknown model of Subsection 6.4.1 to satisfy AD2.1-2. That is, we essentially ignore the stochastic nature of the model and must assume that the disturbance is a sinusoid, however statistically unlikely this may be.

If the disturbance is modeled by an unbounded stochastic process, such as a white process that has a gaussian distribution, then assumptions AD2.1-2 cannot be fulfilled. That is, white gaussian disturbance models cannot be used in the robust estimator.

6.5 Design Choices for the Time-domain Parameter Estimator

In this section, we will discuss the design choices for the robustified time-domain parameter estimator, which was developed in Chapter 4. First, we will discuss the choice of the DFT length for use in the computation of the time-varying bound on the effects of the unstructured uncertainty. Then, we examine the choice of the input/output filter that is used in the parameter estimator.

6.5.1 Choosing the DFT Length for the Time-domain Parameter Estimator

In this subsection, we will discuss the tradeoff that arises when we choose the DFT length N_t for the bounding mechanism in the time-domain parameter estimator. From Eqn. (4.4.23) we find that

$$\bar{e}_2[n] = \bar{e}_{2sum}[n] + \bar{e}_{2rem}[n], \tag{6.5.1}$$

where

$$\bar{e}_{2sum}[n] = \frac{1}{N} \{ \sum_{k=0}^{N-1} \bar{H}_u(e^{j\omega_k T}) |U_N^n(\omega_k)| \}, \text{ for } n = 0, 1, .. \tag{6.5.2}$$

and

$$\bar{e}_{2rem} = 2 u_{max} \sum_{p=N}^{\infty} \bar{h}_u[p]. \tag{6.5.3}$$

First, we will examine the sum of Eqn. (6.5.2) for two different types of input signals.

Example 1: (Single sinusoid case) Let

$$u[n] = \sin(\tilde{\omega} T n), \text{ for } n \geq 0, \tag{6.5.4}$$

where $\omega_p = \tilde{\omega}$, so that for $n \geq N-1$,

$$|U_N^n(\omega_k)| = \begin{cases} N, \text{ if } p=0 \text{ or } p=(N/2) \text{ and } k=p, \\ N/2, \text{ if } p\neq 0 \text{ and } p\neq(N/2) \text{ and } k=p \text{ or } k=N-p, \\ 0, \text{ otherwise.} \end{cases} \tag{6.5.5}$$

where we have assumed that N is even. In this case, Eqn. (6.5.2) becomes

$$\overline{e}_{2sum}[n] = \overline{H}_u(e^{j\omega_p T}), \text{ for } n \geq N-1, \tag{6.5.6}$$

which does not depend on the DFT length N.

Example 2: (Wideband case) Let u[n] be a wideband signal that has constant average energy U_e. That is, we assume

$$U_e = (1/N) \sum_{n=0}^{N-1} u[n]^2 = (1/N^2) \sum_{k=0}^{N-1} |U_N(\omega_k)|^2, \tag{6.5.7}$$

where we have used Parseval's theorem. Further, we assume that

$$|U_N(\omega_p)| = |U_N(\omega_q)|, \text{ for all p and q.} \tag{6.5.8}$$

So, using Eqns. (6.5.7-8) we find

$$|U_N(\omega_k)| = \sqrt{N U_e}, \text{ for } k = 0, \ldots, N-1. \tag{6.5.9}$$

In this case, Eqn. (6.5.2) becomes

$$\overline{e}_{2sum}[n] = \left[\frac{1}{N} \sum_{k=0}^{N-1} \overline{H}_u(e^{j\omega_k T}) \right] \sqrt{N U_e}. \tag{6.5.10}$$

The first term of Eqn. (6.5.10), which is in brackets, is essentially an average which will remain approximately constant for different choices of N. However, the second term of Eqn. (6.5.10) is proportional to the square root of N. In summary, for this input signal, the time-varying bound of Eqn. (6.5.10) grows with the square root of the DFT length N.

From examples 1 and 2 we see that the conservativeness of the bound of Eqn. (6.5.2) depends strongly on the characteristics of the input signal. Example 2 reveals that there is a penalty for choosing N large. We summarize the resulting tradeoff that dictates the choice of the DFT length in Eqns. (6.5.1-3).

TRADEOFF: 1) Choose N small since the time-domain bound can increase with $\sqrt{N}$.

2) Choose N large to make the remainder term $\overline{e}_{2rem}[n]$ of Eqn. (6.5.3) small relative to $\overline{e}_{2sum}[n]$.

The choice of the DFT length for the time-domain parameter estimator will be a balancing of these

two opposing objectives.

6.5.2 Choosing the Input/Ouput Filter

In this subsection, we examine the question of how to choose the filter F(z) of Eqn. (4.2.10) that is used to prefilter the input and output signals before they are used in the parameter estimator part of the robust estimator. In Section 4.2, it was discussed how prefiltering the input and output signals by F(z) prevents a "near differentiation" problem in the parameter estimator. In this section, we will present guidelines for the choice of the filter F(z). For convenience, we repeat the equations for the DARMA model of the discrete-time plant where filtered signals are used. That is, with reference to Eqns. (4.2.10-18),

$$y_f[n] = \phi_f[n-1]^T\theta_0 + e_1[n], \tag{6.5.11}$$

where

$$e_1[n] = [B(q)\,F(q)\,\delta_u(q)]\,u[n] + [A(q)\,F(q)]\,d[n]. \tag{6.5.12}$$

From Eqn. (6.5.12) we see that the filter F(z) can be used to shape the frequency content of the error signal $e_1[n]$. Since the unstructured uncertainty $\delta_u(z)$ is typically large at high frequencies, F(z) will be chosen to be a low-pass filter. In addition, the filter F(z) should roll-off in the same frequency range as the transfer function 1/A(z). If this is not the case, then the transfer function [A(z) F(z)] will magnify the high-frequency components of the disturbance d[n] relative to the low-frequency components in the error signal $e_1[n]$, as can be seen in Eqn. (6.5.12). The bandwidth of F(z), which we will think of as the 3 dB frequency, should not be chosen to be too low since it will attenuate signal energy in the frequency range in which the estimator is trying to identify the plant. These insights lead to a tradeoff in the choice of the filter bandwidth.

TRADEOFF: 1) Choose the filter bandwidth small so as to attenuate the effects of

a) the high-frequency unmodeled dynamics $\delta_u(z)$, and

b) the possibly high-frequency disturbance d[n].

2) Choose the filter bandwidth large so as not to attenuate the input signal energy in the frequency range in which we are trying to identify the plant.

We can now develop a rule of thumb concerning the choice of the filter bandwidth. Assuming that we are only interested in identifying the plant in the frequency range up to the

bandwidth of 1/A(z), we find

RULE OF THUMB: Choose Bandwidth of F(z) ≈ Bandwidth of 1/A(z,θ) where $\theta \in \Theta$, (6.5.13)

where we note that the bandwidth of the transfer function 1/A(z,θ) depends on the, only coarsely known, parameter vector θ. This rule of thumb yields a transfer function A(z)F(z) in Eqn. (6.5.12) that is approximately constant for all frequencies. Of course, this is only a rule of thumb and, if we wanted to identify the plant at frequencies that are higher than the bandwidth of 1/A(z,θ), we would use a filter with a higher bandwidth.

6.6 Design Choices for the Frequency-domain Estimator

In this section, we will discuss the design choices for the frequency-domain bounding methodology, which was developed in Chapter 5. First, we will discuss the choice of the memory length M that is used in the on-line computation of the frequency-domain error bounds. Then, we examine the various tradeoffs involved in the choice of the DFT length for the frequency-domain estimator.

6.6.1 Choice of the Memory Length for the Frequency-domain Bounding Method

In Section 6.2, we showed that a magnitude bounding function on the modeling error of the frequency-domain estimate could be found using Eqns. (5.2.4-5), which we repeat here for convenience.

$$\overline{E}_N^n(\omega_k) = \sum_{p=1}^{M-1} |g_{true}[p]|\,|U_N^{n-p}(\omega_k) - U_N^n(\omega_k)| + 2\,u_{max} \sum_{p=M}^{\infty} p\,|g_{true}[p]|,$$

$$\text{for } k = 0, \ldots, N-1. \qquad (6.6.1)$$

In this subsection, we consider the choice of the integer M, which we will refer to as the memory length of the true plant. The motivation for using Eqn. (6.6.1) is that the bound corresponding to M=1 in Eqn. (6.6.1) is too conservative. That is, if we use M=1, then we are bounding $|E_N^n(\omega_k)|$, the error due to the use of finite-length data, by assuming that the input signal u[n] achieves its worst-case magnitude and phase. By choosing a value of M that is greater than 1 in Eqn. (6.6.1), we use on-line information about u[n], in the form of the DFTs of u[n], to compute a less conservative bound. Our goal in this subsection will be to understand how to choose M so that the second term of Eqn. (6.6.1) is small compared to the first term.

It is advantageous to choose M such that

$$M\,T \approx 5\,\tau_{slow} \tag{6.6.2}$$

where τ_{slow} is the slowest time constant of the true continuous-time plant and T is the sampling period. This choice is illustrated in Figure 6.7, which shows the impulse response of a first-order system along with the choice of M given by Eqn. (6.6.2).

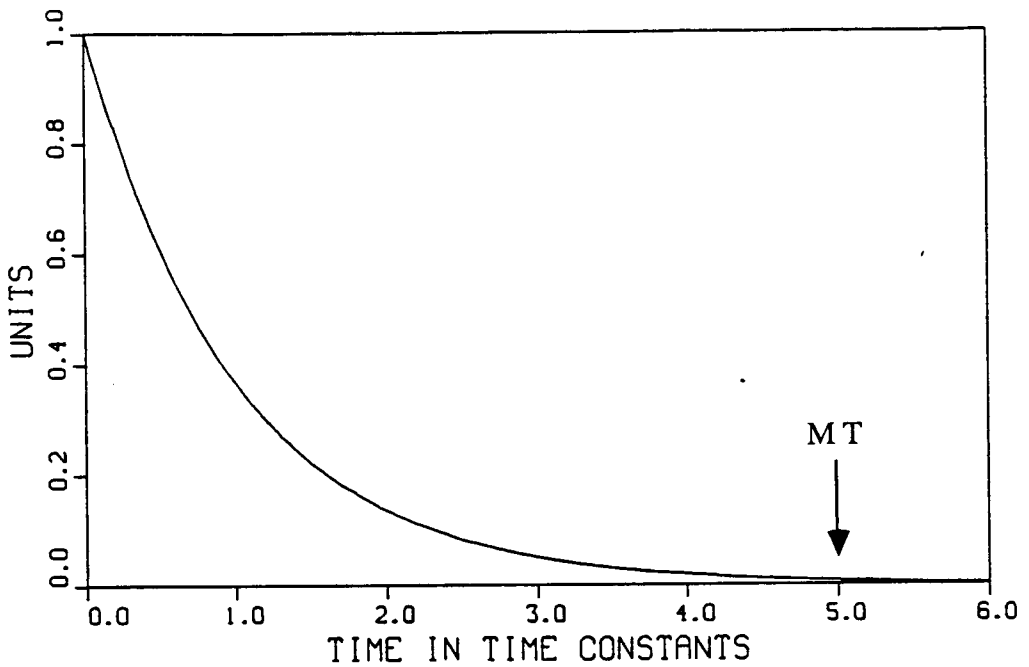

Figure 6.7: Impulse Response and Illustration of Memory Length.

Intuitively, we are choosing M so that, roughly speaking, it is the memory length of the discrete-time plant. That is, for time indicies that are greater than $M = (5\,\tau_{slow} / T)$, the impulse response is very small compared to its values for time indicies that are less than M. We will now show that, for the choice of Eqn. (6.6.2), the infinite summation term is much smaller than the value of the infinite summation term for M=1. That is, we consider the ratio

$$\text{Ratio}(M) = \{ \sum_{p=M}^{\infty} p\,|g_{true}[p]| \} \;/\; \{ \sum_{p=1}^{\infty} p\,|g_{true}[p]| \}. \tag{6.6.3}$$

We assume that the magnitude bounding function on the impulse response of the true plant is a first-order system. So,

$$|g_{true}[n]| \leq b\, e^{-anT} = b\, p^n, \text{ where } p = e^{-aT}. \tag{6.6.4}$$

Then, using Eqn. (C.10) from Appendix C we find that

$$\text{Ratio}(M) = p^{(M-1)} (M - M p + p). \tag{6.6.5}$$

As an example, consider the case where the sampling frequency is chosen to be 20 times the slowest pole, which is 'a' in Eqn. (6.6.4). So, since

$$\omega_s = 2\pi / T = 20\, a, \Rightarrow T = \pi / (10\, a), \tag{6.6.6}$$

we find

$$p = e^{-aT} = e^{-(\pi/10)} = 0.73040. \tag{6.6.7}$$

Using Eqn. (6.6.1) we find that

$$M T \approx 5 / a, \text{ or} \tag{6.6.8}$$

$$M \approx 5 / (a T) = 50 / \pi \approx 16. \tag{6.6.9}$$

From Eqn. (6.6.5) we compute

$$\text{Ratio}(16) = 0.04531 << 1. \tag{6.6.10}$$

Thus we have shown that, in the example considered, by choosing

$$M = \text{integer}(5 / (a T)) \tag{6.6.11}$$

we find that Ratio(M) ≈ 1/20. We consider other cases in the following chart where M is chosen using Eqn. (6.6.11).

Table 6.2: Memory length Choice and the Resulting Ratio(M).

(ω_s / a)	M	Ratio(M)
5	4	0.07253
10	8	0.05246
50	40	0.04170
100	80	0.04060
500	400	0.03975

(6.6.12)

When the slowest pole of the plant is much slower than the sampling frequency, then the discrete-time impulse response doesn't decay for many sample points so a very large value of M is required.

If the plant has a zero at a frequency that is lower than the slowest pole, then we may need to choose M even larger then the value of Eqn. (6.6.11). For example, if the low-frequency zero is much slower than the slowest pole, then the impulse response will have a large peak so the value of, for example 'b' in Eqn. (6.6.4), will be large relative to the case of the lowest frequency pole or

zero being a pole. In fact, Eqn. (6.6.11) is only a starting point when trying to choose M.

Ultimately, we need to choose M large enough so that the remainder term $\overline{E}_{rem}$ in $\overline{E}_{f,N}^{n}(\omega_k)$ becomes small enough for the robust estimator to provide performance-increasing information to the control-law update algorithm. Using Eqns. (5.2.4) and (5.2.17), we find that for $n \geq N-1$,

$$\overline{E}_{f,N}^{n}(\omega_k) = \{ \sum_{p=1}^{M-1} |g_{true}[p]|\, |U_N^{n-p}(\omega_k) - U_N^{n}(\omega_k)| + \overline{E}_{rem} + \overline{\overline{D}}_N(\omega_k) \} / |U_N^{n}(\omega_k)|,$$

$$\text{for } k = 0, \ldots, N-1. \qquad (6.6.13)$$

We see that the remainder term $\overline{E}_{rem}$ enters Eqn. (6.6.13) in the same way as an all-frequency disturbance. Thus, it's not necessary to make $\overline{E}_{rem}$ much smaller than the minimum of the frequency function $\overline{\overline{D}}_N(\omega_k)$. Said another way, we need not choose M to be much larger than the value that makes the error due to the use of finite-length data smaller than the error due to the disturbance. In addition, from Eqn. (6.6.13), we see that the expected size of the input spectrum also affects our choice of M. The larger the input spectrum is, for a fixed u_{max}, the smaller the value of M needs to be to achieve the same additive error bound.

As a final note, we observe that if the input signal u[n] is periodic with period N, then $U_N^{n-p}(\omega_k)=U_N^{n}(\omega_k)$ for all p, and the summation term in Eqn. (6.6.13) will become zero. It is unlikely that the reference signal of the closed-loop system will result in a plant input signal that is periodic with period N. However, as we will later discuss, a periodic probing signal, which enhances identification, could be chosen to have period N.

6.6.2 Choice of the DFT Length for the Frequency-domain Bounding Method

In this subsection, we examine the issues involved in the choice of the DFT length N that is used in the frequency-domain bounding method. Given that we have already chosen the sampling period T, we must choose N so that:

1) The finite-length data intervals used to find the frequency-domain estimate of the plant are long enough to observe the lowest frequency dynamics of the plant.

2) The resolution of the frequency-domain estimate is adequate.

These two goals are both fulfilled by a sufficiently large choice of N. However, we cannot let

$N \rightarrow \infty$ because we must also choose N so that the computational requirements of the algorithm are not excessive. In the following two subsections, we will examine each of the above goals individually.

6.6.3 Finite-length Data and Identification of Very Low-frequency Plant Dynamics

In this subsection, we will examine how N should be chosen so as to be able to identify the very low-frequency dynamics of the plant. That is, the lowest frequency pole or zero of the plant places a restriction on the choice of N. The results of this section will provide answers as to how to choose N so that the robust estimator doesn't yield useless results. That is, if N is chosen to be too small, then the frequency-domain error bounding function $\overline{E}_{f,N}^{n}(\omega_k)$ of Section 5.2 will be very large. In this case, the robust estimator will not be able to provide performance-improving information to the control-law update algorithm. To avoid this situation, we will develop rules of thumb for the choice of N.

First, we develop a lower bound for an intelligent choice of N by considering the lowest frequency dynamics of the plant. Although we may not know the very low-frequency dynamics of the true plant exactly, assumptions AC1.1-2 will, in general, allow us to find bounds on the lowest frequency pole or zero. We denote the magnitude of the real part of the lowest frequency pole or zero of the plant by α_{slow}. Now, consider the case where the plant is excited by an input signal at the frequency $\omega=\alpha_{slow}$. We want to observe at least one cycle of the plant input and output signals at this frequency so that we can identify the plant. Define the slowest cycle time by

$$T_{slow} = 2\pi / \alpha_{slow}. \tag{6.6.14}$$

Then, by choosing N such that

$$NT > T_{slow} \tag{6.6.15}$$

where T is the sampling period, we will observe at least one cycle of the plant input and output signals at the slow frequency α_{slow}. Combining Eqns. (6.6.14-15), we find that

$$N > \omega_s / \alpha_{slow}. \tag{6.6.16}$$

In practice, it will be advantageous to choose N to be larger than the lower bound of Eqn. (6.6.16); however, this equation gives us a rule of thumb with which to work. To illustrate typical values

for N consider the situation where ω_s=10 ω_{tcl}, ω_{tcl}=100 α_{slow}. Then, the rule of thumb of Eqn. (6.6.16) suggests that N > 1000. Clearly, for high-bandwidth control systems that have plants with a large spread in pole locations, very large values of N can be required.

We now examine how the choice of N affects the frequency-domain error bounding function. For convenience we rewrite Eqn. (5.2.17), the frequency-domain error bounding function.

$$\overline{E}_{f,N}^{n}(\omega_k) = (\overline{E}_N^{n}(\omega_k) + \overline{\overline{D}}_N(\omega_k)) / |U_N^{n}(\omega_k)|, \text{ when } n \geq N-1, \quad \text{for } k = 0, \ldots, N-1. \tag{6.6.17}$$

Further, using Corollary 2.1, we define the following conservative bounding function on $|E_N^{n}(\omega_k)|$. That is,

$$|E_N^{n}(\omega_k)| \leq \overline{E}_{wc}, \text{ for } k = 0, \ldots, N-1, \tag{6.6.18}$$

where

$$\overline{E}_{wc} = 2\, u_{max} \sum_{i=1}^{\infty} i\, |g_{true}[i]|, \tag{6.6.19}$$

and the subscript "wc" denotes the fact that this is a conservative "worst-case" bound. The constant bound of Eqn. (6.6.19) doesn't depend on the time index n or the frequency ω_k. Eqn. (6.6.19) corresponds to the remainder term $\overline{E}_{rem}$, for M=1, that was defined in Eqn. (5.2.5). Although the bounding function of Eqn. (5.2.4) is less conservative for values of M that are greater than 1, we will first seek insight using the simpler constant bound $\overline{E}_{wc}$. We rewrite Eqn. (6.6.18) using our worst-case bound.

$$\overline{E}_{wcf,N}^{n}(\omega_k) = (\overline{E}_{wc} + \overline{\overline{D}}_N(\omega_k)) / |U_N^{n}(\omega_k)|, \text{ when } n \geq N-1, \quad \text{for } k = 0, \ldots, N-1. \tag{6.6.20}$$

where the subscript "wcf" denotes the "worst-case frequency-domain" error bounding function. To analyze Eqn. (6.6.20), we first note that the magnitude of the N-point DFT of a signal, as defined by Eqn. (2.1.5), will become larger as N increases. In fact, if the signal is a sinusoid, then the magnitude of the DFT is proportional to N at a given ω_k. So as N$\rightarrow\infty$, both

$$\overline{\overline{D}}_N(\omega_k) \rightarrow \infty, \text{ and} \tag{6.6.21}$$

$$|U_N^n(\omega_k)| \to \infty. \tag{6.6.22}$$

Since $\overline{E}_{wc}$ is a bounded constant that doesn't depend on N, we see from Eqns. (6.6.20-22) that as $N \to \infty$,

$$\overline{E}_{wcf,N}^n(\omega_k) \to \overline{\overline{D}}_N(\omega_k) / |U_N^n(\omega_k)|, \text{ when } n \geq N-1, \quad \text{for } k = 0, \ldots, N-1. \tag{6.6.23}$$

Thus, for sufficiently large N, the frequency-domain error bounding function approaches the frequency-domain disturbance-to-input signal ratio. The constant $\overline{E}_{wc}$ bounds the error due to using finite-length data to compute the frequency-domain estimate. Assume for a moment that the true plant has a finite-length impulse response of length M. Then, as is shown in Figure 6.8, the input signal values, from before the DFT frame, contribute to the values of the output signal in the beginning of the DFT frame and the input signal values, before the end of the DFT frame, contribute to the output signal values for times past the end of the DFT frame. Thus, to obtain an accurate frequency-domain estimate from the finite-length data intervals of N points, we must choose N >> M in order to make these "end effects" small.

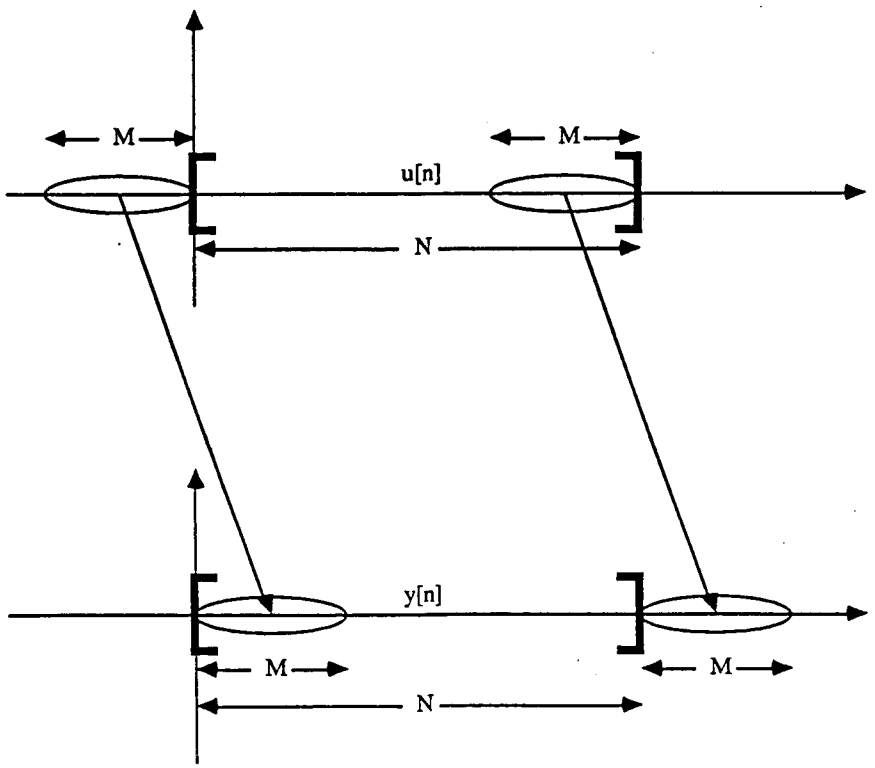

Figure 6.8: Illustration of End-effects in Frequency-domain Estimation.

In Subsection 6.6.1, we developed the rule of thumb of Eqn. (6.6.2) by assuming that the slowest pole or zero of the plant was a pole. This rule of thumb for choosing M can be written as

$$M \approx 5\,\tau_{slow}/T \approx 2\,\pi\,\tau_{slow}/T. \tag{6.6.24}$$

Thus, comparing Eqns. (6.6.24) and (6.6.16) we see that N must be chosen to be greater than M and, in fact, to yield useful frequency-domain error bounds, N must be chosen as follows.

$$\text{RULE OF THUMB 1: Choose } N > \omega_s / \alpha_{slow} \tag{6.6.25}$$

$$\text{where } \alpha_{slow} = 1/\tau_{slow} \tag{6.6.26}$$

That is, α_{slow} is the magnitude of the real part of the slowest pole or zero of the plant. Thus, we have provided two different intuitive arguments for choosing an N that satisfies the above rule of thumb. To gain further insight into the choice of M and N, we present a simple example.

Example: Assume for this example that the true plant is known as follows.

$$g_{true}[n] = b\,e^{-anT} = b\,p^n, \text{ for } n \geq 0, \text{ where } p = e^{-aT}, \tag{6.6.27}$$

where a,b > 0. So,

$$G_{true}(z) = b\,z/(z-p). \tag{6.6.28}$$

Further, assume that u[n]=1, for all n, so that u_{max}=1. Using Eqns. (6.6.19) and (C.11) from Appendix C, we find that

$$\overline{E}_{wc} = 2\sum_{i=1}^{\infty} i\,b\,p^i = 2\,b\,p/(1-p)^2, \tag{6.6.29}$$

which corresponds to a choice of M=1. We will compute, at ω_0=0, the frequency-domain error bounding function given by Eqn. (6.6.20) assuming that the disturbance is zero. That is, using Eqn. (6.6.29) and the periodicity of u[n],

$$\overline{E}_{wcf,N}{}^n(0) = (2\,b\,p/(1-p)^2)/|U_N{}^n(0)|. \tag{6.6.30}$$

It can be shown that

$$|U_N{}^n(0)| = N, \forall n, \text{ and} \tag{6.6.31}$$

$$G_{true}(e^{j\omega_0 T}) = G_{true}(1) = b/(1-p). \tag{6.6.32}$$

So, Eqn. (6.6.30) can be rewritten as

$$\overline{E}_{wcf,N}^{n}(0) = (2\,p / [\,N\,(1 - p)\,]\,)\,G_{true}(1). \tag{6.6.33}$$

Thus, by choosing N sufficiently large, we can make the relative error arbitrarily small. If we choose N to be its bare minimum value of ω_s/a, we find that

$$N = 2\,\pi / (a\,T) = 2\,\pi / -\ln(p). \tag{6.6.34}$$

Assuming that $p \approx 1$, we can use the approximation $-\ln(p) \approx (1-p)$ to show that

$$N \approx 2\,\pi / (1 - p). \tag{6.6.35}$$

Using Eqn. (6.6.35) in (6.6.33) and the fact that $p \approx 1$, yields

$$\overline{E}_{wcf,N}^{n}(0) \approx (1 / \pi)\,G_{true}(1) \approx 0.3\,G_{true}(1). \tag{6.6.36}$$

This additive error bound is relatively large, being on the order of 30% of $G_{true}(1)$.

Since the additive error in the above example was so large, we consider the effects of using different values of N and M. First, we consider the simple case of increasing N. If we choose

$$N = 10\,\omega_s / a >> \omega_s / a, \tag{6.6.37}$$

then

$$\overline{E}_{wcf,N}^{n}(0) \approx (1 / (10\,\pi)\,)\,G_{true}(1) \approx 0.03\,G_{true}(1), \tag{6.6.38}$$

which is a much smaller additive error bound than Eqn. (6.6.36).

Now, we consider the effect of increasing M. For the example of Eqns. (6.6.27-28), we choose to use a value of M that is greater than 1. In this case, using again Eqns. (6.6.19) and (C.11) and the periodicity of u[n], we find

$$\overline{E}_{f,N}^{n}(\omega_k) = 2 \sum_{i=M}^{\infty} i\,b\,p^i = 2\,b\,p^M\,(M - M\,p + p) / (1 - p)^2, \ \forall n, \forall \omega_k. \tag{6.6.39}$$

Following a development similar to that of Eqns. (6.6.30-36), we find that, if we choose $N=\omega_s/a$ and $p \approx 1$, then

$$\overline{E}_{f,N}^{n}(0) \approx ((p^M\,(M - M\,p + p) / \pi)\,G_{true}(1). \tag{6.6.40}$$

So, by choosing M sufficiently large we can make the additive error arbitrarily small in this example. We note that the choice of M that is dictated by the rule $M=\omega_s/a$, will guarantee that

$p^M (M - M p + p)$ is small. For example, if $aT=\pi/10$, then $M=\omega_s/a=20$ and

$$p^M (M - M p + p) = e^{-2\pi} (20 - 19 e^{-\pi/10}) = 0.011. \tag{6.6.41}$$

So, using Eqn. (6.6.40),

$$\overline{E}_{f,N}^{n}(0) \approx (0.011 / \pi) G_{true}(1) \approx 0.004 G_{true}(1). \tag{6.6.42}$$

In summary, we have shown how the choice of N and M affects the additive error at $\omega_0=0$ for a simple example. We have seen how an increase in either N or M will decrease the frequency-domain additive error.

6.6.4 Frequency-domain Resolution

In this subsection, we will develop a rule of thumb for choosing the DFT length N based on the required frequency-domain resolution of the robust estimator. That is, once the sampling frequency ω_s has been chosen, the value of N specifies how many equally spaced frequency points on the interval $[0,\omega_s]$ are used in the frequency-domain bounding methodology of Chapter 5. The choice of N depends on how smooth, in the frequency domain, the plant dynamics are. We can use the results of Subsection 5.7.3 to develop a rule of thumb for the choice of N based on resolution requirements. Using Eqn. (5.7.29), we can bound the largest inter-sample variation of $|\delta_{su}(e^{j\omega T}, \hat{\theta})|$ from $|\delta_{su}(e^{j\omega_k T}, \hat{\theta})|$,

$$| |\delta_{su}(e^{j\omega T}, \hat{\theta})| - |\delta_{su}(e^{j\omega_k T}, \hat{\theta})| | \le (\omega_s / N) \nabla_{su,i}^{n}(\omega_k,\omega_{k+1}),$$

$$\text{for } \omega \in [\omega_k,\omega_{k+1}] \tag{6.6.43}$$

where $\nabla_{su,i}^{n}(\omega_k,\omega_{k+1})$ is defined by Eqn. (5.7.31) which we rewrite here,

$$\nabla_{su,i}^{n}(\omega_k,\omega_{k+1}) = \sup_{\omega \in [\omega_k,\omega_{k+1}]} \{ \nabla_{su}^{n}(e^{j\omega T}) \}. \tag{6.6.44}$$

Thus, if we want to bound the maximum inter-sample variation, we must bound

$$(\omega_s / N) \nabla_{su}^{n}(e^{j\omega T}), \ \forall \omega, \tag{6.6.45}$$

where $\nabla_{su}{}^{n}(e^{j\omega T})$ depends on the on-line computed value of $\Delta_{su}{}^{n}(e^{j\omega T})$ as was developed in Subsection 5.7.2. Now, in the following rule, we want a precomputable bound on the derivative, so we choose to use the worst-case bounding function $\nabla_{su,wc}(e^{j\omega T})$ that is based only on a priori information as shown in Subsection 5.7.1.

RULE OF THUMB 2: Choose N large enough so that $(\omega_s / N)\, \nabla_{su,wc}(e^{j\omega T})$ is sufficiently small for all ω. (6.6.46)

The meaning of "sufficiently small" depends on how large an inter-sample variation is acceptable.

6.6.5 Conclusions on the Choice of the DFT Length for the Frequency-domain Estimator

We now summarize our results concerning the choice of N. The rules of thumb 1 and 2, corresponding to Eqns. (6.6.25) and (6.6.46), respectively, provide lower bounds on the choice of N. Rule of thumb 1 is chosen so that we can accurately identify very low-frequency dynamics and rule of thumb 2 is chosen so that the inter-sample variation of our continuous bounding function on the unstructured uncertainty, is acceptably small. The disadvantage of choosing N or, for that matter, M to be very large is that the number of computations can become prohibitively large. The severity of this computational limit depends on the state of the art in high-speed computing. Computational issues are discussed further in the following section.

6.7 Computational Issues

In this section, we will discuss the computational requirements of the robust estimator. Specifically, we will focus on the main computational bottle-necks in the on-line implementation of the robust estimator. The robust estimator requires considerable design time as well as extensive off-line and on-line calculations. It is the goal of this section to provide an idea of the size of the on-line calculations that are required by the robust estimator.

The main computational burden of the robust estimator is due to the extensive calculations of the frequency-domain bounding method. The chief computational culprit is Eqn. (5.2.4), which we repeat here for convenience,

$$\overline{E}_N^n(\omega_k) = \sum_{p=1}^{M-1} |g_{true}[p]|\,|U_N^{n-p}(\omega_k) - U_N^n(\omega_k)| + \overline{E}_{rem}, \text{ for } k = 0, \ldots, N-1. \qquad (6.7.1)$$

where the remainder term $\overline{E}_{rem}$ can be computed off-line using Eqn. (5.2.5). In the frequency-domain bounding method of Chapter 5, the bounding function of Eqn. (6.7.1) must be computed at every sample time. For a given frequency ω_k, we compute Eqn. (6.7.1) using our a priori bounding function on $|g_{true}[n]|$ and our on-line computed values of the input signal DFT, $U_N^m(\omega_k)$, for m = n-(M-1), n-(M-1)+1, . . , n. Due to the DFT symmetry properties of real-valued signals, we only need to compute Eqn. (6.7.1) for k = 0, . . , N/2. In summary, at every sample time, we must compute a sum of M-1 terms at (N/2)+1 frequencies. So, in Eqn. (6.7.1) we must perform approximately M•(N/2) subtractions, multiplications and additions, at every sample time. Thus, we see that

$$\text{Number of On-line Computations per Sample Time} \approx M \bullet (N/2) \propto M \bullet N. \qquad (6.7.2)$$

This equation reveals how extensive the computational requirements of the robust estimator can become for large values of M and N. However, an important feature of Eqn. (6.7.1) is that it can be computed simultaneously, that is, in parallel, at the (N/2)+1 frequency points. This will allow vast increases in the computation speed of Eqn. (6.7.1). For a parallel implementation of Eqn. (6.7.1), the computation time will only increase in proportion to the memory length M. In Chapters 8 and 9, we will consider two simulation examples. We include the following table to give an idea of how many calculations are required in these examples for Eqn. (6.7.1).

Table 6.3: Number of On-line Computations for Eqn. (6.7.1).

Example	M	N	Number of Multiplications, Subtractions and Additions per Sample Time
Chapter 8, Eqn. (8.1.2)	10	50	250
Chapter 9, Eqn. (9.2.4)	200	1000	100,000

This table illustrates just how different the computational requirements of the frequency-domain bounding method can be for different examples. The example of Chapter 8 has fast discrete-time poles that require only a small value of the memory length M. In addition, the Chapter 8 example has no sharp frequency-domain peaks, so frequency-domain resolution isn't a problem and a small value of N can be used. This simple first-order example is one of the least computationally demanding examples that we could have presented. On the other hand, the example of Chapter 9 is one of the most computationally demanding examples that we could have presented.

The Chapter 9 example potentially has very slow discrete-time poles so the memory length M must be chosen to be large. In addition, the second-order example of Chapter 9 has a potentially sharp frequency-domain peak that requires a large choice of N for frequency-domain resolution. These examples serve as benchmarks for the computational requirements of the frequency-domain bounding method.

As a modification to the basic methodology of Chapter 5, the bounding function of Eqn. (6.7.1) could be computed less frequently than every sample time. This would result in a reduction of real-time computing requirements at the cost of a more conservative bounding function. That is, if we only computed the frequency-domain bounding function of Eqn. (6.7.1), say every five sample times, then we would learn less than if we computed it every sample time.

The computation of Eqn. (6.7.1) represents, by far, the majority of the computational burden of the robust estimator. The on-line calculations that are required by the time-domain parameter estimator of Chapter 4 are quite small compared to the on-line calculations of Eqn. (6.7.1). The one other part of the robust estimator that requires significant computations is the frequency-domain parameter estimator of Section 5.4. This estimator requires the computation of a weighted least-squares fit at (N/2)+1 frequency points. This computation does not represent a bottle-neck for the real-time implementation of the robust estimator since this least-squares fit is computed only infrequently, at the times that the control-law is updated. Thus, even if the computation requires several sample times to perform, it will not greatly affect the performance of the adaptive control system.

In summary, we have seen that the frequency-domain bounding computation of Eqn. (6.7.1), which is the same as Eqn. (5.2.4), is the primary limitation for the real-time implementation of the robust estimator. The examples of this section have provided an idea of just how large the computational requirements of the robust estimator are. In the author's opinion, the robust estimator requires a prohibitively large amount of computation by today's standards. The simulations of Chapters 8 and 9 had to be performed on a Cyber 205 supercomputer. It is hoped that future advances in computer technology will remove this computational barrier to using the robust estimator. What may seem computationally impractical today often becomes practical with such computing advances.

6.8 Conclusion

In this chapter, we have discussed design issues and the specification of the assumed bounds for the robust estimator. In Section 6.5, we examined the tradeoffs involved in the choice of the DFT length N_t that is used in the robustified time-domain parameter estimator. Further, in Section

6.6, we discussed the lower bounds on the choice of the DFT length N_f that is used in the frequency-domain bounding method. We will later see in the simulation chapters that N_t will, in general, be chosen to be smaller than the frequency-domain DFT length N_f. In the robustified time-domain parameter estimator, the bounding mechanism, which uses N_t-point DFTs, needs to track the error signal that it is bounding. This objective results in a relatively small choice of N_t. However, in the frequency-domain bounding methodology we find that there are many reasons to choose the DFT length N_f large. So, if we choose to use the time-domain parameter estimator in combination with the frequency-domain bounding method, then we are forced to compute two different DFTs on-line, one that has N_t points and one that has N_f points.

CHAPTER 7.
A SIMPLE ROBUST ADAPTIVE CONTROLLER

7.1 Introduction

The purpose of this chapter is to tie together the results of the previous chapters. So far, we have presented two methods for generating parameter estimates and, hence, a nominal model, and one method for finding a frequency-domain uncertainty bounding function. Further, we have investigated some of the design choices associated with these parameter estimators and the bounding method. In this chapter we will illustrate, through an example, how the robust estimator would be used in a robust adaptive control system. In addition, we discuss the design of a strategy for adding probing signals to the closed-loop control system to enhance identification. The chapter is organized as follows.

In Section 7.2, we present some stability-robustness results for discrete-time systems. These results are then used in Section 7.3 to develop a simple control-law update algorithm that incorporates an on-line stability-robustness test. The results of Section 7.3 represent a complete robust adaptive controller for a limited class of plants. In Section 7.4, the use of probing signals is discussed. While there are many possible choices for a probing signal, the development of the frequency-domain bounding method gives insight as to what kinds of probing signals will result in improved closed-loop performance, that is, increased bandwidth. The key contributions of this chapter are the development of a robust control-law update algorithm for a limited class of plants, and the investigation of what probing signal strategies should be used with the robust estimator.

7.2 Stability Robustness Issues

In this section, we will develop tools that can be used to conclude that a discrete-time closed-loop system is robustly stable. Further, we will examine the implications of discrete-time stability robustness for the sampled-data system with the continuous-time plant. Specifically, the possibility of hidden oscillations occurring between the time samples of a sampled-data system will be examined.

7.2.1 Discrete-time Stability-Robustness Tests

In this subsection, we will use the results of Appendix F and the bounding function of Chapter 5, to find conditions under which the SISO discrete-time, closed-loop system of Figure 3.3 is robustly stable. From Figure 3.3 and Eqn. (3.7.1), we find that our nominal loop gain is

$$T(z) = G(z,\hat{\theta})\, K(z). \tag{7.2.1}$$

Further, we find our perturbed loop gain,

$$\tilde{T}(z) = G_{true}(z)\, K(z) = G(z,\hat{\theta})\,[1 + \delta_{su}(z,\hat{\theta})]\, K(z) = T(z)\,[1 + \delta_{su}(z,\hat{\theta})]. \tag{7.2.2}$$

We assume that we have a bounding function $\Delta_{su}(e^{j\omega T},\hat{\theta})$ on $|\delta_{su}(e^{j\omega T},\hat{\theta})|$ for all ω. Then, using the definitions of $T(z)$ and $\tilde{T}(z)$ given by Eqns. (7.2.1) and (7.2.2), respectively, we can state the following theorem.

Theorem 7.1: The closed-loop system $\tilde{T}(z) / (1 + \tilde{T}(z))$ has all its poles in the open unit disk if:

1) Assumption AD1.5 of Chapter 3 holds, that is, $G_{true}(z)$ and $G(z,\theta_0)$ have all their poles in the open unit disk, for all $\theta_0 \in \Theta$.

2) $K(z)$ has all its poles in the open unit disk.

3) The nominal closed-loop system, $T(z) / (1 + T(z))$, has all its poles in the open unit disk.

4) a) $$|1 + T^{-1}(e^{j\omega T})| > \Delta_{su}(e^{j\omega T},\hat{\theta}),\ \forall\omega, \text{ or equivalently,} \tag{7.2.3}$$

b) $$|T(e^{j\omega T}) / (1 + T(e^{j\omega T}))| < 1 / \Delta_{su}(e^{j\omega T},\hat{\theta}),\ \forall\omega. \tag{7.2.4}$$

Proof: The proof is an application of the results of Appendix F. Conditions 1 and 2 of the above theorem ensure that conditions 1a and 2 of Theorem F.3 are fulfilled. The stability of the nominal closed-loop system, that is, condition 3 from above, implies that condition 1b of Theorem F.3 is satisfied. Theorem 7.1 follows directly from Theorem F.3 of Appendix F.

Q.E.D.

7.2.2 Implications for Continuous-time

Although the results of the previous subsection enable us to prove asymptotic stability of the discrete-time closed-loop system, we are actually interested in the stability of the underlying sampled-data system with the continuous-time plant. That is, the analysis of the discrete-time system will tell us what is happening at the sampling instants. However, it will not tell us about the continuous-time plant output between these sampling instants. A phenomenon known as "hidden oscillations" or "intersample ripple" can occur, where the continuous-time plant output may oscillate even though the plant output at the sampling times does not. Astrom and Wittenmark

[31, p.116] provide a discussion of this problem. The following is adapted from their text.

They distinguish two cases of the hidden oscillations problem.

Case 1: Open or closed-loop systems, where there is an oscillation in the continuous-time output which cannot be seen in the control signal.

Case 2: Oscillations between the sampling points caused by an oscillation in the control signal.

The first case is due to the fact that for certain values of the sampling period, the discrete-time plant model may have a pole-zero cancellation. If this is the case, then some of the continuous-time open-loop plant modes will not be observable in the discrete-time plant output. A change in the sampling period will solve this problem of unobservability. The second case of hidden oscillations occurs when there are poorly damped plant zeros that are cancelled by the compensator. Astrom and Wittenmark summarize by saying that there are no hidden oscillations, if the unobservable open-loop plant modes are not oscillatory and if unstable or poorly damped plant zeros are not cancelled by the compensator.

7.3 A Simple Control-law Update Algorithm

In this section, we will present a simple control-law update algorithm that can be used in conjunction with the robust estimator to form a complete robust adaptive control system. The main purpose of this section is to illustrate how the robust estimator can be used in a closed-loop adaptive controller. The control-law update algorithm only works for a limited class of plants and is not recommended as a general case algorithm. However, because of its simple form we will be able to automate the update algorithm and, thus, later in Chapter 9, we will be able to perform an illustrative simulation.

7.3.1 Control-law Development

A simple pole-zero cancellation control-law will be developed. Our compensator will be formed by inverting the nominal model and substituting a discrete-time integrator. We will assume that the nominal model is stably invertible for all admissible parameter estimates and that the relative degree of the nominal model is one. We use only the information yielded by the robust estimator in our formulation of the robust control-law update algorithm. We state our simple algorithm in the form of a theorem.

Theorem 7.2: If $G_{true}(z) = G(z, \hat{\theta}) [1 + \delta_{su}(z, \hat{\theta})]$ and (7.3.1)

1) $G_{true}(z)$ has all its poles in the open unit disk,

2) $G(z, \hat{\theta})$ is of relative degree one or less, and has all its poles in the open unit disk for all $\hat{\theta} \in \Theta$,

3) $|\delta_{su}(e^{j\omega T}, \hat{\theta})| \leq \Delta_{su}(e^{j\omega T}, \hat{\theta}), \ \forall \omega,$ (7.3.2)

where $\Delta_{su}(e^{j0}, \hat{\theta}) < 1.$ (7.3.3)

4) $K(z, \hat{\theta}) = G^{-1}(z, \hat{\theta})\, c / (z - (1-\varepsilon_1))$. (7.3.4)

$$\text{where} \quad c = \begin{cases} [\, -(1/x) + \sqrt{(1/x)^2 + 4/x}\,]/2, & \text{if } x > 0 \\ 1, & \text{if } x \leq 0 \end{cases} \tag{7.3.5}$$

$$\text{and} \quad x = \sup_{\omega \in (0, \pi/T]} \{ [\Delta_{su}(e^{j\omega T}, \hat{\theta})^2 - 1] / [\, 2 (1 - \cos(\omega T))\,] \} + \varepsilon_2, \tag{7.3.6}$$

where ε_1 and ε_2 are infinitesimally small positive constants.

Then, the closed-loop system $G_{true}(z)\, K(z, \hat{\theta}) / (1 + G_{true}(z)\, K(z, \hat{\theta}))$ has all its poles in the open unit disk.

Remark 1: The constants ε_1 and ε_2 are included in the above theorem only to satisfy some technical conditions in the proof. In particular, the presence of ε_1 means that K(z) has no poles on the unit circle, thus allowing us to use Theorem 7.1.

Remark 2: In condition 2 of the above theorem, the nominal model is assumed to have a relative degree of one or less so that the compensator will be proper.

Proof: Rewriting Eqns. (7.2.1-2) and using Eqns. (7.3.1) and (7.3.4) we find that

$$T(z) = G(z, \hat{\theta})\, K(z, \hat{\theta}) = c / (z - 1 + \varepsilon_1) \tag{7.3.7}$$

$$\tilde{T}(z) = G_{true}(z)\, K(z, \hat{\theta}) = T(z) [1 + \delta_{su}(z, \hat{\theta})] = (\, c / (z - 1 + \varepsilon_1)\,) [1 + \delta_{su}(z, \hat{\theta})]. \tag{7.3.8}$$

Thus, with reference to 4a of Theorem 7.1, and considering the symmetry and periodicity of Δ_{su},

we must show that

$$|1 + (e^{j\omega T} - 1 + \varepsilon_1) / c| > \Delta_{su}(e^{j\omega T}, \hat{\theta}), \text{ for all } \omega \in [0,\pi/T]. \quad (7.3.9)$$

Now, to simplify the proof, we let $\varepsilon_1 \rightarrow 0$ and derive the limiting form of the inequality of Eqn. (7.3.9). So, we must show that our control law satisfies

$$|1 + (\cos(\omega T) + j \sin(\omega T) - 1) / c| > \Delta_{su}(e^{j\omega T}, \hat{\theta}), \text{ for all } \omega \in [0,\pi/T], \quad (7.3.10)$$

or

$$[1 + (\cos(\omega T) - 1) / c]^2 + (\sin(\omega T) / c)^2 > \Delta_{su}(e^{j\omega T}, \hat{\theta})^2, \text{ for all } \omega \in [0,\pi/T], \quad (7.3.11)$$

or

$$2 (1 - \cos(\omega T)) (1 - c) / c^2 > \Delta_{su}(e^{j\omega T}, \hat{\theta})^2 - 1, \text{ for all } \omega \in [0,\pi/T]. \quad (7.3.12)$$

For $\omega=0$, we find that Eqn. (7.3.12) becomes

$$1 > \Delta_{su}(e^{j0}, \hat{\theta})^2, \quad (7.3.13)$$

regardless of the value of c. The assumption of Eqn. (7.3.3) satisfies the requirement of Eqn. (7.3.13). Next, we consider the requirement of Eqn. (7.3.12) for $\omega \neq 0$. Since

$$1 - \cos(\omega T) > 0, \text{ for } \omega \in (0,\pi/T]. \quad (7.3.14)$$

we can use Eqn. (7.3.12) to see that our requirement has become

$$(1 - c) / c^2 > [\Delta_{su}(e^{j\omega T}, \hat{\theta})^2 - 1] / [\, 2 (1 - \cos(\omega T)) \,], \text{ for all } \omega \in (0,\pi/T], \quad (7.3.15)$$

or, using the definition of Eqn. (7.3.6), we must show that

$$(1 - c) / c^2 \geq x > [\Delta_{su}(e^{j\omega T}, \hat{\theta})^2 - 1] / [\, 2 (1 - \cos(\omega T)) \,], \text{ for all } \omega \in (0,\pi/T]. \quad (7.3.16)$$

Now, if

$$x = (1 - c) / c^2, \quad (7.3.17)$$

then

$$x c^2 + c - 1 = 0, \quad (7.3.18)$$

and, using the quadratic equation, we find that the two possible values of c are given by

$$c = [\, -(1 / x) \pm \sqrt{(1 / x)^2 + 4 / x} \,] / 2. \quad (7.3.19)$$

Eqn. (7.3.5) corresponds to the choice of the '+' sign in Eqn. (7.3.19). If $x \leq 0$, then Eqn.

(7.3.5) would yield a $c \geq 1$; however, we constraint c to be unity in this case; otherwise, the closed-loop nominal system will have a negative real pole.

So far we have shown that, if conditions 3-4 of the theorem are satisfied, then condition 4a of Theorem 7.1 is satisfied. We still need to prove nominal stability. The nominal closed-loop system is given by

$$T_{cl}(z) = G(z,\hat{\theta})\,K(z,\hat{\theta}) / (1 + G(z,\hat{\theta})\,K(z,\hat{\theta})) = c / (z - 1 + c + \varepsilon_1) \qquad (7.3.20)$$

whose pole is $1\text{-}c\text{-}\varepsilon_1$. From Eqn. (7.3.5) we conclude that $0 < c \leq 1$. Thus, the pole of the nominal closed-loop system is in the open unit disk since

$$-1 < -\varepsilon_1 \leq 1 - c - \varepsilon_1 < 1 - \varepsilon_1 < 1. \qquad (7.3.21)$$

Hence, we have shown that condition 3 of Theorem 7.1 is fulfilled. Finally, we see that conditions 1, 2 and 4 of Theorem 7.2 satisfy conditions 1 and 2 of Theorem 7.1. By application of Theorem 7.1 we have proven Theorem 7.2.

Q.E.D.

Remark 3: Theorem 7.2 is not easily extended to cases where the plant has a relative degree that is greater than unity. For the higher relative degree cases it is not possible to decompose the stability-robustness requirement into an inequality of the form of Eqn. (7.3.15) where one side depends only on the compensator gain c and the other side depends only on the uncertainty bounding function and frequency.

Remark 4: In the control-law update algorithm of Theorem 7.2, the compensator gain c can potentially become unity if the uncertainty bounding function $\Delta_{su}{}^{n}(e^{j\omega_k T}, \hat{\theta})$ becomes less than unity for all ω_k. If the gain c becomes unity, then, ignoring the infinitesimally small constant ε_1, the nominal closed-loop transfer function becomes

$$T_{cl}(z) = c / (z - 1 + c). \qquad (7.3.22)$$

So, for c=1,

$$T_{cl}(z) = z^{-1}. \qquad (7.3.23)$$

Thus, the algorithm of Theorem 7.2 can potentially yield a deadbeat system. To avoid this, the update algorithm can be modified to not allow the compensator gain to exceed some target gain $c_t < 1$. In this case, the pole of the nominal closed-loop system will never become faster than $1\text{-}c_t$, and the system will be more robust than in the deadbeat case.

7.3.2 Stability Robustness Tests using Discrete Frequency Points

In this brief subsection, we will address the problem of applying Theorem 7.2 when we have a discrete function of frequency, $\Delta_{su}^{n}(e^{j\omega_k T}, \hat{\theta})$ for k=0, . . , (N/2), instead of a continuous one. This problem was addressed in Section 5.8 where we added a safety factor to the uncertainty bounding function to account for possible inter-sample variations between discrete frequency points. Theorem 7.2 must be modified slightly to account for the use of the discrete uncertainty bounding function. That is, in Theorem 7.2, Eqn. (7.3.6) can be replaced, at a given time index n, by

$$x = \max_{k=1,..,(N/2)} \{ [\overline{\Delta}_{su}^{n}(e^{j\omega_k T}, \hat{\theta})^2 - 1] / [2 (1 - \cos(\omega_k T))] \} + \varepsilon_2, \qquad (7.3.24)$$

where $\overline{\Delta}_{su}^{n}(e^{j\omega_k T}, \hat{\theta})$ is the final uncertainty bounding function including the safety factor, which was developed in Section 5.8, and where again $\varepsilon_2 > 0$ can be made arbitrarily small.

7.4 Probing Signals and Closed-loop Operation

7.4.1 Introduction

In this section, we will discuss the addition of probing signals to enhance identification of the plant in a closed-loop adaptive system. Up to this point in the thesis we have taken a passive attitude with respect to the role of the robust estimator. The robust estimator updates its estimated frequency-domain model when the input signal is rich in some frequency range. However, when the plant input signal is not rich enough to improve on the estimated model, then the robust estimator doesn't update its estimates and, consequently, the control-law is not updated. If we want to enhance identification, that is, enable our robust estimator to learn, we can add a probing signal in the closed-loop. This probing signal will degrade the command-following performance of our closed-loop control system; however, the increased knowledge of the plant will result in better command-following in a later period, provided that the plant remains time-invariant. This trade-off between identification goals and closed-loop performance goals has been studied in the stochastic adaptive control literature as the "dual-control" problem [35], [6]. We do not pursue this stochastic approach but will instead discuss different characteristics of the probing signal that will enable the robust estimator to provide performance-improving information to the control-law update

algorithm. The goal of this section is to show how the robust adaptive control framework of Chapter 3 and the characteristics of the robust estimator impact the choice of a probing signal.

Consider the block diagram of Figure 7.1, which is the same as Figure 3.3 except that we have added the probing signal v[n] at the plant input. There are many possible strategies for choosing a probing signal to enhance identification. The following information can influence our choice of a probing signal:

1) the frequency range of the largest plant uncertainty,
2) the desired bandwidth of the closed-loop system,
3) knowledge of the spectrum of the additive output disturbance d[n],
4) knowledge of the spectrum of the reference signal r[n],
5) the desired speed of the identification procedure.

In addition to the above list, we can also use information that is gathered on-line to help determine our choice of probing signal. Since we compute the DFT of the input signal u[n] on-line, we could keep track of the spectrum of u[n] to see if we needed a probing signal. In the following subsections, we will use assumptions AD1-3 of Section 3.5 (i.e. 1 and 3 above) and an assumed target closed-loop bandwidth, in our development of a strategy for generating a probing signal. We do not assume that we know the spectrum of the reference signal ahead of time.

The rest of the section is organized as follows. In Subsection 7.4.2, we discuss questions of when to introduce probing signals and when to removed them. In Subsection 7.4.3, we will present a specific probing signal strategy that can be used with the simple adaptive control-law update algorithm of Section 7.3. This strategy will later be used in the simulations of the thesis. Since there are potentially many different probing signal strategies, we devote Subsection 7.4.4 to a general discussion of the characteristics of several different strategies.

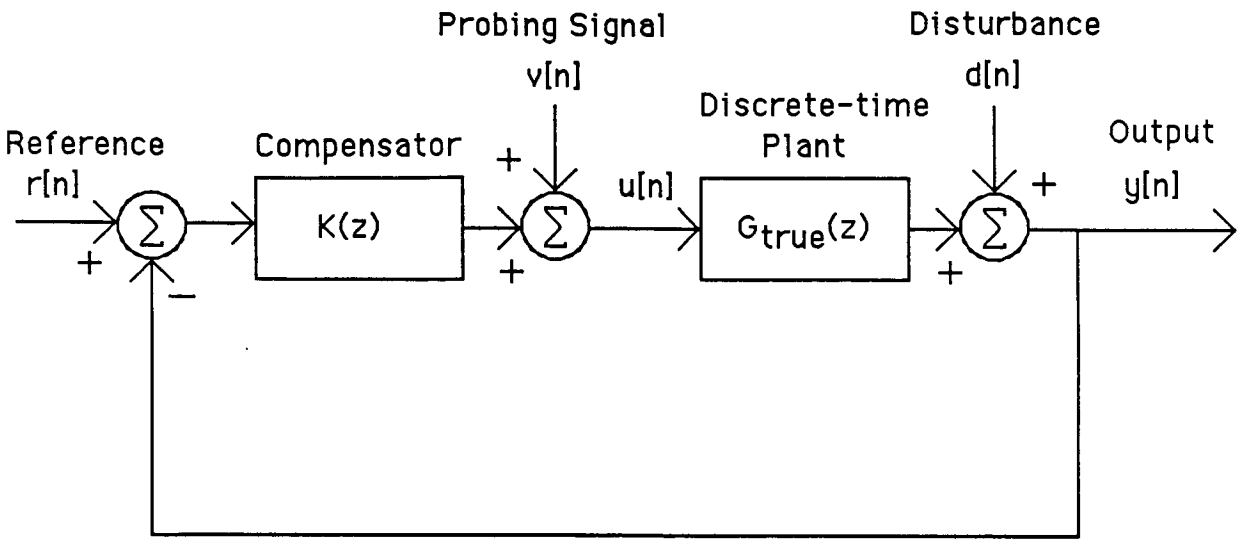

Figure 7.1: Closed-loop Discrete-time System with Probing Signal.

7.4.2 Starting and Stopping Criteria for Probing Signal Strategies

In this subsection, we examine criteria for adding or removing probing signals. In Figure 7.1, if the plant input signal u[n], which at this point is due primarily to the reference signal r[n], is rich enough, then the adaptive control system will yield successively higher bandwidth systems. Unfortunately, this will rarely be the case, so another source of excitation must be introduced. That is, if the adaptive control system doesn't push the bandwidth out on its own, based on the signals due to r[n], the designer may mandate that a probing signal be introduced. It's not clear that one wants to introduce a probing signal in all cases, since the probing signal will disturb the system. However, if the designer determines that he wants some closed-loop bandwidth to be attained in some finite amount of time, then such a signal may be required. Several questions arise in this situation. For example, what criteria should be used to detect when the adaptive control system is not pushing the bandwidth out, and what criteria should be used to stop the addition of the probing signal? We will now address these questions.

Probing Signal Starting Condition

To detect the need for a probing signal, the time progress of the adaptive control system needs to be monitored. We could check the richness of the plant control signal that is due

primarily, at this point, to the reference signal. However, in some situations, it makes more sense to check the progress of the adaptive control system as measured by its ability to increase the closed-loop bandwidth. If we could some how quantify the closed-loop bandwidth in terms of information that is available on-line, then we could perform this check. So, intuitively, we could check the average time rate of change of the closed-loop bandwidth and decide to "turn-on" the probing signal if this rate were not fast enough.

Probing Signal Stopping Condition

An obvious choice for the stopping condition for the probing signal is the attainment of the target closed-loop bandwidth. Of course, this again assumes that we could somehow quantify the closed-loop bandwidth in terms of information that is available on-line.

As an extension to the results of this thesis, in Subsection 10.2.4, we discuss the modification of the robust estimator to handle slowly time-varying plants. In a situation where the plant is slowly time-varying, the uncertainty bounding function can actually become larger if no rich signals are present in the system for a period of time. Thus, the attainment of the target closed-loop bandwidth, at one point in time, isn't the end of the story; rather, the current bandwidth must continually be monitored to see if it falls below its target value. That is, for the slowly time-varying case, we keep checking if the target closed-loop bandwidth is achieved and if it isn't, we introduce the required probing signal. As a final note to this subsection, we point out that there are some problems where the nominal closed-loop bandwidth, or some approximation thereof, is available in the form of the compensator parameters and the estimated plant parameters. For example, in the simple control-law of Section 7.3, the single discrete-time pole of the nominal closed-loop system can be expressed in terms of the known compensator gain c.

7.4.3 A Specific Strategy

In this subsection, we present a strategy for adding a probing signal to enhance identification and hence operation of the robust estimator. We again assume that the probing signal v[n] is added at the plant input as shown in Figure 7.1. Further, we assume that the control-law update algorithm of Section 7.3 is being used and that some target discrete-time pole p_{tcl} has been chosen for the nominal closed-loop system. First, we find out how large that the DFT of the input signal must be to reduce our uncertainty enough to achieve the target closed-loop bandwidth. Then, we use this input signal DFT to compute the DFT magnitude of the probing signal. Our procedure will be to make several assumptions so that we can come up with some idea of what the spectrum of the probing signal should be. Of course, the validity of our results will depend on the validity of our

assumptions, some of which will not be valid in all cases. First, we assume that the input signal is periodic with period N, so that

$$U_N^{n-p}(\omega_k) = U_N^n(\omega_k), \forall\omega_k, \tag{7.4.1}$$

and using Eqn. (5.2.4) we find that

$$\overline{E}_N^n(\omega_k) = \overline{E}_{rem}, \forall\omega_k. \tag{7.4.2}$$

Now, from Eqn. (5.2.17) and (7.4.2) we know that for $n \geq N-1$,

$$\overline{E}_{f,N}^n(\omega_k) = (\overline{E}_{rem} + \overline{\overline{D}}_N(\omega_k)) / |U_N^n(\omega_k)|, \forall\omega_k. \tag{7.4.3}$$

We also assume that

$$G_{cumf,N}^n(\omega_k) = G(e^{j\omega_k T}, \hat{\theta}), \text{ and} \tag{7.4.4}$$

$$\overline{E}_{cumf,N}^n(\omega_k) = \overline{E}_{f,N}^n(\omega_k), \forall\omega_k. \tag{7.4.5}$$

So, using Eqns. (5.5.6) and (7.4.4-5) we find that

$$\Delta_{su}^n(e^{j\omega_k T}, \hat{\theta}) = \overline{E}_{f,N}^n(\omega_k) / |G(e^{j\omega_k T}, \hat{\theta})| \tag{7.4.6}$$

which, combined with Eqn. (7.4.3), yields

$$\Delta_{su}^n(e^{j\omega_k T}, \hat{\theta}) = (\overline{E}_{rem} + \overline{\overline{D}}_N(\omega_k)) / (|U_N^n(\omega_k)| |G(e^{j\omega_k T}, \hat{\theta})|), \forall\omega_k. \tag{7.4.7}$$

Rearranging yields

$$|U_N^n(\omega_k)| = (\overline{E}_{rem} + \overline{\overline{D}}_N(\omega_k)) / (\Delta_{su}^n(e^{j\omega_k T}, \hat{\theta}) |G(e^{j\omega_k T}, \hat{\theta})|), \forall\omega_k. \tag{7.4.8}$$

From Section 7.3, we know that we want

$$\Delta_{su}^n(e^{j\omega_k T}, \hat{\theta}) < |(e^{j\omega_k T} - 1) / c_{tcl} + 1|, \forall\omega_k, \tag{7.4.9}$$

where c_{tcl} is the compensator gain corresponding to the target closed-loop bandwidth. That is, using the compensator of Theorem 7.2 yields a nominal closed-loop system with a single discrete-time pole at 1-c. Thus, if the target discrete-time pole is p_{tcl} for the nominal closed-loop system, then

$$c_{tcl} = 1 - p_{tcl}. \tag{7.4.10}$$

Combining Eqns. (7.4.8-9) yields the requirement that

$$|U_N^n(\omega_k)| > (\overline{E}_{rem} + \overline{\overline{D}}_N(\omega_k)) / (|(e^{j\omega_k T} - 1) / c_{tcl} + 1| |G(e^{j\omega_k T}, \hat{\theta})|), \forall\omega_k. \tag{7.4.11}$$

This equation gives us an idea of what the desired spectrum of the input signal should be so as to

achieve the closed-loop discrete-time pole p_{tcl}. However, what we are really interested in is the desired spectrum of the probing signal.

The transfer function from v[n] to u[n] is given by the sensitivity transfer function,

$$U(z) / V(z) = 1 / (1 + G_{true}(z) K(z, \hat{\theta})). \tag{7.4.12}$$

Thus, if we desire the plant input signal to have some spectrum, we must consider the disturbance rejection properties of the loop when we choose the probing signal v[n]. From Eqn. (7.4.12) we conclude that, to yield an input signal with a DTFT of $U(e^{j\omega T})$, we must use a probing signal v[n] with a DTFT of $V(e^{j\omega T})$ where

$$V(e^{j\omega T}) = [1 + G_{true}(e^{j\omega T}) K(e^{j\omega T}, \hat{\theta})] U(e^{j\omega T}), \forall\omega. \tag{7.4.13}$$

From the results of Chapter 2, we know that for sufficiently large N

$$V_N^n(\omega_k) \approx [1 + G_{true}(e^{j\omega_k T}) K(e^{j\omega_k T}, \hat{\theta})] U_N^n(\omega_k), \forall\omega_k. \tag{7.4.14}$$

Combining Eqns. (7.4.11) and (7.4.14) we find that, to achieve our target closed-loop bandwidth, we want to choose the probing signal such that

$$|V_N^n(\omega_k)| \approx |1 + G_{true}(e^{j\omega_k T}) K(e^{j\omega_k T}, \hat{\theta})| \cdot$$

$$(\overline{E}_{rem} + \overline{D}_N(\omega_k)) / (|(e^{j\omega_k T} - 1) / c_{tcl} + 1| |G(e^{j\omega_k T}, \hat{\theta})|), \forall\omega_k. \tag{7.4.15}$$

Since we do not know $G_{true}(z)$, we use Eqn. (7.3.8) to find

$$G_{true}(e^{j\omega_k T}) K(e^{j\omega_k T}, \hat{\theta}) = [c / (e^{j\omega_k T} - 1)] [1 + \delta_{su}(e^{j\omega_k T}, \hat{\theta})], \forall\omega_k, \tag{7.4.16}$$

where we have set ε_1=0 here. Using the triangle inequality, we write

$$|1 + G_{true}(e^{j\omega_k T}) K(e^{j\omega_k T}, \hat{\theta})| \leq 1 + [c / |e^{j\omega_k T} - 1|] [1 + \overline{\Delta}_{su}(e^{j\omega_k T}, \hat{\theta})], \forall\omega_k. \tag{7.4.17}$$

where we have again used the fact that $\overline{\Delta}_{su}$ is a bounding function on $|\delta_{su}|$. Now, in addition to not knowing $G_{true}(z)$, we do not know the true parameter vector θ_0. That is, while we do know the current parameter vector estimate $\hat{\theta}$, we really want to use the probing signal that will excite the plant well enough to identify the true plant with parameter vector θ_0. To make sure that the probing signal has a large enough spectrum at all frequencies, we choose to use the smallest possible nominal model at all frequencies in Eqn. (7.4.15). Now, we can rewrite Eqn. (7.4.15) using this

smallest nominal model and Eqn. (7.4.17).

$$|V_N^n(\omega_k)| \approx \left(1 + [c / |e^{j\omega_k T} - 1|] [1 + \overline{\Delta}_{su}(e^{j\omega_k T}, \hat{\theta})] \right) \cdot$$

$$\left(\overline{E}_{rem} + \overline{\overline{D}}_N(\omega_k) \right) / \left(|(e^{j\omega_k T} - 1) / c_{tcl} + 1| \inf_{\theta \in \Theta} \{ |G(e^{j\omega_k T}, \theta)| \} \right), \forall \omega_k. \quad (7.4.18)$$

In the above equation, the infimum can be computed off-line. Eqn. (7.4.18) is only computed infrequently, for example, the probing signal might only be updated every N sample times. At these probing signal update times, we use the current compensator gain c, which is updated by the control-law update algorithm, and the current uncertainty bounding function $\overline{\Delta}_{su}$, which is updated by the robust estimator, in order to compute the effect of the current disturbance rejection properties of the closed-loop. In summary, we have computed an approximate expression for the DFT of the probing signal that will yield enough information for the robust estimator to allow the robust control-law update algorithm of Theorem 7.2 to yield a nominal closed-loop system with a discrete-time pole at p_{tcl}.

As a final problem, we must find a time-domain signal that has the DFT magnitude of Eqn. (7.4.18). Here we will work with $V_N(\omega_k)$, the unshifted version of the DFT of v[n]. The inverse DFT of $V_N(\omega_k)$ is given by

$$v[n] = \frac{1}{N} \sum_{k=0}^{N-1} V_N(\omega_k) W_N^{-kn} \qquad \text{for } n = 0, \ldots, N-1. \quad (7.4.19)$$

One way to compute a time-domain signal with DFT magnitude $|V_N(\omega_k)|$ is the following

$$v_1[n] = \frac{1}{N} \sum_{k=0}^{N/2} |V_N(\omega_k)| \sin(2 \pi k n / N), \text{ for } n = 0, \ldots, N-1. \quad (7.4.20)$$

In Eqn. (7.4.20), we only use sinusoids with frequencies up to $\omega_k = \omega_{(N/2)} = (\omega_s/2)$, since symmetry properties give us information for the frequencies from $\omega_{[(N/2)+1]}$ to $\omega_{(N-1)}$. When there are many terms $|V_N(\omega_k)|$ that make significant contributions in the sum of Eqn. (7.4.20), we find that the time-domain signal $v_1[n]$ tends to have peaks, at some time indices, that are much larger than the standard deviation of the signal from its zero average. This occurs at the time

indices where many of the sinusoids add-up. These large time-domain peaks are undesirable so we seek another method for finding a time-domain version of the probing signal. In the second method, which we describe below, we form a time-domain signal by assigning a random phase to the DFT magnitude $|V_N(\omega_k)|$ for each k, and then computing the inverse DFT. So, for method 2 we find the probing signal $v_2[n]$ as follows,

$$v_2[n] = \frac{1}{N} \sum_{k=0}^{N/2} |V_N(\omega_k)| [a_k \cos(2 \pi k n / N) + b_k \sin(2 \pi k n / N)], \quad \text{for } n = 0, \ldots, N-1 \tag{7.4.21}$$

where

$$a_k = \cos(\varphi_k) \tag{7.4.22}$$

$$b_k = \sin(\varphi_k) \tag{7.4.23}$$

so

$$\sqrt{a_k^2 + b_k^2} = 1 \tag{7.4.24}$$

and where φ_k is a random variable that is uniformly distributed on the interval $[0,2\pi]$ for each k. The probing signal $v_2[n]$ of Eqn. (7.4.21) does not have the troublesome peaks of $v_1[n]$ of Eqn. (7.4.20). We note that $v_2[n]$ is effectively the same as passing a white noise signal through a filter with magnitude $|V_N(\omega_k)|$.

We now present a final modification to the probing signal strategy that we have been developing. Since we know what target closed-loop bandwidth we want, we know how small the cumulative frequency-domain error $\overline{E}_{cumf,N}^{n}(\omega_k)$ must become for the worst-case, smallest magnitude nominal model to have a sufficiently small multiplicative uncertainty bounding function. That is, using Eqns. (7.4.5-6) we find

$$|G(e^{j\omega_k T}, \hat{\theta})| \, \Delta_{su}^{n}(e^{j\omega_k T}, \hat{\theta}) = \overline{E}_{cumf,N}^{n}(\omega_k), \; \forall \omega_k. \tag{7.4.25}$$

Now, using the requirement of Eqn. (7.4.9) we find that, if

$$\overline{E}_{cumf,N}^{n}(\omega_k) = |(e^{j\omega_k T} - 1) / c_{tcl} + 1| (\inf_{\theta \in \Theta} \{ |G(e^{j\omega_k T}, \theta)| \}), \tag{7.4.26}$$

for all ω_k, then the target closed-loop bandwidth can be attained for all possible nominal models. This realization suggests the straightforward modification for our probing signal strategy.

> MODIFICATION: If, at time index n, Eqn. (7.4.26) is satisfied for a given frequency ω_k, then the corresponding magnitude coefficient $|V_N(\omega_k)|$ should be set to zero in the time-domain expression for the probing signal.

In this way, we stop unnecessarily exciting the plant at the frequency ω_k since we have already gathered sufficient information at this frequency.

7.4.4 Other Probing Signal Strategies

In this subsection, we provide a more general discussion of probing signal strategies for use with the robust estimator. In the previous section, we saw how the disturbance rejection properties of the closed-loop system affect our choice of a probing signal. Consider a situation where we are using the robust estimator in combination with the control-law of Section 7.3 and the probing signal strategy of Subsection 7.4.3. In this case, we expect the bandwidth of the nominal closed-loop system to increase over time. Initially, the plant estimate will be poor so the compensator gain c will be small to guard against the large modeling uncertainty. Thus, initially the probing signal, which acts as an input disturbance to the plant, will not be rejected by the loop and we will have, roughly speaking, an open-loop identification problem with the probing signal providing most of the plant input signal. In this case, the probing signal need not be large. Needless to say, initially the closed-loop system will have very poor command-following properties because of the low loop gain. Now, as the robust estimator identifies the plant, successively larger values of the compensator gain can be used as the plant uncertainty is decreased. However, a larger compensator gain will result in improved disturbance rejection properties of the closed-loop system. So, as the closed-loop bandwidth increases, we must use successively larger probing signals to gain any new information. That is, the better that we identify, the harder it is to gain any additional information. In practice, what can occur is that the target closed-loop bandwidth can be almost achieved, so that the loop does a good job of rejecting the probing signal. In this case, the probing signal must be very large if we want to actually achieve the target closed-loop bandwidth.

It is stressed again that there are as many probing signal strategies as there are different

adaptive control problems. The choice of a strategy depends on what is known and what the relative importance of different objectives is in a given problem. In this thesis we do not provide a comprehensive treatment of this issue of probing signals. However, since the characteristics of the robust estimator affect the choice of a probing signal strategy, we will discuss several illustrative strategies and point out the different characteristics of each. In each case, we are interested in generating a probing signal that will allow the robust adaptive control system to increase the nominal closed-loop bandwidth to some target value. In the following discussion, we ignore any contribution of the reference signal to the plant input signal and instead compute the spectrum of the probing signal that is required as if it were the only excitation in the system. Thus, we take the viewpoint that, when the probing signal starting condition of Subsection 7.4.2 is true, we introduce a probing signal that we know will do the job until we reach the target closed-loop bandwidth. Again, the problem is that, during the period of time that the probing signal is present, it is disturbing the system. We do not treat this tradeoff rigorously but incorporate it into our arguments as the reason for wanting to use a small time-domain probing signal.

Strategy 1: (Strategy of Subsection 7.4.3)

Description: We compute the required spectrum at the plant input assuming that the plant is the smallest magnitude nominal plant. Then, we use our knowledge of the current disturbance rejection properties of the closed-loop system to compute the required spectrum of the probing signal. The final time-domain version of the probing signal is generated using a sum of all of the required sinusoids.

Characteristics: The above strategy results is a relatively fast adaptation time. In principle, if the assumptions made in the probing signal development of Section 7.4.3 are fulfilled, this strategy can result in the attainment of the target closed-loop bandwidth in roughly the time length of the N-point DFT. However, the time-domain probing signal can be quite large since it is the sum of many sinusoids. In addition, the use of the worst-case, smallest magnitude nominal plant in the computation of the required spectrum means that the probing signal spectrum may be larger than that required for the identification of the true plant. That is, if the true nominal plant rolls-off at a much higher frequency than the assumed worst-case nominal plant, then the probing signal that is computed using this strategy will have an unneccessarily large magnitude in the frequency range between the two different roll-off frequencies.

Strategy 2:

Description: Same as Strategy 1 except that the final time-domain version of the probing signal is generated by using successive N-point time sequences of each of the required sinusoids

alone. That is, given the desired spectrum magnitude $|V_N(\omega_k)|$, we generate the probing signal as follows.

$$v[n] = \begin{cases} |V_N(\omega_0)|, \text{ for } n = 0, \ldots, N-1 \\ |V_N(\omega_1)| \sin(2 \pi n / N), \text{ for } n = N, \ldots, 2N-1 \\ \quad \bullet \bullet \bullet \\ |V_N(\omega_k)| \sin(2 \pi k n / N), \text{ for } n = k \bullet N, \ldots, (k+1) \bullet N - 1 \\ \quad \bullet \bullet \bullet \\ |V_N(\omega_{(N/2)})| \sin(\pi n), \text{ for } n = (N/2) \bullet N, \ldots, (N/2+1) \bullet N - 1 \end{cases} \quad (7.4.27)$$

where N is the DFT length. In this way, we do not have to use a large time-domain probing signal and we are only disturbing the system at one frequency at a time.

Characteristics: The above strategy results is an extremely long adaptation time and is presented only to make a point. There is a tradeoff between the size of the time-domain probing signal and the speed of adaptation (identification). In Strategy 1, the time-domain probing signal is large; however, the target closed-loop bandwidth is achieved in about N sample times. In Strategy 2, the time-domain probing signal is much smaller (potentially only 1/N as big as Strategy 1); however, the target closed-loop bandwidth is not achieved until about (N/2)•N time samples.

Strategy 3:

Description: Same as Strategy 1 except that we use a stage-by-stage learning process with regard to which nominal plant model we use in our computation of the required probing signal spectrum. We are trying to avoid the problem that was described in Strategy 1 concerning the use of the worst-case, smallest magnitude nominal plant. A heuristic approach could be used where we first introduce a probing signal that would result in the achievement of the target closed-loop bandwidth for, say, the largest magnitude nominal plant that we may have. If the probing signal was not rich enough for the adaptive control system to achieve the target closed-loop bandwidth during the first N time samples, then the probing signal would be increased under the assumption that the nominal plant model was somewhat smaller. This process could be carried out in stages over each N time sample period until the required probing signal was reached.

Characteristics: This strategy will result in performance that is similar, but slower than Strategy 1. Stategy 3 requires several N time sample length intervals, depending upon the size of the gradations by which the probing signal is increased at each stage. The advantage is that Strategy 3 requires a smaller probing signal than Strategy 1. Thus, we once again have an example

of the trade-off between adaptation speed and probing signal size.

Later, in Chapter 9, we will use the specific probing signal strategy of Subsection 7.4.3, that is, Strategy 1. It is hoped that the presentation of the other strategies provides insight that may be useful to some future researchers. As will be discussed later in the final chapter of this thesis, the issue of probing signal choice is an area for future research.

7.5 Conclusion

In this chapter, we have given a rather qualitative presentation of some of the remaining issues involved in the development of a complete robust adaptive control system. For illustrative purposes, we have developed a simple control-law update algorithm that can be used in combination with the robust estimator. In addition, for this simple control-law update algorithm, we have suggested an example strategy for the introduction of a probing signal into the closed-loop adaptive system. These results will later be used in the simulation examples of the thesis.

Again, this chapter was meant to tie together the many functional blocks of a complete robust adaptive control system, thereby illustrating the role of the robust estimator. The probing signal discussion of this chapter constitutes only a beginning to the investigation of this issue. However, it is important to emphasize that the robust adaptive control framework that we have provided, allows for the formulation of such probing signal strategies using current frequency-domain information. That is, with reference to the modification that was described at the end of Subsection 7.4.3, we have on-line knowledge of where the plant has been identified well and where it hasn't, in the frequency domain.

CHAPTER 8.
SIMULATIONS OF THE BASIC BUILDING BLOCKS OF THE ROBUST ESTIMATOR

In this chapter, we will illustrate the properties of two of the basic building blocks of the robust estimator by considering several simulation examples. The robust estimator is a complex combination of several simpler building blocks. Later, in Chapter 9, we will perform simulations of the robust estimator as a whole; however, when simulated as a whole, it is difficult to understand the properties of the individual components of the robust estimator. Thus, in order to be able to understand the behavior of the complete robust estimator we must first fully understand the properties and behavior of the robust estimator's individual components. This simulation chapter is a logical follow-on to the signal processing theorems of Chapter 2. We will be simulating the results of Chapter 2 using the design rules and insight of Chapter 6. Specifically, in the present chapter we examine the properties of: 1) the time-domain bounding method of Theorem 2.4 that is used in the time-domain parameter estimator of Chapter 4; and 2) the frequency-domain error bounding method of Theorem 2.2 that is used in Sections 5.2-5.3. We will use a simple first-order plant, with no unmodeled dynamics, and several different types of input signals in the simulations of this chapter. We use many types of input signals so that we can understand the robust estimator's components under many excitation conditions. The understanding gained in this chapter will be very useful in understanding the properties of the robust estimator as a whole in the following chapter.

8.1 Plant Description and Design Choices

8.1.1 Plant Description

Consider the following plant which we will use throughout this chapter.

Continuous-time Plant: $H^c(s) = 1 / (s + 1) \Leftrightarrow h(t) = e^{-t}, t \geq 0.$ (8.1.1)

Choosing the sampling period $T=\pi/5$, corresponding to a sampling frequency $\omega_s=10$ rads/sec., which is ten times the continuous-time pole, we find that the zero-order hold equivalent of the above continuous-time plant is

Discrete-time Plant: $H(z) = r / (z - p) \Leftrightarrow h[n] = g\, p^n, n \geq 1$ (8.1.2)

where

$r = (1 - e^{-T}) = 0.46651;\ p = e^{-T} = 0.53349;$ and $g = r / p = 0.87446.$ (8.1.3)

We compute

$$|H(e^{j\omega_k T})| = r / \sqrt{(\cos(2\pi k / N) - p)^2 + \sin(2\pi k / N)^2}, \text{ for } k = 0, \ldots, N-1. \quad (8.1.4)$$

where again $\omega_k = (k / N)\omega_s$.

In the following simulations we will assume that the input signal u[n] is always less than unity, so $u_{max}=1$ in the signal processing theorems.

8.2 Simulations of Time-domain Bounding

In this subsection, we will present simulation results that illustrate the time-domain bounding mechanism of Theorem 2.4. This theorem is used to find a time-domain bounding function on the error signal, due to the unstructured uncertainty, in the time-domain parameter estimator of Chapter 4. For the purposes of this chapter, we consider the computation of a time-varying bound on |y[n]| where

$$y[n] = h[n] * u[n] \quad (8.2.1)$$

and h[n] is the plant given by Eqn. (8.1.2). With reference to Theorem 2.4, we define the following time-varying bound $\overline{y}[n]$ as follows,

$$|y[n]| \leq \overline{y}[n], n \geq 0, \quad (8.2.2)$$

where

$$\overline{y}[n] = \frac{1}{N} \{ |H(e^{j\omega_0 T})| |U_N^n(\omega_0)| + 2 \sum_{k=1}^{(N/2)-1} |H(e^{j\omega_k T})| |U_N^n(\omega_k)| + |H(e^{j\omega_{(N/2)} T})| |U_N^n(\omega_{(N/2)})| \} + 2 u_{max} \sum_{i=N}^{\infty} |h[i]|. \quad (8.2.3)$$

First, we must choose the DFT length for the time-domain bounding mechanism. To gain insight, we find an equivalent expression for the bound of Eqn. (8.2.3),

$$\overline{y}[n] = \frac{1}{N} \{ \sum_{k=0}^{N-1} |H(e^{j\omega_k T})| |U_N^n(\omega_k)| \} + 2 u_{max} g p^N / (1 - p), \quad (8.2.4)$$

where we have used the results of Appendix C to find a closed-form for the summation,

$$\sum_{i=N}^{\infty} |h[i]| = \sum_{i=N}^{\infty} g p^i = g p^N / (1 - p). \quad (8.2.5)$$

In Section 6.5, we discussed the tradeoff between the two terms of Eqn. (8.2.3). For the parameters of the example that was described in the previous section, we find that for N=6 the second term of Eqn. (8.2.4), i.e. the remainder term, is 0.086428. This is a small number compared to the values of y[n] that we expect to observe. For example, since we assumed that $u_{max}=1$, consider the output of the plant of Eqn. (8.1.2) for a unity magnitude sinusoid at a frequency that is less than 1 rad/sec., i.e. the pole of the plant. In this case, the output y[n] will be on the order of unity. Thus, the remaider term 0.086428 is an order of magnitude smaller than the plant output. We conclude that, based only on the requirements of the time-domain bounding mechanism, a good choice for the DFT length is N=6. In the following subsection we will choose the DFT length for the frequency-domain bounding method to be N=50. In this case, the remainder term is only 8.51416×10^{-14}. However, as was discussed in Section 6.5, the bounding function of Eqn. (8.2.3) tends to increase with N for some wideband excitations, as will be seen in the simulation examples.

Before presenting the actual simulation results, we make some observations concerning the bound of Eqn. (8.2.4) and hence Eqn. (8.2.3).

Observations:

1) Eqn. (8.2.4) is a tight bound on |y[n]| when the significant terms in the sum

$$\sum_{k=0}^{N-1} H(e^{j\omega_k T})\, U_N^n(\omega_k)\, W_N^{-kn}, \qquad (8.2.6)$$

have the same phase.

2) As was observed in Subsection 6.5, if u[n] is a sinusoid with frequency $\omega_k=(k/N)\omega_s$, then $|U_N^n(\omega_k)|$ will be nonzero for only one or two terms in the bounding summation and, consequently, Eqn. (8.2.4) will be a tight bound.

3) As was also observed in Subsection 6.5, if u[n] is a wideband excitation, then the bound of Eqn. (8.2.4) can increase with the square root of N, the DFT length.

Now we present simulations showing the actual value of y[n], as well as the time-varying magnitude bound computed using Eqn. (8.2.3).

Simulation 8.2.1: Sinusoidal Input, N=6

For this simulation we use the sinusoidal input signal

$$u[n] = \sin((2\pi / 5) n) = \sin(2 n T), n \geq 0. \quad (8.2.7)$$

So, since the frequency of this input signal corresponds to ω=2 rads/sec, we find that for $n \geq N-1$, $U_N^n(\omega_k)$ will have energy at 2 rads/sec and ω_s-2=8 rads/sec. However, for our choice of N=6, the discrete frequencies are ω_k= 0, 1.67, 3.33, 5.00, 6.67, and 8.33 rads/sec. This means that for $n \geq N-1=5$, the values of $|U_N^n(\omega_k)|$ will be a result of a two sinc functions, one centered at 2 rads/sec and the other one centered at 8 rads/sec. as was shown for the case of a disturbance in Eqn. (6.4.4). Thus, in terms of the bounding function of Eqn. (8.2.3), $|U_N^n(\omega_k)|$ will be the largest for k=1 with the other terms contributing smaller amounts to the sum. A consequence of this dominance by one term is that the bounding function will be relatively tight, but not as tight as in the case where the sinusoid frequency corresponds to one of the discrete frequencies ω_k. The output signal y[n], as well as the computed bounds $\overline{y}[n]$ and $-\overline{y}[n]$ are shown in Figure 8.1. Since u[n] is zero for $n < 0$, there is a small transient in the bound until n=5 (3.14 secs.) at which time 6 data points have been collected for computing $|U_N^n(\omega_k)|$. As can be seen in Figure 8.1, the bound $\overline{y}[n]$ has a component that oscillates with the same frequency as the input signal u[n].

Simulation 8.2.2: Sinusoidal Input, N=50

For comparison, we again use the sinusoidal signal of Eqn. (8.2.7) and compute the bound $\overline{y}[n]$ using the longer DFT length, N=50. The output signal y[n], as well as the computed bounds $\overline{y}[n]$ and $-\overline{y}[n]$ are shown in Figure 8.2 for N=50. In this case, there is a much longer, more conservative transient in the bound than in the case of N=6. However, we also note that for $n \geq N-1=49$ (30.79 secs.), the bound is a constant and is actually tighter than in the N=6 case. This is a consequence of the fact that for $n \geq N-1$, $|U_N^n(\omega_k)|$ will be nonzero for only k=10 in Eqn. (8.2.3), since for N=50 the sinusoid frequency corresponds exactly to one of the discrete frequencies of the 50-point DFT. That is, for N=50, $\omega_k=\omega_{10}$=2 rads/sec.

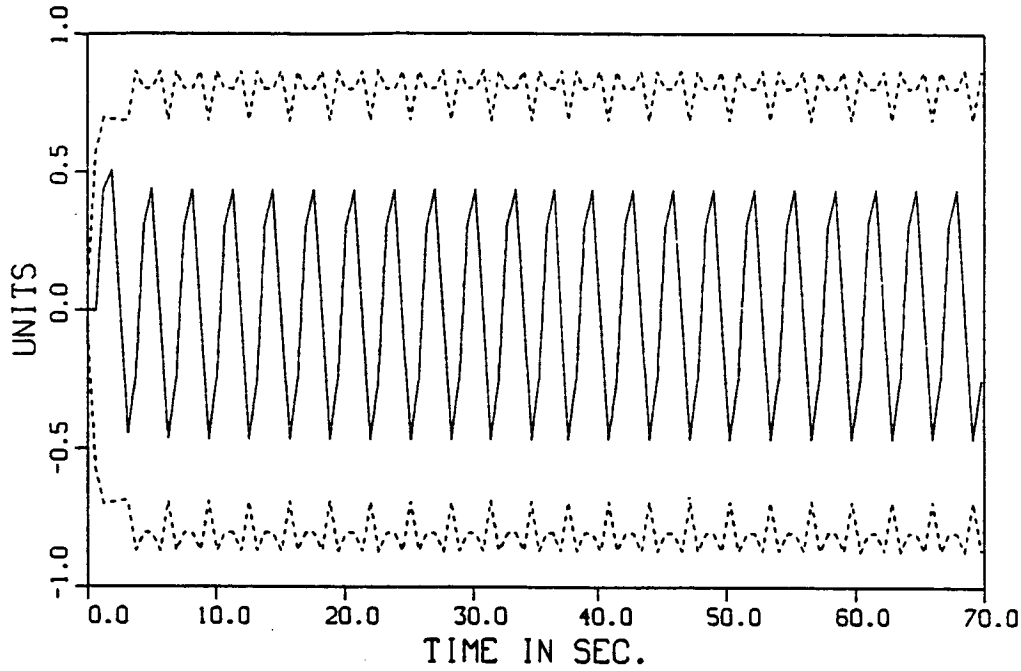

Figure 8.1: Plant Output y[n] and Bounds $\overline{y}[n]$ and $-\overline{y}[n]$ for Sinusoidal Input and N=6.

(y[n] = ——, $\overline{y}[n]$ and $-\overline{y}[n]$ = - - - -)

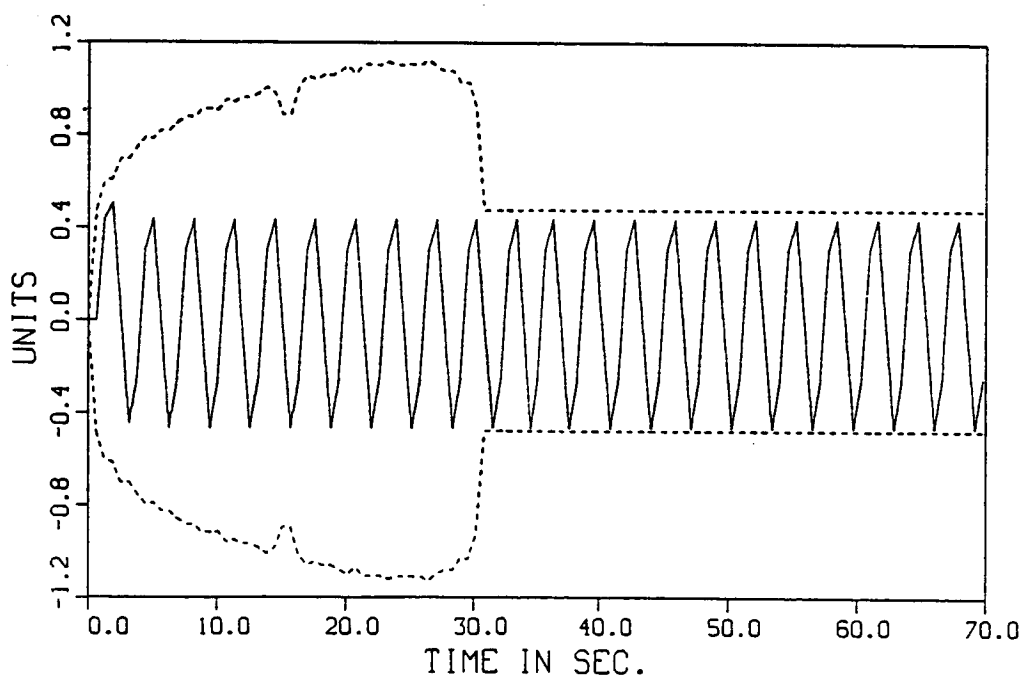

Figure 8.2: Plant Output y[n] and Bounds $\overline{y}[n]$ and $-\overline{y}[n]$ for Sinusoidal Input and N=50.

(y[n] = ——, $\overline{y}[n]$ and $-\overline{y}[n]$ = - - - -)

Simulation 8.2.3: Square-wave Input, for N=6

For this simulation we use the square-wave input signal, u[n]=($\tilde{u}$[n] periodic with period 20) for $n \geq 0$, where

$$\tilde{u}[n] = \begin{cases} 1, \text{ for } 0 \leq n \leq 9 \\ -1, \text{ for } 10 \leq n \leq 19. \end{cases} \tag{8.2.8}$$

The fundamental frequency of u[n] is 0.50 rads/sec., so we expect $U_N^n(\omega_k)$ to have energy at this fundamental frequency and its harmonics at 1.0, 1.5, 2.0, . . , 9.0 and 9.5 rads/sec. However, the actual DFT, $U_N^n(\omega_k)$, will depend on the time index n and the DFT length N. The output signal y[n], as well as the computed bounds $\overline{y}$[n] and -$\overline{y}$[n] are shown in Figure 8.3. Again, since u[n] is zero for $n < 0$, there is a small transient in the bound until n=5 (3.14 secs.) at which time 6 data points have been collected for computing $|U_N^n(\omega_k)|$. The small value of N results in a tight bound. If a larger value of N is used then the bound can be conservative. This possibility is addressed in the next set of simulations.

Simulations 8.2.4-7: Square-wave Input, for N=20, 50, 90 and 100

We use this case of a square-wave input to do a simulation study of the effects of the DFT length N on the bound $\overline{y}$[n]. In Figures 8.4-11 we show both the time-domain bound and $|U_N^n(\omega_k)|$ at n=99 (62.20 secs.), for the cases of the DFT length N being 20, 50, 90 and 100. First, we notice that, if the length of the DFT is the same as a multiple of the period of the input signal u[n], then the time-domain bound reaches a constant steady-state value. That is, for the cases of N=20 and 100, after the initial transient ends at time index N-1, the time-domain bound reaches a constant steady-state value which is the same for both cases. The DFT magnitudes for these cases, see Figures 8.8 and 8.11, show that the discrete frequency points ω_k correspond to the fundamental and harmonic frequencies of the square wave. Thus, the sum of Eqn. (8.2.3) has only 5 nonzero terms and, hence, is a relatively tight bound. For the cases of N=50 and 90, the sum of Eqn. (8.2.3) has many nonzero terms as can be seen from Figures 8.9-10. For these cases, we see from Figures 8.5-6 that the steady-state time-domain bound is more conservative than for

the cases of N=20 and 100. We also observe, from a comparison of the time-domain bounds for the cases of N=50 and 90, that the bound increases with N.

As a final note, we see that for this square-wave input signal the bounding function is more conservative than for the case of a pure sinusoidal input signal. This is because of the difference in the number of significant terms in the sum of Eqn. (8.2.3). Consider the case of N=50 where, as can be seen from Figure 8.9, there are many terms that are significant in the sum of Eqn. (8.2.3). For the sinusoidal input case, there is only one term in the sum for $n \geq N-1$.

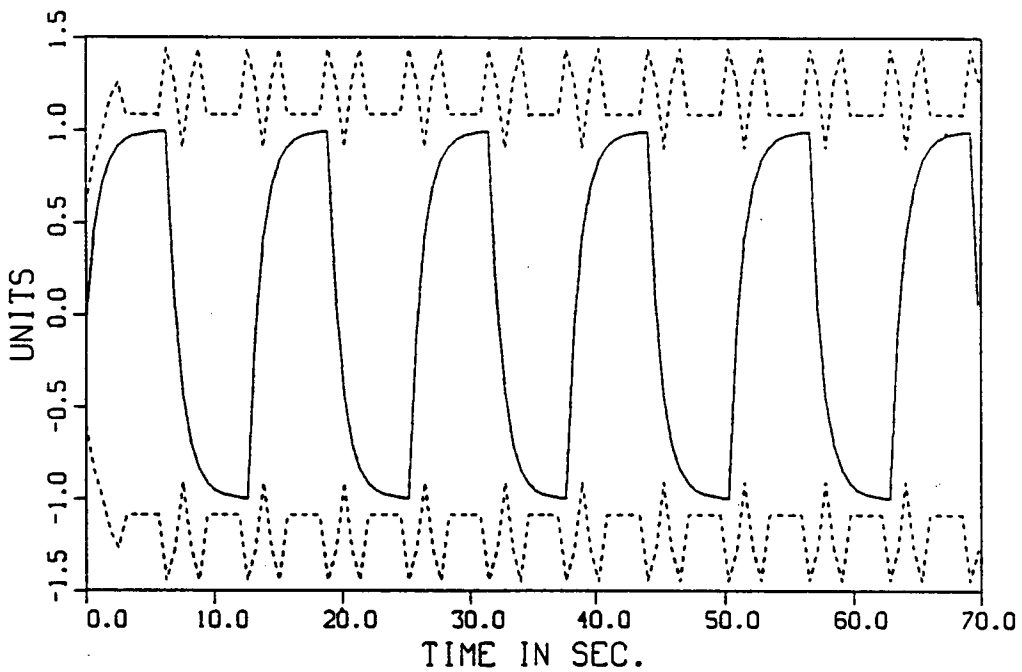

Figure 8.3: Plant Output y[n] and Bounds $\overline{y}[n]$ and $-\overline{y}[n]$ for Square-wave Input and N=6.

(y[n] = ——, $\overline{y}[n]$ and $-\overline{y}[n]$ = - - - -)

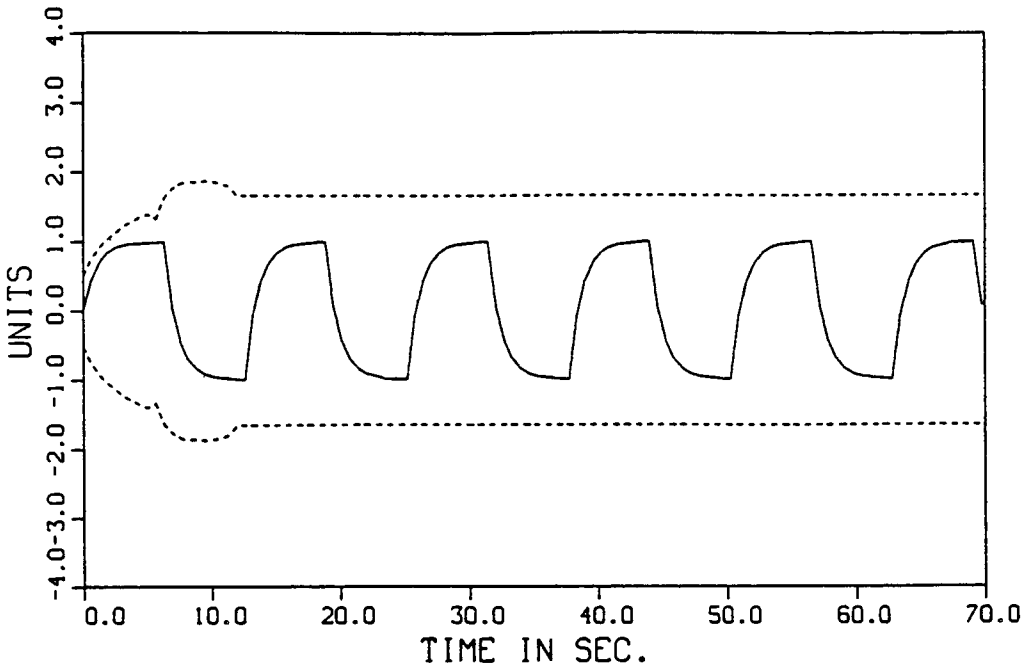

Figure 8.4: Plant Output y[n] and Bounds $\overline{y}[n]$ and $-\overline{y}[n]$ for Square-wave Input and N=20.

(y[n] = ——, $\overline{y}[n]$ and $-\overline{y}[n]$ = - - - -)

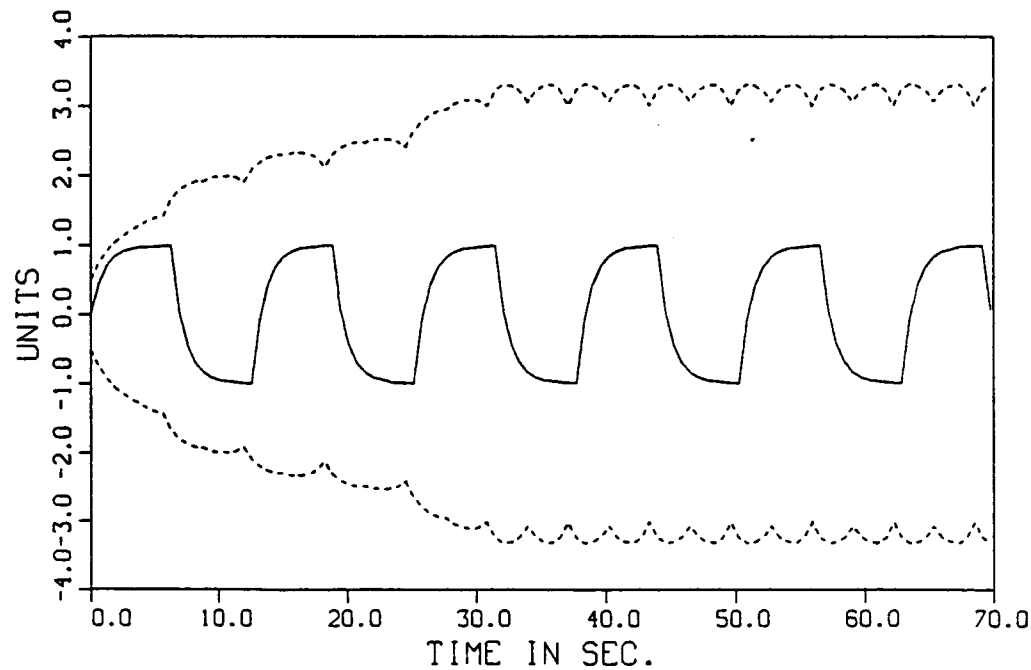

Figure 8.5: Plant Output y[n] and Bounds $\overline{y}[n]$ and $-\overline{y}[n]$ for Square-wave Input and N=50.

(y[n] = ——, $\overline{y}[n]$ and $-\overline{y}[n]$ = - - - -)

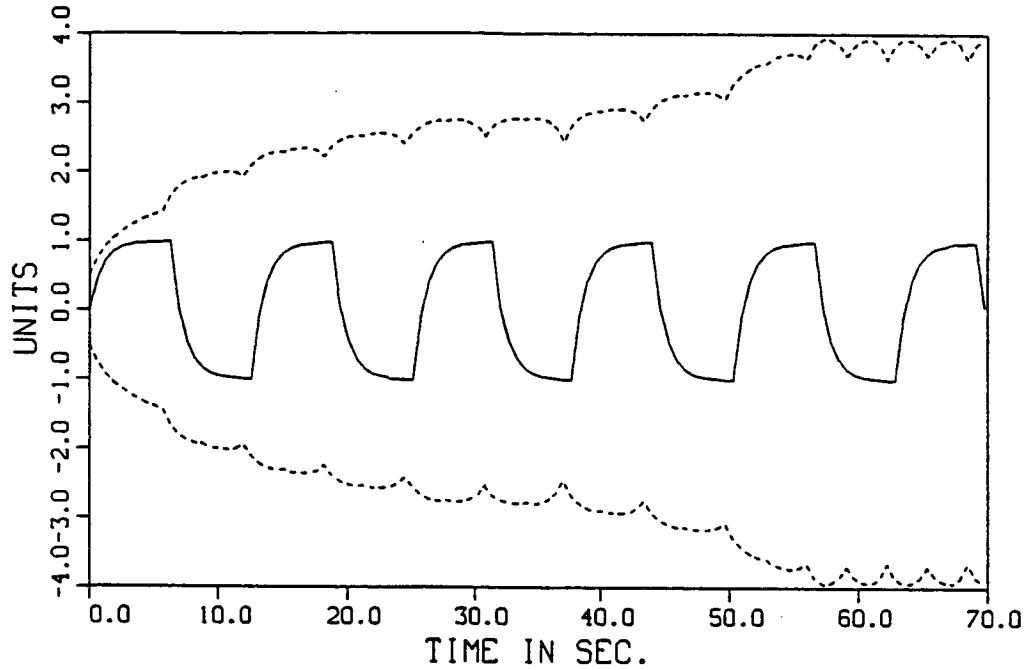

Figure 8.6: Plant Output y[n] and Bounds $\overline{y}[n]$ and $-\overline{y}[n]$ for Square-wave Input and N=90.

(y[n] = ——, $\overline{y}[n]$ and $-\overline{y}[n]$ = - - - -)

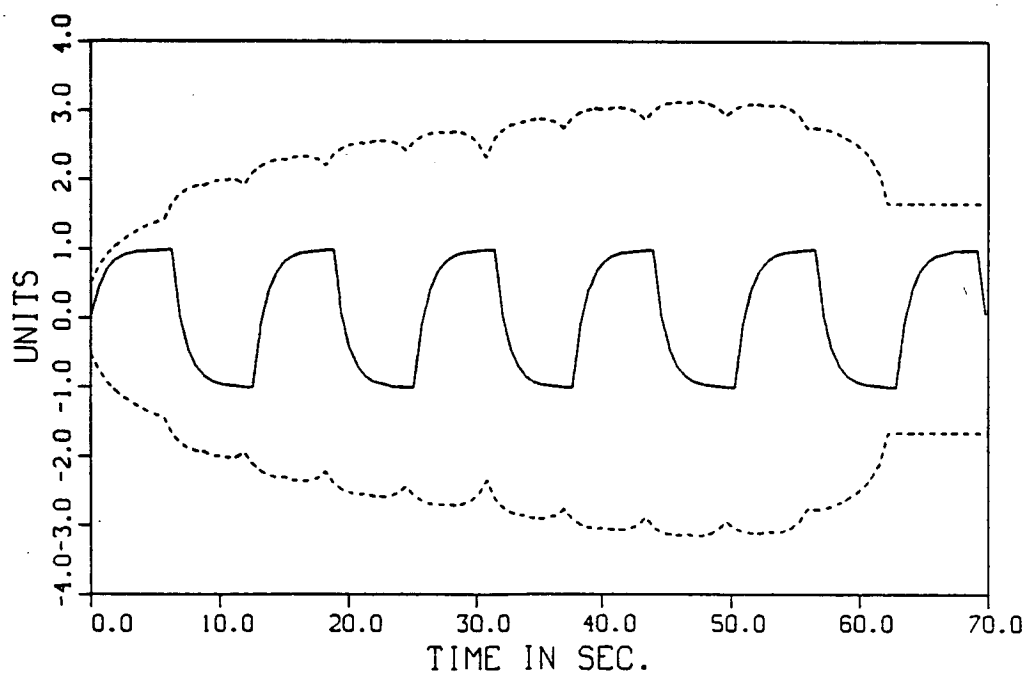

Figure 8.7: Plant Output y[n] and Bounds $\overline{y}[n]$ and $-\overline{y}[n]$ for Square-wave Input and N=100.

(y[n] = ——, $\overline{y}[n]$ and $-\overline{y}[n]$ = - - - -)

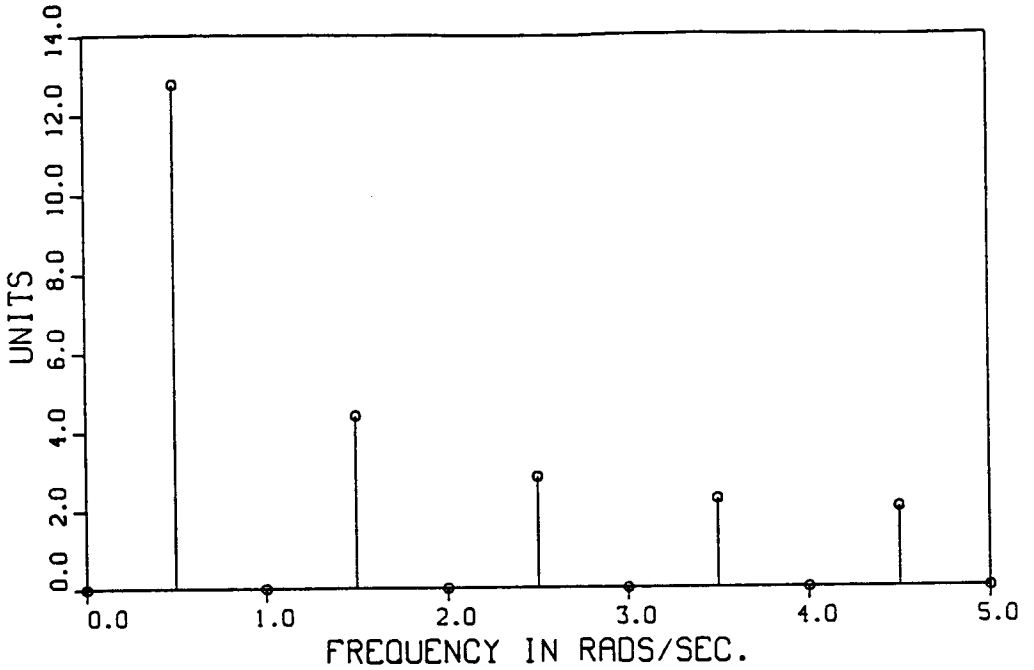

Figure 8.8: $|U_N^n(\omega_k)|$ at n=99 (62.20 secs.) for Square-wave Input and N=20.

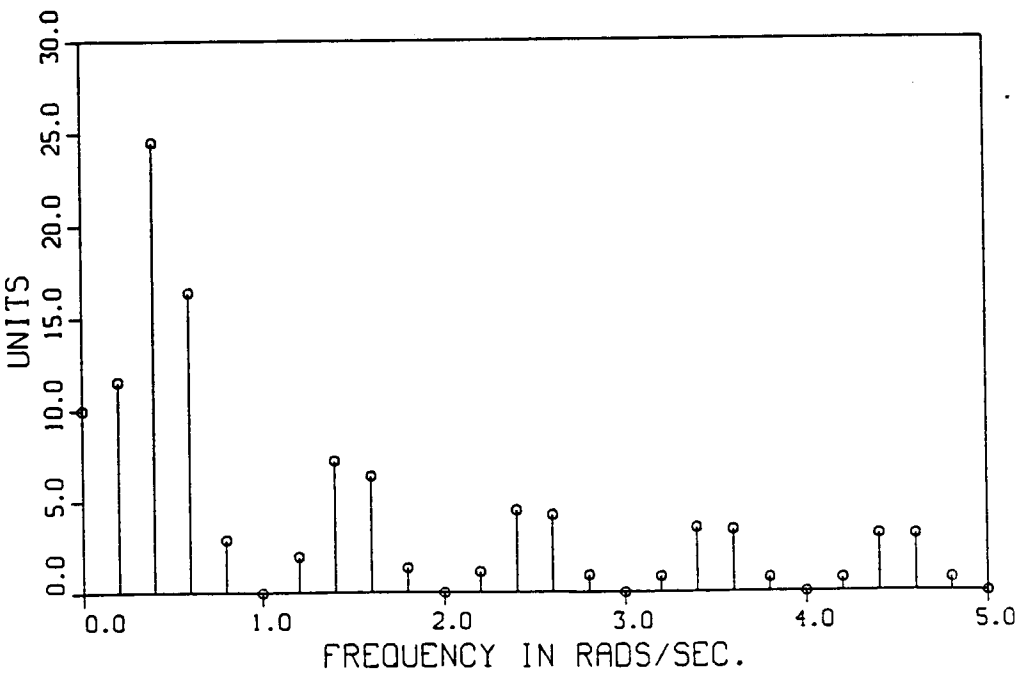

Figure 8.9: $|U_N^n(\omega_k)|$ at n=99 (62.20 secs.) for Square-wave Input and N=50.

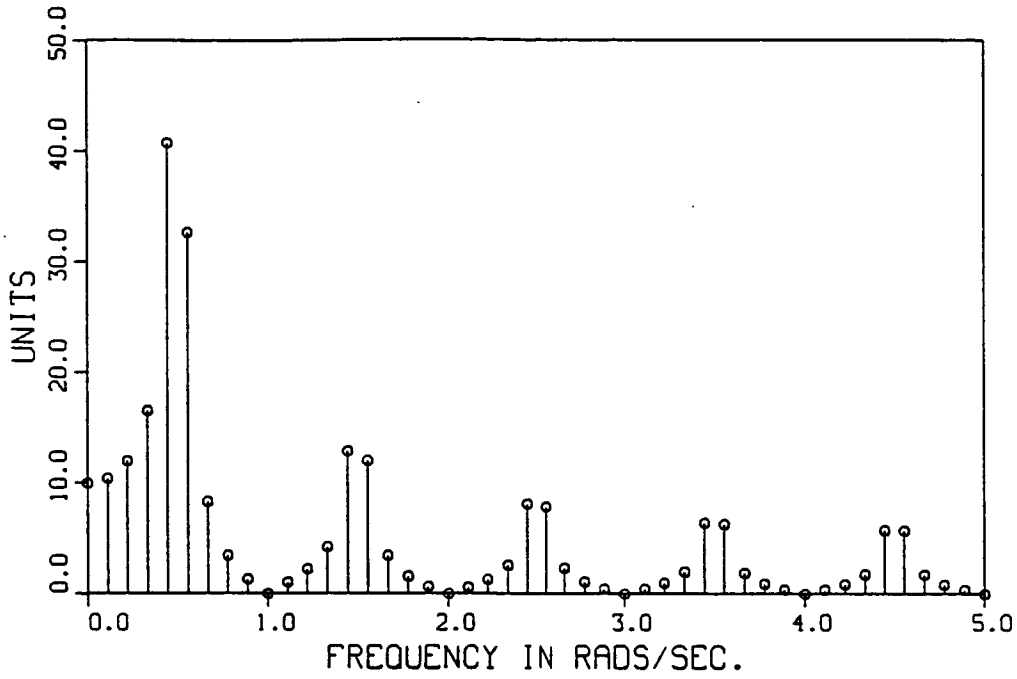

Figure 8.10: $|U_N^n(\omega_k)|$ at n=99 (62.20 secs.) for Square-wave Input and N=90.

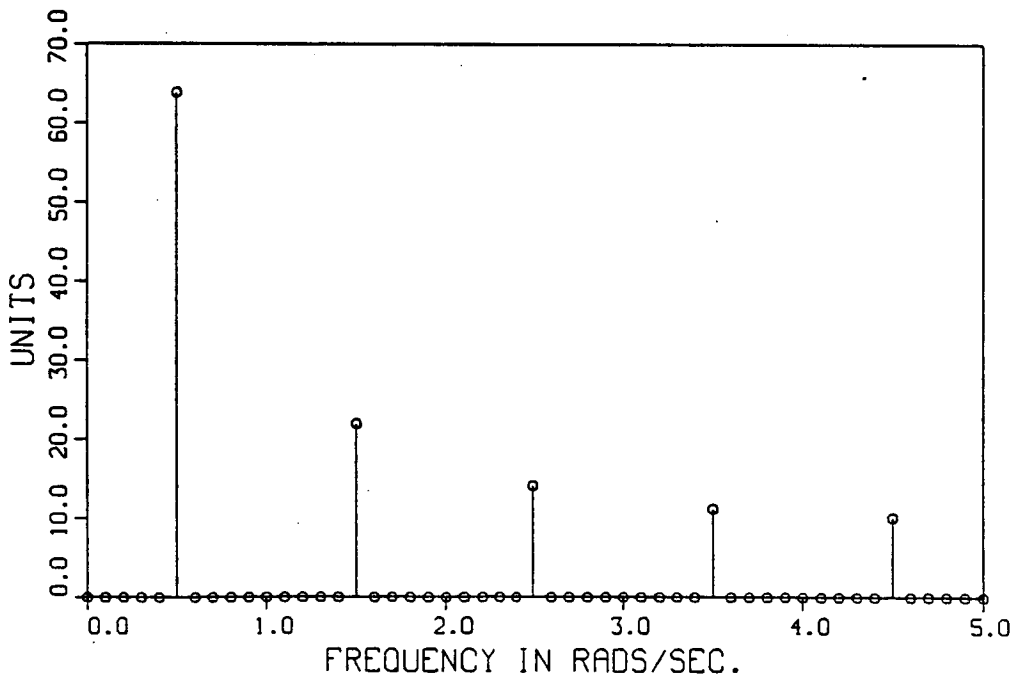

Figure 8.11: $|U_N^n(\omega_k)|$ at n=99 (62.20 secs.) for Square-wave Input and N=100.

Simulation 8.2.8: Impulses Input, for N=6

For this simulation we use the input signal

$$u[n] = 0.02 \sin(\pi n) / \sin(0.02 \pi n), n \geq 0. \quad (8.2.9)$$

where, in practice, we use L'Hopital's rule to find that

$$u[n] = \cos(\pi n) / \cos(0.02 \pi n), \text{ when } \sin(0.02 \pi n) = 0. \quad (8.2.10)$$

This signal is simply a sequence of unit impulses at multiples of 50 time samples, which have alternating sign. The output signal y[n], as well as the computed bounds $\overline{y}[n]$ and $-\overline{y}[n]$ are shown in Figure 8.12 for N=6. From this figure we see that the small value of N results in good tracking for the time-domain bound. For the period of time from n=5 (3.14 secs.) to n=49 (30.78) secs., the bound reduces to the remainder term of 0.086428 in Eqn. (8.2.4).

Simulation 8.2.9: Impulses Input, for N=50

For this simulation we again use the input signal of Eqns. (8.2.9-10) except that now we use the longer DFT length of N=50. For this choice of N and input signal, $|U_N^n(\omega_k)|$ is constant and equal to unity for all k. Thus, the time-domain bound is a constant for all n as shown in Figure 8.13. For this large value of N we get no tracking of the plant output.

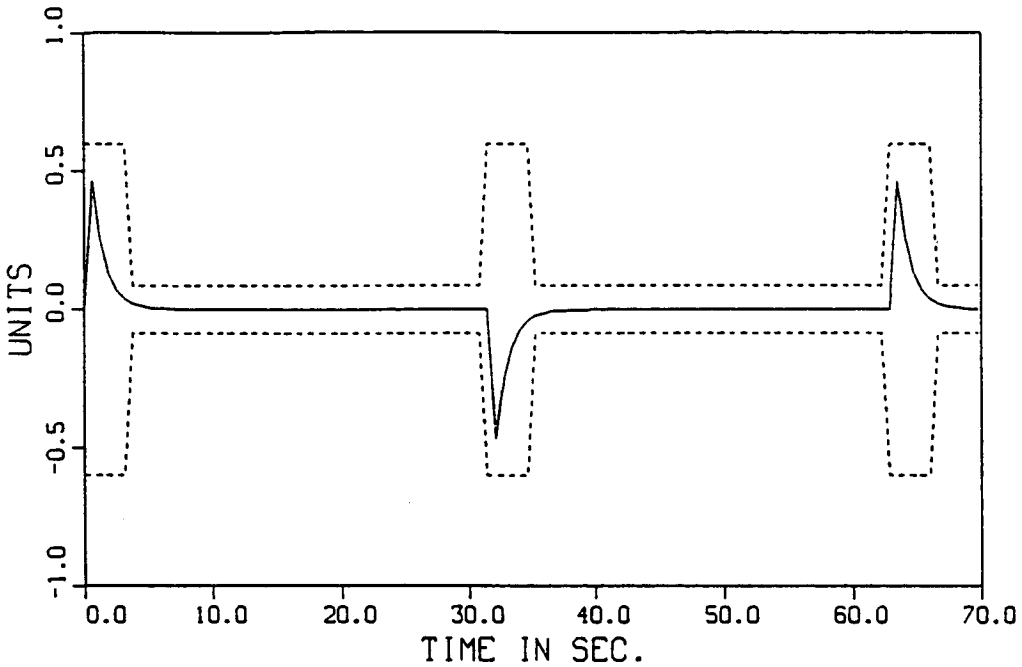

Figure 8.12: Plant Output y[n] and Bounds $\overline{y}[n]$ and $-\overline{y}[n]$ for Impulses Input and N=6.

(y[n] = ——, $\overline{y}[n]$ and $-\overline{y}[n]$ = - - - -)

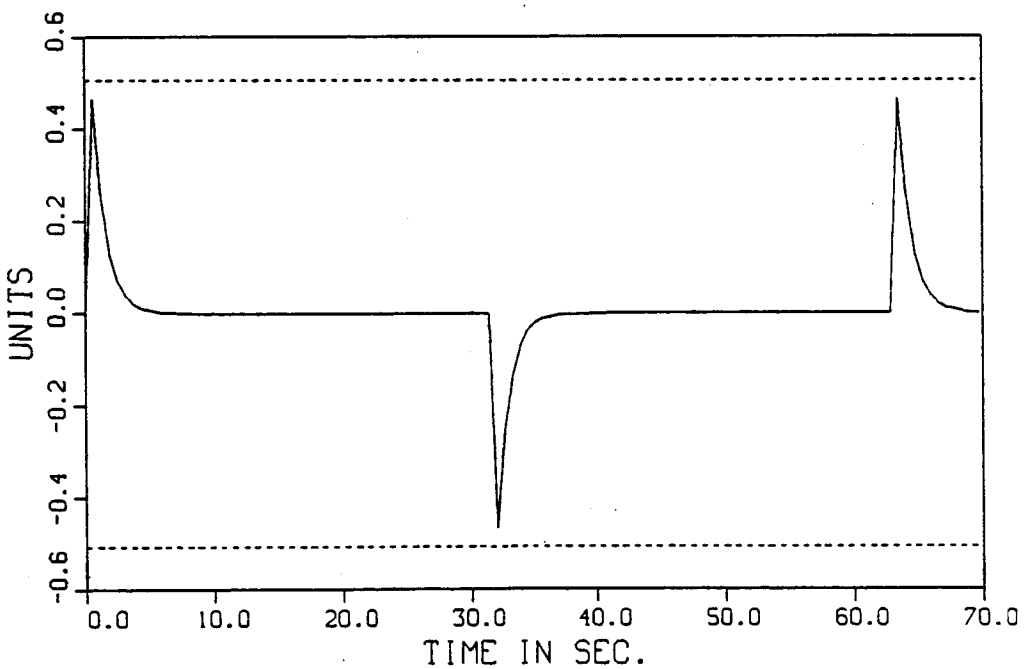

Figure 8.13: Plant Output y[n] and Bounds $\overline{y}[n]$ and $-\overline{y}[n]$ for Impulses Input and N=50.

(y[n] = ——, $\overline{y}[n]$ and $-\overline{y}[n]$ = - - - -)

Simulation 8.2.10: Pseudo-random Input, for N=6

For this simulation we use a pseudo-random input signal. To generate this signal, a pseudo-random signal that was white and had a gaussian probability distribution, with zero mean and standard deviation 0.75, was passed through the following first-order filter, whose pole corresponds to a continuous-time pole of 1 rad/sec for our choice of sampling period.

$$T(z) = 0.46651\, z / (z - 0.53349) \qquad (8.2.11)$$

To yield the signal u[n], the output of this filter was then passed through a saturation function to guarantee that $|u[n]| \leq 1$. The input signal u[n] is shown in Figure 8.14. The output signal y[n], as well as the computed bounds $\overline{y}[n]$ and $-\overline{y}[n]$, are shown in Figure 8.15. For this short DFT length, the bound tracks the actual plant output very well. This is because the bound is based on the values of the input signal at only 6 time indices.

Simulations 8.2.11-12: Pseudo-random Input, for N=50 and 100

For these two simulations we again use the pseudo-random input signal of the previous simulation. We examine the effect of using the longer DFT lengths of 50 and 100 on the conservativeness of the bound. We have previously observed that the bound should increase with the square root of N for the kind of input that we are using in these two simulations. First, in Figure 8.16, we show $|U_N^n(\omega_k)|$ for N=50 and for n=100 (62.83 secs). From this figure we see that many terms in the sum of Eqn. (8.2.3) will be significant, so we expect conservatism in the bound. Now, the output signal y[n], as well as the computed bounds $\overline{y}[n]$ and $-\overline{y}[n]$ are shown in Figures 8.17-18 for the cases of N=50 and 100, respectively. Considering first the case of N=50, we see that the computed bound is conservative once the initial transient is over, although during the transient the bound is quite tight. The bound doesn't vary as much as the actual output signal since its value depends, essentially with equal weight, on the last 50 time samples of the input signal whereas the actual output depends most strongly on the 5 or 6 most recent values of the input, via the plant. Thus, there is a kind of averaging process that is occurring in the computation of the time-varying bound. For the case of N=100, the bound is even more conservative. Comparing Figures 8.17 and 8.18, we see that the steady-state value of the bound increases from roughly 1.4 to 2 as N increases from 50 to 100. This is consistent with our analytically derived prediction that the bound increases with the square root of N.

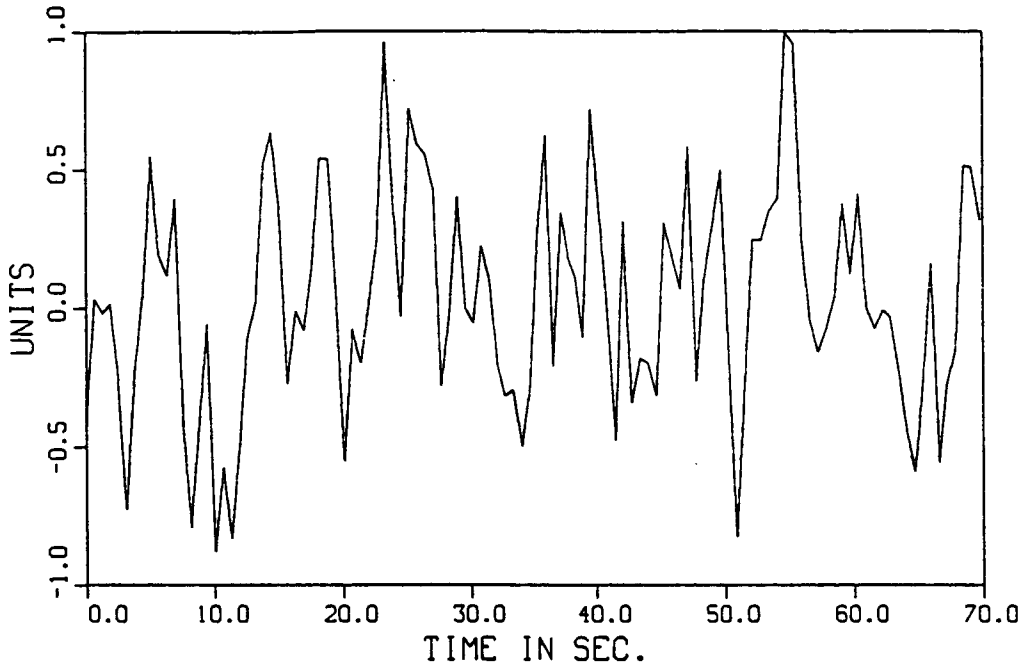

Figure 8.14: Pseudo-random Input u[n].

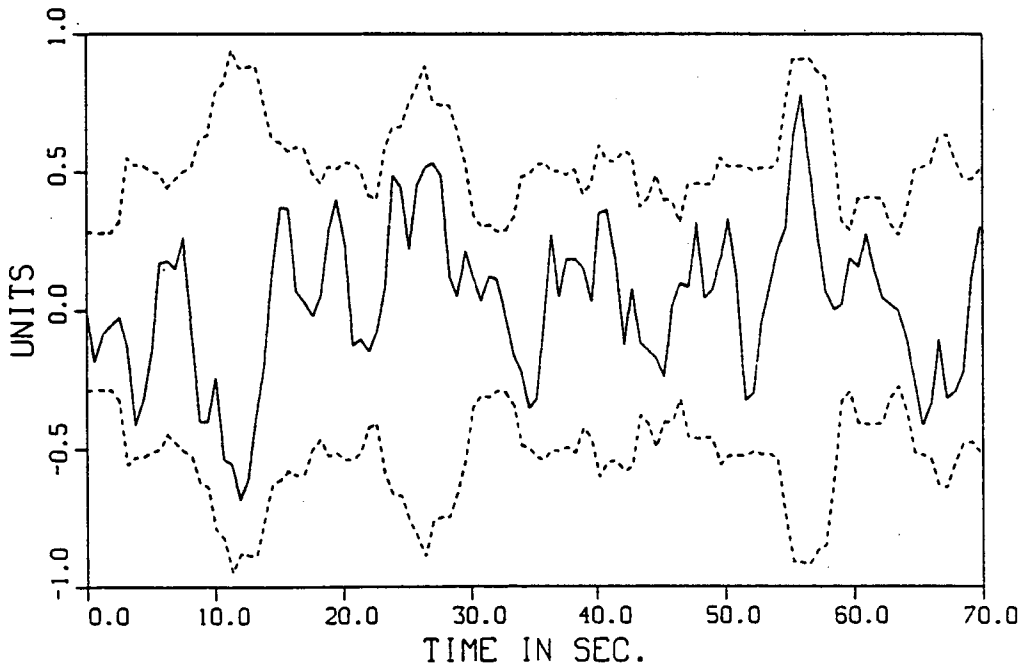

Figure 8.15: Plant Output y[n] and Bounds $\overline{y}[n]$ and $-\overline{y}[n]$ for Pseudo-random Input and N=6.

(y[n] = ——, $\overline{y}[n]$ and $-\overline{y}[n]$ = - - - -)

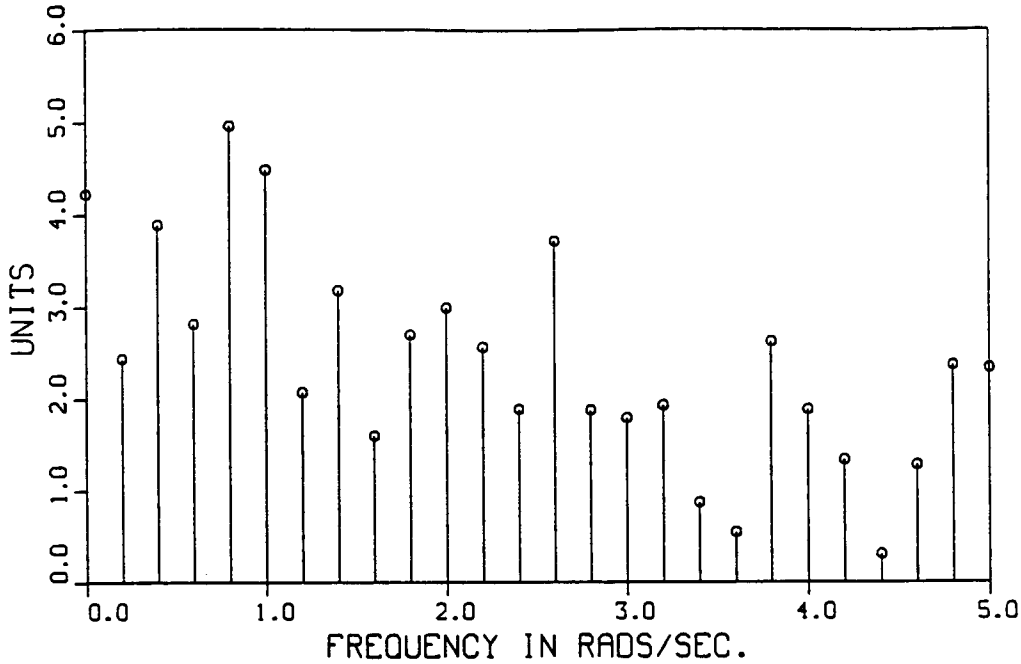

Figure 8.16: $|U_N^n(\omega_k)|$ at n=100 (62.83 secs.) for Pseudo-random Input and N=50.

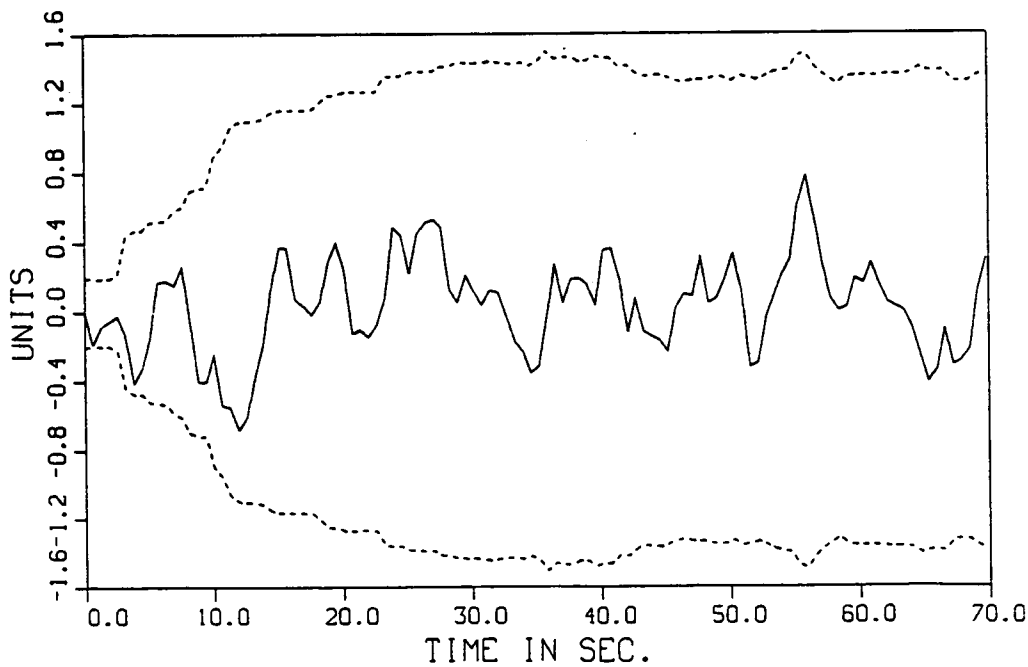

Figure 8.17: Plant Output y[n] and Bounds $\overline{y}[n]$ and $-\overline{y}[n]$ for Pseudo-random Input and N=50.

(y[n] = ——, $\overline{y}[n]$ and $-\overline{y}[n]$ = - - - -)

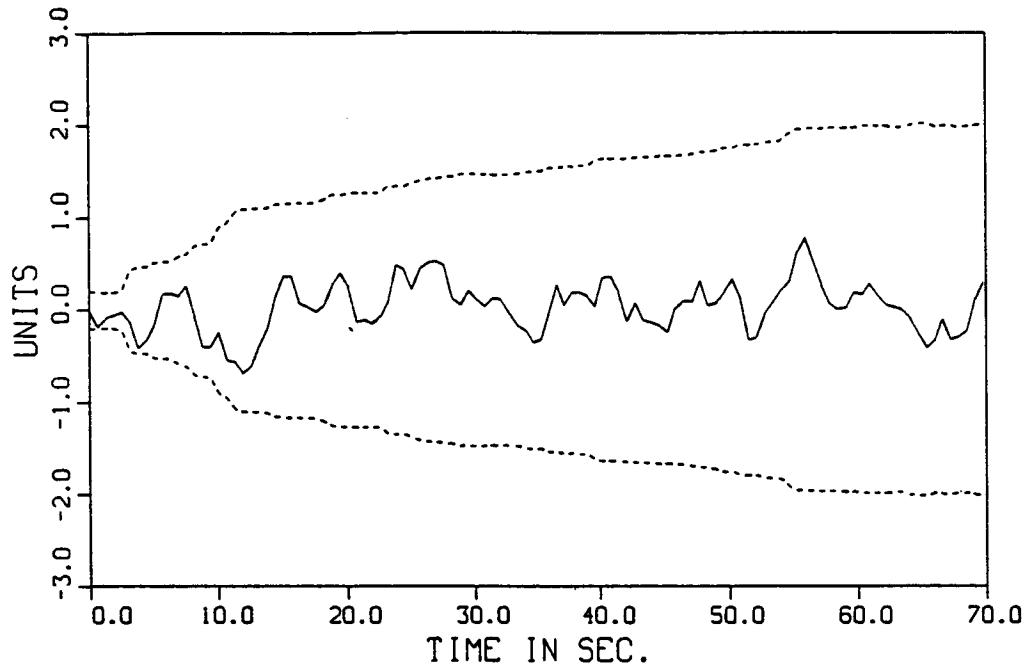

Figure 8.18: Plant Output y[n] and Bounds $\overline{y}[n]$ and $-\overline{y}[n]$ for Pseudo-random Input and N=100.

(y[n] = ——, $\overline{y}[n]$ and $-\overline{y}[n]$ = - - - -)

8.3 Simulations of Frequency-domain Bounding

In this subsection, we will present simulation results that illustrate the frequency-domain bounding method of Theorems 2.1-2. This theorem is used to find a bounding function on the frequency-domain error, due to the use of finite-length data, in the frequency-domain estimator of Chapter 5. For the purposes of this section, we consider the true plant to be the first-order plant H(z) of Section 8.1. From Theorem 2.1,

$$Y_N^n(\omega_k) = H(e^{j\omega_k T})\, U_N^n(\omega_k) + E_N^n(\omega_k), \quad \text{for } k = 0, \ldots, N-1, \tag{8.3.1}$$

where we must find a magnitude bound on the function $E_N^n(\omega_k)$. In Chapter 6, this problem of using finite-length data was viewed as an "end-effects" problem. The result of Corollary 2.1 represents what we will refer to as the "worst-case" bound on the end-effects error. Since we have information about u[n] that is learned on-line, we can compute the tighter bound given by Theorem 2.2 where M is chosen as described in Chapter 6. This frequency-domain bounding function is given by

$$\overline{E}_N^n(\omega_k) = \sum_{i=1}^{M-1} |h[i]|\, |U_N^{n-i}(\omega_k) - U_N^n(\omega_k)| + 2\, u_{max}\, g\, p^M\, (M - M\,p + p) / (1 - p)^2, \quad \text{for } k = 0, \ldots, N-1, \tag{8.3.2}$$

where we have used the results of Appendix C to find a closed-form expression for the summation,

$$\sum_{i=M}^{\infty} i\, |h[i]| = \sum_{i=M}^{\infty} i\, g\, p^i = g\, p^M\, (M - M\,p + p) / (1 - p)^2 \tag{8.3.3}$$

Now, we will discuss the choice of the memory length M and the DFT length N for the frequency-domain bounding method. As was explained in Section 6.6, we choose

$$M = \text{integer}(\omega_s / \alpha_{slow}) = 10, \tag{8.3.4}$$

where α_{slow}=1 rad/sec. in our example. Further, we choose the DFT length for the frequency-domain estimator to be five times the memory length M so as to lessen the effects of using finite-length data. So, we use N=5M=50. Since we assume that u_{max}=1, we find that the remainder term, in Eqn. (8.3.2), is 0.078014 for our choice of M=10. For reference, if M=1, then the remainder term is 4.2871. Note that the remainder term for the case of M=1 corresponds to the definition of the "worst-case" bound $\overline{E}_{wc}$, which was defined in Eqn. (6.6.19).

In the following simulations, we will compute the frequency-domain error bounding function

that was defined in Chapter 5, for the disturbance-free case. That is, we will compute a magnitude bounding function, $\overline{E}_{f,N}^{n}(\omega_k)$, on the magnitude of the error, $E_{f,N}^{n}(\omega_k)$, between the frequency-domain estimate of the plant and the true plant $H(e^{j\omega_k T})$ as shown below.

$$| Y_N^n(\omega_k) / U_N^n(\omega_k) - H(e^{j\omega_k T}) | = |E_{f,N}^n(\omega_k)| \leq \overline{E}_{f,N}^n(\omega_k), \tag{8.3.5}$$

where

$$\overline{E}_{f,N}^n(\omega_k) = \overline{E}_N^n(\omega_k) / |U_N^n(\omega_k)|, \text{ for } k = 0, \ldots, N-1. \tag{8.3.6}$$

For future reference, we use $\overline{E}_{wcf,N}^n(\omega_k)$ to denote the "worst-case frequency-domain" error bounding function generated using M=1 in Eqn. (8.3.2). That is,

$$\overline{E}_{wcf,N}^n(\omega_k) = \overline{E}_{wc} / |U_N^n(\omega_k)| = \{ 2\, u_{max}\, g\, p / (1 - p)^2 \} / |U_N^n(\omega_k)| = 4.2871 / |U_N^n(\omega_k)|, \quad \text{for } k = 0, \ldots, N-1. \tag{8.3.7}$$

Before presenting the simulation results, we will again make several observations.

Observations:

1) For N=50 and the input signals that we will be considering, the worst-case frequency-domain error $\overline{E}_{wcf,N}^n(\omega_k)$ of Eqn. (8.3.7) is not small as compared with the values of $|H(e^{j\omega_k T})|$, so considerable additive error is introduced, if we choose to use the worst-case bounding function.

2) For our choice of M=10, the remainder term of Eqn. (8.3.2) is much smaller than $\overline{E}_{wc}$. Thus, if $U_N^{n-i}(\omega_k) \approx U_N^n(\omega_k)$ and/or if $|u[n]|$ is much smaller than u_{max}, then the bound of Eqn. (8.3.2), using M=10, will yield a much tighter bound than Eqn. (8.3.7).

3) If u[n] is periodic with period N, then $U_N^{n-i}(\omega_k) = U_N^n(\omega_k)$ for all k, for $n-i \geq N-1$.

Now, we present simulations that will show both the actual error function $|E_{f,N}^n(\omega_k)|$ and the time-varying, frequency-domain bounding function $\overline{E}_{f,N}^n(\omega_k)$, which is computed using Eqn. (8.3.2). One difficulty with illustrating our results is that $\overline{E}_{f,N}^n(\omega_k)$ is both a function of time and

frequency. To observe time-variations, we will present the time-varying values of $\overline{E}_{f,N}^{n}(\omega_k)$ at a specific frequency. In addition, we will provide snap-shots of $\overline{E}_{f,N}^{n}(\omega_k)$ versus frequency at a specific time.

Simulation 8.3.1: Sinusoidal Input

For this simulation we use the sinusoidal input signal of Eqn. (8.2.7). Figure 8.19 shows the values of $|E_{f,N}^{n}(\omega_k)|$, $\overline{E}_{f,N}^{n}(\omega_k)$ and $\overline{E}_{wcf,N}^{n}(\omega_k)$, versus the time index n, for the frequency $\omega_k=\omega_{10}=2$ rads/sec. Since the sinusoid has a frequency of 2 rads/sec, it is expected that the actual error will become small as can be seen in Figure 8.19. It is also clear from this figure that the bound $\overline{E}_{f,N}^{n}(\omega_{10})$ is superior to the worst-case bound. That is, even under good excitation conditions, the worst-case bound still doesn't get any smaller than 0.17149. For comparison, the bound $\overline{E}_{f,N}^{n}(\omega_{10})$ becomes 0.0031206 in steady-state, which is a factor of 55 smaller than the worst-case bound. In Figure 8.20 we show $|E_{f,N}^{n}(\omega_k)|$, $\overline{E}_{f,N}^{n}(\omega_k)$ and $\overline{E}_{wcf,N}^{n}(\omega_k)$ versus frequency for the time index n=5 (3.14 secs.). This figure shows that during the transient, there is information at frequencies other than just 2 rads/sec. For $n \geq N-1=49$, $U_N^{n}(\omega_k)$ is zero for all frequencies except ω_{10} so that $|E_{f,N}^{n}(\omega_k)|$ will be infinite at these frequencies, that is, it will provide no information at the frequencies other than $\omega_{10}=2$ rads/sec. In Figure 8.21, we show both the cumulative frequency-domain error bounding function $\overline{E}_{cumf,N}^{n}(\omega_k)$ and the actual error magnitude $|E_{cumf,N}^{n}(\omega_k)|$ between the true plant and the cumulative frequency-domain estimate, both of which were defined in Section 5.3. These cumulative values are shown for time index n=111 (69.74 secs.). This figure again shows how the transient yields information at many frequencies other than just that of the sinusoidal input. The opposite peaks at 4 rads/sec are due to the fact that in Eqn. (8.3.2) the phase cancellations that occur in the actual frequency-domain error function are ignored and, instead, all terms are summed.

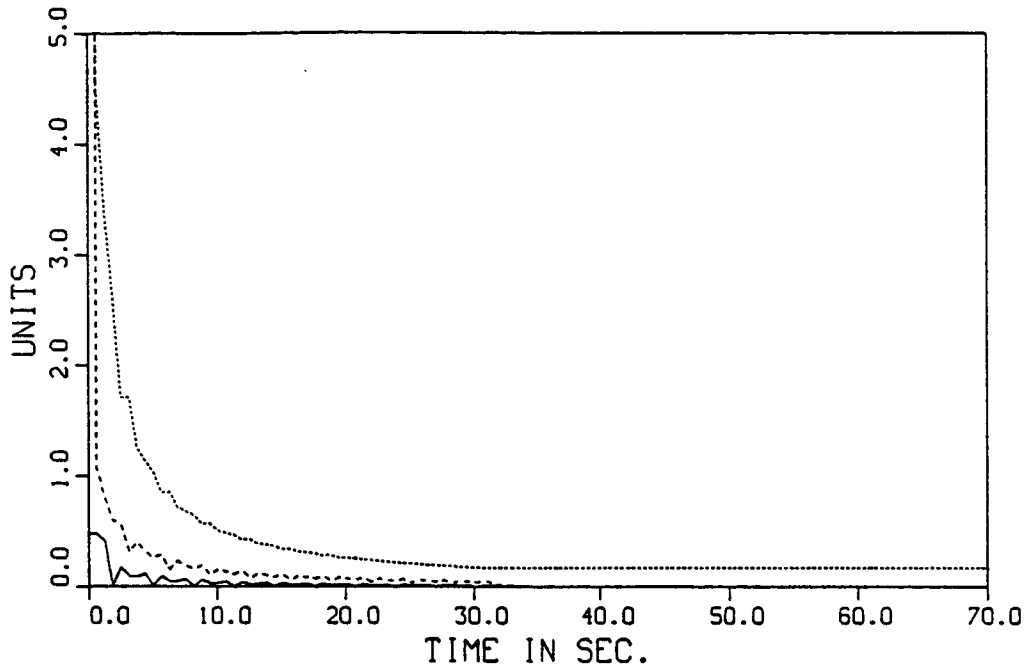

Figure 8.19: Time History of $|E_{f,N}^{n}(\omega_{10})|$, $\overline{E}_{f,N}^{n}(\omega_{10})$ and $\overline{E}_{wcf,N}^{n}(\omega_{10})$ for Sinusoidal Input.

($|E_{f,N}^{n}(\omega_{10})|$ = ——, $\overline{E}_{f,N}^{n}(\omega_{10})$ = - - - -, $\overline{E}_{wcf,N}^{n}(\omega_{10})$ = ...)

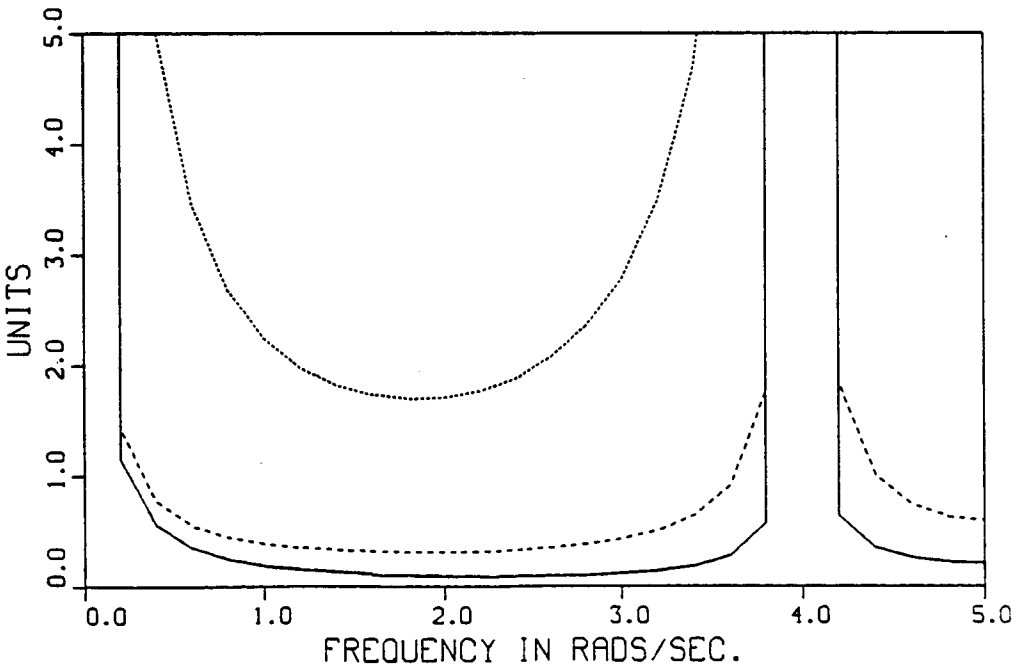

Figure 8.20: Frequency Snapshot of $|E_{f,N}^{5}(\omega_k)|$, $\overline{E}_{f,N}^{5}(\omega_k)$ and $\overline{E}_{wcf,N}^{5}(\omega_k)$ for Sinusoidal Input. ($|E_{f,N}^{5}(\omega_k)|$ = ——, $\overline{E}_{f,N}^{5}(\omega_k)$ = - - - -, $\overline{E}_{wcf,N}^{5}(\omega_k)$ = ...)

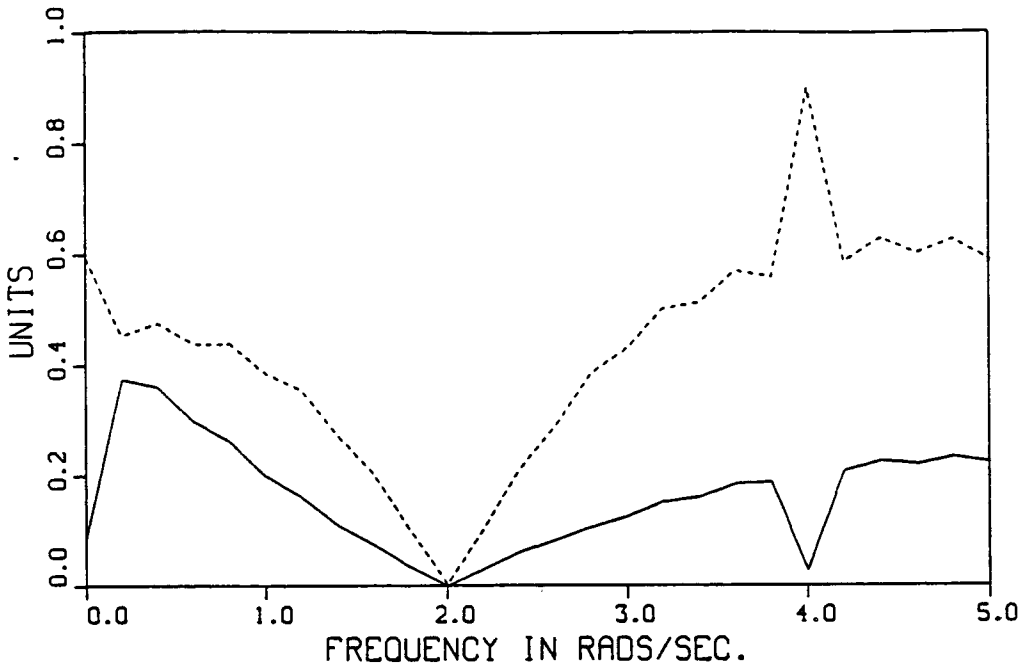

Figure 8.21: Cumulative Error $|E_{cumf,N}^{111}(\omega_k)|$ and Bound $\overline{E}_{cumf,N}^{111}(\omega_k)$ for Sinusoidal Input. ($|E_{cumf,N}^{111}(\omega_k)|$ = ——, $\overline{E}_{cumf,N}^{111}(\omega_k)$ = - - - -)

Simulation 8.3.2: Square-wave Input

For this simulation we use the square-wave input signal of Simulation 8.2.3. Figure 8.22 shows the values of $|E_{f,N}^{n}(\omega_k)|$, $\overline{E}_{f,N}^{n}(\omega_k)$ and $\overline{E}_{wcf,N}^{n}(\omega_k)$ versus the time index n, for the frequency $\omega_k=\omega_{10}=2$ rads/sec. For time indices n=4 (2.51 secs.), 9 (5.65 secs.), 14 (8.80 secs.), 19 (11.94 secs.), ... we see that the input signal has no frequency component at 2 rads/sec, resulting in an infinite value of the frequency-domain error $|E_{f,N}^{n}(\omega_{10})|$. This lack of some frequency components for some time indices is also apparent from Figure 8.9, which shows $|U_N^n(\omega_k)|$ for n=99 (62.20 secs.). In Figure 8.23, we show $|E_{f,N}^{n}(\omega_k)|$, $\overline{E}_{f,N}^{n}(\omega_k)$ and $\overline{E}_{wcf,N}^{n}(\omega_k)$ versus frequency for the time index n=59 (37.07 secs.). The square-wave input used in this simulation results in a large frequency-domain error bound relative to the magnitude of the plant, since it has the worst-case magnitude of 1 for all time and, for some time indices, it has

the worst-case phase from the point of view of our DFT estimation method when using a window length of 50. Consider the situation at n=59, at which time the DFT of $U_N^n(\omega_k)$ contains input data from time indices m=10 to 59. From m=0 to 9 the input signal is +1 and from m=50 to 59 the input signal is -1. Thus, the error nearly achieves its worst-case value at ω=0, since the signs of u[n] at the two ends of the DFT are opposite. That is, in this situation, with respect to our window length, the input signal looks about as unperiodic as it can be, thus yielding large errors for our frequency-domain bounding technique. In Figure 8.24, we show both the cumulative frequency-domain error bounding function $\overline{E}_{cumf,N}^n(\omega_k)$ and the actual error magnitude $|E_{cumf,N}^n(\omega_k)|$ between the true plant and the cumulative frequency-domain estimate, for time index n=111 (69.74 secs.). This figure shows that our bounding technique provides a tight bound on the actual error associated with our cumulative frequency-domain estimate. As expected, the frequency ranges where we do good identification correspond to the frequency ranges where we have input signal energy as can be seen from Figures 8.24 and 8.25. As a final note, by comparing Figures 8.9 and 8.25, we see how $|U_N^n(\omega_k)|$ changes from time index 99 to 100.

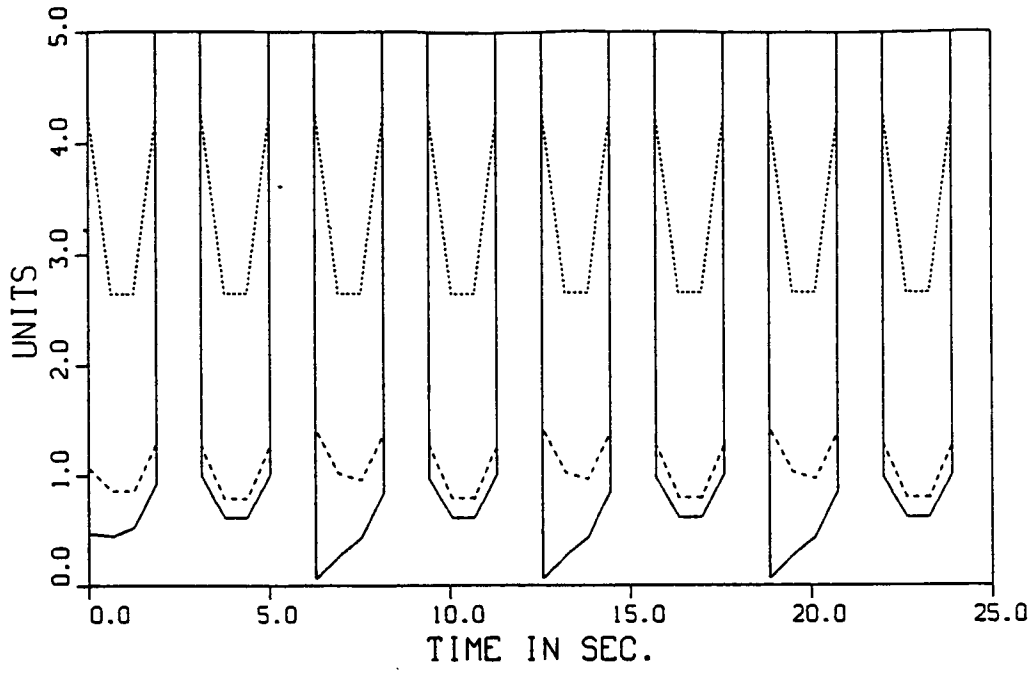

Figure 8.22: Time History of $|E_{f,N}^{n}(\omega_{10})|$, $\overline{E}_{f,N}^{n}(\omega_{10})$ and $\overline{E}_{wcf,N}^{n}(\omega_{10})$ for Square-wave Input. ($|E_{f,N}^{n}(\omega_{10})|$ = ——, $\overline{E}_{f,N}^{n}(\omega_{10})$ = - - - -, $\overline{E}_{wcf,N}^{n}(\omega_{10})$ = ...)

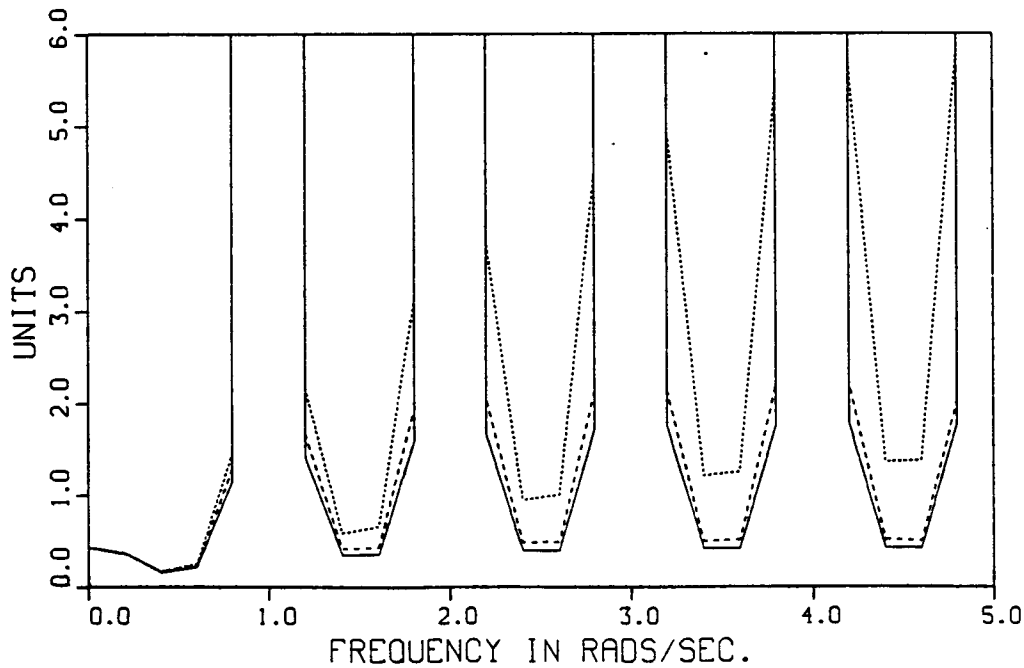

Figure 8.23: Frequency Snapshot of $|E_{f,N}^{59}(\omega_k)|$, $\overline{E}_{f,N}^{59}(\omega_k)$ and $\overline{E}_{wcf,N}^{59}(\omega_k)$ for Square-wave Input. ($|E_{f,N}^{59}(\omega_k)|$ = ——, $\overline{E}_{f,N}^{59}(\omega_k)$ = - - - -, $\overline{E}_{wcf,N}^{59}(\omega_k)$ = ...)

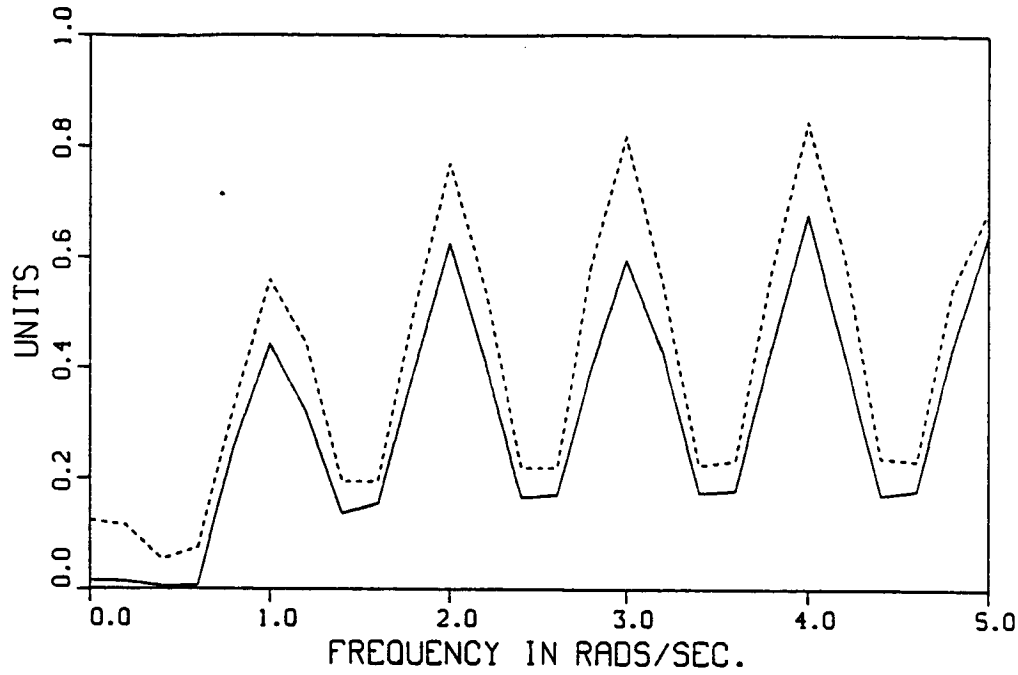

Figure 8.24: Cumulative Error $|E_{cumf,N}^{111}(\omega_k)|$ and Bound $\overline{E}_{cumf,N}^{111}(\omega_k)$ for Square-wave Input. ($|E_{cumf,N}^{111}(\omega_k)| =$ ——, $\overline{E}_{cumf,N}^{111}(\omega_k) =$ - - - -)

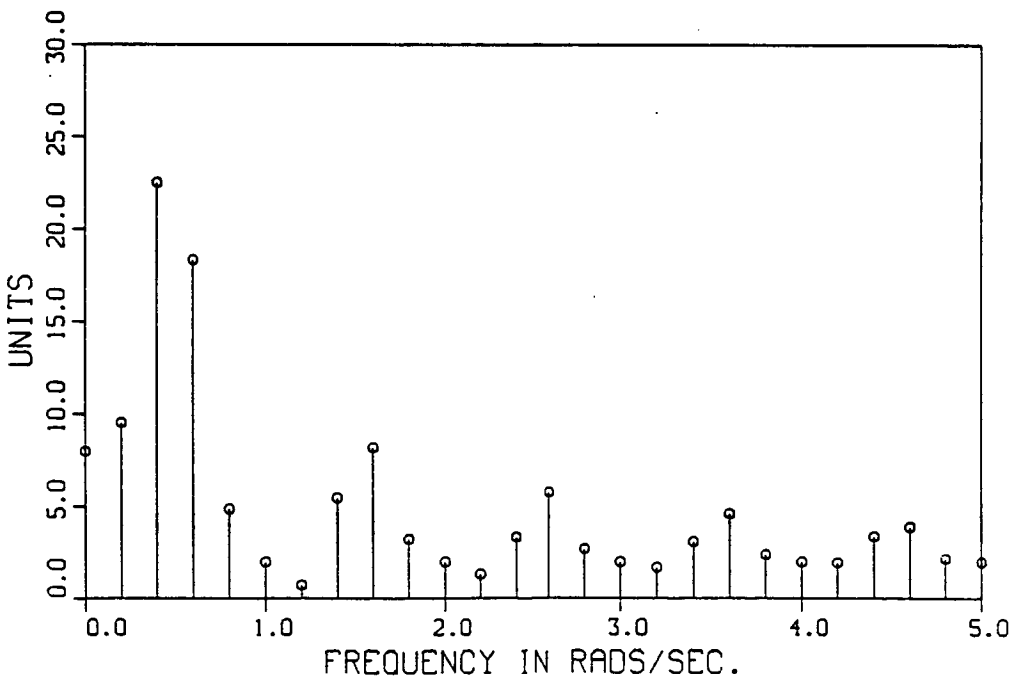

Figure 8.25: $|U_N^n(\omega_k)|$ at n=100 (62.83 secs.) for Square-wave Input.

Simulation 8.3.3: Impulses Input

For this simulation we use the input signal of Eqn. (8.2.9) for which $|U_N^n(\omega_k)|=1$, for all k when N=50. Figure 8.26 shows the values of $|E_{f,N}^n(\omega_k)|$, $\overline{E}_{f,N}^n(\omega_k)$ and $\overline{E}_{wcf,N}^n(\omega_k)$ versus the time index n, for the frequency $\omega_k=\omega_{10}=2$ rads/sec. Our frequency-domain error bounding function works very well as compared with the worst-case bound which has the expected value of 4.2871, since again $|U_N^n(\omega_k)|$ is unity for all frequencies. In Figure 8.26, our bounding function approaches the expected value of 0.078014 during the time periods between the impulses, while the actual error approaches effectively zero during these time periods. For this example, the bounding function $\overline{E}_{f,N}^n(\omega_k)$ shown in Figure 8.26, holds for all frequencies, not just ω_{10}. However, the actual error $|E_{f,N}^n(\omega_k)|$ differs with frequency as can be seen in Figure 8.27, which shows $|E_{f,N}^n(\omega_k)|$, $\overline{E}_{f,N}^n(\omega_k)$ and $\overline{E}_{wcf,N}^n(\omega_k)$ versus frequency for the time index n=100 (62.83 secs.). In this figure, the actual error $|E_{f,N}^n(\omega_k)|$ is simply twice the magnitude of the plant transfer function. At the end of the simulation, see Figure 8.26, the cumulative frequency-domain error bounding function, $\overline{E}_{cumf,N}^n(\omega_k)$, is 0.078014 at all frequencies, while the actual error magnitude $|E_{cumf,N}^n(\omega_k)|$, between the true plant and the cumulative frequency-domain estimate, is zero to the numerical accuracy of the simulation, at all frequencies. That is, from Eqn. (2.2.2) it can be seen that $|E_N^n(\omega_k)|$ will be less than

$$\sum_{i=N}^{\infty} |h[i]| = 4.25708 \times 10^{-14}, \tag{8.3.8}$$

for n=49 since $U_N^{49-p}(\omega_k)=U_N^{49}(\omega_k)$ for p=1, 2, ..., 49, in this example.

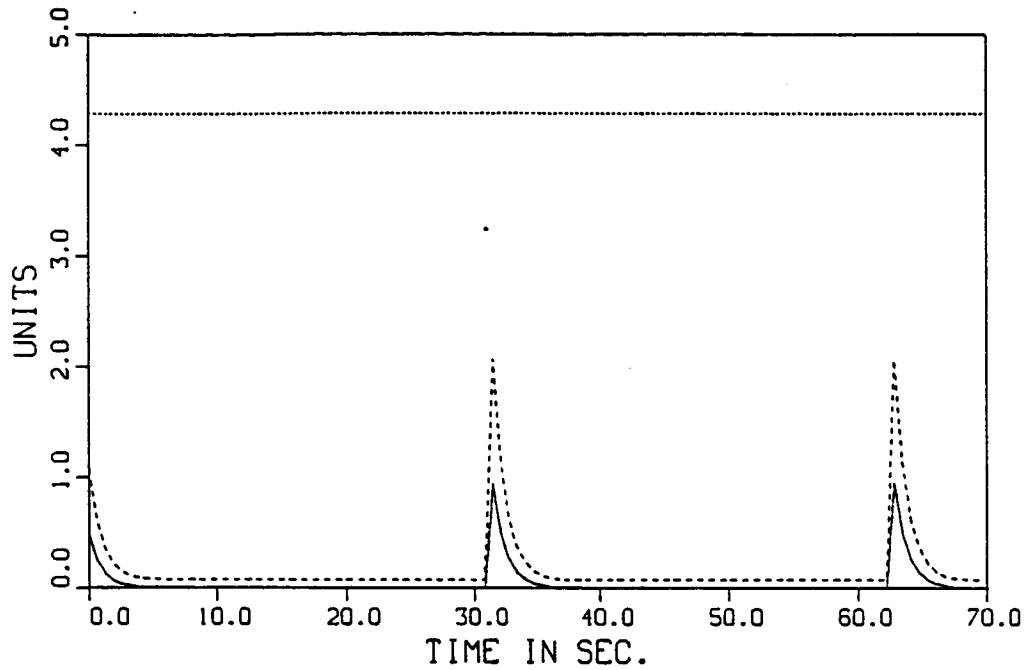

Figure 8.26: Time History of $|E_{f,N}^{n}(\omega_{10})|$, $\overline{E}_{f,N}^{n}(\omega_{10})$ and $\overline{E}_{wcf,N}^{n}(\omega_{10})$ for Impulses Input.

($|E_{f,N}^{n}(\omega_{10})|$ = ——, $\overline{E}_{f,N}^{n}(\omega_{10})$ = - - - -, $\overline{E}_{wcf,N}^{n}(\omega_{10})$ = ...)

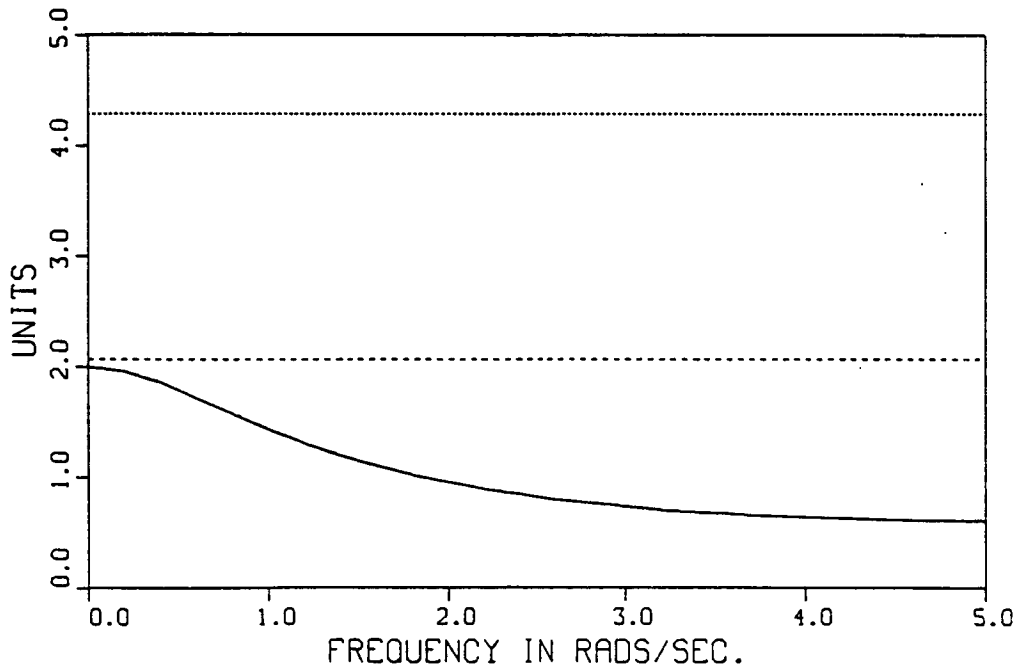

Figure 8.27: Frequency Snapshot of $|E_{f,N}^{100}(\omega_k)|$, $\overline{E}_{f,N}^{100}(\omega_k)$ and $\overline{E}_{wcf,N}^{100}(\omega_k)$ for Impulses Input. ($|E_{f,N}^{100}(\omega_k)|$ = ——, $\overline{E}_{f,N}^{100}(\omega_k)$ = - - - -, $\overline{E}_{wcf,N}^{100}(\omega_k)$ = ...)

Simulation 8.3.4: Pseudo-random Input

For this simulation we use the pseudo-random input signal of Simulation 8.2.10. Figure 8.28 shows the values of $|E_{f,N}^{n}(\omega_k)|$, $\overline{E}_{f,N}^{n}(\omega_k)$ and $\overline{E}_{wcf,N}^{n}(\omega_k)$ versus the time index n, for the frequency $\omega_k=\omega_{10}=2$ rads/sec. In Figures 8.29-30, we show $|E_{f,N}^{n}(\omega_k)|$, $\overline{E}_{f,N}^{n}(\omega_k)$ and $\overline{E}_{wcf,N}^{n}(\omega_k)$ versus frequency for the time indices n=59 (37.07 secs.) and n=74 (46.50 secs.). These figures show: 1) the superiority of our bounding function $\overline{E}_{f,N}^{n}(\omega_k)$ with respect to the worst-case bounding function $\overline{E}_{wcf,N}^{n}(\omega_k)$, and 2) how the bounding function $\overline{E}_{f,N}^{n}(\omega_k)$ provides information in different frequency ranges at different times. In Figure 8.29, the actual error $|E_{f,N}^{n}(\omega_k)|$ is too small to be seen in the plot. In Figure 8.31, we show both the cumulative frequency-domain error bounding function $\overline{E}_{cumf,N}^{n}(\omega_k)$ and the actual error magnitude $|E_{cumf,N}^{n}(\omega_k)|$ between the true plant and the cumulative frequency-domain estimate, for time index n=111 (69.74 secs.). This figure shows that, even for a random type of input signal, the cumulative frequency-domain estimate is quite accurate and our bounding technique provides a useful bound on the actual error corresponding to this estimate. In the passband of the filter used to generate the input signal, that is, for frequencies less than 1 rad/sec., our bounding methodology provides a plant estimate which is guaranteed to have an error magnitude of less than about 5% of the plant's magnitude. Note that the plant has a magnitude of approximately unity for frequencies that are less than 1 rad/sec.

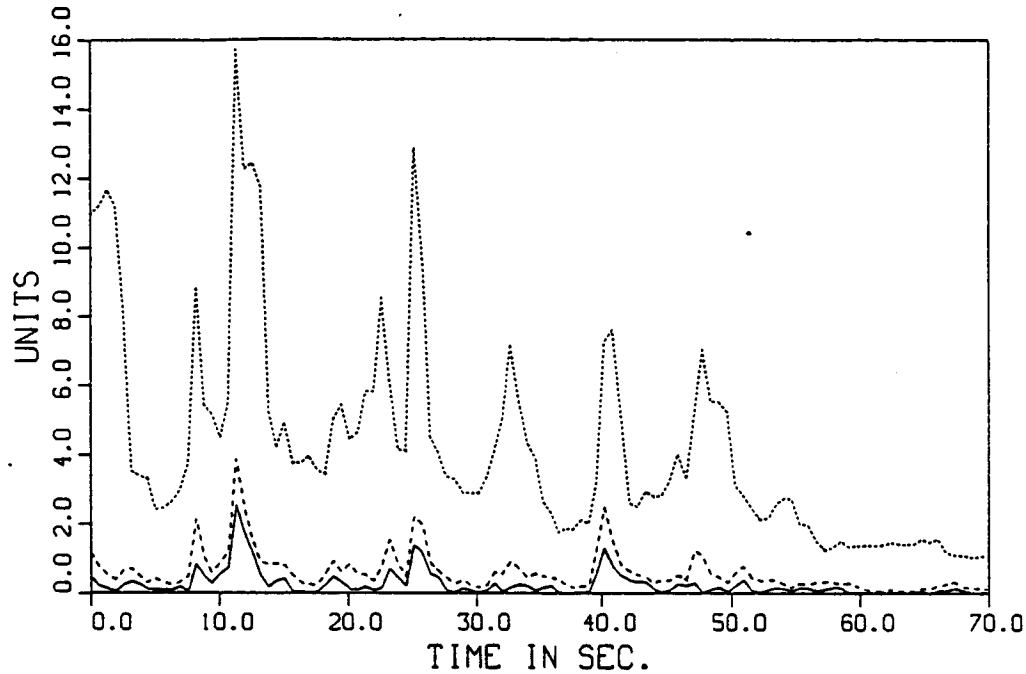

Figure 8.28: Time History of $|E_{f,N}^{n}(\omega_{10})|$, $\overline{E}_{f,N}^{n}(\omega_{10})$ and $\overline{E}_{wcf,N}^{n}(\omega_{10})$ for Pseudo-random Input. ($|E_{f,N}^{n}(\omega_{10})|$ = ——, $\overline{E}_{f,N}^{n}(\omega_{10})$ = - - - -, $\overline{E}_{wcf,N}^{n}(\omega_{10})$ = ...)

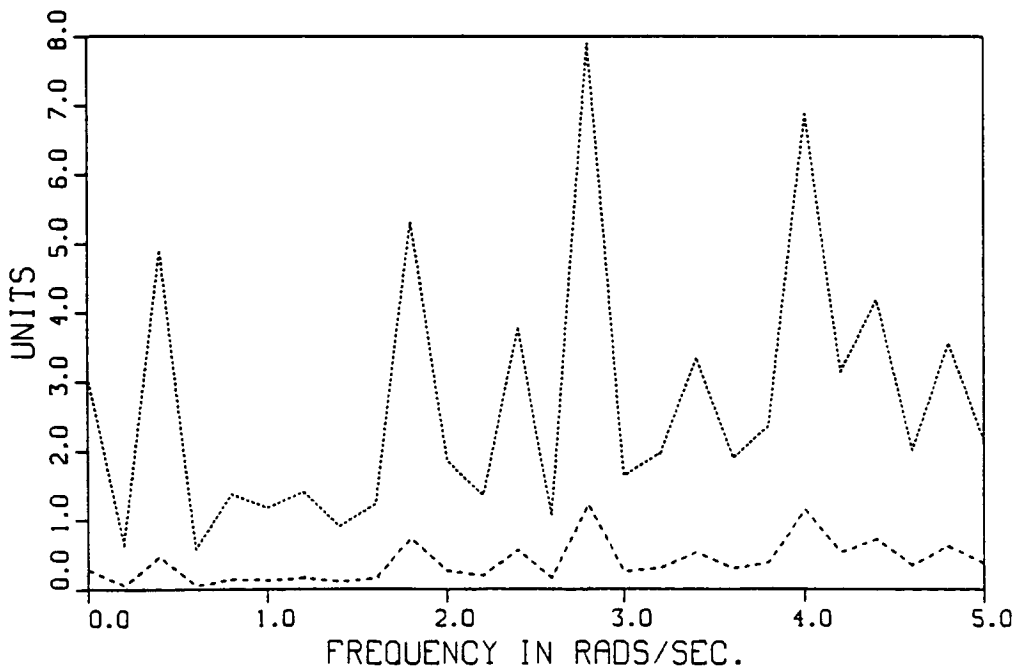

Figure 8.29: Frequency Snapshot of $|E_{f,N}^{59}(\omega_k)|$, $\overline{E}_{f,N}^{59}(\omega_k)$ and $\overline{E}_{wcf,N}^{59}(\omega_k)$ for Pseudo-random Input. ($|E_{f,N}^{59}(\omega_k)|$ = ——, $\overline{E}_{f,N}^{59}(\omega_k)$ = - - - -, $\overline{E}_{wcf,N}^{59}(\omega_k)$ = ...)

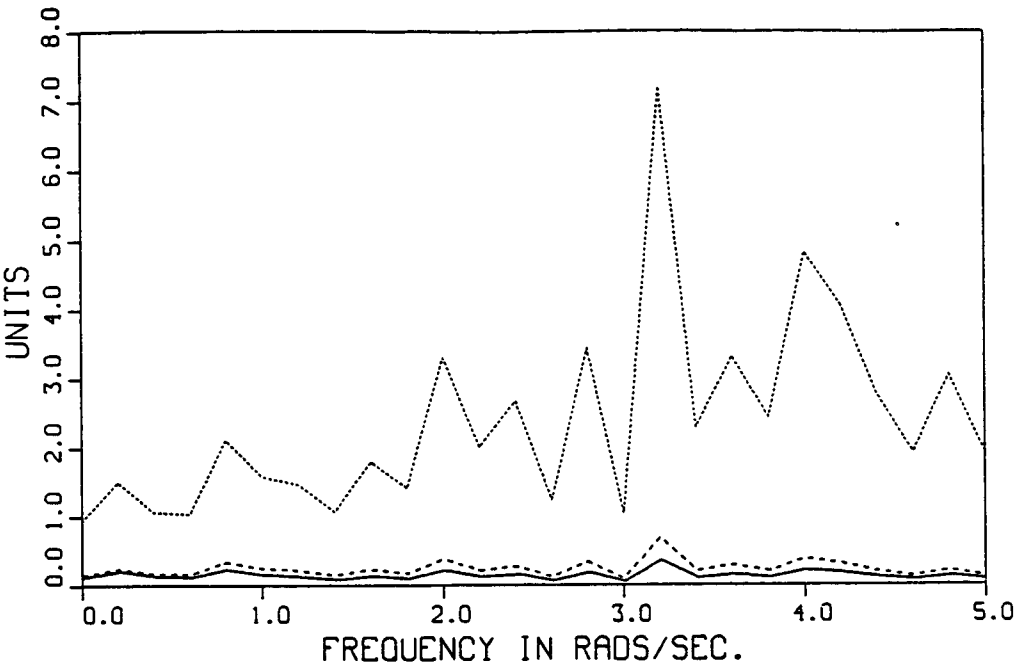

Figure 8.30: Frequency Snapshot of $|E_{f,N}^{74}(\omega_k)|$, $\overline{E}_{f,N}^{74}(\omega_k)$ and $\overline{E}_{wcf,N}^{74}(\omega_k)$ for Pseudo-random Input. ($|E_{f,N}^{74}(\omega_k)|$ = ——, $\overline{E}_{f,N}^{74}(\omega_k)$ = - - - -, $\overline{E}_{wcf,N}^{74}(\omega_k)$ = ...)

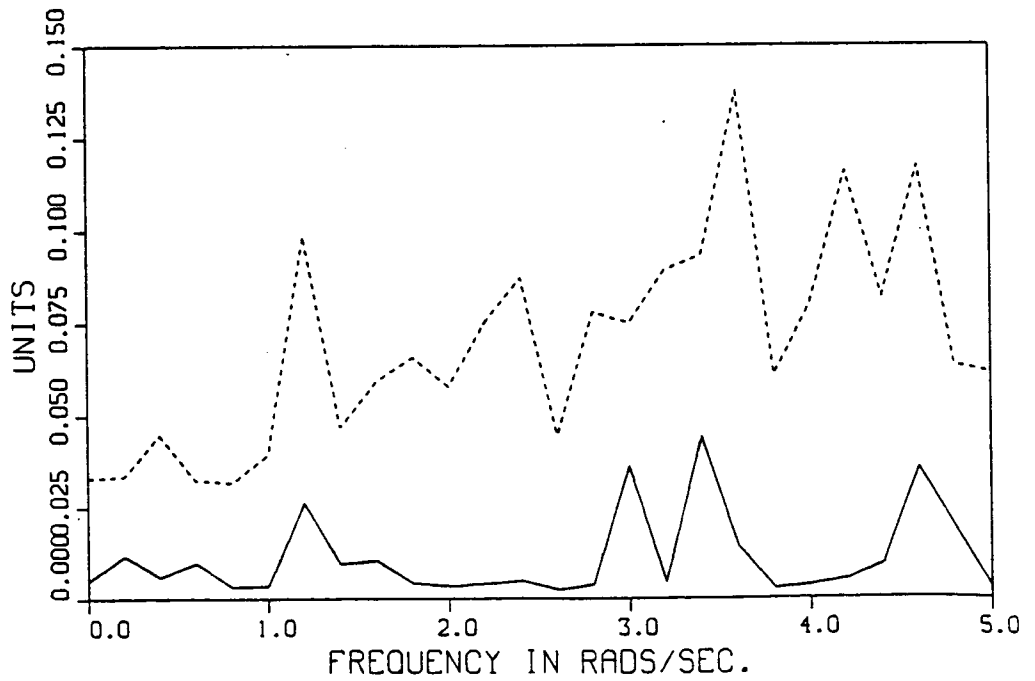

Figure 8.31: Cumulative Error $|E_{cumf,N}^{111}(\omega_k)|$ and Bound $\overline{E}_{cumf,N}^{111}(\omega_k)$ for Pseudo-random Input. ($|E_{cumf,N}^{111}(\omega_k)|$ = ——, $\overline{E}_{cumf,N}^{111}(\omega_k)$ = - - - -)

8.4 Conclusions

In this chapter, we have investigated the basic properties of the time-domain bounding mechanism and the frequency-domain error bounding method. We list the following conclusions concerning the time-domain bound:

1) It is sensitive to relationships between the length of the DFT and the cycle time of any oscillations in the input signal u[n].

2) The more terms that make significant contributions in the frequency sum of Eqn. (8.2.3), the more conservative the time-domain bound tends to be.

3) The time-domain bound increases with the square root of N for pseudo-random types of input signals like the one described in this chapter.

We also summarize our conclusions for the frequency-domain error bounding method:

1) The worst-case frequency-domain error bounding function is too conservative to be of use for moderate choices of the DFT length.

2) The frequency-domain error bounding method of Theorem 2.2 and Eqn. (8.3.2), where M is chosen as described in Chapter 6, yields a useful frequency-domain bounding function for the same DFT length for which the worst-case error bounding function is uselessly conservative.

3) The simulation with the pseudo-random input signal reveals that our frequency-domain error bounding method can perform very well indeed for rich input signals.

These conclusions give us an understanding of the basic properties of both the time-domain bounding mechanism and the frequency-domain bounding method. Having established this understanding, it will be easier to understand the more complex behavior that occurs when the robust estimator is simulated as a whole.

CHAPTER 9
SIMULATIONS OF THE ROBUST ESTIMATOR IN OPEN AND CLOSED LOOP SITUATIONS

9.1 Introduction

In this chapter, we will illustrate the properties of the robust estimator through several simulation examples. First, we present open-loop simulations that illustrate the properties of the robust estimator itself. Then, we present closed-loop simulations of a robust adaptive controller that uses the robust estimator. The chapter is organized as follows.

In Section 9.2, the example plant and disturbance that will be used throughout this chapter, are described and analyzed. This lengthy section includes a development of all of the bounding functions that are used in the robust estimator. Next, the open-loop simulations of the robust estimator are presented in three parts, Sections 9.3 through 9.5. In Sections 9.3 and 9.4, we present simulations that demonstrate the properties of some of the robust estimator's components. These sections are meant to provide insight so that we can understand the simulations of the robust estimator in Section 9.5. Specifically, in Section 9.3, we simulate the time-domain parameter estimator of Chapter 4 that uses the time-varying dead-zone. In this section, the time-domain parameter estimator is simulated for an ideal case, for an unmodeled dynamics alone case and for a disturbance alone case. These simulation results will allow us to understand the individual effects of unmodeled dynamics and a disturbance. In Section 9.4, we present simulations of the frequency-domain bounding methodology alone, without a parameter estimator, so that we can see how the robust estimator would perform if the parameter estimator worked perfectly. Then, in Section 9.5, we present open-loop simulations of the robust estimator as a whole. We present a simulation where the dead-zone based, time-domain parameter estimator is used and a comparable simulation where the frequency-domain parameter estimator is used. The dead-zone based parameter estimator will be shown to perform poorly. The simulation of the dead-zone based, time-domain parameter estimator, in this section, is the logical follow-on to the simulations of individual effects that are presented in Section 9.3. That is, in the robust estimator simulations of Section 9.5, we include both unmodeled dynamics and a disturbance whereas in Section 9.3 we examined these effects individually. A second purpose of Section 9.5 is to show the effect of using different types of unmodeled dynamics on the robust estimator with the frequency-domain parameter estimator. All of the open-loop simulations of Section 9.5 include both unmodeled dynamics and a disturbance.

In Section 9.6, we present closed-loop simulations of an adaptive control system that uses a simple pole-zero cancellation control-law in conjunction with the robust estimator. As in the

open-loop simulations of Section 9.5, all of the closed-loop simulations include both unmodeled dynamics and a disturbance. The major conclusions of this simulation chapter are summarized in Section 9.7. The bottom line of the closed-loop simulations is that the robust estimator can indeed provide performance-improving information to a control-law update algorithm under the "right" excitation conditions. In some of the closed-loop simulations, it will be necessary to introduce a probing signal to enhance identification and, hence, provide the "right" excitation conditions.

9.2 Description and Analysis of Simulation Example

In this section, we describe the simulation example and discuss the satisfaction of the assumptions of the robust estimator (see Chapter 3). In addition, we make several design choices for the implementation of the robust estimator (see Chapter 6). While the main purpose of this section is simply to present the simulation example, several subthemes will be developed. In particular, we will show how the continuous-time unmodeled dynamics map over to discrete-time unmodeled dynamics of approximately the same size, for this example. These results are consistent with the approximations that were presented in Section 3.3.

Since this section is quite lengthy, we outline its organization. The continuous-time nominal plant structure and the continuous-time unmodeled dynamics are described in Subsections 9.2.1 and 9.2.2, respectively. The design choices for the robust estimator, such as the sampling period and the DFT lengths, are discussed in Subsection 9.2.3. In Subsection 9.2.4, we list four cases of the plant example that will be used in our simulations. That is, we use four cases of our plant model that have different combinations of parameter values and unmodeled dynamics. The satisfaction of the various assumptions of the robust estimator, is the topic of Subsection 9.2.5. In Subsections 9.2.6-8, the disturbance and input signals are described. The last subsection, 9.2.9, describes a projection modification which will be used with both the time-domain and frequency-domain parameter estimators.

9.2.1 Description of the Nominal Plant

Consider the following nominal plant which we will use throughout the rest of the chapter.

Continuous-time Nominal Plant:

$$G^c(s) = \frac{\omega_n^2 (s / (2\zeta\omega_n) + 1)}{s^2 + 2\zeta\omega_n s + \omega_n^2} \tag{9.2.1}$$

or

$$G^c(s) = \frac{b^c_0 s + b^c_1}{s^2 - a^c_1 s - a^c_2} \tag{9.2.2}$$

where

$$a^c_1 = -2\zeta\omega_n \; ; \quad b^c_0 = \omega_n / 2\zeta \; ; \quad \text{and} \quad b^c_1 = -a^c_2 = \omega_n^2. \tag{9.2.3}$$

We find that the zero-order hold equivalent of the above continuous-time plant is

Discrete-time Nominal Plant:

$$G(z) = \frac{b_0 z + b_1}{z^2 - a_1 z - a_2} \tag{9.2.4}$$

where

$$a_1 = 2\, e^{-\zeta\omega_n T} \cos\left(\sqrt{1-\zeta^2}\, \omega_n T \right) \tag{9.2.5}$$

$$a_2 = -\, e^{-2\zeta\omega_n T} \tag{9.2.6}$$

$$b_0 = 1 - \left\{ K \sin\left(\sqrt{1-\zeta^2}\, \omega_n T \right) + \cos\left(\sqrt{1-\zeta^2}\, \omega_n T \right) \right\} e^{-\zeta\omega_n T} \tag{9.2.7}$$

$$b_1 = \left\{ K \sin\left(\sqrt{1-\zeta^2}\, \omega_n T \right) - \cos\left(\sqrt{1-\zeta^2}\, \omega_n T \right) \right\} e^{-\zeta\omega_n T} + e^{-2\zeta\omega_n T}$$

$$= 1 - a_1 - a_2 - b_0 \tag{9.2.8}$$

and where

$$K = \left(2\zeta^2 - 1 \right) / \left(2\zeta \sqrt{1-\zeta^2} \right). \tag{9.2.9}$$

The bounded parameter space Θ^c, in which the continuous-time parameter vector $\theta^c = [a^c_1 \; a^c_2 \; b^c_0 \; b^c_1]^T$ is contained, is defined by Eqn. (9.2.3) and the following

$$\Theta^c = \{ \theta^c \mid \theta^c = [a^c_1(\zeta,\omega_n) \; a^c_2(\omega_n) \; b^c_0(\zeta,\omega_n) \; b^c_1(\omega_n)]^T$$

$$\text{where } \zeta \in [0.2, 0.8],\ \omega_n \in [1,2] \text{ rads/sec. and } \zeta\omega_n \geq 0.4 \text{ sec.}^{-1} \}. \tag{9.2.10}$$

Note that there are only two parameters, ζ and ω_n, that regulate the location of the single zero and the two poles. The bounded parameter space Θ, in which the discrete-time parameter vector $\theta = [a_1 \; a_2 \; b_0 \; b_1]^T$ is contained, is defined similarly by Eqns. (9.2.5-9) and the following

$$\Theta = \{ \theta \mid \theta = [a_1(\zeta,\omega_n) \; a_2(\zeta,\omega_n) \; b_0(\zeta,\omega_n) \; b_1(\zeta,\omega_n)]^T$$

$$\text{where } \zeta \in [0.2, 0.8],\ \omega_n \in [1,2] \text{ rads/sec. and } \zeta\omega_n \geq 0.4 \text{ sec.}^{-1} \}. \tag{9.2.11}$$

As was discussed in Subsection 3.3.4, the discrete-time parameter vector θ is the result of a mapping $f(\bullet)$ of the continuous-time parameter vector θ^c. That is, we say that $\theta=f(\theta^c)\in\Theta$, where Θ can be alternatively defined by Eqn. (3.3.30).

As can be seen from Eqn. (9.2.1), the continuous-time plant $G^c(s)$ has two complex poles and a zero on the real axis at $-2\zeta\omega_n$, which is twice the frequency of the real part of the complex pole pair. Throughout the following analysis of the plant, the various supremums that we will need to calculate over the sets Θ^c and Θ, will actually be computed using a 101 point grid. That is, an 11-by-11 point grid of ζ and ω_n will be used where the constraint, $\zeta\omega_n \geq 0.4$ sec.$^{-1}$ eliminates 20 of the original 121 grid points leaving the aforementioned 101 points. In Figure 9.1, the complex pole pair and the zero of $G^c(s,\theta^c)$ are superimposed for all 101 points of the grid. Similarly, in Figure 9.2, the complex pole pair and the zero of the discrete-time nominal plant $G(z,f(\theta^c))$ are superimposed for all 101 points of the grid where we have used a sampling period of $T=\pi/25$ sec., a choice that we will later justify. In Figure 9.3, we show a log-log plot of the maximum and minimum magnitude of $G^c(j\omega,\theta^c)$ versus frequency, for all θ^c in Θ^c. A linear scale version of Figure 9.3 is shown in Figure 9.4 since we will be using a linear scale in the presentation of the simulation results.

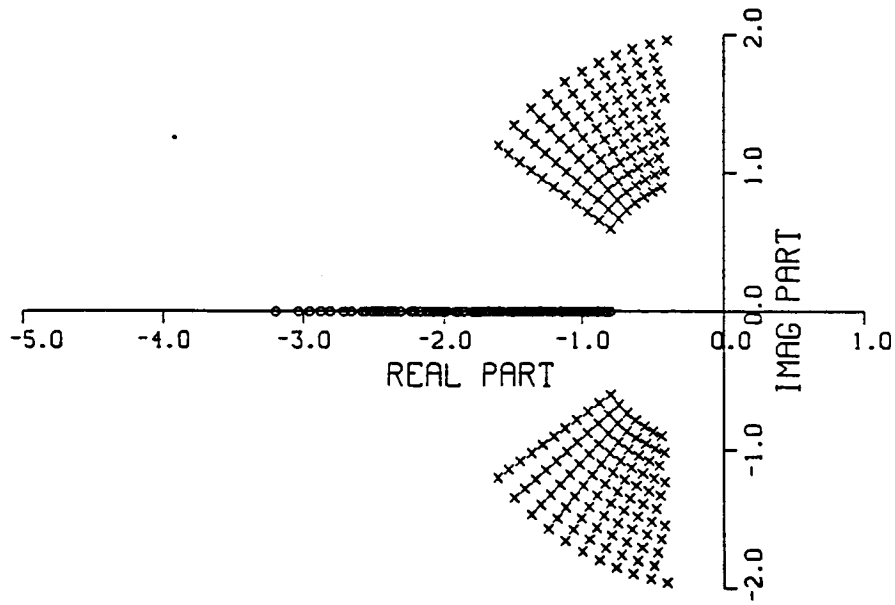

Figure 9.1: Pole-zero Locations of the Continuous-time Nominal Model.

(Pole = ×, Zero = o)

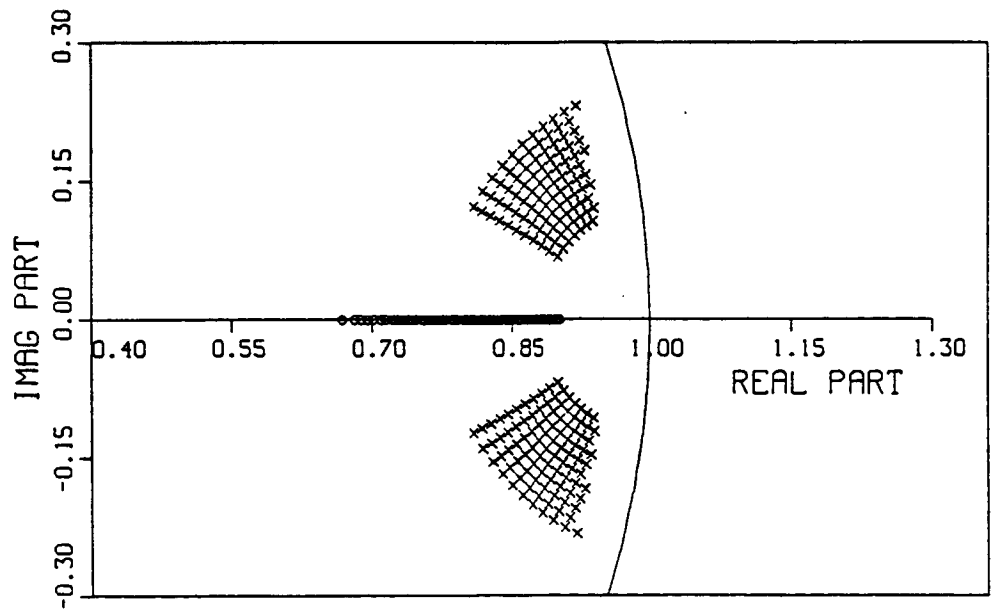

Figure 9.2: Pole-zero Locations of the Discrete-time Nominal Model.

(Pole = ×, Zero = o)

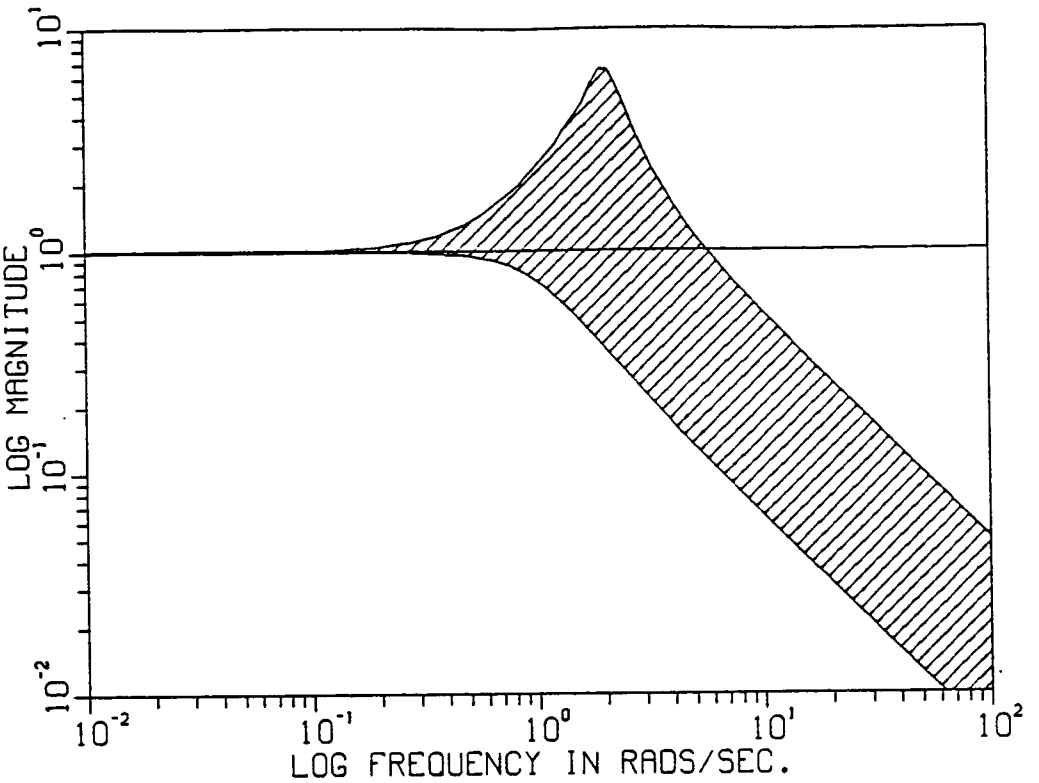

Figure 9.3: Max. and Min. Magnitude of the Continuous-time Nominal Model, Log Scales.

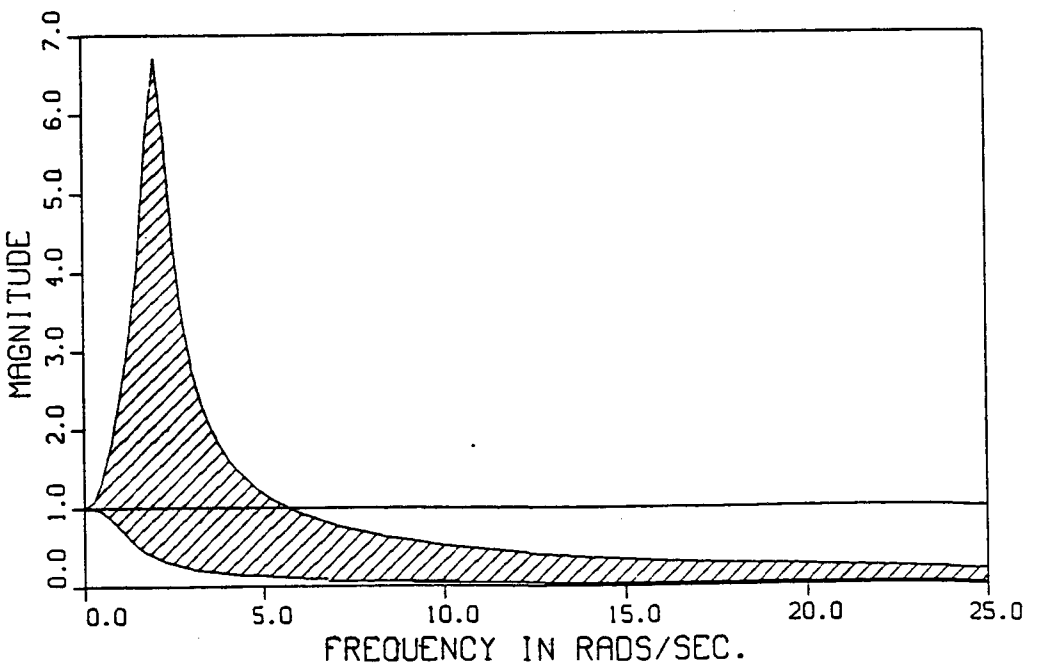

Figure 9.4: Max. and Min. Magnitude of the Continuous-time Nominal Model, Linear Scales.

9.2.2 Description of the Continuous-time Unmodeled Dynamics

In this subsection, we will describe the two types of unmodeled dynamics that we will be using in the simulations to follow. For the purpose of illustration we will consider the hypothetical situation where we know that the unmodeled dynamics are either: 1) a multiplicative second-order system with damping ratio between 0.3 and 1, and a natural frequency that is greater than 50 rads/sec., or 2) a time delay of no greater than 0.04 secs. Our strategy will be to first find continuous-time bounding functions, $\Delta^c_u(j\omega)$ and $\nabla^c_u(j\omega)$, that are valid for both the second-order and the time-delay unmodeled dynamics. Recall that $\Delta^c_u(j\omega)$ and $\nabla^c_u(j\omega)$ are the bounding functions that are required by the continuous-time assumptions of the robust estimator, as described in Section 3.2. Later, we will use $\Delta^c_u(j\omega)$ and $\nabla^c_u(j\omega)$ to find discrete-time bounding functions, $\Delta_u(e^{j\omega T})$ and $\nabla_u(e^{j\omega T})$, that are valid for both the second-order and the time-delay unmodeled dynamics interacting with our uncertain plant.

Consider the bounding function

$$\Delta^c_u(j\omega) = \begin{cases} \omega / 25, & \text{for } \omega < 50 \text{ rads/sec.} \\ 2, & \text{for } \omega \geq 50 \text{ rads/sec.} \end{cases} \qquad (9.2.12)$$

With reference to Example 2 of Subsection 6.3.2, we find that the function of Eqn. (9.2.12) bounds the magnitude of the unstructured uncertainty $\delta^c_u(j\omega)$ of all second-order unmodeled dynamics that have complex poles (i.e. $\zeta < 1$), and a natural frequency that is greater than 50 rads/sec. Figure 9.5 shows the bound of Eqn. (9.2.12) and $|\delta^c_u(j\omega)|$ for second-order unmodeled dynamics with a damping ratio of 0.3 and a natural frequency of 50 rads/sec. In addition, the bounding function of Eqn. (9.2.12) also bounds $|\delta^c_u(j\omega)|$ corresponding to all pure time delays that are less than 0.04 secs. The bound of Eqn. (9.2.12) and $\delta^c_u(j\omega)|$ for a time delay of 0.04 secs. are both shown in Figure 9.6. In Figure 9.7, we show the derivative function $|d\delta^c_u(j\omega)/d\omega|$ for both second-order unmodeled dynamics with a damping ratio of 0.3 and a natural frequency of 50 rads/sec., and for the unmodeled dynamics of a 0.04 sec. time delay. For frequencies less than about 25 rads/sec, $|d\delta^c_u(j\omega)/d\omega|$ is less than 0.04 for both types of unmodeled dynamics.

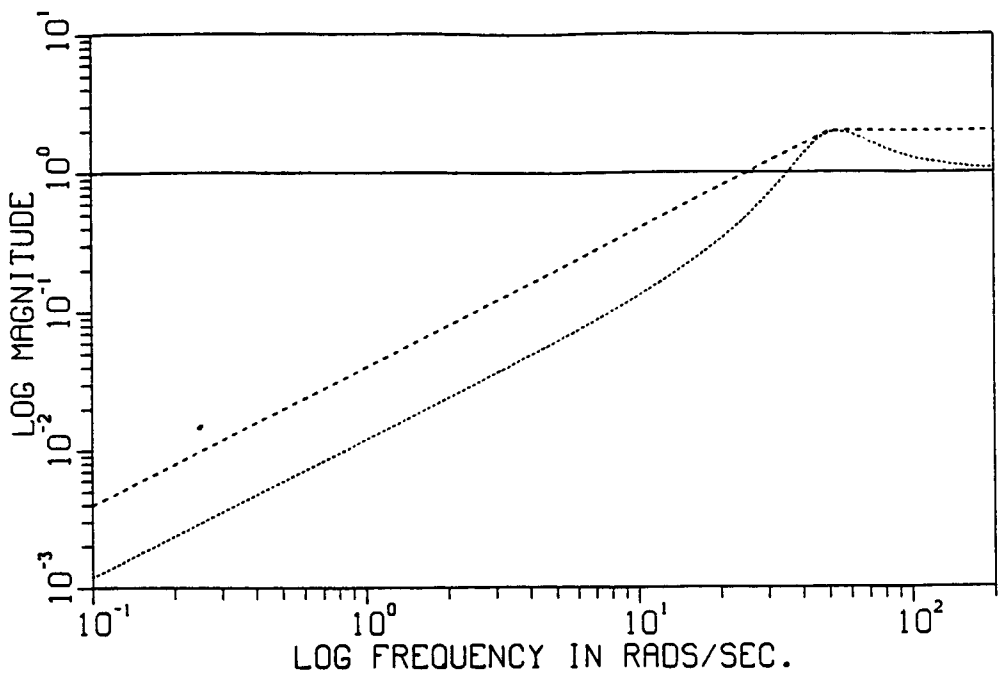

Figure 9.5: $\Delta^c_u(j\omega)$ of Eqn. (9.2.12) and Actual $|\delta^c_u(j\omega)|$ for Second-order Unmodeled Dynamics. ($\Delta^c_u(j\omega)$ = - - - - , $|\delta^c_u(j\omega)|$ = ...)

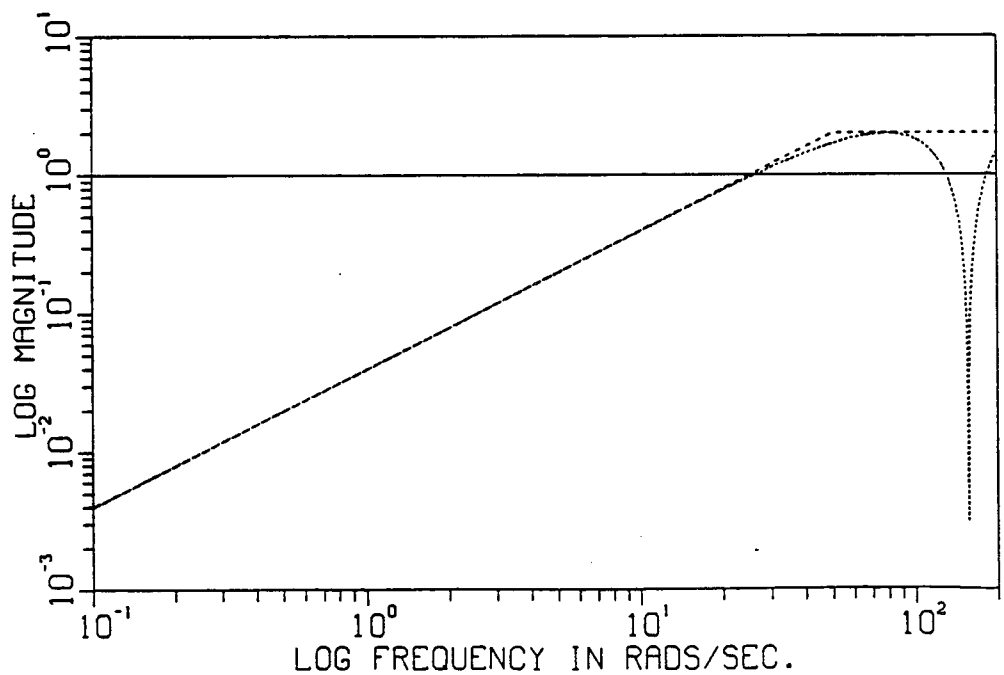

Figure 9.6: $\Delta^c_u(j\omega)$ of Eqn. (9.2.12) and Actual $|\delta^c_u(j\omega)|$ for Time-delay Unmodeled Dynamics.

($\Delta^c_u(j\omega)$ = - - - - , $|\delta^c_u(j\omega)|$ = ...)

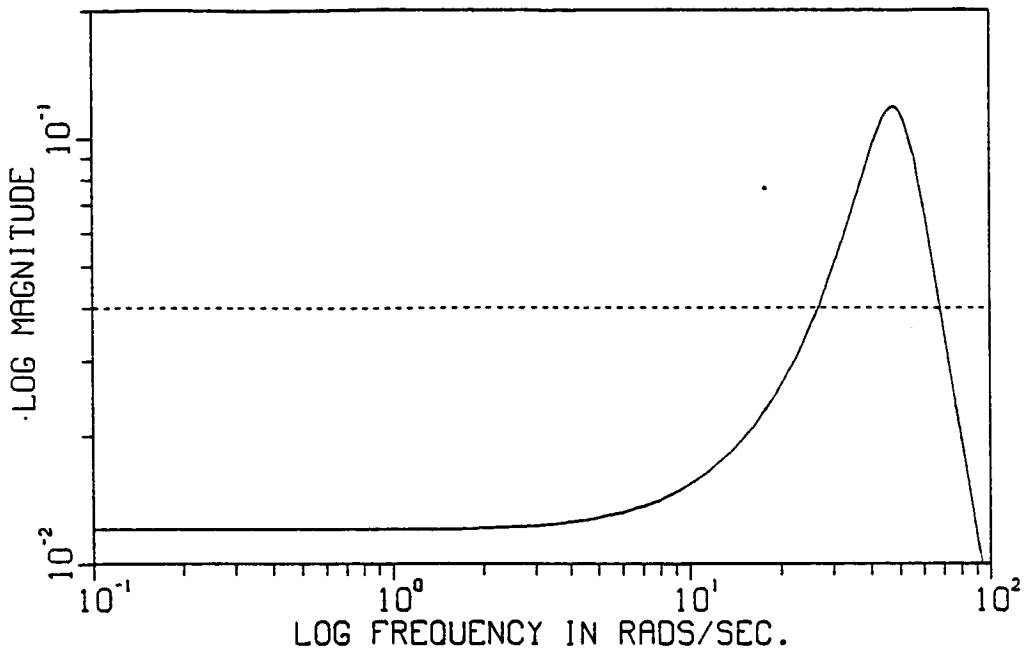

Figure 9.7: Actual $|d\delta^c_u(j\omega)/d\omega|$ for both Second-order and Time-delay Unmodeled Dynamics.

(Second-order $|d\delta^c_u(j\omega)/d\omega|$ = ——, Time-delay $|d\delta^c_u(j\omega)/d\omega|$ = - - - -)

9.2.3 Design Choices

The various design choices that were discussed in a general way in Chapter 6, are now discussed in the context of this simulation example. This subsection is concise since the reasoning behind these design choices was already discussed extensively in Chapter 6.

Choice of Sampling Period

Although we will perform our first simulations in an open-loop scenario, later in this chapter, we will present some closed-loop simulations where we set the target closed-loop bandwidth to ω_{tcl}=5 rads/sec. We want our closed-loop system to have a bandwidth of 5 rads/sec. for all possible nominal plants $G^c(s,\theta^c)$ with θ^c in Θ^c, while being robustly stable to unmodeled dynamics with magnitudes less than the bounding function of Eqn. (9.2.12). Consistent with our discussion in Chapter 6, we choose the sampling frequency ω_s=50 rads/sec., which is ten times the

target closed-loop bandwidth. This choice of sampling frequency corresponds to a sampling period of $T=\pi/25=0.12566$ secs. We note that $(\omega_s/2)=25$ rads/sec., which is the frequency at which the unstructured uncertainty bound of Eqn. (9.2.12) reaches unity. Thus, using the approximation of Eqn. (6.3.25), the discrete-time unstructured uncertainty will be less than unity for all frequencies on the unit circle. With reference to Figures 6.1 and 6.2 of Section 6.2, for our choice of sampling period, $T=\pi/25$, the unmodeled dynamics will have a smaller effect on the discrete-time plant than if we had chosen a faster sampling rate.

Choice of the DFT Length N_t for the Time-domain Bounding Mechanism

In Section 6.5, we discussed the choice of the DFT length for the time-domain bounding mechanism that is used in the time-domain parameter estimator. This DFT length, which we denote by N_t, is chosen by making a tradeoff between the size of the remainder term, and the possible conservatism of the bound for large N_t. For the example of this chapter, we choose $N_t=20$. This DFT length will later be shown, in Subsection 9.3.1, to reduce the remainder term to be the same order of magnitude as the size of the bound itself.

Design of the Input/Output Filter F(z) for the Time-domain Parameter Estimator

As was described in Section 6.5, we must design the input/output filter F(z) that filters both the plant input and the output signals before they are used in the time-domain parameter estimator. In accordance with the rule of thumb given by Eqn. (6.5.3), we choose the filter

$$F(z) = \frac{0.052881\, z^2}{z^2 - 1.64799\, z + 0.70087} \qquad (9.2.13)$$

which has unity D.C. gain and poles that correspond to the continuous-time poles of a second-order system with $\zeta=0.70711$ and $\omega_n=2$ rads/sec., for our choice of sampling period, $T=\pi/25$ secs. With reference to the nominal plant description of Subsection 9.2.1, we see that F(z) and the discretized nominal plant have roughly the same bandwidth. Since the bandwidth of the nominal plant is only coarsely known, this is the best we can do in terms of designing F(z).

Choice of the Memory Length M for the Frequency-domain Bounding Method

From Subsection 9.2.1, we know that the real part of the complex pole pair of the continuous-time nominal plant will be no larger than -0.4 sec.$^{-1}$. That is, we know that the envelope of the impulse response of the true continuous-time plant will decay with a time constant that is no slower than 2.5 secs. since the slowest pole of the nominal plant is also the slowest pole of the true plant. Now, a continuous-time pole of -0.4 sec.$^{-1}$ maps to a discrete-time pole of 0.95098 for our choice of sampling period, $T=\pi/25$ sec. Thus, the slowest pole of the true discrete-time plant is 0.95098, since the unmodeled dynamics are assumed to be at high-frequencies. Using the second approximation of Eqn. (6.6.24), we compute the rule of thumb for a choice of M,

$$\text{integer}((2\pi / T) / 0.4) = \text{integer}(\omega_s / \alpha_{slow}) = 50 \text{ rads/sec.} / 0.4 \text{ sec.}^{-1} = 125 \qquad (9.2.14)$$

where again $-\alpha_{slow}$ is the real part of the slowest pole of the continuous-time plant. This is only a rule of thumb and, in fact, we will choose a larger value of M=175 for our open-loop simulations. This larger value of M will result in a tighter frequency-domain bounding function than if we had just used the rule of thumb value of M. An even larger value of M will be used in the closed-loop simulations as will be discussed later. We use these large values of M because we could potentially have a very difficult identification problem considering our target closed-loop bandwidth of 5 rads/sec. That is, with reference to Figures 9.3-4, if we have the smallest magnitude nominal plant, then we need to reduce the additive error in the frequency-domain to roughly 0.1 at 5 rads/sec. to be able to achieve our target closed-loop bandwidth of 5 rads/sec. This is so because, in order to reduce the multiplicative modeling uncertainty to be unity at a given frequency, we must reduce the additive error to be roughly the same size as the nominal model at that frequency, depending on the phase. So, considering our discussion of Subsection 6.6.5 and Eqn. (6.6.13), we see that it is advantageous to choose a larger value of M to help make the achievable additive error be as small as possible.

Choice of the DFT Length N_f for the Frequency-domain Bounding Method

In Subsections 6.6.2 and 6.6.3, we derived two rules of thumb concerning a lower bound for the choice of the DFT length for the frequency-domain bounding method. We denote this DFT length by N_f, to distinguish it from N_t, which is the DFT length for the time-domain bounding mechanism. From Eqns. (6.6.25-26), and (9.2.14), we find that the first rule of thumb suggests

that N_f be chosen such that

$$N_f > 125. \tag{9.2.15}$$

The second rule of thumb, which is given by Eqn. (6.6.44), is based on frequency-domain resolution requirements. From Figure 9.4, we expect that we will have to choose a large value of N_f to guard against inter-sample variations in the vicinity of 2 rads/sec. Eqn. (5.7.11) can be used to compute the "worst-case" a priori bounding function $\nabla_{su,wc}(e^{j\omega T})$ and, thus, give us an idea of what value of N is required. Note that in Eqn. (5.7.11), we must use the bounding functions, $\Delta_u(e^{j\omega T})$ and $\nabla_u(e^{j\omega T})$, whose development will be described in a future subsection. In any event, using these bounding functions and Eqn. (5.7.11), we can compute $(\omega_s/N)\nabla_{su,wc}(e^{j\omega T})$ for N=1000, as is shown in Figure 9.8. From this figure, we see that if the worst-case bounding function $\nabla_{su,wc}(e^{j\omega T})$ were used instead of the on-line computed bounding function $\nabla_{su}{}^n(e^{j\omega T})$ of Eqn. (5.7.18), then we would have to add a safety factor on the order of unity in the frequency range near 2 rads/sec. That is, in Eqn. (5.8.3) the additive safety factor would be $(\omega_s/2N)\nabla_{su,wc}(e^{j\omega T})$, or half the values in Figure 9.8. Clearly, the frequency-domain resolution requirements place the lower bound on our choice of the DFT length. Judging that the values of Figure 9.8 are sufficiently small for our purposes, we choose N_f=1000. This DFT length will be used in the frequency-domain bounding method and, hence, the frequency-domain parameter estimator, throughout the rest of the chapter.

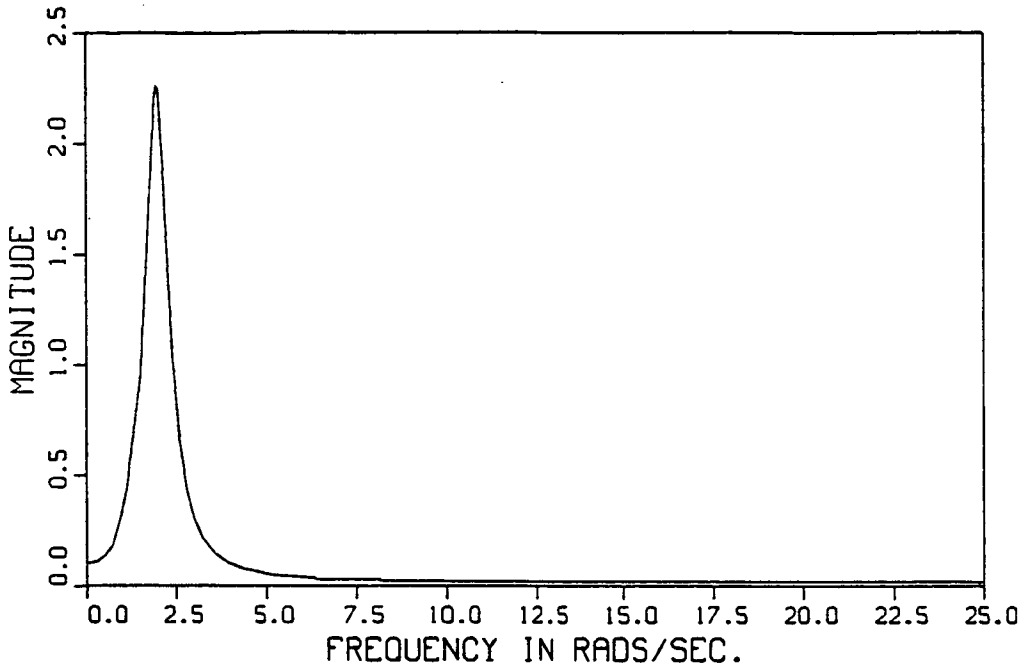

Figure 9.8: The Worst-case Bound $(\omega_s/N)\nabla_{su,wc}(e^{j\omega T})$ for N=1000.

9.2.4 Description of Four Cases for Simulation

In this subsection, we will describe four cases of the true plant that we will use in our simulations. In these cases, we consider two different nominal models. We use a fast nominal model with ζ=0.2 and ω_n=2 rads/sec., which has a sharp frequency-domain peak because of the small damping ratio. In addition, we use a slow nominal model with ζ=0.8 and ω_n=1 rad/sec., which doesn't have a frequency-domain peak because of the large damping ratio. The pole-zero locations for these nominal models are shown in Figures 9.9 and 9.10. These nominal models were chosen because they have very different characteristics. In Figures 9.3 and 9.4, the fast system corresponds to the maximum magnitude of the nominal model, except for a small frequency range just before the 2 rads/sec. peak. In these figures, the slow nominal model corresponds to the minimum magnitude. We will use these nominal models with different types of unmodeled dynamics. We denote the ideal case of no unmodeled dynamics as Case 1 where we choose ζ=0.2 and ω_n=2 rads/sec. in the nominal model of Eqn. (9.2.1) to yield:

Case 1: (ζ=0.2 and ω_n=2 rads/sec. and no unmodeled dynamics)

$$G^c_{true}(s) = \frac{4\,(s/0.8 + 1)}{s^2 + 0.8\,s + 4} \tag{9.2.16}$$

whose zero-order hold equivalent for the sampling period T=π/25 sec. is given by:

Case 1: (ζ=0.2 and ω_n=2 rads/sec. and no unmodeled dynamics)

$$G_{true}(z) = \frac{0.62189\,z - 0.56211}{z^2 - 1.84458\,z + 0.90436} \tag{9.2.17}$$

For Case 2, we use ζ=0.2 and ω_n=2 rads/sec. in the nominal model of Eqn. (9.2.1) and second-order unmodeled dynamics with a damping ratio of 0.3 and a natural frequency of 50 rads/sec.

Case 2: (ζ=0.2 and ω_n=2 rads/sec. and second-order unmodeled dynamics)

$$G^c_{true}(s) = \frac{4\,(s/0.8 + 1)}{s^2 + 0.8\,s + 4} \cdot \frac{2500}{s^2 + 30\,s + 2500} \tag{9.2.18}$$

whose zero-order hold equivalent for the sampling period T=π/25 sec. is given by:

Case2: (ζ=0.2 and ω_n=2 rads/sec. and second-order unmodeled dynamics)

$$G_{true}(z) = \frac{0.57666\,z^3 - 0.65109\,z^2 + 0.12783\,z - 0.0096407}{z^4 - 2.13562\,z^3 + 1.46426\,z^2 - 0.30573\,z + 0.020849} \tag{9.2.19}$$

For Case 3, we use ζ=0.2 and ω_n=2 rads/sec. in the nominal model of Eqn. (9.2.1) and use the unmodeled dynamics of a 0.04 sec. time delay.

Case 3: (ζ=0.2 and ω_n=2 rads/sec. and 0.04 sec. time-delay unmodeled dynamics)

$$G^c_{true}(s) = \frac{4\,(s/0.8 + 1)}{s^2 + 0.8\,s + 4} \cdot e^{-s(0.04)} \tag{9.2.20}$$

whose zero-order hold equivalent for the sampling period $T=\pi/25$ sec. is given by:

Case 3: ($\zeta=0.2$ and $\omega_n=2$ rads/sec. and 0.04 sec. time-delay unmodeled dynamics)

$$G_{true}(z) = \frac{0.42626\, z^2 - 0.18581\, z - 0.18068}{z\,(z^2 - 1.84458\, z + 0.90436)} \qquad (9.2.21)$$

For Case 4, we use $\zeta=0.8$ and $\omega_n=1$ rad/sec. in the nominal model of Eqn. (9.2.1) and use the same second-order unmodeled dynamics that were used in Case 2 above.

Case 4: ($\zeta=0.8$ and $\omega_n=1$ rad/sec. and second-order unmodeled dynamics)

$$G^c_{true}(s) = \frac{(s/1.6 + 1)}{s^2 + 1.6\, s + 1} \cdot \frac{2500}{s^2 + 30\, s + 2500} \qquad (9.2.22)$$

whose zero-order hold equivalent for the sampling period $T=\pi/25$ sec. is given by:

Case 4: ($\zeta=0.8$ and $\omega_n=1$ rad/sec. and second-order unmodeled dynamics)

$$G_{true}(z) = \frac{0.072471\, z^3 - 0.075668\, z^2 + 0.014760\, z - 0.0011052}{z^4 - 2.09462\, z^3 + 1.36583\, z^2 - 0.27961\, z + 0.018855} \qquad (9.2.23)$$

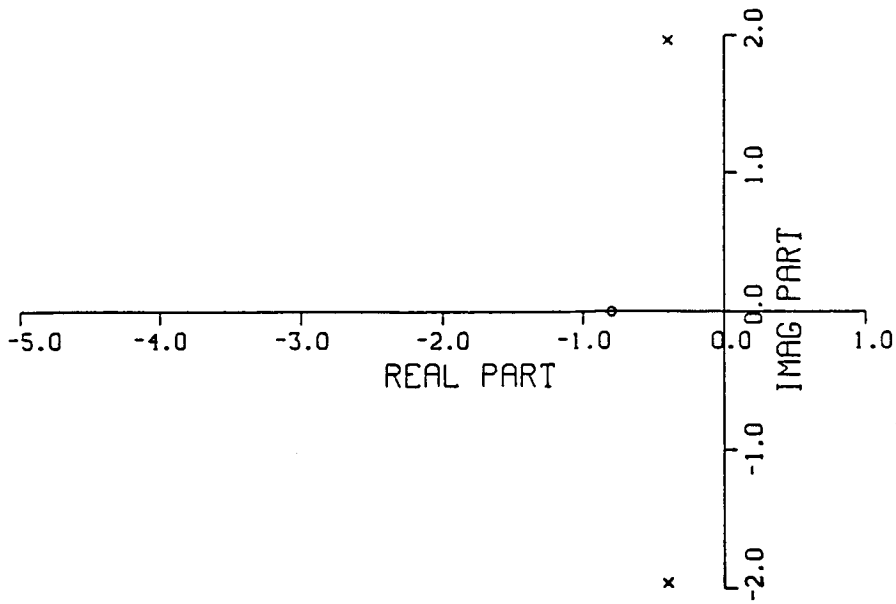

Figure 9.9: Pole-zero Locations of the Fast Continuous-time Nominal Model, ζ=0.2 and ω_n=2 rads/sec. (Pole = x, Zero = o)

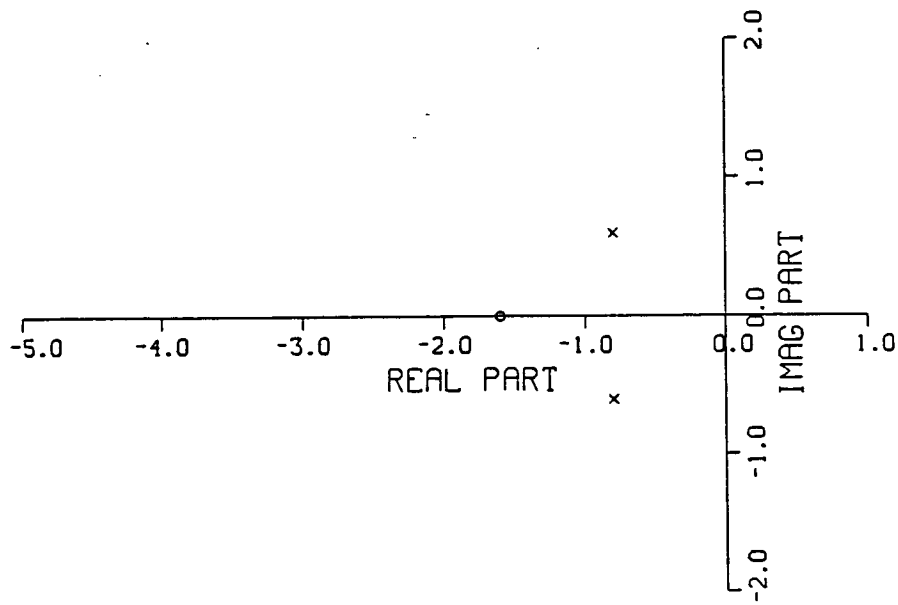

Figure 9.10: Pole-zero Locations of the Slow Continuous-time Nominal Model, ζ=0.8 and ω_n=1 rad/sec. (Pole = x, Zero = o)

9.2.5 Satisfaction of the Robust Estimator Plant Assumptions

In this subsection, we will discuss the satisfaction of the various plant assumptions of Chapter 3. The assumptions AD1.1-1.2 of Subsection 3.6 are satisfied by the results of Subsection 9.2.1. Further, since the continuous-time nominal model is stable for all parameter variations in Θ^c, for our example, and since the unmodeled dynamics are stable, we conclude that the true discrete-time system is stable and, hence, assumption AD1.5 is satisfied. We must still find the bounding functions of assumptions AD1.3-4, and AD1.6-7.

Satisfying Assumption AD1.3: Finding $\Delta_u(e^{j\omega T})$

The bounding techniques of Subsection 3.3.2, specifically Eqn. (3.3.17), could be used to find the discrete-time bounding function $\Delta_u(e^{j\omega T})$ from the continuous-time bounding function $\Delta^c{}_u(j\omega)$. However, the resulting bounding function can be conservative and it requires much work to compute the various supremums. In practice, the approximation of Eqn. (3.3.19) is useful. We choose to not use this equation since it is not a guaranteed bound. Instead, we will consider some specific cases so that we can find a rigorous bound. We will find that for the cases considered, the approximation of Eqn. (3.3.19) turns out to be rigorously true. In the following development, we will use Cases 2-4, which were described in Subsection 9.2.4, to find the discrete-time bounding function $\Delta_u(e^{j\omega T})$. In Figure 9.11, we show $|\delta^c{}_u(j\omega)|$ for the second-order unmodeled dynamics and $|\delta_u(e^{j\omega T})|$ for both Cases 2 and 4. We see from this figure that $|\delta_u(e^{j\omega T})| \approx |\delta^c{}_u(j\omega)|$ for both Cases 2 and 4. In Figure 9.12, we show $|\delta^c{}_u(j\omega)|$ for the time-delay unmodeled dynamics and $|\delta_u(e^{j\omega T})|$ for Case 3. Again, we see from this figure that $|\delta_u(e^{j\omega T})| \approx |\delta^c{}_u(j\omega)|$ for the time-delay unmodeled dynamics. For these three cases, the continuous-time bounding function of Eqn. (9.2.12) in the frequency range 0 to $\omega_s/2$ can be used as the discrete-time bounding function for Cases 2-4. That is, we will use the bounding function,

$$\Delta_u(e^{j\omega T}) = \omega / 25, \text{ for } 0 \le \omega \le 25 \text{ rads/sec.} \qquad (9.2.24)$$

in the following work. While we can only guarantee that the above bounding function is valid for

Cases 2-4, which is all of the cases that we will be simulating, it is likely that this bounding function also holds for all variations of the continuous-time parameters in Θ^c. We base this statement on the fact that we have used, in a sense, the most different nominal models in Θ^c that we could have. It seems likely that all other parameter variations in Θ^c will yield bounding functions that lie between the bounding functions resulting from the fast and slow nominal model cases, or at least not greatly differ from this range.

Satisfying Assumption AD1.4: Finding $\nabla_u(e^{j\omega T})$

The bounding techniques of Subsection 3.3.3, specifically Eqn. (3.3.25), could be used to find a discrete-time bounding function $\nabla_u(e^{j\omega T})$ from the continuous-time bounding functions $\Delta^c{}_u(j\omega)$ and $\nabla^c{}_u(j\omega)$. However, the resulting bounding function can be very conservative and it requires a great deal of work to compute. In practice, the approximation of Eqn. (3.3.23) is useful. We choose to not use this equation since it is not a guaranteed bound. Instead, as in the case of $\Delta_u(e^{j\omega T})$, we will consider some specific cases so that we can find a rigorous bound. We will again use Cases 2-4 to find the discrete-time bounding function $\nabla_u(e^{j\omega T})$. In Figure 9.13, we show $|d\delta^c{}_u(j\omega)/d\omega|$ for the second-order unmodeled dynamics and $|d\delta_u(e^{j\omega T})/d\omega|$ for both Cases 2 and 4. We see that $|d\delta_u(e^{j\omega T})/d\omega| \approx |d\delta^c{}_u(j\omega)/d\omega|$ for both Cases 2 and 4. Similarly, in Figure 9.14, we show $|d\delta^c{}_u(j\omega)/d\omega|$ for the time-delay unmodeled dynamics and $|d\delta_u(e^{j\omega T})/d\omega|$ for Case 3. Again, we see that $|d\delta_u(e^{j\omega T})/d\omega| \approx |d\delta^c{}_u(j\omega)/d\omega|$. The actual $|d\delta_u(e^{j\omega T})/d\omega|$ for Cases 2-4 is always less than about 0.04. We choose to use the bound,

$$\nabla_u(e^{j\omega T}) = 0.05, \text{ for } 0 \leq \omega \leq 25 \text{ rads/sec.} \tag{9.2.25}$$

in what follows. As was the case for $\Delta_u(e^{j\omega T})$, we can only guarantee that the bounding function of Eqn. (9.2.25) is valid for Cases 2-4; however, it is again likely that this bounding function also holds for all variations of the continuous-time parameters in Θ^c.

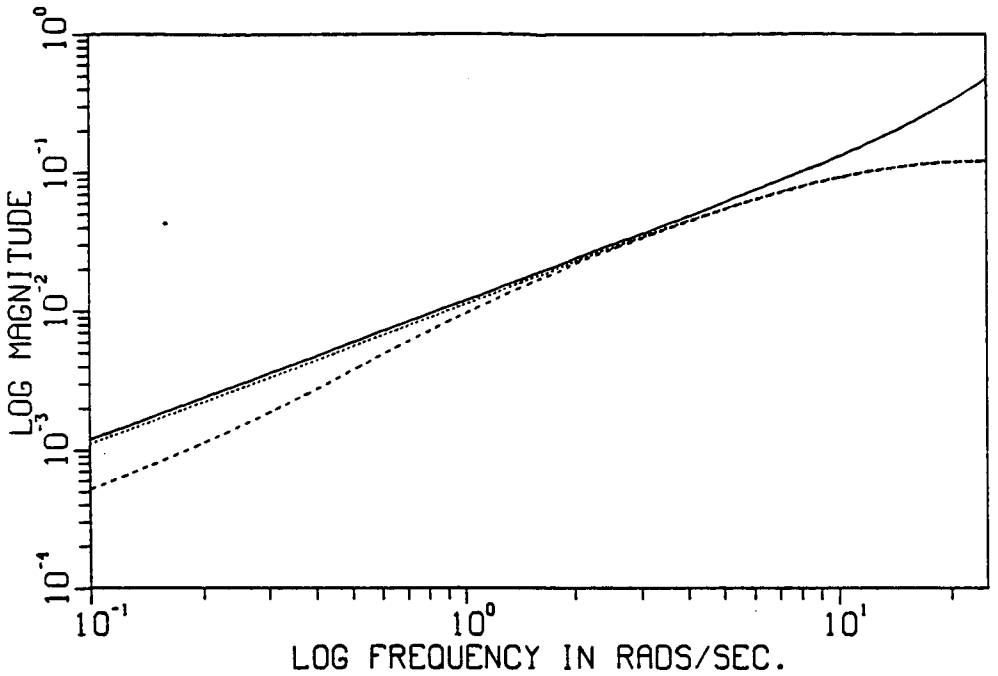

Figure 9.11: Continuous and Discrete-time Unmodeled Dynamics Magnitudes, for 2nd-order Case. ($|\delta^{c}_{u}(j\omega)|$ = ——, $|\delta_{u}(e^{j\omega T})|$ for Case 2 = - - - - , $|\delta_{u}(e^{j\omega T})|$ for Case 4 = ...)

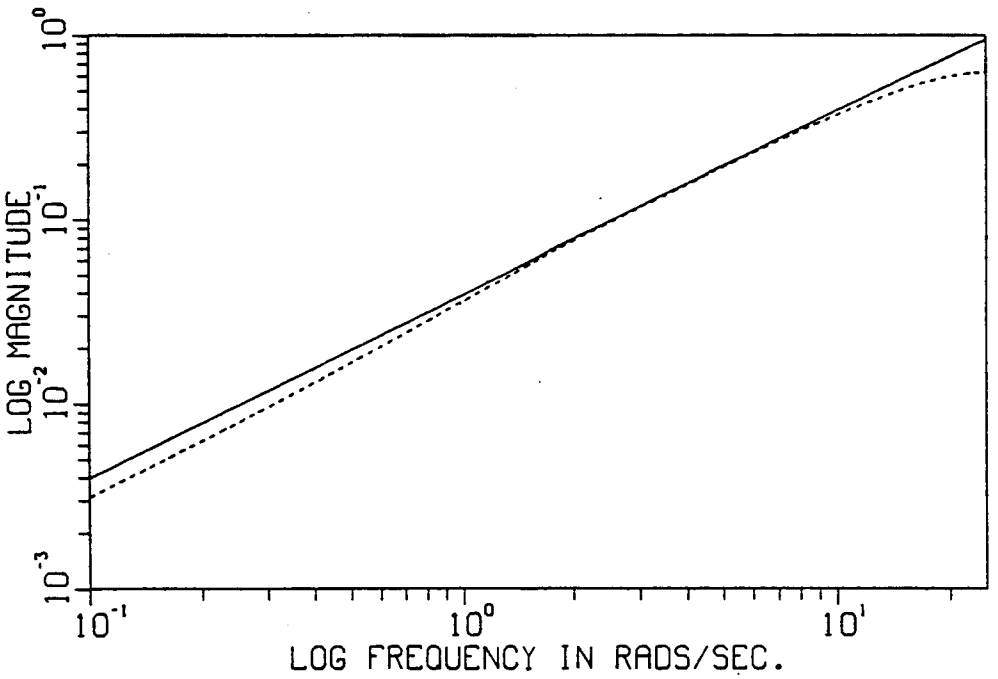

Figure 9.12: Continuous and Discrete-time Unmodeled Dynamics Magnitudes, for Time-delay Case. ($|\delta^{c}_{u}(j\omega)|$ = ——, $|\delta_{u}(e^{j\omega T})|$ for Case 3 = - - - -)

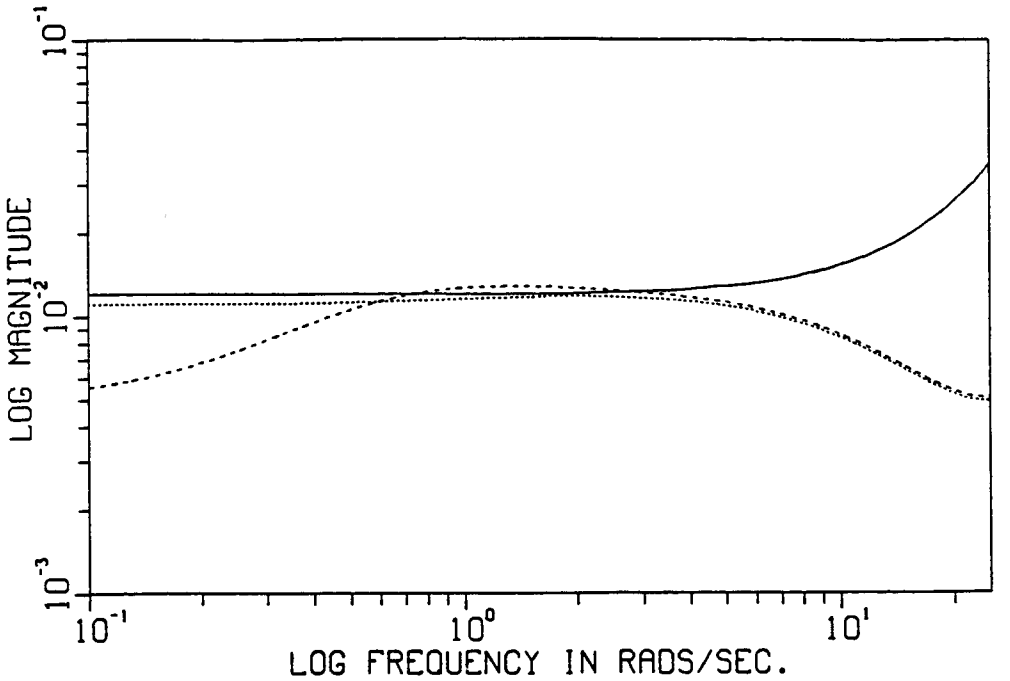

Figure 9.13: Continuous and Discrete-time Derivative Magnitudes, for 2nd-order Case.

($|d\delta^c{}_u(j\omega)/d\omega|$ = ——, $|d\delta_u(e^{j\omega T})/d\omega|$ for Case 2 = - - - - , $|d\delta_u(e^{j\omega T})/d\omega|$ for Case 4 = ...)

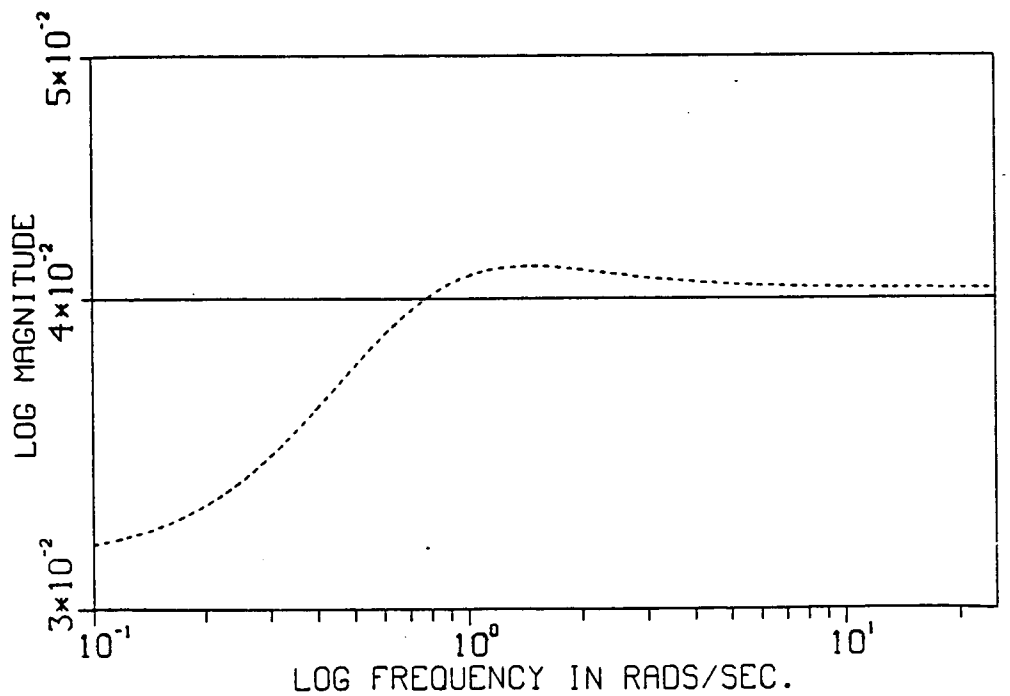

Figure 9.14: Continuous and Discrete-time Derivative Magnitudes, for Time-delay Case.

($|d\delta^c{}_u(j\omega)/d\omega|$ = ——, $|d\delta_u(e^{j\omega T})/d\omega|$ for Case 3 = - - - -)

Satisfying Assumption AD1.6: Finding a Bounding Function on $|g_{true}[n]|$

We again appeal to Cases 1-4 to satisfy assumption AD1.6, that is, to find a bounding function on $|g_{true}[n]|$. We will bound $|g_{true}[n]|$ using a first-order system with a discrete-time pole of 0.95098, which is the slowest possible pole of $g_{true}[n]$ as was discussed in Subsection 9.2.3. We use Cases 1-4 to find the gain of the first-order bounding function. Figures 9.15, 9.16 and 9.17 show the impulse responses of the true discrete-time plant $g_{true}[n]$ for Cases 2, 3 and 4, respectively, where the impulse responses of the appropriate nominal plants g[n], that is, the plants without unmodeled dynamics, are also superimposed on each graph. For example, the impulse response of the plant of Case 1, which is shown as a solid line in Figure 9.15, is the impulse response of the nominal plant of Case 2. From Figures 9.15-17 we choose the gain g of the bounding function on $|g_{true}[n]|$ as follows:

$$|g_{true}[n]| \le \overline{g}_{true}[n] = g\, p^n, \quad \text{for } n \ge 1, \tag{9.2.26}$$

where

$$g = 0.75 \quad \text{and} \quad p = 0.95098 \tag{9.2.27}$$

Satisfying Assumption AD1.7: Finding a Bounding Function on $|h_{g\delta}[n,\theta]|$

As for assumption AD1.6, we will appeal to Cases 2-4 to satisfy assumption AD1.7, which is the assumption of a bounding function on the impulse response of the additive plant error, that is, the error between the true plant and the nominal model. First, we recall the definition of Eqn. (4.4.7).

$$h_{g\delta}[n,\theta] = g[n,\theta] * \tilde{\delta}_u[n] = g_{true}[n] - g[n,\theta] \tag{9.2.28}$$

From our earlier work concerning $|g_{true}[n]|$ and, hence, $|g[n,\theta]|$, we know that the envelope of $|h_{g\delta}[n,\theta]|$ is bounded by a first-order system with a discrete-time pole of 0.95098. To find the gain of the first-order system, the actual impulse response $h_{g\delta}[n,\theta]$ was computed for Cases 2-4. From these results we choose the gain 'a' of the bounding function on $|h_{g\delta}[n]|$ as follows:

$$|h_{g\delta}[n,\theta]| \le \overline{h}_{g\delta}[n] = a\, b^n, \quad \text{for } n \ge 1, \tag{9.2.29}$$

where

$$a = 0.25 \text{ and } b = 0.95098 \tag{9.2.30}$$

We have presented this bounding function for completeness. In the general method that was described in Subsection 4.4.2, we use this bounding function $\overline{h}_{g\delta}[n]$ to find a bounding function on $|h_u[n]|$. However, in the development of this chapter, we will not actually use this result, since later, in Subsection 9.3.1, we use Cases 2-4 to find the required bounding function on $|h_u[n]|$ directly. The bounding function that is found in this way is less conservative than the bounding function yielded by the general method of Subsection 4.4.2. Later, in Subsection 9.3.1, this will enable us to find a tighter bound on the remainder term of Eqn. (9.3.16).

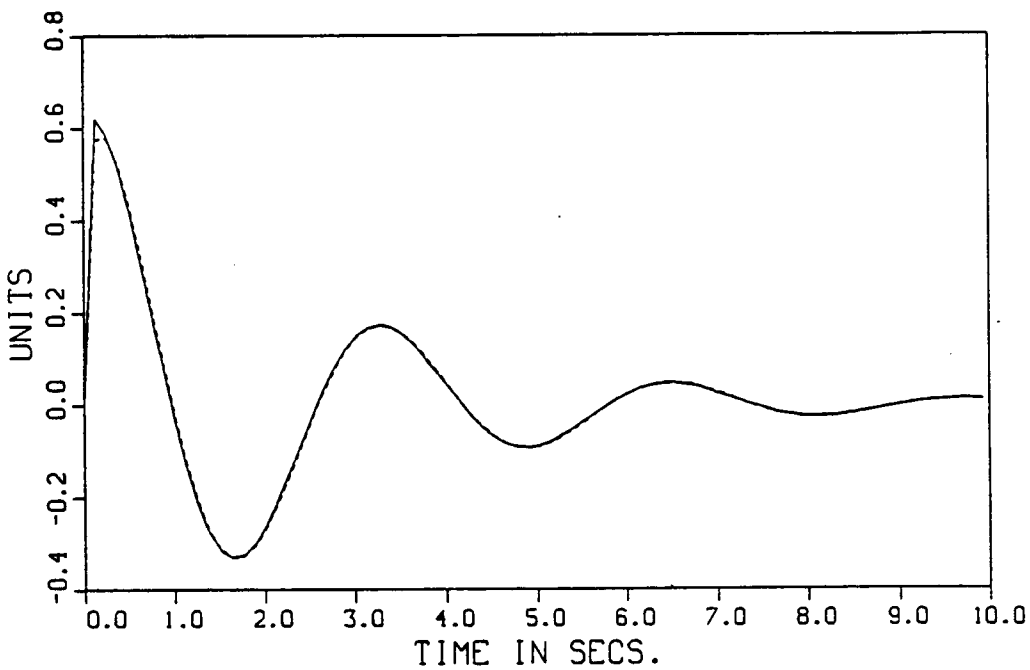

Figure 9.15: Discrete-time Impulse Responses, for Case 2.
(g[n] for Case 2 = ——, $g_{true}[n]$ for Case 2 = - - - -)

In this figure, we can only see differences between the two impulse reponses during the first few sample times.

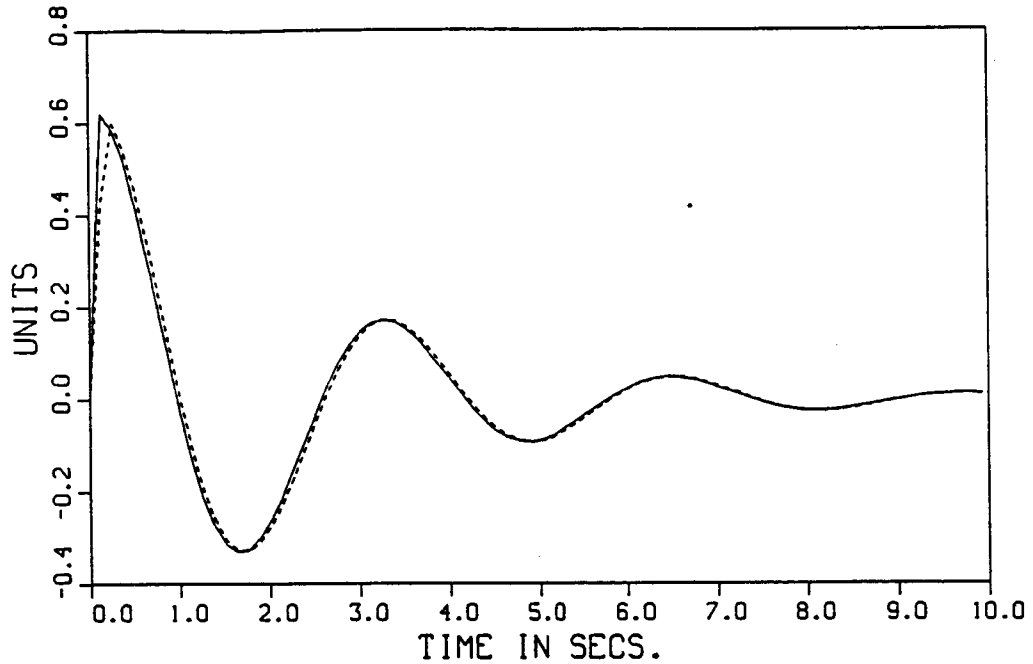

Figure 9.16: Discrete-time Impulse Responses, for Case 3.
(g[n] for Case 3 = ——, $g_{true}[n]$ for Case 3 = - - - -)

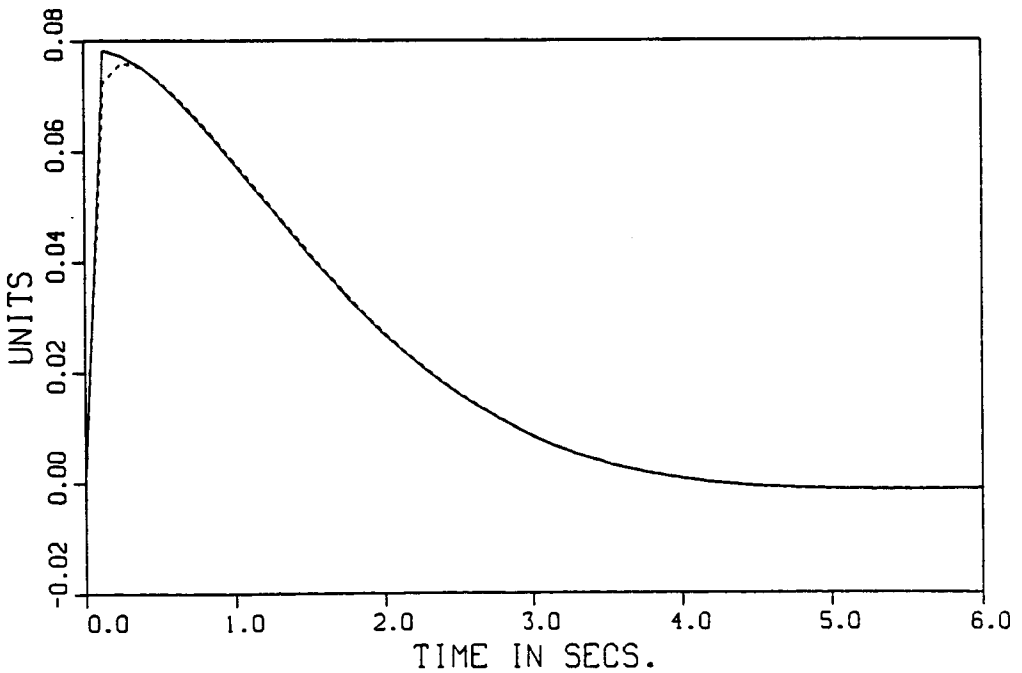

Figure 9.17: Discrete-time Impulse Responses, for Case 4.
(g[n] for Case 4 = ——, $g_{true}[n]$ for Case 4 = - - - -)

9.2.6 Description of the Disturbance

In this subsection, we will describe the disturbance that corrupts the output of the plant. Since the simulations will be implemented in discrete-time, we will work entirely with a discrete-time disturbance signal. We choose a disturbance that has most of its energy in the low-frequency range. We make this choice so that there is some hope of identifying the plant at frequencies beyond the open-loop bandwidth of the plant. In the frequency range above where the plant transfer function rolls-off, we need a high signal-to-noise ratio in order to find a useful bound on the additive frequency-domain estimation error. Said another way, in order to reduce the multiplicative uncertainty to unity at some frequency, we must have a noise-to-signal ratio, $D_N(\omega_k)/U_N(\omega_k)$, at that frequency that is roughly of the same order of magnitude as the plant transfer function (see Eqn. (5.2.17)). We produce the low-frequency disturbance by using a low-pass filter which has discrete-time poles that correspond to the continuous-time poles of a second-order system with ζ=0.70711 and ω_n=2 rads/sec. Thus, the disturbance filter has a bandwidth that is greater than or equal to the bandwidth of the nominal plant model in which ω_n is between 1 and 2 rads/sec.

Figure 9.18 shows how the disturbance signal will be produced. The discrete-time disturbance signal will be generated by using a pseudo-random signal that is uncorrelated in time and that has a gaussian probability distribution with zero mean and a standard deviation of $0.75 \cdot d_{factor}$, where d_{factor} denotes the disturbance scaling factor. This pseudo-random signal will be passed through the low-pass filter,

$$F_d(z) = \frac{0.052881\, z^2}{z^2 - 1.64799\, z + 0.70087} \tag{9.2.31}$$

which we have chosen to be the same as the input/output filter F(z) of Subsection 9.2.3. The actual disturbance signal d[n] is then generated by passing the output of this filter through a saturation function to guarantee that $|d[n]| \leq d_{factor}$. This disturbance signal is shown in Figure 9.19 for d_{factor}=1. Since the disturbance filter $F_d(z)$ has roughly the same bandwidth as the partially known plant $G_{true}(z)$, we can view the disturbance as a wideband process noise or a wideband input noise to the plant.

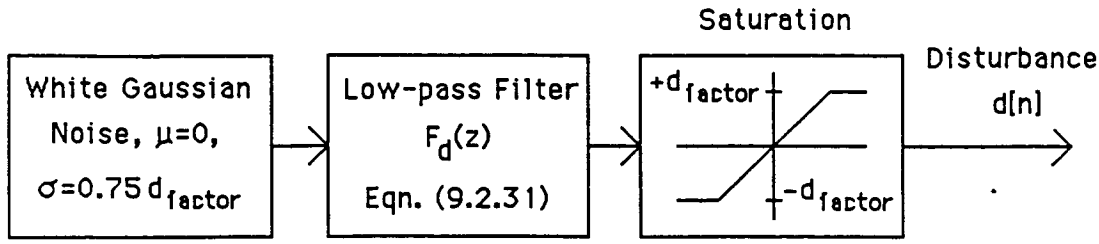

Figure 9.18: Disturbance Signal Generation.

9.2.7 Satisfaction of the Robust Estimator Disturbance Assumptions

In this subsection, we will discuss the satisfaction of the disturbance assumptions of Section 3.6. Since we are starting with a discrete-time disturbance to perform our simulations, we do not require the methods of Section 3.5. For the disturbance of Subsection 9.2.6, we are assured that assumption AD2.1 is satisfied by construction, since

$$|d[n]| \leq d_{max} = d_{factor}, \tag{9.2.32}$$

where again d_{factor} is the disturbance scaling factor. The bounding functions of assumption AD2.2 are found empirically by computing the actual DFTs of d[n] for very large samples, that is, for at least as long as the longest of our simulations. For example, the bound $\overline{\overline{D}}_N(\omega_k)$ at a specific frequency ω_k is chosen as the maximum value of $|D_N^n(\omega_k)|$ that is empirically observed for all time indices n that are less than 2500. The bounding function $\overline{\overline{D}}_N(\omega_k)$ for $N=N_f=1000$ that results from this procedure is shown in Figure 9.20.

To find the family of bounding functions, $\overline{D}_N^{+n}(\omega_k)$, corresponding to n=0 to N-2, we empirically compute, at each time index n, the maximum value of the DFT over frequency of the unfiltered disturbance, that is, the disturbance before it is passed through the low-pass filter $F_d(z)$. These values for n=0 to N-2 are then made to be nonincreasing. At a given time index n, the bounding function $\overline{D}_N^{+n}(\omega_k)$ is generated by scaling the magnitude of the frequency response of the low-pass filter $F_d(z)$ by the maximum value of the DFT over frequency, at time index n, of the unfiltered disturbance. This complicated procedure is not of major importance but it is required, if the robust estimator is to yield useful information during the first N-1 time samples of the simulation when it is starting up.

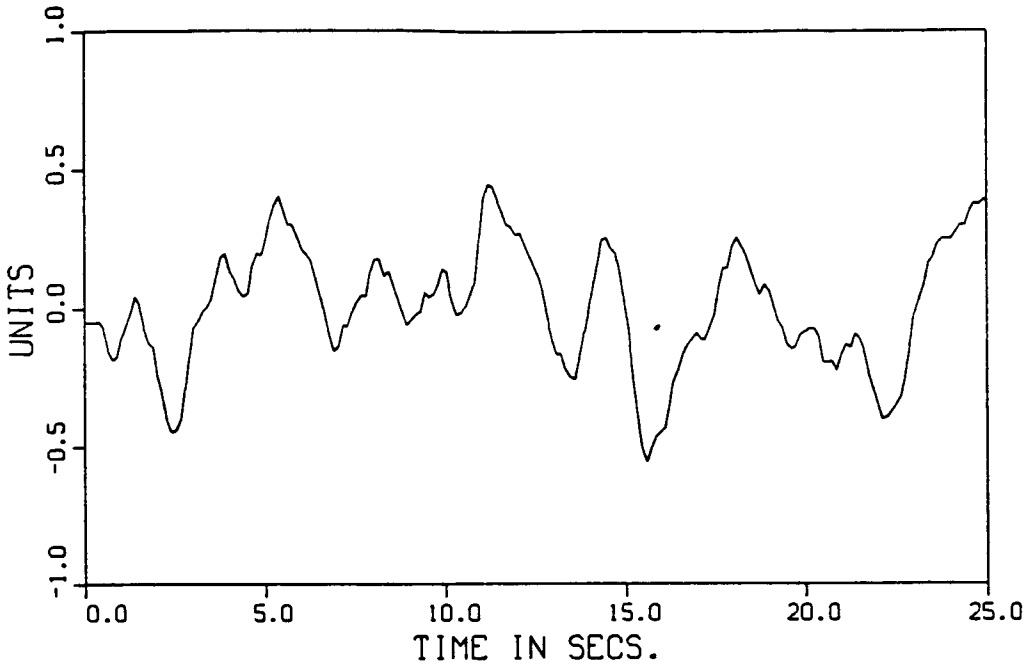

Figure 9.19: Disturbance d[n] for d_{factor}=1.

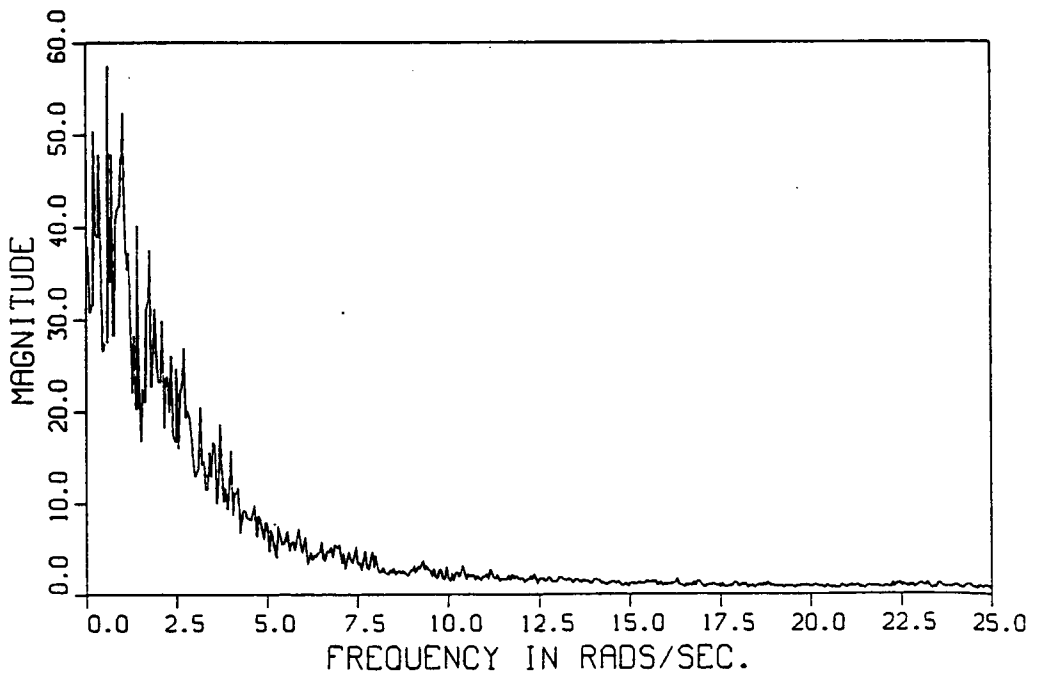

Figure 9.20: Disturbance DFT Bounding Function $\overline{\overline{D}}_N(\omega_k)$ for N=1000.

9.2.8 Description of the Input/Reference Signal

In this brief subsection, we describe the chirp-like signals that will be used as the plant input signal in the open-loop simulations and as the reference signal in the closed-loop simulations. In the open-loop simulations, the plant input signal u[n] will be generated as follows

$$u[n] = \begin{cases} +1, & \text{if } \sin(\rho \bullet (n \text{ modulo } N_f)^2) \geq 0 \text{ and } n \geq 0, \\ -1, & \text{if } \sin(\rho \bullet (n \text{ modulo } N_f)^2) < 0 \text{ and } n \geq 0, \\ 0, & \text{if } n < 0. \end{cases} \quad (9.2.33)$$

where N_f=1000 and where

$$\rho = \pi / (2\, N_f) = \pi / 2000 = 0.0015708 \quad (9.2.34)$$

This signal is shown in Figure 9.21 for time indices n=0 to 250 (31.42 secs.). At the time indices just before n=1000 (125.66 secs.), u[n] oscillates between -1 and +1 changing every sample time. Thus, just before n=1000 the input signal oscillates with frequency $\omega_s/2$. The magnitude of the DFT of the input signal, $|U_N^n(\omega_k)|$, is shown in Figure 9.22 for N=N_f=1000 and n=N-1=999.

We make several observations concerning this signal. First, since u[n] is periodic with period N_f, we find that $U_{Nf}^n(\omega_k) = U_{Nf}^{n-p}(\omega_k)$ for p=1,..,M-1 when $n \geq N_f$-1+M-1. This means that the frequency-domain bounding method can work well since $\overline{E}_{Nf}^n(\omega_k)$ in Eqn. (5.2.4) reduces to $\overline{E}_{rem}$ for $n \geq N_f$-1+M-1. Secondly, we observe that u[n] has energy at all frequencies, as can be seen in Figure 9.22. In the open-loop simulations, we will see that u[n] is rich enough for the robust estimator to yield useful information. We also note that u[n] has energy at high frequencies that will excite the unmodeled dynamics. So this input signal will exercise the part of the time-domain bounding mechanism that bounds the effect of high-frequency signals interacting with the unmodeled dynamics. Lastly, we observe from Eqn. (9.2.33) that assumption AD3.1 of Section 3.6 is satisfied as follows for the open-loop simulations.

$$|u[n]| \leq u_{max} = 1, \forall n. \quad (9.2.35)$$

The reference signal r[n] that will be used in the closed-loop simulations will be a scaled version of the signal given by Eqn. (9.2.33). The reference signal will be discussed further in Subsection 9.6.2.

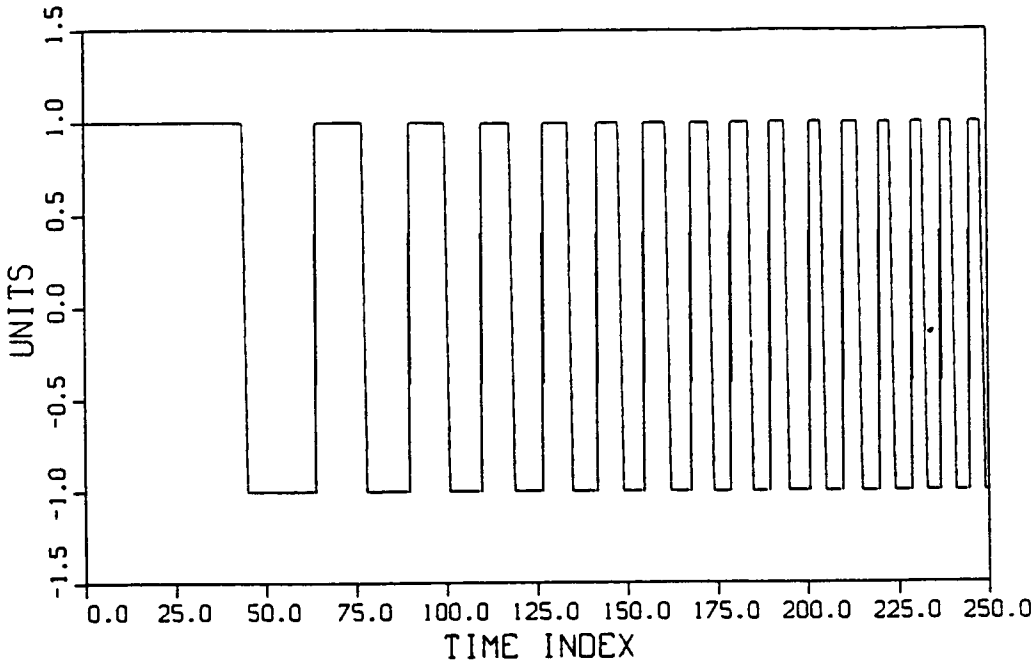

Figure 9.21: Open-loop Plant Input Signal u[n].

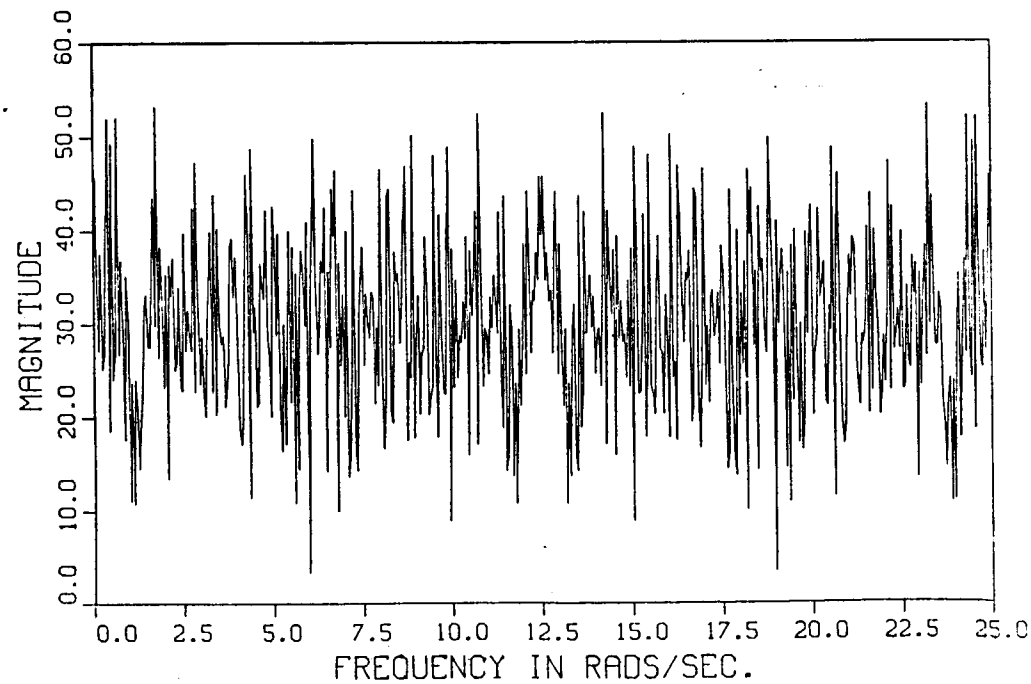

Figure 9.22: Input Signal DFT Magnitude $|U_N^n(\omega_k)|$ for N=1000 and n=999.

9.2.9 Projecting the Parameter Vector Estimate onto the Parameter Space Θ

In this subsection, we will describe a feature that will be used in both the time-domain and the frequency-domain parameter estimators. This feature is necessary since both of our parameter estimators estimate the three discrete-time parameters, a_1, a_2 and b_0, which depend on only two continuous-time parameters, ζ and ω_n. Note that the fourth discrete-time parameter, b_1, is a linear function of the other three discrete-time parameters as is shown in Eqn. (9.2.8). The point is that our parameter estimators do not include the nonlinear relationships of Eqns. (9.2.5-7) and thus they can yield estimates that are not in the set Θ. However, we know that the estimate of the parameter vector should be in the set Θ, since the true parameter vector is, that is, $\theta_0 \in \Theta$. To eliminate this discrepancy, we take the raw result of the parameter estimator and project it onto the set Θ. To find this set we plot the discrete-time plant parameters a_1, a_2 and b_0 for the 101 grid points discussed in Subsection 9.2.1. Since these three parameters vary with only two variables, ζ and ω_n, the set Θ is a 2-dimensional surface in $\mathbf{R}^3$. The 101 grid points are shown in Figure 9.23. We also show, for perspective, a prism that contains Θ. To project the raw parameter vector estimate onto the set Θ we will choose the grid point in Θ that is closest to the parameter vector estimate in the sense of the following measure of distance,

$$\text{Distance} = \sqrt{[\,(a_1^* - \hat{a}_1)/\Delta a_1\,]^2 + [\,(a_2^* - \hat{a}_2)/\Delta a_2\,]^2 + [\,(b_0^* - \hat{b}_0)/\Delta b_0\,]^2} \qquad (9.2.36)$$

where the 'starred' quantities represent the elements of the parameter vector at a grid point and

$$\Delta a_1 = 0.26501,\ \Delta a_2 = 0.23546 \text{ and } \Delta b_0 = 0.54354 \qquad (9.2.37)$$

This measure of distance normalized the individual parameter distances by the maximum variation of that parameter over the 101 grid points. This is a simple first-order correction to compensate for the fact that some parameters vary more than others.

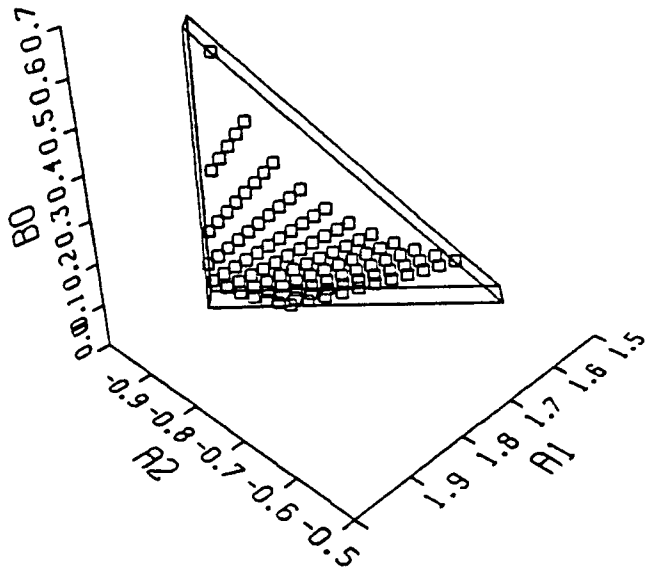

Figure 9.23: The Parameter Space Θ with 101 Grid Points.

9.3 Open-loop Simulations of the Time-domain Parameter Estimator

In this section, we will present our simulation results of the dead-zone based, time-domain parameter estimator of Chapter 4. Specifically, we will simulate the time-domain parameter estimator in three situations: 1) an ideal case, 2) an unmodeled dynamics only case, and 3) a disturbance only case. Later, in Section 9.5, we will simulate the robust estimator that uses the time-domain parameter estimator, in the presence of "both" unmodeled dynamics and a disturbance. This simulation will be a logical follow-on to the simulations of the present section, in which we examine the "individual" effects of unmodeled dynamics and a disturbance. In Chapter 8, we simulated the time-domain bounding mechanism that is used in the robustified time-domain parameter estimator that we study in this section. Recall that the time-domain parameter estimator is one of the two ways that we can generate parameters for the nominal model.

The main purposes of the following simulations are: 1) to see how tight the time-domain bounds on the various equation error signals are, and 2) to see how the individual effects of unmodeled dynamics and a disturbance degrade the performance of the time-domain parameter estimator relative to the ideal case. One of the major conclusions of this section, is that the dead-zone based time-domain parameter estimator performs poorly in the presence of the relatively mild case of unmodeled dynamics that is used here. This is discussed further in the conclusions. Before we present the actual simluation results, we must complete the preparations for the time-domain parameter estimator.

9.3.1 Preparation for the Time-domain Parameter Estimator

In this subsection, we will complete the preparations and a priori calculations for the time-domain parameter estimator of Chapter 4. Specifically, we will compute the various frequency and time domain bounding functions that are required by the time-domain parameter estimator. In addition, in this subsection we modify the parameter estimator to include a priori knowledge of the continuous-time plant.

Off-line Computation of $\overline{H}_d(e^{j\omega_k T})$

Recall that $\overline{H}_d(e^{j\omega_k T})$ is the magnitude bounding function on the transfer function from the disturbance d[n] to the equation error $e_1[n]$. Using Eqns. (3.6.4) and (9.2.4), we find that

$$A(z,\theta) = 1 - a_1 z^{-1} - a_2 z^{-2} \tag{9.3.1}$$

and from Eqns. (4.3.3) and (9.2.13)

$$H_d(z,\theta) = A(z,\theta)\,F(z) = \frac{0.052881\,(z^2 - a_1 z - a_2)}{z^2 - 1.64799\,z + 0.70087} \qquad (9.3.2)$$

where a_1 and a_2 are parameters in the vector θ that vary according to Eqns. (9.2.5-6). The magnitude bounding function on $\overline{H}_d(e^{j\omega_k T})$, which was defined in Eqn. (4.3.5), was computed by finding the maximum magnitude of $|H_d(e^{j\omega_k T},\theta)|$ at each frequency over the 101 point parameter grid that was described in Subsection 9.2.1. Thus, we had to compute (N/2)+1=501 maximums, each being a maximum over 101 points. The bounding function $\overline{H}_d(e^{j\omega_k T})$ is shown in Figure 9.24. Noting that the vertical scale in this figure doesn't begin at zero, we see that the bounding function doesn't change much with frequency, since it is always between 0.53 and 0.60. Thus, the error signal $e_3[n]$ will be approximately a scaled version of the disturbance d[n].

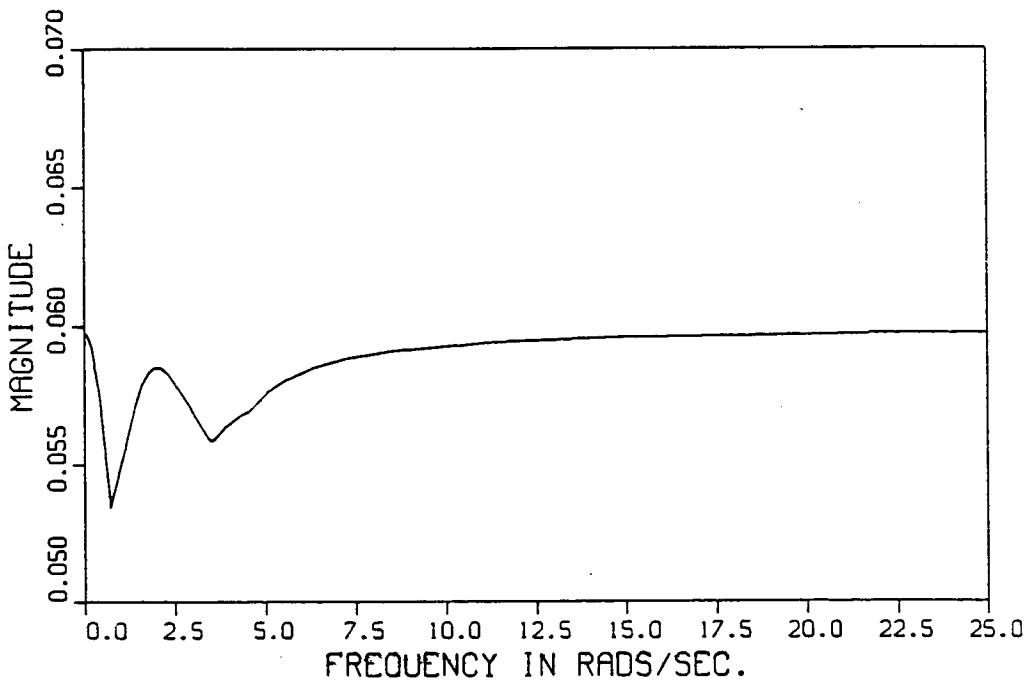

Figure 9.24: Frequency-domain Bounding Function $\overline{H}_d(e^{j\omega_k T})$.

Off-line Computation of the Impulse Response Bounding Function $\overline{h}_d[n]$

Recall that $\overline{h}_d[n]$ is the bounding function on the impulse response from the disturbance d[n] to the equation error $e_1[n]$. From Eqn. (9.3.2) we find that the impulse response $h_d[n,\theta]$, which corresponds to the transfer function $H_d(z,\theta)$, is given by

$$h_d[n,\theta] = 0.052881 \{ \delta[n] + 6.75685 [(1.64799 - a_1) (0.83718)^n \sin(0.17772\, n) u_{-1}[n-1] + (-0.70087 - a_2) (0.83718)^{(n-1)} \sin(0.17772\, (n-1)) u_{-1}[n-2]] \} \quad (9.3.3)$$

where $\delta[n]$ and $u_{-1}[n-1]$ denote the unit impulse and unit step, respectively. For the parameter variations described in Subsection 9.2.1, it can be shown that

$$a_1 \in [1.61716, 1.88217] \text{ and } a_2 \in [-0.90436, -0.66890]. \quad (9.3.4)$$

Using Eqns. (9.3.3-4) we find that

$$|h_d[n,\theta]| \leq 0.052881\, \delta[n] + 0.17052\, (0.83718)^n\, u_{-1}[n-1]. \quad (9.3.5)$$

This bounding function is not very tight so we will use some of the cases that were described in Subsection 9.2.4 to find a tighter bounding function. Consider the two cases:

Case A: $\zeta = 0.2$ and $\omega_n = 2$ rads/sec. $\Rightarrow a_1 = 1.84458$ and $a_2 = -0.90436$ (9.3.6)

Case B: $\zeta = 0.8$ and $\omega_n = 1$ rad/sec. $\Rightarrow a_1 = 1.80358$ and $a_2 = -0.81786$ (9.3.7)

Case A corresponds to the nominal model parameters for Cases 1-3 of Subsection 9.2.1 and Case B corresponds to the nominal model parameters for Case 4 of Subsection 9.2.1. In Figure 9.25, we show $h_d[n,\theta]$ for Cases A and B, along with the empirically chosen bounding function $\overline{h}_d[n]$ where

$$|h_d[n,\theta]| \leq \overline{h}_d[n] = g\, p^n, \text{ for } n \geq 0, \quad (9.3.8)$$

and

$$g = 0.06 \text{ and } p = 0.83718 \quad (9.3.9)$$

Thus, this bounding function is valid for all of the cases that we will be simulating. It is about a factor of 3 smaller than the bounding function that is computed via Eqn. (9.3.5).

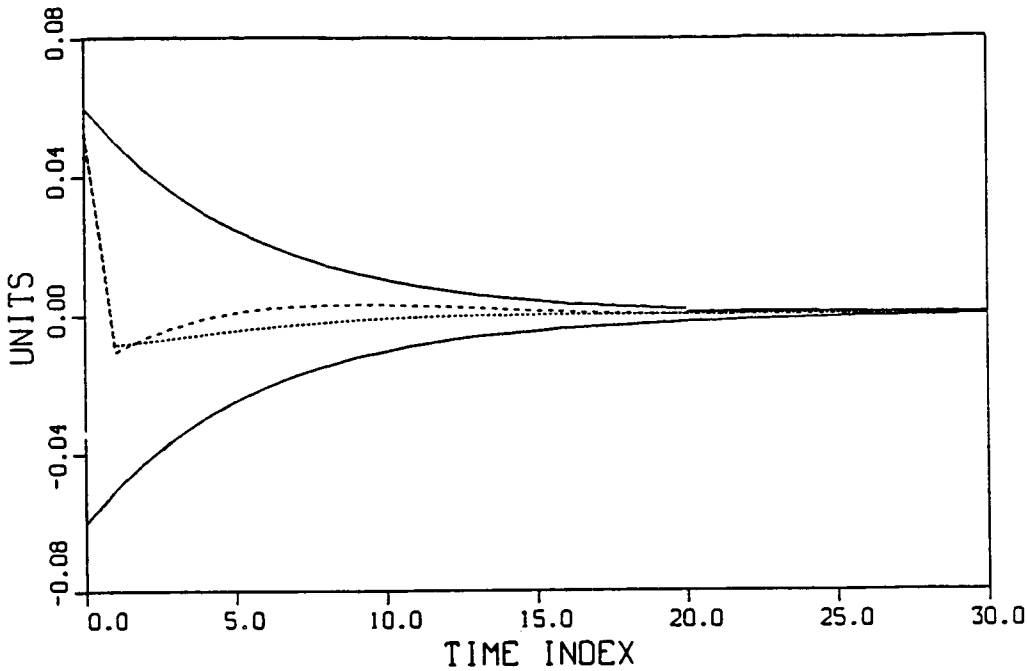

Figure 9.25: Impulse Response $h_d[n,\theta]$ for Cases A and B, and Bounding Function $\overline{h}_d[n]$.

($\overline{h}_d[n]$ and $-\overline{h}_d[n]$ = ——, $h_d[n,\theta]$ for Case A = - - - - , $h_d[n,\theta]$ for Case B = ...)

Off-line Computation of the Error Bound $\overline{e}_3[n]$

The constant $\overline{e}_3$ that bounds the steady-state effect of the disturbance in the error signal $e_1[n]$ is computed using Eqn. (4.3.13). To compute this bound we use the bounding function $\overline{\overline{D}}_N(\omega_k)$ for $N=N_t=20$, which can be empirically generated as was described in Subsection 9.2.7. Eqn. (4.3.13) yields

$$\overline{e}_3 = 0.130760 \cdot d_{factor} \tag{9.3.10}$$

We can bound the remainder term of Eqn. (4.3.13) using Eqns. (4.3.12), (9.2.32) and (9.3.8-9), as shown.

$$2\, d_{max} \sum_{p=N_t}^{\infty} \overline{h}_d[p] \le 2 \cdot d_{factor} \cdot 0.06\, (0.83718)^{20} / (1 - 0.83718) = 0.021079 \cdot d_{factor} \tag{9.3.11}$$

So, the remainder term is about a sixth of the value of the steady-state bound itself.

The time-varying bound $\overline{e}_3[n]$ that is used during the start-up period from n=0 to N_t-2 is computed off-line using Eqn. (4.3.11). It can then be stored for use on-line. To compute this time-varying bound we use the family of bounding functions, $\overline{D}_N^{+n}(\omega_k)$, corresponding to n=0 to N_t-2, which can be empirically generated as was described in Subsection 9.2.7.

Off-line Computation of the Bounding Function $\overline{H}_u(e^{j\omega_k T})$

Recall that $\overline{H}_u(e^{j\omega_k T})$ is the magnitude bounding function on the transfer function from the input u[n] to the equation error $e_1[n]$. This bounding function is used to compute a bound on the effect of the unmodeled dynamics on the equation error. Using Eqns. (3.6.3) and (9.2.4), we find that

$$B(z,\theta) = b_0 z^{-1} + b_1 z^{-2} \tag{9.3.12}$$

and from Eqns. (4.4.1) and (9.2.13),

$$H_u(z,\theta) = B(z,\theta) F(z) \delta_u(z) = \frac{0.052881 (b_0 z + b_1)}{z^2 - 1.64799 z + 0.70087} \delta_u(z). \tag{9.3.13}$$

where b_0 and b_1 are parameters in the vector θ that vary according to Eqns. (9.2.7-8). As for $\overline{H}_d$, we compute the magnitude bounding function on $\overline{H}_u(e^{j\omega_k T})$, which was defined in Eqn. (4.4.3), by finding the maximum magnitude of $|H_u(e^{j\omega_k T},\theta)|$ at each frequency over the 101 point parameter grid described in Subsection 9.2.1. The bounding function $\overline{H}_u(e^{j\omega_k T})$ is shown in Figure 9.26.

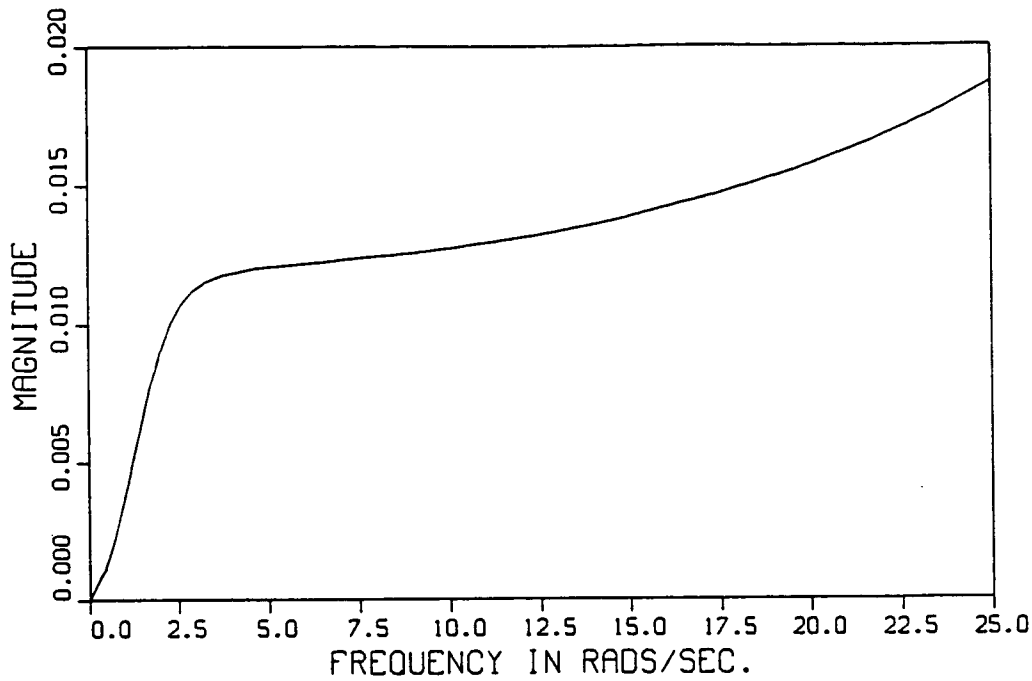

Figure 9.26: Frequency-domain Bounding Function $\overline{H}_u(e^{j\omega_k T})$.

Off-line Computation of the Impulse Response Bounding Function $\overline{h}_u[n]$

Recall that $\overline{h}_u[n]$ is the bounding function on the impulse response from the input u[n] to the equation error $e_1[n]$. This bounding function is used to compute a bound on the effect of the unmodeled dynamics on the equation error. We must find a magnitude bound on the impulse response $h_u[n,\theta]$ corresponding to the transfer function $H_u(z,\theta)$. Instead of using the results of Subsection 4.4.2, which will yield a conservative bound, we will again make use of the cases that were described in Subsection 9.2.4. In Figure 9.27, we show $h_u[n,\theta]$ for Cases 2-4, along with the empirically chosen bounding function $\overline{h}_u[n]$ where

$$|h_u[n,\theta]| \leq \overline{h}_u[n] = g\,p^n, \text{ for } n \geq 0, \tag{9.3.14}$$

and

$$g = 0.015 \text{ and } p = 0.83718 \tag{9.3.15}$$

This bounding function is valid for all of the cases that we will be simulating.

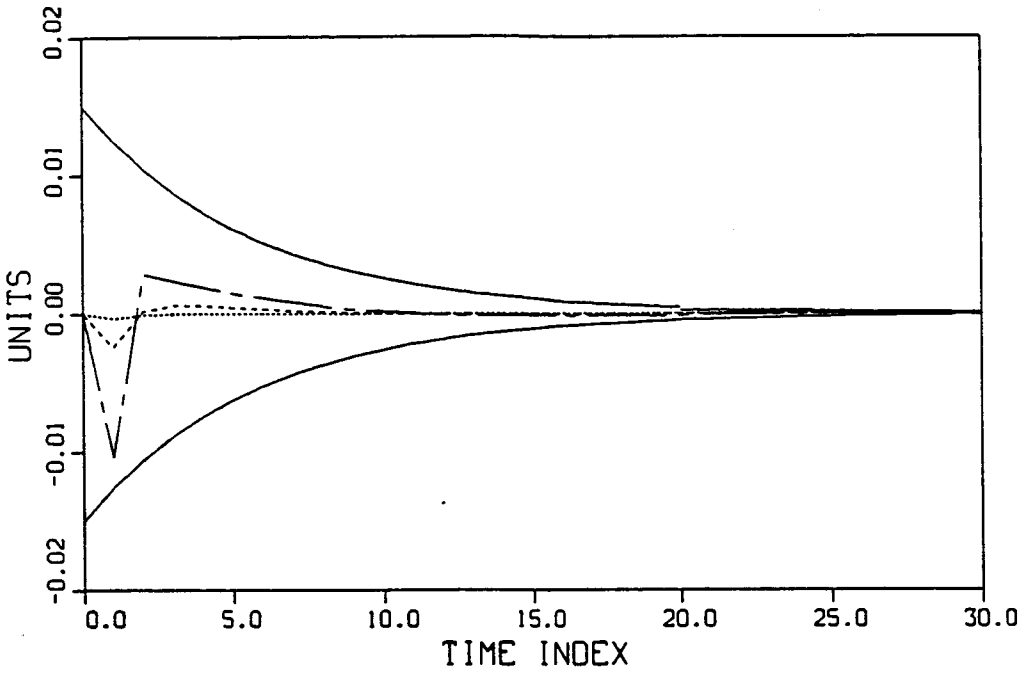

Figure 9.27: Impulse Response $h_u[n,\theta]$ for Cases 2-4, and Bounding Function $\overline{h}_u[n]$.

($\overline{h}_u[n]$ and $-\overline{h}_u[n]$ = ——, $h_u[n]$ for Case 2 = - - - - , $h_u[n]$ for Case 3 = — — — ,
$h_u[n]$ for Case 4 = ...)

Preparation for the On-line Computation of the Time-varying Error Bound $\overline{e}_2[n]$

The time-varying bounding function $\overline{e}_2[n]$ that bounds the effect of the unstructured uncertainty in the error signal $e_1[n]$, is computed on-line using Eqn. (4.4.23). The bounding function of Figure 9.26 and the magnitude of the input signal DFT, $U_N^n(\omega_k)$, which is computed on-line, are used to compute the time-varying bound. We can bound the remainder term of Eqn. (4.4.23) using Eqn. (9.3.14-15), the facts that u_{max}=1 and N_t=20, and the results of Appendix C as shown.

$$2\,u_{max} \sum_{p=N_t}^{\infty} \overline{h}_u[p] \le 2 \bullet 0.015\,(0.83718)^{20} / (1 - 0.83718) = 0.0052698 \qquad (9.3.16)$$

This remainder term is small compared to the values of the time-varying bound $\overline{e}_2[n]$ that we will

observe in the simulations. The on-line computational requirements for computing $\overline{e_2}[n]$ are quite small compared to the requirements of the frequency-domain bounding part of the robust estimator. With reference to Eqn. (4.4.23), we only have to perform about $N_t/2=5$ multiplications and additions at each sample time. Of course, we also must compute the N_t-point DFTs of the input and output signals; however, these computations are easily implemented using the recursion of Eqn. (2.1.11).

Modification of the Time-domain Parameter Estimator Based on a priori Information

The time-domain parameter estimator that was described in Chapter 4 could be used to find estimates of the four parameters, a_1, a_2, b_0 and b_1. However, from our problem description of Subsection 9.2.1, we know that the D.C. gain of the nominal plant $G^c(s,\theta^c)$ is unity for all θ^c in Θ^c. Further, since the high-frequency unmodeled dynamics are assumed to have no effect on the D.C. gain of the plant in our problem, we see that the D.C. gains of the continuous and discrete-time plants are unity. This means that the four parameters of the discrete-time plant are not independent. Using Eqn. (9.2.4) and the fact that G(z)=1 for z=1, we know that

$$b_1 = 1 - a_1 - a_2 - b_0 \tag{9.3.17}$$

as was previously noted in Eqn. (9.2.8). This a priori known constraint allows us to use a parameter estimator that only estimates the three parameters, a_1, a_2 and b_0. We will now derive a modified form of the linear regression equation that describes the plant by incorporating this constraint. Using Eqns. (4.2.17) and (9.3.17), we see that

$$\begin{aligned} y_f[n] &= \phi_f[n-1]^T\theta_0 + e_1[n] = a_1\, y_f[n-1] + a_2\, y_f[n-2] + b_0\, u_f[n-1] + b_1\, u_f[n-2] + e_1[n] \\ &= a_1 (y_f[n-1] - u_f[n-2]) + a_2 (y_f[n-2] - u_f[n-2]) + b_0 (u_f[n-1] - u_f[n-2]) + u_f[n-2] + e_1[n]. \end{aligned} \tag{9.3.18}$$

Rewriting this equation yields

$$(y_f[n] - u_f[n-2]) =$$

$$a_1 (y_f[n-1] - u_f[n-2]) + a_2 (y_f[n-2] - u_f[n-2]) + b_0 (u_f[n-1] - u_f[n-2]) + e_1[n] \tag{9.3.19}$$

which can be expressed as

$$y_{fm}[n] = \phi_{fm}[n-1]^T\theta_{0m} + e_1[n] \tag{9.3.20}$$

where

$$y_{fm}[n] = y_f[n] - u_f[n-2] \tag{9.3.21}$$

$$\phi_{fm}[n-1] = [\ (y_f[n-1] - u_f[n-2])\ \ (y_f[n-2] - u_f[n-2])\ \ (u_f[n-1] - u_f[n-2])\ ]^T \tag{9.3.22}$$

$$\theta_{0m} = [\ a_1\ \ a_2\ \ b_0\ ]^T \tag{9.3.23}$$

and where the subscript 'm' stands for 'modified' form of the parameter estimator. In the following simulations the modified linear regression of Eqns. (9.3.20-23) will be used. For the sake of clarity we will drop the subscript 'm' notation throughout the discussion of the following simulations. That is, in the various figures the modified output of Eqn. (9.3.21) and the modified parameter vector of Eqn. (9.3.23) will be referred to as $y_f[n]$ and θ_0, respectively.

Choice of Algorithm Constants for the Time-domain Parameter Estimator

In the dead-zone based, time-domain parameter estimator of Chapter 4, there are several constants that must be chosen. With reference to the algorithm of Section 4.5, we choose α=0.50 and, hence, β=1.4142. The constant α multiplies the additive update to the parameter vector estimate so we call it the adaptation gain. The constant β multiplies the dead-zone width. The larger β is, the less often the parameter estimates are updated. As discussed in Remark 1 of Section 4.5, we choose these values as a result of a trade-off between the adaptation gain α and the size of the dead-zone as controlled by the parameter β. In the regularized constant trace modification to the least-squares algorithm, which is described in Subsection 4.5.3, we choose the constants c_0=10 and c_1=30.

Subsection Summary

In this preparatory subsection, we have developed all of the necessary bounding functions and computed all of the necessary quantities for use of the robustified time-domain parameter estimator of Chapter 4. In the following subsections we will use this information to simulate the parameter estimator.

9.3.2 Simulations of the Time-domain Parameter Estimator

In this subsection, we will simulate the time-domain parameter estimator of Chapter 4 using the modification discussed in Subsection 4.5.3. Thus, we simulate the robustified least-squares parameter estimator with the regularized constant trace modification. The chirp-like input signal u[n] of Subsection 9.2.8 will be used in all of the simulations in this subsection. We shall perform simulations of the time-domain parameter estimator for three cases: 1) ideal case, with no disturbance or unmodeled dynamics, 2) unmodeled dynamics only case, with no disturbance, and 3) disturbance only case, with no unmodeled dynamics. The case of both unmodeled dynamics and a disturbance will be simulated later, in Subsection 9.5.2, when we consider the robust estimator as a whole.

Simulation 9.3.1: Ideal Case, No Disturbance, No Unmodeled Dynamics

For this simulation we will use Case 1 of Subsection 9.2.4, and will not introduce any disturbance. This situation of no unmodeled dynamics and no unmeasurable disturbance provides us with a baseline by which to judge the performance and behavior of the later simulations which will include the effects of unmodeled dynamics and an unmeasurable disturbance. In this ideal case, we set-up the parameter estimator using the knowledge that the error signal $e_1[n]$ is always zero. Thus, the dead-zone mechanism is not used in the algorithm for this simulation.

For clarity of presentation, we define the individual parameter errors. Keeping with the notation of our definition of $\tilde{\theta}[n]$ in Eqn. (4.5.4), we define

$$\tilde{a}_1[n] = \hat{a}_1[n] - a_1 \tag{9.3.24}$$

$$\tilde{a}_2[n] = \hat{a}_2[n] - a_2 \tag{9.3.25}$$

$$\tilde{b}_0[n] = \hat{b}_0[n] - b_0 \tag{9.3.26}$$

where the 'hatted' variables represent the estimates. We now present our results.

In Figure 9.28, we show the input signal u[n] and the output signal y[n]. We note the large amplitude of the plant output when the input signal excites the resonance at 2 rads/sec. Beyond 15 secs., as the input signal frequency increases, the plant output response decreases in size, as expected. For the initial parameter estimates we used the values that correspond to the choice of ζ=0.8 and ω_n=1 rad/sec. These values are quite different from those of the true simulation plant, which are ζ=0.2 and ω_n=2 rads/sec. In Figure 9.29 we show the parameter errors as defined

above. For reference, we list the true values, initial estimates and initial errors of the parameters. In addition, we show the parameter errors at n=200 (25.13 secs.) and n=2500 (314.16 secs.).

Table 9.1: Parameter Estimates of the Time-domain Algorithm for the Ideal Case.

	θ_0	$\hat{\theta}[0]$	$\tilde{\theta}[0]$	$\tilde{\theta}[200]$	$\tilde{\theta}[2500]$
a_1	1.84458	1.80358	-0.04100	0.00488	0.0
a_2	-0.90436	-0.81786	0.08650	-0.00257	0.0
b_0	0.62189	0.07834	-0.54355	-0.00234	0.0

From Figure 9.29, we see that the parameter errors almost reach zero in 25 seconds. The simulation was run for a total of 314 seconds at which time the parameters had converged to zero, to within the numerical accuracy of the simulation. This simulation shows us how well the parameter estimator works for the ideal case of no disturbance and no unmodeled dynamics.

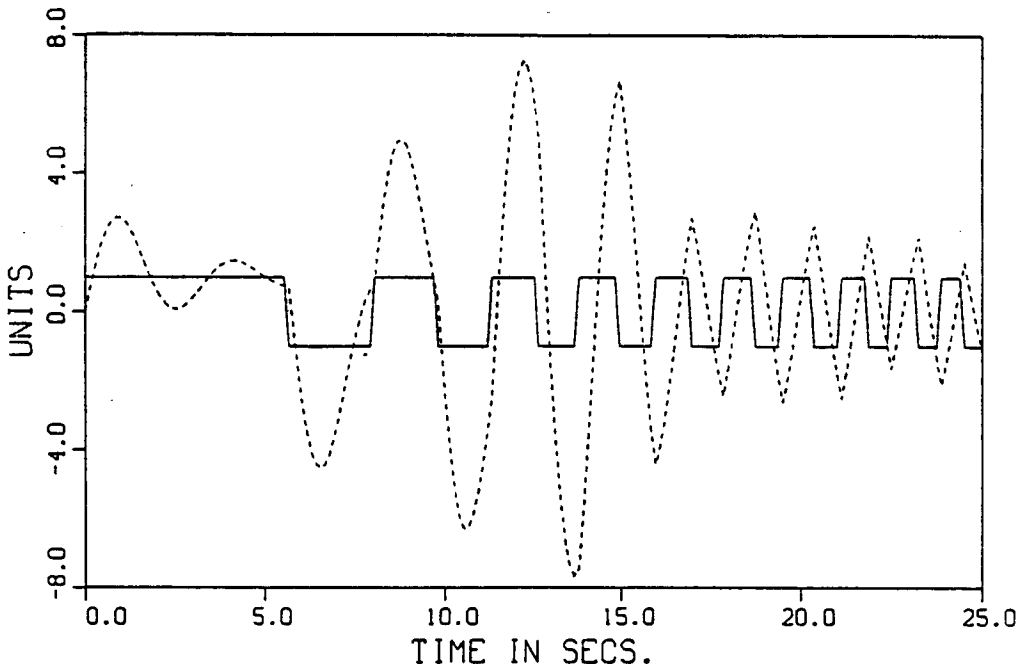

Figure 9.28: Parameter Estimator Simulation, u[n] and y[n] for Ideal Case.
(u[n] = ——, y[n] = - - - -)

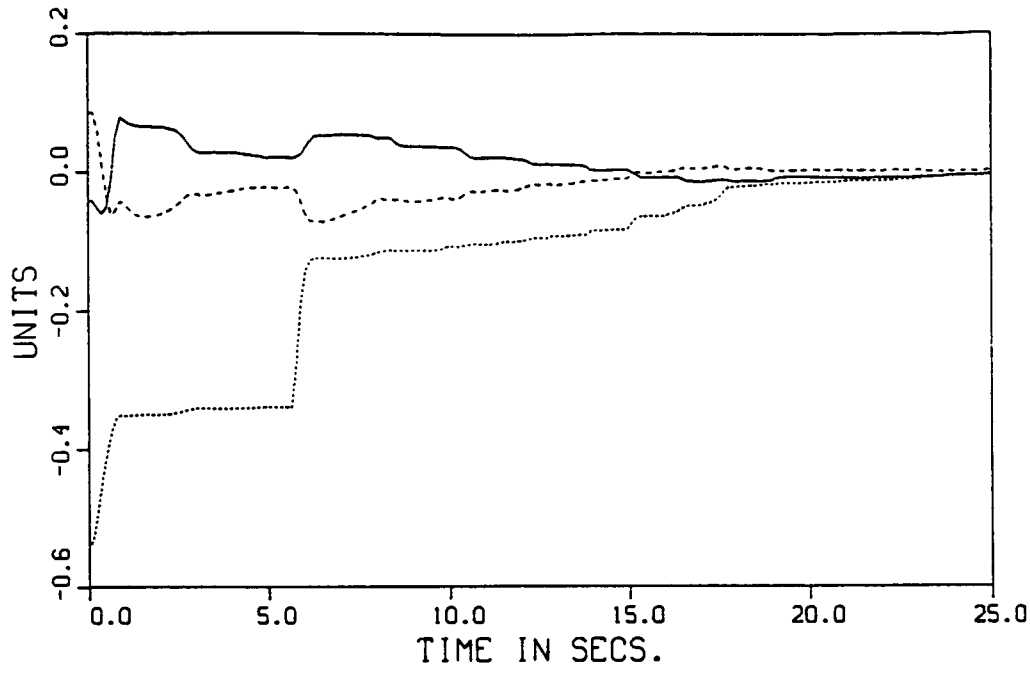

Figure 9.29: Parameter Errors for Ideal Case.

($\tilde{a}_1[n]$ = ——, $\tilde{a}_2[n]$ = - - - -, $\tilde{b}_0[n]$ = ...)

Simulation 9.3.2: Unmodeled Dynamics Case, No Disturbance

For this simulation we will use Case 3 of Subsection 9.2.4 and will not introduce any disturbance. That is, we use the case of time-delay unmodeled dynamics but no disturbance, so that we can isolate the effect of the unmodeled dynamics alone. For this simulation, we set-up the parameter estimator using the knowledge that the error signal $e_3[n]$, due to the disturbance, is always zero. Thus, the dead-zone mechanism is used only to bound the effect of unmodeled dynamics for this simulation. We now present our results.

The 0.04 sec. time delay has only a small effect on the plant output. The time histories of the input signal u[n] and the output signal y[n] are almost the same as those of Figure 9.28 and for this reason they are not shown. For the initial parameter estimates we again used the values that correspond to the choice of ζ=0.8 and ω_n=1 rad/sec. In Figure 9.30, we show the parameter errors. For reference, we list the true values, initial estimates and initial errors of the parameters. In addition, we show the parameter errors at n=200 (25.13 secs.) and n=2500 (314.16 secs.).

Table 9.2: Parameter Estimates of the Time-domain Algorithm for the Unmodeled Dynamics Case.

	θ_0	$\hat{\theta}[0]$	$\tilde{\theta}[0]$	$\tilde{\theta}[200]$	$\tilde{\theta}[2500]$
a_1	1.84458	1.80358	-0.04100	0.01115	0.02172
a_2	-0.90436	-0.81786	0.08650	-0.01921	-0.02789
b_0	0.62189	0.07834	-0.54355	-0.37421	-0.32506

Comparing Figures 9.29 and 9.30, we see that the parameter errors are quite large for the present simulation. Later, in the simulation of the robust estimator with the time-domain parameter estimator (see Section 9.5.2), we will see that the large estimation error for the b_0 parameter does indeed matter in the sense that it results in large frequency-domain errors. The above table shows that, even after a long time, the parameter estimates are still poor. We can understand this poor performance by looking at the operation of the dead-zone mechanism.

In Figure 9.31, we show the magnitude bound $\overline{e}_1[n]$ and the actual error signal $e_1[n]$, which is due entirely to the effects of unmodeled dynamics in this simulation. This figure reveals that the time-domain bounding mechanism is conservative. To provide a broader view of the operation of this time-domain bounding mechanism, we present Figure 9.32, which shows the magnitude bound $\overline{e}_1[n]$ and the actual error signal $e_1[n]$ for a duration 10 times longer than Figure 9.31. In this figure, the dips in the magnitude bound occur just after the input signal has the same period for at least N_t time samples. In this situation, the time-domain bounding mechanism sees a pure fundamental frequency resulting in a tight bound. In Figure 9.33, we show both the prediction error e[n] and the threshold signal $\beta\overline{e}_1[n]$. The dead-zone signal $\upsilon[n]$ of Subsection 4.5.2, is shown in Figure 9.34. Comparing Figures 9.33 and 9.34, we see how the dead-zone signal is nonzero only when the magnitude of the prediction error e[n] is larger than the threshold signal $\beta\overline{e}_1[n]$. Figure 9.34 shows us that the parameter estimator is turned off almost all of the time. Since the parameters are updated for only a few short time intervals, it is not surprising that the parameter estimator yields poor parameter estimates. This simulation reveals the poor performance of the dead-zone based parameter estimator for even a relatively mild case of unmodeled dynamics. It appears that the conservativeness of the time-domain bounding mechanism is a major contributor to this poor performance.

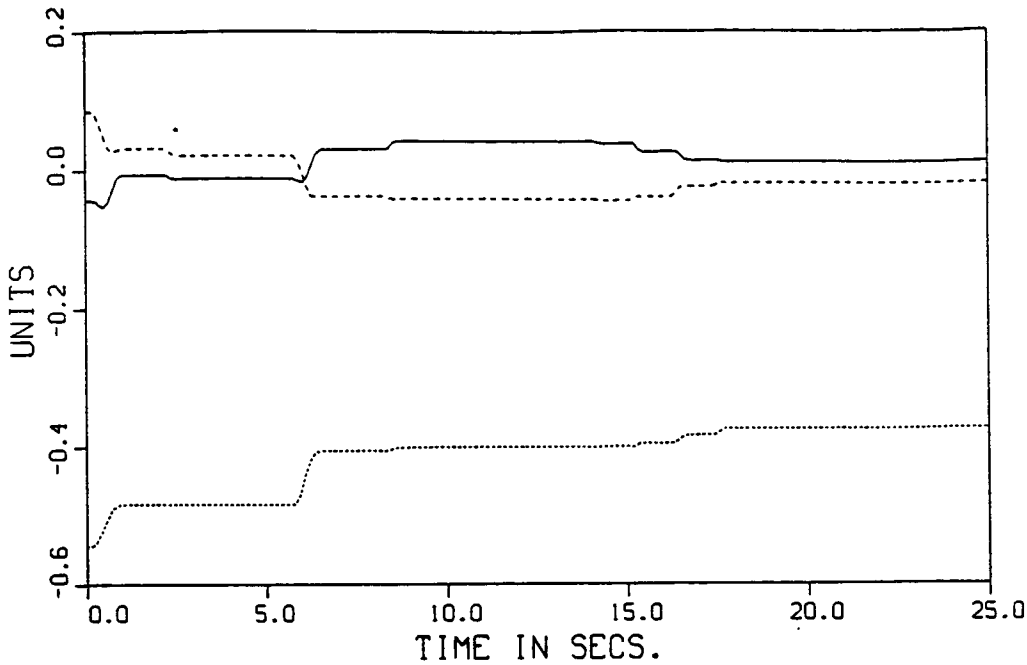

Figure 9.30: Parameter Errors for Unmodeled Dynamics Alone Case.

($\tilde{a}_1[n]$ = ——, $\tilde{a}_2[n]$ = - - - - , $\tilde{b}_0[n]$ = ...)

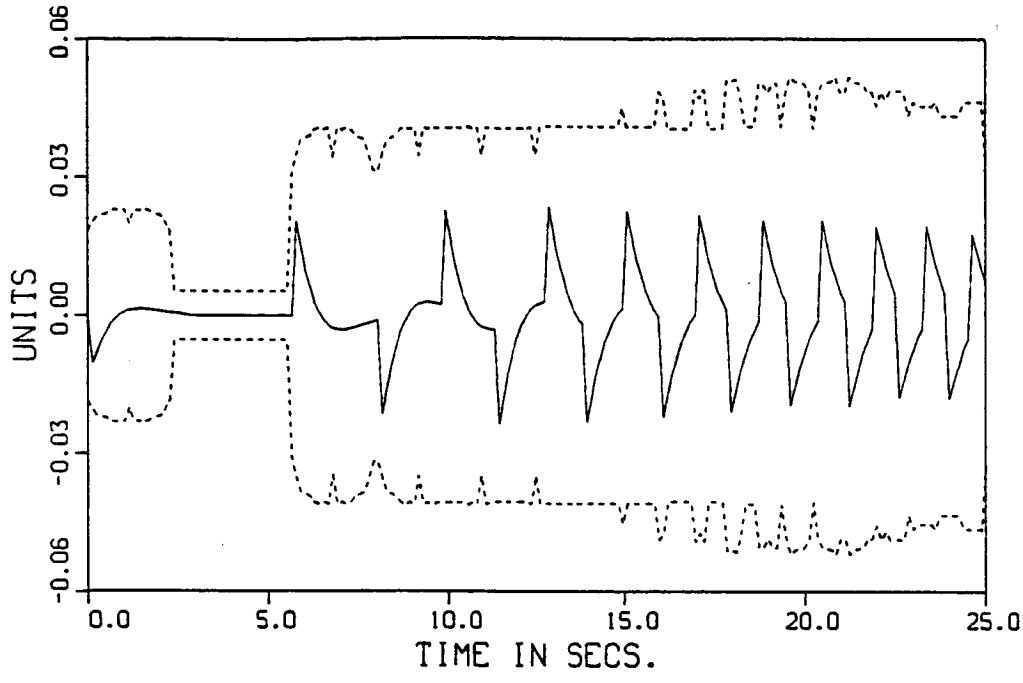

Figure 9.31: Error $e_1[n]$ and Bound $\overline{e}_1[n]$ for Unmodeled Dynamics Alone Case, Short Plot.

($e_1[n]$ = ——, $\overline{e}_1[n]$ and $-\overline{e}_1[n]$ = - - - -)

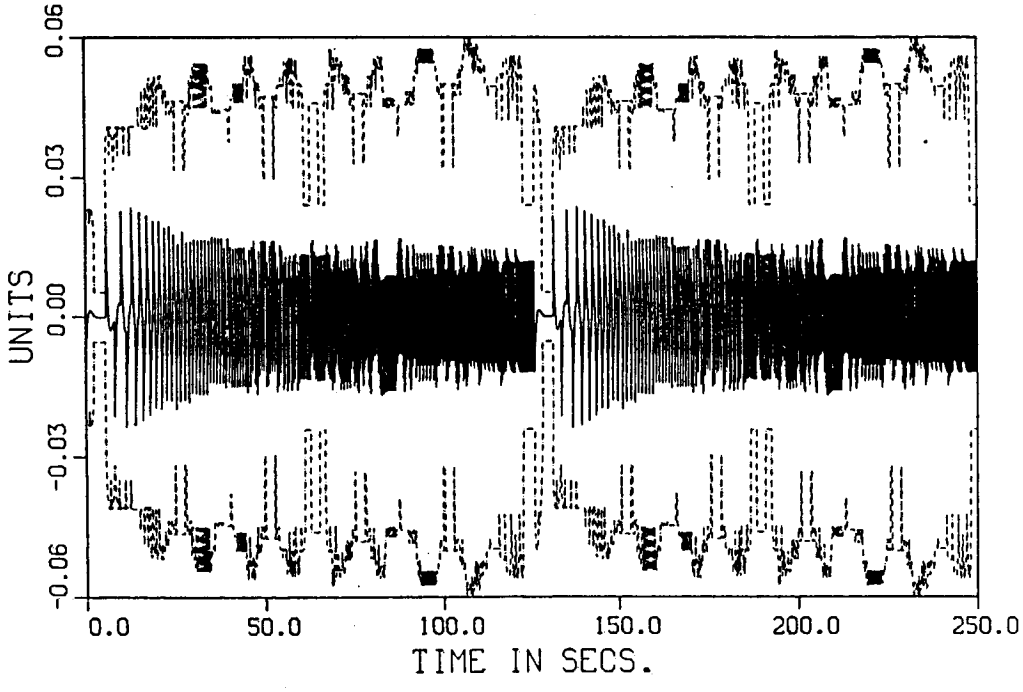

Figure 9.32: Error $e_1[n]$ and Bound $\overline{e}_1[n]$ for Unmodeled Dynamics Alone Case, Long Plot.

($e_1[n]$ = ——, $\overline{e}_1[n]$ and $-\overline{e}_1[n]$ = - - - -)

These figures show us the conservatism of our time-domain bound on $|e_1[n]|$, for this case.

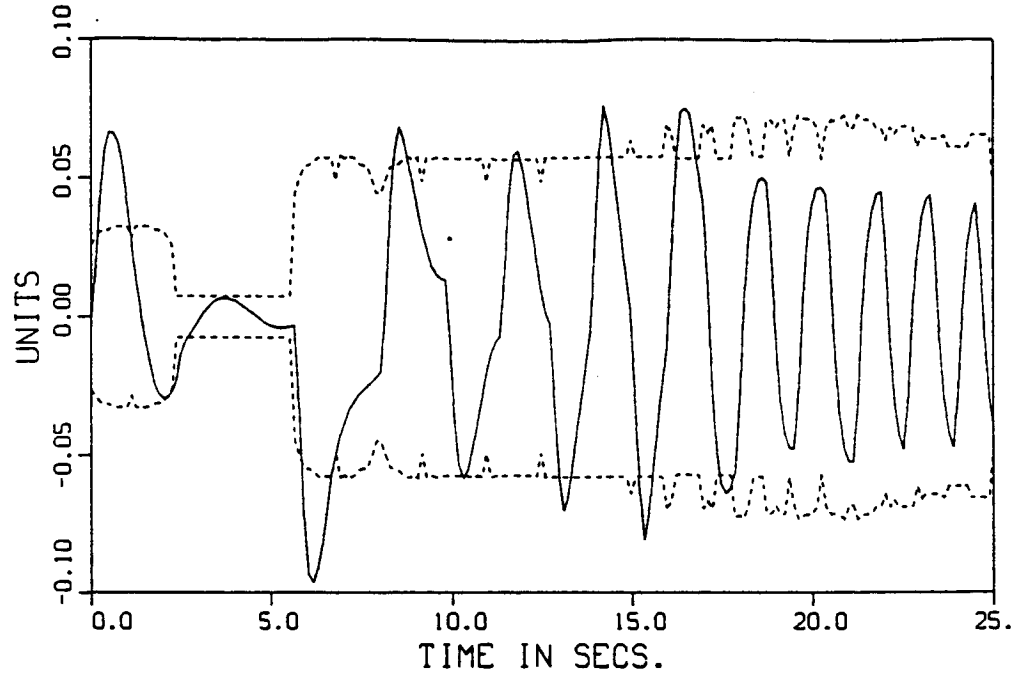

Figure 9.33: Prediction Error e[n] and Threshold $\beta\overline{e}_1[n]$ for Unmodeled Dynamics Alone Case.

(e[n] = ——, $\beta\overline{e}_1[n]$ and $-\beta\overline{e}_1[n]$ = - - - -)

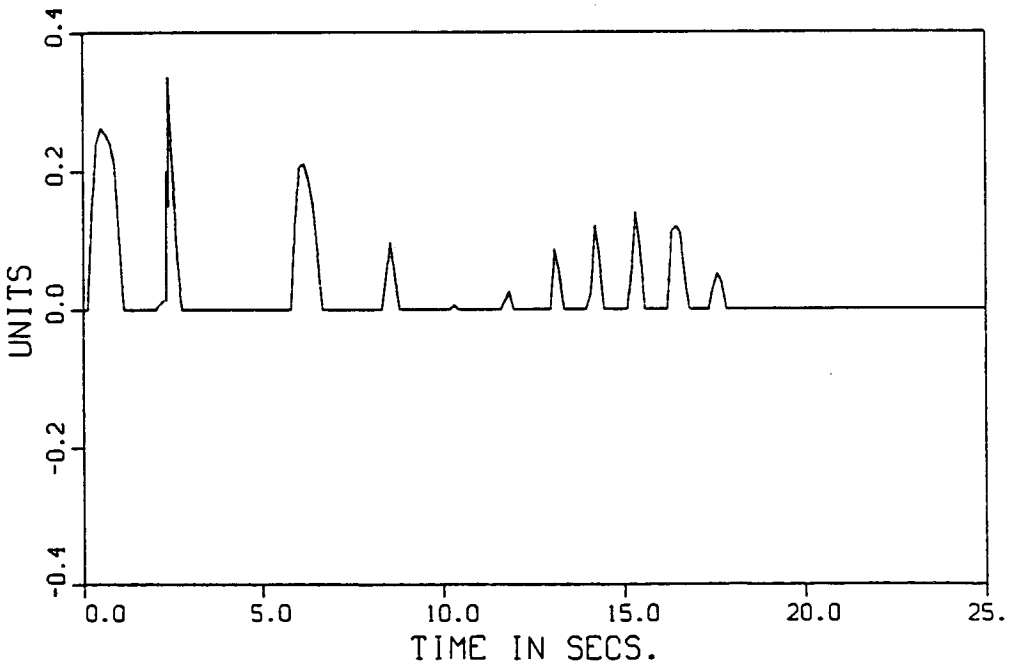

Figure 9.34: Dead-zone Signal $\upsilon[n]$ for Unmodeled Dynamics Alone Case.

The dead-zone signal is nonzero only when the magnitude of the prediction error is greater than the threshold signal.

Simulation 9.3.3: Disturbance Case, No Unmodeled Dynamics

For this simulation we will use Case 1 of Subsection 9.2.4, and will introduce a disturbance. That is, we use the case of no unmodeled dynamics, so that we can isolate the effect of the disturbance alone. For this simulation, we set-up the parameter estimator using the knowledge that the error signal $e_2[n]$, due to the unmodeled dynamics, is always zero. Thus, the dead-zone mechanism is used only to bound the effect of the disturbance for this simulation. The disturbance that was described in Subsection 9.2.6 will be used in this simulation with a scaling factor of d_{factor}=0.1. This is a small disturbance signal as can be seen from Figure 9.19, since for the first 25 secs. the disturbance magnitude doesn't even exceed 0.06, including the scaling factor. Recall that the input signal u[n] has unity magnitude. We now present our results.

The disturbance has only a small effect on the plant output, so the time histories of the input signal u[n] and the output signal y[n] are again almost the same as those of Figure 9.28. For the initial parameter estimates we again used the values that correspond to the choice of ζ=0.8 and ω_n=1 rad/sec. In Figure 9.35, we show the parameter errors. For reference, we list the true values, initial estimates and initial errors of the parameters. In addition, we show the parameter errors at n=200 (25.13 secs.) and n=2500 (314.16 secs.).

Table 9.3: Parameter Estimates of the Time-domain Algorithm for the Disturbance Case.

	θ_0	$\hat{\theta}[0]$	$\tilde{\theta}[0]$	$\tilde{\theta}[200]$	$\tilde{\theta}[2500]$
a_1	1.84458	1.80358	-0.04100	-0.02261	0.00681
a_2	-0.90436	-0.81786	0.08650	0.00255	-0.00822
b_0	0.62189	0.07834	-0.54355	-0.16399	-0.09797

Comparing Figures 9.29 and 9.35, we see that the parameter error is small for each of the parameters a_1 and a_2, but is still relatively large for b_0. The above table shows that even after a long time, the parameter estimate of b_0 is still not good. To gain insight, we investigate the operation of the dead-zone mechanism.

In Figure 9.36, we show the magnitude bound $\overline{e}_1[n]$ and the actual error signal $e_1[n]$, which is due entirely to the effects of the disturbance in this simulation. This figure reveals that the disturbance bound introduces considerable conservatism for this simulation. In Figure 9.37, we show both the prediction error e[n] and the threshold signal $\beta\overline{e}_1[n]$. The dead-zone signal $\upsilon[n]$ is shown in Figure 9.38. Comparing Figures 9.37 and 9.38, we again see how the dead-zone signal is nonzero only when the magnitude of the prediction error e[n] is larger than the threshold signal

$\beta\overline{e}_1[n]$. Figure 9.38 shows us that the parameter estimator is turned off for much of the time but not nearly as much as in the case of the previous simulation. Since the bound $\overline{e}_1[n]$ is overly conservative, the dead-zone disables the parameter estimator when there is still useful information in the input/output data. This simulation shows that the parameter estimator can perform marginally well when the disturbance is small.

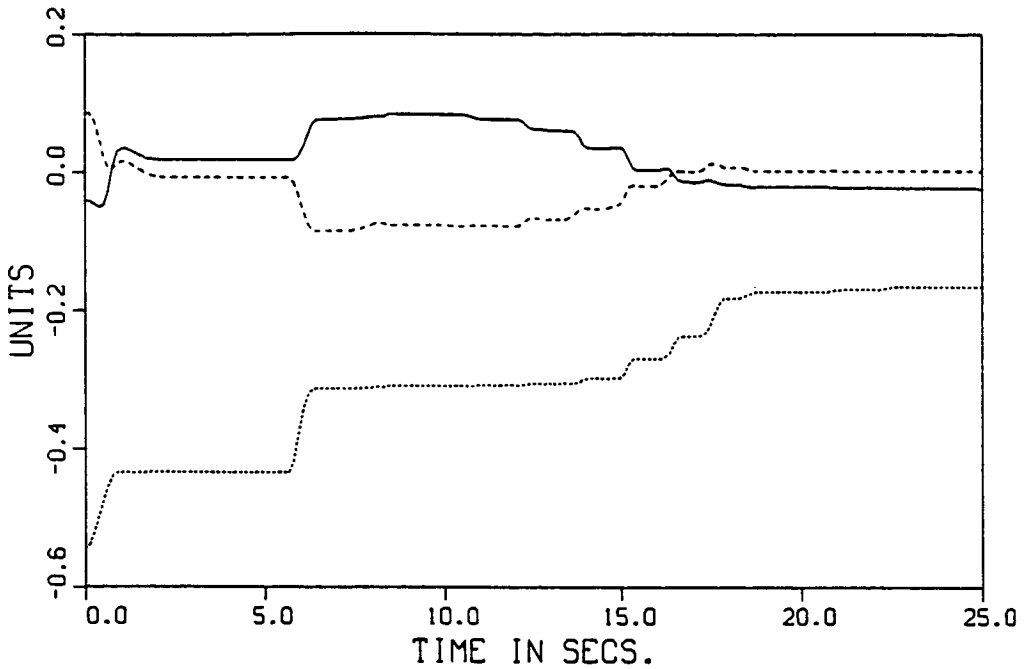

Figure 9.35: Parameter Errors for Disturbance Alone Case.

($\tilde{a}_1[n]$ = ——, $\tilde{a}_2[n]$ = - - - -, $\tilde{b}_0[n]$ = ...)

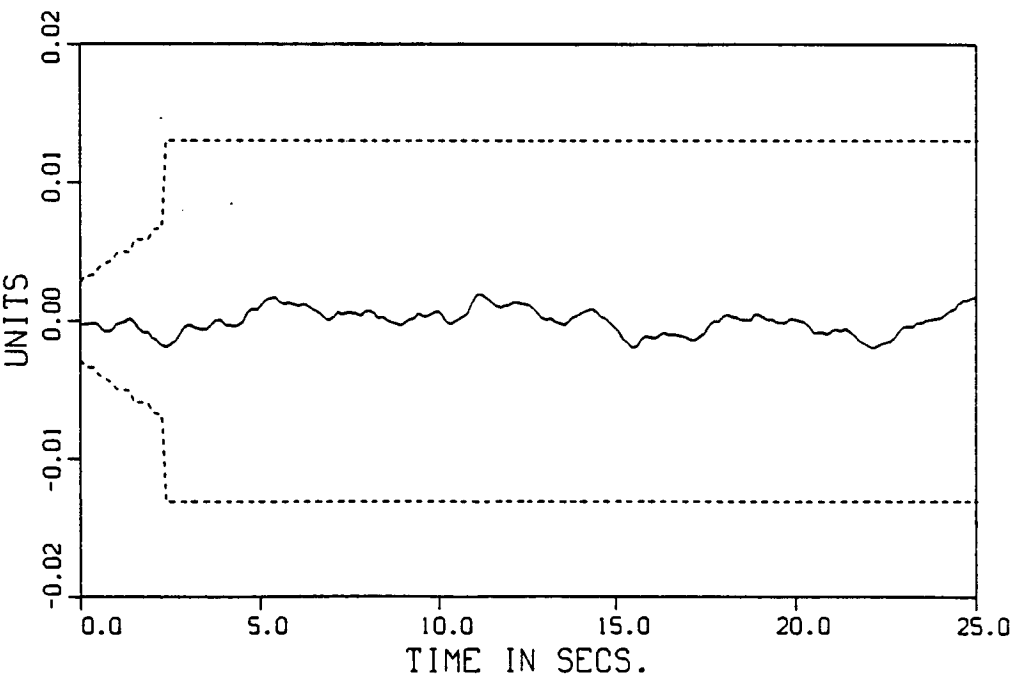

Figure 9.36: Error $e_1[n]$ and Bound $\overline{e}_1[n]$ for Disturbance Alone Case.

($e_1[n]$ = ——, $\overline{e}_1[n]$ and $-\overline{e}_1[n]$ = - - - -)

This figure show us the conservatism of our time-domain bound on $|e_1[n]|$, for this case.

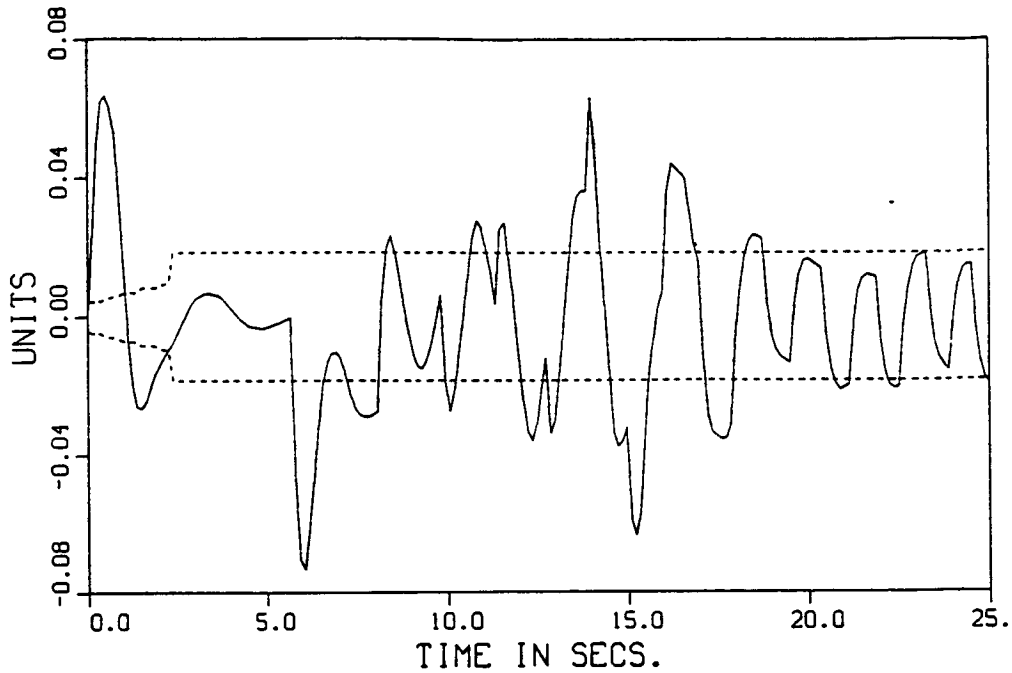

Figure 9.37: Prediction Error e[n] and Threshold $\beta\overline{e_1}[n]$ for Disturbance Alone Case.

(e[n] = ——, $\beta\overline{e_1}[n]$ and $-\beta\overline{e_1}[n]$ = - - - -)

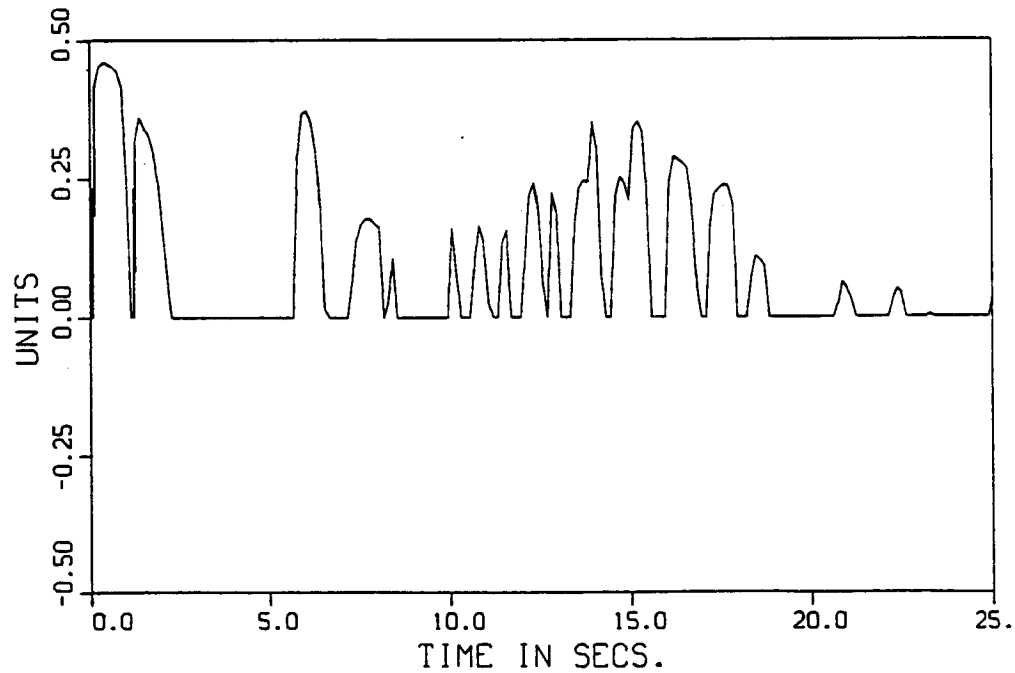

Figure 9.38: Dead-zone Signal $\upsilon[n]$ for Disturbance Alone Case.

The dead-zone signal is nonzero only when the magnitude of the prediction error is greater than the threshold signal.

9.3.3 Conclusion

In this section, we have studied the properties of the dead-zone based, time-domain parameter estimator, through the use of several simulations. We have examined the individual effects of unmodeled dynamics and a disturbance on the time-domain parameter estimator. Later, in the robust estimator simulation of Subsection 9.5.2, we will simulate the time-domain parameter estimator in the presence of both unmodeled dynamics and a disturbance. The understanding that was gained in the present section will help us to understand this later simulation of the complete robust estimator using the time-domain parameter estimator. We summarize our conclusions concerning the simulations of the present section.

1) The time-domain parameter estimator is frequently 'turned-off' for even a relatively mild case of unmodeled dynamics, thus resulting in poor parameter estimates.

2) The time-domain bounding mechanism can be very conservative in the case of a pseudo-random type of disturbance. Thus, the resulting disturbance bound will be conservative and will result in degraded parameter estimates.

The most important of these conclusions is the one concerning the poor performance of the dead-zone based parameter estimator for mild cases of unmodeled dynamics. It is the author's opinion that there exist some inherent difficulties with using a dead-zone approach to guard against the effects of unmodeled dynamics. Since the effects of the unmodeled dynamics vary greatly with frequency, it seems more appropriate to try to weed out their effects using a frequency-domain approach. To further justify this viewpoint, we present the following thought experiment.

Consider a disturbance-free situation in which the plant input signal contains some small sinusoidal component that produces some small sinusoidal component in the plant output signal. We assume that there are other, larger components of the input signal that drive the time-domain bounding mechanism of the parameter estimator, thus resulting in some large error bound. The large error bound will disable the parameter estimator. That is, the time-domain contribution of the small sinusoid is smaller than the time-domain signal due to the interaction of the total input signal with the unmodeled dynamics. However, a frequency transform of the data can still provide useful information at the frequency of the small sinusoidal component. Thus, from the point of view of the dead-zone based parameter estimator there is no useful information in the input/output data, but from a frequency-domain viewpoint there is. These arguments help justify our choice of the frequency-domain parameter estimator of Section 5.4 over the dead-zone based parameter estimator that was simulated in this chapter. Later, our simulation results for the frequency-domain parameter estimator will further justify this choice.

As a final note we emphasize that the dead-zone based parameter estimator is only one type of time-domain parameter estimator. We do not mean to imply that time-domain techniques are

inferior to frequency-domain techniques. We are only saying that the dead-zone based parameter estimator doesn't perform well, in our simulations.

9.4 Open-loop Simulations of the Frequency-domain Uncertainty Bounding Method

In this section, we will simulate the frequency-domain bounding method that was developed in Chapter 5. Specifically, we will implement the part of the robust estimator that generates the multiplicative uncertainty bounding function. However, we will use the actual values of the parameters in the nominal model. That is, the simulations of this section show how the robust estimator would work if the parameter estimator always gave the true parameters. Later, this will allow us to see how much conservatism is due to the frequency-domain bounding method itself, and how much is due to the parameter estimator. We will see that for our choices of the DFT length N_f and the memory length M, the frequency-domain bounding function yields a multiplicative uncertainty bounding function that is much less than unity and, hence, is useful for updating the control-law in a closed-loop adaptive control context. That is, we will see that the frequency-domain bounding method performs well. Before presenting the simulation results, we must take care of some preparations for the frequency-domain bounding method.

9.4.1 Preparation for the Frequency-domain Uncertainty Bounding Method

In this subsection, we will complete the preparations and a priori calculations for the frequency-domain uncertainty bounding method of Chapter 5. Specifically, we will compute the various frequency and time-domain bounding functions that are required by the frequency-domain uncertainty bounding method.

Computation of the Error Bounding Function

The error bounding function of Eqn. (5.2.4) will be computed using the on-line computed DFT of the input signal, $U_N^n(\omega_k)$, and the bounding function on the impulse response of the true plant, which is given by Eqns. (9.2.26-7). Recall that Eqn. (5.2.4) is the key equation that is used to compute the frequency-domain bounding function. The remainder term of Eqn. (5.2.5) is computed using Eqns. (9.2.26-7), the fact that $u_{max}=1$, and the results of Appendix C. Thus, the remainder term is given by

$$\bar{E}_{rem} = 2\, u_{max} \sum_{i=M}^{\infty} i\ \bar{g}_{true}[i] = 2\, g\, p^{M} (M - M\, p + p) / (1 - p)^2. \qquad (9.4.1)$$

where from Eqn. (9.2.27), g=0.75 and p=0.95098. This remainder term is shown in Figure 9.39 as a function of the memory length M. In addition, we present the following table for the larger values of M.

Table 9.4: The Remainder Term $\bar{E}_{rem}$ as a Function of the Memory Length M.

M	$\bar{E}_{rem}$
1	593.55381
100	23.97108
125	8.25089
150	2.75484
175	0.89977
200	0.28901
225	0.09163
250	0.02874
275	0.00894
300	0.00276

For the open-loop simulations of this section, we use M=175 which corresponds to a remainder term of 0.89977. As mentioned previously, this remainder term looks like a constant disturbance over all frequencies, to the frequency-domain estimator.

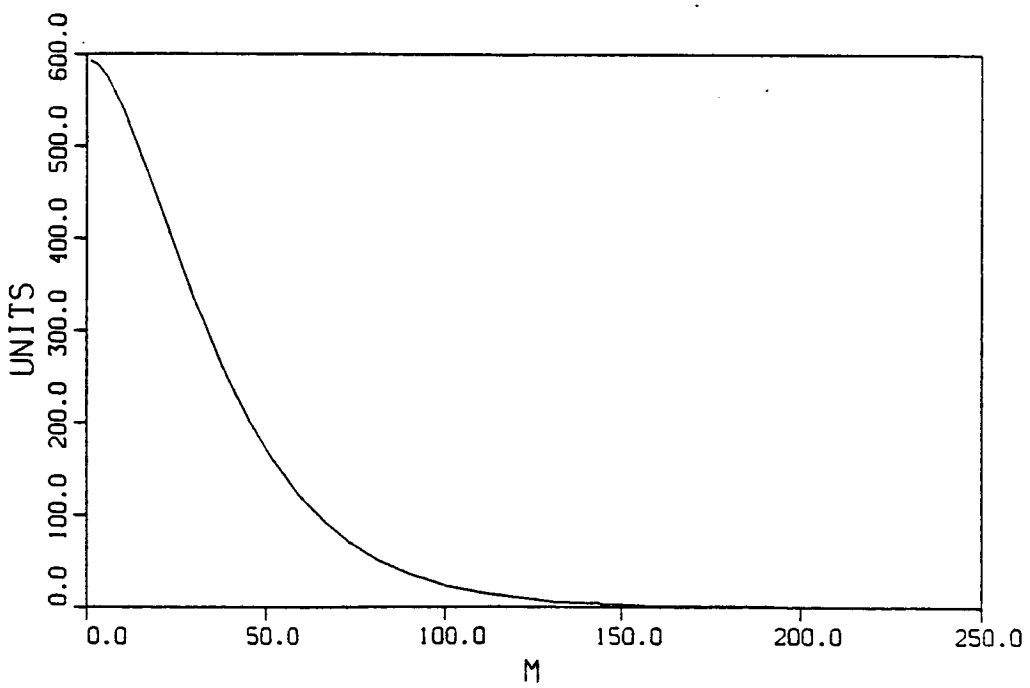

Figure 9.39: Remainder Term $\bar{E}_{rem}$ as a Function of the Memory Length M.

Computation of the Interval form of the Smoothness Condition $\nabla_{su,i}^{n}(\omega_k,\omega_{k+1})$

The bounding function $\nabla_{su}^{n}(e^{j\omega_k T})$ will be computed on-line. Recall that this bounding function is used to both smooth out sharp peaks in the raw uncertainty bounding function and to compute the additive safety factor that guards against inter-sample variations. The methods of Subsection 5.7.2 will be used to compute the bounding function $\nabla_{su}^{n}(e^{j\omega_k T})$; however, to compute the interval form of the smoothness condition $\nabla_{su,i}^{n}(\omega_k,\omega_{k+1})$ we must use an approximation to Eqn. (5.7.31). Since we are using a large number of frequency points in this simulation, little error is introduced by the following approximation.

$$\nabla_{su,i}^{n}(\omega_k,\omega_{k+1}) = \max\{\nabla_{su}^{n}(e^{j\omega_k T}), \nabla_{su}^{n}(e^{j\omega_{k+1} T})\} \approx \sup_{\omega\in[\omega_k,\omega_{k+1}]} \{\nabla_{su}^{n}(e^{j\omega T})\} \quad (9.4.2)$$

Subsection Summary

In this preparatory subsection, we have developed all of the necessary bounding functions and computed all of the necessary quantities for use of the frequency-domain uncertainty bounding method of Chapter 5. In the following sections of this chapter, we will use this information to simulate the frequency-domain bounding method.

9.4.2 Simulation of the Frequency-domain Uncertainty Bounding Method with True Parameter Estimates

In this subsection, we will simulate the frequency-domain uncertainty bounding method of Chapter 5 using the "true" parameters, not estimates. That is, instead of using a parameter estimator, we use the true parameter values which we know from the start in this controlled situation. This approach will allow us to evaluate the performance of the frequency-domain bounding method independently of the performance of the parameter estimator. In this subsection, we simulate the main method of Chapter 5, including the smoothing computations of Section 5.7 and the addition of the safety factor that was described in Section 5.8. We do not implement any of the modifications with regard to the robust uncertainty bounding discussion of Subsection 5.6.3. The input signal u[n] of Subsection 9.2.8 will be used in all of the simulations in this subsection. We shall perform simulations of the frequency-domain bounding method for two cases in this

section: 1) ideal case, with no disturbance or unmodeled dynamics, and 2) disturbance only case, with no unmodeled dynamics. Later, in Section 9.5, the complete robust estimator will be simulated.

Simulation 9.4.1: Ideal Case, No Disturbance, No Unmodeled Dynamics

For this simulation we will use Case 1 of Subsection 9.2.4 and will not introduce any disturbance. In this ideal case, we expect the frequency-domain bounding method to work very well. With no disturbance, the only source of error with regard to our frequency-domain estimate is the use of finite-length data. For initial values, we set the cumulative frequency-domain estimate to the frequency response of the nominal model for ζ=0.8 and ω_n=1 rad/sec., and set the corresponding cumulative frequency-domain bounding function to the best bounding function that can be found using only a priori knowledge of the plant. That is, we can find some large initial bounding function on the frequency-domain error based on our assumptions concerning the structured and unstructured uncertainty of the plant. Note that we start the frequency-domain bounding method with parameter values that are very far from the true values of ζ=0.2 and ω_n=2 rads/sec. We now present our results.

In this simulation, the time histories of the input signal u[n] and the output signal y[n] are the same as those of Figure 9.28. As in Chapter 8, we will present the time histories of the frequency-domain errror and error bound, at a given frequency. In Figure 9.40, we show the time histories of the frequency-domain error bound, $\overline{E}_{f,N}^{n}(\omega_k)$, and the actual error magnitude, $|E_{f,N}^{n}(\omega_k)|$, at ω_k=2 rads/sec. In Figure 9.41, we show the same quantities for ω_k=20 rads/sec. These figures show how the frequency-domain error bounding function decreases sooner for low frequencies than for high frequencies in our example. This occurs because the input signal is a low-frequency signal initially but then becomes an increasingly higher frequency signal for later times. In Figures 9.40-41, there is a marked decrease in the bounds at n=999 (125.54 secs.) when the first DFT frame of 1000 time samples is filled. Since the input signal has the same period as the length of the DFT, the bounds remain constant after time index $n=N_f-1+M-1=1173$, or after 147.40 secs. These results show us that the frequency-domain bounding method yields its best results after something on the order of N_f+M sample times have passed. This gives us an idea of how fast the bounding method learns.

In Figure 9.42, we show frequency-domain snapshots of the cumulative frequency-domain

error bounding function, $\overline{E}_{cumf,N}^{n}(\omega_k)$, and the actual error magnitude, $|E_{cumf,N}^{n}(\omega_k)|$, for n=999 (125.54 secs.). In Figure 9.43, we show the same functions for n=2500 (314.16 secs.). From Figure 9.42, we see that the both the cumulative bounding function and the error function are still quite large at n=999. However, from Figure 9.43, we see that at n=2500, both the cumulative bounding function and the error function are small. In fact, the actual cumulative error function is so small that it can't be seen on the scale of Figure 9.43. A comparison of Figures 9.43 and 9.22, which shows the DFT magnitude of the input signal, reveals the expected result that we obtain the best estimates at the frequencies where the input signal has the most energy.

We now present the final results of the frequency-domain uncertainty bounding method, the bounding functions $\Delta_{su}^{n}(e^{j\omega_k T})$ and $\overline{\Delta}_{su}^{n}(e^{j\omega_k T})$ on $|\delta_{su}(e^{j\omega_k T})|$. In Figure 9.44, we show the raw bounding function $\Delta_{su}^{n}(e^{j\omega_k T})$, which is defined by Eqn. (5.5.6), for n=2500 (314.16 secs.). In Figure 9.45, we show the final bounding function $\overline{\Delta}_{su}^{n}(e^{j\omega_k T})$ for n=2500 (314.16 secs.), after the smoothing of $\Delta_{su}^{n}(e^{j\omega_k T})$ and the addition of the safety factor, as described in Sections 5.7-8. Comparing Figures 9.44 and 45, we see how the smoothing procedure has removed the sharp peaks in Figure 9.44. Further, from this comparison, the addition of the safety factor in Figure 9.45 is apparent, particularly in the frequency range from 0 to 2.5 rads/sec. These results show us how well the frequency-domain bounding method works for the ideal case of no disturbance and no unmodeled dynamics. The final bounding function is quite small being much less than unity. This means that for our choice of N_f and M the frequency-domain bounding method works very well.

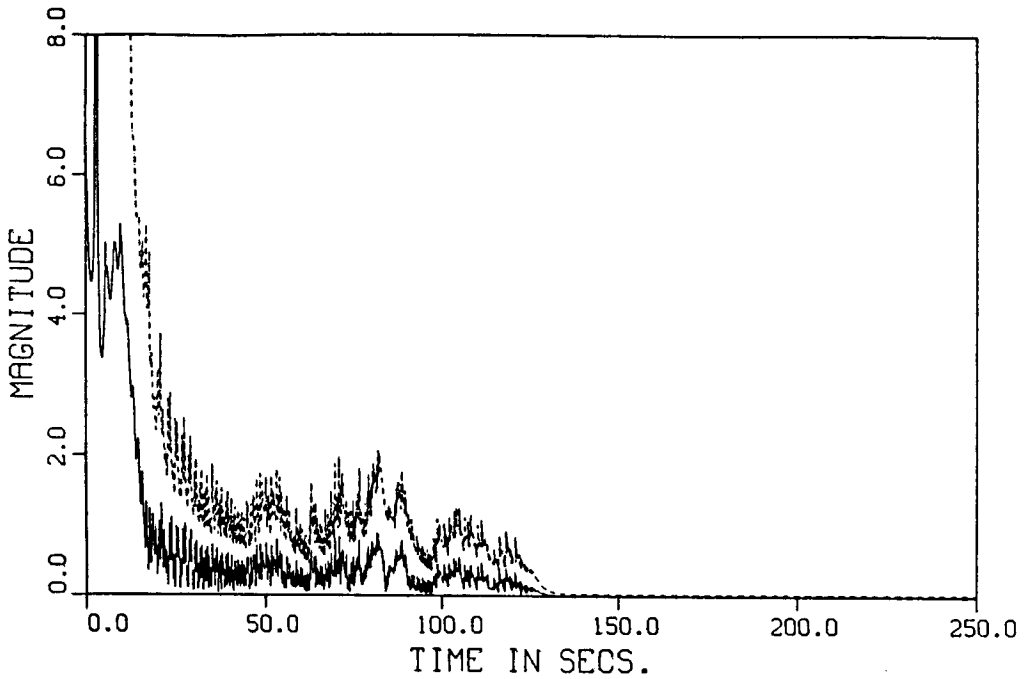

Figure 9.40: Time History of $|E_{f,N}^{n}(\omega_k)|$ and $\overline{E}_{f,N}^{n}(\omega_k)$ for ω_k=2 rads/sec., and Ideal Case.

($|E_{f,N}^{n}(\omega_k)|$ = ——, $\overline{E}_{f,N}^{n}(\omega_k)$ = - - - -)

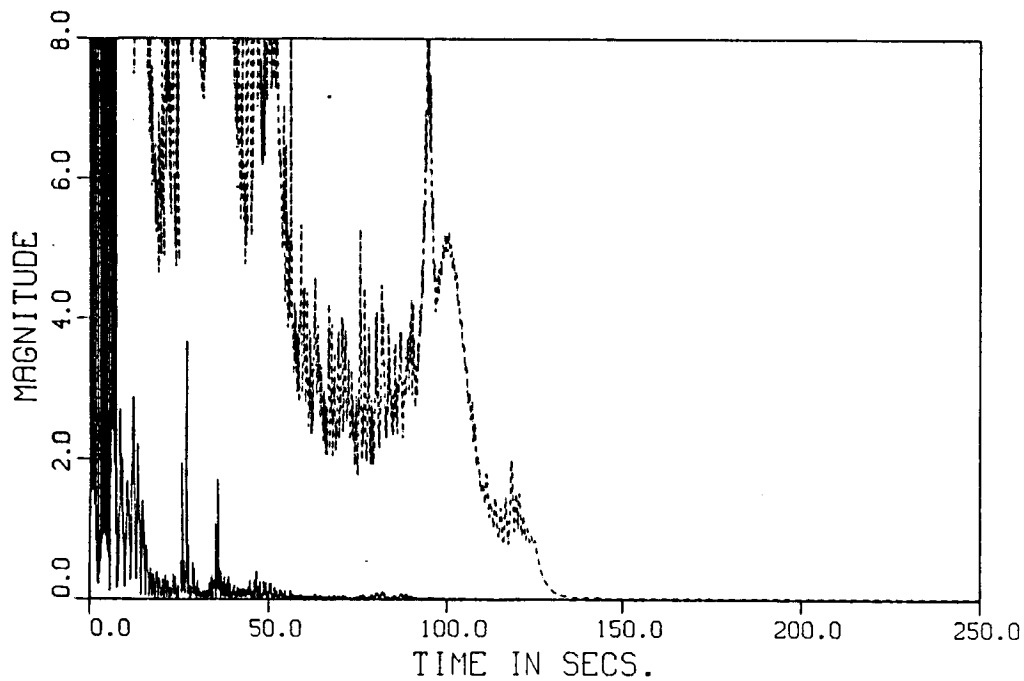

Figure 9.41: Time History of $|E_{f,N}^{n}(\omega_k)|$ and $\overline{E}_{f,N}^{n}(\omega_k)$ for ω_k=20 rads/sec., and Ideal Case.

($|E_{f,N}^{n}(\omega_k)|$ = ——, $\overline{E}_{f,N}^{n}(\omega_k)$ = - - - -)

These figures show how fast the bounding method learns at different frequencies.

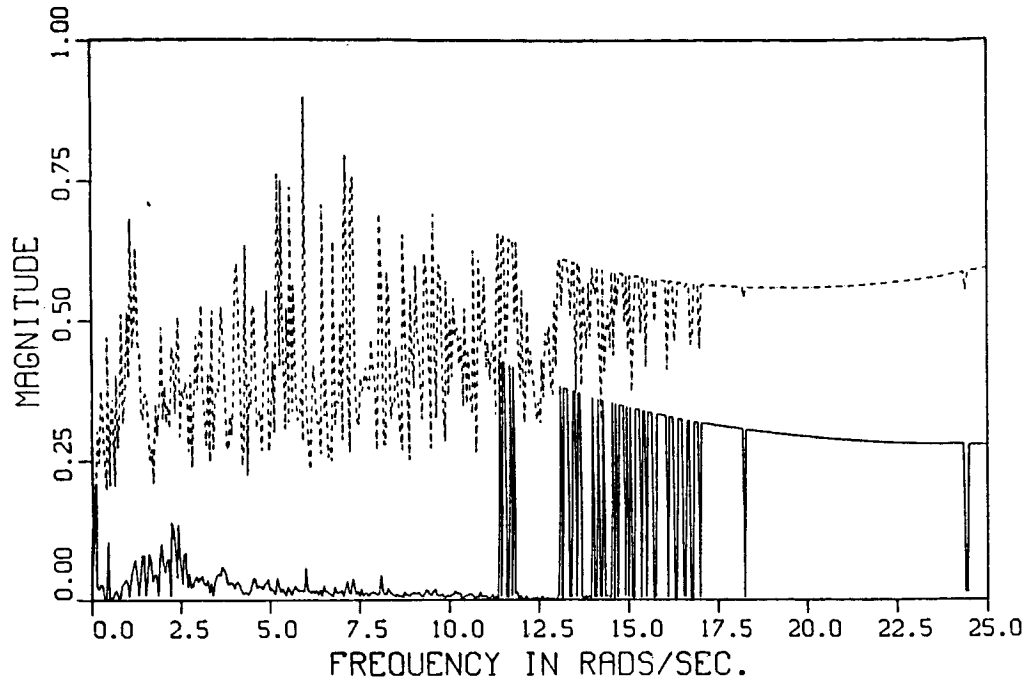

Figure 9.42: Frequency Snapshot of $|E_{cumf,N}^{n}(\omega_k)|$ and $\overline{E}_{cumf,N}^{n}(\omega_k)$ for n=999, and Ideal Case. ($|E_{cumf,N}^{n}(\omega_k)|$ = ——, $\overline{E}_{cumf,N}^{n}(\omega_k)$ = - - - -)

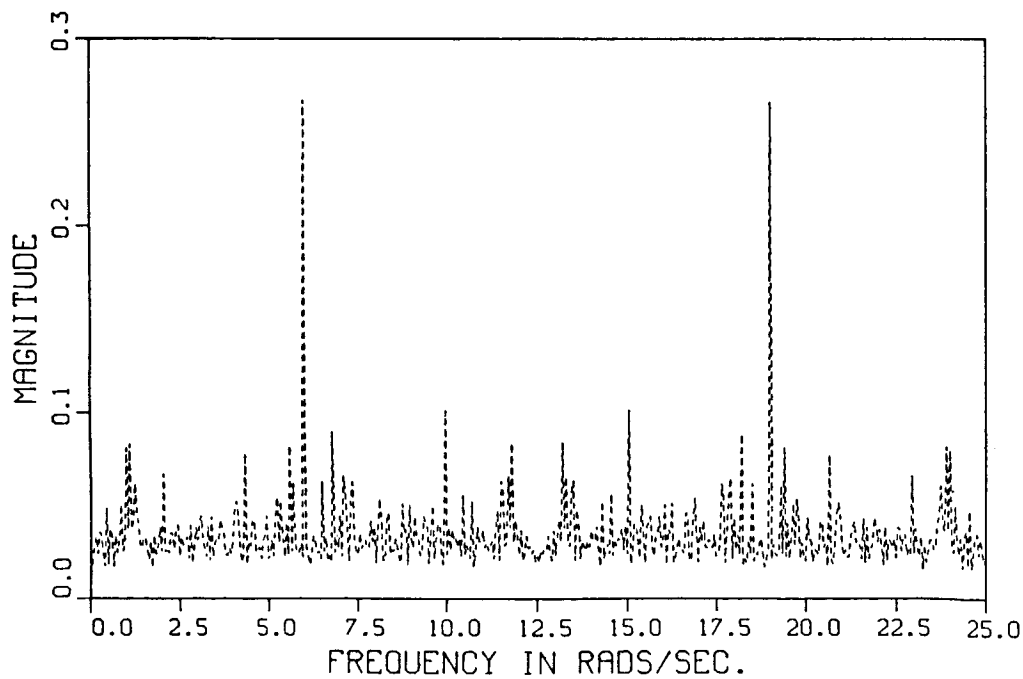

Figure 9.43: Frequency Snapshot of $|E_{cumf,N}^{n}(\omega_k)|$ and $\overline{E}_{cumf,N}^{n}(\omega_k)$ for n=2500, and Ideal Case. ($|E_{cumf,N}^{n}(\omega_k)|$ = —— [too small to see], $\overline{E}_{cumf,N}^{n}(\omega_k)$ = - - - -)

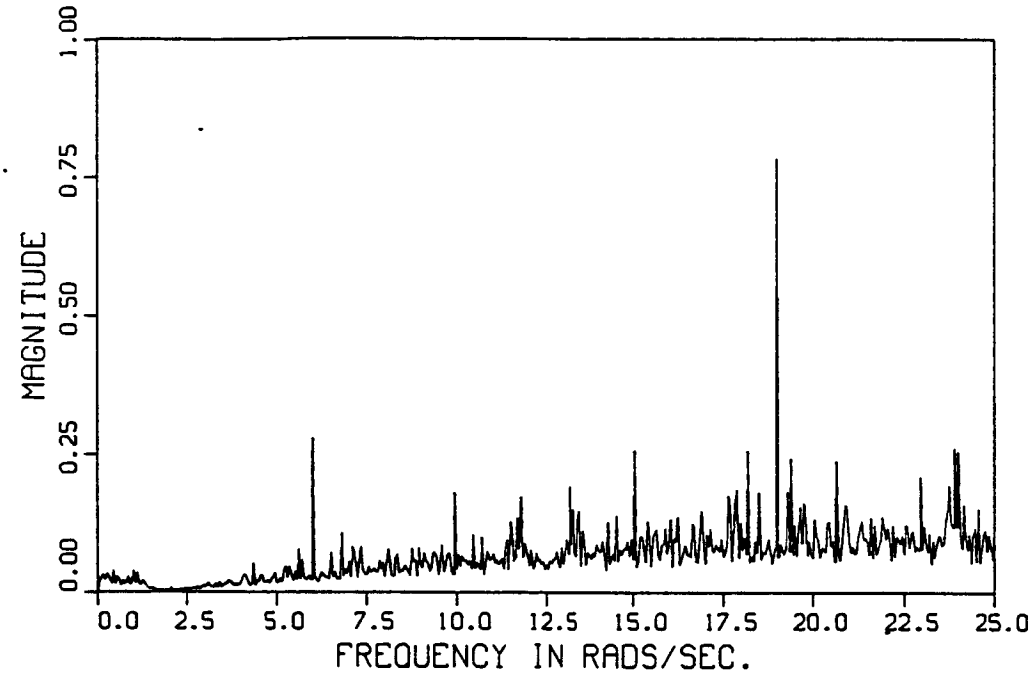

Figure 9.44: Raw Uncertainty Bounding Function $\Delta_{su}^{n}(e^{j\omega_k T})$ for n=2500, and Ideal Case.

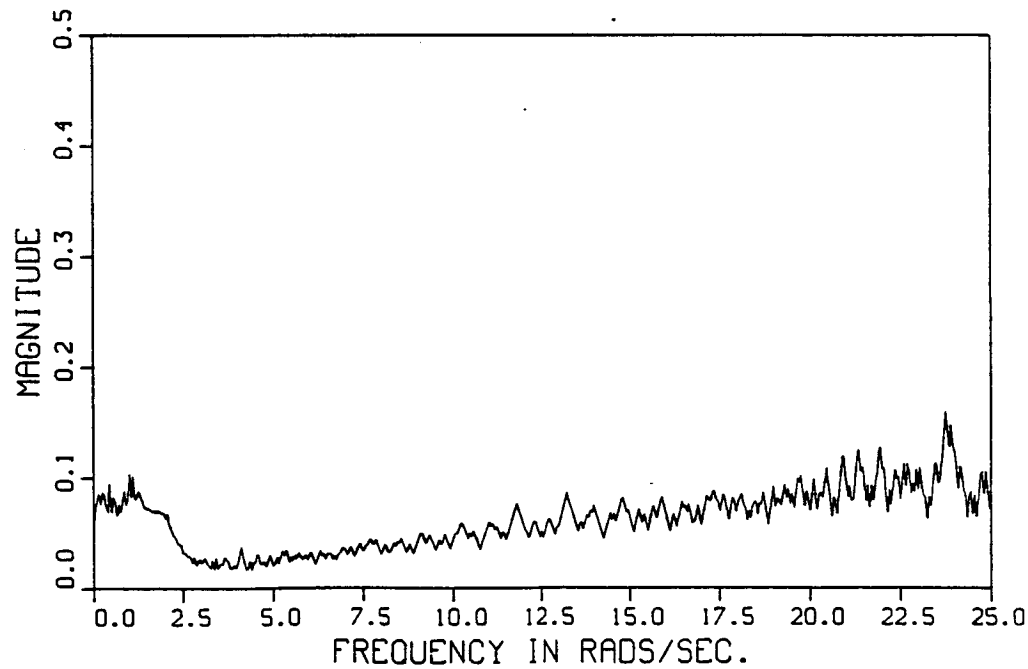

Figure 9.45: Final Uncertainty Bounding Function $\overline{\Delta}_{su}^{n}(e^{j\omega_k T})$ for n=2500, and Ideal Case.

Simulation 9.4.2: Disturbance Case, No Unmodeled Dynamics

For this simulation we will use Case 1 of Subsection 9.2.4, and will introduce the disturbance of Subsection 9.2.6 with a scaling factor of d_{factor}=0.1. In this disturbance case, we do not expect the frequency-domain bounding method to work as well as in the ideal case, in the frequency range where the disturbance has its energy. We use the same initial values for the frequency-domain method as in the previous simulation. We now present our results.

In this simulation, the time histories of the input signal u[n] and the output signal y[n] are similar to those of Figure 9.28, since the disturbance is small. The time histories of the frequency-domain error bound, $\overline{E}_{f,N}^{n}(\omega_k)$, and the actual error magnitude, $|E_{f,N}^{n}(\omega_k)|$, are qualitatively similar to those of the previous simulation so we do not show them. In Figure 9.46, we show frequency-domain snapshots of the cumulative frequency-domain error bounding function, $\overline{E}_{cumf,N}^{n}(\omega_k)$, and the actual error magnitude, $|E_{cumf,N}^{n}(\omega_k)|$, for n=2500 (314.16 secs.). Comparing Figures 9.43 and 9.46, we see that the functions are larger in the disturbance case than in the ideal case of no disturbance, as expected. Comparing these two figures with the disturbance DFT magnitude, which is shown in Figure 9.20 (not including the scaling factor of 0.1), we see how the disturbance corrupts the estimate primarily in the low-frequency range.

Now, for the disturbance case, we present the final results of the frequency-domain uncertainty bounding method, the bounding functions $\Delta_{su}^{n}(e^{j\omega_k T})$ and $\overline{\Delta}_{su}^{n}(e^{j\omega_k T})$ on $|\delta_{su}(e^{j\omega_k T})|$. In Figure 9.47, we show the raw bounding function $\Delta_{su}^{n}(e^{j\omega_k T})$ for n=2500 (314.16 secs.). In Figure 9.48, we show the final bounding function $\overline{\Delta}_{su}^{n}(e^{j\omega_k T})$ for n=2500 (314.16 secs.), after the smoothing of $\Delta_{su}^{n}(e^{j\omega_k T})$ and the addition of the safety factor. Comparing Figures 9.47-48, we see again how the smoothing procedure has removed the sharpest peaks in Figure 9.47. The presence of the disturbance is most pronounced in the low frequency range from 0 to 2.5 rads/sec. A comparison of Figures 9.45 and 9.48 reveals the degradation of the uncertainty bounding function that is due to the presence of the disturbance. These results show us how the disturbance affects the performance of the frequency-domain bounding method. We note that, even in the presence of the disturbance, the final bounding function is smaller than unity and, hence, useful.

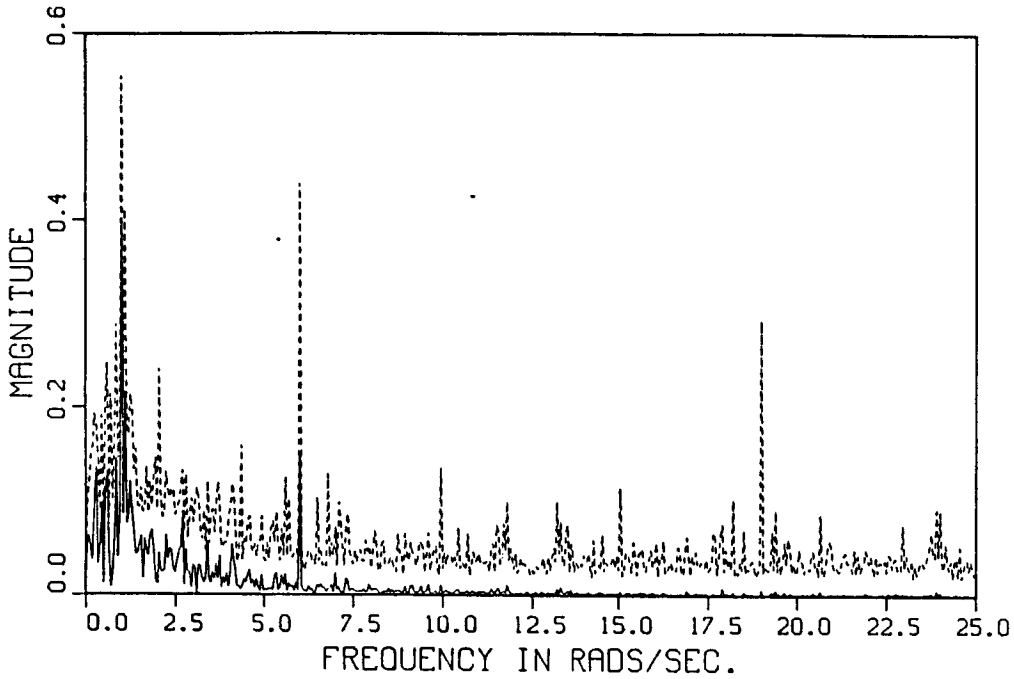

Figure 9.46: Frequency Snapshot of $|E_{cumf,N}^{n}(\omega_k)|$ and $\overline{E}_{cumf,N}^{n}(\omega_k)$ for n=2500, and Disturbance Case. ($|E_{cumf,N}^{n}(\omega_k)|$ = ——— , $\overline{E}_{cumf,N}^{n}(\omega_k)$ = - - - -)

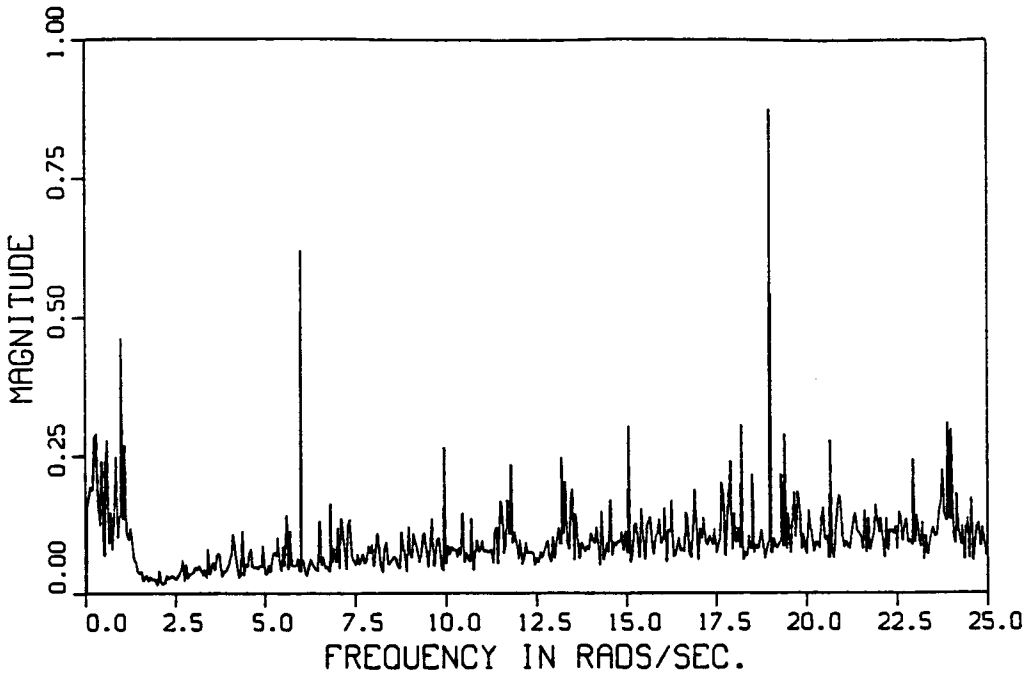

Figure 9.47: Raw Uncertainty Bounding Function $\Delta_{su}{}^{n}(e^{j\omega_k T})$ for n=2500, and Disturbance Case.

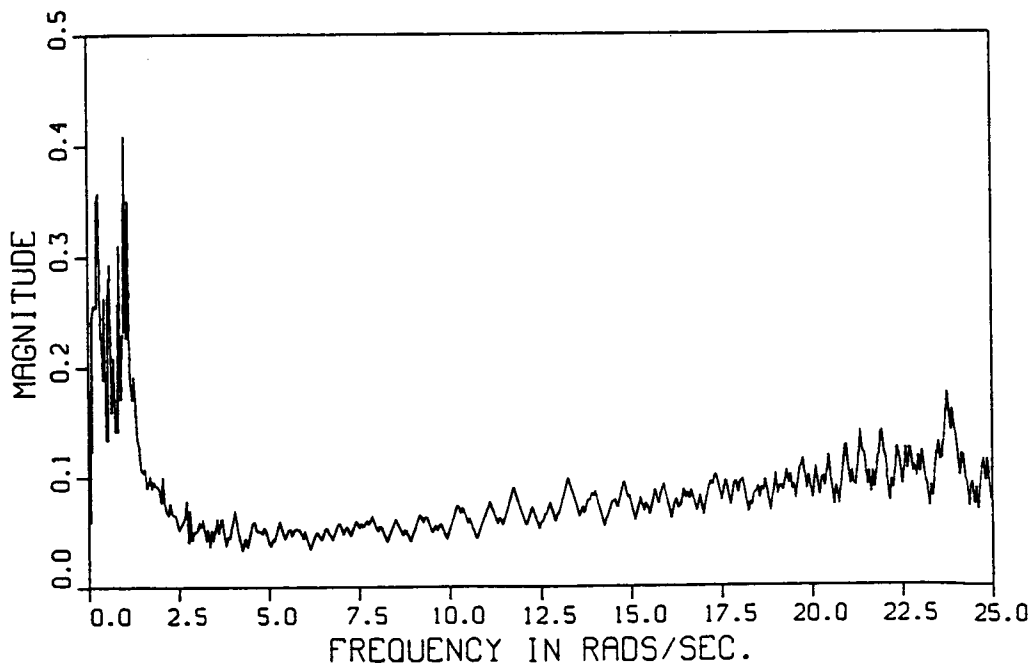

Figure 9.48: Final Uncertainty Bounding Function $\overline{\Delta}_{su}{}^{n}(e^{j\omega_k T})$ for n=2500, and Disturbance Case.

9.4.3 Conclusion

In this section, we have studied the properties of the frequency-domain uncertainty bounding method, through the use of two simulations. We have seen that the frequency-domain bounding method performs well. We summarize our conclusions concerning these simulations.

1) In the disturbance-free case, the frequency-domain bounding method yielded a multiplicative uncertainty bounding function that is much less than unity and, hence, useful for control design. This verifies that our choices of M and N_f are sufficiently large.

2) In the disturbance case, we saw how the low-frequency disturbance resulted in a larger multiplicative uncertainty bounding function than in the disturbance-free case. This shows how the presence of the disturbance affects the closed-loop bandwidth that is achievable using the frequency-domain uncertainty bounding method.

These conclusions are encouraging and indicate that the frequency-domain uncertainty bounding method holds promise. However, the robust estimator also includes a parameter estimator. The results of this section show that, if 1) the parameter estimator yields the true parameter values and 2) the input signal is rich, such as in these simulations, then the frequency-domain bounding method can yield a useful bounding function on the multiplicative modeling uncertainty. By useful we mean a bounding function that is, for example, less than unity for frequencies that are lower than the target closed-loop bandwidth. This will allow the robust adaptive control system to increase the closed-loop bandwidth using the knowledge provided by the robust estimator.

9.5 Open-loop Simulations of Both Types of the Robust Estimator

9.5.1 Introduction

In this section, we will simulate the robust estimator using both types of the parameter estimator, one time-domain and one frequency-domain. This will provide a comparison of the two kinds of parameter estimators. In Section 9.3, we saw that the dead-zone based time-domain parameter estimator did not perform well in our simulations. We expect the frequency-domain parameter estimator to perform better than the time-domain parameter estimator. A second objective of this section is to see how the robust estimator (using the frequency-domain parameter estimator) performs for several different types of unmodeled dynamics.

9.5.2 Simulation of the Robust Estimator using the Time-domain Parameter Estimator

In this subsection, we will simulate the robust estimator using the time-domain parameter estimator of Chapter 4 and the modification discussed in Subsection 4.5.3. That is, we use the robustified least-squares parameter estimator with the regularized constant trace modification. The input signal u[n] of Subsection 9.2.8 will be used in this simulation. We simulate the robust estimator in a situation where both unmodeled dynamics and a disturbance are present. This simulation is the logical follow-on to the simulations of Section 9.3, where the effects of the unmodeled dynamics and the disturbance were considered individually.

Simulation 9.5.1: Robust Estimator using the Time-domain Parameter Estimator, Case 3

For this simulation we will use Case 3 of Subsection 9.2.4, and will introduce a disturbance. That is, we use the case of time-delay unmodeled dynamics. The disturbance that was described in Subsection 9.2.6 will be used in this simulation with a scaling factor of d_{factor}=0.1. For initial values in the frequency-domain bounding part of the robust estimator, we set the cumulative frequency-domain estimate to the frequency response of the nominal model for ζ=0.8 and ω_n=1 rad/sec., and set the corresponding cumulative frequency-domain bounding function to the best bounding function that can be found using only a priori knowledge of the plant. Thus, we start the frequency-domain bounding method with parameter values that are very far from the true values of ζ=0.2 and ω_n=2 rads/sec. We now present our results.

The 0.04 sec. time delay has only a small effect on the plant output. The time histories of

the input signal u[n] and the output signal y[n] are almost the same as those of Figure 9.28. For the initial parameter estimates we again used the values that correspond to the choice of ζ=0.8 and ω_n=1 rad/sec. In Figure 9.49, we show the parameter errors. For reference, in Table 9.5 we list the true values, initial estimates and initial errors of the parameters. In addition, we show the parameter errors at n=200 (25.13 secs.) and n=2500 (314.16 secs.). In Table 9.6, we again show the true parameter values and the values at n=2500; however, we also show the nearest grid point θ^*, of the 101 grid points, that the estimate is projected to. In addition, we show the projected parameter errors, that is, $\tilde{\theta}^*[2500] = \theta^*[2500] - \theta_0$.

Table 9.5: Parameter Estimates of the Time-domain Algorithm for Case 3 and a Disturbance.

	θ_0	$\hat{\theta}[0]$	$\tilde{\theta}[0]$	$\tilde{\theta}[200]$	$\tilde{\theta}[2500]$
a_1	1.84458	1.80358	-0.04100	0.01910	0.02768
a_2	-0.90436	-0.81786	0.08650	-0.02353	-0.03477
b_0	0.62189	0.07834	-0.54355	-0.43629	-0.41353

Table 9.6: Projected Parameter Estimates of the Time-domain Algorithm for Case 3 and a Disturbance.

	θ_0	$\hat{\theta}[2500]$	$\tilde{\theta}[2500]$	$\theta^*[2500]$	$\tilde{\theta}^*[2500]$
a_1	1.84458	1.87225	0.02768	1.88217	0.03759
a_2	-0.90436	-0.93913	-0.03477	-0.90028	0.00410
b_0	0.62189	0.20836	-0.41353	0.18132	-0.44057

Comparing Figures 9.29 and 9.49, we see that the parameter errors are quite large for the present simulation. The above tables show that even after a long time, the parameter estimates are still poor. The projection onto the grid of 101 points doesn't help improve the parameter estimates overall. To gain insight, we investigate the operation of the dead-zone mechanism.

In Figure 9.50, we show the magnitude bound $\bar{e}_1[n]$ and the actual error signal $e_1[n]$, which is due to both the effects of unmodeled dynamics and the disturbance in this simulation. The components of the magnitude bound $\bar{e}_1[n]$ and the actual error signal $e_1[n]$ are shown in Figures 9.51-52. Recall that $\bar{e}_2[n]$ and $\bar{e}_3[n]$ bound the effect of the unmodeled dynamics and the disturbance, respectively. From these figures, we see that the unmodeled dynamics bounding signal is the major component of $\bar{e}_1[n]$. In Figure 9.53, we show both the prediction error e[n] and the threshold signal $\beta\bar{e}_1[n]$. The dead-zone signal $\upsilon[n]$ of Subsection 4.5.2, is shown in

Figure 9.54. As before, by comparing Figures 9.53 and 9.54, we see how the dead-zone signal is nonzero only when the magnitude of the prediction error e[n] is larger than the threshold signal $\beta\overline{e_1}[n]$. Further, by comparing Figure 9.54 with Figures 9.34 and 9.38, which show the dead-zone signal for the previous cases, we see that in the present simulation the parameter estimator is turned-off even more than in either of the previous two simulations of the time-domain parameter estimator. As before, since the parameters are updated for only a few short time intervals, it is not surprising that the parameter estimator yields poor parameter estimates. We now present our frequency-domain results.

The cumulative frequency-domain error bounding function at n=2500 (314.16 secs.) is the same for this simulation as it was in Simulation 9.4.1, where $\overline{E}_{cumf,N}{}^{n}(\omega_k)$ is shown in Figure 9.46. This is not surprising since the frequency-domain error bounding function depends only on the input u[n] and the disturbance d[n]. In addition, the actual error magnitude, $|E_{cumf,N}{}^{n}(\omega_k)|$, is also the same for this simulation as it was in Simulation 9.4.1. The additive error in the frequency-domain and our bound on it, both depend only on the input signal and the disturbance, not the plant. In Figure 9.55, we show the final bounding function $\overline{\Delta}_{su}{}^{n}(e^{\omega_k T})$ for n=2500 (314.16 secs.), after the smoothing of $\Delta_{su}{}^{n}(e^{\omega_k T})$ and the addition of the safety factor, as described in Sections 5.7-8. This uncertainty bounding function is very large and would allow only a very low closed-loop bandwidth to be achieved in a closed-loop adaptive control context. The problem with the performance of the robust estimator in this simulation is the poor performance of the dead-zone based parameter estimator. The frequency-domain bounding method part of the robust estimator works well, but the dead-zone based time-domain parameter estimator works so poorly that the resulting uncertainty bounding function is uselessly conservative. Fortunately, as we will see in the next subsection, the frequency-domain parameter estimator works much better than the dead-zone based parameter estimator.

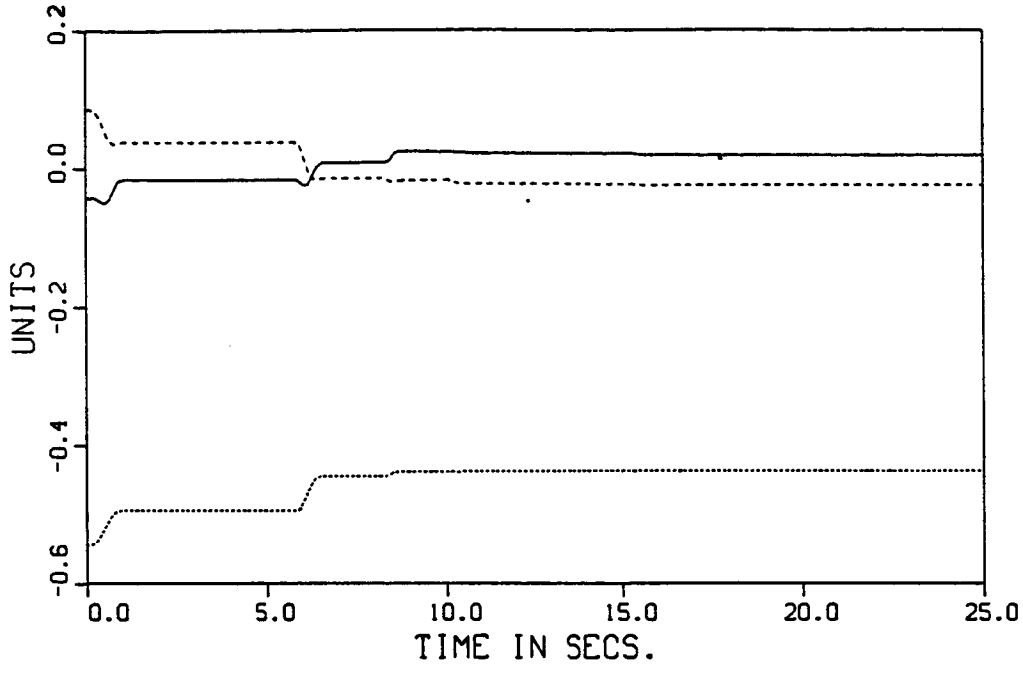

Figure 9.49: Parameter Errors for Robust Estimator.

($\tilde{a}_1[n]$ = ——, $\tilde{a}_2[n]$ = - - - -, $\tilde{b}_0[n]$ = ...)

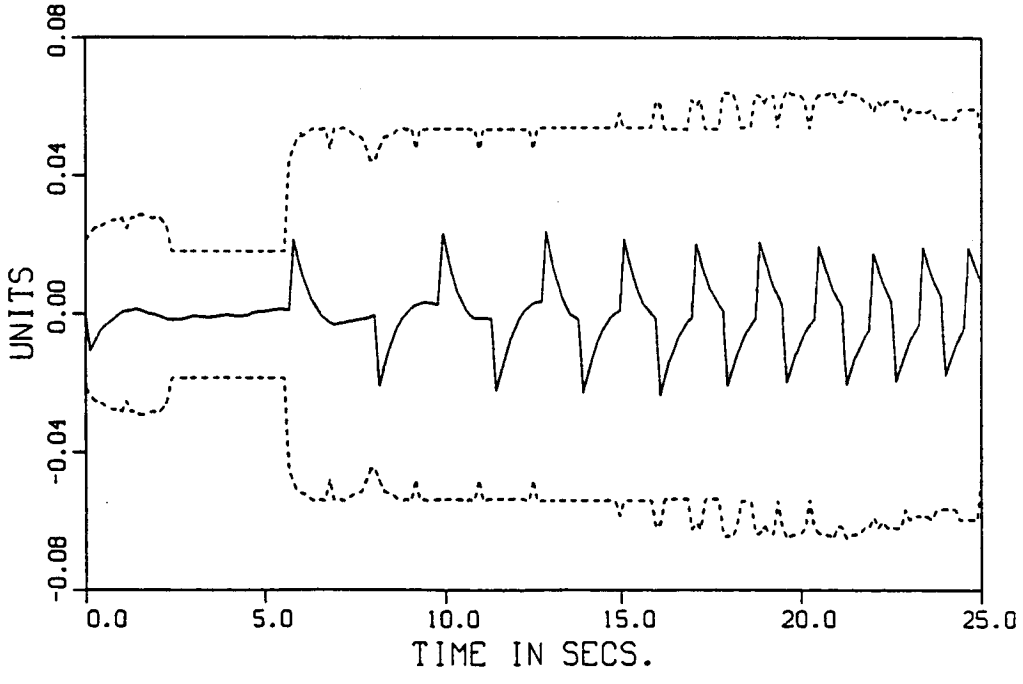

Figure 9.50: Error $e_1[n]$ and Bound $\overline{e}_1[n]$ for Robust Estimator.

($e_1[n]$ = ——, $\overline{e}_1[n]$ and $-\overline{e}_1[n]$ = - - - -)

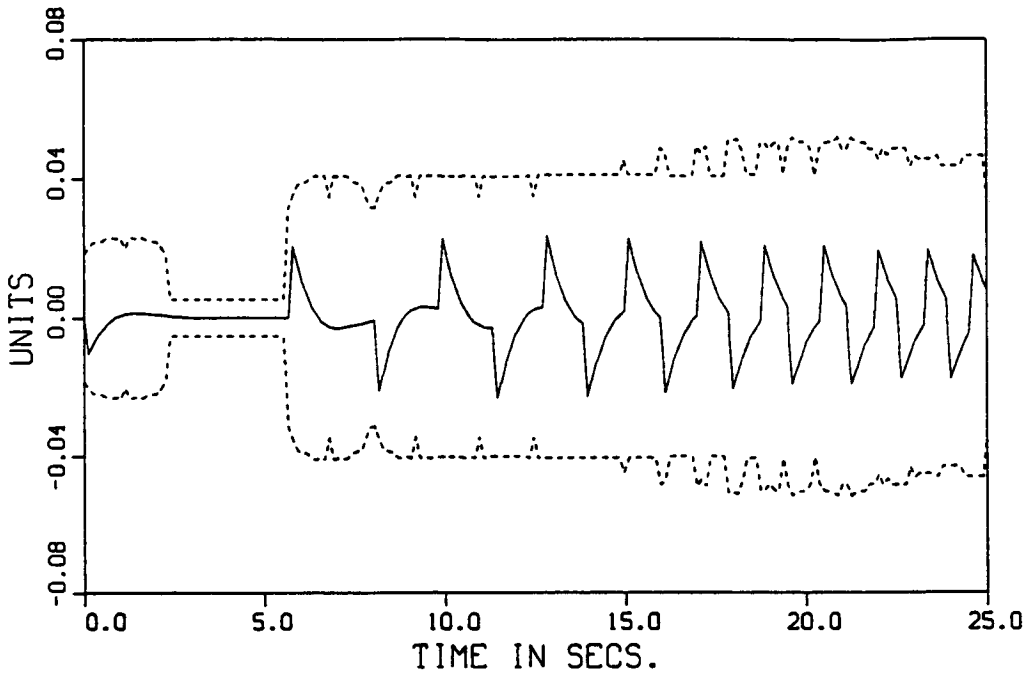

Figure 9.51: Error $e_2[n]$ and Bound $\overline{e}_2[n]$, due to Unmodeled Dynamics, for Robust Estimator.

($e_2[n]$ = ——, $\overline{e}_2[n]$ and $-\overline{e}_2[n]$ = - - - -)

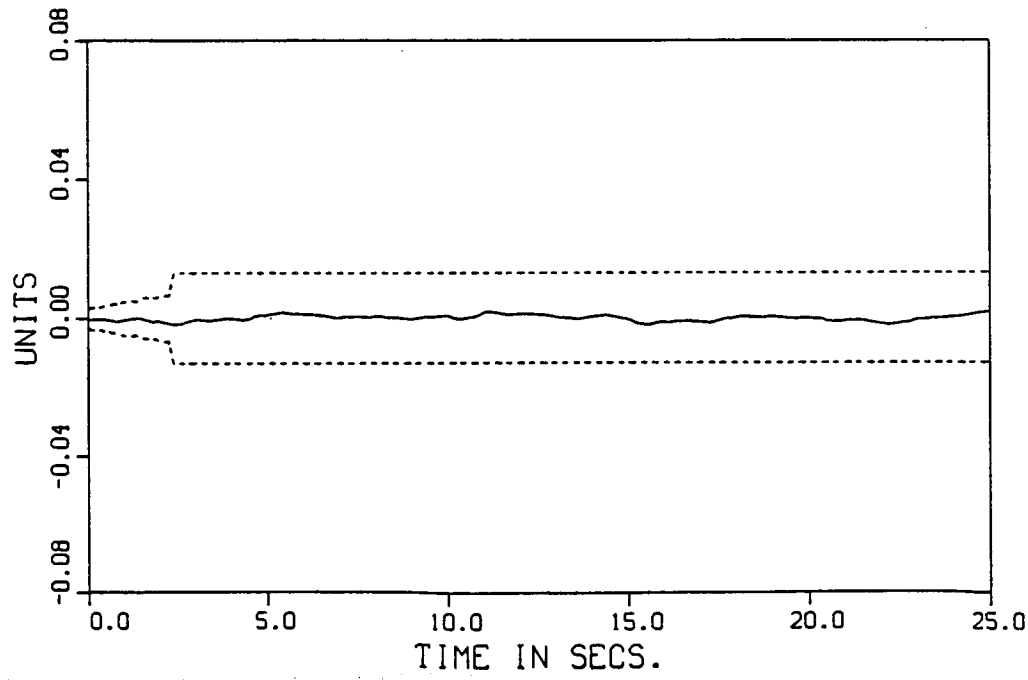

Figure 9.52: Error $e_3[n]$ and Bound $\overline{e}_3[n]$, due to Disturbances, for Robust Estimator.

($e_3[n]$ = ——, $\overline{e}_3[n]$ and $-\overline{e}_3[n]$ = - - - -)

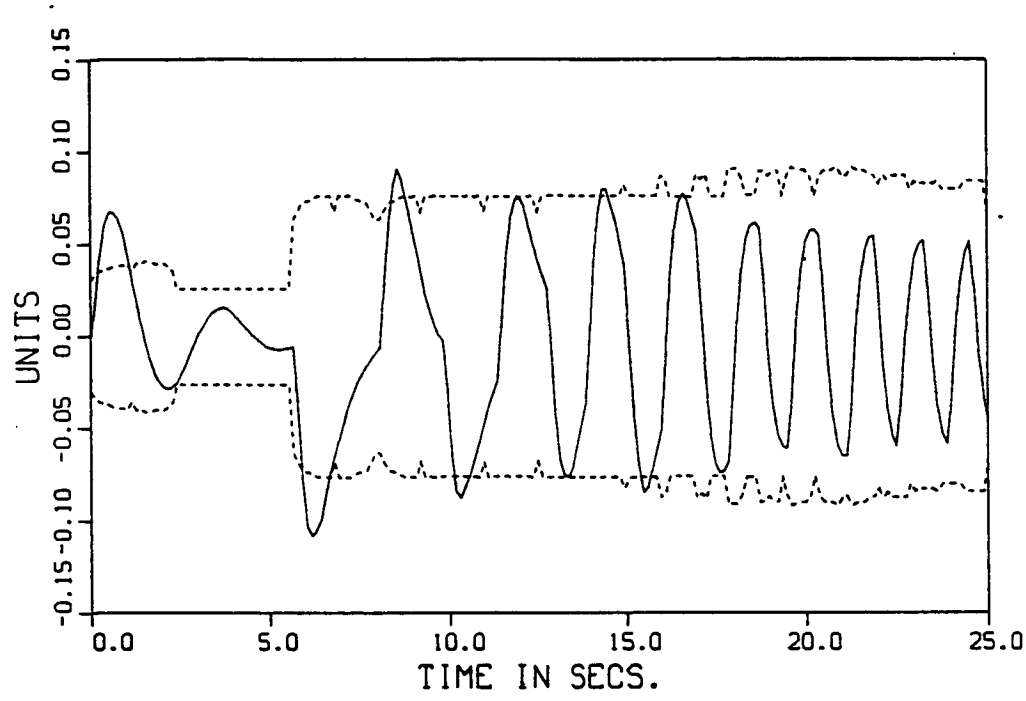

Figure 9.53: Prediction Error e[n] and Threshold $\beta\overline{e_1}[n]$ for Robust Estimator.

(e[n] = ——, $\beta\overline{e_1}[n]$ and $-\beta\overline{e_1}[n]$ = - - - -)

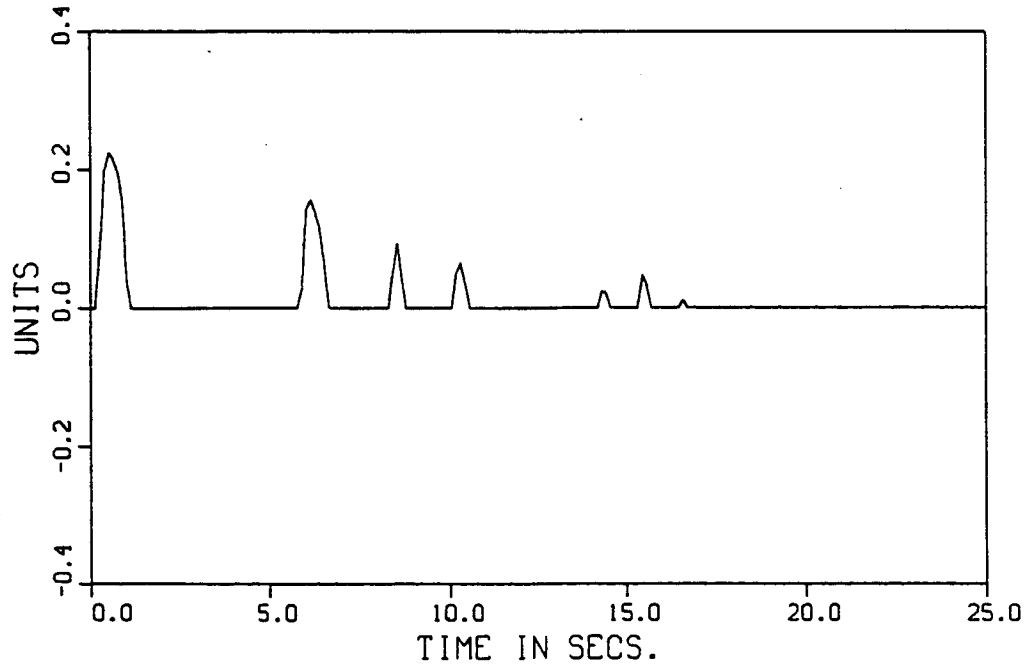

Figure 9.54: Dead-zone Signal $\upsilon[n]$ for Robust Estimator.

The dead-zone signal is nonzero only when the magnitude of the prediction error is greater than the threshold signal.

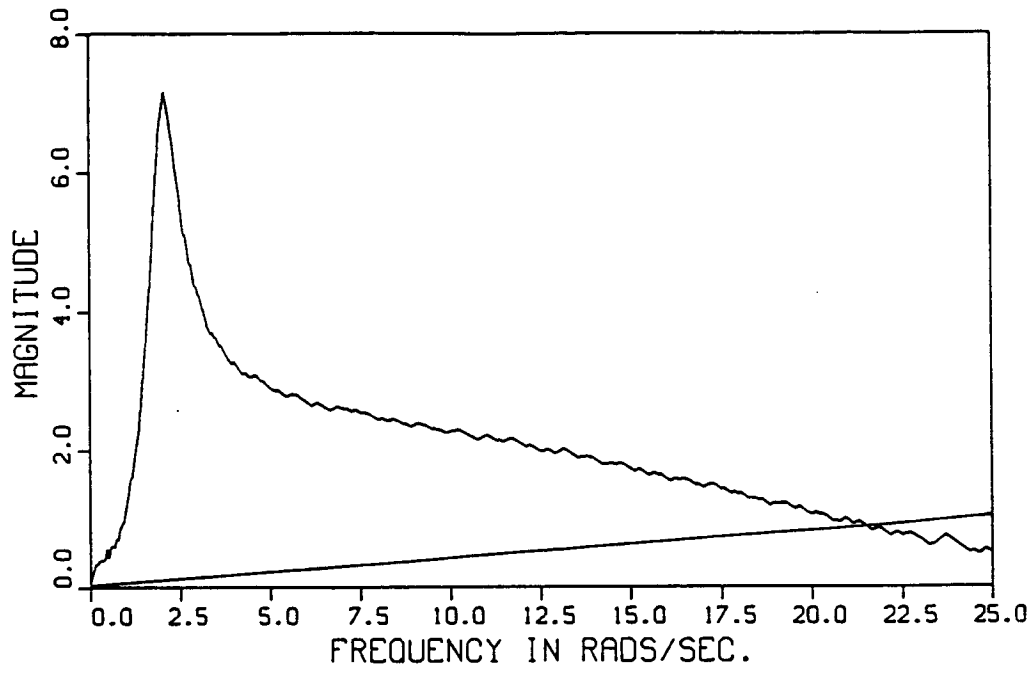

Figure 9.55: Final Uncertainty Bounding Function $\overline{\Delta}_{su}^{n}(e^{\omega_k T})$ for n=2500, Robust Estimator using Time-domain Parameter Estimator, Case 3. Straight line is a priori bound Δ_u.

9.5.3 Simulation of the Robust Estimator using the Frequency-domain Parameter Estimator

In this subsection, we will simulate the robust estimator using the frequency-domain parameter estimator that was described in Section 5.4. The input signal u[n] of Subsection 9.2.8 will be used in all of the simulations in this subsection. In addition, the disturbance that was described in Subsection 9.2.6 will again be used with a scaling factor of d_{factor}=0.1, in all of the simulations in this subsection. Since the input u[n] and the disturbance d[n] are the same for all three of the simulations of this section, the cumulative frequency-domain error bounding function at n=2500 (314.16 secs.) is also the same. This error bounding function is also the same as it was in Simulation 9.4.1, where $\overline{E}_{cumf,N}^{n}(\omega_k)$ is shown in Figure 9.46. In addition, the actual error magnitude, $|E_{cumf,N}^{n}(\omega_k)|$, is the same for the three simulations of this subsection as it was in Simulation 9.4.1. In this subsection, we simulate the robust estimator (using the frequency-domain parameter estimator) for three different cases of unmodeled dynamics. However, first we must choose the weighting function in the frequency-domain parameter

estimator.

Choice of the Frequency-weighting Function in the Frequency-domain Parameter Estimator

We must choose the frequency-weighting function f(ω) that is used in Eqn. (5.4.13) to find the diagonal frequency weighting matrix W. As was discussed in Section 5.4, if we wanted to choose a weighting function that yields a least-squares fit between the cumulative frequency-domain estimate and the true frequency-domain estimate, then we would choose the function to be

$$1 / |e^{2j\omega T} - a_1 e^{j\omega T} - a_2|, \tag{9.5.1}$$

where, of course, we don't know the true parameters a_1 and a_2. Since there are high-frequency unmodeled dynamics in our true plant, we want to de-emphasize the measured frequency-domain information at high frequencies. Thus, ideally, we don't choose Eqn. (9.5.1) but, rather, we choose a weighting function that has, for example, a single-pole roll-off above and beyond the two pole roll-off of Eqn. (9.5.1). We choose

$$f(\omega) = |4 / (j\omega + 4)|^3. \tag{9.5.2}$$

This weighting function will result in a better fit at low-frequencies than at high frequencies in the frequency-domain parameter estimator. In Figure 9.56, we show this weighting function f(ω).

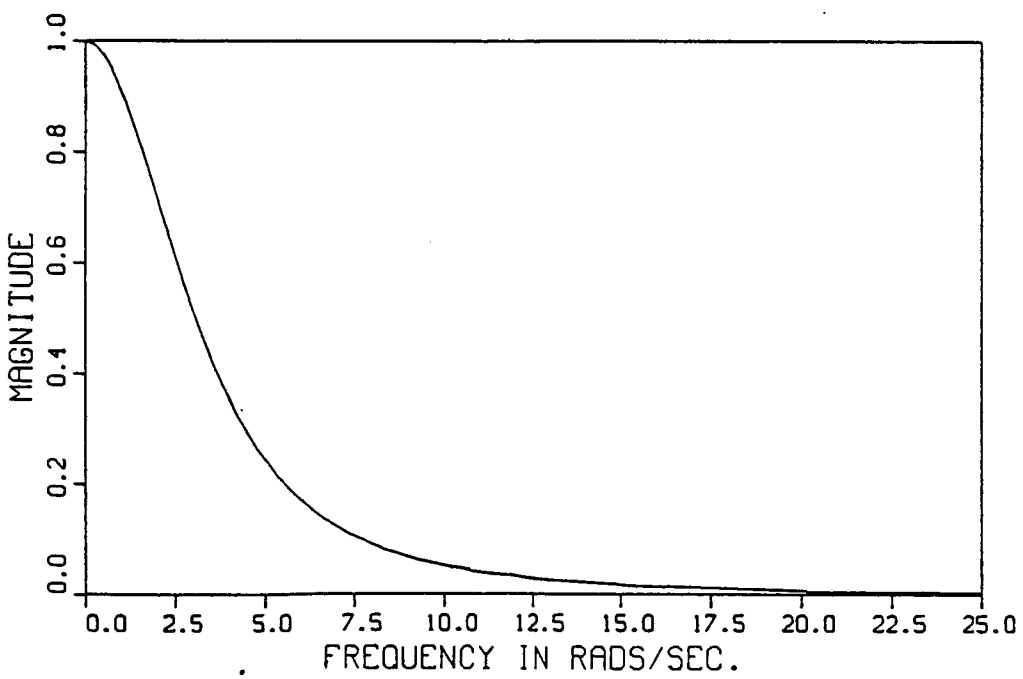

Figure 9.56: Weighting Function f(ω) for Frequency-domain Parameter Estimator.

Modification of the Frequency-domain Parameter Estimator Based on a Priori Information

The frequency-domain parameter estimator that was described in Section 5.4 could be used to find estimates of the four parameters, a_1, a_2, b_0 and b_1. However, as was the case for the time-domain parameter estimator (see Subsection 9.3.1), we can make use of a priori information to modify the frequency-domain parameter estimator. From the problem description of Subsection 9.2.1, we know that the D.C. gain of the plant is unity. So, using Eqn. (9.2.4) and the fact that G(z)=1 for z=1, we know that

$$b_1 = 1 - a_1 - a_2 - b_0 \tag{9.5.3}$$

as was previously noted in Eqn. (9.2.8). This a priori known constraint allows us to use a parameter estimator that only estimates the three parameters, a_1, a_2 and b_0. We will now develop a modified form of the frequency-domain parameter estimator of Section 5.4. Using Eqns. (5.4.3-4) and (9.5.3), we find that

$$z^2 G(z,\theta_0) - 1 = [\, z\,G(z,\theta_0) - 1 \quad G(z,\theta_0) - 1 \quad z - 1 \,]\,[\, a_1 \;\; a_2 \;\; b_0 \,]^T \tag{9.5.4}$$

or

$$z^2 G(z,\theta_0) - 1 = [\, z\,G(z,\theta_0) - 1 \quad G(z,\theta_0) - 1 \quad z - 1 \,]\,\theta_{0m} \tag{9.5.5}$$

where

$$\theta_{0m} = [\, a_1 \;\; a_2 \;\; b_0 \,]^T \tag{9.5.6}$$

and where the subscript 'm' stands for 'modified' form of the parameter estimator. The definition of Eqn. (9.5.6) is the same as that of Eqn. (9.3.23) for the modified time-domain parameter estimator. The development of the modified frequency-domain parameter estimator proceeds the same as the development of Section 5.4, except that Eqn. (9.5.5) is used in place of Eqn. (5.4.5). In the following simulations, the modified frequency-domain parameter estimator will be used. For the sake of clarity we will drop the subscript 'm' notation throughout the discussion of the following simulations.

Simulation 9.5.2: Robust Estimator using the Frequency-domain Parameter Estimator, Case 3

For this simulation we will use Case 3 of Subsection 9.2.4, which has time-delay unmodeled dynamics, and will introduce a disturbance with a scaling factor of d_{factor}=0.1. For initial values in the frequency-domain bounding part of the robust estimator, we set the cumulative frequency-domain estimate to the frequency response of the nominal model for ζ=0.8 and ω_n=1

rad/sec., and set the corresponding cumulative frequency-domain bounding function to the best bounding function that can be found using only a priori knowledge of the plant. Thus, we start the frequency-domain bounding method with parameter values that are very far from the true values of ζ=0.2 and ω_n=2 rads/sec. We now present our results.

Again, the 0.04 sec. time delay has only a small effect on the plant output. The time histories of the input signal u[n] and the output signal y[n] are almost the same as those of Figure 9.28. The frequency-domain parameter estimator was actually used only at the end of the simulation. In the following table we list the true parameter values, and the parameter estimates and errors at n=2500 (314.16 secs.).

Table 9.7: Parameter Estimates of the Frequency-domain Algorithm for Case 3 and a Disturbance.

	θ_0	$\hat{\theta}$[2500]	$\tilde{\theta}$[2500]	θ^*[2500]	$\tilde{\theta}^*$[2500]
a_1	1.84458	1.86098	0.01640	1.84458	0.0
a_2	-0.90436	-0.92211	-0.01775	-0.90436	0.0
b_0	0.62189	0.55545	-0.06644	0.62189	0.0

In addition, we show the nearest grid point θ^*, of the 101 grid points, that the estimate is projected to. Since the resulting grid point happens to correspond to the true parameter values for this simulation, the final parameter vector error $\tilde{\theta}^*$ is zero. We now present our frequency-domain results.

In Figure 9.57, we show the final bounding function $\overline{\Delta}_{su}{}^n(e^{\omega_k T})$ for n=2500 (314.16 secs.), after the smoothing of $\Delta_{su}{}^n(e^{\omega_k T})$ and the addition of the safety factor, as described in Sections 5.7-8. This uncertainty bounding function is much smaller than that of Figure 9.55 for the robust estimator using the dead-zone based time-domain parameter estimator. This significant difference is due to the superior performance of the frequency-domain parameter estimator as compared with the dead-zone based one. The uncertainty bounding function of Figure 9.57 is always less than unity and would be useful for increasing the bandwidth in a closed-loop adaptive control context.

A Comparison of the Dead-zone based Time-domain Parameter Estimator and the Frequency-domain Parameter Estimator

The previous two simulations, Simulations 9.5.1 and 9.5.2, are the same except that the dead-zone based time-domain parameter estimator has been used in the first simulation and the

frequency-domain parameter estimator has been used in the second one. That is, we can compare the parameter estimates of the two different types of parameter estimators for the plant of Case 3 with a disturbance. We summarize the results of these two simulations below where the data from Tables 9.5-7 has been used.

Table 9.8: Comparison at n=2500 of the Parameter Estimates of the Time-domain and the Frequency-domain Algorithms for Case 3 and a Disturbance.

	Time-domain	Freq.-domain	Time-domain	Freq.-domain
	$\tilde{\theta}[2500]$	$\tilde{\theta}[2500]$	$\tilde{\theta}^*[2500]$	$\tilde{\theta}^*[2500]$
a_1	0.02768	0.01640	0.03759	0.0
a_2	-0.03477	-0.01775	0.00410	0.0
b_0	-0.41353	-0.06644	-0.44057	0.0

In this table, we see that at the end of the simulations, the raw parameter errors $\tilde{\theta}[2500]$ of the dead-zone based time-domain parameter estimator are much larger than the raw estimates of the frequency-domain parameter estimator. In addition, we see that the errors of the projected parameter estimates $\tilde{\theta}^*[2500]$ of the dead-zone based time-domain parameter estimator are also much larger than the raw estimates of the frequency-domain parameter estimator. In particular, we note that the dead-zone based parameter estimator yields a very poor estimate of the b_0 parameter, as compared with the frequency-domain parameter estimator.

These results tell us that over a long period of time, the frequency-domain parameter estimator is likely to yield much better estimates. These results do not tell us how quickly the frequency-domain parameter estimator arrives at its estimates as compared with the time-domain parameter estimator. However, by construction, the frequency-domain parameter estimator improves its estimates as fast as the robust estimator improves its frequency-domain estimate. That is, the estimates of the frequency-domain estimator are found by performing a frequency-domain fit to the evolving frequency-domain estimate of the plant. Thus, the speed of the frequency-domain parameter estimator is as fast as it needs to be in the sense that it yields accurate estimates when the frequency-domain bounding function becomes small.

Simulation 9.5.3: Robust Estimator using the Frequency-domain Parameter Estimator, Case 2

For this simulation we will use Case 2 of Subsection 9.2.4, which has second-order unmodeled dynamics, and will introduce a disturbance with a scaling factor of d_{factor}=0.1. We use the same initial values for the frequency-domain method as in the previous simulation. We now present our results.

The second-order unmodeled dynamics have only a small effect on the plant output. The time histories of the input signal u[n] and the output signal y[n] are almost the same as those of Figure 9.28. In the following table we list the true parameter values, and the parameter estimates and errors at n=2500 (314.16 secs.).

Table 9.9: Parameter Estimates of the Frequency-domain Algorithm for Case 2 and a Disturbance.

	θ_0	$\hat{\theta}[2500]$	$\tilde{\theta}[2500]$	$\theta^*[2500]$	$\tilde{\theta}^*[2500]$
a_1	1.84458	1.84961	0.00503	1.84458	0.0
a_2	-0.90436	-0.90966	-0.00530	-0.90436	0.0
b_0	0.62189	0.60184	-0.02005	0.62189	0.0

In addition, we show the nearest grid point θ^*, of the 101 grid points, that the estimate is projected to. Since the resulting grid point happens to correspond to the true parameter values for this simulation, the final parameter vector error $\tilde{\theta}^*$ is zero. Comparing the values of $\tilde{\theta}[2500]$, we see that the parameter errors for this simulation are about a factor of 3 smaller than for the previous simulation. This is because the second-order unmodeled dynamics have a smaller effect than the time-delay unmodeled dynamics. We now present our frequency-domain results.

In Figure 9.58, we show the final bounding function $\overline{\Delta}_{su}{}^{n}(e^{\omega_k T})$ for n=2500 (314.16 secs.), after smoothing and the addition of the safety factor. This uncertainty bounding function is smaller than that of Figure 9.57 since again the second-order unmodeled dynamics are smaller than the time-delay unmodeled dynamics, as can be seen in Figures 9.11-12. The uncertainty bounding function of Figure 9.58 is always much less than unity and would be useful for increasing the bandwidth in a closed-loop adaptive control context.

Simulation 9.5.4: Robust Estimator using the Frequency-domain Parameter Estimator, Case 4

For this simulation we will use Case 4 of Subsection 9.2.4, which has second-order unmodeled dynamics, and will introduce a disturbance with a scaling factor of d_{factor}=0.1. Recall that Case 4 differs from Case 2 in that the nominal model parameters are different. For initial values in the frequency-domain bounding part of the robust estimator, we set the cumulative frequency-domain estimate to the frequency response of the nominal model for ζ=0.2 and ω_n=2 rads/sec., and set the corresponding cumulative frequency-domain bounding function to the best bounding function that can be found using only a priori knowledge of the plant. Thus, we start the frequency-domain bounding method with parameter values that are very far from the true values of

ζ=0.8 and ω_n=1 rad/sec. We note that this is a different set of initial conditions than was used for Simulations 9.4.1-2, and 9.5.1-3. This means that the cumulative frequency-domain bounding function will be different, initially, for this simulation than for the previous simulations. However, for this simulation, the input signal is large enough so that the initial conditions make no contribution to the the cumulative frequency-domain bounding function at n=2500 (314.16 secs.). Thus, $\overline{E}_{cumf,N}{}^{n}(\omega_k)$ and $|E_{cumf,N}{}^{n}(\omega_k)|$ are the same at n=2500 as in Simulation 9.4.2. We now present the rest of our results.

The time histories of the input signal u[n] and the output signal y[n] are shown in Figure 9.59. In the following table we list the true parameter values, and the parameter estimates and errors at n=2500 (314.16 secs.).

Table 9.10: Parameter Estimates of the Frequency-domain Algorithm for Case 4 and a Disturbance.

	θ_0	$\hat{\theta}$[2500]	$\tilde{\theta}$[2500]	θ^*[2500]	$\tilde{\theta}^*$[2500]
a_1	1.80358	1.83871	0.03513	1.84111	0.03753
a_2	-0.81786	-0.85058	-0.03272	-0.85571	-0.03785
b_0	0.07834	0.07709	-0.00125	0.10109	0.02275

In addition, we show the nearest grid point θ^*, of the 101 grid points, that the estimate is projected to. The projected parameter estimate doesn't yield the true parameter values in this simulation, although the true parameter values do correspond to one of the 101 grid points. Instead, the projected parameter vector θ^*[2500] corresponds to the continuous-time parameters of ζ=0.62 and ω_n=1 rad/sec. So, the parameter estimator gets ω_n correct, but is off on the value of ζ by -0.18, since the true value is ζ=0.8. We also see from these results that the projection of the parameter vector estimate didn't help reduce the parameter errors, since the raw parameter errors $\tilde{\theta}$[2500] are smaller than the projected parameter errors $\tilde{\theta}^*$[2500]. The parameter estimation results of this simulation are considered satisfactory in light of the difficult identification problem that occurs here. The frequency-domain values of the plant transfer function are much less sensitive to changes in ζ when it is close to unity than when it is close to zero. What really matters is how good our final frequency-domain results are.

In Figure 9.60, we show the final bounding function $\overline{\Delta}_{su}{}^{n}(e^{\omega_k T})$ for n=2500 (314.16 secs.), after smoothing and the addition of the safety factor. This uncertainty bounding function is

larger than that of Figure 9.58, which corresponds to the ζ=0.2, ω_n=2 rads/sec. case. Thus, even though we have used the same second-order unmodeled dynamics in Simulations 9.5.3 and 9.5.4, we get a larger multiplicative uncertainty bounding function in the later case. There are two causes for this result: 1) the parameter estimator yields slightly erroneous values in Simulation 9.5.4, and 2) the true plant of Simulation 9.5.4 rolls off at a lower frequency than that of Simulation 9.5.3.

Recall that in both simulations the additive error bounding function $\overline{E}_{cumf,N}{}^{n}(\omega_k)$ is the same. So, since the true plant of Simulation 9.5.4 is smaller at high frequencies then that of Simulation 9.5.3, the resulting multiplicative error bounding function will be larger. As a final note, we see that the uncertainty bounding function of Figure 9.60 is still always less than unity and would be useful for increasing the bandwidth in a closed-loop adaptive control context.

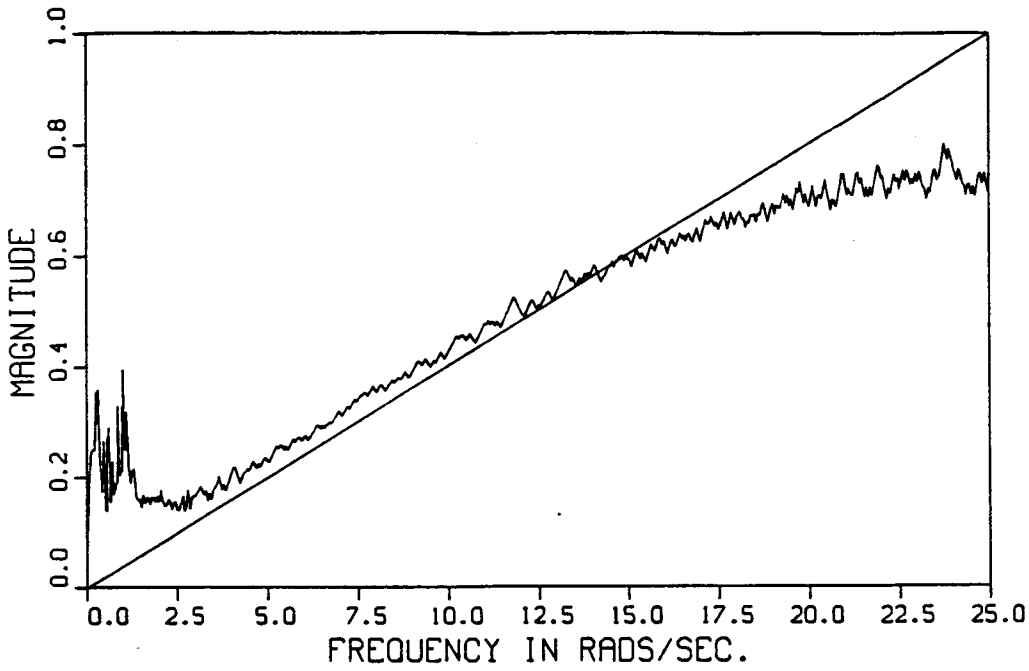

Figure 9.57: Final Uncertainty Bounding Function $\overline{\Delta}_{su}{}^{n}(e^{\omega_k T})$ for n=2500, Robust Estimator using Frequency-domain Parameter Estimator, Case 3. Straight line is a priori bound Δ_u.

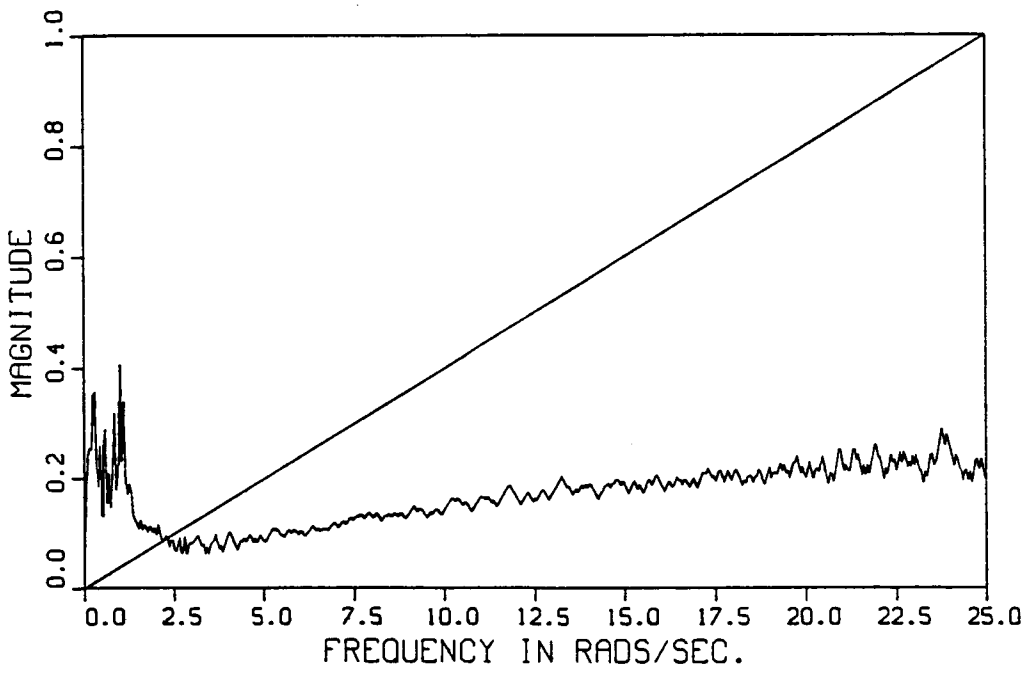

Figure 9.58: Final Uncertainty Bounding Function $\overline{\Delta}_{su}{}^{n}(e^{\omega_k T})$ for n=2500, Robust Estimator using Frequency-domain Parameter Estimator, Case 2. Straight line is a priori bound Δ_u.

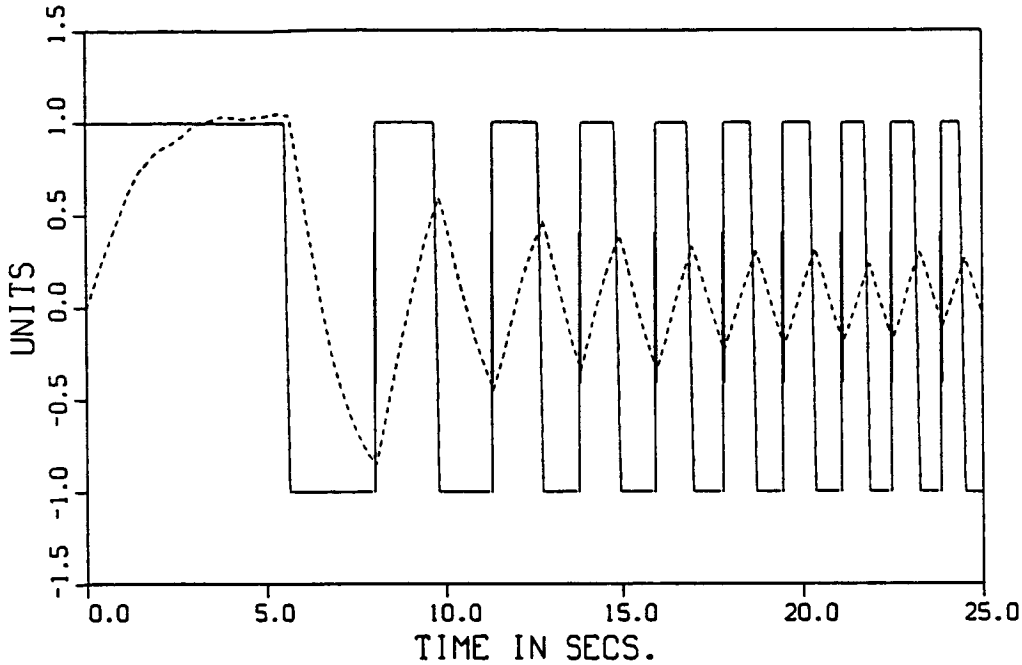

Figure 9.59: Plant Input u[n] and Output y[n] for Case 4, with a Disturbance.
(u[n] = ——, y[n] = - - - -)

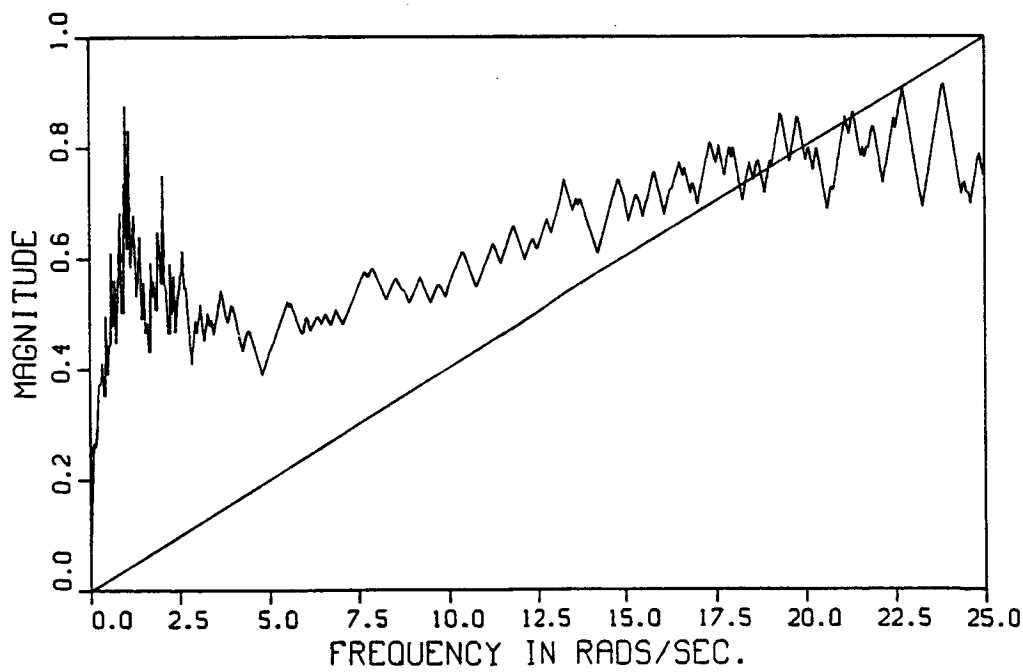

Figure 9.60: Final Uncertainty Bounding Function $\overline{\Delta}_{su}{}^{n}(e^{\omega_k T})$ for n=2500, Robust Estimator using Frequency-domain Parameter Estimator, Case 4. Straight line is a priori bound Δ_u.

9.5.4 Conclusion

In this section, we have studied the properties of the robust estimator through four simulations, one using the dead-zone based time-domain parameter estimator and the rest using the frequency-domain parameter estimator. We summarize our conclusions concerning these simulations.

1) The frequency-domain parameter estimator performs better than the dead-zone based parameter estimator.

2) The robust estimator (using the frequency-domain parameter estimator) works well and can yield a multiplicative uncertainty bounding function that is less than unity and, hence, useful for control design.

3) Since the additive error bound (at a given frequency) that the robust estimator can achieve is governed by the input signal and the disturbance alone, a smaller multiplicative error bound (at a given frequency) will result for a plant that is larger (at a given frequency).

These simulations show that the robust estimator (using a frequency-domain parameter estimator) can provide us with a useful bounding function on the multiplicative modeling uncertainty. Again, by useful we mean a bounding function that is, for example, less than unity for frequencies that are lower than the target closed-loop bandwidth. As we will see in the next section, this will allow the robust adaptive control system to increase the closed-loop bandwidth using the knowledge provided by the robust estimator.

9.6 Closed-loop Simulations using the Robust Estimator

9.6.1 Introduction

In this section, we will demonstrate that the robust estimator can be used in a robust adaptive controller to provide improved closed-loop performance as compared with a non-adaptive controller. In the simulations of this section, we will only use the robust estimator that uses the frequency-domain parameter estimator. We do this because, in the open-loop simulations, the frequency-domain parameter estimator was seen to perform better than the dead-zone based one. Several closed-loop simulations will be performed using the simple adaptive controller that was described in Chapter 7. In addition, we will implement a variation of the probing signal strategy that was developed in Section 7.4.3. The primary purpose of this section is to evaluate the behavior of the robust estimator in a closed-loop scenario and, hence, to see if it holds promise for adaptive control. In the following simulations, we aim to show the strengths as well as the weaknesses of the robust estimator.

9.6.2 Description of the Closed-loop Adaptive System and Performance Goals

Description of the Basic Closed-loop System

In this subsection, we describe the closed-loop adaptive system that will be simulated in the following subsections. Figure 9.61 shows the block diagram of the complete robust adaptive control system. We use the following simple pole-zero cancellation compensator,

$$K(z,\hat{\theta}) = G^{-1}(z,\hat{\theta})\, c / (z - 1), \tag{9.6.1}$$

which was developed in Section 7.3. We assume that the constants ε_1 and ε_2 of Theorem 7.2 are effectively zero in this subsection. In Eqn. (9.6.1), the compensator gain c will be determined using Eqn. (7.3.5) and Eqn. (7.3.24) in place of Eqn. (7.3.6), with ε_2=0. The compensator will be updated every 100 sample times or every 12.57 secs. This is considered infrequent since, as was discussed in Subsection 9.2.3, the slowest possible time constant of the true plant is 2.5 secs. While this does make the closed-loop system time-varying, it has been shown that, if the system varies "sufficiently slowly", then the exponential stability of the frozen-time systems implies the exponential stability of the slowly time-varying system. See [36] for a derivation of an upper bound on the variation rate for a slowly varying discrete-time system. So, if we guarantee that each compensator update yields a robustly stable LTI system and we vary the compensator slowly

enough, then the time-varying system is exponentially stable.

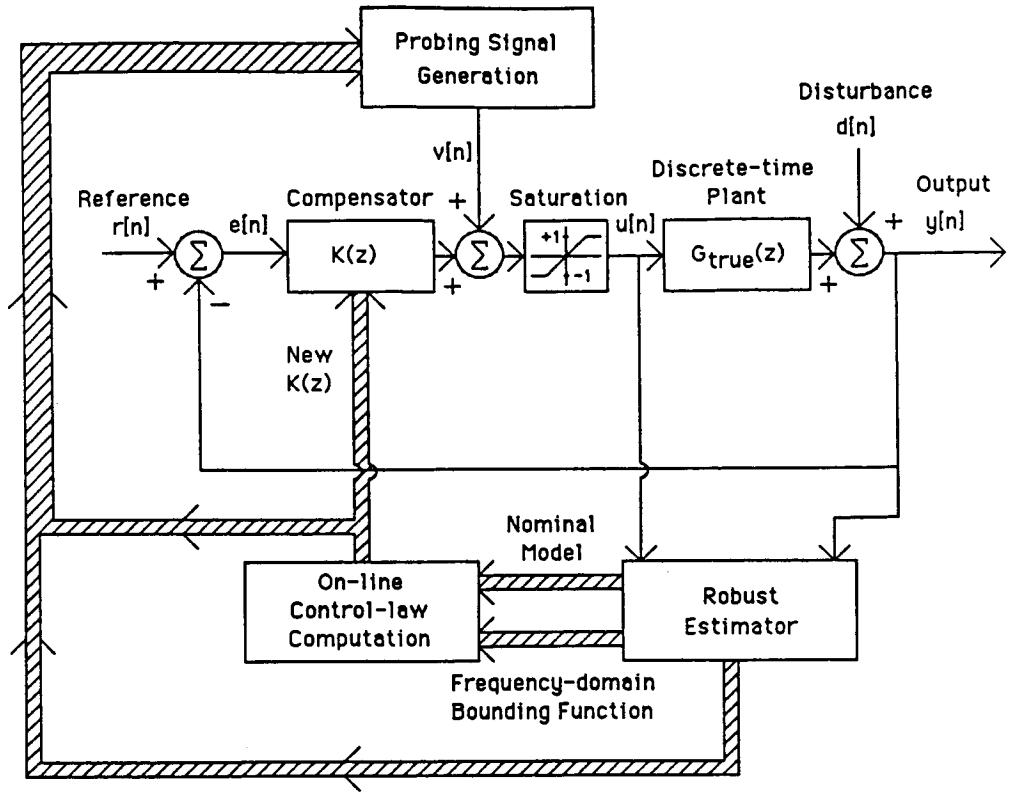

Figure 9.61: Complete Robust Adaptive Control System with Probing Signal.

The saturation block in Figure 9.61 is introduced because we must know a bound on the plant input signal u[n] as was assumed in AD3.1 of Chapter 3. We do not consider this a major limitation of the theory in that most physical systems have saturating actuators anyway. In the following simulations, we will attempt to avoid saturation at the plant input. One ramification of this is that the reference signal r[n] must be chosen to be much smaller than the input signal that was used in the previous simulations of this chapter. To avoid saturating at the input, for a system with the target closed-loop bandwidth of 5 rads/sec., we choose the reference signal r[n] to be one tenth of the input signal that was described in Subsection 9.2.8. Further, we also reduce the disturbance to be a tenth of the disturbance that was used in the previous simulations. That is, in all of the following simulations we use the disturbance signal of Subsection 9.2.7 with d_{factor}=0.01, as compared with d_{factor}=0.1 for the previous simulations. Recalling our discussion of how the remainder term $\overline{E}_{rem}$ looks like a constant disturbance term at all frequencies, we must also reduce this term. From the table in Subsection 9.4.1, we choose the memory length M=200, as compared with M=175 that was used in the previous simulations. This choice reduces $\overline{E}_{rem}$ by a factor of 3

to yield a value of 0.28901 for M=200. We scaled down our reference and disturbance signals by the same amount so that the signal-to-noise ratio of the closed-loop simulations was similar to that of the previous open-loop simulations.

In the following simulations we simulate the robust estimator using the frequency-domain parameter estimator. We use the projection method that was described in Subsection 9.2.9 and the weighting function of Eqn. (9.5.2) in the frequency-domain parameter estimator. In the frequency-domain bounding method we include the smoothing and safety factor modifications that were described in Sections 5.7 and 5.8, respectively. The robust uncertainty modification of Section 5.6 is not used in the simulations. Instead, we use the less conservative modification of making sure that the final uncertainty bounding function doesn't become less than the a priori bounding function on the unstructured uncertainty, $\Delta_u(e^{\omega_k T})$. That is, we denote the final uncertainty bounding function that is used by the control-law update algorithm by $\overline{\Delta}_{su}{}^n(e^{\omega_k T})_{new}$ where

$$\overline{\Delta}_{su}{}^n(e^{\omega_k T})_{new} = \max\{\, \overline{\Delta}_{su}{}^n(e^{\omega_k T}), \Delta_u(e^{\omega_k T}) \,\}, \tag{9.6.2}$$

and where $\overline{\Delta}_{su}{}^n(e^{\omega_k T})$ is the final bounding function yielded by the robust estimator.

Description of the Probing Signal Strategy

In the following simulations we will introduce a probing signal for some cases. We will use a modified form of the probing signal strategy that was developed in Section 7.4.3. First, we discuss the modifications and then we discuss the starting, stopping and updating conditions of the probing signal strategy.

The DFT magnitude of the probing signal, $|V_N{}^n(\omega_k)|$, will be generated using the following equation which is the same as Eqn. (7.4.18) except for the presence of the scaling factor γ.

$$|V_N{}^n(\omega_k)| = \gamma \cdot (1 + [c / |e^{j\omega_k T} - 1|\,] [1 + \overline{\Delta}_{su}{}^n(e^{j\omega_k T}, \hat{\theta})_{new}]) \cdot$$

$$(\overline{E}_{rem} + \overline{\overline{D}}_N(\omega_k)) / (|(e^{j\omega_k T} - 1) / c_{tcl} + 1| \inf_{\theta \in \Theta} \{|G(e^{j\omega_k T}, \theta)|\}), \forall \omega_k. \tag{9.6.3}$$

Recall that in our original derivation of $|V_N{}^n(\omega_k)|$ we assumed that: 1) the plant input signal was periodic with period N {see Eqn. (7.4.1)} and 2) that the nominal model fit the cumulative

frequency-domain estimate exactly {see Eqn. (7.4.4)}. Since these assumptions are not satisfied in the following simulations, we introduce the aforementioned scaling factor. We choose γ=10 in Eqn. (9.6.3) so that we stand a better chance of meeting our target closed-loop bandwidth. In addition, we choose the (continuous-time) target closed-loop bandwidth to be 5 rads/sec. With reference to Eqn. (7.3.20), we know that the nominal closed-loop system is

$$T_{cl}(z) = c / (z - 1 + c). \tag{9.6.4}$$

So, if we want this system to have a discrete-time pole that corresponds to the continuous-time target bandwidth, we must choose the target closed-loop compensator gain c_{tcl} as follows,

$$c_{tcl} = 1 - e^{-(5 \text{ rads/sec.})T} = 0.46651 \tag{9.6.5}$$

where we have used Eqn. (7.4.10). This is the value of c_{tcl} that we use in Eqn. (9.6.3).

As a second modification to the original probing signal strategy, we use a reduced number of sinusoids in our generation of a time-domain signal. With reference to Eqn. (7.4.21), we use the following equation to generate the time-domain probing signal,

$$v[n] = \frac{1}{N} \sum_{k=1}^{N/4} |V_N(\omega_k)| [a_k \cos(2 \pi k n / N) + b_k \sin(2 \pi k n / N)], \tag{9.6.6}$$

$$\text{for } n = 0, \ldots, N-1$$

where a_k and b_k are found using Eqns. (7.4.22-23). We choose not to excite the system at high frequencies since we will then be exciting the unmodeled dynamics of the plant. We also don't excite the system at ω=0 since we already know the D.C. gain of the true plant. By only exciting the system for frequencies that are less than $\omega_k=\omega_{(N/4)}$=12.5 rads/sec., we prevent ourselves from learning about the plant at high frequencies, unless of course the reference signal introduces high-frequency signals. This can cause problems as we will see later in the simulations. A benefit of this reduced excitation modification is a smaller time-domain probing signal.

A third and final modification concerns the selective turning-off of the probing signals for certain frequencies. We turn-off a given sinsoidal frequency when

$$\overline{E}_{cumf,N}^{n}(\omega_k) \le \eta \, |(e^{j\omega_k T} - 1) / c_{tcl} + 1| (\inf_{\theta \in \Theta} \{ |G(e^{j\omega_k T}, \theta)| \}). \tag{9.6.7}$$

This equation differs from Eqn. (7.4.26) in that we have introduced a scaling factor η, which we choose to be 0.5 in the following simulations. We use this scaling factor to make sure that after adding the safety factor of Section 5.8, we still have a small enough uncertainty bounding function

to be able to achieve our target closed-loop bandwidth. Now we discuss starting, stopping and updating conditions for the probing signal strategy.

In the following simulations we want things to happen in a finite time frame, so for the cases that use the probing signal we start the probing signal at time 0. The probing signal is updated every N=1000 time samples, or every 125.66 secs. That is, in Eqn. (9.6.2) we use the most recent values of the compensator gain c and the uncertainty bounding function $\overline{\Delta}_{su}{}^{n}(e^{j\omega_k T}, \hat{\theta})_{new}$. Updating the probing signal more often than the DFT length can cause problems. For example, if the probing signal were updated 10 times during the 1000 point DFT, then the transitions change the frequency content of the whole 1000 point signal. The probing signal is turned off as soon as the target compensator gain c_{tcl}= 0.46651 is achieved.

Adaptive Control and Closed-loop Performance Goals

We briefly discuss the overall goal of the robust adaptive control system. The goal of the robust adaptive control system is to reduce the structured uncertainty to zero and thus allow improved closed-loop control. Ideally, we would like to have the uncertainty bounding function Δ_{su} approach the a priori bounding function Δ_u on the unstructured uncertainty alone. If the uncertainty were reduced to the a priori bounding function Δ_u of Eqn. (9.2.24), which is never greater than unity, then the control-law update algorithm would yield a compensator gain of c=1. As was discussed in Remark 4 of Section 7.3, this would yield a deadbeat system, that is, the nominal closed-loop system would become simply a delay of one sampling period, $T_{cl}(z)=z^{-1}$. In the following simulations we will allow the adaptive control system to become deadbeat if it can reduce the uncertainty sufficiently. However, alternatively we could disallow the compensator gain c from becoming larger than the target gain of 0.46651. If this is modification is used, the resulting system is more robust than a deadbeat system.

9.6.5 Simulations using Case 2

In this subsection, we simulate the closed-loop adaptive system that was described above using the true plant of Case 2 of Subsection 9.2.4, which includes second-order unmodeled dynamics. Recall that the nominal model of Case 2 corresponds to the continuous-time parameters ζ=0.2 and ω_n=2 rads/sec. In addition, we introduce a disturbance with d_{factor}=0.01. We perform

two simulations, one without and one with the probing signal. For initial values, in both simulations, we set the cumulative frequency-domain estimate to the frequency response of the nominal model for ζ=0.8 and ω_n=1 rad/sec., and set the corresponding cumulative frequency-domain bounding function to the best bounding function that can be found using only a priori knowledge of the plant. Thus, we start the frequency-domain bounding method with parameter values that are very far from the true values of ζ=0.2 and ω_n=2 rads/sec.

Simulation 9.6.1: Case 2, with a Disturbance, without a Probing Signal

In this simulation we do not use a probing signal, but rely solely on the reference signal r[n] for excitation. First, we present a time history of the simulation in Table 9.11. In this table, we show the compensator gain that is computed by the control-law update algorithm every 100 time samples. As noted in the table, the compensator is not updated when the newly computed compensator gain is smaller than the current compensator gain. We also show the values of the continuous-time parameters that correspond to the nearest point in the 101 point projection grid. For insight, we compute the value of the continuous-time pole that corresponds to the discrete-time pole of the nominal closed-loop system. We compute

$$\text{Continuous-time Bandwidth} = -(1/T)\ln(1-c), \tag{9.6.8}$$

where c is the current compensator gain. From this table we see that the frequency-domain parameter estimator is able to find the true parameters of the nominal plant model by time n=2200 (276.46 secs.). In addition, the adaptive system is able to increase the bandwidth from 0.10 rad/sec to 2.49 rads/sec. However, we don't achieve our desired closed-loop bandwidth of 5 rads/sec. in the time frame of the simulation. It is possible that the system could eventually reach this target closed-loop bandwidth, as the sucessively higher bandwidth compensators are introduced. Using a priori information only we are stuck with the low nominal bandwidth of 0.10 rad/sec. for our control-law design methodology and our choice of initial conditions. Excited only by the relatively small reference signal r[n], the adaptive system is able to increase the bandwidth and thus yield better command-following properties for the closed-loop system. This improvement in command following can be seen in Figure 9.62, where we show the reference signal r[n] and the plant output y[n] on a broken time scale. Compare the command following for the time intervals just after 0, 125 and 250 secs. The tracking error,

$$e_t[n] = r[n] - y[n], \tag{9.6.9}$$

is shown in Figure 9.63, where we see that the error reaches zero faster just after 250 secs. than it does just after 0 secs. In Figure 9.64, we show the cumulative frequency-domain error bounding

function, $\overline{E}_{cumf,N}{}^{n}(\omega_k)$, and the actual error magnitude, $|E_{cumf,N}{}^{n}(\omega_k)|$, for n=2500 (314.16 secs.). The effect of the disturbance is clearly evident in the frequency range from 0 to 2.5 rads/sec. At higher frequencies, we can still see visages of the smooth a priori bounding function that was used to initialize the frequency-domain bounding method. In Figure 9.65, we show the bounding function $\overline{\Delta}_{su}{}^{n}(e^{j\omega_k T})$ yielded by the robust estimator along with a straight-line representing the lower bound, $\Delta_u(e^{j\omega_k T})$, that we enforce via Eqn. (9.6.2). Clearly, for this example, the modification of Eqn. (9.6.2) has no effect. From Figure 9.65, we see how the low-frequency peak, which is due to the disturbance, limits the bandwidth to 2.49 rads/sec.

Table 9.11: Simulation 9.6.1 - Case 2, with a Disturbance, without a Probing Signal. True Continuous-time Parameters, $\zeta = 0.2$ and $\omega_n = 2$ rads/sec.

(* denotes no compensator update)

Time Index n	Time t (secs.)	Computed Compensator Gain	Continuous-time Parameter Estimates ζ	ω_n	Continuous-time Bandwidth (rads/sec.)
0	0	0.01213	0.80	1.0	0.10
100	12.57	0.01213 *	0.80	1.0	0.10
200	25.13	0.01988	0.38	1.1	0.16
300	37.70	0.03430	0.32	1.3	0.28
400	50.27	0.03449	0.32	1.3	0.28
500	62.83	0.04213	0.26	1.6	0.34
600	75.40	0.04213 *	0.26	1.6	0.34
700	87.96	0.04382	0.26	1.6	0.36
800	100.53	0.05318	0.26	1.6	0.43
900	113.10	0.05318 *	0.26	1.6	0.43
1000	125.66	0.05318 *	0.26	1.6	0.43
1100	138.23	0.05540	0.26	1.6	0.45
1200	150.80	0.06531	0.26	1.6	0.54
1300	163.36	0.06712	0.26	1.6	0.55
1400	175.93	0.07491	0.26	1.7	0.62
1500	188.50	0.07349 *	0.26	1.7	0.62
1600	201.06	0.07349 *	0.26	1.7	0.62
1700	213.63	0.07349 *	0.26	1.7	0.62
1800	226.20	0.07227 *	0.26	1.8	0.62
1900	238.76	0.07696	0.26	1.8	0.64
2000	251.33	0.08663	0.26	1.8	0.72
2100	263.89	0.08663 *	0.26	1.8	0.72
2200	276.46	0.18548	0.20	2.0	1.63
2300	289.03	0.18548 *	0.20	2.0	1.63
2400	301.59	0.26857	0.20	2.0	2.49
2500	314.16	0.26857 *	0.20	2.0	2.49

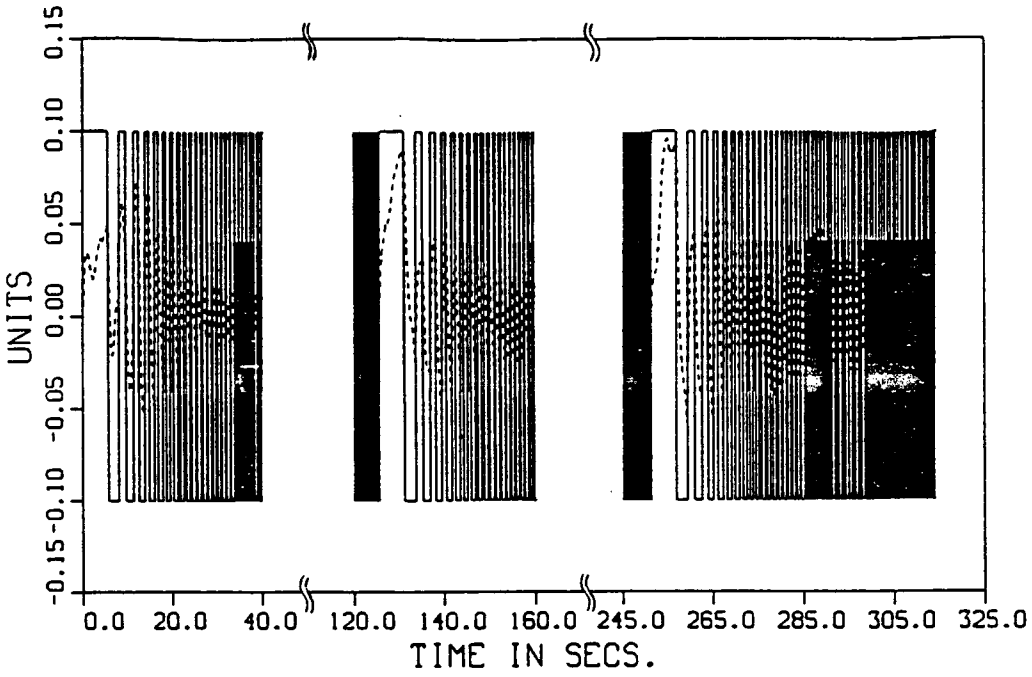

Figure 9.62: Reference r[n] and Plant Output y[n] for Case 2, Without Probing Signal.
(r[n] = ——, y[n] = - - - -)

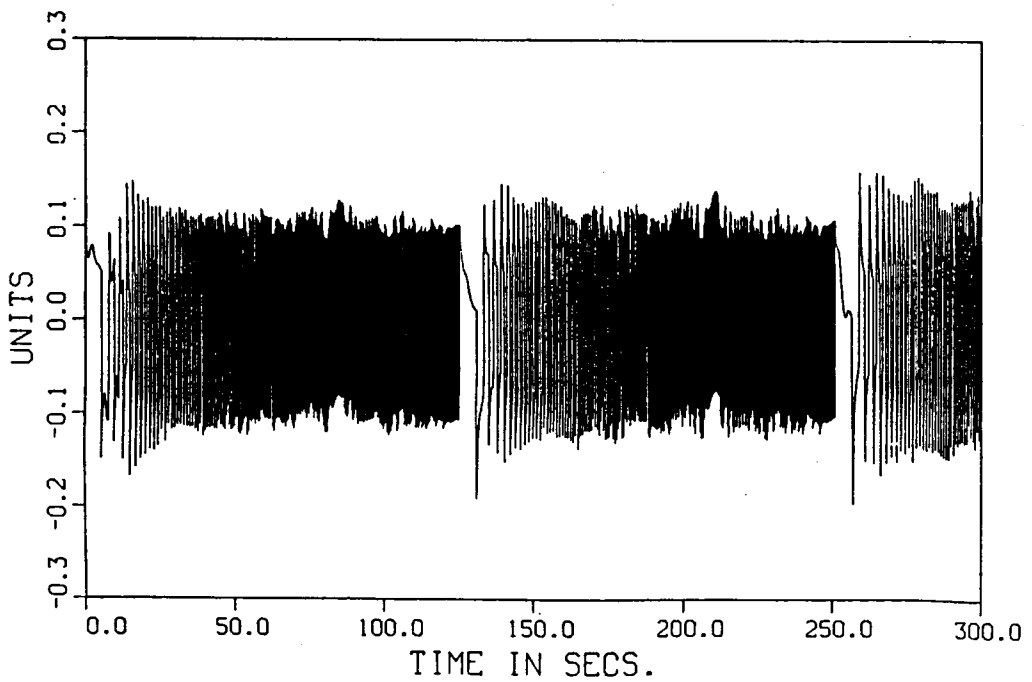

Figure 9.63: Tracking Error, $e_t[n] = r[n] - y[n]$, for Case 2, Without Probing Signal.

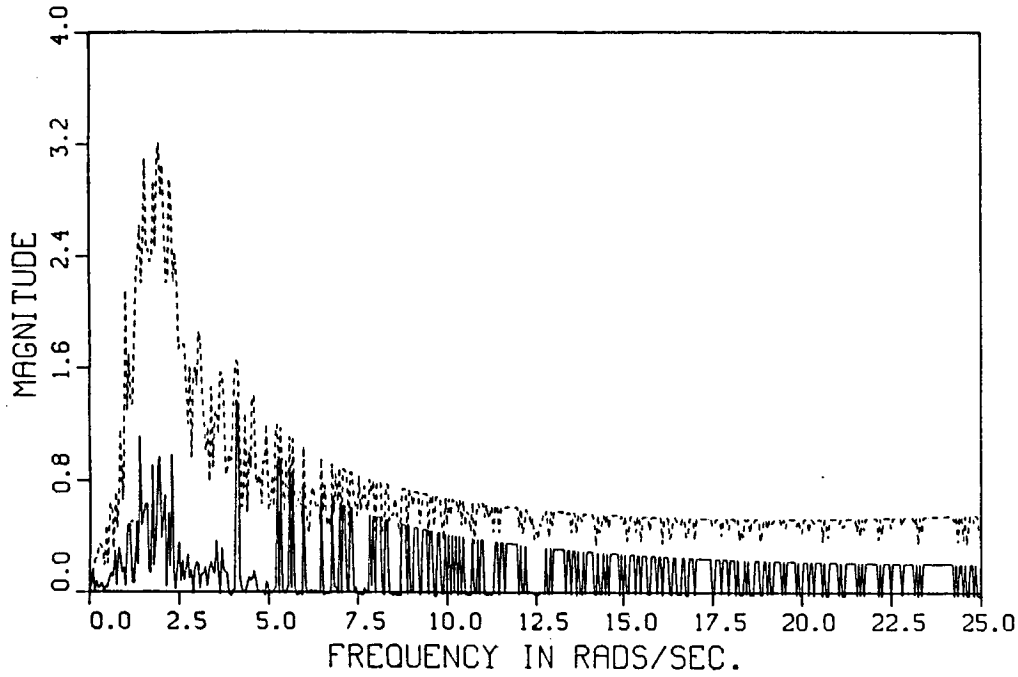

Figure 9.64: $|E_{cumf,N}^{n}(\omega_k)|$ and $\overline{E}_{cumf,N}^{n}(\omega_k)$ for n=2500, Case 2, Without Probing Signal.

($|E_{cumf,N}^{n}(\omega_k)|$ = ——, $\overline{E}_{cumf,N}^{n}(\omega_k)$ = - - - -)

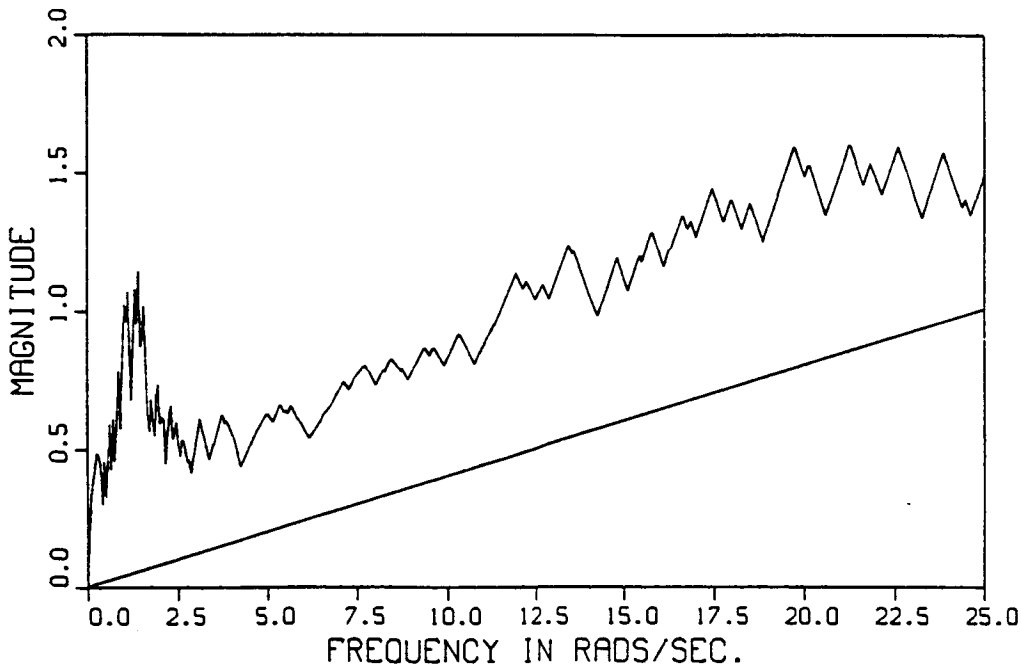

Figure 9.65: $\overline{\Delta}_{su}^{n}(e^{\omega_k T})$ for n=2500, Case 2, Without Probing Signal. Straight line is a priori bound Δ_u.

Simulation 9.6.2: Case 2, with a Disturbance and a Probing Signal

In this simulation we use the probing signal strategy that was described in Subsection 9.6.5. Since the probing signal doesn't excite high frequencies (i.e. above 12.5 rads/sec.), we can only gain high-frequency knowledge of the plant from the excitation due to the reference signal. A time history of the simulation is presented in Table 9.12. From this table we see that the frequency-domain parameter estimator is able to find the true parameters of the nominal plant model by time n=900 (113.10 secs.). As expected, the probing signal allows the robust estimator to find the true parameter values in a much shorter time than in the previous simulation. In addition, the adaptive system is able to greatly increase the closed-loop bandwidth from the low initial value of 0.10 rad/sec. At the end of the simulation, the nominal closed pole of the discrete-time system is zero, which corresponds to an infinite continuous-time bandwidth via the relationship $z=e^{sT}$. However, we must recall that the nominal closed-loop system still has a delay of one sampling period. The increases in bandwidth that occur after the probing signal is turned off are due to the excitation of the reference signal. As was discussed previously, we could have prevented the system from becoming deadbeat by not allowing the compensator gain to become any larger than the value that achieves our target closed-loop bandwidth.

From this simulation, we see that the probing signal gets things started for the adaptive control system, but is turned-off at n=1100 (138.23 secs.) when the nominal closed-loop bandwidth exceeds our target value. Comparing the results of this simulation with the previous one, we see that the probing signal has indeed helped the robust estimator identify the system and yield a high-performance closed-loop system. However, in the following time-domain figures, we will see how the probing signal also greatly disturbs the system, preventing any semblance of command-following when the probing signal is present.

In Figure 9.66, we show the probing signal v[n]. The signal is only updated once at n=1000 (125.66 secs.) and is changed very little at this time, since the compensator gain c is still small. The reference signal r[n] and the plant output y[n] are shown, on a broken time scale, in Figure 9.67. From this figure, it can be seen that, after the probing signal is turned off, the command following appears to be good. From Table 9.12, we know that after n=2200 (276.46 secs.) the nominal closed-loop system is simply a delay. In Figure 9.68, we show r[n] and y[n] again, on a shorter time scale, to show that the actual closed-loop system indeed performs like a delay of T=0.126 secs. except for the presence of the unmodeled dynamics. The tracking error is shown in Figure 9.69, where the effects of the probing signal are again apparent. Note that the tracking error doesn't go to zero because of the unavoidable delay in the discrete-time closed-loop system. These time-domain figures show how much the probing signal disturbs the system in this example. If we used a smaller probing signal, then we would have to wait longer for the closed-loop bandwidth to

increase. We now consider our frequency-domain results.

In Figure 9.70, we show the cumulative frequency-domain error bounding function, $\overline{E}_{cumf,N}^{n}(\omega_k)$, and the actual error magnitude, $|E_{cumf,N}^{n}(\omega_k)|$, for n=2500 (314.16 secs.). We see how the probing signal has provided accurate information for frequencies below 12.5 rads/sec. At frequencies above 12.5 rads/sec, the bounding function is larger, since only the reference signal excites the system for these frequencies. In Figure 9.71, we show the bounding function $\overline{\Delta}_{su}^{n}(e^{j\omega_k T})$ yielded by the robust estimator along with a straight-line representing the lower bound, $\Delta_u(e^{j\omega_k T})$, that we enforce via Eqn. (9.6.2). For this example, the modification of Eqn. (9.6.2) has an effect and prevents the uncertainty bounding function that is used in the control-law update, from becoming less than $\Delta_u(e^{j\omega_k T})$. Comparing Figures 9.65 and 9.71, we see how the probing signal has counteracted the effect of the disturbance in the low-frequency range. For insight, we investigate the disturbance rejection properties of the closed-loop system at different time indices.

In Figure 9.72, we show the magnitude of the nominal sensitivity transfer function,

$$S(z) = (z - 1) / (z - 1 + c), \qquad (9.6.10)$$

for time indices n=0, n=500 (62.83 secs.), n=1100 (138.23 secs.), n=2100 (263.89 secs.) and n=2200 (276.46 secs.). That is, at the different time indices shown in Table 9.12, the compensator gain c will have different values corresponding to different nominal sensitivity transfer functions. We show the sensitivity transfer functions to make a point. From Figure 9.72 we see that, as time increases, the closed-loop does an increasingly good job of rejecting disturbances in the low-frequency range. This means that to produce the same effect at the plant input u[n], the probing signal v[n] will need to be made increasingly larger to compensate for the fact that it is being rejected by the closed-loop system. In the present simulation, we don't get to see this occur, since the probing signal turns off before the loop can effectively reject it.

Table 9.12: Simulation 9.6.2 - Case 2, with a Disturbance and a Probing Signal.
True Continuous-time Parameters, $\zeta = 0.2$ and $\omega_n = 2$ rads/sec.

(* denotes no compensator update)
(¤ denotes probing signal turn-off)

Time Index n	Time t (secs.)	Computed Compensator Gain	Continuous-time Parameter Estimates ζ	ω_n	Continuous-time Bandwidth (rads/sec.)
0	0	0.01213	0.80	1.0	0.10
100	12.57	0.01698	0.44	1.0	0.14
200	25.13	0.02256	0.38	1.1	0.18
300	37.70	0.04243	0.32	1.3	0.35
400	50.27	0.04213 *	0.26	1.6	0.35
500	62.83	0.04303	0.26	1.6	0.35
600	75.40	0.04180 *	0.26	1.7	0.35
700	87.96	0.04155 *	0.26	1.8	0.35
800	100.53	0.04155 *	0.26	1.8	0.35
900	113.10	0.03990 *	0.20	2.0	0.35
1000	125.66	0.03990 *	0.20	2.0	0.35
1100	138.23	0.53177 ¤	0.20	2.0	6.04
1200	150.80	0.53177 *	0.20	2.0	6.04
1300	163.36	0.53177 *	0.20	2.0	6.04
1400	175.93	0.53177 *	0.20	2.0	6.04
1500	188.50	0.53177 *	0.20	2.0	6.04
1600	201.06	0.53177 *	0.20	2.0	6.04
1700	213.63	0.53177 *	0.20	2.0	6.04
1800	226.20	0.53177 *	0.20	2.0	6.04
1900	238.76	0.53177 *	0.20	2.0	6.04
2000	251.33	0.53177 *	0.20	2.0	6.04
2100	263.89	0.65683	0.20	2.0	8.51
2200	276.46	1.00000	0.20	2.0	∞
2300	289.03	1.00000 *	0.20	2.0	∞
2400	301.59	1.00000 *	0.20	2.0	∞
2500	314.16	1.00000 *	0.20	2.0	∞

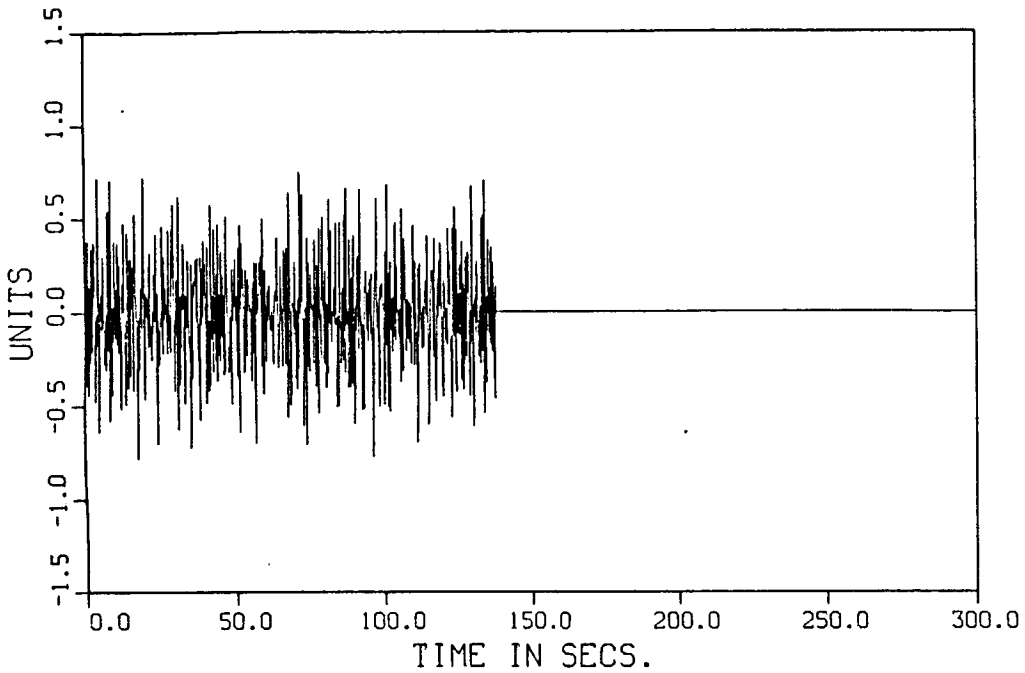

Figure 9.66: Probing Signal v[n] for Case 2 Simulation.

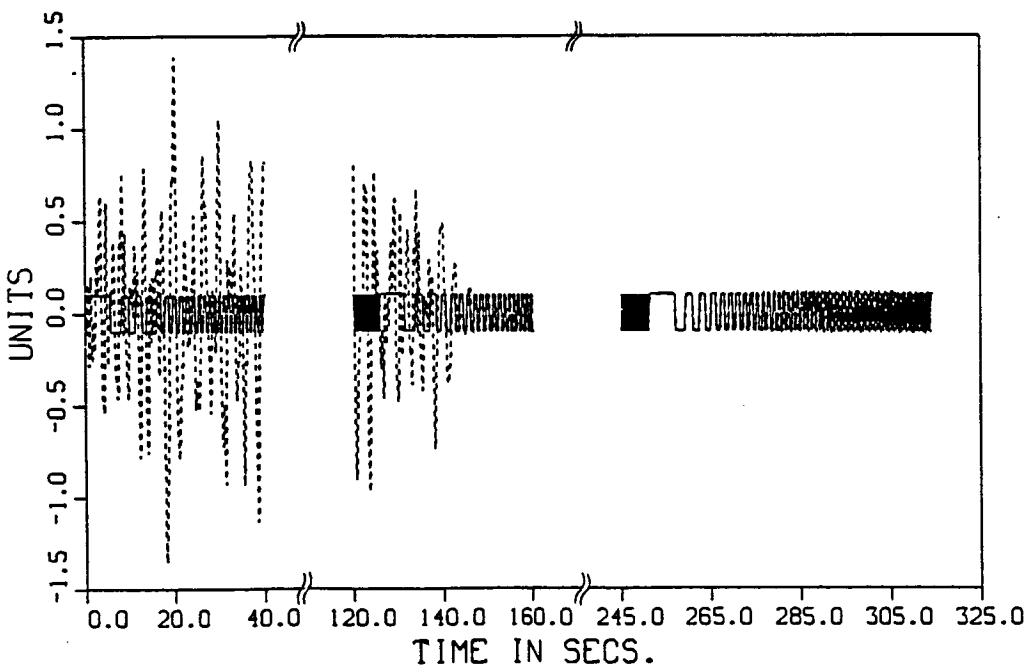

Figure 9.67: Reference r[n] and Plant Output y[n] for Case 2, With Probing Signal, Long Plot.
(r[n] = ——, y[n] = - - - -)

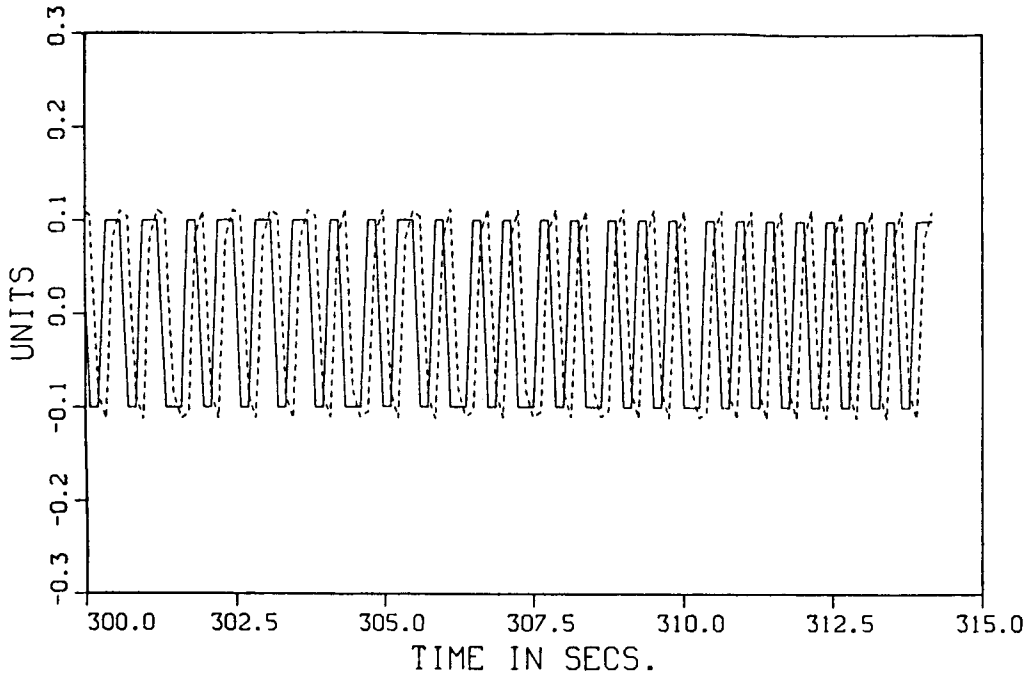

Figure 9.68: Reference r[n] and Plant Output y[n] for Case 2, With Probing Signal, Short Plot.
(r[n] = ——, y[n] = - - - -)

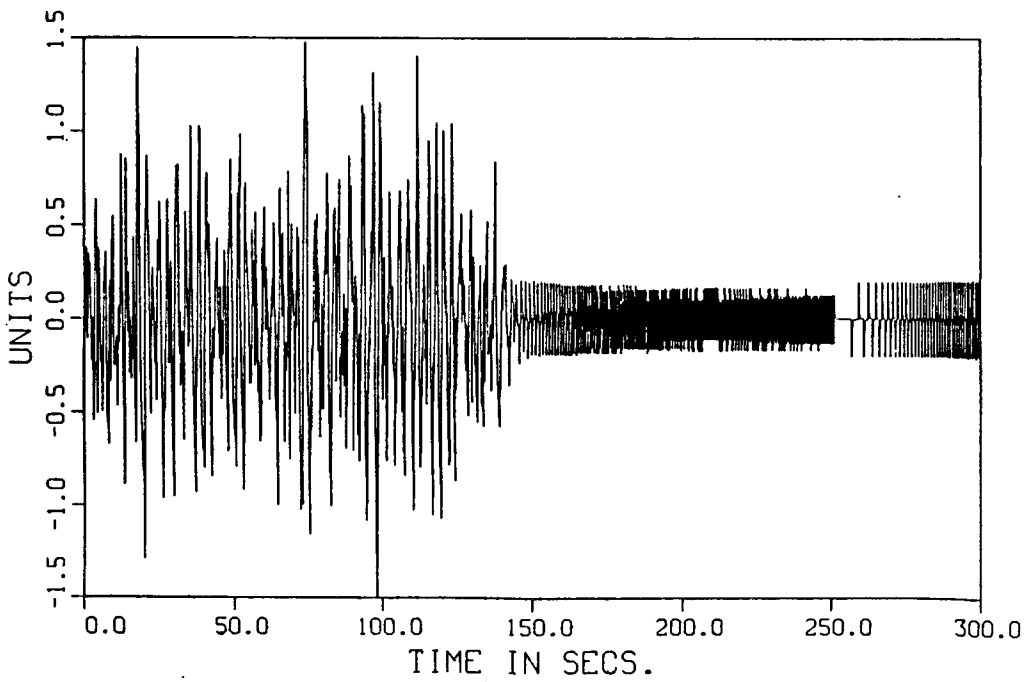

Figure 9.69: Tracking Error, $e_t[n] = r[n] - y[n]$, for Case 2, With Probing Signal.

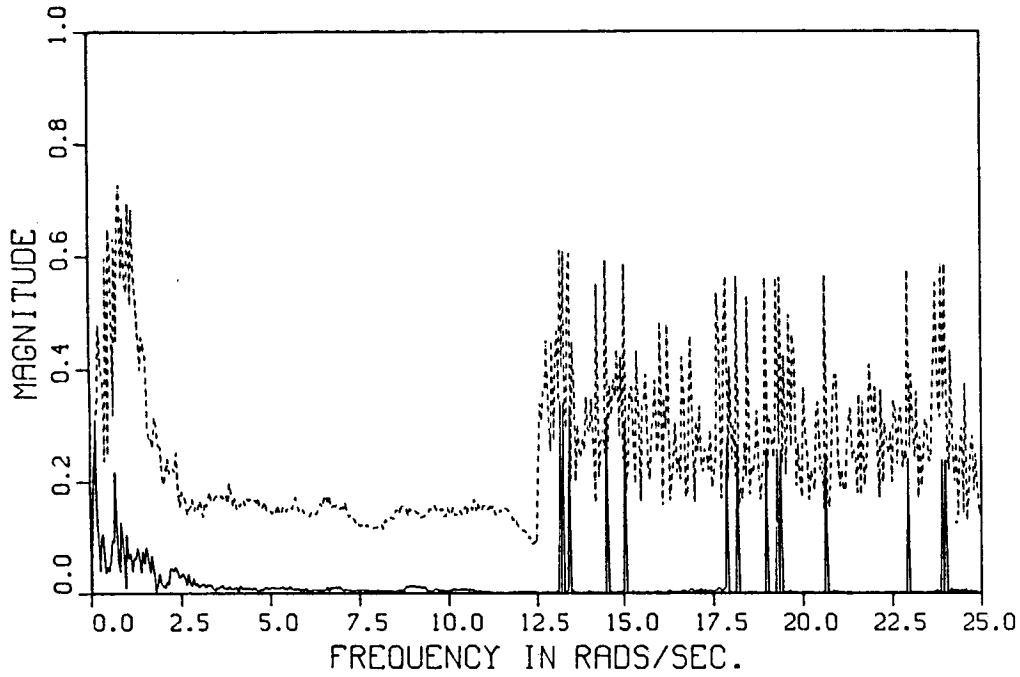

Figure 9.70: $|E_{cumf,N}^{n}(\omega_k)|$ and $\overline{E}_{cumf,N}^{n}(\omega_k)$ for n=2500, Case 2, With Probing Signal.

($|E_{cumf,N}^{n}(\omega_k)| =$ ——, $\overline{E}_{cumf,N}^{n}(\omega_k) =$ - - - -)

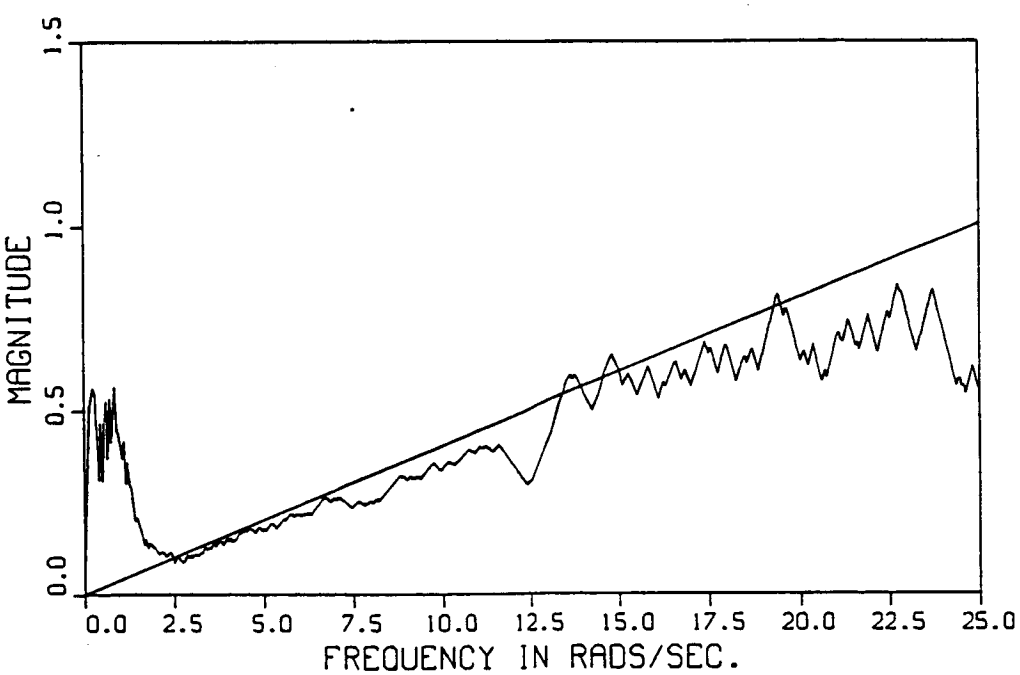

Figure 9.71: $\overline{\Delta}_{su}^{n}(e^{\omega_k T})$ for n=2500, Case 2, With Probing Signal. Straight line is a priori bound Δ_u.

C-4

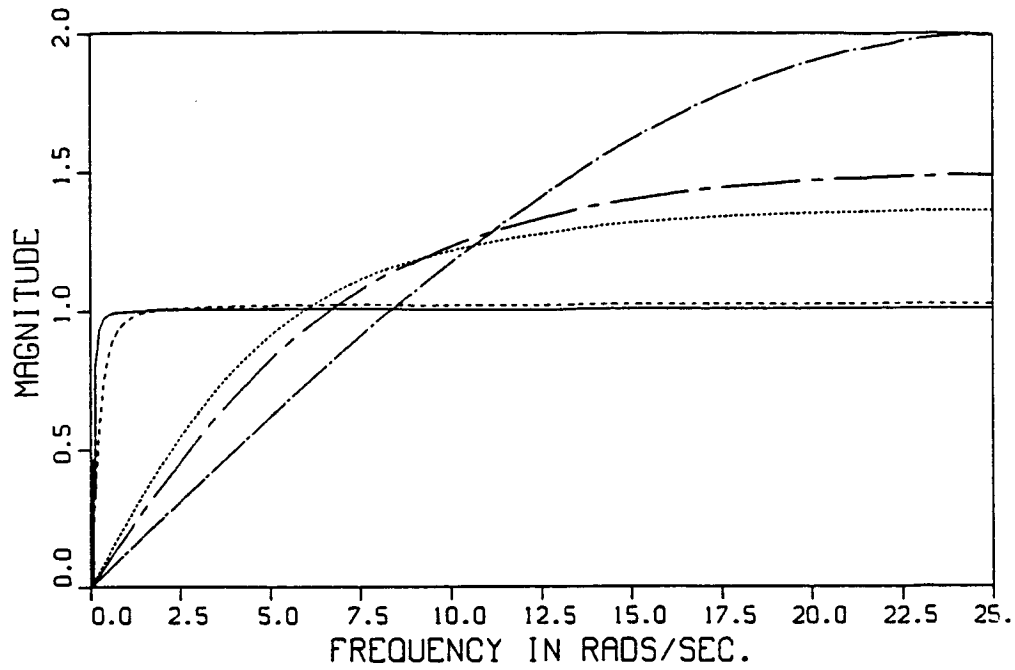

Figure 9.72: Sensitivity Transfer Functions for Case 2, With Probing Signal, for Different Time Indices. (0 = ——, 500 = - - - - , 1100 = ..., 2100 = — — —, 2200 = — - —)

9.6.6 Simulations using Case 4

In this subsection, we simulate the closed-loop adaptive system using the true plant of Case 4 of Subsection 9.2.4, which includes second-order unmodeled dynamics. Recall that the nominal model of Case 4 corresponds to the continuous-time parameters ζ=0.8 and ω_n=1 rad/sec. In addition, we introduce a disturbance with d_{factor}=0.01. We perform two simulations, one without and one with the probing signal. For initial values, in both simulations, we set the cumulative frequency-domain estimate to the frequency response of the nominal model for ζ=0.2 and ω_n=2 rads/sec., and set the corresponding cumulative frequency-domain bounding function to the best bounding function that can be found using only a priori knowledge of the plant. Thus, we start the frequency-domain bounding method with parameter values that are very far from the true values of ζ=0.8 and ω_n=1 rad/sec. From our open-loop simulation results, we expect the robust estimator to have much more difficulty identifying Case 4, than it did with Case 2 in the previous subsection. Again, this is because Case 4 rolls-off at a lower frequency than Case 2.

Simulation 9.6.3: Case 4, with a Disturbance, without a Probing Signal

In this simulation we do not use a probing signal but rely solely on the reference signal r[n] for excitation. First, we present a time history of the simulation in Table 9.13. From this table we see that the frequency-domain parameter estimator is not able to find the true parameters of the nominal plant model. In addition, the robust adaptive controller is not able to increase the compensator gain and, hence, the nominal closed-loop bandwidth. Consequently, the system exhibits very poor command-following properties as can be seen in Figure 9.73, which shows the tracking error.

One cause for the poor performance of the robust estimator is our initial choice of compensator. For ζ=0.2 and ω_n=2 rads/sec., the plant-inverting compensator greatly attenuates the frequency components around 2 rads/sec. since this is where the nominal model corresponding to ζ=0.2 and ω_n=2 rads/sec. has a large peak. In this simulation, it might have been wise to update the compensator even if the newly computed compensator gain is not less than the current gain. That is, the frequency response of a lower gain compensator might be more desirable from an excitation viewpoint than the compensator that has a notch at 2 rads/sec. In Figure 9.74, we show the cumulative frequency-domain error bounding function, $\overline{E}_{cumf,N}^{n}(\omega_k)$, and the actual error magnitude, $|E_{cumf,N}^{n}(\omega_k)|$, for n=2500 (314.16 secs.). The large peak in this figure is due to the poor compensator (from an excitation viewpoint) and the effects of the disturbance. At higher frequencies, we can still see visages of the smooth a priori bounding function that was used to initialize the frequency-domain bounding method. In Figure 9.75, we show the bounding function $\overline{\Delta}_{su}^{n}(e^{j\omega_k T})$ yielded by the robust estimator along with $\Delta_u(e^{j\omega_k T})$. For this example, the modification of Eqn. (9.6.2) has no effect. From Figure 9.75, we see how that the uncertainty bounding function is larger than unity for all frequencies greater than about 1 rad/sec. Clearly, this bounding function is not very useful for increasing the bandwidth of the system.

Table 9.13: Simulation 9.6.3 - Case 4, with a Disturbance, without a Probing Signal.
True Continuous-time Parameters, $\zeta = 0.8$ and $\omega_n = 1$ rad/sec.

(* denotes no compensator update)

Time Index n	Time t (secs.)	Computed Compensator Gain	Continuous-time Parameter Estimates ζ	ω_n	Continuous-time Bandwidth (rads/sec.)
0	0	0.13292	0.20	2.0	1.13
100	12.57	0.13292 *	0.20	2.0	1.13
200	25.13	0.05843 *	0.20	2.0	1.13
300	37.70	0.05849 *	0.20	2.0	1.13
400	50.27	0.06017 *	0.26	1.8	1.13
500	62.83	0.06839 *	0.26	1.8	1.13
600	75.40	0.06578 *	0.38	1.9	1.13
700	87.96	0.06578 *	0.38	1.9	1.13
800	100.53	0.06578 *	0.38	1.9	1.13
900	113.10	0.06578 *	0.38	1.9	1.13
1000	125.66	0.05804 *	0.44	1.8	1.13
1100	138.23	0.05730 *	0.56	1.8	1.13
1200	150.80	0.05468 *	0.68	1.5	1.13
1300	163.36	0.05468 *	0.68	1.5	1.13
1400	175.93	0.05468 *	0.68	1.5	1.13
1500	188.50	0.05468 *	0.68	1.5	1.13
1600	201.06	0.05468 *	0.68	1.5	1.13
1700	213.63	0.05468 *	0.68	1.5	1.13
1800	226.20	0.05538 *	0.68	1.5	1.13
1900	238.76	0.05538 *	0.68	1.5	1.13
2000	251.33	0.05868 *	0.62	1.5	1.13
2100	263.89	0.05868 *	0.62	1.5	1.13
2200	276.46	0.05868 *	0.62	1.5	1.13
2300	289.03	0.05673 *	0.62	1.5	1.13
2400	301.59	0.05673 *	0.62	1.5	1.13
2500	314.16	0.05673 *	0.62	1.5	1.13

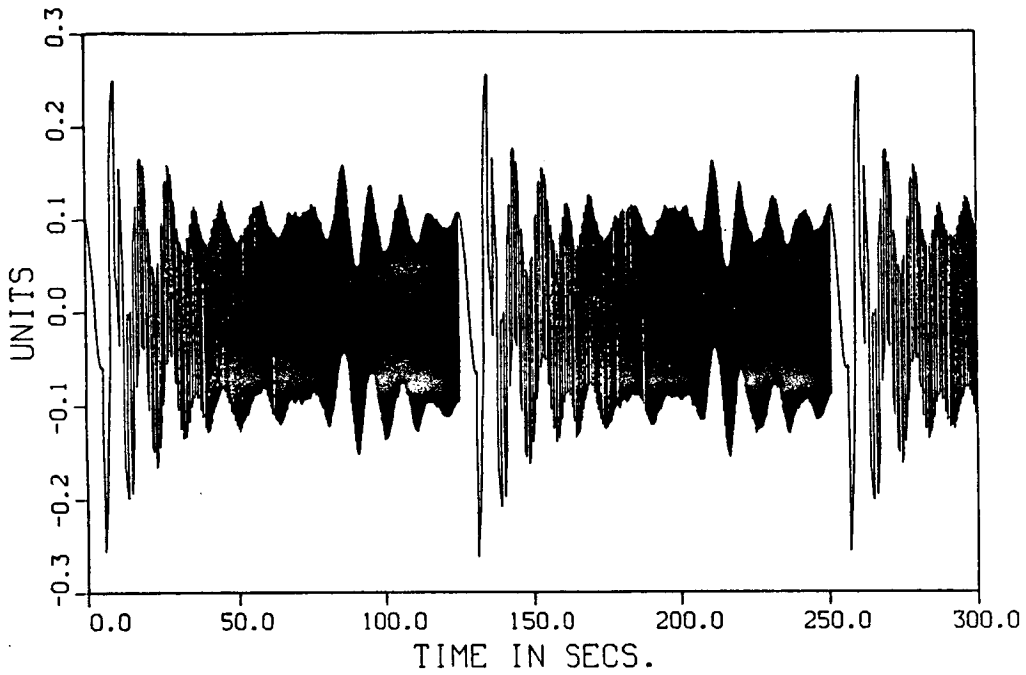

Figure 9.73: Tracking Error, $e_t[n] = r[n] - y[n]$, for Case 4, Without Probing Signal.

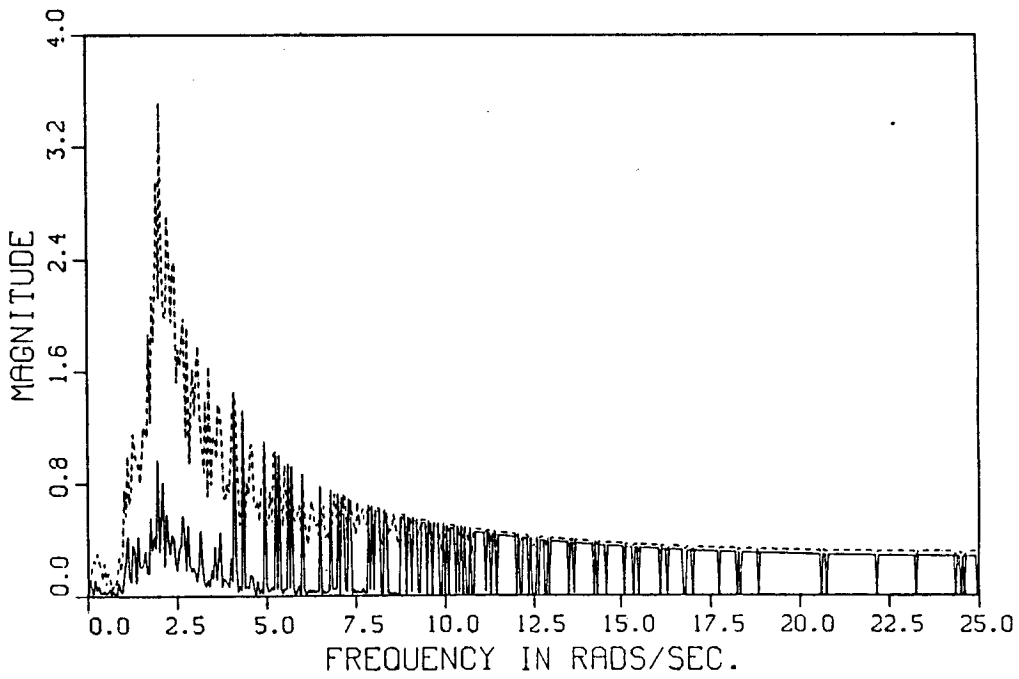

Figure 9.74: $|E_{cumf,N}^{n}(\omega_k)|$ and $\overline{E}_{cumf,N}^{n}(\omega_k)$ for n=2500, Case 4, Without Probing Signal.

($|E_{cumf,N}^{n}(\omega_k)|$ = ——, $\overline{E}_{cumf,N}^{n}(\omega_k)$ = - - - -)

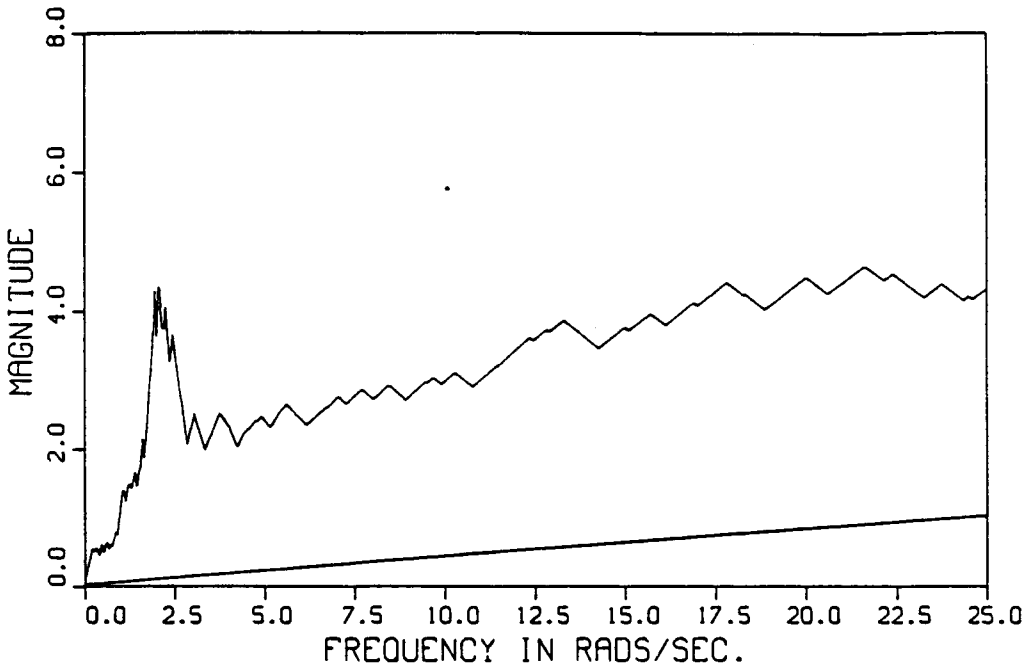

Figure 9.75: $\overline{\Delta}_{su}{}^{n}(e^{\omega_k T})$ for n=2500, Case 4, Without Probing Signal. Straight line is a priori bound Δ_u.

Simulation 9.6.4: Case 4, with a Disturbance and a Probing Signal

In this simulation, we use the probing signal strategy that was described in Subsection 9.6.5. A time history of the simulation is presented in Table 9.14. From this table we see that the frequency-domain parameter estimator is not able to find the true parameters of the nominal plant; however, it is able to find the correct value of ζ=0.8. This partial knowledge combined with the frequency-domain bounding information allows the adaptive system to increase the closed-loop bandwidth from the initial value of 1.13 rads/sec to 2.44 rads/sec. As can be seen from the table, the first 1000 sample times of the probing signal result in no increase in the closed-loop bandwidth. The probing signal is updated at n=1000, that is, a new compensator gain and uncertainty bounding function are used in Eqn. (9.6.3). This updated probing signal, which is again updated at n=2000, results in the bandwidth increase at n=2200. Since the target closed-loop bandwidth is not reached, the probing signal is not turned off and continues to disturb the system until the end of the simulation. This performance is not very impressive, but the understanding that we gain from this simulation provides clues for making improvements in our probing signal strategy.

In Figure 9.76, we show the probing signal v[n]. This signal is updated at n=1000 (125.66

secs.) and n=2000 (251.33 secs.). The tracking error is shown in Figure 9.77, where the effects of the probing signal are again apparent. Since the probing signal overwhelms the reference signal in this example, we cannot observe any kind of command following performance. However, for times greater than n=2200 (276.46 secs.), when the compensator is updated, the system seems to do a better job of rejecting the probing signal. To understand the poor performance of this simulation we must consider our frequency-domain results.

In Figure 9.78, we show the cumulative frequency-domain error bounding function, $\overline{E}_{cumf,N}^{n}(\omega_k)$, and the actual error magnitude, $|E_{cumf,N}^{n}(\omega_k)|$, for n=2500 (314.16 secs.). We see how the probing signal has provided accurate information for frequencies below 12.5 rads/sec. However, the robust estimator has not been able to learn any information about the plant for frequencies greater than 12.5 rads/sec. For these frequencies the cumulative frequency-domain estimate is still equal to the initial value. So, for frequencies above 12.5 rads/sec. the cumulative frequency-domain estimate, at n=2500 (314.16 secs.) is equal to the frequency response of the nominal model for ζ=0.2 and ω_n=2 rads/sec. When the parameter estimator performs its frequency-domain fit to the cumulative frequency-domain estimate it sees no peak but the erroneous information at high frequencies results in a large error for the ω_n estimate. This helps explain the fact that the frequency-domain parameter estimator correctly estimates ζ to be 0.8 but yields a grossly incorrect value of ω_n=2 rads/sec instead of the true value of 1 rad/sec. One solution to this problem would be to actually have the probing signal excite the true plant at high frequencies, thus enabling the frequency-domain estimator to perform better. This would help us in the example of this simulation, because the structured uncertainty is large at high frequencies. However, this increased excitation approach will result in a larger probing signal that will saturate the plant input in this simulation. If the plant input signal saturates, then some frequency components of the probing signal will be reduced resulting in insufficient excitation at those frequencies.

In Figure 9.79, we show the bounding function $\overline{\Delta}_{su}^{n}(e^{j\omega_k T})$ yielded by the robust estimator along with $\Delta_u(e^{j\omega_k T})$. For this example, the modification of Eqn. (9.6.2) has no effect. Comparing Figures 9.75 and 9.79, we see that the probing signal has helped greatly to reduce the uncertainty bounding function, particularly in the low-frequency range. From Figure 9.79, it can be shown that it is the large values of the uncertainty bounding function at high frequencies that limit the bandwidth of the system. The probing signal must be extended further into the high

frequency range to obtain the target closed-loop bandwidth in this example.

A Note for the Curious Reader

The perceptive reader will notice that the cumulative frequency-domain bounding function is updated for frequencies greater than 12.5 rads/sec in Simulation 9.6.3 (no probing signal) but is not updated in this frequency range in Simulation 9.6.4 (with a probing signal). Since the reference signal r[n] is the same in both simulations, this is a curious result. The author believes that in Simulation 9.6.4, the mild saturation that occurs at the plant input is the cause of this phenomenon. As can be seen from Figure 9.74, for frequencies greater than 12.5 rads/sec, the improvement in the cumulative frequency-domain error bounding function is very small. That is, the reference signal provides just enough signal to learn something at these high frequencies in the no probing signal case. In the probing signal case, a small amount of saturation occurs at the plant input, thereby reducing the richness of the reference signal enough so that no updating occurs at high frequencies. To test this theory, the reference signal was increased slightly in the probing signal case and it was indeed observed that some updating then occurred for frequencies greater than 12.5 rads/sec.

Table 9.14: Simulation 9.6.4 - Case 4, with a Disturbance and a Probing Signal.
True Continuous-time Parameters, $\zeta = 0.8$ and $\omega_n = 1$ rad/sec.

(* denotes no compensator update)

Time Index n	Time t (secs.)	Computed Compensator Gain	Continuous-time Parameter Estimates ζ	ω_n	Continuous-time Bandwidth (rads/sec.)
0	0	0.13292	0.20	2.0	1.13
100	12.57	0.07629 *	0.20	2.0	1.13
200	25.13	0.06486 *	0.26	1.9	1.13
300	37.70	0.05558 *	0.32	1.9	1.13
400	50.27	0.04759 *	0.32	1.9	1.13
500	62.83	0.05739 *	0.38	1.9	1.13
600	75.40	0.05298 *	0.44	1.8	1.13
700	87.96	0.05618 *	0.50	1.8	1.13
800	100.53	0.05618 *	0.50	1.8	1.13
900	113.10	0.04639 *	0.80	2.0	1.13
1000	125.66	0.04639 *	0.80	2.0	1.13
1100	138.23	0.07299 *	0.80	2.0	1.13
1200	150.80	0.12444 *	0.80	2.0	1.13
1300	163.36	0.12444 *	0.80	2.0	1.13
1400	175.93	0.12444 *	0.80	2.0	1.13
1500	188.50	0.12444 *	0.80	2.0	1.13
1600	201.06	0.12444 *	0.80	2.0	1.13
1700	213.63	0.12444 *	0.80	2.0	1.13
1800	226.20	0.12444 *	0.80	2.0	1.13
1900	238.76	0.12444 *	0.80	2.0	1.13
2000	251.33	0.12444 *	0.80	2.0	1.13
2100	263.89	0.12444 *	0.80	2.0	1.13
2200	276.46	0.26425	0.80	2.0	2.44
2300	289.03	0.26425 *	0.80	2.0	2.44
2400	301.59	0.26425 *	0.80	2.0	2.44
2500	314.16	0.26425 *	0.80	2.0	2.44

The probing signal never turns off in this simulation.

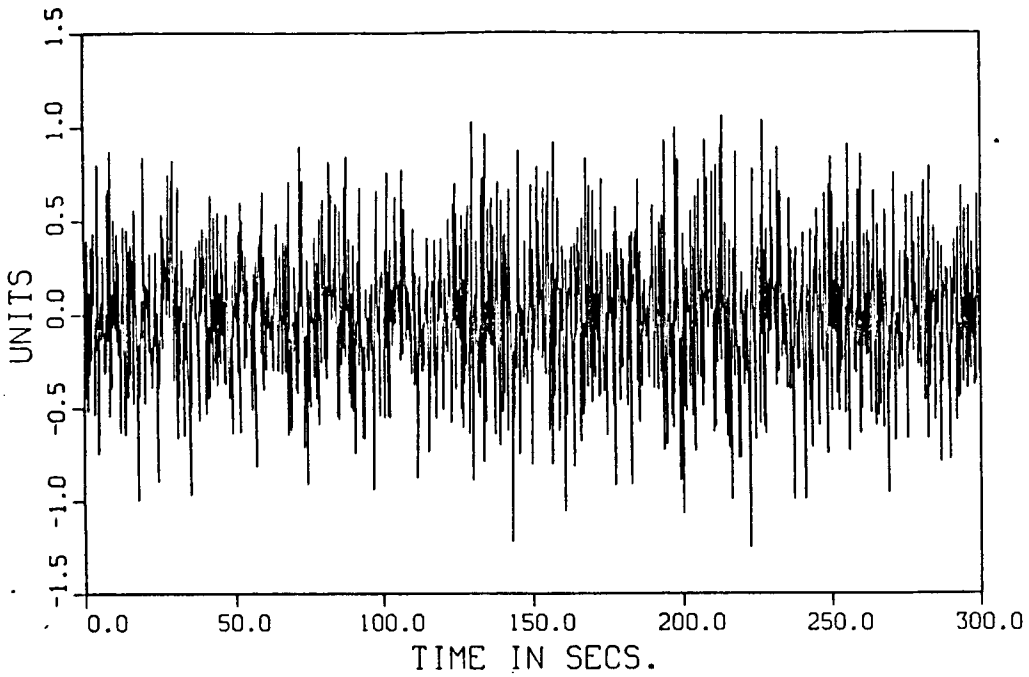

Figure 9.76: Probing Signal v[n] for Case 4 Simulation.

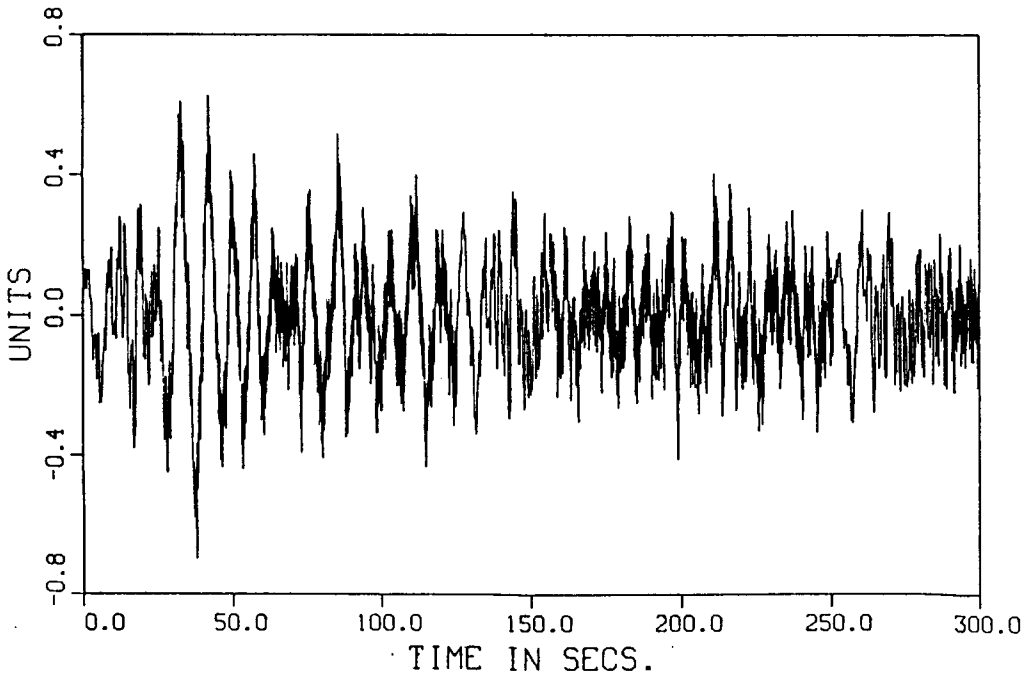

Figure 9.77: Tracking Error, $e_t[n] = r[n] - y[n]$, for Case 4, With Probing Signal.

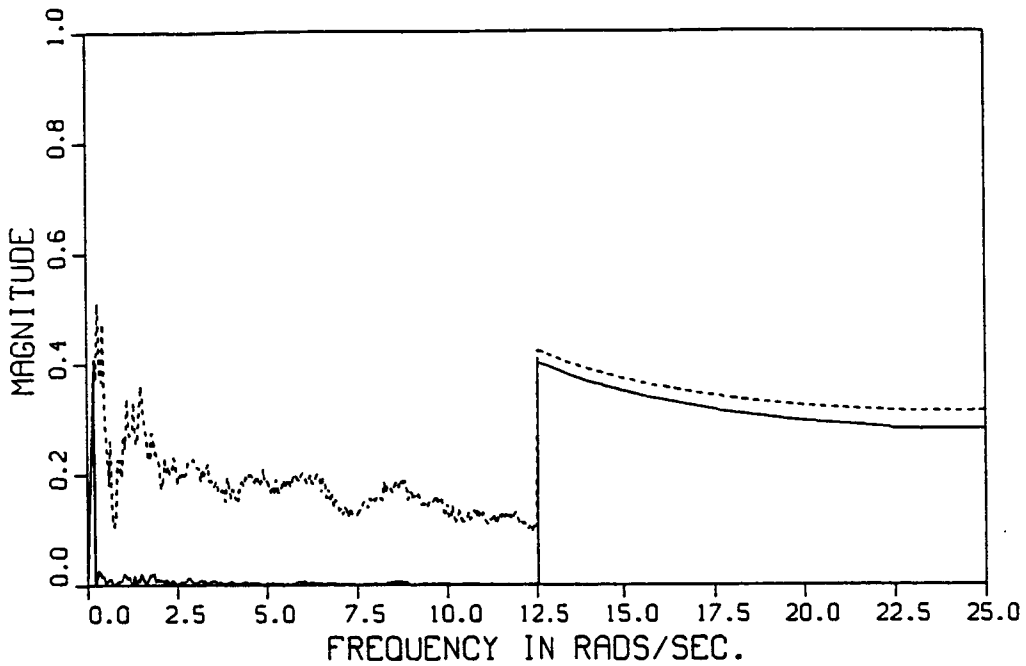

Figure 9.78: $|E_{cumf,N}^{n}(\omega_k)|$ and $\overline{E}_{cumf,N}^{n}(\omega_k)$ for n=2500, Case 4, With Probing Signal.

($|E_{cumf,N}^{n}(\omega_k)|$ = ——, $\overline{E}_{cumf,N}^{n}(\omega_k)$ = - - - -)

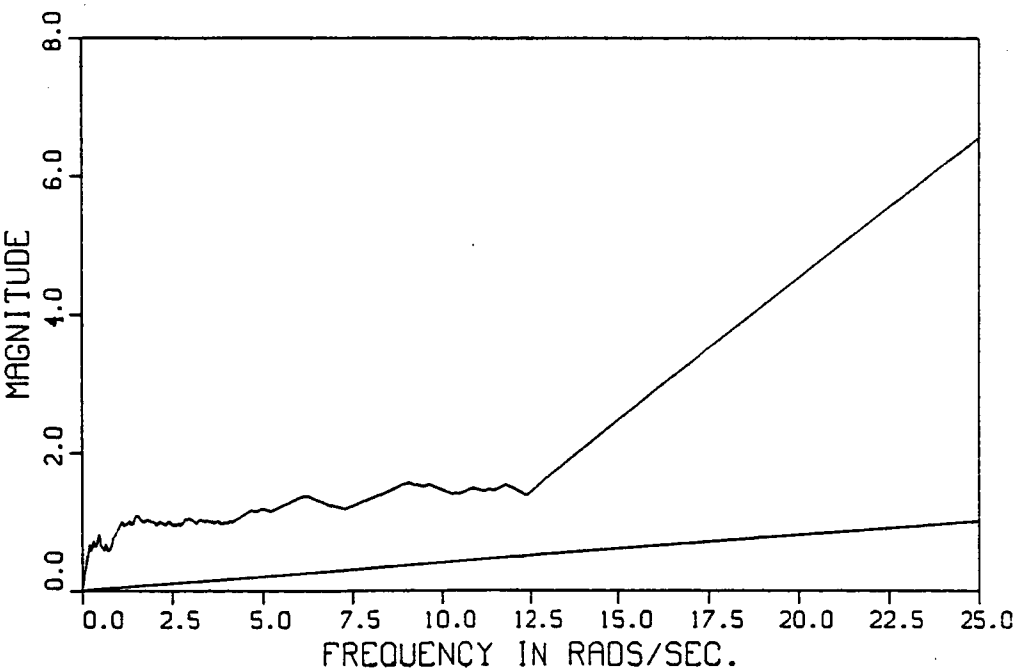

Figure 9.79: $\overline{\Delta}_{su}^{n}(e^{\omega_k T})$ for n=2500, Case 4, With Probing Signal. Straight line is a priori bound Δ_u.

9.6.5 Conclusion of Closed-loop Simulation Subsection

In this subsection, we have studied the properties of the robust estimator in a closed-loop scenario. We summarize our conclusions concerning the performance of the robust adaptive control system that uses the robust estimator.

1) For Case 2 (ζ=0.2 and ω_n=2 rads/sec.) with no probing signal, the system improves the nominal bandwidth some but not as much as the target value of 5 rads/sec.

2) For Case 2 (ζ=0.2 and ω_n=2 rads/sec.) with a probing signal, the system quickly improves the nominal bandwidth to the target value of 5 rads/sec., at the expense of greatly disturbing the system for the period of identification.

3) For Case 4 (ζ=0.8 and ω_n=1 rad/sec.) with no probing signal, the system cannot improve the nominal bandwidth.

4) For Case 4 (ζ=0.8 and ω_n=1 rad/sec.) with a probing signal, the system improves the bandwidth some, but not as much as the target value of 5 rads/sec. The probing signal continues to greatly disturb the system throughout the simulation.

As previously mentioned for 4) above, the problem was that the probing signal wasn't rich enough for frequencies that are greater than 12.5 rads/sec. These simulations show us that, for some examples, the robust adaptive control system can increase the bandwidth without the probing signal while for other examples a probing signal must be introduced. Alternative probing signal strategies that result in a longer identification time, but that disturb the system much less, were discussed in Section 7.4.4. We reserve our more global conclusions for the final section of this chapter.

9.7 Conclusions

In this chapter, we have considered a non-trivial plant example and shown how the robust estimator can be used in open-loop and closed-loop situations to identify the plant. The bottom line is that a robust adaptive control system that uses the robust estimator can increase the closed-loop bandwidth and, hence, improve the performance of a system under the right excitation conditions. In some situations the reference signal may supply sufficient excitation to increase the bandwidth at a desired rate but in other situations a probing signal must be added to achieve a target closed-loop bandwidth within a certain amount of time. For hard identification problems, the required excitation signals will be large if the plant is to be identified in a short amount of time. For example, the problem of identifying the plant transfer function of Case 4 in the region near the

target closed-loop bandwidth of 5 rads/sec., is difficult since the plant transfer function has rolled off considerably by this frequency. In any event, the robust adaptive control system using the robust estimator will provide improved performance when the plant input signal is rich enough. When the plant input is not rich, then the robust adaptive controller simply becomes the best control system that we could design (using our design method) given the current state of our plant knowledge.

The closed-loop results of this chapter were found using our pragmatic fix of not letting the uncertainty bounding function become less than the a priori bounding function on the unstructured uncertainty. If the robust uncertainty bounding function $\hat{\Delta}_{su}{}^{n}(e^{j\omega_k T})$ of Subsection 5.6.3 had been used instead, then the closed-loop bandwidths attained by the adaptive control system would have been smaller. This is because $\hat{\Delta}_{su}{}^{n}(e^{j\omega_k T})$ is more conservative than the uncertainty bounding function that was used in this chapter.

A final issue that we mention is the large computational burden of the robust estimator. As was discussed in Section 6.7, one of the major components of this computational burden is the computation of the error bounding function of Eqn. (5.2.4). As an example, consider the closed-loop simulations of this chapter where M=200 and N=1000. At every sample time, the sum of Eqn. (5.2.4) has about 200 terms and this sum must be computed at about N/2=500 frequency points. So, for Eqn. (5.2.4) alone, we must perform the operations of subtraction and multiplication and addition, 100,000 times each. Simulation 9.6.1, which was 2500 sampling periods in length, required about 12 minutes of CPU time on a Cyber 205 supercomputer. Since the simulation time scale runs to 314 secs., we see that the Cyber 205 is too slow, for real-time control, by a factor of 2!

CHAPTER 10.
CONCLUSIONS AND FUTURE RESEARCH

10.1 Conclusions

In this thesis, we have developed a new method for identifying a partially known plant, in the presence of unmodeled dynamics and an unmeasurable disturbance. Our entire development was motivated by the need to provide identification guarantees in a robust adaptive control system. The robust estimator was developed to provide: 1) a nominal plant model, and 2) a frequency-domain bounding function on the modeling error. The nominal plant model is required because current control-law design methodologies require such a finite-dimensional nominal model. In the future, new control-law design methodologies may not require an explicit nominal model. The frequency-domain bounding function on the modeling error is required for the frequency-domain stability-robustness tests. These tests allow us to guarantee that the nominal closed-loop control system is robustly stable to the modeling error. Next, we summarize the major results of the thesis.

In Chapter 2, we developed several new signal processing theorems. In particular, we found a way to bound the effects of using finite-length data in frequency-domain estimation. We also found a time-domain bound on the output of a system, using a magnitude bounding function on the frequency response of the system. This result was based on the work of Orlicki [14]. In Chapter 3, we stated the robust estimation problem. First, we started with a set of assumptions concerning the continuous-time plant and disturbance. Then, an analogous set of assumptions was developed in discrete-time using the original continuous-time assumptions. In this way, we tried to remain faithful to our goal of controlling a continuous-time plant. The robust estimator problem was then stated in discrete-time.

Given the statement of the robust estimation problem, we investigated two approaches for providing parameter estimates for the nominal plant model, one using time-domain methods and one using frequency-domain methods. In Chapter 4, we developed a dead-zone based parameter estimator that uses time-domain methods and in Chapter 5, we presented a frequency-domain method for computing parameter estimates. In the simulations, the frequency-domain parameter estimator worked much better than did the dead-zone based parameter estimator. In Chapter 5, we also developed the frequency-domain method for bounding the modeling uncertainty. The pragmatic design choices for the methods of Chapters 4 and 5 were addressed in a closed-loop adaptive control context, in Chapter 6.

Having completed the development of the robust estimator itself, in Chapter 7 we addressed the more global problem of robust adaptive control. We developed a simple adaptive control

system that uses the robust estimator as a component. In addition, the issue of adding probing signals to enhance identification was discussed. Since the performance of the robust estimator was not apparent from its development, we performed extensive simulations in order to understand its properties.

In Chapter 8, some of the basic building blocks that are used in the time-domain parameter estimator and the frequency-domain bounding method, were simulated and analyzed. This understanding enabled us to provide explanations of the more complex simulations that were presented in Chapter 9. The robust estimator was simulated in both open-loop and closed-loop situations in Chapter 9. The overall conclusion is that when the plant input signal is rich enough, the robust estimator can be used in a robust adaptive control system to provide significant performance increases, as measured by increases in the bandwidth of the system. When the plant input signal isn't inherently rich, the designer must face the tradeoff of adding a probing signal that enhances identification but disturbs the system. The results of this thesis have demonstrated that a robust estimator based adaptive control system can provide useful performance increases for non-trivial plant examples that have have unmodeled dynamics and an unmeasurable disturbance.

10.2 Directions for Future Research

In this section, we will discuss areas for future research on the problem of robust adaptive control. There are several unfinished issues concerning the development of a robust adaptive control system that uses the robust estimator.

10.2.1 Robust Control Methods

The robust adaptive control scheme that was discussed in Chapter 3 and shown in Figure 3.4, requires a control-law design method that can be implemented in an on-line manner. That is, we require a completely automated robust control design methodology that can use the information from the robust estimator to yield a system that is robustly stable to the effects of the modeling uncertainty. Currently, there exist robust control design methods, such as the LQG/LTR methodology [2], that can be used in an off-line manner to achieve robust control designs. However, the author is not aware of any methods that do this in a completely automated way. So, as a first step, an automated robust control design methodology must be developed.

As a second issue for robust control research, we suggest the development of a robust control design method that is performed entirely in the frequency-domain. In the development of the frequency-domain bounding method, we had to add a term to account for the difference between the frequency response of the nominal model and the cumulative frequency-domain

estimate. If we didn't need to use a nominal model for control design but worked directly with the frequency-domain estimate, then we wouldn't have to introduce this extra term that adds to the conservativeness of our bounding function.

10.2.2 Probing Signal Requirements

The issue of probing signal requirements was addressed in Chapter 7 but work remains to be done in this area. In Chapter 7, we provided insight as to what the excitation requirements of the robust estimator are. However, the issue of how to choose the probing signal requires additional study. In particular, the following questions require further examination.

1) What kind of tradeoff should be made between:
   a) enhancing identification now via a probing signal (leading to better control performance later), and
   b) disturbing the system with such a probing signal?
2) How should we determine when to introduce or take away a probing signal?
3) How can we monitor the current richness of the plant input signal and use this knowledge in our choice of a probing signal?

There has been considerable literature on "optimal inputs" for identification, see Mehra [41]. However, in the specific context of an adaptive controller that uses the robust estimator, work remains to be done.

10.2.3 Treatment of Unstable Plants

One of the starting assumptions for the development of the robust estimator was the assumption that the true plant was stable. This assumption is required by the frequency-domain estimation method. The plant has to be stable so that the most recent plant input data, which determines the DFT of the input signal, has the strongest effect on the most recent plant output data, which determines the DFT of the output signal. If the plant is unstable, it is the data from the distant past that most strongly influences the current value of the plant output. In this case, the frequency-domain estimate based on finite-length DFTs would not yield any useful information.

One solution to this problem is to identify the closed-loop transfer function and then use this estimate to infer an estimate of the true plant transfer function. For example, the true closed-loop transfer function is given by

$$T_{cl,true}(z) = G_{true}(z)\,K(z) / (\,1 + G_{true}(z)\,K(z)\,), \qquad (10.2.1)$$

so we find

$$G_{true}(z) = T_{cl,true}(z) / [\, K(z) \,(\, 1 - T_{cl,true}(z) \,)\,]. \qquad (10.2.2)$$

Thus, by using the robust estimator to estimate the closed-loop transfer function, which we know is stable by our choice of compensator, we can learn about the possibly unstable true plant via Eqn. (10.2.2). However, to learn anything, the additive error bound on $T_{cl,true}(e^{j\omega T})$ must be small enough so that the denominator of Eqn. (10.2.2) cannot be zero. In this indirect way, we can still use the robust estimator to identify an unstable plant.

10.2.4 Treatment of Slowly Time-varying Plants

The results of this thesis were derived assuming that the plant was linear and time-invariant, that is, we assumed that the plant parameters were constant. In practice, a plant may have slowly time-varying parameters. Indeed, parameter drift is one reason for using adaptive control. To apply the results of this thesis to slowly time-varying plants, several changes must be made. We sketch some possible approaches to this time-varying problem.

The part of the robust estimator that is most directly affected by this slowly time-varying problem is the updating of the cumulative frequency-domain bounding function. In Section 5.3, we set the cumulative frequency-domain bounding function to the smallest value of the frequency-domain bounding function that was observed since time zero. Thus, the cumulative bounding function could have values, at certain frequencies, that were found from data of the distant past. A question for future researches would be how to use knowledge of the maximum rate of change of the plant parameters to discount the past values of the frequency-domain bounding function. One could add an additional error term that increases as a frequency-domain bounding function (for a given time) becomes more and more outdated.

10.3 Some Parting Thoughts on Adaptive Control

In this brief final section of the thesis, we discuss and speculate on the usefulness of the thesis results as they relate to the robust adaptive control problem. As has been emphasized, the thesis research was begun with the mandate to develop some sort of guarantees at the identification stage of a robust adaptive controller, so that we could guarantee stability of the closed-loop system in the presence of unmodeled dynamics and an unmeasurable disturbance. This guarantee of robust stability comes at a great price. The robust estimator requires considerable design time and extensive off-line and on-line calculations. In order to provide some idea of how much work is required in the robust estimator design process, we will discuss the major design steps. We will only consider the design of a robust estimator that uses the frequency-domain parameter estimator.

The first major step in the application of the robust estimator results is the specification of the assumptions of Section 3.6. Recall that these assumptions include the specification of a nominal model structure along with a bounded parameter space. In addition, several bounding functions, some in the frequency-domain and some in the time-domain, are required. Given this information, the designer must choose the sampling period, the DFT length, the memory length M, a weighting function for the frequency-domain parameter estimator, and an appropriate target closed-loop bandwidth. Figure 5.4, which is included at the end of Chapter 5, provides a summary of the parts of the robust estimator (using the frequency-domain parameter estimator). Most of the calculations are done on-line. Key off-line calculations are: 1) the analytical computation of the remainder term of Eqn. (5.2.5), and 2) the computation of the supremums of two transfer function magnitudes, at each frequency, as $\hat{\theta}$ and θ_0 vary over the parameter space Θ {see $|H_{su1}|$ in Eqn. (5.6.14) and $|H_{su3}|$ in Eqn. (5.7.18)}. With all this off-line work done, one can implement the complete robust estimator, which again is summarized in Figure 5.4. As was discussed in Section 6.7, the robust estimator requires extensive on-line computations that are dominated by the computation of the frequency-domain bounding function of Eqn. (5.2.4). In the author's opinion, it is the extensive on-line calculations that are the biggest deterrent to using the robust estimator. The design procedure and the robust estimator algorithm itself are complex; however, this is unavoidable considering the type of guarantees that are provided. We are asking our adaptive control algorithm to be robust to the effects of unmodeled dynamics and an unmeasurable disturbance, so we expect a more complex algorithm than the standard "ideal case" model reference adaptive controllers.

In summary, it is the author's opinion that the prohibitively large computational requirements of the robust estimator make it an unattractive option for adaptive control in the short term. However, as the computational capabilities of computers increase, the robust estimator will become increasingly appealing. Thus, the author believes that in the long run we may find that the extensive computations of the robust estimator are a necessity if we want to obtain a truly robust adaptive control system.

Appendix A: Treatment of Infinite Summations

In this appendix, we consider computational methods for evaluating infinite summations. These summations arise from the frequency-domain folding that occurs when the continuous-time unmodeled dynamics are translated to discrete-time. First, we present a method for finding a closed-form expression for an infinite summation, using a result from complex analysis. This complex analysis approach can only be applied in some cases. So, to handle the cases that can't be treated using this approach, we will then show how to bound the infinite summation by integrating a function that bounds the summation terms.

Computing an Closed-form Expression Using Complex Analysis

From Theorem 4.1 of Astrom and Wittenmark [31] we know that if $F^c(s)$ is a continuous-time transfer function and $F(z)$ is the correponding pulse transfer function, then

$$F(e^{j\omega T}) = \frac{1}{T} \sum_{r=-\infty}^{\infty} F^c(j\omega + jr\omega_s). \tag{A.1}$$

Further, if we choose

$$F^c(s) = 1 / s^2 \tag{A.2}$$

then, from Appendix B of Franklin and Powell [30], we find that

$$F(z) = T z / (z - 1)^2. \tag{A.3}$$

From Eqns. (A.1-3) we find that

$$T e^{j\omega T} / (\cos(\omega T) - 1 + j \sin(\omega T))^2 = \frac{1}{T} \sum_{r=-\infty}^{\infty} - 1 / (\omega + r\omega_s)^2. \tag{A.4}$$

Taking the magnitude of both sides of this equation and using the fact that

$$\begin{aligned} | \cos(\omega T) - 1 + j \sin(\omega T) |^2 &= \cos(\omega T)^2 - 2 \cos(\omega T) + 1 + \sin(\omega T)^2 \\ &= 2 (1 - \cos(\omega T)) \\ &= 4 \sin(\omega T/2)^2 \end{aligned} \tag{A.5}$$

yields

$$T / (4 \sin(\omega T/2)^2) = \frac{1}{T} \sum_{r=-\infty}^{\infty} 1 / (\omega + r\omega_s)^2. \tag{A.6}$$

After some manipulation we find that

$$\pi^2 / \sin(\pi \omega / \omega_s)^2 = \sum_{r=-\infty}^{\infty} 1 / ((\omega / \omega_s) + r)^2, \tag{A.7}$$

or letting $\rho = \omega / \omega_s$

$$\pi^2 / \sin(\pi \rho)^2 = \sum_{r=-\infty}^{\infty} 1 / (\rho + r)^2. \tag{A.8}$$

We can differentiate Eqn. (A.8) to arrive at expressions for infinite summations of higher-order reciprocal powers. Under certain requirements, which are satisfied by the functions in Eqn. (A.8), we can differentiate both sides of Eqn. (A.8) yielding

$$\pi^3 \cos(\pi \rho) / \sin(\pi \rho)^3 = \sum_{r=-\infty}^{\infty} 1 / (\rho + r)^3. \tag{A.9}$$

Further, differentiating both sides of Eqn. (A.9) we find that

$$\pi^4 (1 + 2 \cos(\pi \rho)^2) / (3 \sin(\pi \rho)^4) = \sum_{r=-\infty}^{\infty} 1 / (\rho + r)^4. \tag{A.10}$$

This process can be continued for higher-order reciprocal powers.

A final detail that must be addressed, is the behavior of Eqns. (A.8-10) as $\rho \rightarrow 0$. Since, for example, the summation in Eqn. (A.8) will have a term $1/\rho^2$ that approaches infinity as $\rho \rightarrow 0$, we must consider instead the summation

$$[\pi^2 / \sin(\pi \rho)^2] - [1 / \rho^2] = \sum_{\substack{r=-\infty \\ r \neq 0}}^{\infty} 1 / (\rho + r)^2. \tag{A.11}$$

Taking the limit as $\rho \rightarrow 0$ on both sides of Eqn. (A.11) yields after some manipulation

$$\sum_{\substack{r=-\infty \\ r \neq 0}}^{\infty} 1 / r^2 = \pi^2 / 3. \tag{A.12}$$

Using a similar process for Eqn. (A.10) yields

$$\sum_{\substack{r=-\infty \\ r\neq 0}}^{\infty} 1/r^4 = \pi^4/45. \tag{A.13}$$

In Eqn. (A.9), the terms for negative r cancel the terms for positive r so that we find

$$\sum_{\substack{r=-\infty \\ r\neq 0}}^{\infty} 1/r^3 = 0. \tag{A.14}$$

In conclusion, we see that for even reciprocal powers we can use equations like (A.8) and (A.10) to achieve magnitude bounding in our frequency-folding equations but for odd reciprocal powers we need another approach. This is because in Eqn. (A.9) the terms are negative for negative r.

Integral Bounding Approach

We will now show how an infinite summation can be bounded by integrating a function that bounds the terms of the infinite summation. This method can be used to treat the cases of odd reciprocal powers. The author first saw this method in [37]. Assuming that $n > 1$ is a real number and $N \geq 2$ is an integer, it can be shown that

$$\sum_{r=N}^{\infty} 1/r^n < \int_{N-1}^{\infty} (1/x^n)\,dx = 1/[(n-1)(N-1)^{n-1}]. \tag{A.15}$$

Now, consider the infinite summation

$$\sum_{r=-\infty}^{\infty} 1/|\rho+r|^n = \sum_{r=-(N-1)}^{N-1} 1/|\rho+r|^n + \sum_{r=N}^{\infty} [1/|\rho+r|^n + 1/|r-\rho|^n]. \tag{A.16}$$

If $0 \leq \rho \leq 1$, then

$$\sum_{r=N}^{\infty} 1/|\rho+r|^n \leq \sum_{r=N}^{\infty} 1/r^n \tag{A.17}$$

and

$$\sum_{r=N}^{\infty} 1/|r-\rho|^n \leq \sum_{r=N}^{\infty} 1/(r-1)^n. \tag{A.18}$$

From Eqns. (A.15-18) we conclude that if $0 \leq \rho \leq 1$, $n > 1$ and $N \geq 3$, then

$$\sum_{r=-\infty}^{\infty} 1/|\rho + r|^n \leq \sum_{r=-(N-1)}^{N-1} 1/|\rho + r|^n + [1/(n-1)][1/(N-1)^{n-1} + 1/(N-2)^{n-1}]. \quad (A.19)$$

The first term on the right-hand side of the above equation must still be computed numerically. However, the contribution of the infinite summation term on the right-hand side of Eqn. (A.16) is bounded by the easily computable term in Eqn. (A.19) and can now be used to handle the summations with odd reciprocal powers.

Appendix B: Impulse Response Bounding Integrals

In this appendix, we derive results for bounding a discrete-time impulse response given a bounding function on the continuous-time impulse response. From Franklin and Powell [30,p.62] we find that, if the zero-order hold equivalence is used, then the discrete-time impulse response $g_{true}[n]$ is related to the continuous-time impulse response $g_{true}(t)$ as follows.

$$g_{true}[n] = \int_{(n-1)T}^{nT} g_{true}(t)\, dt, \quad \forall n. \tag{B.1}$$

We assume that $g_{true}(t)$ satisfies the magnitude bound of the form of assumption AC1.6 of Chapter 3,

$$|g_{true}(t)| \leq \sum_{i=1}^{I_0^c} b_i\, t^{(r_i)}\, e^{(-a_i t)}, \text{ for } t \geq 0, \tag{B.2}$$

where r_i is a positive integer, and $b_i > 0$, $a_i > 0$ (i.e. poles in the open left-half plane), and r_i are known for $i=1, \ldots, I_0^c$. Then, we find that

$$|g_{true}[n]| \leq \int_{(n-1)T}^{nT} |g_{true}(t)|\, dt \tag{B.3}$$

$$\leq \sum_{i=1}^{I_0^c} b_i \int_{(n-1)T}^{nT} t^{(r_i)}\, e^{(-a_i t)}, \text{ for } n \geq 1. \tag{B.4}$$

We now consider several cases of Eqn. (B.4).

Case 1. ($r = 0$, single-pole case)

$$b \int_{(n-1)T}^{nT} e^{-at}\, dt = (b/a)\,(1 - e^{-aT})\, e^{-aT(n-1)}, \text{ for } n \geq 1. \tag{B.5}$$

From formula 521. of [38] we know that,

$$\int t^r e^{-at}\, dt = -e^{-at} \sum_{p=0}^{r} r!\, t^{r-p} / ((r-p)!\, a^{p+1}). \tag{B.6}$$

This formula can be used to evaluate Eqn. (B.4) for more complex cases than $r=0$. We have computed a few cases as follows.

Case 2. (r = 1, double-pole case)

$$b \int_{(n-1)T}^{nT} t e^{-at}\, dt = (b/a) \{ [(1/a)(1 - e^{-aT}) - T] + [nT (1 - e^{-aT})] \} e^{-aT(n-1)}, \text{ for } n \geq 1. \tag{B.7}$$

Case 3. (r = 2, triple-pole case)

$$b \int_{(n-1)T}^{nT} t^2 e^{-at}\, dt = (b/a) \{ [T^2 - 2T/a + (2/a^2)(1 - e^{-aT})]$$

$$+ n(2T) [-T + (1/a)(1 - e^{-aT})] + n^2T^2 (1 - e^{-aT}) \} e^{-aT(n-1)}, \text{ for } n \geq 1. \tag{B.8}$$

We note that in all of the above cases, $g_{true}[n]=0$, for $n \leq 0$ since $g_{true}(t)$ is causal and there is no feedthrough term in Eqn. (B.2). The above results could also have been derived by finding the inverse z-transform of the zero-order hold equivalent of the bounding function in Eqn. (B.2).

Appendix C: Summation Equations

In this appendix, we summarize several useful results concerning the evaluation of infinite and finite series of the geometric type. We will consider several specific cases and then describe the method for the general case. Under the conditions stated, it can easily be seen that all of the following series are convergent via the ratio test. See Rudin [39].

Case 1. We define

$$S_1 = \sum_{i=r_0}^{r_1} x^i, \tag{C.1}$$

where r_0 and r_1 are positive integers, $r_0 < r_1$, and $|x| < 1$ if $r_1 \to \infty$. We find that

$$S_1 x = \sum_{i=r_0}^{r_1} x^{i+1} = \sum_{j=r_0+1}^{r_1+1} x^j = S_1 - x^{r_0} + x^{r_1+1}. \tag{C.2}$$

So,

$$S_1 = (x^{r_0} - x^{r_1+1}) / (1 - x). \tag{C.3}$$

Special Case 1a. If $r_1 \to \infty$, then

$$S_1 = x^{r_0} / (1 - x). \tag{C.4}$$

Special Case 1b. If $r_0 = 0$, and $r_1 \to \infty$, then

$$S_1 = 1 / (1 - x). \tag{C.5}$$

Case 2.

$$S_2 = \sum_{i=r_0}^{r_1} i\, x^i. \tag{C.6}$$

We find that

$$\frac{dS_1}{dx} = \sum_{i=r_0}^{r_1} i\, x^{i-1}. \tag{C.7}$$

So,

$$S_2 = x \frac{dS_1}{dx}, \tag{C.8}$$

and it can be shown that

$$S_2 = [\, x^{r_0} (r_0 - r_0 x + x) + x^{r_1+1} (-r_1 + r_1 x - 1) \,] / (1 - x)^2. \tag{C.9}$$

Special Case 2a. If $r_1 \to \infty$, then

$$S_2 = x^{r_0} (r_0 - r_0 x + x) / (1 - x)^2. \tag{C.10}$$

Special Case 2b. If $r_0 = 0$, and $r_1 \to \infty$, then

$$S_2 = x / (1 - x)^2. \tag{C.11}$$

Case 3.

$$S_3 = \sum_{i=r_0}^{r_1} i^2 x^i. \tag{C.12}$$

As in Case 2, we find that

$$S_3 = x \frac{dS_2}{dx}, \tag{C.13}$$

and it can be shown that

$$S_3 = [\, r_0^2 x^{r_0} + (-2 r_0^2 + 2 r_0 + 1) x^{r_0+1} + (r_0 - 1)^2 x^{r_0+2}$$
$$- (r_1 + 1)^2 x^{r_1+1} + (2 r_1^2 + 2 r_1 - 1) x^{r_1+2} - r_1^2 x^{r_1+3} \,] / (1 - x)^3. \tag{C.14}$$

Special Case 3a. If $r_1 \to \infty$, then

$$S_3 = [\, r_0^2 x^{r_0} + (-2 r_0^2 + 2 r_0 + 1) x^{r_0+1} + (r_0 - 1)^2 x^{r_0+2} \,] / (1 - x)^3. \tag{C.15}$$

Special Case 3b. If $r_0 = 0$, and $r_1 \to \infty$, then

$$S_3 = x (1 + x) / (1 - x)^3. \tag{C.16}$$

General Case. For some integer $n \geq 1$, the sum

$$S_n = \sum_{i=r_0}^{r_1} i^{(n-1)} x^i. \tag{C.17}$$

can be found by induction, since

$$S_n = x \left(dS_{(n-1)} / dx \right), \tag{C.18}$$

and S_1 is given by Eqn. (C.3).

Appendix D: Discrete-time Impulse Response Bounding

In this appendix, we show how to find a bounding function on the impulse response of a system that is composed of two systems. We assume knowledge of a magnitude bounding function on each of the impulse responses. We define

$$h_3[n] = h_1[n]*h_2[n] = \sum_{m=0}^{n} h_1[m]\, h_2[n-m] = \sum_{p=0}^{n} h_2[p]\, h_1[n-p]. \tag{D.1}$$

where we assume that $h_1[n]$ and $h_2[n]$ are causal transfer functions. Further, we assume that the following magnitude bounding functions are known for $h_1[n]$ and $h_2[n]$,

$$|h_1[n]| \le \overline{h_1}[n], \ \forall n \tag{D.2}$$

$$|h_2[n]| \le \overline{h_2}[n], \ \forall n \tag{D.3}$$

where both $\overline{h_1}[n]$ and $\overline{h_2}[n]$ are of the form,

$$\sum_{i=1}^{I_0} g_i\, n^{(r_i)}\, p_i^n, \tag{D.4}$$

where r_i is a positive integer, $g_i > 0$, and $0 < p_i < 1$. In this appendix, we consider several different cases of Eqn. (D.4) for $h_1[n]$ and $h_2[n]$. In each case, we seek a magnitude bounding function on $h_3[n]$. From Eqns. (D.1-3) we find,

$$|h_3[n]| \le \overline{h_3}[n], \ \forall n \tag{D.5}$$

where,

$$\overline{h_3}[n] = \sum_{m=0}^{n} \overline{h_1}[m]\, \overline{h_2}[n-m]. \tag{D.6}$$

Now, we consider some specific cases.

Case 1. (both first-order)

$$\overline{h_1}[n] = g_1\, p_1^n, \text{ for } n \ge 0 \tag{D.7}$$

$$\overline{h_2}[n] = g_2\, p_2^n, \text{ for } n \ge 0. \tag{D.8}$$

From Eqn. (D.6) we find,

$$\overline{h_3}[n] = \sum_{m=0}^{n} g_1 p_1^m g_2 p_2^{n-m}. \quad (D.9)$$

So,

$$\overline{h_3}[n] = \{ g_1 g_2 \sum_{m=0}^{n} (p_1/p_2)^m \} p_2^n. \quad (D.10)$$

We consider two possibilities in Eqn. (D.10):

Case 1a. ($p_1 \neq p_2$) In this case, using Eqn. (C.3) from Appendix C we find that

$$\overline{h_3}[n] = \{ g_1 g_2 [(1 - (p_1/p_2)^{n+1}) / (1 - (p_1/p_2))] \} p_2^n, \quad (D.11)$$

or

$$\overline{h_3}[n] = \{ g_1 g_2 / (p_2 - p_1) \} (p_2^{n+1} - p_1^{n+1}). \quad (D.12)$$

We note that a more conservative, but simpler bounding function can be found, as follows,

$$\overline{h_3}[n] < (g_1 g_2 / |p_2 - p_1|) (\max(p_1, p_2))^{n+1}. \quad (D.13)$$

Case 1b. ($p_1 = p_2$) In this case, from Eqn. (D.10),

$$\overline{h_3}[n] = \{ g_1 g_2 (n+1) \} p_1^n. \quad (D.14)$$

Case 2. (one second-order, one first-order)

$$\overline{h_1}[n] = g_1 n p_1^n, \text{ for } n \geq 0 \quad (D.15)$$

$$\overline{h_2}[n] = g_2 p_2^n, \text{ for } n \geq 0. \quad (D.16)$$

From Eqn. (D.6) we find,

$$\overline{h_3}[n] = \sum_{m=0}^{n} g_1 m p_1^m g_2 p_2^{n-m}. \quad (D.17)$$

So,

$$\overline{h_3}[n] = \{ g_1 g_2 \sum_{m=0}^{n} m (p_1/p_2)^m \} p_2^n. \quad (D.18)$$

We consider two possibilities in Eqn. (D.18):

Case 2a. ($p_1 \neq p_2$) In this case, using Eqn. (C.9) from Appendix C we find that

$$\overline{h}_3[n] = \{ g_1 g_2 [(p_1/p_2) + (p_1/p_2)^{n+1} (-n + n (p_1/p_2) - 1)] / (1 - (p_1/p_2))^2] \} p_2^n, \quad (D.19)$$

or

$$\overline{h}_3[n] = \{ g_1 g_2 / (p_2 - p_1)^2 \} [p_1 p_2^{n+1} + (n p_1 - (n + 1) p_2) p_1^{n+1}]. \quad (D.20)$$

We note that a more conservative, but simpler bounding function can be found, as follows,

$$\overline{h}_3[n] < \{ g_1 g_2 (n+1) / (p_2 - p_1)^2 \} (\max(p_1, p_2))^{n+2}. \quad (D.21)$$

Case 2b. ($p_1 = p_2$) In this case, we use L'Hospital's rule twice to find from Eqn. (D.20),

$$\overline{h}_3[n] = \{ g_1 g_2 / 2 \} n (n+1) p_1^n, \quad (D.22)$$

or

$$\overline{h}_3[n] = \{ g_1 g_2 / 2 \} (n^2 + n) p_1^n. \quad (D.23)$$

Case 3. (both second-order)

$$\overline{h}_1[n] = g_1 n p_1^n, \text{ for } n \geq 0 \quad (D.24)$$

$$\overline{h}_2[n] = g_2 n p_2^n, \text{ for } n \geq 0. \quad (D.25)$$

From Eqn. (D.6) we find,

$$\overline{h}_3[n] = \sum_{m=0}^{n} g_1 m p_1^m g_2 (n-m) p_2^{n-m}. \quad (D.26)$$

So,

$$\overline{h}_3[n] = g_1 g_2 \{ [\sum_{m=0}^{n} m (p_1/p_2)^m] n p_2^n - [\sum_{m=0}^{n} m^2 (p_1/p_2)^m] p_2^n \}. \quad (D.27)$$

We consider two possibilities in Eqn. (D.27):

Case 3a. ($p_1 \neq p_2$) In this case, using Eqns. (C.9) and (C.15) from Appendix C we find after much algebra that

$$\overline{h}_3[n] = \{ g_1 g_2 / (p_2 - p_1)^3 \} [(n - 1) (p_1 p_2^{n+2} - p_1^{n+2} p_2) + (n + 1) (p_1^{n+1} p_2^2 - p_1^2 p_2^{n+1})]. \quad (D.28)$$

We note that a more conservative but simpler bounding function can be found, as follows,

$$\overline{h}_3[n] < \{ g_1 g_2 (2 n) / |p_2 - p_1|^3 \} (\max(p_1, p_2))^{n+3}. \quad (D.29)$$

Case 3b. ($p_1 = p_2$) In this case, we use L'Hospital's rule three times to find from Eqn. (D.27),

$$\overline{h}_3[n] = \{ g_1 g_2 / 6 \} (n-1) n (n+1) p_1^n, \quad (D.30)$$

or

$$\overline{h}_3[n] = \{ g_1 g_2 / 6 \} (n^3 - n) p_1^n. \quad (D.31)$$

Appendix E: Proof of Theorems 4.1 and 4.2

In this appendix, we present a complete proof of Theorem 4.1. An outline of this proof has appeared in the literature in parts, see [17] and [18]. In the following proof of property 1 the parameter $\bar{\varepsilon}$, which appears in the algorithm and proof in [17,18], does not appear. This parameter is unnecessary and can be eliminated as we have done in our statement of the algorithm and the proof. In Eqn. (E.23) we arrive at an expression that depends only on the parameter α whereas the proof of [17,18] arrives at an expression that also includes $\bar{\varepsilon}$. As a note for the reader we observe that, since the matrix P is symmetric and positive definite, the maximum and minimum singular values of P are equal to the maximum and minimum eigenvalues of P, respectively. Thus, the condition number of P is equivalently defined as the ratio of either the singular values or the eigenvalues.

We conclude the appendix with a proof of Theorem 4.2. This proof is largely the same as the proof of Theorem 4.1 so only the modifications are mentioned. Goodwin et al. [1] have previously proven most of the properties of Theorem 4.2.

Proof of Theorem 4.1:

Proof of Property 1: From Eqn. (4.5.5) we recall that

$$e[n] = -\phi_f[n-1]^T \tilde{\theta}[n-1] + e_1[n] = -\tilde{\theta}[n-1]^T \phi_f[n-1] + e_1[n], \text{ where} \tag{E.1}$$

$$\tilde{\theta}[n] = \hat{\theta}[n] - \theta_0. \tag{E.2}$$

Subtracting θ_0 from each side of Eqn. (4.5.7) and using Eqn. (E.1) we find that

$$\tilde{\theta}[n] = \tilde{\theta}[n-1] + \frac{\upsilon[n] P[n-2] \phi_f[n-1]}{1 + \phi_f[n-1]^T P[n-2] \phi_f[n-1]} (-\phi_f[n-1]^T \tilde{\theta}[n-1] + e_1[n]). \tag{E.3}$$

Using the matrix inversion lemma,

$$(A + B C)^{-1} = A^{-1} - A^{-1} B (I + C A^{-1} B)^{-1} C A^{-1}, \tag{E.4}$$

and Eqn. (4.5.8) which we repeat here for convenience,

$$P[n-1] = P[n-2] - \frac{\upsilon[n] P[n-2] \phi_f[n-1] \phi_f[n-1]^T P[n-2]}{1 + \phi_f[n-1]^T P[n-2] \phi_f[n-1]}, \tag{E.5}$$

we find that

$$P[n-1]^{-1} = P[n-2]^{-1} + \frac{\upsilon[n]\,\phi_f[n-1]\,\phi_f[n-1]^T}{1 + (1-\upsilon[n])\,\phi_f[n-1]^T\,P[n-2]\,\phi_f[n-1]}. \tag{E.6}$$

Using Eqns. (E.3) and (E.5) it can be shown that

$$\tilde{\theta}[n] = P[n-1]\,P[n-2]^{-1}\,\tilde{\theta}[n-1] + \frac{\upsilon[n]\,P[n-2]\,\phi_f[n-1]\,e_1[n]}{1 + \phi_f[n-1]^T\,P[n-2]\,\phi_f[n-1]}. \tag{E.7}$$

We now define the candidate Lyapunov function,

$$V[n] = \tilde{\theta}[n]^T\,P[n-1]^{-1}\,\tilde{\theta}[n], \tag{E.8}$$

which is non-negative since P is symmetric and positive definite. Using Eqns. (E.7-8) we compute,

$$V[n] - V[n-1] = (\tilde{\theta}[n] - \tilde{\theta}[n-1])^T\,P[n-2]^{-1}\,\tilde{\theta}[n-1] + \frac{\upsilon[n]\,\tilde{\theta}[n]^T\,P[n-1]^{-1}\,P[n-2]\,\phi_f[n-1]\,e_1[n]}{1 + \phi_f[n-1]^T\,P[n-2]\,\phi_f[n-1]}. \tag{E.9}$$

Using Eqns. (4.5.7) and (E.7) in (E.9) yields

$$V[n] - V[n-1] = \{\,\upsilon[n] / (\,1 + \phi_f[n-1]^T\,P[n-2]\,\phi_f[n-1]\,)\,\}\,\{\,\phi_f[n-1]^T\,\tilde{\theta}[n-1]\,e[n] + \tilde{\theta}[n-1]^T\,\phi_f[n-1]\,e_1[n] + \frac{\upsilon[n]\,\phi_f[n-1]^T\,P[n-2]\,P[n-1]^{-1}\,P[n-2]\,\phi_f[n-1]\,e_1[n]^2}{1 + \phi_f[n-1]^T\,P[n-2]\,\phi_f[n-1]}\,\}. \tag{E.10}$$

Eqns. (E.1) and (E.6) are then used to find

$$V[n] - V[n-1] = \{\,\upsilon[n] / (\,1 + \phi_f[n-1]^T\,P[n-2]\,\phi_f[n-1]\,)\,\}\,\{\,(\,e_1[n] - e[n]\,)\,(\,e_1[n] + e[n]\,) + \frac{\upsilon[n]\,\phi_f[n-1]^T\,P[n-2]\,\phi_f[n-1]\,e_1[n]^2}{1 + \phi_f[n-1]^T\,P[n-2]\,\phi_f[n-1]}$$

$$+ \frac{\upsilon[n]^2 \, (\phi_f[n-1]^T P[n-2] \phi_f[n-1])^2 \, e_1[n]^2}{\{ 1 + \phi_f[n-1]^T P[n-2] \phi_f[n-1] \} \{ 1 + (1-\upsilon[n]) \phi_f[n-1]^T P[n-2] \phi_f[n-1] \}} \}$$

(E.11)

This reduces to

$$V[n] - V[n-1] = \{ \upsilon[n] / (1 + \phi_f[n-1]^T P[n-2] \phi_f[n-1]) \} \{ e_1[n]^2 - e[n]^2 + \frac{\upsilon[n] \, \phi_f[n-1]^T P[n-2] \phi_f[n-1] \, e_1[n]^2}{1 + (1-\upsilon[n]) \phi_f[n-1]^T P[n-2] \phi_f[n-1]} \}. \quad \text{(E.12)}$$

We reduce Eqn. (E.12) further to find

$$V[n] - V[n-1] = \{ \upsilon[n] / (1 + \phi_f[n-1]^T P[n-2] \phi_f[n-1]) \} \cdot \{ \frac{1 + \phi_f[n-1]^T P[n-2] \phi_f[n-1]}{1 + (1-\upsilon[n]) \phi_f[n-1]^T P[n-2] \phi_f[n-1]} e_1[n]^2 - e[n]^2 \}. \quad \text{(E.13)}$$

We will show that the right-hand side of Eqn. (E.13) is non-positive. However, we must first make some observations. We observe from the properties of the deadzone function 'f' of Eqn. (4.5.6), the definition of $\upsilon[n]$ and Eqns. (4.5.10-11) that

$$1 \leq \frac{1 + \phi_f[n-1]^T P[n-2] \phi_f[n-1]}{1 + (1-\upsilon[n]) \phi_f^T[n-1] P[n-2] \phi_f[n-1]} \leq \frac{1}{1 - \alpha} = \beta^2. \quad \text{(E.14)}$$

Since $\overline{e_1}[n]$ is a bound on $|e_1[n]|$, we use Eqns. (E.13-14) to find

$$V[n] - V[n-1] \leq \{ \upsilon[n] / (1 + \phi_f[n-1]^T P[n-2] \phi_f[n-1]) \} \{ \beta^2 \overline{e_1}[n]^2 - e[n]^2 \}. \quad \text{(E.15)}$$

We observe that if $|e[n]| \geq \beta \overline{e_1}[n]$, then

$$| f\{ \beta \overline{e_1}[n], e[n] \} | = | |e[n]| - \beta \overline{e_1}[n] | \quad \text{(E.16)}$$

$$\Rightarrow | f\{ \beta \overline{e_1}[n], e[n] \} | |e[n]| = | \beta \overline{e_1}[n] |e[n]| - e[n]^2 | \quad \text{(E.17)}$$

$$\Rightarrow - f\{ \beta \overline{e_1}[n], e[n] \} e[n] = \beta \overline{e_1}[n] |e[n]| - e[n]^2, \quad \text{(E.18)}$$

where we have used the properties of the deadzone to determine the signs in Eqn. (E.18). Further, if $|e[n]| \geq \beta \overline{e_1}[n]$, then

$$\beta\, \overline{e_1}[n]\, |e[n]| - e[n]^2 \geq \beta^2\, \overline{e_1}[n]^2 - e[n]^2. \tag{E.19}$$

Thus, if $|e[n]| \geq \beta\, \overline{e_1}[n]$, then

$$-f\{\, \beta\, \overline{e_1}[n], e[n]\,\}\, e[n] \geq \beta^2\, \overline{e_1}[n]^2 - e[n]^2. \tag{E.20}$$

Multiplying both sides of Eqn. (E.20) by the non-negative number $f\{\, \beta\, \overline{e_1}[n], e[n]\,\}/e[n]$ we find that

$$-f\{\, \beta\, \overline{e_1}[n], e[n]\,\}^2 \geq (\, f\{\, \beta\, \overline{e_1}[n], e[n]\,\} / e[n]\,)\, (\, \beta^2\, \overline{e_1}[n]^2 - e[n]^2\,) \tag{E.21}$$

for all e[n]. If $|e[n]| < \beta\, \overline{e_1}[n]$ then both sides of the above inequality are zero. From Eqns. (4.5.9-10) we find that

$$\upsilon[n] = \alpha\, f\{\, \beta\, \overline{e_1}[n], e[n]\,\} / e[n]. \tag{E.22}$$

Combining Eqns. (E.15) and (E.22) and then using Eqn. (E.21) we find that

$$\mathbf{V}[n] - \mathbf{V}[n-1] \leq -\alpha\, f\{\, \beta\, \overline{e_1}[n], e[n]\,\}^2 / (\, 1 + \phi_f[n-1]^T\, P[n-2]\, \phi_f[n-1]\,). \tag{E.23}$$

From Eqn. (E.23) we conclude that the non-negative function $\mathbf{V}[n]$ is non-increasing and hence

$$\tilde{\theta}[n]^T\, P[n-1]^{-1}\, \tilde{\theta}[n] \leq \tilde{\theta}[n-1]^T\, P[n-2]^{-1}\, \tilde{\theta}[n-1]. \tag{E.24}$$

From Eqn. (E.6) we find

$$P[n]^{-1} = P[n-1]^{-1} + \frac{\upsilon[n+1]\, \phi_f[n]\, \phi_f[n]^T}{1 + (1-\upsilon[n+1])\, \phi_f[n]^T\, P[n-1]\, \phi_f[n]}, \tag{E.25}$$

where we note that $\upsilon[n+1]$ is non-negative and always less than unity so the second term on the right-hand side is positive semi-definite. From (E.25) and the fact that P is symmetric and positive definite, we find that

$$\sigma_{min}\{P[n]^{-1}\} \geq \sigma_{min}\{P[n-1]^{-1}\} \geq \sigma_{min}\{P[-1]^{-1}\}, \tag{E.26}$$

where $\sigma_{min}\{\bullet\}$ denotes the minimum singular value of a matrix and later we will use $\sigma_{max}\{\bullet\}$ to denote the maximum singular value of a matrix. Using Eqn. (E.26) and then (E.24) we find

$$\sigma_{min}\{P[-1]^{-1}\}\, \|\tilde{\theta}[n]\|^2 \leq \sigma_{min}\{P[n-1]^{-1}\}\, \|\tilde{\theta}[n]\|^2 \tag{E.27}$$

$$\leq \tilde{\theta}[n]^T\, P[n-1]^{-1}\, \tilde{\theta}[n] \tag{E.28}$$

$$\leq \tilde{\theta}[0]^T\, P[-1]^{-1}\, \tilde{\theta}[0] \tag{E.29}$$

$$\leq \sigma_{max}\{P[-1]^{-1}\} \| \tilde{\theta}[0] \|^2. \tag{E.30}$$

Therefore,

$$\| \tilde{\theta}[n] \|^2 \leq \kappa\{P[-1]\} \| \tilde{\theta}[0] \|^2, \tag{E.31}$$

and hence

$$\| \tilde{\theta}[n] \| \leq \sqrt{\kappa\{P[-1]\}} \| \tilde{\theta}[0] \|, \tag{E.32}$$

where

$$\kappa\{P[-1]\} = \sigma_{max}\{P[-1]\} / \sigma_{min}\{P[-1]\} = \sigma_{max}\{P[-1]^{-1}\} / \sigma_{min}\{P[-1]^{-1}\}. \tag{E.33}$$

This establishes property 1 of Theorem 4.1. The result stated in Remark 2 of Chapter 4 follows directly using the initial time of n-2 instead of 0 in Eqns. (E.27-32).

Proof of Property 2: Using Eqn. (E.23) and summing from 1 to N yields

$$V[N] - V[0] \leq - \sum_{n=1}^{N} \alpha f\{ \beta \bar{e}_1[n], e[n] \}^2 / (1 + \phi_f[n-1]^T P[n-2] \phi_f[n-1]). \tag{E.34}$$

Since we know that

$$- (V[N] - V[0]) < \infty, \ \forall N \tag{E.35}$$

we conclude that the summation of positive terms in Eqn. (E.34) is finite for all N. This implies that

$$\lim_{n \to \infty} \frac{f\{ \beta \bar{e}_1[n], e[n] \}^2}{1 + \phi_f[n-1]^T P[n-2] \phi_f[n-1]} = 0, \tag{E.36}$$

which establishes property 2.

Proof of Property 3: For this part of the proof we must first develop some preliminary results. Since

$$\frac{f\{ \beta \bar{e}_1[n], e[n] \}^2}{1 + \phi_f[n-1]^T P[n-2] \phi_f[n-1]} = \frac{(1 + \phi_f[n-1]^T P[n-2] \phi_f[n-1]) f\{ \beta \bar{e}_1[n], e[n] \}^2}{(1 + \phi_f[n-1]^T P[n-2] \phi_f[n-1])^2}, \tag{E.37}$$

we find from Eqn. (E.34-5) that for all N,

$$\sum_{n=1}^{N} \frac{(1+\phi_f[n-1]^T P[n-2]\,\phi_f[n-1])\, f\{\beta \bar{e}_1[n], e[n]\}^2}{(1+\phi_f[n-1]^T P[n-2]\,\phi_f[n-1])^2} =$$

$$\sum_{n=1}^{N} \frac{f\{\beta \bar{e}_1[n], e[n]\}^2}{(1+\phi_f[n-1]^T P[n-2]\,\phi_f[n-1])^2} + \sum_{n=1}^{N} \frac{\phi_f[n-1]^T P[n-2]\,\phi_f[n-1]\, f\{\beta \bar{e}_1[n], e[n]\}^2}{(1+\phi_f[n-1]^T P[n-2]\,\phi_f[n-1])^2} < \infty. \tag{E.38}$$

Further, from Eqn. (E.34) we find

$$\sum_{n=1}^{N} \frac{f\{\beta \bar{e}_1[n], e[n]\}^2}{(1+\phi_f[n-1]^T P[n-2]\,\phi_f[n-1])^2} \le \sum_{n=1}^{N} \frac{f\{\beta \bar{e}_1[n], e[n]\}^2}{1+\phi_f[n-1]^T P[n-2]\,\phi_f[n-1]} < \infty. \tag{E.39}$$

We conclude from Eqns. (E.38-9) that for all N,

$$\sum_{n=1}^{N} \frac{\phi_f[n-1]^T P[n-2]\,\phi_f[n-1]\, f\{\beta \bar{e}_1[n], e[n]\}^2}{(1+\phi_f[n-1]^T P[n-2]\,\phi_f[n-1])^2} < \infty. \tag{E.40}$$

This implies that

$$\lim_{n\to\infty} \frac{\phi_f[n-1]^T P[n-2]\,\phi_f[n-1]\, f\{\beta \bar{e}_1[n], e[n]\}^2}{(1+\phi_f[n-1]^T P[n-2]\,\phi_f[n-1])^2} = 0. \tag{E.41}$$

Now, from Eqn. (4.5.7),

$$\|\tilde{\theta}[n] - \tilde{\theta}[n-1]\|^2 = \frac{\upsilon[n]^2\, \phi_f[n-1]^T P[n-2]^2\, \phi_f[n-1]\, e[n]^2}{(1+\phi_f[n-1]^T P[n-2]\,\phi_f[n-1])^2}. \tag{E.42}$$

Using the fact that

$$\upsilon[n]^2\, e[n]^2 = \alpha^2\, f\{\beta \bar{e}_1[n], e[n]\}^2 \tag{E.43}$$

and, from Eqn. (E.26), the fact that

$$\sigma_{max}\{P[n]\} \le \sigma_{max}\{P[-1]\}, \tag{E.44}$$

we can show that

$$\| \tilde{\theta}[n] - \tilde{\theta}[n-1] \|^2 \leq \frac{\phi_f[n-1]^T P[n-2] \phi_f[n-1] f\{ \beta \bar{e}_1[n], e[n] \}^2}{(1 + \phi_f[n-1]^T P[n-2] \phi_f[n-1])^2} (\alpha^2 \sigma_{max}\{P[-1]\}). \quad \text{(E.45)}$$

Eqns. (E.41) and (E.45) allow us to conclude that

$$\lim_{n \to \infty} \| \hat{\theta}[n] - \hat{\theta}[n-1] \|^2 = 0, \quad \text{(E.46)}$$

and hence

$$\lim_{n \to \infty} \| \hat{\theta}[n] - \hat{\theta}[n-1] \| = 0, \quad \text{(E.47)}$$

which establishes property 3.

Preparation for the Proof of Theorem 4.2:

Before proceeding with the basic proof, we will first present two lemmas that will be used in the proof of Theorem 4.2. Both of the following lemmas have been stated by Goodwin et al. See [17] and [18] for the statements of Lemmas 1 and 2, respectively.

Lemma 1: The convergence results of properties 2 and 3 of Theorem 4.1 (or 4.2) hold for algorithms that modify the P matrix if the modification algorithm satisfies the following properties:

1) P is increased at modification, that is, $P[n-1] \geq \bar{P}[n-1]$, where $\bar{P}[n-1]$ is the least-squares projection matrix.

2) P has an upper bound, that is, $\sigma_{max}\{P[n-1]\}$ is bounded.

Proof: Substituting $\bar{P}[n-1]$ for $P[n-1]$ up until Eqn. (E.24) in the proof of property 1 of Theorem 4.1, we see that

$$\tilde{\theta}[n]^T \bar{P}[n-1]^{-1} \tilde{\theta}[n] \leq \tilde{\theta}[n-1]^T P[n-2]^{-1} \tilde{\theta}[n-1] - \alpha f\{ \beta \bar{e}_1[n], e[n] \}^2 / (1 + \phi_f[n-1]^T P[n-2] \phi_f[n-1]). \quad \text{(E.48)}$$

From 1) above we know that

$$P[n-1]^{-1} \leq \overline{P}[n-1]^{-1} \tag{E.49}$$

so that

$$\tilde{\theta}[n]^T P[n-1]^{-1} \tilde{\theta}[n] \leq \tilde{\theta}[n]^T \overline{P}[n-1]^{-1} \tilde{\theta}[n]]. \tag{E.50}$$

Combining Eqns. (E.48) and (E.50) yields

$$\tilde{\theta}[n]^T P[n-1]^{-1} \tilde{\theta}[n] \leq \tilde{\theta}[n-1]^T P[n-2]^{-1} \tilde{\theta}[n-1] - \alpha f\{ \beta \overline{e}_1[n], e[n] \}^2 / (1 + \phi_f[n-1]^T P[n-2] \phi_f[n-1]). \tag{E.51}$$

Using Eqn. (E.51) the proofs of properties 2 and 3 follow exactly the same as in Theorem 4.1 with the exception of Eqns. (E.44-45). Since Eqn. (E.44) is not necessarily true for the modified algorithm, we instead write

$$\| \tilde{\theta}[n] - \tilde{\theta}[n-1] \|^2 \leq \frac{\phi_f[n-1]^T P[n-2] \phi_f[n-1] f\{ \beta \overline{e}_1[n], e[n] \}^2 (\alpha^2 \sigma_{max}\{P[n-1]\})}{(1 + \phi_f[n-1]^T P[n-2] \phi_f[n-1])^2} \tag{E.52}$$

where we know that $\sigma_{max}\{P[n-1]\}$ is bounded from 2) above. The proof of property 3 can then be completed.

Lemma 2: The modified algorithm defined by the use of Eqns. (4.5.17-19) has the following properties:

$$1)\ \sigma_{max}\{P[n-1]\} \leq \text{trace}\{P[n-1]\} = c_1,\ n \geq 1. \tag{E.53}$$

$$2)\ P[n-1] \geq \overline{P}[n-1],\ n \geq 1. \tag{E.54}$$

Proof: From Eqns. (4.5.17) and (4.5.20) we find that if $\tau > c_0$, then

$$\text{trace}\{P[n-1]\} = \text{trace}\{\overline{P}[n-1]\} + c_1 - \tau = \tau + c_1 - \tau = c_1, \tag{E.55}$$

and if $\tau < c_0$, then

$$\text{trace}\{P[n-1]\} = (c_0 / \tau)\, \text{trace}\{\overline{P}[n-1]\} + (c_1 - c_0) = c_0 + c_1 - c_0 = c_1. \tag{E.56}$$

Further, we know that

$$\sum_{i=1}^{m} \sigma_i\{P[n-1]\} = \sum_{i=1}^{m} \lambda_i\{P[n-1]\} = \text{trace}\{P[n-1]\}, \tag{E.57}$$

where σ_i and λ_i denote the singular values and eigenvalues, respectively. We find that

$$\sigma_{max}\{P[n-1]\} \leq \text{trace}\{P[n-1]\}. \tag{E.58}$$

This concludes the proof of property 1 of Lemma 2.

As was shown in the proof of property 1 of Theorem 4.1, Eqn. (4.5.19) has the property that

$$\overline{P}[n-1] \leq P[n-1] \tag{E.59}$$

$$\Rightarrow \text{trace}\{\overline{P}[n-1]\} \leq \text{trace}\{P[n-1]\}. \tag{E.60}$$

Now, from Eqn. (4.5.18) we know that

$$\text{trace}\{P[-1]\} = c_1. \tag{E.61}$$

Thus, from Eqns. (4.5.17) and (E.60-1) and property 1, we find that

$$\tau \leq c_1. \tag{E.62}$$

Using Eqns. (E.62) and (4.5.20) and the fact that $c_1 > c_0$, we see that

$$P[n-1] = k_0 \overline{P}[n-1] + k_1 I, \tag{E.63}$$

where

$$k_0 = 1 \text{ and } k_1 = ((c_1 - \tau)/m) \geq 0, \text{ if } \tau > c_0, \text{ and} \tag{E.64}$$

$$k_0 = (c_0/\tau) \geq 1 \text{ and } k_1 = ((c_1 - c_0)/m) > 0, \text{ if } \tau < c_0. \tag{E.65}$$

This establishes property 2 of Lemma 2.

Proof of Theorem 4.2: We will not prove the properties of this theorem in order. First, since Lemma 2 shows that the modified algorithm satisfies the requirements of Lemma 1, we conclude that properties 2 and 3 of Theorem 4.2 are true. Now, we proceed with the proof of property 1. Using the results of Lemmas 1 and 2, we find from Eqn. (E.51) that

$$\tilde{\theta}[n]^T P[n-1]^{-1} \tilde{\theta}[n] \leq \tilde{\theta}[n-1]^T P[n-2]^{-1} \tilde{\theta}[n-1]. \tag{E.66}$$

This equation is then used to find

$$\sigma_{min}\{P[n-1]^{-1}\}\,\|\tilde{\theta}[n]\|^2 \le \tilde{\theta}[n]^T P[n-1]^{-1}\,\tilde{\theta}[n] \tag{E.67}$$

$$\le \tilde{\theta}[0]^T P[-1]^{-1}\,\tilde{\theta}[0] \tag{E.68}$$

$$\le \sigma_{max}\{P[-1]^{-1}\}\,\|\tilde{\theta}[0]\|^2. \tag{E.69}$$

Therefore,

$$\|\tilde{\theta}[n]\|^2 \le (\,\sigma_{max}\{P[n-1]\,/\,\sigma_{min}\{P[-1]\}\,)\,\|\tilde{\theta}[0]\|^2, \tag{E.70}$$

and hence

$$\|\tilde{\theta}[n]\| \le \sqrt{\sigma_{max}\{P[n-1]\,/\,\sigma_{min}\{P[-1]\}}\;\|\tilde{\theta}[0]\|. \tag{E.71}$$

From Eqn. (4.5.18),

$$\sigma_{min}\{P[-1]\} = c_1\,/\,m. \tag{E.72}$$

Thus, using property 1 of Lemma 1 we find that

$$\|\tilde{\theta}[n]\| \le \sqrt{m}\;\|\tilde{\theta}[0]\|. \tag{E.73}$$

This completes the proof of Theorem 4.2. The result stated in Remark 4 of Chapter 4 follows directly using the initial time of n-2 instead of 0 in Eqns. (E.67-71).

Appendix F: Discrete-time Stability-Robustness Tests

In this appendix, we will develop tests that can be used to guarantee the stability robustness of a discrete-time closed-loop system. We will state SISO discrete-time versions of the continuous-time stability-robustness tests developed by Lehtomaki et al. [40]. The following development parallels that of reference [40].

Consider the system of Figure F.1. We assume that both the SISO loop transfer function T(z) and the perturbed loop transfer function $\tilde{T}(z)$ have state space representations (A, b, c^T) and $(\tilde{A}, \tilde{b}, \tilde{c}^T)$, respectively, so that

$$T(z) = c^T (zI - A)^{-1} b \tag{F.1}$$

and the perturbed transfer function

$$\tilde{T}(z) = \tilde{c}^T (zI - \tilde{A})^{-1} \tilde{b}. \tag{F.2}$$

Further, we define the open and closed-loop polynomials,

$$\phi_{OL}(z) = \det(zI - A), \tag{F.3}$$

$$\phi_{CL}(z) = \det(zI - A + b c^T). \tag{F.4}$$

The polynomials $\tilde{\phi}_{OL}(z)$ and $\tilde{\phi}_{CL}(z)$ are defined analogously for the perturbed transfer function. The appropriate Nyquist contour D_R in the z-plane is shown in Figure F.2 where D_R avoids zeros of $\phi_{OL}(z)$ on the unit circle by 1/R radius indentions. Lastly, we define $T(z,\varepsilon)$ as a rational transfer function that is continuous in z and ε for ε in [0,1] and for all z in D_R. $T(z,\varepsilon)$ also satisfies the following conditions:

$$T(z,0) = T(z) \tag{F.5}$$

and

$$T(z,1) = \tilde{T}(z). \tag{F.6}$$

Theorem F.1: The polynomial $\tilde{\phi}_{CL}(z)$ has no zeros outside the open unit disk if the following conditions hold:

1) a) $\phi_{OL}(z)$ and $\tilde{\phi}_{OL}(z)$ have the same number of zeros outside the open unit disk.

   b) if $\tilde{\phi}_{OL}(e^{j\omega_a T}) = 0$, then $\phi_{OL}(e^{j\omega_a T}) = 0$.

c) $\phi_{CL}(z)$ has no zeros outside the open unit disk (i.e. nominal stability).

2) $1 + T(z,\varepsilon) \neq 0$, for all ε in [0,1] and for all $z \in D_R$ with R sufficiently large.

Proof: The proof of Theorem F.1 is analogous to the proof of the similar continuous-time result. The discrete-time version of the Nyquist criterion, see Ackermann [32], is used in the proof.

Q.E.D.

Now, let

$$\tilde{T}(z) = T(z)\,[1 + \delta(z)] \tag{F.7}$$

so,

$$\delta(z) = [\tilde{T}(z) - T(z)] / T(z). \tag{F.8}$$

We define a magnitude bounding function on $\delta(z)$ on the unit circle. That is,

$$|\delta(e^{j\omega T})| \leq \Delta(e^{j\omega T}), \forall\omega. \tag{F.9}$$

Theorem F.1 can be used to prove the following theorems.

Theorem F.2: The polynomial $\tilde{\phi}_{CL}(z)$ has no zeros outside the open unit disk if the following conditions hold:

1) condition 1) of Theorem F.1 holds.

2) $|1 + T^{-1}(z)| > |\delta(z)|, \ \forall z \in D_R$.

Theorem F.3: The closed-loop system $\tilde{T}(z) / (1 + \tilde{T}(z))$ has all its poles in the open unit disk if:

1) a) $\phi_{OL}(z)$ and $\tilde{\phi}_{OL}(z)$ have the same number of zeros outside the open unit disk.

b) $\phi_{CL}(z)$ has no zeros outside the open unit disk (i.e. nominal stability).

2) $\phi_{OL}(e^{j\omega T}) \neq 0, \forall\omega$.

3) a) $|1 + T^{-1}(e^{j\omega T})| > \Delta(e^{j\omega T}), \forall\omega$, or equivalently,

b) $|T(e^{j\omega T}) / (1 + T(e^{j\omega T}))| < 1 / \Delta(e^{j\omega T}), \forall\omega$.

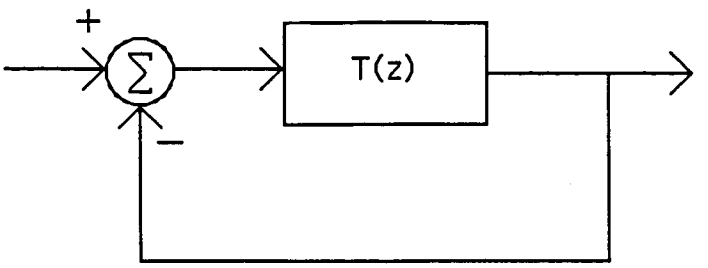

Figure F.1: Closed-loop System.

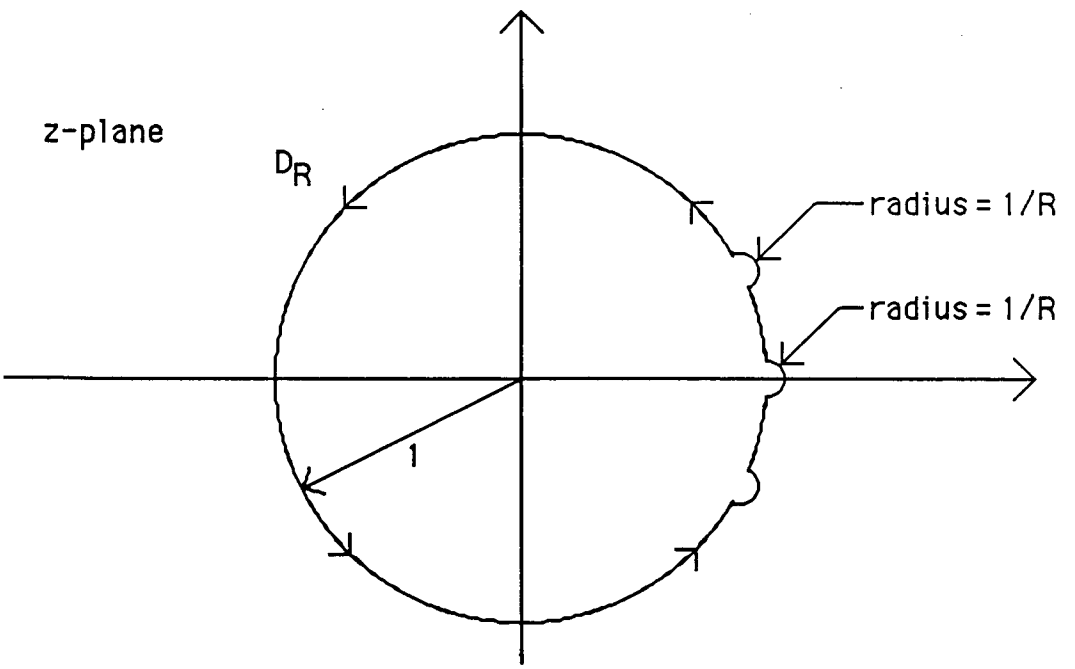

Figure F.2: Discrete-time Nyquist Contour.

REFERENCES

[1] G. C. Goodwin, D. J. Hill and M. Palamiswami, "Towards an Adaptive Robust Controller", Proc. of IFAC Identification and System Parameter Estimation Conf., 1985, York, UK, pp. 997-1002.

[2] M. Athans, "A Tutorial on the LQG/LTR Method", Proc. American Control Conference, Seattle, Washington, June 1986, pp. 1289-1296.

[3] K. S. Narendra and L. S. Valavani, "Stable Adaptive Controller Design - Direct Control", IEEE Trans. on Automatic Control, vol. AC-23, pp. 570-583, Aug. 1978.

[4] K. S. Narendra, Y. H. Lin and L. S. Valavani, "Stable Adaptive Controller Design, Part II: Proof of Stability", IEEE Trans. on Automatic Control, vol. AC-25, pp. 440-448, June 1980.

[5] A. Feuer and A. S. Morse "Adaptive Control of Single-Input Single-Output Linear Systems", IEEE Trans. on Automatic Control, vol. AC-23, pp. 557-570, Aug. 1978.

[6] K. J. Astrom and B. Wittenmark, "On Self-Tuning Regulators", Automatic, vol. 9, pp. 185-199, 1973.

[7] K. J. Astrom, U. Borisson, L. Ljung and B. Wittenmark, "Theory and Applications of Self-Tuning Regulators", Automatic, vol. 13, pp. 457-476, 1977.

[8] G. C. Goodwin, P. J. Ramadge and P. E. Caines, "Discrete Time Multivariable Adaptive Control", IEEE Trans. on Automatic Control, vol. AC-25, pp. 449-456, June 1980.

[9] C. E. Rohrs, L. Valavani, M. Athans and G. Stein, "Robustness of Adaptive Control Algorithms in the Presence of Unmodeled Dynamics", Proc. 21st IEEE Conf. on Decision and Control, Orlando, Florida, Dec. 1982, pp. 3-11.

[10] C. E. Rohrs, L. Valavani, M. Athans and G. Stein, "Robustness of Continuous Time Adaptive Control Algorithms in the Presence of Unmodeled Dynamics", IEEE Trans. on Automatic Control, vol. AC-30, pp. 881-889, Sept. 1985.

[11] P. A. Ioannou and P. V. Kokotovic, Adaptive Systems with Reduced Models, Springer-Verlag Series, Lecture Notes in Control and Information Sciences, 1983.

[12] B. B. Peterson and K. S. Narendra, "Bounded Error Adaptive Control", IEEE Trans. on Automatic Control, vol. AC-27, pp. 1161-1168, Dec. 1982.

[13] G. C. Goodwin and K. S. Sin, Adaptive Filtering, Prediction and Control, Prentice-Hall, Englewood Cliffs: N.J. 1984.

[14] D. M. Orlicki, L. Valavani, M. Athans and G. Stein, "Adaptive Control With Variable Dead-zone Nonlinearities", Proc. American Control Conference, San Diego, California, June 1984, pp. 1893-1898.

[15] D. M. Orlicki, "Model Reference Adaptive Control Systems Using a Dead-zone Nonlinearity", Ph. D. thesis, LIDS-TH-1455, MIT, April 1985.

[16] G. Kreisselmeier and B. D. O. Anderson, "Robust Model Reference Adaptive Control", IEEE Trans. on Automatic Control, vol. AC-31, pp. 127-133, Feb. 1986.

[17] G. C. Goodwin, D. J. Hill, D. Q. Mayne and R. H. Middleton, Adaptive Robust Control (Convergence, Stability and Performance), Technical Report EE8544, Dec. 1985, Univ. of Newcastle, N.S.W. 2308 Australia.

[18] G. C. Goodwin, R. Lozano Leal, D. Q. Mayne and R. H. Middleton, "Rapprochement between Continuous and Discrete Model Reference Adaptive Control", Automatica, vol. 22, pp. 199-207, 1986.

[19] K. J. Astrom, "Auto-tuning, Adaptation and Expert Control", Proc. American Control Conf., Boston, Mass., June 1985, pp. 1514-1519.

[20] R. Isermann and K.-H. Lachmann, "Parameter-adaptive Control with Configuration Aids and Supervision Functions", Automatica, vol. 21, pp. 625-638, 1985.

[21] C. E. Rohrs, G. Stein and K. J. Astrom, "Uncertainty in Sampled Systems", Proc. American Control Conf., Boston, Mass., June 1985, pp. 95-97.

[22] C. E. Rohrs, G. Stein and K. J. Astrom, "A Practical Robustness Theorem for Adaptive Control", Proc. American Control Conference, Boston, Mass., June 1985, pp. 979-983.

[23] P. Young, "Parameter Estimation for Continuous-Time Models - A Survey", Automatica, vol. 17, pp. 23-39, 1981.

[24] L. Ljung and K. Glover, "Frequency Domain Versus Time Domain Methods in System Identification", Automatica, vol. 17, pp. 71-86, 1981.

[25] L. Ljung, "On the Estimation of Transfer Functions", Automatica, vol. 21, pp. 677-698, 1985.

[26] L. Ljung, System Identification - Theory for the User, Prentice-Hall, Englewood Cliffs, N.J., 1986.

[27] I. Gustavsson, L. Ljung and T. Soderstrom, "Identification of Processes in Closed Loop - Identifiability and Accuracy Aspects", Automatica, vol. 13, pp. 59-75, 1977.

[28] A. V. Oppenheim and R. V. Schafer, Digital Signal Processing, Prentice-Hall, Englewood Cliffs, N.J., 1975.

[29] L. R. Rabiner and B. Gold, Theory and Application of Digital Signal Processing, Prentice-Hall, Englewood Cliffs, N.J., 1975.

[30] G. F. Franklin and D. J. Powell, Digital Control of Dynamic Systems, Addison-Wesley, Reading, Mass., 1980.

[31] K. J. Astrom and B. Wittenmark, Computer Controlled Systems, Prentice-Hall, Englewood Cliffs, N.J., 1984.

[32] J. Ackermann, Sampled-Data Control Systems, Springer-Verlag, Berlin, 1985.

[33] G. Strang, Linear Algebra and its Applications, Academic Press, New York, N.Y., 1980.

[34] J. C. Doyle and G. Stein, "Multivariable Feedback Design: Concepts for a Classical/Modern Synthesis", IEEE Trans. on Automatic Control, vol. AC-26, pp. 4-16, Feb. 1981.

[35] Y. Bar-Shalom and E. Tse, "Dual Effect, Certainty Equivalence and Separation in Stochastic Control", IEEE Trans. on Automatic Control, vol. AC-19, pp. 494-500, Oct. 1974.

[36] C. A. Deseor, "Slowly Varying Discrete System $x_{i+1} = A_i x_i$", Electronics Letters, vol. 6, no. 11, pp. 339-340, May 1970.

[37] P. M. Thompson, "Conic Sector Analysis of Hybrid Control Systems", Ph. D. thesis, LIDS-TH-1242, MIT, Sept. 1982.

[38] W. H. Beyer, editor, CRC Standard Mathematical Tables, 26th Edition, CRC Press, Boca Raton, Florida, 1981.

[39] W. Rudin, Principles of Mathematical Analysis, McGraw-Hill Book Co., New York, N.Y., 1976.

[40] N. A. Lehtomaki, D. A. Castanon, B. C. Levy, G. Stein, N. R. Sandell, Jr. and M. Athans, "Robustness and Modeling Error Characterization", IEEE Trans. on Automatic Control, vol. AC-29, pp. 212-220, March 1984.

[41] R. K. Mehra, "Optimal Input Signals for Parameter Estimation in Dynamic Systems - Survey and New Results", IEEE Trans. on Automatic Control, vol. AC-19, pp. 753-768, Dec. 1974.